Published in Journals: Energies,
Journal of Marine Science and Engineering, Processes

Topic Reprint

# Marine Renewable Energy

Edited by
Eugen Rusu, Kostas Belibassakis and George Lavidas

mdpi.com/topics

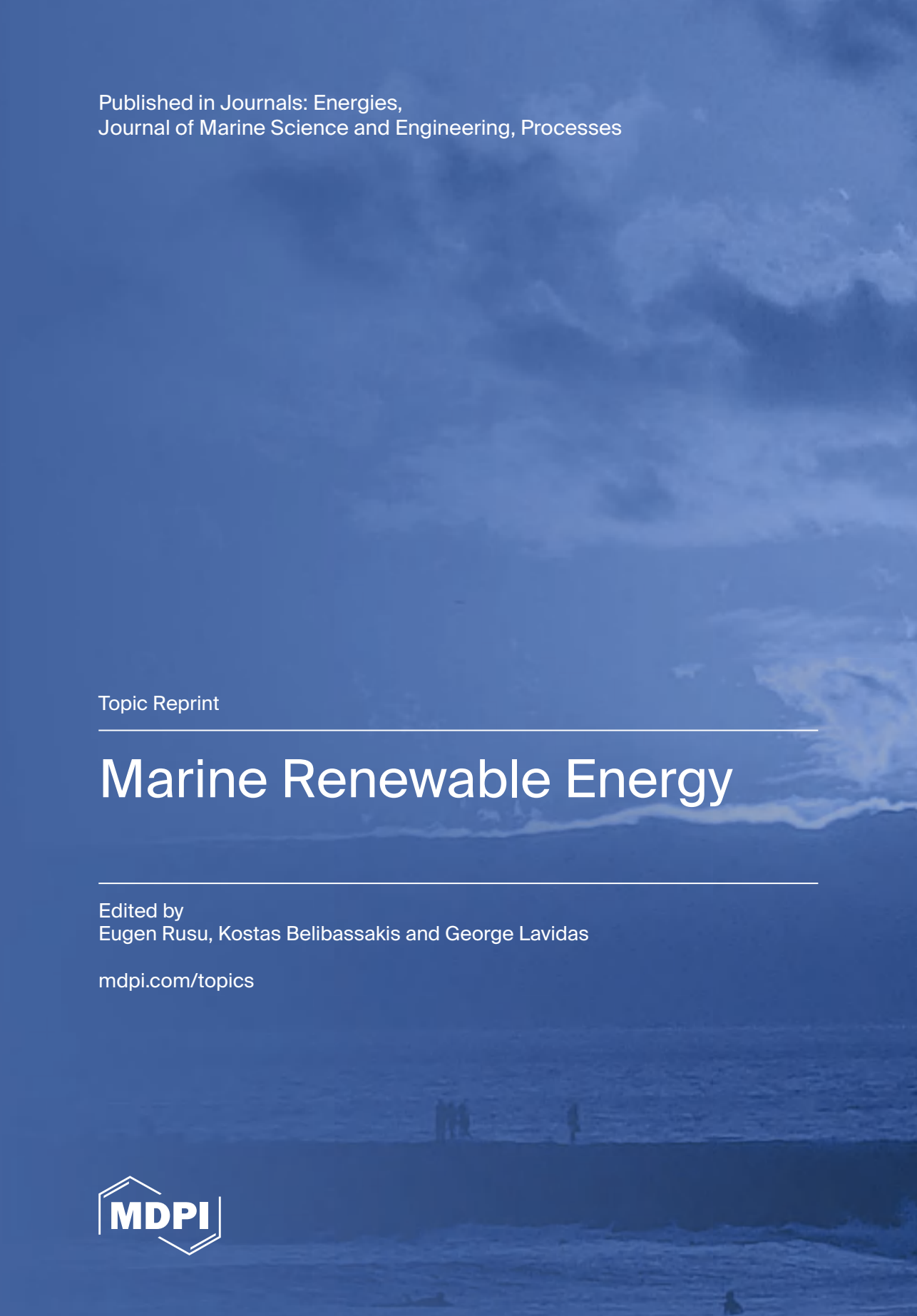

# Marine Renewable Energy

# Marine Renewable Energy

Editors

**Eugen Rusu**
**Kostas Belibassakis**
**George Lavidas**

MDPI

Basel • Beijing • Wuhan • Barcelona • Belgrade • Novi Sad • Cluj • Manchester

*Editors*

Eugen Rusu
University Dunarea de Jos of Galati
Galați, Romania

Kostas Belibassakis
National Technical University of Athens
Athens, Greece

George Lavidas
Delft University of Technology (TU Delft)
Delft, The Netherlands

*Editorial Office*
MDPI
St. Alban-Anlage 66
4052 Basel, Switzerland

This is a reprint of articles from the Topic published online in the open access journals *Journal of Marine Science and Engineering* (ISSN 2077-1312), *Processes* (ISSN 2227-9717), and *Energies* (ISSN 1996-1073) (available at: https://www.mdpi.com/topics/marine).

For citation purposes, cite each article independently as indicated on the article page online and as indicated below:

Lastname, A.A.; Lastname, B.B. Article Title. *Journal Name* **Year**, *Volume Number*, Page Range.

**ISBN 978-3-0365-9134-6 (Hbk)**
**ISBN 978-3-0365-9135-3 (PDF)**
**doi.org/10.3390/books978-3-0365-9135-3**

Cover image courtesy of Eugen Rusu

© 2023 by the authors. Articles in this book are Open Access and distributed under the Creative Commons Attribution (CC BY) license. The book as a whole is distributed by MDPI under the terms and conditions of the Creative Commons Attribution-NonCommercial-NoDerivs (CC BY-NC-ND) license.

# Contents

Journal of
*Marine Science and Engineering*

MDPI

*Article*

# Vertical Stiffness Functions of Rigid Skirted Caissons Supporting Offshore Wind Turbines

**AbdelRahman Salem [1,2], Saleh Jalbi [3,*] and Subhamoy Bhattacharya [2]**

[1] Arcadis Consulting, London CR0 1EA, UK; abdelrahman.salem@arcadis.com
[2] Department of Civil and Environmental Engineering, University of Surrey, Guildford GU2 7XH, UK; S.Bhattacharya@surrey.ac.uk
[3] Sea & Land Project Engineering, London SE1 1UN, UK
* Correspondence: saleh.jalbi@seaandland.co.uk

**Abstract:** Suction Bucket Jackets (SBJs) need to be fundamentally designed to avoid rocking modes of vibration about the principal axes of the set of foundations and engineered towards sway-bending modes of tower vibration. Whether or not such type of jackets exhibit rocking modes depends on the vertical stiffness of the caissons supporting them. This paper therefore derives closed form solutions for vertical stiffness in three types of ground profiles: linear, homogenous, and parabolic. The expressions are applicable to suction caissons having an aspect ratio (depth: diameter) between 0.2 and 2 (i.e., $0.2 < L/D < 2$). The work is based on finite element analysis followed by non-linear regression. The derived expressions are then validated and verified using studies available in literature. Finally, an example problem is taken to demonstrate the application of the methodology whereby fundamental natural frequency of SBJ can be obtained. These formulae can be used for preliminary design and can also be used to verify rigorous finite element analysis during detailed design.

**Keywords:** suction caissons; vertical stiffness functions; natural frequency; jackets; offshore wind turbines

**Citation:** Salem, A.; Jalbi, S.; Bhattacharya, S. Vertical Stiffness Functions of Rigid Skirted Caissons Supporting Offshore Wind Turbines. *J. Mar. Sci. Eng.* **2021**, *9*, 573. https://doi.org/10.3390/jmse9060573

Academic Editor: Eugen Rusu

Received: 27 April 2021
Accepted: 18 May 2021
Published: 26 May 2021

**Publisher's Note:** MDPI stays neutral with regard to jurisdictional claims in published maps and institutional affiliations.

**Copyright:** © 2021 by the authors. Licensee MDPI, Basel, Switzerland. This article is an open access article distributed under the terms and conditions of the Creative Commons Attribution (CC BY) license (https://creativecommons.org/licenses/by/4.0/).

## 1. Introduction

The European Union's (EU) strategy to fight climate change and air pollution issues has accelerated the investments into sustainable energy sources. This is essentially to meet the targets of 55% reduction in the greenhouse emissions by 2030 as well as paving the way for climate neutrality by 2050 [1]. Offshore wind in Europe in particular has witnessed a substantial growth, with the UK leading the market (10,428 MW cumulative capacity) and is expected to add 15 GW capacity in the next 5 years. Countries with large offshore wind developments also include Germany (7689 MW capacity), Belgium (2261 MW capacity), and the Netherlands (2611 MW capacity) [2]. Other global leaders include mainland China (approximately 10 GW capacity) [3]. There are new entries to the market including Taiwan (through the Formosa 1 and 2 offshore wind farms) and in the final planning stages for the East Coast of the United States.

This growing demand for renewable energy is responsible for the rapid pace of the technological developments emerging in the industry. Such developments mainly target the turbine size and installations in deeper waters. Wind Europe [2] has stated that the rated capacity of OWT has been enhanced by 102% in the last 20 years. At present, the newly-installed turbines have an average rated capacity of 7.8 MW, though most new installments have turbine capacities exceeding 10 MW. Monopiles support 81% of all installed OWT in Europe [2]. Yet, for some locations, their design poses several engineering challenges and environmental issues to satisfy the requirements needed to support larger wind turbines in deeper waters. This explains the continuous efforts to innovate in this field. Recently, the trend in the construction of new wind farms has considered OWTs supported on jackets as an attractive alternative to conventional monopiles in deeper waters.

Jackets supported on piles or caissons, illustrated in Figure 1, are suitable for water depths of 30–60 m which allow them to be potentially used for future rounds of wind energy developments [4]. Aberdeen and Borkum Riffgrund 2 offshore wind farms are recent developments utilising caisson jackets foundations to support 8 MW turbines [5]. Other on-going projects include Seagreen and Zhuanghe 2.

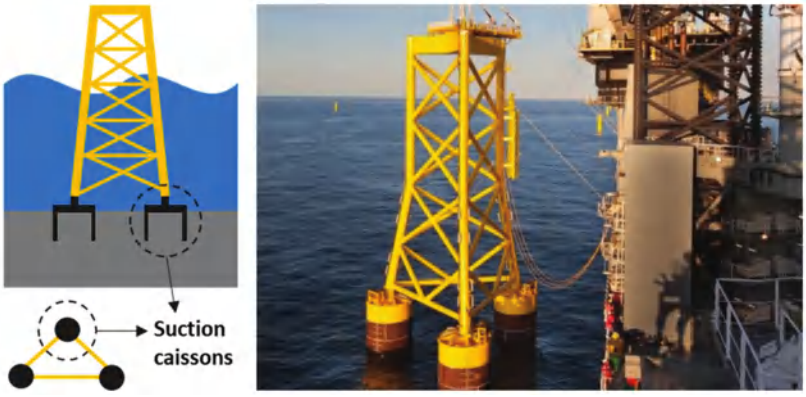


**Figure 1.** Schematic of a 3-legged jacket on suction caissons reproduced from [6], with permission from Ørsted, 2019.

There is an inherent difference in the way monopiles and jackets resist overturning moments due to lateral loads. As illustrated in Figure 2, single foundations (typically monopiles) transfer the loads via overturning moments to the surrounding soil. On the other hand, multiple foundations such as jacket on piles/caissons mainly transfer the loads through axial push-pull interaction. This obvious difference will later drive the simple mechanical modelling of the system where the foundation is replaced by equivalent springs for analysis purposes. Hence whilst the lateral stiffness plays a major role in the dynamic performance of monopile supported offshore wind turbines, the vertical stiffness plays a more detrimental role in jackets due to the propensity of rocking type of vibrations. It has shown by Jalbi and Bhattacharya that low-frequency rocking modes of jacket vibration must be avoided as it may coincide with the low frequency 1P rotor frequency and more importantly the peak wave frequency [7].

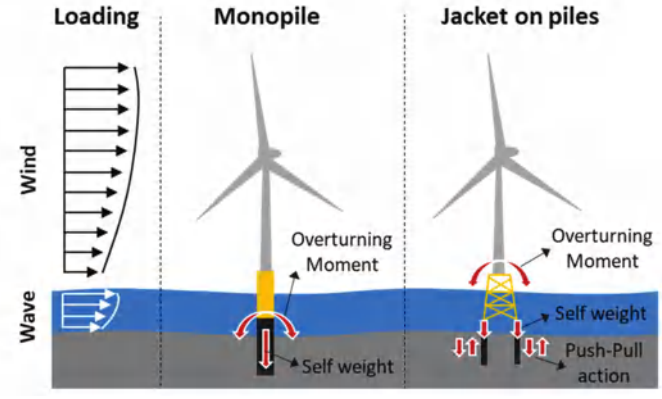


**Figure 2.** Load transfer in different foundation systems.

Current design aims to place the natural frequency of the bottom-fixed structures within the soft-stiff band, see Bhattacharya [4] for fundamentals of design. It is well

established in literature that the natural frequency of the system is reliant on the support condition (i.e. foundation stiffness) which in turn is a function of the properties of the foundation and subsoil. Considering the dynamic sensitivity of the OWTs, modes of vibration are considered a key element in the design procedure. Similar to the load transfer process discussed above, the modes of vibration of an OWT system are primarily dependent on the foundation and superstructure stiffness [8].

Studies carried out by Bhattacharya et al. [9] showed that the first eigenfrequency of vibration for OWTs supported on multiple shallow foundations (such as jackets on three or four suction caissons) correspond to low frequency rocking modes of vibration about the principle axes. The work is based on scaled model tests on three types of foundations: monopiles, tetrapods (4-legged jacket on caissons), and asymmetric tripods (3-legged seabed frame on caissons). Rocking modes of vibration are also reported in offshore structures such as the Brent B Condeep platform, see [4].

As mentioned before, rocking modes of vibration tend to have a lower frequency and may interfere with the 1P (rotor) frequency range and wave frequency, see Figure 3 for schematics. This is particularly challenging for large turbines where the soft-stiff target frequency is shifting towards the wave frequency. For example, a typical 8 MW turbine will have a target of 0.22 Hz and a 12 MW turbine will have a target frequency in the range of 0.15 Hz. Furthermore, wave loads will have a higher energy of excitation and may impose serious fatigue damage on the structure if rocking modes are allowed. It is therefore advisable to avoid rocking modes for jackets supported on shallow foundations. In addition, for asymmetric arrangements, scaled model tests showed that they have experienced two closely-spaced natural frequencies associated with the rocking modes of vibration [10]. This corresponds to the variability of the ground reflected in the vertical stiffness of the foundation. Not only does it widen the range of frequencies that can be excited by the loading conditions but also may introduce an additional design problem such as the beating phenomenon and both can have an impact in the fatigue limit state. Moreover, through analytical methods, Jalbi et al. [11] and Jalbi and Bhattacharya [7] showed that that a jacket may be engineered towards a no-rocking solution by optimising two parameters: (a) ratio of vertical stiffness of the foundation stiffness to lateral superstructure stiffness; and (b) aspect ratio of the jacket-tower geometry. A low value of vertical foundation stiffness values together with a low aspect ratio will promote a rocking mode of vibration.

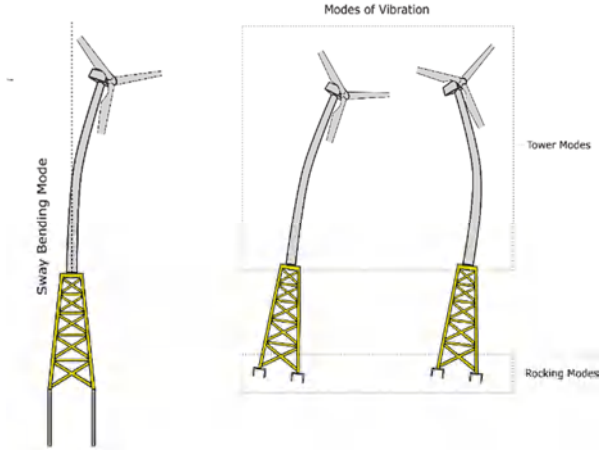


**Figure 3.** Vibration modes in different foundation systems.

From the discussions above, it is essential to have a method to calculate the vertical stiffness of foundations early on in the design stages of a project. Hence, given the importance of SSI on the dynamic performance, the objectives of the paper are as follows:

(1) Carry out review of the current methods in literature to predict the vertical stiffness of rigid caissons.
(2) Provide static vertical stiffness functions for caissons of aspect ratio between 0.2 and 2 i.e., $0.2 < L/D < 2$ for three types of ground: homogeneous, parabolic and linear profiles. This is based on the approach laid out in Eurocodes for ground types (see Eurocode 8 Part 5) and also a gap in the literature.
(3) Demonstrate the application of the developed methodology through a step-by-step solved example in the context of predicting the natural frequency of the system.

It should be noted that the solutions provided in this paper are intended for the concept design stage and for initial sizing of the foundation when information about the structure and the ground profile is scarce. As the design progresses from conceptual to detailed design, a higher computational complexity of the analysis is required to further optimise the foundations. This includes using refined soil constitutive models incorporated in 3D finite element analysis (FEA) packages. In addition, this would also require more input such as site-specific ground investigations and geotechnical laboratory testing.

*Background Literature*

Ideally, each assessment of the composite system should encompass an independent numerical analysis for the structure and foundation. For instance, the analysis of the latter would likely involve modelling the soil as continuum which is typically carried out using advanced geotechnical finite element methods. However, the limitation of the high computational cost and modelling complexities make it impractical to be utilised in preliminary design stages, yet useful in verifying the final design of the foundation. Consequently, both approaches (i.e., analytical and numerical solutions) tend to idealise the structural dynamics problem through replacing the foundation by a set of lumped springs or in the case of deep foundations distributed springs. The overall stability and foundation stiffness can be purely expressed in terms of functions that describe the force resultants and their conjugate displacements and rotations of these lumped springs. Figure 4 illustrates the breakdown of the structure-foundation problem.

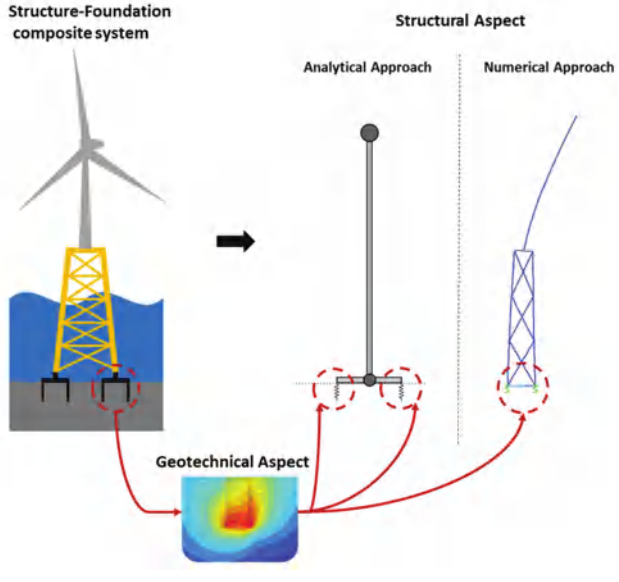


**Figure 4.** Breakdown of the structure-foundation problem.

The work of this paper continues the efforts of the research group which aims at providing simplified expressions for the computation of the foundation stiffness. For

instance, Shadlou and Bhattacharya [12] studied the lateral dynamic stiffness of deep foundations and proposed spring stiffness functions for both rigid and flexible monopiles. In their model, the foundation is replaced by four springs; $K_L$ (lateral spring), $K_R$ (rocking spring), $K_V$ (vertical spring) and $K_{LR}$ (cross-coupling spring) to capture the degrees of freedom. This methodology was later utilised by Arany et al. [13] in designing monopile foundations. Similarly, Jalbi et al. [14] obtained static stiffness functions for the lateral stiffness terms of a rigid monopod caissons. Moreover, Jalbi and Bhattacharya [15] provided closed form solutions to calculate the natural frequency of jackets supported on multiple foundations incorporating soil-structure interaction (SSI). The foundation flexibility was represented by a set of vertical springs which emphasizes the importance of predicting the vertical stiffness of foundations. Thus, it is now essential to continue the work and obtain the vertical stiffness components of the foundations.

The assessment of static and dynamic vertical spring constants has been the subject of extensive studies in the field of machine foundations and seismic analysis. Most of the elastic solutions available in the literature provide guidance regarding surface and embedded footings. Generally, most literature reports that stiffness decreases with increasing strains and increasing forcing frequencies. However, work on the elastic and non-linear stiffness of a skirted caisson is inadequate. Bell [16] presented a comprehensive review of the existing stiffness coefficients of surface footings, whereas the effect of embedment of the circular footings was extensively discussed in Gazetas [17]. On the other hand, there is less work assessing the stiffness of suction caisson foundations. These foundations are quite similar to the embedded-type foundations with the difference of the soil mass is trapped beneath the lid and within the enclosed volume. Two extreme models could be adopted to represent the caissons: one in which the lid is treated as a rigid circular foundation on the surface while ignoring the effect of the skirts, and another in which the caisson is completely rigid. The latter was analysed by Doherty et al. [18] who provided tabulated coefficients for completely rigid caisson. The analyses incorporated practical variation in soil stiffness, embedment depth and Poisson's ratios. It also provided correction factors to account for the skirt flexibility. Skau et al. [19] focused on the effect of caisson flexibility following the observations of the extensive behaviour monitoring for Borkum Riffrung 01 -Suction Bucket Jacket (BKR01-SBJ). An elastic correction to the response of a rigid foundation response was suggested to address the foundation flexibility particularly due to the lid which appeared to significantly influence the total vertical stiffness of the system. Table 1 summarises the vertical stiffness formulae found by different researchers for different foundation types including some additional guidance found for deep foundations.

**Table 1.** Methods to estimate the vertical stiffness of the foundation in literature.

| | Source (Year) [Reference] | Formulae and Their Applications |
|---|---|---|
| Surface Foundation | Lysmer (1965) [20]<br>Spence (1968) [21] | Circular rigid footing on surface of homogenous elastic half-space:<br>$k_v = \frac{2G_sD}{1-y_s}$<br>To account for the roughness of the footing base that allow full transmission of shear stress, Spence [21] proposed the following:<br>$k_v = \frac{2G_sD\ \ln(3-4\,y_s)}{1-2y_s}$<br>The results from this analytical solution showed up to 10% increase in stiffness values at low $y_s$ values |
| | Gazetas (1983) [22]<br>DNVGL (2019) [23] | Circular footing on stratum over bedrock:<br>$k_v = \frac{2G_sD}{1-y_s}\left(1+1.28\frac{D}{2H}\right)$ |
| | Gazetas (1991) [17] | Arbitrary shaped foundation on surface of homogenous half-space:<br>$k_v = \frac{2G_sl}{1-y_s}\left(0.73+1.54\chi^{0.75}\right)$<br>where $\chi = A_b/4l^2$, l is the base-length of the circumscribed rectangle and $A_b$ is the area |

**Table 1.** *Cont.*

| | Source (Year) [Reference] | Formulae and Their Applications |
|---|---|---|
| Shallow Embedded Foundation | Gazetas (1983) [22]<br>DNVGL (2019) [23] | Circular rigid footing embedded in homogenous stratum over bedrock; Developed for machine-type inertial loading.<br>Range of validity: L/D<1<br>$k_v = \frac{2G_sD}{1-y_s}\left(1+1.28\frac{D}{2H}\right)\left(1+\frac{L}{D}\right)\left[1+\left(0.85-\frac{0.28L}{0.5D}\right)\left(\frac{L}{H-L}\right)\right]$ |
| | Wolf (1988) [24]<br>Wolf and Deeks (2004) [25] | General prismatic footing embedded in a linear elastic half space<br>$k_v = \frac{G_sb}{1-y_s}\left(3.1\left(\frac{l}{b}\right)^{0.75}+1.6\right)\left(1+\left(0.25+0.25\frac{b}{l}\right)\left(\frac{e}{b}\right)^{0.8}\right)$<br>where 2l, 2b are the base dimensions of circumscribed rectangle and e is the embedment depth. This formulation was later simplified by Wolf and Deeks [25];<br>$k_v = \frac{2G_sD}{1-y_s}\left(1+1.08\left(\frac{e}{D}\right)\right)$ |
| | Gazetas (1991) [17] | Arbitrary shaped foundation embedded in half-space<br>$k_v = k_{v,\,surface}\left[1+\left(\frac{1}{2l}\right)\left(\frac{L}{b}\right)+(1+1.3\chi)\right]\left[1+0.2\left(\frac{A_w}{A_b}\right)^{2/3}\right]$<br>where $k_{v,\,surface}$ is obtained using the equation provided earlier by Gazetas [17]for surface footings, b is the base-width of the circumscribed rectangle, $\chi = A_b/4l^2$ and $A_w$ is the actual sidewall-soil contact area; for constant effective-contact height, d, along the perimeter: $A_w$ = (d) × (perimeter).<br>Based on Gazetas' methodology, Bordón et al. [26] developed a simplified formula for the stiffness of a rigid cylinderical foundation embedded in homogenous soil to study the group effect of multi-bucket foundations:<br>$k_v = \frac{2G_sD\ \ln(3-4\,y_s)}{1-2y_s}\left[1+1.12(1-0.84y_s)\left(\frac{L}{D}\right)^{0.84}\right]$ |
| Deep foundation | Fleming et al. (1992) [27] | Embedded piles considering shaft friction only:<br>$k_v = \frac{2\pi LG_s}{y}$ where *St* is between 3 and 5 |
| | Shama & El Naggar (2015) [28] | Single pile under axial load for seismic design of highway bridges:<br>$k_v = \frac{1.25E_pA}{L}$ |

N.B: $K_V$ is vertical stiffness of the foundation, $G_s$ is shear modulus of the soil, $y_s$ is Poisson's ratio of the medium, D is diameter, L is embedment depth, H is thickness of the soil layer and $E_p$ is modulus of elasticity of pile material.

From the table above, it is evident that the available methodologies are limited either by the shape of the footing and the idealised soil profiles which do not reflect the actual heterogeneity in the soil. This paper aims to tackle one aspect of that where solutions are provided for rigid caissons through numerical modelling. The solutions provide the vertical stiffness $K_v$ are for homogeneous, parabolic, and linear ground profiles.

## 2. Numerical Modelling

Finite element method using Plaxis 3D (continuum approach) was utilised to model the soil-structure interaction. The size of the soil contour is specified such that any stress increase on the boundary is absorbed without rebounding and disturbing the model results. Suryasentana et al. [29] presented a mesh domain of 80D (D is the diameter of the suction caisson) for both diameter and depth to analyse vertically loaded foundations, while Latini et al. [30] used 100D and 30D for the diameter and depth respectively. Moreover, Sloan [31] adopted 5D for the mesh dimensions when analysing vertically loaded rigid circular footing. This clearly shows the wide range of possibilities to eliminate the boundary effects. Considering the scope of this analysis, all the models have been set up with an extent of the soil domain 10D and depth of 15D; as shown in Figure 5 (which has been obtained through trial and error). Despite the symmetry of the problem, a full model was adopted as to avoid a rotation of the caisson if the point load was placed at the centre.

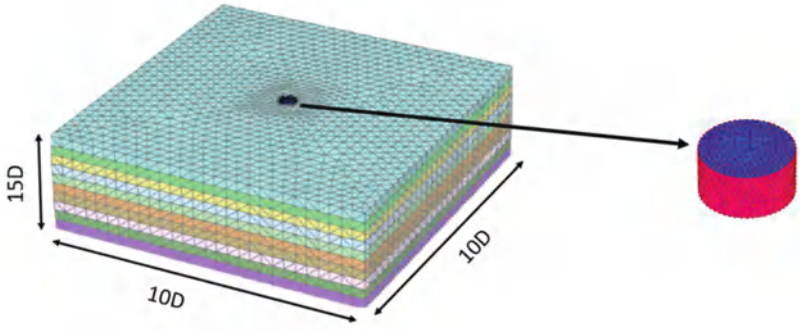


**Figure 5.** Mesh dimensions and shape of caissons.

Generally, the stiffness of the foundation dictating the dynamic stability of the system, is characterised by a non-linear nature. It is dependent on the strain levels; generated from the load cycles due to the soil-structure interaction, as well as the forcing frequency (expressed in terms of static and dynamic stiffness) [32]. Since the natural frequency is associated with relatively small amplitude of vibrations (linear range), the initial foundation stiffness would be sufficient for this purpose [13]. Similarly, OWTs are considered a very low frequency application compared to seismic actions based on design charts provided in [12,20,33–36]. Hence, the effect of the forcing frequency on the stiffness values can be ignored and the static stiffness value can effectively be adopted. Based on the above justifications, the soil is modelled as a linear elastic material. This model is based on Hooke's law of isotropic elasticity and requires the identification of two basic elastic parameters; Young's modulus (E) and Poisson's ratio ($v_s$) which can be determined using conventional site investigation techniques [37].

To encompass the realistic variation of the shear modulus of the soil with depth, three idealisations of the ground profile were adopted:

- *Homogenous soil*: typical for overconsolidated clays that show constant variation in stiffness with depth and can be easily defined on Plaxis 3D;
- *Linear inhomogeneity*: common for normally consolidated clay, sometimes referred to as Gibson soil where the stiffness increases linearly with depth [18]; and
- *Parabolic inhomogeneity*: is an intermediate condition which is typical for sandy soils [12]. Unlike the other two ground profiles, the soil stratum has to be discretised into multiple layers on Plaxis 3D to incorporate the parabolic variation of the soil stiffness. 10 distinct layers of 0.1H thickness each (H is the depth of the soil stratum equivalent to 15D) were used to model the soil stratum. For each layer, an initial stiffness and linear slope were used to mimic the parabolic behaviour.

Figure 6 illustrates the three ground profiles described above where the values of Young's modulus for the different ground profile intersect at one diameter depth. For all the cases, Poisson' ratio was assumed to be uniform within each model and the soil density was set to a constant value of 18 kN/m$^3$.

The structure forming the foundation, which consists of the skirt and the lid, has been treated under the assumption of being rigid for all the models. In other words, the response of the foundation system due to the applied loads is solely due to the deformations in the soil (no structural deformations of the caisson lid and skirt). This also includes the soil enclosed within the skirt. This assumption is considered valid considering the low aspect ratio of the caissons modelled and the high flexural and shear stiffness of the steel compared to those of the soil. Doherty et al. [18] investigated the effect of the skirt flexibility on the response of a caisson foundation. Results showed that the vertical stiffness values of both cases are almost similar for low aspect ratios of the caisson which reinforces and validates the previous assumption. In addition, the bucket lid can in-reality deflect and alter the

foundation stiffness where the recent in-situ observations by Shonberg et al. [38] confirmed that the suction bucket's structural elements stiffness has an effect on the performance and can be idealised as pair of vertical springs in series, such that $\frac{1}{k_{total}} = \frac{1}{k_{lid}} + \frac{1}{k_{soil-skirt}}$. However, for simplicity, a lumped vertical spring compiling both elements is adopted for this study rather than treating them separately.

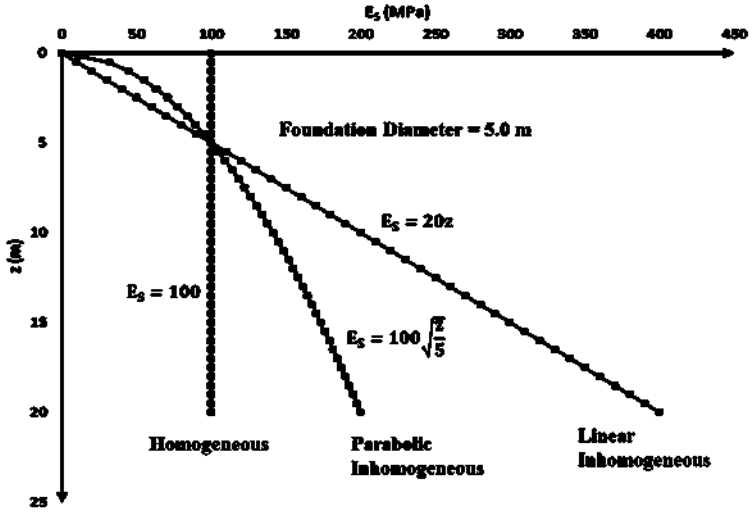


**Figure 6.** Variation in stiffness with depth.

Furthermore, the push-pull nature for OWT supported on jackets requires the estimation of the stiffness in both tension and compression, yet this study assumes that the vertical stiffness is the same for both tension and compression as the intention is to use these values for low amplitude vibrations. In reality, the computed compressive stiffness should be higher due to the additional contribution of the bearing below the lid. Other factors should further be investigated involving the impact of the grouted connections and its imperfections, interaction between the adjacent jacketed caissons and imperfect contact at the interface of the soil and foundation. All these factors form a strong basis for the continuation of the work produced in this study. Nevertheless, it may be reminded that the solutions provided in this paper are intended for the concept design stage and for initial sizing of the foundation when information about the structure and the ground profile is limited.

*Methodology Verification and Comparison of Results*

Normalized values for $K_V$ are plotted against L/D for $0.2 < L/D < 2$ considering the three different ground profiles. The results are then compared to the solutions provided by Wolf and Deeks [25] and DNVGL [23] which are in turn based on the work of Gazetas [22]. Figure 7 shows the stiffness coefficients plotted for homogeneous profile at two Poisson's ratios (0.2 and 0.499). All the simulated cases are summarised in Appendix A.

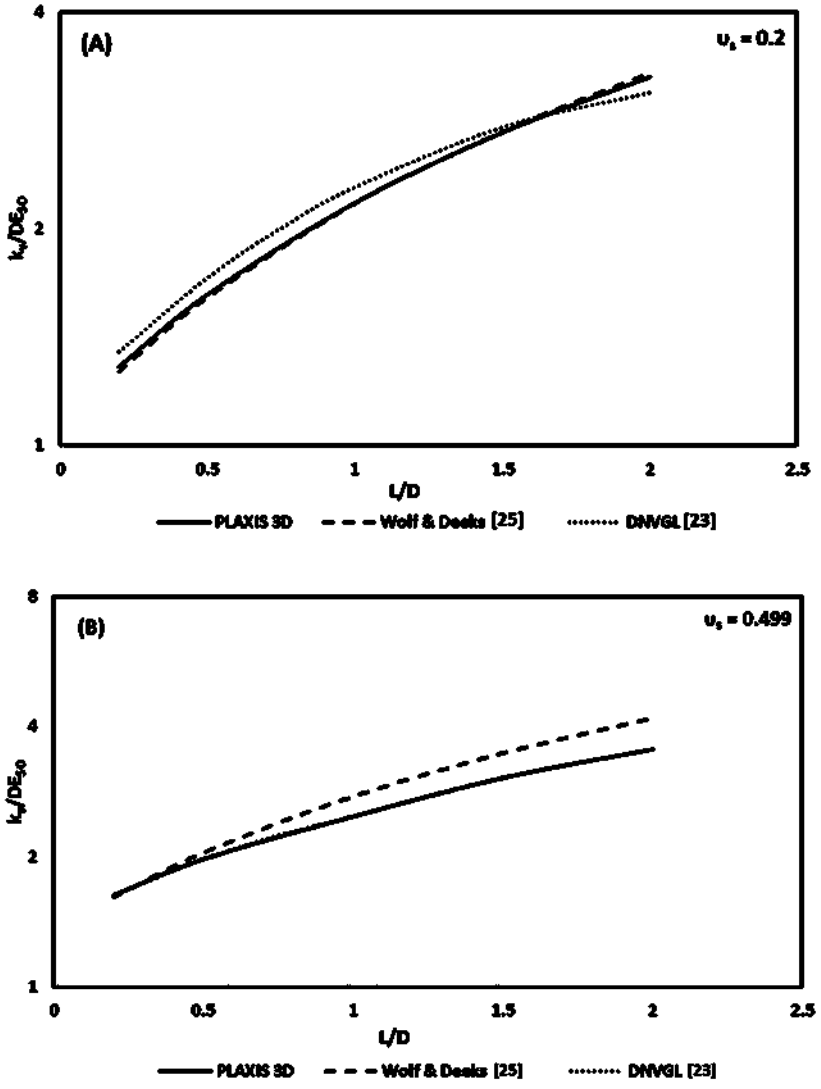


**Figure 7.** Vertical static stiffness functions for rigid caissons in homogeneous ground profiles at two Poisson's ratios (**A**) $\upsilon_s$ = 0.2, and (**B**) $\upsilon_s$ = 0.499.

The numerical model compares well with the formulations provided in the literature which justifies the method of extraction, the mesh used, the extent of the boundary conditions, and the rigid body assumption applied in the finite element model. Any discrepancy can be justified in terms of the foundation geometry implemented; where both Wolf and Deeks [25] and DNVGL [23] used a solid embedded foundation rather than a skirted caisson with soil mass enclosed within it. Another reason could be the effect of the Poisson ratio.

The impact of Poisson's ratio on the computed stiffness coefficients was evident from the FE analysis. Therefore, normalised values for the vertical foundation stiffness coefficients in a homogeneous stratum were plotted against $\upsilon_s$, as shown in Figure 8. The results were normalised against their respective values at $\upsilon_s$ = 0.1. The aspect ratio (L/D) also appears to influence the effect of Poisson's ratio as also shown in Figure 8. For all L/D

cases, the stiffness decreases with increasing $\upsilon_s$ until $\upsilon_s$ = 0.4 and then slightly increases. Both Gazetas [22] and Wolf and Deeks [25] considered the effect of the soil's Poisson's ratio on the stiffness coefficients and incorporated it in their proposed impedance functions. Their proposed functions show similarity with the trend predicted by this study, yet, the impact of the Poisson's ratio is observed to be slightly lower than the abovementioned literature. Accordingly, a correction factor $f(\upsilon_s)$, function of both $\upsilon_s$ and L/D, will be developed in the subsequent section.

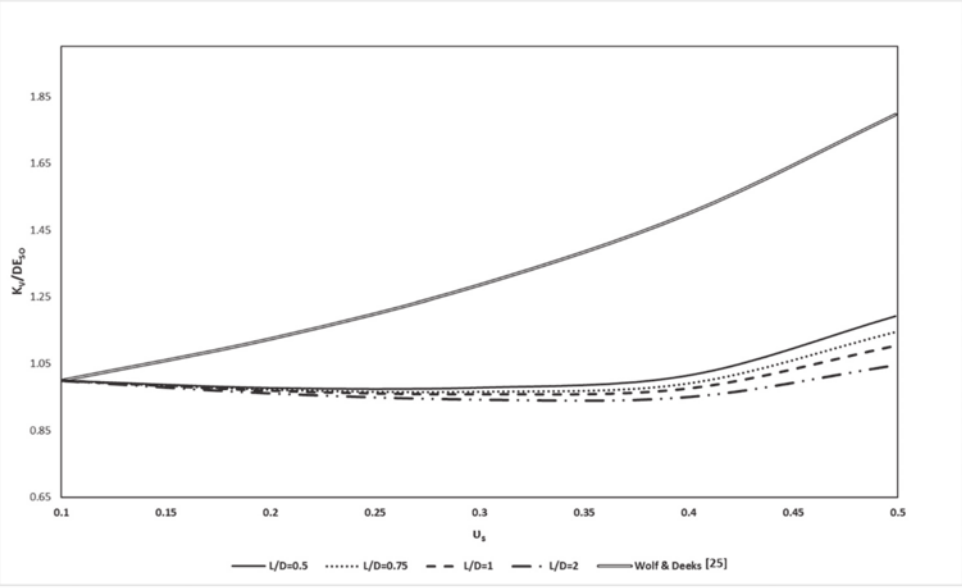


**Figure 8.** Variation of vertical stiffness ($K_v$) with Poisson's ratio ($\upsilon_s$) and aspect ratio (L/D).

## 3. Development of the Static Stiffness Functions and Correction Factors

Functions for the vertical stiffness were developed using non-linear regression analysis on the normalised set of stiffness coefficients. A diameter of 5m was adopted and the soil stiffness at 1m depth was set as 100 (MPa), see Figure 5. The study then plots the change of the vertical stiffness with increasing L (L values include 2.5, 5, 7.5 and 10 m) and $\upsilon_s$ (0.1 to 0.49).

First, a new correction factor due to Poisson's ratio, $f(\upsilon_s)$, will be presented. The reason for this correction is to clarify how the Poisson's ratio modifies the vertical stiffness for different ranges of caisson dimensions. Thus, Figure 8 shows that $f(\upsilon_s)$ is not only a function the Poisson's ratio itself but also a function of L/D. This has not been extensively discussed in literature where the correction factor was only a function of the Poisson's ratio itself. Consequently, revised $f(\upsilon_s)$ functions dependent on both L/D and $\upsilon_s$ are suggested herein.

From Figure 8, the best fit curve for the Poisson's ratio correction was a cubic function in the form of $f(\upsilon_s) = a_0\upsilon_s^3 - a_1\upsilon_s^2 + a_2\upsilon_s + a_3$. The values of the coefficients $a_0$, $a_1$, $a_2$, and $a_3$ were recorded for L/D = 0.5, 0.75, 1,1.5, 2 normalized at L/D = 0.5. The coefficients for L/D = 0.5 are $a_0$ = 10.028, $a_1$ = -5.8814, $a_2$ = 0.9092, and $a_3$ = 0.96. Figure 9 shows the normalized values for $a_0$, $a_1$, $a_2$, and $a_3$, thus simulating the dependency of $f(\upsilon_s)$ on L/D. From the figure, it is evident that $a_0$ and $a_1$ follow a similar trend and where given the same logarithmic function whilst $a_2$ followed a different trend and was given another logarithmic function. Finally, a constant value of 1 was given for $a_3$.

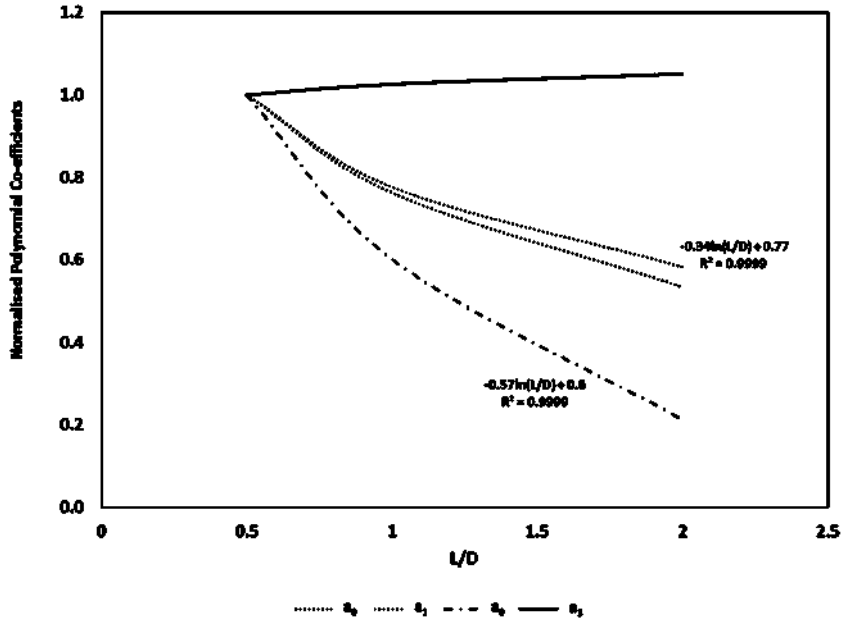


**Figure 9.** Variation of the polynomial coefficients with L/D.

As a result, from the analysis above, the Poisson's ratio correction may be summarized using Equation (1):

$$f(\upsilon_s) = \left[\left(10\upsilon_s^3 - 5.88\upsilon_s^2\right)\left(-0.34\ln\frac{L}{D} + 0.77\right)\right] + 0.91\upsilon_s\left(-0.57\ln\frac{L}{D} + 0.6\right) + 1 \quad (1)$$

It may be noted that the same methodology was repeated in parabolic and linear inhomogeneous ground profiles where the $f(\upsilon_s)$ obtained was in close proximity to the one shown in Equation (1). Similarly, a few trials on higher aspect ratios (L/D > 2) showed no noticeable change in the formulations:

Subsequently, the normalized values of $\frac{K_V}{DE_{SO}f(\upsilon_s)}$ were then computed and plotted against L/D for all ground profiles. Therefore, a best fit curve was applied in the form of a power function. Even though previous literature did not specifically use power functions for static vertical stiffness functions of shallow caissons, it still performs accurately for the rigid caissons as the $R^2$ values shown show a good correlation as shown in Figure 10 and the solutions are summarized in Table 2.

$$f(\upsilon_s) = \left[\left(10\upsilon_s^3 - 5.88\upsilon_s^2\right)\left(-0.34\ln\frac{L}{D} + 0.77\right)\right] + 0.91\upsilon_s\left(-0.57\ln\frac{L}{D} + 0.6\right) + 1$$

**Table 2.** Vertical stiffness for shallow skirted foundations exhibiting rigid behaviour.

| Ground profile | $\frac{K_V}{DE_{SO}f(\upsilon_s)}$ |
|---|---|
| Homogeneous | $2.31\left(\frac{L}{D}\right)^{0.52}$ |
| Parabolic | $2.16\left(\frac{L}{D}\right)^{0.96}$ |
| Linear | $2.37\left(\frac{L}{D}\right)^{1.28}$ |

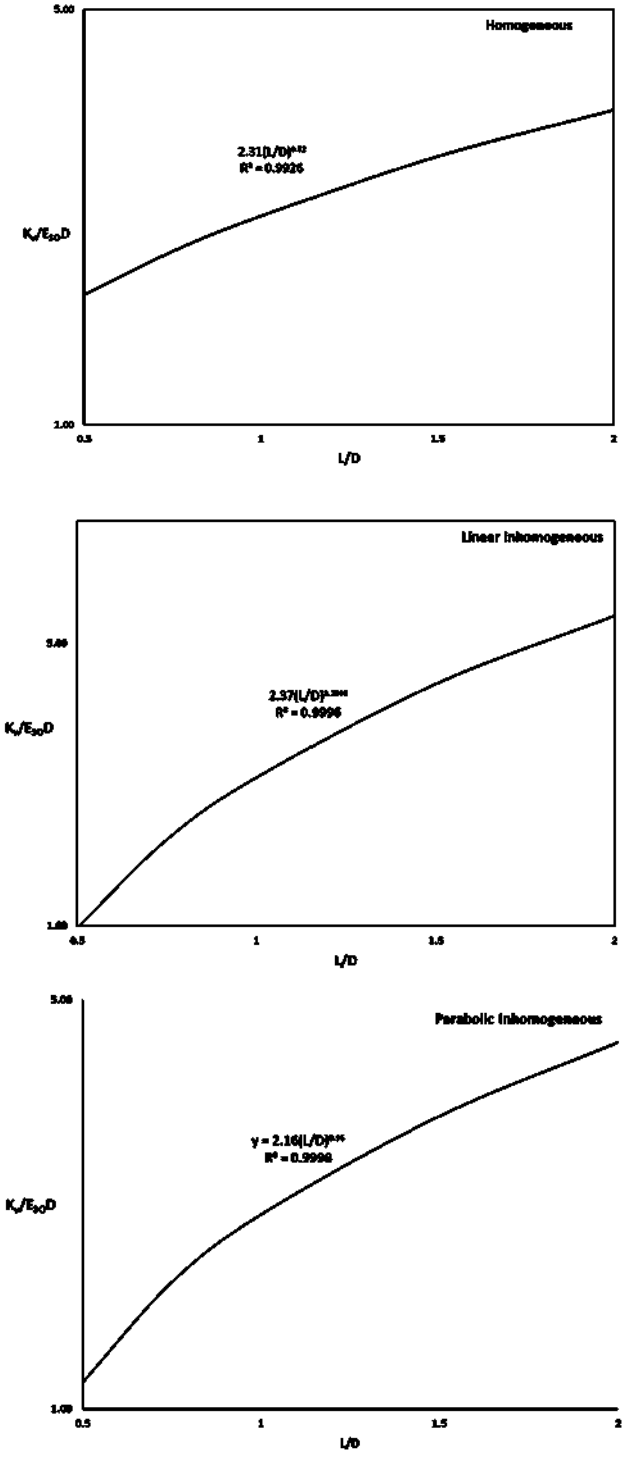


**Figure 10.** Best fit curves for the vertical stiffness functions.

## 4. Discussion and Validation of the Results

The functions provided in Table 2 were used to calculate $K_V$ for the simulated cases and the highest recorded percentage was found to be below 10% which is considered of low practical significance. The results are also checked against the coefficients provided by [18] and summarized in Table 3. As shown in the table, the results generally show a good match with the obtained results while being applicable for a wide range of Poisson's ratio. Slight discrepancies exist at the higher Poisson ratio, and this is explained by the difference in the Poisson's ratio correction between the proposed method and existing literature.

**Table 3.** Comparison of vertical stiffness at $\upsilon_s = 0.2$ and $\upsilon_s = 0.499$. Data from Doherty et al. (2005) [18].

| Case | | $\frac{K_V}{DE_{SO}}$ | | | $\frac{K_V}{DE_{SO}}$ | |
|---|---|---|---|---|---|---|
| | | Doherty, et al., 2005 [18] | Proposed method | | Doherty et al., 2005 [18] | Proposed method |
| L/D = 0.5 Homogeneous | $\upsilon_s = 0.2$ | 1.61 | 1.65 | $\upsilon_s = 0.499$ | 1.81 | 1.98 |
| L/D = 0.5 Linear | | 1.38 | 1.00 | | 2.10 | 1.199 |
| L/D = 2 Homogeneous | | 3.29 | 3.146 | | 2.86 | 3.21 |
| L/D = 2 Linear | | 6.72 | 5.47 | | 7.60 | 5.58 |

## 5. Application of the Methodology

In order to demonstrate the application of the proposed vertical stiffness functions, a solved example in the context of the prediction of the natural frequency of an OWT system is presented in this section. A 5 MW turbine supported on a symmetrical four-legged jacket was considered for design in deep waters, as shown in Figure 11. Details about the turbine specification and an approximate jacket dimensions were found in Jonkman et al. [39] and Alati et al. [40], respectively, and summarised in Table 4.

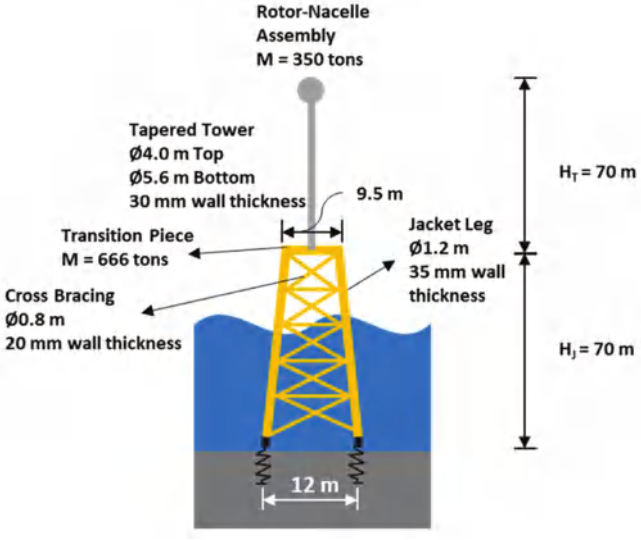


**Figure 11.** Example problem.

**Table 4.** Main input parameters of the example (Data from Jonkman et al. [39]; Alati et al. [40]).

| Parameter | Value | Unit |
|---|---|---|
| Height of the jacket ($h_J$) | 70 | m |
| Jacket bottom width ($L_{bottom}$) | 12 | m |
| Jacket top width ($L_{top}$) | 9.5 | m |
| Area of jacket leg ($A_C$) | 0.1281 | $m^2$ |
| Distributed mass of the jacket including diagonals ($m_J$) | 8150 | kg/m |
| Tower height ($h_T$) | 70 | m |
| Bottom diameter of the tower ($D_{bottom}$) | 5.6 | m |
| Top diameter of the tower ($D_{top}$) | 4.0 | m |
| Distributed mass of the tower ($m_T$) | 3730 | kg/m |
| Mass of Rotor-Nacelle Assembly ($M_{RNA}$) | 350 | tons |
| Mass of transition piece ($M_{TP}$) | 666 | tons |

A homogeneous stratum over bedrock is assumed with all the foundation dimensions and soil properties summarised in Table 5.

**Table 5.** Foundation details for the example problem.

| Parameter | Value | Unit |
|---|---|---|
| Foundation depth (L) | 4 | m |
| Foundation diameter (D) | 4 | m |
| Depth to bed rock (H) | 50 | m |
| Soil Young's modulus (Es) | 40 | MPa |
| Soil Poisson's ratio (vs) | 0.28 | Non-dimensional |

Using the equations provided in Table 2, a preliminary estimate of the vertical stiffness for a rigid caisson foundation (with L/D = 1) is obtained as shown below:

$$\begin{aligned} f(\upsilon_s) &= \left[\left(10\upsilon_s^3-5.88\upsilon_s^2\right)\left(-0.34\ln\tfrac{L}{D}+0.77\right)\right]+0.91\upsilon_s\left(-0.57\ln\tfrac{L}{D}+0.6\right)+1 \\ &= \left[\left(10(0.28)^3-5.88(0.28)^2\right)(-0.34\ln(1)+0.77)\right]+0.91(0.28)(-0.57\ln(1)+0.6)+1 = 0.97 \end{aligned}$$

$$K_V = 2.31\left(\tfrac{L}{D}\right)^{0.52} D E_S f(\upsilon_s) = 2.31(1)^{0.52}(4)(40)(0.97) = 0.36\ \tfrac{GN}{m}$$

The target natural frequency of the system for a soft-stiff design should ultimately be between 0.2 and 0.35 Hz to avoid 1P/3P frequencies. Following the methodology suggested by Jalbi and Bhattacharya [15], a closed-form solution of the first natural frequency of the system which considers the soil-structure interaction can be obtained as follows:

$$f_0 = C_J \times f_{fb}$$

where $f_{fb}$ is the fixed base natural frequency and $C_J$ is the foundation flexibility parameter that is dependent on the vertical stiffness of the springs ($K_V$).

For the purpose of this explanatory example, the computed fixed base natural frequency is 0.303 Hz and the $C_J$ is equal to 0.77. Hence, the first natural frequency of the system (with the SSI effect) is calculated to be $f_0 = C_J \times f_{fb} = 0.77 \times 0.303 = 0.23$ Hz, refer to Appendix A for the detailed calculation of the example. Although, the estimated value of the natural frequency falls within the targeted range, it is still in close proximity to the 1P frequency.

For further detailed analysis group effects can also be incorporated and readers are referred to Bordón et al. [26] which suggests formulations on how to incorporate foundation group effects correction factors which are dependent on the caisson aspect ratio, diameter and spacing. These formulations are also presented in the Appendix A. This will further lower the natural frequency and the design may have to be refined in order to allow for the additional 10% safety margin as per the DNVGL [23] recommendations. Subsequently, the FLS and ULS criteria should also be checked.

## 6. Conclusions

Offshore wind turbines supported on multiple shallow foundations can exhibit undesirable rocking modes of vibration strongly dependent on the vertical stiffness of the foundation. In this paper, numerical analysis is carried out to explore the axial behaviour of skirted caisson foundations for three idealised ground profiles (homogeneous, linear inhomogeneous and parabolic inhomogeneous) where the soil stiffness varies with depth. A set of static vertical stiffness functions and correction factors due to Poisson's ratio are derived. The results are validated against numerical and analytical solutions found in the literature. These formulations can be utilised for optimising the caisson's dimensions for feasibility studies purposes and preliminary design stages of a project. An explanatory example is provided to illustrate the usage of the derived formulation whereby natural frequency of a typical jacket supported OWT structure is calculated.

**Author Contributions:** Conceptualization, A.S., S.J. and S.B.; methodology, A.S. and S.J.; software, A.S.; validation, A.S. and S.J.; formal analysis, A.S. and S.J.; investigation, A.S. and S.J.; resources, S.B.; data curation, A.S.; writing—original draft preparation, A.S. and S.J.; writing—review and editing, S.B.; visualization, A.S.; supervision, S.B.; project administration, S.B.; funding acquisition, A.S. and S.J. All authors have read and agreed to the published version of the manuscript.

**Funding:** This research received no external funding.

**Institutional Review Board Statement:** Not applicable.

**Informed Consent Statement:** Not applicable.

**Data Availability Statement:** Not applicable.

**Conflicts of Interest:** The authors declare no conflict of interest.

## Nomenclature

| | |
|---|---|
| L | Foundation Depth |
| D | Foundation Diameter |
| R | Foundation Radius |
| Pile | Foundation with L/D > 2 |
| Caisson | Foundation with 0.2 < L/D < 2 |
| $E_{SO}$ | initial soil Young's modulus at 1D depth |
| $E_S$ | Vertical distribution of soil's Young's modulus |
| $f_{FB}$ | Fixed base (cantilever) natural frequency |
| $C_J$ | Foundation flexibility parameter |
| $m_{RNA}$ | Mass of Rotor Nacelle assembly |
| $m_T$ | Mass of tower |
| $D_{Bottom}$ | Tower bottom diameter |
| $D_{Top}$ | Tower top diameter |
| $\upsilon_s$ | Soil Poisson's ratio |
| $K_V$ | Vertical stiffness of the foundation |

## Appendix A.

### *Appendix A.1. Summary of the Analysis Performed*

**Table A1.** Summary of the Analysis Performed.

| Ground Profiles | $E_{SO}$ (MPa) | L/D (D = 5 m) | $v_s$ |
|---|---|---|---|
| Homogeneous<br>Parabolic Inhomogeneous<br>Linear Inhomogeneous | 100 | 0.2, 0.5, 0.75, 1, 1.5, 2 | 0.1, 0.2, 0.3, 0.4, 0.499 |

### *Appendix A.2. Obtaining the Natural Frequency*

*Step 1*: Calculate the fixed base natural frequency:

$$f_{fb} = \frac{1}{2\pi}\sqrt{\frac{3EI_{T-J}}{(0.243m_{eq}h_{total} + M_{RNA})(h_{total})^3}} = \frac{1}{2\pi}\sqrt{\frac{3 \times 1.635 \times 10^{12}}{[0.243(4200 \times 140) + 350000](140)^3}} = 0.303\text{Hz}$$

This is also presentative of the natural frequency if the jacket is supported on deep embedded piles

*Step 2*: Calculate $C_J$ for the stiffness of the springs:

Using the equations provided in Table 3, a preliminary estimate of the vertical stiffness for a rigid caisson foundation (with L/D = 1) is obtained as shown below;

$$\begin{aligned} f(\upsilon_s) &= \left[\left(10\upsilon_s^3 - 5.88\upsilon_s^2\right)\left(-0.34\ln\tfrac{L}{D} + 0.77\right)\right] + 0.91\upsilon_s\left(-0.57\ln\tfrac{L}{D} + 0.6\right) + 1 \\ &= \left[\left(10(0.28)^3 - 5.88(0.28)^2\right)(-0.34\ln(1) + 0.77)\right] + 0.91(0.28)(-0.57\ln(1) + 0.6) + 1 = 0.97 \end{aligned}$$

$$K_V = 2.31\left(\tfrac{L}{D}\right)^{0.52} DE_S f(\upsilon_s) = 2.31(1)^{0.52}(4)(40)(0.97) = 0.36\ \tfrac{GN}{m}$$

$$K_{V1,2} = 0.36 \times 2 = 0.72\ \frac{GN}{m}$$

$$\text{For } \alpha = 1,\ K_R = K_{V1,2}L^2\left[\frac{\alpha}{1+\alpha}\right] = 0.72 \times 12^2 \times \left[\frac{1}{1+1}\right] = 52\ \text{GNm}$$

$$\tau = \frac{K_R h_{total}}{EI_{T-J}} = \frac{52 \times 10^9 \times 140}{1.635 \times 10^{12}} = 4.45$$

$$C_J = \sqrt{\frac{\tau}{\tau + 3}} = \sqrt{\frac{4.45}{4.45 + 3}} = 0.77$$

$$f_0 = C_J \times f_{fb} = 0.77 \times 0.303 = 0.23\text{Hz}$$

Readers are refered to Jalbi and Bhattacharya [15] for the step-by-step derivation of $EI_{T\text{-}J}$ and $K_R$. In essence, the vertical spring stiffness was factored by 2 as the method converts the 3D representation of the system into 2D. Therefore, each spring in Figure 11 is representative of two caisson foundations.

*Additional Step:* Bordón et al. [26] propose the following method to calculate group effects correction factors:

$$\text{Group Effect Factor} = \frac{1}{1 + 0.06(1 + 3.08N)\left[\left(1 + 1.2(L/D)^{0.53}\right)/(s/D)\right]}$$

where N is the number of foundations and s is the spacing. For the solved example, this results in reducing the vertical stiffness of the foundations by a factor of 0.63. This further reduces the natural frequency to 0.21 Hz after the repition of the calculation above.

## References


1. European Commission. 2030 Climate & Energy Framework. 2020. Available online: https://ec.europa.eu/clima/policies/strategies/2030_en#tab-0-0 (accessed on 26 May 2021).
2. Wind Europe. *The European Offshore Wind Industry. Key Trends and Statistics 2019*; windeurope.org: Brussels, Belgium, 2019. Available online: https://windeurope.org/wp-content/uploads/files/about-wind/statistics/WindEurope-Annual-Offshore-Statistics-2019.pdf (accessed on 24 May 2021).
3. Global Wind Energy Council. *Global Wind Report*; Global Wind Energy Council: Brussels, Belgium, 2021.
4. Bhattacharya, S. *Design of Foundations for Offshore Wind Turbines*; John Wiley & Sons Ltd.: Chichester, UK, 2019.
5. 4COffshore Limited. Global Offshore Wind Farms Database. 2021. Available online: http://www.4coffshore.com/windfarms/ (accessed on 15 May 2021).
6. Orsted. Our Experience with Suction Bucket Jacket Foundations. 2019. Available online: https://orsted.com/en/our-business/offshore-wind/wind-technology/suction-bucket-jacket-foundations (accessed on 26 May 2021).
7. Jalbi, S.; Bhattacharya, S. Minimum foundation size and spacing for jacket supported offshore wind turbines considering dynamic design criteria. *Soil Dyn. Earthq. Eng.* **2019**, *123*, 193–204. [CrossRef]
8. Bhattacharya, S. Civil Engineering Aspects of a Wind Farm and Wind Turbine Structures. In *Wind Energy Engineering: A Handbook for Onshore and Offshore Wind Turbines*; Elsevier: London, UK, 2017.
9. Bhattacharya, S.; Nikitas, N.; Garnsey, J.; Alexander, N.; Cox, J.; Lombardi, D.; Wood, D.M.; Nash, D. Observed dynamic soil–structure interaction in scale testing of offshore wind turbine foundations. *Soil Dyn. Earthq. Eng.* **2013**, *54*, 47–60. [CrossRef]
10. Bhattacharya, S.; Cox, J.A.; Lombardi, D.; Wood, D. Dynamics of offshore wind turbines supported on two foundations. *Geotech. Eng.* **2011**, *166*, 159–169. [CrossRef]
11. Jalbi, S.; Nikitas, G.; Bhattacharya, S.; Alexander, N. Dynamic design considerations for offshore wind turbine jackets supported on multiple foundations. *Mar. Struct.* **2019**, *67*, 102631. [CrossRef]
12. Shadlou, M.; Bhattacharya, S. Dynamic stiffness of monopiles supporting offshore wind turbine generators. *Soil Dyn. Earthq. Eng.* **2016**, *88*, 15–32. [CrossRef]
13. Arany, L.; Bhattacharya, S.; Macdonald, J.; Hogan, S.J. Design of monopiles for offshore wind turbines in 10 steps. *Soil Dyn. Earthq. Eng.* **2017**, *92*, 126–152. [CrossRef]
14. Jalbi, S.; Shadlou, M.; Bhattacharya, S. Impedance functions for rigid skirted caissons supporting offshore wind turbines. *Ocean Eng.* **2018**, *150*, 21–35. [CrossRef]
15. Jalbi, S.; Bhattacharya, S. Closed form solution for the first natural frequency of offshore wind turbine jackets supported on multiple foundations incorporating soil-structure interaction. *Soil Dyn. Earthq. Eng.* **2018**, *113*, 593–613. [CrossRef]
16. Bell, R.W. The analysis of offshore foundations subject to combined loading. In *Degree of Master of Science*; University of Oxford: Oxford, UK, 1991.
17. Gazetas, G. Formulas and Charts for Impedances of Surface and Embedded Foundations. *J. Geotech. Eng.* **1991**, *117*, 1363–1381. [CrossRef]
18. Doherty, J.; Houlsby, G.; Deeks, A. Stiffness of flexible caisson foundations embedded in nonhomogeneous elastic soil. *J. Geotech. Geoenvironmental Eng.* **2005**, *131*, 1498–1508. [CrossRef]
19. Skau, K.S.; Jostad, H.P.; Eiksund, G.; Sturum, H. Modelling of soil-structure-interaction for flexible caissons for offshore wind turbines. *Ocean Eng.* **2019**, *171*, 273–285. [CrossRef]
20. Lysmer, J. Vertical Motions of Rigid Footings. Ph.D. Thesis, University of Michigan, Ann Arbor, MI, USA, 1965.
21. Spence, D.A. Self similar solutions to adhesive contact problems with incremental loading. *Proc. R. Soc. Lond. Ser. A* **1968**, *305*, 55–80.
22. Gazetas, G. Analysis of machine foundation vibrations: State of the art. *Int. J. Soil Dyn. Earthq. Eng.* **1983**, *2*, 2–42. [CrossRef]
23. DNVGL. *DNVGL-RP-C212 Offshore Soil Mechanics and Geotechnical Engineering*; DNVGL AS: Oslo, Norway, 2019.
24. Wolf, J.P. *Soil Structure Interaction Analysis in Time Domain*; Electrowatt Engineering Services Ltd.: Zurich, Switzerland, 1988.
25. Wolf, J.P.; Deeks, A.J. *Foundation Vibration Analysis: A Strength-of-Materials Approach*; Elsevier: Oxford, UK, 2004.
26. Bordón, J.D.R.; Aznarez, J.J.; Padron, L.A.; Maeso, O.; Bhattacharya, S. Closed-form stiffnesses of multi-bucket foundations for OWT including group effect correction factors. *Mar. Struct.* **2019**, *65*, 326–342. [CrossRef]
27. Fleming, W.G.; Weltman, A.J.; Randolph, M.F.; Elson, W.K. *Piling Engineering*; Blackie and Son: London, UK, 1992.
28. Shama, A.A.; El Naggar, H. Bridge Foundations. *Encycl. Earthq. Eng.* **2015**, *1*, 298–317.
29. Suryasentana, S.; Byrne, B.; Burd, H.; Shonberg, A. Simplified model for stiffness of suction caisson foundations under 6 dof loading. In Proceedings of the SUT OSIG 8th International Conference, London, UK, 12–14 September 2017.
30. Latini, C.; Cisternino, M.; Zania, V. Vertical dynamic stiffness of offshore foundations. In Proceedings of the 26th International Ocean and Polar Engineering Conference, Rhodes, Greece, 26 June–1 July 2016; pp. 775–780.
31. Sloan, S.W. Numerical Analysis of Incompressible and Plastic Solids Using Finite Elements. Ph.D. Thesis, Cambridge University, Cambridge, UK, 1981.
32. Bhattacharya, S.; Wang, L.; Liu, J.; Hong, Y. Civil engineering challenges associated with design of offshore wind turbines with special reference to China. In *Wind Energy Engineering: A Handbook for Onshore and Offshore Wind Turbines*; Elsevier: London, UK, 2017.
33. Latini, C.; Zania, V. Vertical dynamic impedance of suction caissons. *Soils Found.* **2019**, *59*, 1113–1127. [CrossRef]

34. Latini, C.; Zania, V. Dynamic lateral response of suction caissons. *Soil Dyn. Earthq. Eng.* **2017**, *100*, 59–71. [CrossRef]
35. Anoyatis, G.; Mylonakis, G.; Lemnitzer, A. Soil reaction to lateral harmonic pile motion. *Soil Dyn. Earthq. Eng.* **2016**, *87*, 164–179. [CrossRef]
36. Lysmer, J.; Udaka, T.; Seed, H.B.; Hwang, R. *FLUSH-A Computer Program for Complex Response Analysis of Soft-Structure Systems*; University of California: Berkeley, CA, USA, 1974.
37. Plaxis 3D. *Materials Models Manual*; Bentley Systems International Limited: Dublin, Ireland, 2018.
38. Shonberg, A.; Harte, M.; Aghakouchak, A.; Brown, C.S.D.; Andrade, M.P.; Lingaard, M.A. Suction bucket jackets for offshore wind turbines: Applications from in-situ observations. In Proceedings of the TC-209 Workshop—19th ICSMGE, Seoul, Korea, 20 September 2017.
39. Jonkman, J.; Buttefield, S.; Musial, W.; Scott, G. *Definition of a 5-MW Reference Wind Turbine for Offshore System Development*; National Renewable Energy Laboratory (NREL): Golden, CO, USA, 2009.
40. Alati, N.; Failla, G.; Arena, F. Seismic analysis of offshore wind turbines on bottom-fixed support structures. *Philos. Trans. R. Soc. A* **2015**, *373*, 20140086. [CrossRef] [PubMed]

Journal of
*Marine Science and Engineering*

MDPI

*Article*

# Dynamic Analysis on Pile Group Supported Offshore Wind Turbine under Wind and Wave Load

**Yusha Shi [1], Wenjuan Yao [2,*] and Guoliang Yu [3,*]**

[1] School of Mechanics and Engineering Science, Shanghai University, Shanghai 200444, China; shiyushawork@gmail.com
[2] Shanghai Institute of Applied Mathematics and Mechanics, Shanghai University, Shanghai 200444, China
[3] SKLOE, CISSE, School of Naval Architecture, Ocean & Civil Engineering, Shanghai Jiao Tong University, Shanghai 200240, China
* Correspondence: wjyao@shu.edu.cn (W.Y.); yugl@sjtu.edu.cn (G.Y.)

**Abstract:** With growing demand for renewable wind energy, the number of offshore wind turbines increased rapidly in recent years. This paper uses the improved Tajimi model and transfer matrix method to analyze the dynamic response of pile group supported offshore wind turbine under wind and wave load. The vibration equation of the structure is established by tower discretization. The calculation result is compared with the numerical simulation result. The horizontal displacement of the structure under loads with different frequencies can be obtained. The wind speed and the foundation impedance are found important to the structure displacement. The pile–pile interaction factor depends on the pile spacing, the pile embedment ratio, and the incidence angle.

**Keywords:** offshore wind turbine; pile–pile interaction factor; wind load; wave load; transfer matrix method

**Citation:** Shi, Y.; Yao, W.; Yu, G. Dynamic Analysis on Pile Group Supported Offshore Wind Turbine under Wind and Wave Load. *J. Mar. Sci. Eng.* **2022**, *10*, 1024. https://doi.org/10.3390/jmse10081024

Academic Editors: Eugen Rusu, Kostas Belibassakis and George Lavidas

Received: 6 July 2022
Accepted: 23 July 2022
Published: 26 July 2022

**Publisher's Note:** MDPI stays neutral with regard to jurisdictional claims in published maps and institutional affiliations.

**Copyright:** © 2022 by the authors. Licensee MDPI, Basel, Switzerland. This article is an open access article distributed under the terms and conditions of the Creative Commons Attribution (CC BY) license (https://creativecommons.org/licenses/by/4.0/).

## 1. Introduction

New energy development and utilization have become the main focus of all human beings with the consumption of traditional energy. As one kind of renewable and clean energy, wind energy is developing rapidly. With abundant energy reserves and the farmland-free characteristic, offshore wind energy source has better development prospect rather than onshore wind energy. Offshore wind turbine (OWT) developed rapidly in China. From 2014–2018, the installed offshore wind turbine in China increased average of 60.5% per year.

OWTs are mainly under wind load and wave load [1], sometimes even earthquake load [2]. The structure of OWT can be divided into two parts, the tower above the seawater and the foundation partially submerged in the seawater, and partially embedded in the soil. The tower is under wind load, whereas the foundation is under wave load and soil reaction [3]. OWT is a slender structure, which means its dynamic response will be significantly influenced by the load frequency. In OWT design, it is needed to calculate the OWT structure natural frequency to prevent it falls within the frequency ranges of main loads [4]. As shown in Figure 1, the peak frequency of the wind load is usually within 0.01 Hz. The peak frequency of the wave load is 0.08 Hz~0.2 Hz. Definitions of 1P frequency and 3P frequency are presented below:

(1) The barycenter of blades and the turbine might slightly shift from the rotating shaft, which will produce eccentric force, and its frequency is equal to the frequency of the turbine rotation frequency. This frequency is called the 1P frequency [5–7]. Since an OWT has different rotation speeds, the 1P frequency is not a single frequency but a frequency range, which is related to the highest and lowest value of the rotation speed.
(2) Rotating blades will produce the air turbulence load. Once a blade runs across a certain location, a turbulence load will be created. This load is usually called 2P or 3P

load. Most OWTs are three-blade structures, and the model used in this paper is the same, so it is a 3P frequency.

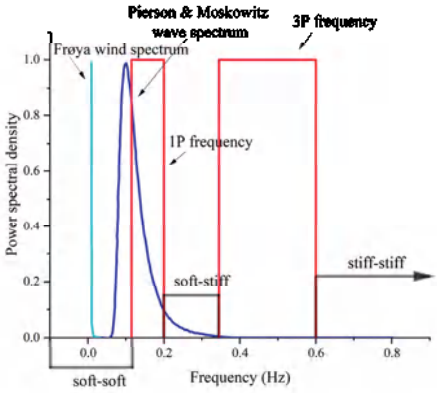


**Figure 1.** Frequency spectrum of the dynamic loads [4].

As shown in Figure 1, in OWT design, three different design methods are considered, which are "soft-soft", "soft-stiff", and "stiff-stiff" methods. Most installed OWTs adopted "soft-stiff" design method. Therefore, it is needed to analyze the dynamic response of OWT under different frequencies.

Previous research mainly focused on the study of monopile-supported OWTs. The numerical method is used to analyze the overall dynamic structure response, including the finite element method [8] (FEM) and boundary element method (BEM). Kjørlaug [9] used SAP2000 to analyze the acceleration and structure natural frequency of OWT under lateral and vertical earthquake loads. Corciulo [10] used the OpenSees simulation platform to investigate the dynamic response of OWT under wind and wave load. Zuo [11] used ABAQUS to establish the model of OWT including blades and analyzed the dynamic response of OWT under operating and steady conditions. Galvin [12] used the FEM-BEM method and analyzed the dynamic response of OWT under earthquake load.

Another analysis method is the analytical method. The OWT structure can be divided into the superstructure and the foundation to investigate its dynamic response [13]. As for the foundation, the P-y curve method is used in early research [14,15]. This method is still widely used [6,16]. Andersen [17] simplified the pile–soil interaction as the equivalent coupled spring model and obtained the structure natural frequency. Adhikari and Bhattacharya [18,19] established the foundation model with elastic supports based on the Euler–Bernoulli beam, used horizontal and rotation springs to simulate the foundation reaction, and validated the result with the experimental result [20].

The foundation of OWT is partially embedded in the soil, and the dynamic equation of different pile parts is different. By using the transfer matrix method [21–23], the dynamic response of different pile parts can be connected. Wang [24] analyzed the onshore wind turbine structure natural frequency using the transfer matrix method. Huang [25] analyzed the dynamic response of the pile group supported OWT using the transfer matrix method.

This paper used the Morison equation to calculate the wave load applied to the pile, and calculates the pile–soil interaction using an improved Tajimi soil model [26,27]. By using the transfer matrix method, the dynamic response of the pile group embedded in the soil and submerged in the seawater are connected, and the overall pile group impedance is obtained. The stable forced vibration equation of the multiple-degree-of-freedom OWT system is established by discretizing the tower into multiple segments. By substituting the pile group impedance into the equation, the dynamic response of OWT under different load frequencies is obtained. For the pile group, the pile–pile interaction factor is calculated, which considers the influence of the passive pile on the active pile.

The calculated result is compared with the FEM result to validate the correctness of the proposed calculation method.

## 2. Proposed Calculation Method

### 2.1. Model Establishment

As shown in Figure 2, the pile group supported 3.6 MW offshore wind turbine can be divided into two parts. The first part is the pile group foundation, which is partially embedded in the soil and partially submerged in the seawater. The second part is the superstructure, which is under distributed and thrust wind load.

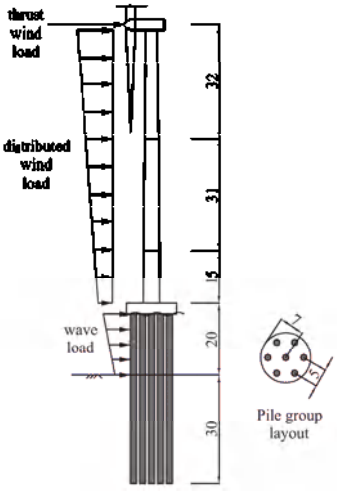


**Figure 2.** Pile group supported 3.6 MW offshore wind turbine.

### 2.2. Pile Submerged in the Seawater

The pile diameter of the pile group is relatively small compared with the wavelength ($D/L_{wl} \leq 0.2$). Therefore, the wave load applied to the pile can be calculated by the Morison equation. For linear waves, at height z of the cylinder, the horizontal wave load $q_G(z)$ can be calculated according to Equation (1) [28]:

$$q_G(z) = \frac{1}{2}C_D\rho_w D\left(\frac{\pi H_w}{T}\frac{\cosh(KZ_w)}{\sinh(KL_w)}\right)^2 \cos\theta|\cos\theta|dz + C_M\frac{\pi D^2}{4}\frac{2\pi^2 H_w}{T^2}\frac{\cosh(KZ_w)}{\sinh(KL_w)}\sin\theta dz \quad (1)$$

where $C_D$ is the drag coefficient, $C_M$ is the inertia coefficient, $\theta = -\omega t$, $\rho_w$ is the density of the seawater, $D$ is the pile diameter, $H_w$ is the wave height, $T$ is the wave period, and $K = \frac{2\pi}{L_{wl}}$, where $L_{wl}$ is the wavelength. This paper mainly discusses the dynamic response of the pile under different frequencies; therefore, it is needed to calculate the maximum horizontal wave load applied to the whole pile body. The wave load applied to the whole pile body can be calculated according to Equation (2) [28]:

$$F_T = \int_0^{L_w} q_G(z) = F_{HD}\cos\theta|\cos\theta| + F_{HI}\sin\theta \quad F_{HD} = C_D\frac{\gamma D{H_w}^2}{2}K_1, F_{HI} = C_M\frac{\gamma\pi D^2 H_w}{8}K_2 \quad (2)$$

where $K_1 = \frac{2KL_w+\sinh 2KL_w}{8\sinh 2KL_w}$ and $K_2 = \tanh KL_w$. As shown in Equation (2), the value of $\theta$ to determine the maximum of $F_{HD}$ and $F_{HI}$ is not the same. Therefore, it is needed to determine the value of $\theta$ when the total wave force is the largest. According to the calculation, the maximum total wave force depends on the value of $F_{HD}$ and $F_{HI}$.

(1) When $F_{HI} \geq 2F_{HD}$, the maximum total wave force happens when $\theta = \pi/2$, and the maximum total wave force $F_{T\max}$ equals $F_{HI}$.
(2) When $F_{HI} < 2F_{HD}$, the maximum total wave force happens when $\theta = \arcsin(F_{HI}/F_{HD})$, $F_{\max} = F_{HD}\left(1 + \frac{1}{4}\left(\frac{F_{HI}}{F_{HD}}\right)^2\right)$.

In engineering, $F_{HI} < 2F_{HD}$ is rarely seen. Therefore, in this paper, we consider $F_{HI} \geq 2F_{HD}$, which means $F_{T\max} = F_{HI}$. Then, we can calculate the wave load applied to the cylinder at height z when the maximum total wave load happens [28]:

$$q_G(z) = C_M \frac{\pi D^2}{4} \frac{2\pi^2 H_w}{T^2} \frac{\cosh(KZ_w)}{\sinh(KL_w)} \tag{3}$$

Equation (3) is used for single piles in the seawater. However, the wave load applied to the pile group can be complex due to the pile–pile interaction and pile–cap interaction. According to the research [29], considering the pile–pile interaction, this paper considers the wave load applied to each pile within the pile group as 0.8 times the wave load applied to the single pile, and Equation (3) can be modified as:

$$q_G(z) = 0.8C_M \frac{\pi D^2}{4} \frac{2\pi^2 H_w}{T^2} \frac{\cosh(KZ_w)}{\sinh(KL_w)} \tag{4}$$

Based on the water–soil interface, the local coordinate system is established, and the $z$ axis is towards the seabed. The pile submerged in the seawater can be divided into n parts, and the length of each part is $h_i$. According to dynamic equilibrium conditions, the dynamic equation of each pile section can be obtained:

$$\frac{d^4 w_i^{a1}}{dz^4} + 4\gamma^4 w_i^{a1}(z) = \frac{q_G(z)}{E_p I_p} \tag{5}$$

where $w$ is the lateral displacement of the pile section, superscript $a1$ denotes the first part of the active pile, and $\gamma = \left(\frac{-m_p\omega^2}{4E_pI_p}\right)^{1/4}$, where $\omega$ is the load frequency, $m_p$ is the unit mass of the pile body, $E_p$ is the modulus of elasticity of the pile, and $I_p$ is the cross-section inertia moment of the pile. The solution of Equation (5) is the superposition of general solution and particular solution, as shown in Equation (6):

$$w_i^{a1}(z) = e^{(-1+i)\gamma z} A_{1i}^{a1} + e^{(-1-i)\gamma z} A_{2i}^{a1} + e^{(1-i)\gamma z} A_{3i}^{a1} + e^{(1+i)\gamma z} A_{4i}^{a1} + q'_G(z) \tag{6}$$

where $q'_G = a_p q_G, a_p = \frac{1}{E_p I_p (K^4 + 4\gamma^4)}$, $A_{1i}^{a1}$, $A_{2i}^{a1}$, $A_{3i}^{a1}$, $A_{4i}^{a1}$ are undetermined coefficients, which can be obtained according to boundary conditions.

According to differential relations, we can obtain the lateral displacement $w$, rotation angle $\theta$, bending moment $M$, and shearing force $Q$ of the pile section. For simplicity, we define $M = \overline{M}/E_pI_p$ and $Q = \overline{Q}/E_pI_p$ to represent the equivalent bending moment and shearing force. Written in matrix form:

$$\begin{Bmatrix} w_i^{a1} \\ \phi_i^{a1} \\ M_i^{a1} \\ Q_i^{a1} \\ 1 \end{Bmatrix} = \left\{ t_i^{a1} \right\} \begin{Bmatrix} A_{1i}^{a1} \\ A_{2i}^{a1} \\ A_{3i}^{a1} \\ A_{4i}^{a1} \\ 1 \end{Bmatrix} \tag{7}$$

where the matrix $\left\{ t_i^{a1} \right\}$ is shown in Appendix A.

Equation (7) can be used to calculate each pile section of the pile body. The transfer matrix between the pile top and pile tip of each pile section can then be obtained, as shown in Equation (8):

$$\begin{Bmatrix} w^{a1}(h_i) \\ \phi^{a1}(h_i) \\ M^{a1}(h_i) \\ Q^{a1}(h_i) \\ 1 \end{Bmatrix} = \left\{ t_i^{a1}(h_i) \right\} \left\{ t_i^{a1}(0) \right\}^{-1} \begin{Bmatrix} w^{a1}(0) \\ \phi^{a1}(0) \\ M^{a1}(0) \\ Q^{a1}(0) \\ 1 \end{Bmatrix} \tag{8}$$

Let $\{T_i^{a1}\} = \left\{ t_i^{a1}(h_i) \right\} \left\{ t_i^{a1}(0) \right\}^{-1}$ and $T^{a1} = T_n^{a1} \cdots T_i^{a1} \cdots T_2^{a1} T_1^{a1}$; the transfer matrix between the pile tip (water–soil interface) and the pile top (water–air interface) can then be obtained, as shown in Equation (9):

$$\begin{Bmatrix} w^{a1}(L_w) \\ \phi^{a1}(L_w) \\ M^{a1}(L_w) \\ Q^{a1}(L_w) \\ 1 \end{Bmatrix} = \{T^{a1}\} \begin{Bmatrix} w^{a1}(0) \\ \phi^{a1}(0) \\ M^{a1}(0) \\ Q^{a1}(0) \\ 1 \end{Bmatrix} \tag{9}$$

Thus, we obtain the transfer matrix of the active pile submerged in the seawater. The solution can also be used for the passive pile and the active pile under the influence of the passive pile. Let $\{T^{p1}\} = \{T^{a1}\} = \{\overline{T}^{a1}\}$, written in matrix form:

$$\begin{aligned} \begin{Bmatrix} w^{p1}(L_w) \\ \phi^{p1}(L_w) \\ M^{p1}(L_w) \\ Q^{p1}(L_w) \\ 1 \end{Bmatrix} &= \{T^{p1}\} \begin{Bmatrix} w^{p1}(0) \\ \phi^{p1}(0) \\ M^{p1}(0) \\ Q^{p1}(0) \\ 1 \end{Bmatrix} \\ \begin{Bmatrix} \overline{w}^{a1}(L_w) \\ \overline{\phi}^{a1}(L_w) \\ \overline{M}^{a1}(L_w) \\ \overline{Q}^{a1}(L_w) \\ 1 \end{Bmatrix} &= \{\overline{T}^{a1}\} \begin{Bmatrix} \overline{w}^{a1}(0) \\ \overline{\phi}^{a1}(0) \\ \overline{M}^{a1}(0) \\ \overline{Q}^{a1}(0) \\ 1 \end{Bmatrix} \end{aligned} \tag{10}$$

where $w^{p1}$ is the lateral displacement of the passive pile and $\overline{w}^{a1}$ is the lateral displacement of the active pile under the influence of the passive pile.

### *2.3. Pile Embedded in the Soil*

#### 2.3.1. Pile–Soil Interaction

The pile embedded in the soil is under lateral reaction of the soil. To investigate the influence of the soil cut-off frequency, this paper adopts the soil model proposed by Anoyatis [26]. This model uses the improved Tajimi soil model, considers the soil as a three-dimensional continuum, and considers the influence of soil vertical displacement on the lateral soil displacement. The proposed dynamic Winkler modulus can reflect the vibration of spring coefficient and damping coefficient around the soil cut-off frequency. The proposed calculation method is shown in the equation below:

$$\begin{aligned} k^* &= \pi G_s^* s \left[ s + 4 \frac{Y_1'(s)}{Y_0'(s)} \right] \\ s &= \frac{1}{2(\eta_s)\chi} \sqrt{a_{cutoff}^2 - \frac{a_0^2}{1+2i\beta_s}} \end{aligned} \tag{11}$$

where $G_s^* = G_s(1 + 2i\beta_s)$, $\beta_s$ is the soil material damping, valued 0.05 in this paper, $Y'_1(s)$ and $Y'_0(s)$ are the first and zero order modified Bessel function of the second kind, $\eta_s = \sqrt{2 - \nu_s / 1 - \nu_s}$, where $\upsilon_s$ is Poisson's ratio, $a_{cutoff} = (\pi/2)(L/D)^{-1}$, where $L$ is the

pile length, and $\chi$ is the dimensional coefficient, valued according to Poisson's ratio, valued 3 in this paper.

As shown in Figure 3, the dynamic response of the pile embedded in the soil can be divided into four steps:

(1) The horizonal displacement of the active pile under the pile top dynamic load;
(2) The passive pile is influenced by the incident wave from the active pile displacement after the soil attenuation;
(3) The horizontal displacement of the passive pile;
(4) The active pile is influenced by the secondary wave from the passive pile displacement after soil attenuation.

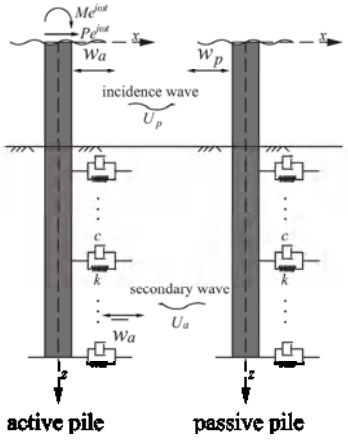


**Figure 3.** Pile–pile interaction.

2.3.2. Active Pile Displacement

The dynamic equation of the active pile under horizontal dynamic load can be written as:

$$\frac{d^4 w_i^{a2}}{dz^4} + 4\gamma^4 w_i^{a2}(z) = 0 \tag{12}$$

where $\gamma = \left(\frac{k+i\omega c - m_p\omega^2}{4E_p I_p}\right)^{1/4}$, $k = \mathrm{Re}(k^*)$, $wc = \mathrm{IM}(k^*)$, and $w_i^{a2}$ means the lateral displacement of the active pile embedded in the soil. The solution of Equation (12) is written below:

$$w_i^{a2}(z) = e^{(-1+i)\gamma z}A_{a2} + e^{(-1-i)\gamma z}B_{a2} + e^{(1-i)\gamma z}C_{a2} + e^{(1+i)\gamma z}D_{a2} \tag{13}$$

where $A_{a2}$, $B_{a2}$, $C_{a2}$, $D_{a2}$ are undetermined coefficients, which can be determined according to boundary conditions.

Similarly, according to differential relations, we can obtain the lateral displacement, rotation angle, bending moment, and shearing force of the active pile embedded in the soil. Written in matrix form:

$$\begin{Bmatrix} w_i^{a2} \\ \phi_i^{a2} \\ M_i^{a2} \\ Q_i^{a2} \\ 1 \end{Bmatrix} = \left\{ t_i^{a2} \right\} \begin{Bmatrix} A_{a2} \\ B_{a2} \\ C_{a2} \\ D_{a2} \\ 1 \end{Bmatrix} \tag{14}$$

where the matrix $\left\{t_i^{a2}\right\}$ is shown in Appendix A. The transfer matrix between the pile top and pile tip of each pile section is shown in Equation (15):

$$\begin{Bmatrix} w_i^{a2}(h_i) \\ \phi_i^{a2}(h_i) \\ M_i^{a2}(h_i) \\ Q_i^{a2}(h_i) \\ 1 \end{Bmatrix} = \left\{t_i^{a2}(h_i)\right\}\left\{t_i^{a2}(0)\right\}^{-1} \begin{Bmatrix} w_i^{a2}(0) \\ w_i^{a2}(0) \\ M_i^{a2}(0) \\ Q_i^{a2}(0) \\ 1 \end{Bmatrix} \tag{15}$$

Let $\{T_i^{a2}\} = \left\{t_i^{a2}(h_i)\right\}\left\{t_i^{a2}(0)\right\}^{-1}$ and $T^{a2} = T_n^{a2} \cdots T_i^{a2} \cdots T_2^{a2} T_1^{a2}$; the transfer matrix between the active pile tip and top (soil-water surface) can be obtained:

$$\begin{Bmatrix} w^{a2}(H) \\ \phi^{a2}(H) \\ M^{a2}(H) \\ Q^{a2}(H) \\ 1 \end{Bmatrix} = \{T^{a2}\} \begin{Bmatrix} w^{a2}(0) \\ \phi^{a2}(0) \\ M^{a2}(0) \\ Q^{a2}(0) \\ 1 \end{Bmatrix} \tag{16}$$

2.3.3. Soil Attenuation Function and Soil Displacement

For the soil S m away from the active pile, its attenuation function and soil displacement can be calculated according to the following equation:

$$U_p(S,z) = \psi w^{a2}(z) = \left[\psi(S,0^\circ)\cos\theta^2 + \psi(S,90^\circ)\sin\theta^2\right] w^{a2}(z) \tag{17}$$

where

$$\psi(S,0^\circ) = \sqrt{\frac{R}{S}} \exp\left(\frac{-\beta\omega(R-S)}{V_{La}}\right) \exp\left(\frac{-i\omega(R-S)}{V_{La}}\right) \tag{18}$$

$$\psi(S,90^\circ) = \sqrt{\frac{R}{S}} \exp\left(\frac{-\beta\omega(R-S)}{V_s}\right) \exp\left(\frac{-i\omega(R-S)}{V_s}\right) \tag{19}$$

where $R$ is the radius of the pile, $S$ is the distance between the active pile and passive pile, $\beta$ is the soil damping, $V_{La}$ and $V_s$ are the shear wave velocity and Lysmer's simulation velocity [30], $V_{La} = \frac{3.4}{\pi(1-v)} V_s$, and $\theta$ is the angle of incidence, which will influence the pile–pile interaction factor, as shown in Figure 4.

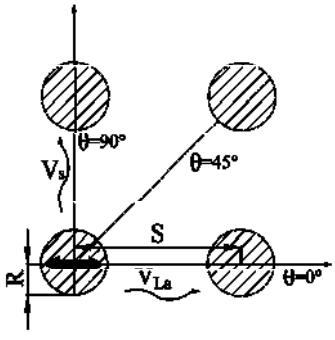


**Figure 4.** Pile–pile interaction.

The soil displacement around the passive pile after the soil attenuation can then be obtained. In pile groups, $\theta$ can be different between different piles, which will be considered when calculating the overall impedance of the pile group.

2.3.4. Passive Pile Displacement

The displacement of the passive pile due to the soil displacement can be calculated according to the following equation:

$$\frac{d^4 w_i^{p2}}{dz^4} + 4\gamma^4 w_i^{p2}(z) - \frac{(k+i\omega c)}{E_p I_p} U_p(S,z) = 0 \tag{20}$$

Substitute Equation (17) into Equation (20), the solution can be obtained:

$$\begin{aligned} w_i^{p2}(z) = \; & e^{(-1+i)\gamma z} A_{p2} + e^{(-1-i)\gamma z} B_{p2} + e^{(1-i)\gamma z} C_{p2} + e^{(1+i)\gamma z} D_{p2} + \\ & \tfrac{(k+i\omega c)\psi z}{E_p I_p} [(1-i)e^{(-1+i)\gamma z} A_{a2} + (1+i)e^{(-1-i)\gamma z} B_{a2} + \\ & (-1+i)e^{(1-i)\gamma z} C_{a2} + (-1-i)e^{(1+i)\gamma z} D_{a2}] \end{aligned} \tag{21}$$

where $A_{p2}$, $B_{p2}$, $C_{p2}$, $D_{p2}$ are undetermined coefficients.

Written in matrix form:

$$\begin{Bmatrix} w_i^{p2} \\ \phi_i^{p2} \\ M_i^{p2} \\ Q_i^{p2} \\ 1 \end{Bmatrix} = \left\{ t_i^{a2} \right\} \begin{Bmatrix} A_{p2} \\ B_{p2} \\ C_{p2} \\ D_{p2} \\ 1 \end{Bmatrix} + \left\{ t_i^{p2} \right\} \begin{Bmatrix} A_{a2} \\ B_{a2} \\ C_{a2} \\ D_{a2} \\ 1 \end{Bmatrix} \tag{22}$$

where the matrix $\left\{ t_i^{p2} \right\}$ is shown in Appendix A. The transfer matrix between passive pile segment tip and top can be obtained after the following calculation:

$$\begin{Bmatrix} w_i^{p2}(h_i) \\ \phi_i^{p2}(h_i) \\ M_i^{p2}(h_i) \\ Q_i^{p2}(h_i) \\ 1 \end{Bmatrix} = T_{i1}^{p2} \begin{Bmatrix} w_i^{p2}(0) \\ \phi_i^{p2}(0) \\ M_i^{p2}(0) \\ Q_i^{p2}(0) \\ 1 \end{Bmatrix} + T_{i2}^{p2} \begin{Bmatrix} w_i^{a2}(0) \\ w_i^{a2}(0) \\ M_i^{a2}(0) \\ Q_i^{a2}(0) \\ 1 \end{Bmatrix} \tag{23}$$

where

$$\begin{aligned} T_{i1}^{p2} &= t_i^{a2}(h_i) \left( t_i^{a2}(0) \right)^{-1} \\ T_{i2}^{p2} &= \left( t_i^{p2}(h_i) - t_i^{a2}(h_i) \left( t_i^{a2}(0) \right)^{-1} t_i^{p2}(0) \right) \left( t_i^{a2}(0) \right)^{-1} \end{aligned} \tag{24}$$

The transfer matrix between the passive pile tip and top (soil-water surface) can then be obtained:

$$\begin{Bmatrix} w^{p2}(H) \\ \phi^{p2}(H) \\ M^{p2}(H) \\ Q^{p2}(H) \\ 1 \end{Bmatrix} = T_1^{p2} \begin{Bmatrix} w^{p2}(0) \\ \phi^{p2}(0) \\ M^{p2}(0) \\ Q^{p2}(0) \\ 1 \end{Bmatrix} + T_2^{p2} \begin{Bmatrix} w^{a2}(0) \\ w^{a2}(0) \\ M^{a2}(0) \\ Q^{a2}(0) \\ 1 \end{Bmatrix} \tag{25}$$

where $T_1^{p2} = T_{n1}^{p2} \cdots T_{i1}^{p2} \cdots T_{21}^{p2} T_{11}^{p2}$, $T_2^{p2} = T_{n2}^{p2} \cdots T_{i2}^{p2} \cdots T_{22}^{p2} T_{12}^{p2}$.

2.3.5. Active Pile Displacement Due to Secondary Wave

The passive pile displacement will produce secondary wave, which will influence the active pile displacement. The soil displacement around the active pile can be calculated according to the following equation:

$$U_a(S,z) = \psi w^{p2}(z) = \left[ \psi(S, 0^\circ) \cos\theta^2 + \psi(S, 90^\circ) \sin\theta^2 \right] w^{p2}(z) \tag{26}$$

The dynamic equation can be written as:

$$\frac{d^4\overline{w}_i^{a2}}{dz^4} + 4\gamma^4\overline{w}_i^{a2}(z) - \frac{(k+i\omega c)}{E_p I_p}U_a(S,z) = 0 \tag{27}$$

where $\overline{w}^{a2}$ is the lateral displacement of the active pile under the influence of the passive pile. The solution to Equation (27) is:

$$\begin{aligned}\overline{w}_i^{a2}(z) = \quad & e^{(-1+i)\gamma z}\overline{A}_{a2} + e^{(-1-i)\gamma z}\overline{B}_{a2} + e^{(1-i)\gamma z}\overline{C}_{a2} + e^{(1+i)\gamma z}\overline{D}_{a2} + \\ & \tfrac{(k+i\omega c)\psi z}{16E_p I_p\gamma^3}[(1-i)e^{(-1+i)\gamma z}A_{p2} + (1+i)e^{(-1-i)\gamma z}B_{p2} + \\ & (-1+i)e^{(1-i)\gamma z}C_{p2} + (-1-i)e^{(1+i)\gamma z}D_{p2}] + \\ & \tfrac{(k+i\omega c)\psi z^2}{512E_p I_p\gamma^6}[(1-i)^2e^{(-1+i)\gamma z}A_{a2} + (1+i)^2e^{(-1-i)\gamma z}B_{a2} + \\ & (-1+i)^2e^{(1-i)\gamma z}C_{a2} + (-1-i)^2e^{(1+i)\gamma z}D_{a2}]\end{aligned} \tag{28}$$

where $\overline{A}_{a2}$, $\overline{B}_{a2}$, $\overline{C}_{a2}$, $\overline{D}_{a2}$ are undetermined coefficients.

Written in matrix form:

$$\begin{aligned}&\begin{Bmatrix}\overline{w}_i^{a2}\\ \overline{\phi}_i^{a2}\\ \overline{M}_i^{a2}\\ \overline{Q}_i^{a2}\\ 1\end{Bmatrix} = \{t_i^{a2}\}\begin{Bmatrix}\overline{A}_{a2}\\ \overline{B}_{a2}\\ \overline{C}_{a2}\\ \overline{D}_{a2}\\ 1\end{Bmatrix} + \tfrac{1}{16\gamma^3}\left\{t_i^{p2}\right\}\begin{Bmatrix}A_{p2}\\ B_{p2}\\ C_{p2}\\ D_{p2}\\ 1\end{Bmatrix} + \\ &\left(\left\{\overline{t}_i^{a2}\right\} + \tfrac{3i}{1024\gamma^7}\begin{Bmatrix}(1-i)^2 & 0 & 0 & 0\\ 0 & (1+i)^2 & 0 & 0\\ 0 & 0 & (-1+i)^2 & 0\\ 0 & 0 & 0 & (-1-i)^2\end{Bmatrix}\left\{t_i^{p2}\right\}\right)\begin{Bmatrix}A_{a2}\\ B_{a2}\\ C_{a2}\\ D_{a2}\\ 1\end{Bmatrix}\end{aligned} \tag{29}$$

where the matrix $\left\{\overline{t}_i^{a2}\right\}$ is shown in Appendix A.

Let:

$$\begin{aligned}&\{t_i^1\} = \{t_i^{a2}\}\\ &\{t_i^2\} = \tfrac{1}{16\gamma^3}\left\{t_i^{p2}\right\}\\ &\{t_i^3\} = \left\{\overline{t}_i^{a2}\right\} + \tfrac{3i}{1024\gamma^7}\begin{Bmatrix}(1-i)^2 & 0 & 0 & 0\\ 0 & (1+i)^2 & 0 & 0\\ 0 & 0 & (-1+i)^2 & 0\\ 0 & 0 & 0 & (-1-i)^2\end{Bmatrix}\left\{t_i^{p2}\right\}\end{aligned} \tag{30}$$

Equation (29) can be simplified:

$$\begin{Bmatrix}\overline{w}_i^{a2}\\ \overline{\phi}_i^{a2}\\ \overline{M}_i^{a2}\\ \overline{Q}_i^{a2}\\ 1\end{Bmatrix} = \left\{t_i^1\right\}\begin{Bmatrix}\overline{A}_{a2}\\ \overline{B}_{a2}\\ \overline{C}_{a2}\\ \overline{D}_{a2}\\ 1\end{Bmatrix} + \left\{t_i^2\right\}\begin{Bmatrix}A_{p2}\\ B_{p2}\\ C_{p2}\\ D_{p2}\\ 1\end{Bmatrix} + \left\{t_i^3\right\}\begin{Bmatrix}A_{a2}\\ B_{a2}\\ C_{a2}\\ D_{a2}\\ 1\end{Bmatrix} \tag{31}$$

The transfer matrix between active pile segment tip and top can then be obtained:

$$\begin{Bmatrix} \overline{w}_i^{a2}(h_i) \\ \overline{\phi}_i^{a2}(h_i) \\ \overline{M}_i^{a2}(h_i) \\ \overline{Q}_i^{a2}(h_i) \\ 1 \end{Bmatrix} = T_{i1} \begin{Bmatrix} \overline{w}_i^{a2}(0) \\ \overline{\phi}_i^{a2}(0) \\ \overline{M}_i^{a2}(0) \\ \overline{Q}_i^{a2}(0) \\ 1 \end{Bmatrix} + T_{i2} \begin{Bmatrix} w_i^{p2}(0) \\ w_i^{p2}(0) \\ M_i^{p2}(0) \\ Q_i^{p2}(0) \\ 1 \end{Bmatrix} + T_{i3} \begin{Bmatrix} w_i^{a2}(0) \\ w_i^{a2}(0) \\ M_i^{a2}(0) \\ Q_i^{a2}(0) \\ 1 \end{Bmatrix} \tag{32}$$

where

$$\begin{aligned} T_{i1} = \;& t_i^1(h_i)\left(t_i^1(0)\right)^{-1} \\ T_{i2} = \;& \left(t_i^2(h_i) - t_i^1(h_i)\left(t_i^1(0)\right)^{-1} t_i^2(0)\right)\left(t_i^{a2}(0)\right)^{-1} \\ T_{i3} = \;& -\left(t_i^2(h_i) - t_i^1(h_i)\left(t_i^1(0)\right)^{-1} t_i^2(0)\right)\left(t_i^{a2}(0)\right)^{-1} t_i^{p2}(0)\left(t_i^{a2}(0)\right)^{-1} + \\ & \left(t_i^3(h) - t_i^1(h)\left(t_i^1(0)\right)^{-1} t_i^3(0)\right)\left(t_i^{a2}(0)\right)^{-1} \end{aligned} \tag{33}$$

The transfer matrix between the active pile tip and top (soil–water surface) due to the secondary wave can then be obtained:

$$\begin{Bmatrix} \overline{w}^{a2}(H) \\ \overline{\phi}^{a2}(H) \\ \overline{M}^{a2}(H) \\ \overline{Q}^{a2}(H) \\ 1 \end{Bmatrix} = T_1 \begin{Bmatrix} \overline{w}^{a2}(0) \\ \overline{\phi}^{a2}(0) \\ \overline{M}^{a2}(0) \\ \overline{Q}^{a2}(0) \\ 1 \end{Bmatrix} + T_2 \begin{Bmatrix} w^{p2}(0) \\ w^{p2}(0) \\ M^{p2}(0) \\ Q^{p2}(0) \\ 1 \end{Bmatrix} + T_3 \begin{Bmatrix} w^{a2}(0) \\ w^{a2}(0) \\ M^{a2}(0) \\ Q^{a2}(0) \\ 1 \end{Bmatrix} \tag{34}$$

where $T_1 = T_{n1} \cdots T_{i1} \cdots T_{21} T_{11}$, $T_2 = T_{n2} \cdots T_{i2} \cdots T_{22} T_{12}$, $T_3 = T_{n3} \cdots T_{i3} \cdots T_{23} T_{13}$.

### *2.4. Overall Dynamic Response of the Pile Group*

The transfer matrix of pile submerged in the seawater and pile embedded in the soil are obtained in Sections 2.3 and 2.4. According to the continuity condition at the water–soil interface, the dynamic response of these two pile parts can be connected, and the overall dynamic response of the pile can be obtained.

#### 2.4.1. Active Pile

For the active pile, the continuity condition is:

$$\begin{Bmatrix} w^{a2}(0) \\ \phi^{a2}(0) \\ M^{a2}(0) \\ Q^{a2}(0) \\ 1 \end{Bmatrix} = \begin{Bmatrix} w^{a1}(L_w) \\ \phi^{a1}(L_w) \\ M^{a1}(L_w) \\ Q^{a1}(L_w) \\ 1 \end{Bmatrix} \tag{35}$$

Substituting Equations (10) and (35) into Equation (16), the overall transfer matrix can be obtained:

$$\begin{Bmatrix} w^a(L) \\ \phi^a(L) \\ M^a(L) \\ Q^a(L) \\ 1 \end{Bmatrix} = \{T^{a2}\}\{T^{a1}\} \begin{Bmatrix} w^a(0) \\ \phi^a(0) \\ M^a(0) \\ Q^a(0) \\ 1 \end{Bmatrix} \tag{36}$$

Substituting boundary conditions:

$$\begin{aligned} M_{z=0} &= \left.\frac{d^2w(z)}{dz^2}\right|_{z=0} = 0 \\ Q_{z=0} &= \left.\frac{d^3w(z)}{dz^3}\right|_{z=0} = 0 \\ w_{z=L} &= w(z)\big|_{z=L} = 0 \\ \theta_{z=L} &= \left.\frac{dw(z)}{dz}\right|_{z=L} = 0 \end{aligned} \tag{37}$$

Equation (36) can then be solved, and the displacement, rotation angle, bending moment and the shearing force of the active pile top can be obtained; the value of single pile swaying impedance $K^*_{hh}$, rocking impedance $K^*_{rr}$, swaying-rocking impedance $K^*_{hr}$, and rocking-swaying impedance $K^*_{rh}$ can then be obtained.

2.4.2. Passive Pile

For the passive pile, the continuity condition is:

$$\begin{Bmatrix} w^{p2}(0) \\ \phi^{p2}(0) \\ M^{p2}(0) \\ Q^{p2}(0) \\ 1 \end{Bmatrix} = \begin{Bmatrix} w^{p1}(L_w) \\ \phi^{p1}(L_w) \\ M^{p1}(L_w) \\ Q^{p1}(L_w) \\ 1 \end{Bmatrix} \tag{38}$$

Substituting Equations (10), (11) and (38) into Equation (25), the overall transfer matrix can be obtained:

$$\begin{Bmatrix} w^{p}(L) \\ \phi^{p}(L) \\ M^{p}(L) \\ Q^{p}(L) \\ 1 \end{Bmatrix} = \left\{T_1^{p2}\right\}\left\{T^{p1}\right\}\begin{Bmatrix} w^{p}(0) \\ \phi^{p}(0) \\ M^{p}(0) \\ Q^{p}(0) \\ 1 \end{Bmatrix} + \left\{T_2^{p2}\right\}\left\{T^{a1}\right\}\begin{Bmatrix} w^{a}(0) \\ \phi^{a}(0) \\ M^{a}(0) \\ Q^{a}(0) \\ 1 \end{Bmatrix} \tag{39}$$

Substituting the solution to Equation (36) and boundary conditions (37), the equation can then be solved, and the displacement, rotation angle, bending moment, and the shearing force of the passive pile top can be obtained.

2.4.3. Active Pile under Secondary Wave

For the active pile under secondary wave:

$$\begin{Bmatrix} \overline{w}^{a2}(0) \\ \overline{\phi}^{a2}(0) \\ \overline{M}^{a2}(0) \\ \overline{Q}^{a2}(0) \\ 1 \end{Bmatrix} = \begin{Bmatrix} \overline{w}^{a1}(L_w) \\ \overline{\phi}^{a1}(L_w) \\ \overline{M}^{a1}(L_w) \\ \overline{Q}^{a1}(L_w) \\ 1 \end{Bmatrix} \tag{40}$$

Substituting Equations (10), (11) and (40) into Equation (34), the overall transfer matrix can be obtained:

$$\begin{Bmatrix} \overline{w}^{a}(L) \\ \overline{\phi}^{a}(L) \\ \overline{M}^{a}(L) \\ \overline{Q}^{a}(L) \\ 1 \end{Bmatrix} = T_1\{\overline{T}^{a1}\}\begin{Bmatrix} \overline{w}^{a}(0) \\ \overline{\phi}^{a}(0) \\ \overline{M}^{a}(0) \\ \overline{Q}^{a}(0) \\ 1 \end{Bmatrix} + T_2\{T^{p1}\}\begin{Bmatrix} w^{p}(0) \\ \phi^{p}(0) \\ M^{p}(0) \\ Q^{p}(0) \\ 1 \end{Bmatrix} + T_3\{T^{a1}\}\begin{Bmatrix} w^{a}(0) \\ \phi^{a}(0) \\ M^{a}(0) \\ Q^{a}(0) \\ 1 \end{Bmatrix} \tag{41}$$

Substituting the solutions to Equations (36) and (39), and boundary conditions (37), the equation can be solved. The displacement, rotation angle, bending moment, and the shearing force of the active pile top under the secondary wave can be obtained.

2.4.4. Pile–Pile Interaction and Pile Group Dynamic Response

The pile–pile interaction factor is defined as [31]:

$$\alpha^G = \frac{w^p}{w^a} \tag{42}$$

where $w_a$ is the displacement of the active pile and $w_p$ is the displacement of the passive pile. To reflect the influence of the passive pile to the active pile, the definition of the pile–pile interaction factor is modified as [32]:

$$\begin{array}{l} \alpha^G = \frac{w^p}{w^a - \overline{w}^a} = \frac{w^p}{(1-\kappa)w^a} \\ \kappa = \frac{\overline{w}^a}{w^a} \end{array} \tag{43}$$

where $\overline{w}_a$ is the displacement of active pile under secondary wave.

Suppose the number of piles of the pile group is n, the cap is rigid, and the mass of the cap is ignored. Under the lateral harmonic load $Pe^{i\omega t}$, the lateral displacement of the pile group $w^G$ can be considered equal to the displacement of each pile $w^i$, which means $w^1 = w^i = w^G$. In the pile group, each pile plays the role of both active pile and passive pile, so the single pile displacement can be calculated:

$$w^i = \left(1 - \sum_{j=1, j\neq i}^{n} \kappa_{ij}\right) w^i + \sum_{j=1, j\neq i}^{n} \alpha_{ij}^G w^j \tag{44}$$

The dynamic equation of the pile group can be written in matrix form:

$$\frac{1}{K_{hh}^*} \begin{bmatrix} 1 - \sum\limits_{j=1, j\neq 1}^{n} \kappa_{1j} & \alpha_{12}^G & \cdots & \alpha_{1n}^G \\ \alpha_{21}^G & 1 - \sum\limits_{j=1, j\neq 2}^{n} \kappa_{2j} & \cdots & \alpha_{2n}^G \\ \vdots & \vdots & \vdots & \vdots \\ \alpha_{n1}^G & \alpha_{n2}^G & \cdots & 1 - \sum\limits_{j=1, j\neq n}^{n} \kappa_{nj} \end{bmatrix} \begin{Bmatrix} P_1 \\ P_2 \\ \vdots \\ P_n \end{Bmatrix} = \begin{Bmatrix} w^1 \\ w^2 \\ \vdots \\ w^n \end{Bmatrix} \tag{45}$$

where $K_{hh}^*$ is the single pile impedance, which can be obtained by solving the Equation (36), $P_j$ is the load distributed to pile $j$, and $a_{ij}^G$ is the interaction factor between pile $i$ and $j$, $i \neq j$. The load applied to the pile group is the sum of the load applied to each pile:

$$P = \sum_{j=1}^{n} P_j \tag{46}$$

Then, Equation (45) can be solved, and the horizontal pile group impedance can be calculated:

$$K_G^* = P / w_G = K_G + iC_G \tag{47}$$

According to the previous research [31], the swaying interaction factor, the sway-rocking interaction factor, and the rock-swaying interaction factor between piles can be ignored. Therefore, $K_{rr}^*$, $K_{hr}^*$ $K_{rh}^*$ are the sum of single pile calculation results. The pile group impedance matrix can then be obtained:

$$K^* = \begin{Bmatrix} K_G^* & K_{hr}^* \\ K_{rh}^* & K_{rr}^* \end{Bmatrix} \tag{48}$$

### 2.5. Superstructure Dynamic Response

#### 2.5.1. Distributed Wind Load

The distributed wind load $F_d(z)$ can be calculated according to the equation below [33]:

$$F_d(z) = 1/2\rho_a C_D D_T(z) V^2(z) \tag{49}$$

where $\rho_d$ is the density of the air, valued 1.225 kg/m$^3$ in this paper, $C_D$ is the drag coefficient, valued according to the Reynolds number and structure surface roughness, i.e., 1.2 in this paper, $V$ (m/s) is the average wind speed, and $D_T$ (m) is the tower diameter, the value of which changes with increasing tower height.

The wind profile [34] can be calculated according to the following equation:

$$V(z) = V_a(\frac{z}{H_a})^{\alpha_w} \tag{50}$$

where $V_a$ is the wind speed at height $H_a$ and $\alpha_w$ is the power law coefficient, valued 0.12 in open seas with waves.

#### 2.5.2. Thrust Wind Load

The wind load applied to the blades and turbine will produce lateral load, which can be considered as the concentrated load $F_b$, calculated according to Equation (51) [35]:

$$F_b = 1/2\rho_a \pi R_T^2 V_T^2 C_T(\lambda_s) \tag{51}$$

where $V_T$ is the wind speed at the tower top, $R_T$ is the blade radius, and $C_T$ is the thrust coefficient, which is related to the tip speed ratio $\lambda_s$, as shown in Figure 5.

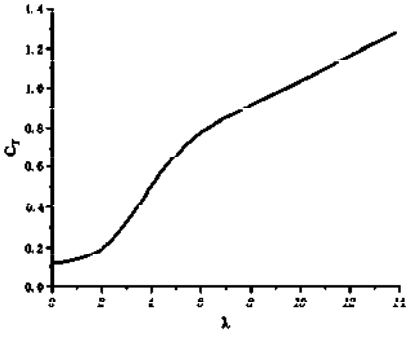


**Figure 5.** Thrust coefficient $C_T$-tip speed ratio $\lambda_s$ curve [35].

#### 2.5.3. Tower Dynamic Response

The tower can be divided into n segments, numbered 1~$n$ from the bottom to the top. As shown in Figure 6, for the $i$ ($i = 1, 2 \cdots n$)th segment, the number of its bottom point is $i$, and the number of its top point is $i + 1$. Consider each segment as equal cross-section beam, where $H_i$ is the length of the $i$th segment. $H_i$ is valued differently between segments to account for the varied cross-section geometry. The mass of each segment is concentrated to the bottom point, and the $2 \times 2$ mass matrix of each segment can be obtained, including the mass and moment of inertia. The mass of blades is considered as the concentrated mass point $m_{n+1}$ at the tower top. Similarly, the distributed loads applied to each segment are concentrated to the bottom point, and the load matrix of each segment can be obtained, including the force and bending moment. The load matrix at the tower top includes the thrust wind force.

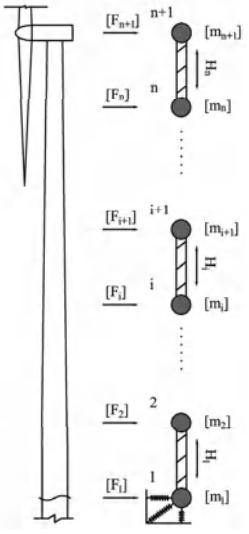


**Figure 6.** Tower discretization.

The swaying-rocking equation of this system with 2($n$+1) degrees of freedom can be written in matrix form [25]:

$$\begin{bmatrix} \overline{K}_{11} & \overline{K}_{12} & & & & & & \\ \overline{K}_{21} & \overline{K}_{22} & \overline{K}_{23} & & & & & \\ & \ddots & \ddots & \ddots & & & & \\ & & \overline{K}_{i,j-1} & \overline{K}_{i,j} & \overline{K}_{i,j+1} & & & \\ & & & \ddots & \ddots & \ddots & & \\ & & & & \overline{K}_{n,n-1} & \overline{K}_{n,n} & \overline{K}_{n,n+1} & \\ & & & & & \overline{K}_{n+1,n} & \overline{K}_{n+1,n+1} \end{bmatrix} \begin{Bmatrix} u_1 \\ u_2 \\ \vdots \\ u_i \\ \vdots \\ u_n \\ u_{n+1} \end{Bmatrix} = \begin{Bmatrix} F_1 \\ F_2 \\ \vdots \\ F_i \\ \vdots \\ F_n \\ F_{n+1} \end{Bmatrix} \tag{52}$$

where $u_i$ is the point displacement matrix, including the horizontal displacement and rotation angle. The stiffness in Equation (52) can be calculated according to equations below.

For the first line:

$$\overline{K}_{11} = K_{11} + K^* - \omega^2 m_1 \tag{53}$$

$$\overline{K}_{12} = K_{12} \tag{54}$$

For the second to $n$th line:

$$\overline{K}_{i,i-1} = K_{i,i-1} \tag{55}$$

$$\overline{K}_{i,i} = K_{i,i} - \omega^2 m_i \tag{56}$$

$$\overline{K}_{i,i+1} = K_{i,i+1} \tag{57}$$

For $n+1$th line:

$$\overline{K}_{n+1,n} = K_{n+1,n} \tag{58}$$

$$\overline{K}_{n+1,n+1} = K_{n+1,n+1} - \omega^2 m_{n+1} \tag{59}$$

where

$$K_{i,i-1} = \begin{bmatrix} -12E_pI_{i-1}/H_{i-1}^3 & -6E_pI_{i-1}/H_{i-1}^2 \\ 6E_pI_{i-1}/H_{i-1}^2 & 2E_pI_{i-1}/H_{i-1} \end{bmatrix} \tag{60}$$

$$K_{i,i} = \begin{bmatrix} 12E_pI_i/H_i^3 & 6E_pI_i/H_i^2 \\ 6E_pI_i/H_i^2 & 4E_pI_i/H_i \end{bmatrix} + \begin{bmatrix} 12E_pI_{i-1}/H_{i-1}^3 & -6E_pI_{i-1}/H_{i-1}^2 \\ -6E_pI_{i-1}/H_{i-1}^2 & 4E_pI_{i-1}/H_{i-1} \end{bmatrix} \tag{61}$$

$$K_{i,j+1} = \begin{bmatrix} -12E_pI_i/H_i^3 & 6E_pI_i/H_i^2 \\ -6E_pI_i/H_i^2 & 2E_pI_i/H_i \end{bmatrix} \quad (62)$$

When $i = 1$, Equation (60) is invalid, and the second part of Equation (61) should be removed. When $i = n + 1$, Equation (57) is invalid, and the first part of Equation (61) should be removed. Substitute the foundation impedance matrix $K^*$ into Equation (53), the equation can then be solved, and the displacement of the tower can be obtained.

## 3. Validation

The calculation result is compared with the FEM result to validate the correctness of the proposed calculation model. ABAQUS simulation software is used in this paper. A pile group supported OWT [25] is used for validation. The total mass of blades and turbine is 177.1 ton, and the tower is divided into three segments, as shown in Table 1. The pile group consists of seven piles, as shown in Figure 2. The pile diameter is 1.7 m and the pile wall thickness is 30 mm. The elastic modulus of the steel is 210 GPa and the density of the steel is 7800 kg/m$^3$. The pile length embedded in the soil is 30 m nad the pile length submerged in the seawater is 20 m. The elastic modulus of the soil is 40 MPa, the Poisson's ratio of the soil is 0.3, and the density of the soil is 1800 kg/m$^3$. As shown in Figure 7, the offshore wind turbine model is established.

**Table 1.** Tower parameters.

| Tower Parts | Length (m) | Bottom Diameter | Top Diameter | Tower Wall Thickness |
|---|---|---|---|---|
| Upper segment | 32 | 3.9 | 3.1 | 50 |
| Middle segment | 31 | 4.5 | 3.9 | 50 |
| Bottom segment | 15 | 4.5 | 4.5 | 50 |

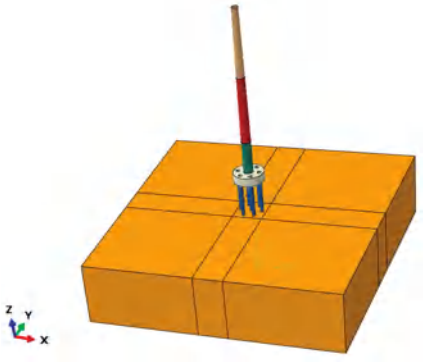


**Figure 7.** FEM numerical simulation model.

Since the overall displacement of the offshore wind turbine is relatively small, linear modal analysis is used to calculate its structure natural frequency. The deformation of soil foundation is also small during the dynamic analysis; therefore, the change of soil foundation stiffness is not considered, and the small strain linear elastic model is used for the soil.

For the tower, the eight-node S8R shell element is used. The tower is divided into three parts, as shown in Table 1. For each part, the tower diameter changes linearly with increasing height. To prevent the separation between tower parts, a bonding constraint is added between the interfaces, including the interface between the bottom tower part and the cap. The blades are simplified as the concentrated force applied to the tower top. The pile foundation is modeled as solid element to better simulate the pile–soil interaction. For the side face of the soil, the lateral displacement is constrained; for the bottom side of the

soil, displacements of all directions are constrained. The pile–soil interaction is set as small sliding, penalty contact, while the coefficient is set as 0.4.

The dead weight is applied to the model according to parameters presented in Table 1, and the wave load is also applied to the structure. Here, we use FORTRAN to write a subroutine to accurately input wave load according to Equation (4). The offshore wind turbine is fine meshed. As for the soil, the soil around the pile is refined, as shown in Figure 8.

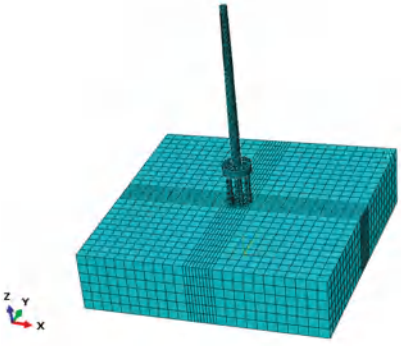


**Figure 8.** Meshing of the model.

After establishing the FEM model, the modal analysis is performed, and the first 10 structure natural frequencies are obtained. Here, we focus on the first lateral structure natural frequency. Then, we applied a 10 kN horizontal harmonic thrust wind load to the tower top, and the tower top displacement and load frequency curve can be obtained.

As shown in Figure 9, the FEM result and the calculating result are in good agreement, with only some differences being observed for the maximum tower displacement, which validates the correctness of the calculating result. The structure natural frequency can also be obtained from Figure 9, which falls within the "soft-stiff" design frequency range.

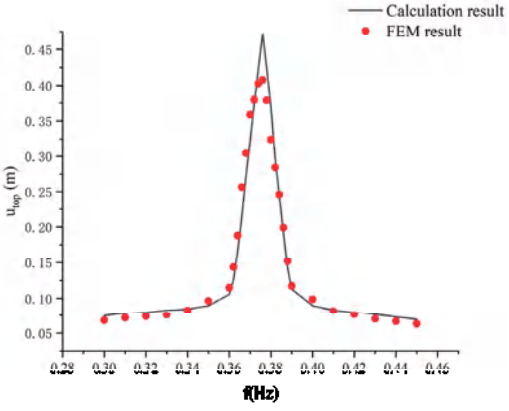


**Figure 9.** Comparison between the calculation result and FEM result.

## 4. Parametric Analysis

### *4.1. Tower Displacement*

The tower displacement under different wind speeds is studied. The wind speed at sea level is 4 m/s, 8 m/s, and 12 m/s, respectively. The percentage of the thrust wind load is 96.31%, and the percentage of the distributed wind load is 3.69%. As shown in Figure 10, the tower displacement is largely influenced by the wind speed. When the wind speed is 4 m/s, the increasing rate of tower displacement is relatively small. When the wind speed

is 8 m/s, the increasing rate rises to a certain degree. When the wind speed is 12 m/s, the increasing rate is significantly larger than the increasing rate when the wind speed is 4 m/s.

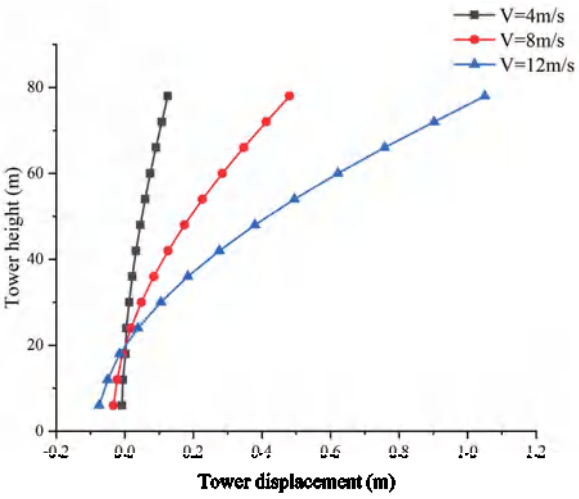


**Figure 10.** The influence of the wind speed on the tower displacement.

The influence of the foundation impedance on the tower displacement is also studied. Define $\alpha_K = K'^*/K^*$, where $K'^*$ is the modified foundation impedance matrix and $\alpha_K$ is valued from 0.1~2 to analyze the influence of the foundation impedance on the maximum tower displacement. As shown in Figure 11, when the foundation impedance is relatively small, the tower displacement is large. With increasing foundation impedance, the tower displacement decreases rapidly. Additionally, with increasing foundation impedance, the tower displacement decreasing speed slows. When the foundation impedance reaches 2.0 its original impedance, the tower displacement remains almost unchanged.

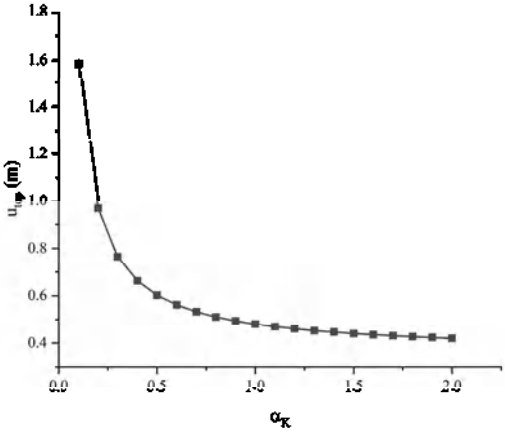


**Figure 11.** The influence of the foundation impedance on the tower displacement.

*4.2. Pile–Pile Interaction Factor*

The regressive solution (the pile is considered completely embedded in the soil) of the proposed calculation model is compared with the solution of Kaynia [36]. In this section, parameters below are used for calculation: the ratio of elastic modulus of the pile to elastic modulus of the soil $E_p/E_s = 1000$, the ratio of the pile length to the pile diameter

$L/D = 20$, and Poisson's ratio is 0.4. The ratio of the density of the pile to the density of the soil $\rho_p/\rho_s = 1.3$, while the damping ratio $\beta_s = 0.05$. The pile spacing $S = 2D$, the pile embedment ratio $L_w/L = 0.3$. The dimensionless frequency $a_0 = \omega D/V_s$ is used for analysis. Here, we consider the influence of three parameters on the pile–pile interaction factor: pile spacing, pile embedment ratio, and the angle of incidence $\theta$.

As shown in Figure 12, when the pile spacing $S/D = 10$, the calculating result of this paper and the result from the literature are in good agreement, which validates the correctness of the calculation method. When the pile spacing $S/D = 5$, some differences can be observed compared with the results from the literature. Furthermore, when $S/D = 2$, the difference becomes more significant, especially in low frequencies. This is because when the pile spacing decreases, the influence of the passive pile on the active pile is more significant, which changes the horizontal displacement of the active pile. This analysis demonstrates that when the pile spacing is small, the influence of the passive pile on the active pile is important and cannot be ignored.

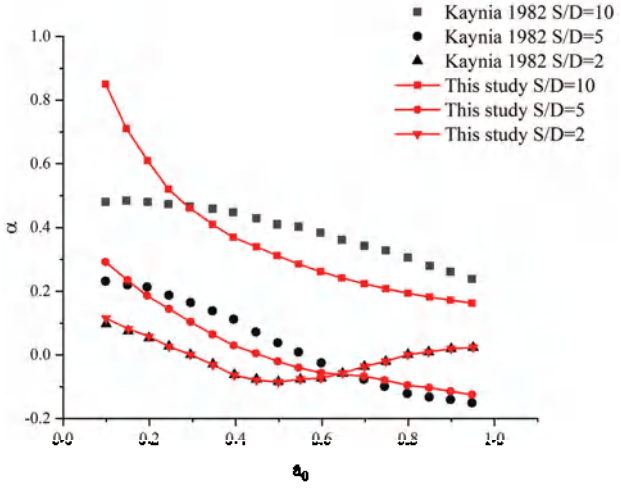


**Figure 12.** Pile–pile interaction under different pile spacings.

The influence of the pile embedded ratio is studied. As shown in Figure 13, when the pile is completely embedded, the pile–pile interaction factor decreases with increasing load frequency, and the value remains positive. When $L_w/L = 0.1$, the pile–pile interaction factor $\alpha$ at all frequencies largely decreases. When $L_w/L = 0.2$, $\alpha$ changes obviously. With increasing load frequency, $\alpha$ decreases rapidly when closing to a certain frequency and rises after reaching the lowest point. When $L_w/L = 0.3$, the curve moves from a mainly middle-high frequency to a middle-low frequency. This analysis demonstrates that $\alpha$ is sensitive to the pile embedment ratio. When the pile embedment ratio is relatively small, the change of $\alpha$ with increasing frequency is simple; when the pile embedment ratio is relatively large, the change of $\alpha$ becomes complex.

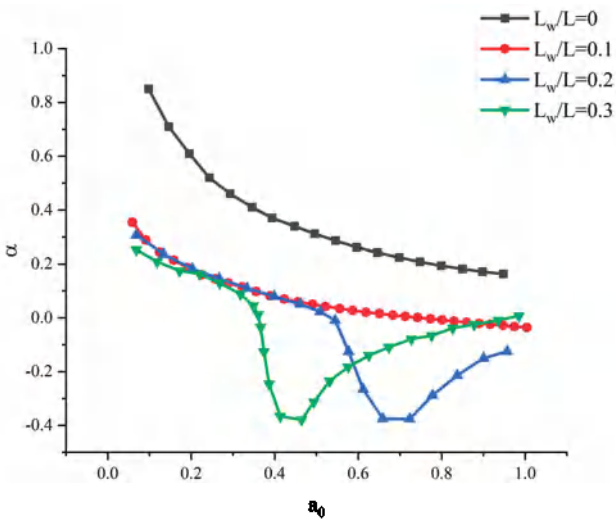


**Figure 13.** Pile–pile interaction under different pile embedded ratios.

The influence of different incidences angle $\theta$ is studied, i.e., $0^\circ$, $45^\circ$, and $90^\circ$, respectively. As shown in Figure 14, when $\theta = 0^\circ$, the curve fluctuates significantly, the minimum value of $\alpha$ is the smallest among three angles, and the maximum value of $\alpha$ is the largest among three angles. When $\theta = 90^\circ$, the value of $\alpha$ is slightly smaller than that of $\theta = 0^\circ$. When $\theta = 45^\circ$, the change of $\alpha$ is moderate, and no significant fluctuation is observed.

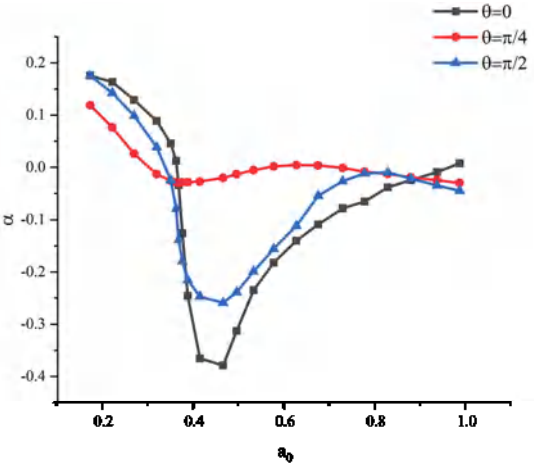


**Figure 14.** Pile–pile interaction under different incidence angles.

*4.3. Dynamic Foundation Impedance*

As shown in Figure 15, with increasing load frequency, the change of horizonal foundation impedance is not obvious. When the load frequency is around soil cut-off frequency, the horizontal foundation impedance slightly decreases. The foundation impedance is very sensitive to the pile length submerged in the seawater. With an increasing pile embedment ratio, the foundation impedance decreases significantly.

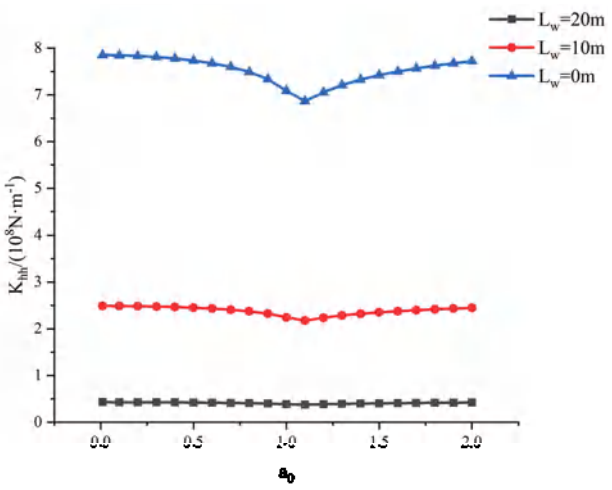


**Figure 15.** The influence of the pile length in seawater on the foundation impedance.

Meanwhile, the wave load can influence the foundation impedance to a certain degree. As shown in Figure 16, when the wave load is relatively small (wavelength $L_{wl} = 75$ m, wave height $H_w = 4$ m), the influence of wave load on the foundation impedance is not significant. When the wave load is relatively large (wavelength $L_{wl} = 120$ m, wave height $H_w = 8$ m), the influence of wave load on the foundation impedance is significant.

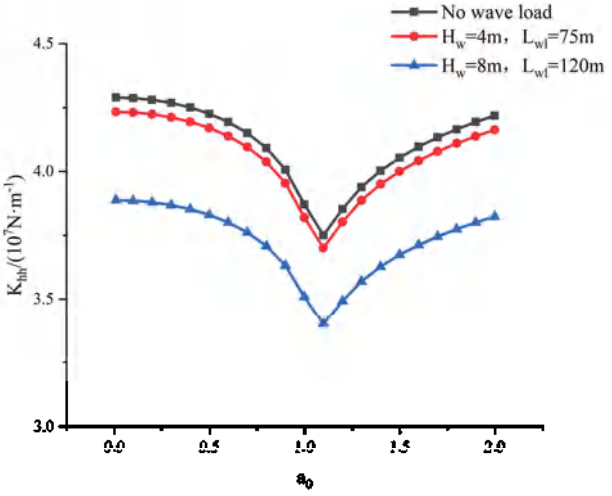


**Figure 16.** The influence of the wave load on the foundation impedance.

## 5. Conclusions

This paper establishes the model of pile group supported OWT under wind and wave load; the main findings are presented below:

(1) With increasing wind speed, the tower displacement increases significantly. The influence of foundation impedance on the tower displacement is more significant when the foundation impedance is relatively small.

(2) The pile–pile interaction factor depends largely on the pile spacing. When the pile spacing is large, the influence of the passive pile on the active pile can be ignored; when the pile spacing is small, a secondary wave effect should be considered for the pile–pile interaction factor.

(3) When the pile embedded ratio is large, the pile–pile interaction is more obvious. When the incidence angle is 45°, the pile–pile interaction is less significant compared with that of 0° and 90°.
(4) The foundation impedance decreases significantly with an increasing pile embedment ratio.
(5) The influence of wave load on the foundation impedance is more obvious when the wave load is large.

**Author Contributions:** Conceptualization, W.Y.; Data curation, Y.S.; Formal analysis, Y.S.; Funding acquisition, W.Y.; Investigation, G.Y.; Methodology, Y.S.; Project administration, G.Y.; Resources, G.Y.; Software, Y.S.; Supervision, W.Y.; Validation, Y.S.; Visualization, Y.S.; Writing—original draft, Y.S.; Writing—review and editing, Y.S. and W.Y. All authors have read and agreed to the published version of the manuscript.

**Funding:** This study was financially supported by the Key Projects of the National Natural Science Foundation of China (Grant No. 11932010).

**Institutional Review Board Statement:** Not applicable.

**Informed Consent Statement:** Not applicable.

**Data Availability Statement:** Not applicable.

**Conflicts of Interest:** The authors declare no conflict of interest.

## Appendix A

$$\{t_i^{q1}\} = \begin{Bmatrix} e^{(-1+i)\gamma z} & e^{(-1-i)\gamma z} & e^{(1-i)\gamma z} & e^{(1+i)\gamma z} & q'_G(z) \\ (-1+i)\gamma e^{(-1+i)\gamma z} & (-1-i)\gamma e^{(-1-i)\gamma z} & (1-i)\gamma e^{(1-i)\gamma z} & (1+i)\gamma e^{(1+i)\gamma z} & K\frac{\sinh(Kz)}{\cosh(Kz)}q'_G(z) \\ (-1+i)^2\gamma^2 e^{(-1+i)\gamma z} & (-1-i)^2\gamma^2 e^{(-1-i)\gamma z} & (1-i)^2\gamma^2 e^{(1-i)\gamma z} & (1+i)^2\gamma^2 e^{(1+i)\gamma z} & K^2 q'_G(z) \\ (-1+i)^3\gamma^3 e^{(-1+i)\gamma z} & (-1-i)^3\gamma^3 e^{(-1-i)\gamma z} & (1-i)^3\gamma^3 e^{(1-i)\gamma z} & (1+i)^3\gamma^3 e^{(1+i)\gamma z} & K^3\frac{\sinh(Kz)}{\cosh(Kz)}q'_G(z) \\ 0 & 0 & 0 & 0 & 1 \end{Bmatrix}$$

$$\{t_i^{q2}\} = \begin{Bmatrix} e^{(-1+i)\gamma z} & e^{(-1-i)\gamma z} & e^{(1-i)\gamma z} & e^{(1+i)\gamma z} & 0 \\ (-1+i)\gamma e^{(-1+i)\gamma z} & (-1-i)\gamma e^{(-1-i)\gamma z} & (1-i)\gamma e^{(1-i)\gamma z} & (1+i)\gamma e^{(1+i)\gamma z} & 0 \\ (-1+i)^2\gamma^2 e^{(-1+i)\gamma z} & (-1-i)^2\gamma^2 e^{(-1-i)\gamma z} & (1-i)^2\gamma^2 e^{(1-i)\gamma z} & (1+i)^2\gamma^2 e^{(1+i)\gamma z} & 0 \\ (-1+i)^3\gamma^3 e^{(-1+i)\gamma z} & (-1-i)^3\gamma^3 e^{(-1-i)\gamma z} & (1-i)^3\gamma^3 e^{(1-i)\gamma z} & (1+i)^3\gamma^3 e^{(1+i)\gamma z} & 0 \\ 0 & 0 & 0 & 0 & 1 \end{Bmatrix}$$

$$\left\{t_i^{p2}\right\} = \frac{(k+i\omega c)\psi}{E_p I_p} \begin{Bmatrix} z(1-i)e^{(-1+i)\gamma z} & z(1+i)e^{(-1-i)\gamma z} \\ (1-i)e^{(-1+i)\gamma z} + z(2i\gamma)e^{(-1+i)\gamma z} & (1+i)e^{(-1-i)\gamma z} + z(-2i\gamma)e^{(-1-i)\gamma z} \\ (4i\gamma)e^{(-1+i)\gamma z} - 2z(i+1)\gamma^2 e^{(-1+i)\gamma z} & (-4i\gamma)e^{(-1-i)\gamma z} + 2z(i-1)\gamma^2 e^{(-1-i)\gamma z} \\ -6(i+1)\gamma^2 e^{(-1+i)\gamma z} + 4z\gamma^3 e^{(-1+i)\gamma z} & 6(i-1)\gamma^2 e^{(-1-i)\gamma z} + 4z\gamma^3 e^{(-1-i)\gamma z} \\ 0 & 0 \\ z(-1+i)e^{(1-i)\gamma z} & z(-1-i)e^{(1+i)\gamma z} \quad 0 \\ (-1+i)e^{(1-i)\gamma z} + z(2i\gamma)e^{(1-i)\gamma z} & (-1-i)e^{(1+i)\gamma z} + z(-2i\gamma)e^{(1+i)\gamma z} \quad 0 \\ (4i\gamma)e^{(1-i)\gamma z} + 2z(i+1)\gamma^2 e^{(1-i)\gamma z} & (-4i\gamma)e^{(1+i)\gamma z} - 2(i-1)\gamma^2 z e^{(1+i)\gamma z} \quad 0 \\ 6(i+1)\gamma^2 e^{(1-i)\gamma z} + 4z\gamma^3 e^{(1-i)\gamma z} & -6(i-1)\gamma^2 e^{(1+i)\gamma z} + 4\gamma^3 z e^{(1+i)\gamma z} \quad 0 \\ 0 & 0 \quad 1 \end{Bmatrix}$$

$$\left\{\bar{t}_i^{a2}\right\} = \frac{(k+i\omega c)\psi}{512E_pI_p\gamma^6}\left\{\begin{array}{r} -2iz^2e^{(-1+i)\gamma z} \\ -4ize^{(-1+i)\gamma z} + 2(i+1)\gamma z^2e^{(-1+i)\gamma z} \\ -4ie^{(-1+i)\gamma z} + 8(i+1)\gamma ze^{(-1+i)\gamma z} - 4\gamma^2z^2e^{(-1+i)\gamma z} \\ 12(1+i)\gamma e^{(-1+i)\gamma z} - 24\gamma^2ze^{(-1+i)\gamma z} + 4(1-i)\gamma^3z^2e^{(-1+i)\gamma z} \\ 0 \\ 2iz^2e^{(-1-i)\gamma z} \\ 4ize^{(-1-i)\gamma z} + 2(1-i)\gamma z^2e^{(-1-i)\gamma z} \\ 4ie^{(-1-i)\gamma z} + 8(1-i)\gamma ze^{(-1-i)\gamma z} - 4\gamma^2z^2e^{(-1-i)\gamma z} \\ 12(1-i)\gamma e^{(-1-i)\gamma z} - 24\gamma^2ze^{(-1-i)\gamma z} + 4(1+i)\gamma^3z^2e^{(-1-i)\gamma z} \\ 0 \\ -2iz^2e^{(1-i)\gamma z} \\ -4ize^{(1-i)\gamma z} - 2(i+1)\gamma z^2e^{(1-i)\gamma z} \\ -4ie^{(1-i)\gamma z} - 8(i+1)\gamma ze^{(1-i)\gamma z} - 4\gamma^2z^2e^{(1-i)\gamma z} \\ -12(1+i)\gamma e^{(1-i)\gamma z} - 24\gamma^2ze^{(1-i)\gamma z} - 4(1-i)\gamma^3z^2e^{(1-i)\gamma z} \\ 0 \end{array}\right.$$

$$\left.\begin{array}{rr} 2iz^2e^{(1+i)\gamma z} & 0 \\ -4ize^{(1+i)\gamma z} + 2(i-1)\gamma z^2e^{(1+i)\gamma z} & 0 \\ -4ie^{(1+i)\gamma z} + 8(1-i)\gamma ze^{(1+i)\gamma z} + 4\gamma^2z^2e^{(1+i)\gamma z} & 0 \\ 12(1-i)\gamma e^{(1+i)\gamma z} + 24\gamma^2ze^{(1+i)\gamma z} + 4(1+i)\gamma^3z^2e^{(1+i)\gamma z} & 0 \\ 0 & 1 \end{array}\right\}$$

## References


1. Feyzollahzadeh, M.; Mahmoodi, M.; Yadavar-Nikravesh, S.; Jamali, J. Wind load response of offshore wind turbine tow-ers with fixed monopile platform. *J. Wind Eng. Ind. Aerodyn.* **2016**, *158*, 122–138. [CrossRef]
2. Zheng, X.Y.; Li, H.; Rong, W.; Li, W. Joint earthquake and wave action on the monopile wind turbine foundation: An experimental study. *Mar. Struct.* **2015**, *44*, 125–141. [CrossRef]
3. Gupta, B.K.; Basu, D. Offshore wind turbine monopile foundations: Design perspectives. *Ocean Eng.* **2020**, *213*, 107514. [CrossRef]
4. Bhattacharya, S. Challenges in Design of Foundations for Offshore Wind Turbines. *Eng. Technol. Ref.* **2014**, *1*, 922. [CrossRef]
5. Lombardi, D.; Bhattacharya, S.; Wood, D.M. Dynamic soil–structure interaction of monopile supported wind turbines in cohesive soil. *Soil Dyn. Earthq. Eng.* **2013**, *49*, 165–180. [CrossRef]
6. Damgaard, M.; Bayat, M.; Andersen, L.; Ibsen, L. Assessment of the dynamic behaviour of saturated soil subjected to cyclic loading from offshore monopile wind turbine foundations. *Comput. Geotech.* **2014**, *61*, 116–126. [CrossRef]
7. Bouzid, D.A.; Bhattacharya, S.; Otsmane, L. Assessment of natural frequency of installed offshore wind turbines using nonlinear finite element model considering soil-monopile interaction. *J. Rock Mech. Geotech. Eng.* **2018**, *10*, 333–346. [CrossRef]
8. Alkhoury, P.; Soubra, A.H.; Rey, V.; Aït-Ahmed, M. A full three-dimensional model for the estimation of the natural fre-quencies of an offshore wind turbine in sand. *Wind Energy* **2021**, *24*, 699–719. [CrossRef]
9. Kjørlaug, R.A.; Kaynia, A.M. Vertical earthquake response of megawatt-sized wind turbine with soil-structure interaction effects. *Earthq. Eng. Struct. Dyn.* **2015**, *44*, 2341–2358. [CrossRef]
10. Corciulo, S.; Zanoli, O.; Pisanò, F. Transient response of offshore wind turbines on monopiles in sand: Role of cyclic hy-dro–mechanical soil behaviour. *Comput. Geotech.* **2017**, *83*, 221–238. [CrossRef]
11. Zuo, H.; Bi, K.; Hao, H. Dynamic analyses of operating offshore wind turbines including soil-structure interaction. *Eng. Struct.* **2018**, *157*, 42–62. [CrossRef]
12. Galvín, P.; Romero, A.; Solís, M.; Domínguez, J. Dynamic characterisation of wind turbine towers account for a monopile foundation and different soil conditions. *Struct. Infrastruct. Eng.* **2017**, *13*, 942–954. [CrossRef]
13. Kausel, E. Early history of soil–structure interaction. *Soil Dyn. Earthq. Eng.* **2010**, *30*, 822–832. [CrossRef]
14. Reese, L.C. Non-dimensional solutions for laterally loaded piles with soil modulus assumed proportional to depth. In Proceedings of the 8th Texas Conference on Soil Mechanics and Foundation Engineering, Austin, TX, USA, 14–15 September 1956.
15. McClelland, B.; Focht, J. Soil modulus for laterally loaded piles. *J. Soil Mech. Found. Div.* **1956**, *82*, 1081-1–1081-22. [CrossRef]
16. Darvishi-Alamouti, S.; Bahaari, M.R.; Moradi, M. Natural frequency of offshore wind turbines on rigid and flexible monopiles in cohesionless soils with linear stiffness distribution. *Appl. Ocean Res.* **2017**, *68*, 91–102. [CrossRef]
17. Andersen, L.V.; Vahdatirad, M.; Sichani, M.T.; Sørensen, J.D. Natural frequencies of wind turbines on monopile founda-tions in clayey soils—A probabilistic approach. *Comput. Geotech.* **2012**, *43*, 1–11. [CrossRef]
18. Adhikari, S.; Bhattacharya, S. Vibrations of wind-turbines considering soil-structure interaction. *Wind Struct. Int. J.* **2011**, *14*, 85–112. [CrossRef]

19. Adhikari, S.; Bhattacharya, S. Dynamic Analysis of Wind Turbine Towers on Flexible Foundations. *Shock Vib.* **2012**, *19*, 37–56. [CrossRef]
20. Bhattacharya, S.; Adhikari, S. Experimental validation of soil–structure interaction of offshore wind turbines. *Soil Dyn. Earthq. Eng.* **2011**, *31*, 805–816. [CrossRef]
21. Nogami, T.; Paulson, S.K. Transfer matrix approach for nonlinear pile group response analysis. *Int. J. Numer. Anal. Methods Geomech.* **1985**, *9*, 299–316. [CrossRef]
22. Zhang, L.; Gong, X.-N.; Yang, Z.-X.; Yu, J.-L. Elastoplastic solutions for single piles under combined vertical and lateral loads. *J. Cent. South Univ. Technol.* **2011**, *18*, 216–222. [CrossRef]
23. Zhang, L.; Zhao, M.; Zou, X. Behavior of Laterally Loaded Piles in Multilayered Soils. *Int. J. Géoméch.* **2015**, *15*, 06014017. [CrossRef]
24. Wang, M.; Wang, Z.; Zhao, H. Analysis of Wind-Turbine Steel Tower by Transfer Matrix. In Proceedings of the 2009 International Conference on Energy and Environment Technology, Guilin, China, 16–18 October 2009.
25. Huang, M.; Zhong, R. Coupled horizontal-rocking vibration pf partially embedded pile groups and its effect on resonance of offshore wind turbine structures. *Chinsese J. Geotech. Eng.* **2014**, *36*, 286–294.
26. Anoyatis, G.; Mylonakis, G.; Lemnitzer, A. Soil reaction to lateral harmonic pile motion. *Soil Dyn. Earthq. Eng.* **2016**, *87*, 164–179. [CrossRef]
27. Anoyatis, G.; Lemnitzer, A. Dynamic pile impedances for laterally–loaded piles using improved Tajimi and Winkler for-mulations. *Soil Dyn. Earthq. Eng.* **2017**, *92*, 279–297. [CrossRef]
28. Shuqing, W.; Bingchen, L. *Wave Mechanics for Ocean Engineering*; China Ocean University Press: Qingdao, China, 2013. (In Chinese)
29. Xin-xin, L.; Da-peng, S.; Xue-jiao, X.; Hao, W.; Yu-cheng, L. Experimental study of irregular wave force loads on high rise pile platform. *J. Waterw. Harb.* **2013**, *34*, 277–284. (In Chinese)
30. Dobry, R.; Gazetas, G. Dynamic Response of Arbitrarily Shaped Foundations. *J. Geotech. Eng.* **1986**, *112*, 109–135. [CrossRef]
31. Mylonakis, G.; Gazetas, G. Lateral Vibration and Internal Forces of Grouped Piles in Layered Soil. *J. Geotech. Geoenvironmental Eng.* **1999**, *125*, 16–25. [CrossRef]
32. Luan, L.; Zheng, C.; Kouretzis, G.; Ding, X. Dynamic analysis of pile groups subjected to horizontal loads considering coupled pile-to-pile interaction. *Comput. Geotech.* **2020**, *117*, 103276. [CrossRef]
33. Van Binh, L.; Ishihara, T.; Van Phuc, P.; Fujino, Y. A peak factor for non-Gaussian response analysis of wind turbine tower. *J. Wind Eng. Ind. Aerodyn.* **2008**, *96*, 2217–2227. [CrossRef]
34. Veritas, N. *Environmental Conditions and Environmental Loads*; Det Norske Veritas Oslo: Høvik, Norway, 2000.
35. Jara, F.A.V. *Model Testing of Foundations for Offshore Wind Turbines*; Oxford University: Oxford, UK, 2006.
36. Kaynia, A.M. *Dynamic Stiffness and Seismic Response of Pile Groups*; Massachusetts Institute of Technology: Cambridge, MA, USA, 1982.

Journal of
*Marine Science and Engineering*

MDPI

*Article*

# Topology Optimization-Driven Design for Offshore Composite Wind Turbine Blades

**Jian Song *, Junying Chen, Yufei Wu and Lixiao Li ***

College of Civil and Transportation Engineering, Shenzhen University, Shenzhen 518060, China
* Correspondence: jiansong@szu.edu.cn (J.S.); llxiao2021@gmail.com (L.L.)

**Abstract:** With the increase in wind turbine power, the size of the blades is significantly increasing to over 100 m. It is becoming more and more important to optimize the design for the internal layout of large-scale offshore composite wind turbine blades to meet the structural safety requirements while improving the blade power generation efficiency and achieving light weight. In this work, the full-scale internal layout of an NREL 5 MW offshore composite wind turbine blade is elaborately designed via the topology optimization method. The aerodynamic wind loads of the blades were first simulated based on the computational fluid dynamics. Afterwards, the variable density topology optimization method was adopted to perform the internal structure design of the blade. Then, the first and second generation multi-web internal layouts of the blade were reversely designed and evaluated in accordance with the stress level, maximum displacement of blade tip and fatigue life. In contrast with the reference blade, the overall weight of the optimized blade was reduced by 9.88% with the requirements of stress and fatigue life, indicating a better power efficiency. Finally, the vibration modal and full life cycle of the designed blade were analyzed. The design conception and new architecture could be useful for the improvement of advanced wind turbines.

**Keywords:** offshore wind turbine blade; composites; computational fluid dynamics; topology optimization; fatigue life

**Citation:** Song, J.; Chen, J.; Wu, Y.; Li, L. Topology Optimization-Driven Design for Offshore Composite Wind Turbine Blades. *J. Mar. Sci. Eng.* **2022**, *10*, 1487. https://doi.org/10.3390/jmse10101487

Academic Editors: Eugen Rusu, Kostas Belibassakis and George Lavidas

Received: 28 March 2022
Accepted: 1 August 2022
Published: 13 October 2022

**Publisher's Note:** MDPI stays neutral with regard to jurisdictional claims in published maps and institutional affiliations.

**Copyright:** © 2022 by the authors. Licensee MDPI, Basel, Switzerland. This article is an open access article distributed under the terms and conditions of the Creative Commons Attribution (CC BY) license (https://creativecommons.org/licenses/by/4.0/).

## 1. Introduction

Wind energy is one of the most mature forms of renewable energy and is an effective strategy to alleviate energy shortages, reduce environmental pollution and improve climate conditions [1–3]. The utilization of onshore wind energy has encountered bottlenecks due to the restriction of land wind resources, noise and environmental pollution. Hence, in the last two decades, offshore wind farms have been rapidly growing. In 2021, new installations of more than 6 GW were generated all over the world [4]. For the offshore wind turbine, the blade is one of the most important components to convert wind kinetic energy into electrical energy. However, approximately 20% of the failures in wind turbine components occurs in the blades [5,6]. Nowadays, the blade length in offshore wind turbines has dramatically grown over 100 m, resulting in major concerns about the blades' resistance to damage over a life period of 20–25 years [7]. Compared to the onshore wind turbine blades, offshore wind turbine blade damage may happen in different parts due to static, vibration and fatigue loadings [8,9]. Moreover, it is great of importance to lighten the weight of the blades to reduce transportation costs.

Extensive studies for the design of the optimal offshore wind turbine blades have been carried out in recent years [10–13]. Each blade includes skin and web structures, where the skin structure determines the aerodynamic characteristics and the web structure provides the stiffness and strength requirements of the blade. Naung et al. [14] proposed a highly efficient nonlinear frequency-domain solution approach for elaborating the aerodynamic and aeromechanical performances of an oscillating wind turbine blade aerofoil. In comparison to the time-domain method, the frequency-domain method was not only

accurate but also computationally very efficient as the computation time was declined by 90%. Furthermore, Naung et al. [15] also investigated the influence of the wake of neighboring turbines on the aerodynamics of a wind turbine within windfarms based on the aforesaid frequency-domain method. The corresponding conclusions had been also obtained, namely that the frequency-domain solution method provided accurate results while reducing the computational cost by one to two orders of magnitude in comparison with the conventional time-domain method. In addition, Nakhchi and Naung et al. [16] also developed direct numerical simulations (DNS) to reveal the aerodynamic performance, transition to turbulence, and to capture the laminar separation bubble occurring on a wind turbine blade. Mamouri et al. [17,18] designed different shapes of wind turbine airfoil by incorporating entropy generation analysis. Chen et al. [19] performed the lay-up thickness size optimization for a 2 MW composite wind turbine blade with the objective of mass saving based on the particle swarm optimization method. Yet, only the blade stiffness and blade tip displacement were considered, and the extension of weight reduction was limited in accordance with the change of lay-up thickness. Ghiasi et al. [20] carried out the optimization design for the lay-up selection of a composite wind turbine blade with the objective of maximum stiffness. The results found that gradient-based methods were faster than others, but the optimal solution may be a local optimal value. In addition to the composite skin optimization, Zhang et al. [21] compared the maximum deformation, frequency and stress between the single-web and twin-web structures inside an 8 MW wind turbine blade, and the results showed that it was better to choose the twin-web structure form for large-size wind turbine blades. Liao et al. [22] employed an improved particle swarm algorithm (PSA) with the FAST program to optimize the thickness and location of the layers in the spar caps of wind turbine blades. The comparison of the results between the optimal and reference blades indicated that the optimization method was a feasible strategy to obtain the global optimization solution. The aforementioned studies focused on the local structural optimization design of wind turbine blades, whereas investigations on the structural optimization design of blades with the objective of weight reduction are considerably insufficient.

In the structural optimization design, topology optimization design is an effective way to obtain a reasonable internal layout of the blade, which can provide a new configuration and solution for engineering structural design [23]. Nowadays, the main topology optimization methods include the variable thickness method [24], homogenization method [25] and variable density method [26]. Generally, the variable thickness method and homogenization method are basically used for comparatively simple structures. For the variable density method, it has been integrated in finite element simulation software, i.e., ANSYS Workbench. Joncas et al. [27] adopted the topology optimization method to design the end part configuration of a thermoplastic composite wind turbine blade under waving moment and pendulum moment loading. Burton et al. [28] also adopted the topology optimization method to design the inner-surface structures of a wind turbine blade, and the optimization configuration was a non-prismatic structure. Yu et al. [29] designed a novel honeycomb-filled main beam cavity of a wind turbine blade based on the variable density topology optimization method [26], and a reasonable layout of honeycomb cells was obtained and the weight of the optimal blade was reduced by 8.41%. Zhang et al. [30] used the variable density topology optimization method to optimize the thickness and location of the main beam and twin-web of a wind turbine blade, and the optimal configuration showed that the webs play a key supporting role for maintaining the aerodynamic shape of the blade and the overall weight of blade obviously decreased though the dimension and location of the inner webs. However, the challenges remain about how many webs should be placed in the blades and the layout of the related webs.

To address this, Aage et al. [31] adopted the variable density topology optimization method to successfully design the internal structure of an aeroplane wing based on the full-scale internal structure. From this viewpoint, in this work, we report the design of the internal layout of a 5 MW offshore wind turbine blade with the objective of maximum

stiffness using the variable density topology optimization method. The aerodynamic loads of blades were obtained though computational fluid dynamics (CFD) simulation. Afterwards, the internal structure of the blade was optimized using the variable density topology optimization, and two multi-web internal layouts were obtained through the reverse design inspired by the topology optimization results. Finally, by validating the performance indexes with respect to stress level, maximum displacement and fatigue life, the multi-web structural layout of the second generation optimal wind turbine blade was an optimal feasible structure, which answered the key scientific issues of how many webs should be placed inside the blade and where to array the related webs. We hope the design method and findings could provide novel and efficient routes to high-performance offshore wind turbine blades.

## 2. Analytical Preliminaries

### 2.1. Topology Optimization Method

The variable density topology optimization problem [32] can be expressed as follows:

$$\begin{aligned} &\min_{\rho_e} \phi(\rho) = U^T K U = \sum_{e=1}^{N} (\rho_e)^P u_e^T k_0 u_e \\ &s.t. \begin{cases} KU = F \\ \sum\limits_{e=1}^{N} \rho_e V_e \le V^*, 0 \le \rho_{\min} \le \rho_e \le 1 \end{cases} \end{aligned} \tag{1}$$

where $\phi$ means a sum of each element's compliance. $U$, $K$ and $F$ mean the global displacement, stiffness matrix and force vectors, respectively. $k_0$ and $u_e$ mean the element stiffness matrix and displacement vector. $\rho$ means the design variable vector, viz element density vector. $N$ means the element amount of design domain. $V_e$ and $V^*$ mean the unit element volume and total volume for the design domain. To make sure of the numerically stable iteration, $\rho_{\min} = 0.001$ is chosen as the lower limitation of design variable. Additionally, a convolution-type filtering operation is used to filter the holes, viz.

$$\rho_e = \frac{\sum_{i \in N_e} w(r_i, r_e) v_i x_i}{\sum_{i \in N_e} w(r_i, r_e) v_i} \tag{2}$$

where $N_e = \{ i \| r_i - r_e \| \le R \}$ means a neighborhood set within the radius, $R$. $r_i$ and $r_e$ mean the spatial central coordinate of elements $i$ and $e$, respectively. $w(r_i, r_e) = R - \| r_i - r_e \|$ means the weighting function. $v_i$ is the volume of element $i$.

### 2.2. CFD Model of Reference Composite Wind Turbine Blade

#### 2.2.1. Control Equation, Geometric Model of Composite Wind Turbine Blade and Flow Field for CFD Simulation

In this work, the Navier–Stokes equation (RANS) based on Reynolds stress averaging was used to solve the flow field of the wind turbine blade, see Equation (1).

$$\frac{\partial}{\partial t}(\rho \vec{u}) + \nabla \cdot (\rho \vec{u} \vec{u}) = -\nabla p + \nabla \left( \mu \left( \nabla \vec{u} + \nabla \vec{u}^T \right) - \frac{2}{3} \mu (\nabla \cdot \vec{u}) \right) + \vec{F} \tag{3}$$

where $\vec{F}$ is the external force applied to the fluid.

The wind turbine in this work is the NREL offshore 5 MW baseline wind turbine developed by National Renewable Energy Laboratory (NREL) [33]. The length of composite blade in the NREL 5 MW machine is about 61.63 m. The blade is artificially divided into 17 airfoils from the root to the tip, namely: Cylinder, Du40, Du35, Du30, Du25, Du21 and NACA64, respectively. Note: The detailed geometric parameters corresponding to the aforesaid airfoils can be found in Table S1, Supporting Information (SI).

The geometric model of the composite wind turbine blade can be established as follows: ① Translate the aerodynamic center of the airfoil to the coordinate origin; ② Rotate and

transform the airfoil coordinate in accordance with the twist and chord; ③ Calculate the 3D coordinate of nodes using the following equation:

$$\begin{cases} x' = c \cdot \frac{|x - x_{\text{Aero}}|}{x - x_{\text{Aero}}} \sqrt{(x - x_{\text{Aero}})^2 + y^2} \cos\left(\arctan\frac{y}{x - x_{\text{Aero}}} + \beta\right) \\ y' = c \cdot \frac{|x - x_{\text{Aero}}|}{x - x_{\text{Aero}}} \sqrt{(x - x_{\text{Aero}})^2 + y^2} \sin\left(\arctan\frac{y}{x - x_{\text{Aero}}} + \beta\right) \\ z = r \end{cases} \quad (4)$$

where $x$ and $y$ mean the normalized coordinates; $x'$ and $y'$ mean the 3D coordinates; $x_{\text{Aero}}$ means the aerodynamic center of the airfoil to the coordinate origin; $c$ and $\beta$ mean the chord and twist. Based on the aforesaid method, the 3D geometric model of composite wind turbine blade can be established using the Siemens NX 10.0 software, see Figure 1a,b.

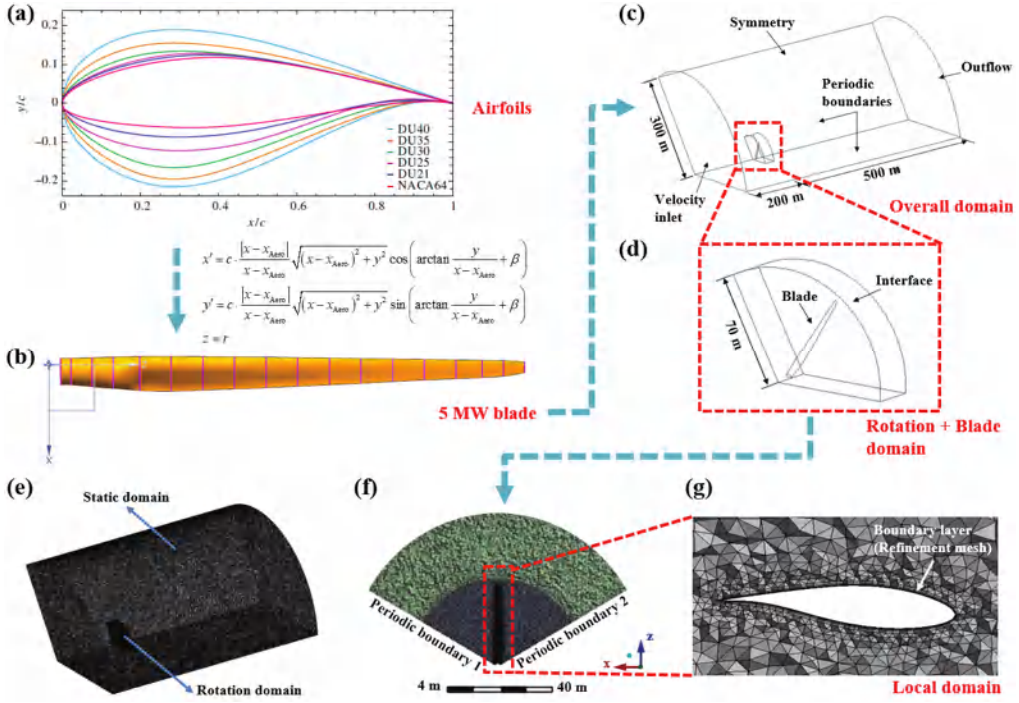


**Figure 1.** Establishment of 5 MW wind turbine blade. (**a**) Normalized section data of airfoils. (**b**) Wind turbine blade. (**c**) Geometric overall domain. (**d**) Geometric rotation and blade domains. (**e**,**f**) Stereogram and side view of fluent mesh models. (**g**) Local fluent mesh view of blade.

The flow domain for the CFD simulation of a composite wind turbine blade was defined as: ① The effects of tower and nacelle were not considered in this work; ② One-third model was chosen for the CFD simulation to reduce the computation time. Figure 1c exhibits the dimensions and boundary conditions of the CFD model, where the model consists of a rotation domain and a stationary domain. The data can be passed though the interface. The radiuses of the rotation and stationary domains were 70 m and 300 m, respectively. The inlet was 200 m from the hub center and the outlet was 500 m from the hub center.

The fluent mesh model for the CFD simulation of the composite wind turbine blade was obtained as follows: The aforesaid domains were meshed using unstructured tetrahedral element type based on the ANSYS Meshing tool. Note: although some scholars [34,35] meshed blades using the structured mesh, the unstructured mesh for

blade and fluid is available by calculating Y+ values at different speeds and comparing the results of the output torque and power curves, which can obtain reasonable simulation results, see Figure 2. The mesh sizes for the rotation and stationary domains were 3 m and 1 m, respectively. Furthermore, the meshes in the symmetry surfaces, named Side_wai1 and Side_nei1, Side_nei1 and Side_nei2, were completely controlled by the periodic mesh matching using the periodic boundary constraint command to ensure that the periodic surface nodes correspond to each other, see Figure 1e,f. In order to better simulate the flow near the wall surface of the blade, the meshes around the blade surfaces were refined and fifteen expansion layers with a growth rate of 1.9 were set. The height of the first layer was $1 \times 10^{-5}$ m, see Figure 1g.

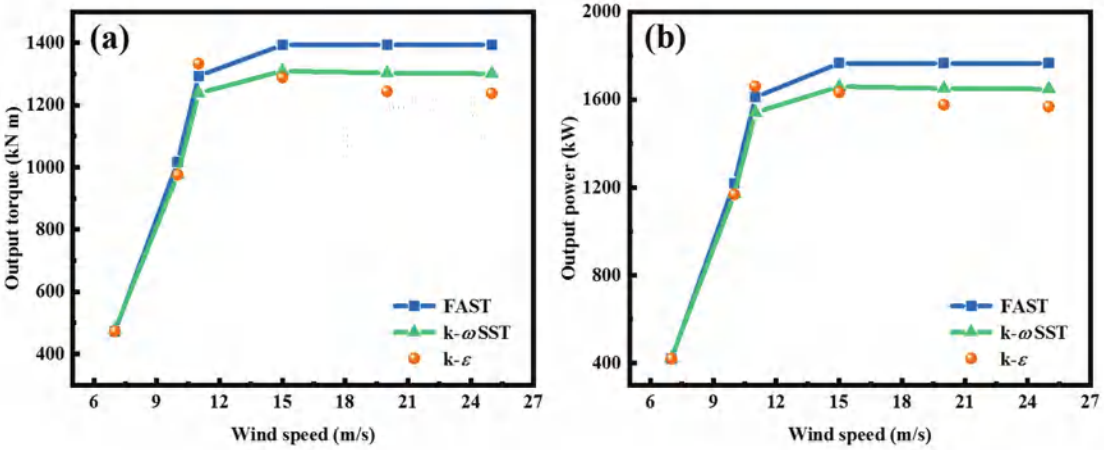


**Figure 2.** Output responses of composite wind turbine blade based on the k-$\omega$ SST and k- models and FAST. (**a**) Output torque response. (**b**) Output power response. Note: the simulation model is one third of wind turbine.

2.2.2. Mesh Quality and Independence Verifications

The mesh quality of the constructed CFD model was checked by using the $y^+$ value [36], which can be calculated as:

$$y^+ = u_* y / \nu \quad (5)$$

where $u_*$ is the friction speed; $y$ is the nearest wall; $\nu$ is the kinematic viscosity of fluid. If the $y^+$ is less than 1, the mesh quality is reasonable. The $y^+$ values were calculated under the wind speeds of 7 m/s, 11.4 m/s, 15 m/s, 20 m/s and 25 m/s, respectively, see Figure S1, SI. All the values were less than 1, indicating that the constructed CFD meshing models under different wind speeds were reasonable. Apart from the validation of mesh quality, the mesh independence was also carried out to find out an appropriate mesh size in this work. The case under the wind speed of 11.4 m/s was chosen, where the wind turbine speed is 12.1 RPM and the pitch angle is 0°. Four mesh sizes of 0.3 m, 0.2 m, 0.1 m and 0.07 m were adopted to mesh the blade surface, and the interface surface and outer surface meshes were set as 3 m and 6 m, respectively. After meshing, the amount of elements corresponding to the aforementioned mesh sizes were 3.63 million, 4.17 million, 578 million and 808 million, respectively. Table S2 (SI) shows the relationship between mesh number and calculated wind turbine torque. In view of the computation time and accuracy, the mesh size of 0.1 m was taken for the blade surface in the subsequent study of this work.

2.2.3. Calculation Method for the CFD Simulation

Considering that the subsequent topology optimization of wind turbine blade is a static solution question, the moving reference frame (MRF) method was adopted in this

work. Specifically, the rotation speed of the wind turbine is attached to the rotation domain, and the flow fluxes originated from the stationary domain can be translated by the interface. Compared to the non-constant slip grid method, the MRF method is a constant calculation method, which is simpler, faster with less computation time to produce acceptable results in a short time. The method has been used in CFD simulations of static wind turbine blade [37,38].

### *2.3. Finite Element Model of Reference Composite Wind Turbine Blade*

#### 2.3.1. Mechanical Properties of Composite Materials of Wind Turbine Blades

Glass fiber reinforced resin unidirectional composites were used as the skin material of blade in this work. The mechanical properties and corresponding allowable values of composites can be found in Table 1.

**Table 1.** Mechanical properties and allowable values.

| Mechanical Properties of Composites | | | | Allowable Values of Composites | | | |
|---|---|---|---|---|---|---|---|
| **Items** | **Values** | **Items** | **Values** | **Items** | **Values** | **Items** | **Values** |
| $E_x$ | $4.5 \times 10^4$ MPa | $\mu_{xz}$ | 0.3 | $TS_x$ | $1.1 \times 10^3$ MPa | $CS_z$ | −120 MPa |
| $E_y$ | $1.0 \times 10^4$ MPa | $G_{xy}$ | $5.0 \times 10^3$ MPa | $TS_y$ | 35 MPa | $GS_{xy}$ | 80 MPa |
| $E_z$ | $1.0 \times 10^4$ MPa | $G_{yz}$ | $3.8 \times 10^3$ MPa | $TS_z$ | 35 MPa | $GS_{yz}$ | 46 MPa |
| $\mu_{xy}$ | 0.3 | $G_{xz}$ | $5.0 \times 10^3$ MPa | $CS_x$ | −680 MPa | $GS_{xz}$ | 80 MPa |
| $\mu_{yz}$ | 0.4 | $\rho$ | 2000 kg·m$^3$ | $CS_y$ | −120 MPa | - | - |

Note: "*TS*", "*CS*" and "*GS*" indicate the tension, compression and shear strength.

#### 2.3.2. Finite Element Model of Wind Turbine Blade

As the wind turbine blade has a complex geometric configuration, the ANSYS Meshing was used to generate tetrahedral elements for the internal room of the blade in this work. Furthermore, to weaken the influence of mesh dependence on the blade, the mesh size was chosen as 0.07 m. Finally, the total number of elements and nodes were 4.85 million and 6.69 million. The corresponding model can be found in Figure S2, SI.

### *2.4. Design and Validation Cases of Wind Turbine Blade*

Three load cases are considered in this work, viz.:

(1) DLC-1 (Worst working case)

According to the IEC 61400-1 standard [39], the reference wind turbine is in the 1A IWC wind class, which means it can only withstand wind gusts up to 21% of its rated speed. Therefore, the first load case is when the wind turbine is operating under rated case in severe gusts, in which the gusts suddenly occur so that the blades do not have enough time to change pitch. As it is of great importance for the safety of turbine, this case is also used as the design condition for topology optimization in this work. The related parameters are given in Table 2.

**Table 2.** Operation parameters in different load cases.

| Load Case | Rotation Speed (RPM) | Pitch Angle (°) | Wind Speed (m/s) |
|---|---|---|---|
| DLC-1 (Design) | 12.1 | 0 | 13.8 |
| DLC-2 | 12.1 | 23.3 | 25 |
| DLC-3 | 0 | 89.3 | 37.5 |

Note: In DLC-1 case, wind speed = Rated wind speed + maximum allowable gust (11.4 + 21% × 11.4); in DLC-2 case, wind speed = cut-out wind speed; in DLC-3 case, wind speed = speed of typhoon.

(2) DLC-2 (Cut-out wind speed working case)

This case is the cut-out wind speed condition. This is the highest wind speed that the wind turbine can reach before opening the propeller to the downwind position and shutting it down. In this case, blade tip deflection is relatively small. The tip deflection

acceleration is even less than that in DLC-1, and therefore the inertial load can be ignored in this case. In this work, this case was used as a verification design case, and the related parameters are listed in Table 2.

(3) DLC-3 (Shutdown working case)

This case is the parking brake condition, at which the blade is in the downwind position and the incoming wind is typhoon speed (37.5 m/s). Here, the downwind position is the pitch angle of the blade that is not affected by any torque. In this work, this case was also adopted as a verification design case, and the relevant parameters are shown in Table 2.

## 3. Results

### *3.1. CFD Simulation of Wind Turbine Blade*

In this work, two turbulence models, viz. k-$\omega$ SST and k-$\varepsilon$, were adopted to elaborate the rationality of CFD simulation. Furthermore, the rationality analyses in terms of output torque and power were compared with the results obtained from the FAST software. Figure 2a illustrates the output torque curves based on the k-$\omega$ SST and k-$\varepsilon$ models and FAST as the increase in wind speed, and the corresponding data are also listed in Table 3. It can be seen from Figure 2a and Table 3 that the predicted torque values of turbine blade based on the k-$\omega$ SST and k-$\varepsilon$ turbulence models under the different wind speeds were close to the values based on the FAST. The k-$\omega$ SST model had a higher prediction accuracy in comparison with the k-$\varepsilon$ model. Compared to the values obtained from the FAST, the errors of output torque based on the k-$\omega$ SST model in the wind speed range of 7–25 m/s were less than 7%. The predicted values for the k-$\varepsilon$ turbulence model at high wind speeds were relatively low, and the related errors in the wind speed range of 15–25 m/s were within 7–12%.

**Table 3.** Output torques based on the k-$\omega$ SST and k-$\varepsilon$ models and FAST.

| Wind Speed (m/s) | Pitch Angle (°) | Wind Turbine Torque | | | | |
|---|---|---|---|---|---|---|
| | | **FAST** | **k-$\omega$ SST** | **Error** | **k-$\varepsilon$** | **Error** |
| 7 | 0 | 472.70 | 479.05 | 1.34% | 473.61 | 0.19% |
| 10 | 0 | 1017.03 | 976.36 | 4.00% | 976.36 | 4.00% |
| 11 | 0 | 1293.77 | 1238.20 | 4.30% | 1333.51 | 3.07% |
| 15 | 10.45 | 1393.37 | 1309.79 | 6.00% | 1289.05 | 7.49% |
| 20 | 17.47 | 1393.37 | 1302.96 | 6.49% | 1244.32 | 10.70% |
| 25 | 23.57 | 1393.37 | 1300.84 | 6.64% | 1237.86 | 11.16% |

Apart from the output torque performance, the output power performance of the turbine blade based on the k-$\omega$ SST and k-$\varepsilon$ models and FAST was also evaluated. The output power can be calculated as the following formula:

$$P = M\omega \tag{6}$$

where $M$ is the torque of blade; $\omega$ is rotation speed. Figure 2b and Table 4 show the output power values of the turbine blade based on the k-$\omega$ SST and k-$\varepsilon$ models and FAST, respectively. It can be noted that both the models simulated the output power performance relatively well, and the maximum errors were basically within 10%. However, the error based on the k-$\varepsilon$ model at the wind speed of 25 m/s was 11.16%, probably resulting in a relatively dangerous result. Consequently, the k-$\omega$ SST turbulence model was adopted in this work.

**Table 4.** Output power based on the k-$\omega$ SST and k-$\varepsilon$ models and FAST.

| Wind Speed (m/s) | Pitch Angle (°) | Wind Turbine Power | | | | |
|---|---|---|---|---|---|---|
| | | FAST | k-$\omega$ SST | Error | k-$\varepsilon$ | Error |
| 7 | 0 | 419.20 | 424.86 | 1.35% | 420.03 | 0.2% |
| 10 | 0 | 1217.67 | 1168.75 | 4.02% | 1168.75 | 4.02% |
| 11 | 0 | 1611.07 | 1541.70 | 4.31% | 1660.39 | 3.06% |
| 15 | 10.45 | 1765.53 | 1659.65 | 6.00% | 1633.37 | 7.49% |
| 20 | 17.47 | 1765.57 | 1651.00 | 6.49% | 1576.69 | 10.70% |
| 25 | 23.57 | 1765.57 | 1648.30 | 6.64% | 1568.50 | 11.16% |

### 3.2. Structural Responses of Wind Pressure on the Surface of Wind Turbine Blade

According to the design case shown in Table 2 where the pitch angle of the wind turbine blade was adjusted to 0° and the meshing strategy discussed in Section 2.2.2, the structural responses of wind pressure on the surface of blade were obtained based on the k-$\omega$ SST turbulence model (Section 3.1). Figure 3 illustrates the pressure surface and suction surface contours of turbine blade under the aerodynamic external load. From Figure 2, the pressure was mainly concentrated in the blade root and trailing edge, while the suction force in the middle of the blade was mainly focused on the blade edge. The maximum pressure and suction force were 2723 and 5729 Pa, respectively.

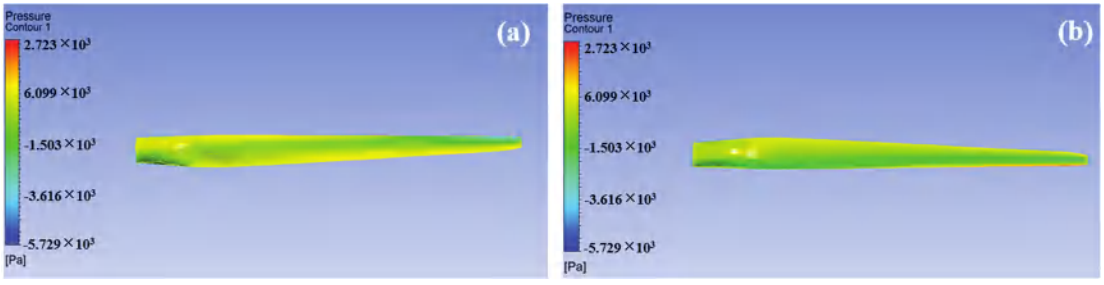


**Figure 3.** (**a**) Pressure surface contour. (**b**) Suction surface contour.

### 3.3. Topology Optimization Results of Internal Configuration of Wind Turbine Blade

Figure 4 exhibits the topology optimization results of the wind turbine blade. The outer shell of the blade was completely retained (Figure 4a), and in the internal configuration appeared obvious strip-shaped "gap" and "hole" regions along the axial direction of the blade (Figure 4b), which indicated several webs should be set in these regions. Furthermore, from the left and right enlarged views, some vertical webs should be retained in order to improve the bending resistance. Figure 4c shows the specific internal views cut from 12 various locations from the root to the tip of blade. More obviously, some web-like structures were retained though the topology optimization design.

Based on the aforesaid analysis, the preliminary design of the webs inside the blade in accordance with the topology optimization (Figure 4b,c) was subsequently carried out, see Figure 5. Taking into account seven cross-sections at different locations along the axis direction, the internal web structure of the blade from the root to tip generally changes from the single-web mode to twin-web mode and then to the single-web mode (Figure 5a,b), respectively. However, there are some discontinuous regions among the transition regions of webs, see Figure 5a. Consequently, we proposed to connect the discontinuous region "①" by using a twin-web structure and also arranging the twin-web structure in the region "②", but other regions were filled by the single-web structure. Four webs were reversely designed and the specific sizes of the web cross-sections were determined by the seven cross-sections shown in Figure 5b, in which the corresponding locations along the blade were at 6.70, 17.13, 28.18, 50.28, 56.69, 70.30 and 74.71%, respectively. Ultimately, according

to the dimensions of the different cross-sections shown in Figure 5b, the first generation turbine blade inspired by topology optimization was constructed by Boolean operation between the designed web structures and blade boundary, see Figure 5c. The corresponding finite element model of the blade is exhibited in Figure 5c.

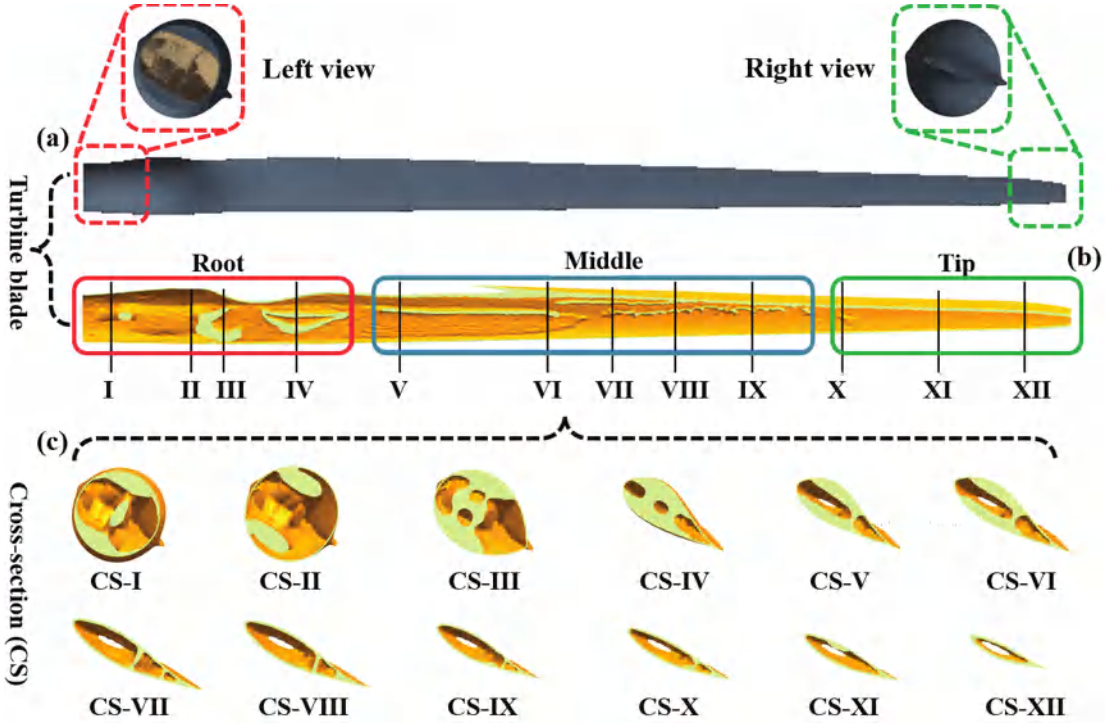


**Figure 4.** Topology optimization results of the wind turbine blade. (**a**) External shell structure. Inset: the enlarged left and right views. (**b**) Retained materials in the internal blade. (**c**) Cross-section views at different axis locations.

### *3.4. Validation of Performance Indexes for the First Generation Wind Turbine Blade*

The designed first generation wind turbine blade was firstly validified in the DLC-1 case (Table 2) to ensure the feasibility of the reverse design structure. If it was a feasible solution, the design was further validified in the DLC-2 and DLC-3 cases. Otherwise, the aforesaid design strategy was repeated until all the work cases were satisfied.

Figure 6 and Table 5 show the simulation results of the first generation wind turbine blade in the DLC-1 case. From Figure 6a and Table 5, the stress levels in the X direction were the largest, resulting from the waving force (i.e., wind speed incoming flow direction). The maximum tensile and compressive stresses were 45.56 and 49.72 MPa, which are less than the corresponding allowable stress of GFRP. The maximum tensile and compressive stresses in the Y direction were 27.49 and 16.76 MPa, and the values in the Z direction were 17.66 and 12.72 MPa, respectively. The aforementioned stress values were within the allowable stress ranges. Moreover, the maximum displacement of the blade tip was 4.38 m, which was also less than 9 m. Thus, the overall stress and displacement indexes met the design requirements. Figure 6b illustrates the stress contours of the web of the first generation blade. The stresses in the X, Y and Z directions were less than the overall stresses, indicating that the reverse designed web structure satisfied the stress requirements. Figure 6c exhibits the local stress contours of the web in the X, Y and Z directions. It can be seen that the high stress levels were concentrated at the web notch location, which was

due to the discontinuity of the designed web. Likewise, all the local stresses were within the requirements of stress. Based on the above-mentioned results, the preliminary design of the first generation turbine blade driven by the topology optimization was reasonable, but the blade is prone to fatigue damage in the long-term service. Thus, the fatigue life should be also considered as an important evaluation index of safety. Figure 6d and Table 5 demonstrate the fatigue life results in the X, Y and Z directions. The minimum fatigue lives in the X and Y directions were $1.27 \times 10^9$ and $6.45 \times 10^8$, both of which meet the fatigue life requirements. However, from Figure 6d, the fatigue life levels at the discontinuous location of the web were considerably lower. The minimum fatigue life in the Z direction was $8.97 \times 10^7$, which does not meet the requirement. Therefore, the first generation blade structure at the local position should be further modified. In this work, we directly connected the middle discontinuous region using a web structure and the second generation wind turbine blade was generated, see Figure 6e.

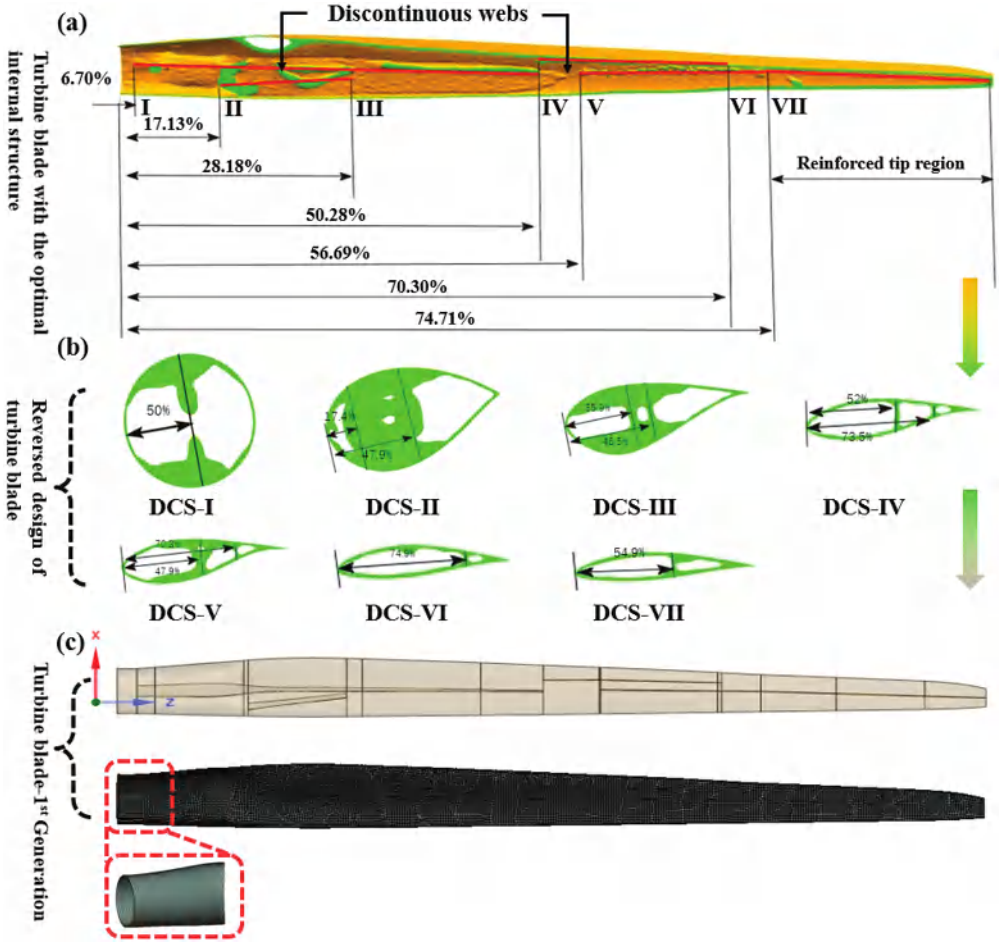


**Figure 5.** Reverse design of the wind turbine blade. (**a**) Turbine blade with the optimal internal structure. (**b**) Reverse design of turbine blade inspired by the topology optimization. (**c**) First generation turbine blade.

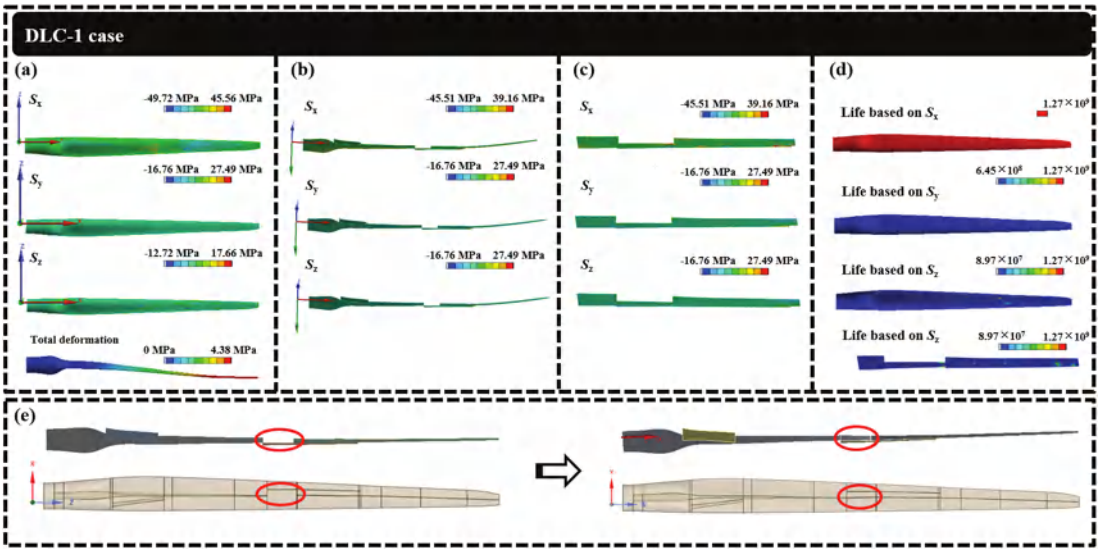


**Figure 6.** Validation of performance indexes for the first generation wind turbine blade in the DLC-1 case. (**a**) Stress and deformation contours of overall turbine blade. (**b**) Stress contours of internal structure. (**c**) Stress contours of localized regions of internal structure. (**d**) Fatigue life contours of whole turbine blade (**e**) The second generation design of the wind turbine blade.

**Table 5.** Simulation results of the first generation wind turbine blade in the DLC-1 case.

| Direction | Overall Stress of Blade | | Localized Stress of Web | | Min. Fatigue Life | Disp. of Tip |
|---|---|---|---|---|---|---|
| | Max. TS | Max. CS | Max. TS | Max. CS | | |
| X | 45.56 MPa | 49.72 MPa | 39.16 MPa | 45.51 MPa | $1.27\times10^9$ | |
| Y | 27.49 MPa | 16.76 MPa | 27.49 MPa | 16.76 MPa | $6.45\times10^8$ | 4.38 m |
| Z | 17.66 MPa | 12.72 MPa | 27.49 MPa | 16.76 MPa | $8.97\times10^7$ | |

Figure 7 shows the simulation results of the second generation wind turbine blade in the DLC-1, 2 and 3 cases. Table 6 compared results of performance indexes between the first and second generation wind turbine blades in the DLC-1 case. Compared with the performance indexes of the first generation blade in the DLC-1 case, the overall maximum tensile stress of the blade in the X direction was slightly changed, but the maximum compressive stress in the Y direction was reduced by 18.79%. It is worth noting that the maximum localized tensile and compressive stresses of the web in the Z direction were remarkably decreased by 97.05 and 95.17%, respectively. Furthermore, the maximum displacement of the blade tip was 4.03 m, which was also reduced by 7.99%. All the stress and displacement indexes met the design requirements. Importantly, after connecting the discontinuous region by the additional web, the minimal fatigue life of the web was $2.25 \times 10^8$, significantly improved by 150.84%, which achieved the requirement of fatigue life.

In addition, the overall stress contours of the second blade in the X, Y and Z directions were similar to those of the first blade (Figure 7a,b). The stress levels in the X direction were higher than those in the Y and Z directions. From Figure 7c, the stress levels at the local region in three directions were relatively uniform, indicating that the stress concentration had been accommodated by adding additional web structure in this region. Furthermore, the maximum tensile stresses were still less than the allowable ones. In summary, the design strategy for the internal structure of the second generation wind turbine blade is

a feasible solution. In the following discussion, the performance indexes of the blade are further evaluated in the DLC-2 and DLC-3 cases.

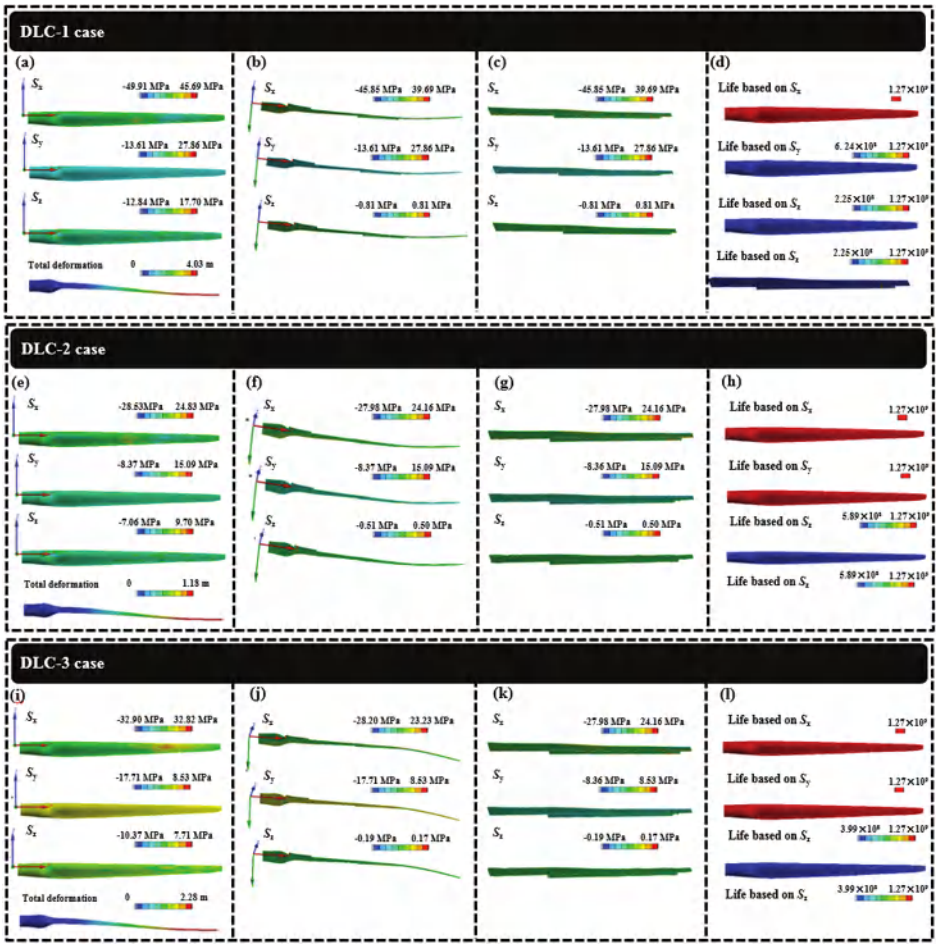


**Figure 7.** Validation of performance indexes for the second generation wind turbine blade in the DLC-1, DLC-2 and DLC-3 cases. (**a**,**e**,**i**) Stress and deformation contours of whole turbine blade. (**b**,**f**,**j**) Stress contours of internal structure. (**c**,**g**,**k**) Stress contours of localized regions of internal structure. (**d**,**h**,**l**) Fatigue life contours of whole turbine blade.

Figure 7 and Table 7 exhibit the validation results of the second blade in the X, Y and Z directions in the DLC-2 case. The overall stress distribution contours of the blade in the X, Y and Z directions were totally consistent with those of the first blade, and the maximum tensile and compressive stresses meet the stress requirements. The maximum displacement was only 1.18 m, which also meets the design allowable value. Compared to the performance indexes of the first blade, the stress and deformation responses of the second blade were relatively lower. It should be noted that the wind turbine obtained an additional torque in this case, and the outer part of the blade had a negative angle of attack which to some extent counteracted the internal lift. Although the turbine operated at a higher wind speed, the aerodynamic load acting at the blade tip was weaker than that in the DLC-1 case. Additionally, the minimal fatigue life also achieved the design requirement. Consequently, all the performance indexes of the second turbine blade met

the design requirements, confirming that it was also a feasible solution in the DLC-2 case. In addition, Figure 7 and Table 7 also show the validation results of the second blade in the X, Y and Z directions in the DLC-3 case. In this case, the wind turbine was suffering from typhoon conditions, and the blade was in the down pitch stop state. The maximum displacement of blade tip was 2.28 m and the minimum fatigue life was $3.90 \times 10^8$, both of which met the design requirements. Furthermore, it can be seen from the stress contours that the middle stress levels in the X direction were slightly higher, giving an indication of stress concentration in the region. However, those in the Y and Z directions were relatively uniform. All the stress indexes were within the requirements. Therefore, the second turbine blade was also a feasible design in the DLC-3 case.

**Table 6.** Compared results of performance indexes between the first and second generation wind turbine blades in the DLC-1 case.

| Item | Overall Stress of Blade | | Localized Stress of Web | | Min. Fatigue Life | Disp. of Tip |
|---|---|---|---|---|---|---|
| | Max. TS | Max. CS | Max. TS | Max. CS | | |
| First X | 45.56 MPa | 49.72 MPa | 39.16 MPa | 45.51 MPa | $1.27\times10^9$ | 4.38 m (first); 4.03 m (second); Δ = −7.99% |
| Second X | 45.77 MPa | 49.91 MPa | 36.69 MPa | 45.85 MPa | $1.27\times10^9$ | |
| Δ X | +0.46% | +0.38% | −6.31% | +0.75% | 0% | |
| First Y | 27.49 MPa | 16.76 MPa | 27.49 MPa | 16.76 MPa | $6.45\times10^8$ | |
| Second Y | 27.86 MPa | 13.61 MPa | 27.86 MPa | 13.61 MPa | $6.24\times10^8$ | |
| Δ Y | +1.35% | −18.79% | +1.35% | −18.79% | −3.26% | |
| First Z | 17.66 MPa | 12.72 MPa | 27.49 MPa | 16.76 MPa | $8.97\times10^7$ | |
| Second Z | 17.70 MPa | 12.84 MPa | 0.81 MPa | 0.81 MPa | $2.25\times10^8$ | |
| Δ Z | +0.23% | +0.94% | −97.05% | −95.17% | +150.84% | |

**Table 7.** Simulation results of the second generation wind turbine blade in the DLC-1, 2 and 3 cases. Unit in stress: MPa, in displacement of tip: m.

| Case | Direction | Overall Stress of Blade | | Localized Stress of Web | | Min. Fatigue Life | Disp. of Tip |
|---|---|---|---|---|---|---|---|
| | | Max. TS | Max. CS | Max. TS | Max. CS | | |
| DLC-1 | X | 45.77 | 49.91 | 36.69 | 45.85 | 1.27e9 | 4.03 |
| | Y | 27.86 | 13.61 | 27.86 | 13.61 | 6.24e8 | |
| | Z | 17.70 | 12.84 | 0.81 | 0.81 | 2.25e8 | |
| DLC-2 | X | 24.83 | 28.53 | 24.16 | 27.98 | 1.27e9 | 1.18 |
| | Y | 15.09 | 8.37 | 15.09 | 8.36 | 1.27e9 | |
| | Z | 9.70 | 7.06 | 0.50 | 0.51 | 5.98e8 | |
| DLC-2 | X | 32.82 | 32.90 | 24.16 | 27.98 | 1.27e9 | 2.28 |
| | Y | 8.53 | 17.71 | 15.09 | 8.36 | 1.27e9 | |
| | Z | 7.71 | 10.37 | 0.50 | 0.51 | 3.90e8 | |

Note: "Disp" means displacement. "TS" and "CS" mean tensile stress, compressive stress.

In summary, a novel turbine blade with the optimal web structure guided by the topology optimization was accomplished.

## 4. Discussion

### *4.1. Comparison of Performance Indexes between the Novel and Reference Turbine Blades*

Table 8 lists the compared results of the performance indexes between the novel and reference turbine blades. Overall, the stress levels of the novel blade were lower than those of the reference blade. Note: a positive value in Table 8 represents the increase in performance index. The displacement values of the novel blade in various load cases were larger than those of the reference blade, indicating that a more flexible blade was obtained in this work. Importantly, the weight of the novel blade was reduced by 9.88% relative to the reference blade, which is a significant benefit in decreasing the cost of turbine blades. Therefore, the novel wind turbine blade driven by topology optimization in this

work has predictably better power efficiency than the reference blade without the loss of load-bearing capacity.

**Table 8.** Compared results of performance indexes between the novel and reference turbine blades. Unit in stress: MPa, in displacement of tip: m, in overall weight: kg.

| Case | Dir. | Item | Overall Blade Stress | | Localized Web Stress | | Disp. of Tip | Overall Weight |
|---|---|---|---|---|---|---|---|---|
| | | | Max. TS | Max. CS | Max. TS | Max. CS | | |
| DLC-1 | X | Ref. blade | 32.70 | 30.60 | 14.30 | 16.00 | 3.42 (Ref.) 4.03 (New) Δ: 17.84% | 21,247 (Ref.); 19,148 (New) Δ: −9.88% |
| | | Nov. blade | 45.769 | 49.91 | 36.69 | 45.85 | | |
| | | Δ | 39.97% | 63.10% | 156.57% | 186.56% | | |
| | Y | Ref. blade | 13.10 | 19.50 | 13.10 | 19.50 | | |
| | | Nov. blade | 27.86 | 13.61 | 27.86 | 13.61 | | |
| | | Δ | 112.67% | −30.21% | 112.67% | −30.21% | | |
| | Z | Ref. blade | 19.30 | 13.60 | 0.15 | 0.18 | | |
| | | Nov. blade | 17.70 | 12.84 | 0.81 | 0.81 | | |
| | | Δ | −8.29% | −5.59% | 440.00% | 350.00% | | |
| DLC-2 | X | Ref. blade | 18.90 | 15.70 | 8.85 | 9.70 | 1.08 (Ref.) 1.18 (New) Δ: 9.26% | |
| | | Nov. blade | 24.83 | 28.53 | 24.16 | 27.98 | | |
| | | Δ | 31.38% | 81.72% | 172.99% | 188.45% | | |
| | Y | Ref. blade | 7.15 | 10.40 | 7.15 | 10.40 | | |
| | | Nov. blade | 15.09 | 8.37 | 15.09 | 8.36 | | |
| | | Δ | 111.05% | −19.52% | 111.05% | −19.62% | | |
| | Z | Ref. blade | 10.80 | 6.14 | 0.07 | 0.08 | | |
| | | Nov. blade | 9.70 | 7.06 | 0.50 | 0.51 | | |
| | | Δ | −10.19% | 14.98% | 614.29% | 537.50% | | |
| DLC-3 | X | Ref. blade | 23.80 | 25.50 | 6.08 | 5.61 | 1.94 (Ref.) 2.28 (New) Δ: 17.53% | |
| | | Nov. blade | 32.82 | 32.90 | 24.16 | 27.98 | | |
| | | Δ | 37.90% | 29.02% | 297.37% | 398.75% | | |
| | Y | Ref. blade | 7.67 | 5.29 | 7.67 | 5.29 | | |
| | | Nov. blade | 8.53 | 17.71 | 15.09 | 8.36 | | |
| | | Δ | 11.21% | 234.78% | 96.74% | 58.03% | | |
| | Z | Ref. blade | 9.96 | 7.42 | 0.09 | 0.09 | | |
| | | Nov. blade | 7.71 | 10.37 | 0.50 | 0.51 | | |
| | | Δ | −22.59% | 39.76% | 455.56% | 466.67% | | |

Note: "Dir.", "Ref." and "Nov." mean "Direction", "Reference" and "Novel", respectively.

### *4.2. Modal Analysis of the Novel Wind Turbine Blade*

As the decrease of blade weight, the vibration problem of the novel wind turbine blade should be discussed to further identify the dynamic properties. In this work, the modal analysis was also carried out based on the novel blade, see Figure 8 and Table 9. It can be seen from Figure 8, the first six orders of the novel turbine blade include: first order waving vibration, second order pendulum vibration, third order waving vibration, fourth order waving vibration, fifth order waving vibration and sixth waving pendulum, which are similar to those of the reference blade. The vibration types of the blade are mainly dominated by waving and pendulum vibrations. Moreover, from Table 9, it can be seen that the first six order frequencies were well in agreement with those of the reference blade, indicating that the designed internal layout is reasonable.

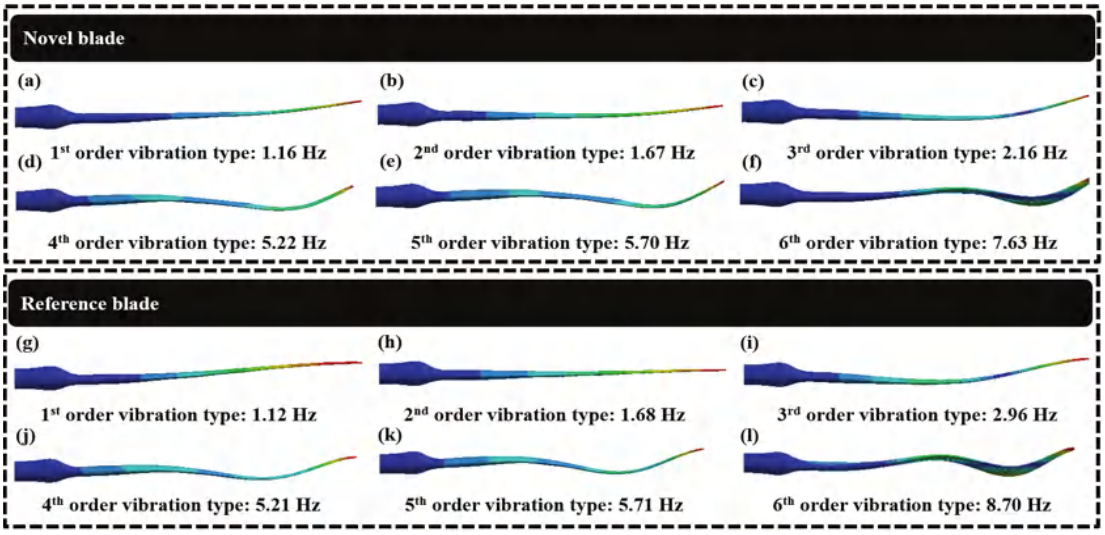


**Figure 8.** Vibration types of the novel and reference turbine blades.

**Table 9.** Comparison of frequency between the novel and reference turbine blades.

| Order | Frequency (Hz) | | Order | Frequency (Hz) | |
|---|---|---|---|---|---|
| | Ref. Blade | Nov. Blade | | Ref. Blade | Nov. Blade |
| 1 | 1.12 | 1.16 | 4 | 5.21 | 5.22 |
| 2 | 1.68 | 1.67 | 5 | 5.71 | 5.70 |
| 3 | 2.96 | 2.16 | 6 | 8.70 | 7.63 |

*4.3. Full Life Cycle Assessment of the Novel Wind Turbine Blade*

The service life of a wind turbine is generally more than 20 years. During long-term service, wind turbine blades are always subjected to complex aerodynamic loads induced by wind, with the result that it is very susceptible to fatigue damage and failure. Hence, to ensure the long-term service safety, a full life-cycle assessment of the novel wind turbine blade should be discussed in this work. According to the wind speed data of a full year in Guangdong Province, the wind speed range from 5–25 m/s was considered in this work, see Table 10. The statistical duration of wind speed in an hour can be obtained through the Weibull distribution, see Table S3, SI. Based on the finite element analysis given in Section 3, the stress responses of the novel blade were obtained, see Table 10. Considering the S-N curve of GFRP used as the shell composite material (Table S4, SI), the fatigue lives of turbine blades corresponding to the wind speed were calculated though the Goodman curve, see Table 10. Afterwards, the fatigue damage with respect to each wind speed was obtained via the ratio of stress range in the Weibull distribution and the related fatigue life (Table 10). Finally, the full life of the novel blade over 20 years was evaluated based on the linear P-M accumulative damage theory, viz:

$$Y = \frac{N}{N' \times \omega \times 60} = \frac{1/(\sum \gamma_i / N_i)}{N' \times \omega \times 60} = \frac{1/(\frac{0.197}{1.70\times10^8} + \frac{0.15}{1.60\times10^8} + \frac{0.101}{1.05\times10^8} + \frac{0.061}{1.08\times10^8})}{7250\times12.1\times60} = 21.9 \text{ Year} \quad (7)$$

where $Y$ is the full life; $\omega$ is the rated speed of turbine blade, taken as 12.1 RPM (Table 2); $N'$ is the sum of duration of wind speed in hours; $\gamma_i$ is the stress range Weibull distribution; $N_i$ is the fatigue life corresponding to wind speed. Consequently, the full life over the 20 years is 21.9 years, which meets the design requirement of 20 years.

**Table 10.** Wind speed distribution and fatigue damage in a year.

| Wind Speed (m/s) | Duration of Wind Speed (h) | Max. Stress (MPa) | Min. Stress (MPa) | Stress Range Weibull Distribution | Fatigue Limitation (MPa) | Fatigue Life | Fatigue Damage |
|---|---|---|---|---|---|---|---|
| 5 | 1526 | 12.84 | 3.85 | 0.210 | 40.4 | $>2 \times 10^8$ | 0 |
| 7 | 1613 | 21.18 | 6.35 | 0.222 | 40.4 | $>2 \times 10^8$ | 0 |
| 9 | 1425 | 42.43 | 12.73 | 0.197 | 40.4 | $1.70 \times 10^8$ | $1.16 \times 10^{-9}$ |
| 11 | 1090 | 42.64 | 12.79 | 0.150 | 40.4 | $1.60 \times 10^8$ | $9.38 \times 10^{-10}$ |
| 13 | 734 | 47.86 | 14.36 | 0.101 | 40.4 | $1.05 \times 10^8$ | $9.62 \times 10^{-10}$ |
| 15 | 439 | 42.54 | 12.76 | 0.061 | 40.4 | $1.08 \times 10^8$ | $5.65 \times 10^{-10}$ |
| 17 | 235 | 36.24 | 10.87 | 0.032 | 40.4 | $>2 \times 10^8$ | 0 |
| 19 | 113 | 33.89 | 10.17 | 0.016 | 40.4 | $>2 \times 10^8$ | 0 |
| 21 | 49 | 23.87 | 7.16 | 0.007 | 40.4 | $>2 \times 10^8$ | 0 |
| 23 | 19 | 28.33 | 8.50 | 0.003 | 40.4 | $>2 \times 10^8$ | 0 |
| 25 | 7 | 33.3 | 9.99 | 0.001 | 40.4 | $>2 \times 10^8$ | 0 |

## 5. Conclusions

This work develops an innovative multi-web internal layout for the offshore wind turbine blade in accordance with the variable density topology optimization method, which theoretically answers the proposed scientific issues about how many webs need to be used inside the blade and where the related webs should be laid out. The following conclusions can be summarized as follows:

1. The surface pressure was obtained based on the CFD simulation, and the two turbulence models, viz. k-$\omega$ SST and k-$\varepsilon$, were adopted. By comparing the output torques and power, the k-$\omega$ SST model was chosen to calculate the surface pressure distribution. Moreover, the simulation results obtained from the CFD were also validated in comparison with those calculated from the FAST.
2. The topology optimization model was established based on the full-scale internal structure of offshore wind turbine blade, considering stress, displacement and fatigue life constraints.
3. After the full-scale topology optimization, two multi-web layouts were theoretically obtained driven by the optimal topological configuration for the first time. By validation, the second generation optimal blade completely met all the requirements and the weight was reduced by 9.88% relative to the reference blade, which was a significant benefit in decreasing the cost of turbine blades.
4. Vibration modal and full life cycle of the novel blade were also evaluated. The first six vibration types of the novel blade were consistent with those of the reference blade, further indicating that the designed internal layout was reasonable. Moreover, the full life cycle of the novel blade is 21.9 years, theoretically verifying that the novel blade is able to service more than 20 years in the given sea domain.

**Supplementary Materials:** The following supporting information can be downloaded at: https://www.mdpi.com/article/10.3390/jmse10101487/s1, Figure S1: $y^+$ values for evaluating the mesh quality under the different wind speeds; Figure S2: Illustration of the relationship between the amount of element and torque; Table S1: Distributed blade aerodynamic properties in NREL 5 MW wind turbine blade; Table S2: Mesh independence analysis; Table S3: Statistic duration of wind speed in hour; Table S4: S-N data of GFRP.

**Author Contributions:** J.S.: writing—original draft, reviewing, project administration and supervision; J.C.: writing—original draft, reviewing and validation; Y.W.: review, editing and validation; L.L.: conceptualization and supervision. All authors have read and agreed to the published version of the manuscript.

**Funding:** The support for this research has been provided by the National Natural Science Foundation of China (Grant No. 51905350), the Shenzhen Science and Technology Program (Grant No. KQTD20200820113004005), Shenzhen Key Laboratory of Structure Safety and Health Monitoring of Marine Infrastructures (Grant No. ZDSYS20201020162400001) and the National Natural Science Foundation of Guangdong Province (Grant No. 2022A1515011499) are gratefully acknowledged.

**Institutional Review Board Statement:** Not applicable.

**Informed Consent Statement:** Not applicable.

**Data Availability Statement:** Not applicable.

**Conflicts of Interest:** The authors declare that they have no known competing financial interests or personal relationships that could have appeared to influence the work reported in this paper.

## References


1. Oh, K.Y.; Nam, W.; Ryu, M.S.; Kim, J.Y.; Epureanu, B.I. A review of foundations of offshore wind energy convertors: Current status and future perspectives. *Renew. Sustain. Energy Rev.* **2018**, *88*, 16–36. [CrossRef]
2. Liu, P.; Meng, F.R.; Barlow, C.Y. Wind turbine blade end-of-life options: An economic comparison. *J. Clean. Prod.* **2022**, *180*, 106202. [CrossRef]
3. Mishnaevsky, L.; Johansen, N.F.; Fraisse, A.; Faster, S.; Jensen, T.; Bendixen, B. Technologies of Wind Turbine Blade Repair: Practical Comparison. *Energies* **2022**, *15*, 1767. [CrossRef]
4. Dyrholm, M. *GWEC | Global Wind Report*; Global Wind Energy Council: Brussels, Belgium, 2021.
5. Chou, J.S.; Chiu, C.K.; Huang, I.K.; Chi, K.N. Failure analysis of wind turbine blade under critical wind loads. *Eng. Fail. Anal.* **2013**, *27*, 99–118. [CrossRef]
6. Liu, Y.; Hajj, M.; Bao, Y. Review of robot-based damage assessment for offshore wind turbines. *Renew. Sustain. Energy Rev.* **2022**, *158*, 112187. [CrossRef]
7. Rafiee, R.; Hashemi, M.R. Failure analysis of a composite wind turbine blade at the adhesive joint of the trailing edge. *Eng. Fail. Anal.* **2021**, *121*, 105148. [CrossRef]
8. Roh, C.; Ha, Y.J.; Ahn, H.J.; Kim, K.H. A Comparative Analysis of the Characteristics of Platform Motion of a Floating Offshore Wind Turbine Based on Pitch Controllers. *Energies* **2022**, *15*, 716. [CrossRef]
9. Guo, Y.; Wang, H.; Lian, J. Review of integrated installation technologies for offshore wind turbines: Current progress and future development trends. *Energy Convers. Manag.* **2022**, *255*, 115319. [CrossRef]
10. Asim, T.; Islam, S.Z.; Hemmati, A.; Khalid, M.S. A Review of Recent Advancements in Offshore Wind Turbine Technology. *Energies* **2022**, *15*, 579. [CrossRef]
11. Ibrahimbegovic, A. Flexible Blades Wind-Turbines: Giant Installations and System-of-Systems Approach to Optimizing Wind-Energy Farms. In *CIGOS 2021, Emerging Technologies and Applications for Green Infrastructur*; Springer: Berlin/Heidelberg, Germany, 2022; pp. 3–27.
12. Zhu, J.; Cai, X.; Ma, D.; Zhang, J.; Ni, X. Improved structural design of wind turbine blade based on topology and size optimization. *Int. J. Low-Carbon Technol.* **2022**, *17*, 69–79. [CrossRef]
13. Chen, J.; Kim, M.H. Review of Recent Offshore Wind Turbine Research and Optimization Methodologies in Their Design. *J. Mar. Sci. Eng.* **2021**, *10*, 28. [CrossRef]
14. Naung, S.W.; Erfanian Nakhchi Toosi, M.; Rahmati, M. An Experimental and Numerical Study on the Aerodynamic Performance of Vibrating Wind Turbine Blade with Frequency-Domain Method. *J. Appl. Comput. Mech.* **2021**, *7*, 1737–1750.
15. Naung, S.W.; Nakhchi, M.E.; Rahmati, M. High-fidelity CFD simulations of two wind turbines in arrays using nonlinear frequency domain solution method. *Renew. Energy* **2021**, *174*, 984–1005. [CrossRef]
16. Nakhchi, M.E.; Naung, S.W.; Rahmati, M. High-resolution direct numerical simulations of flow structure and aerodynamic performance of wind turbine airfoil at wide range of Reynolds numbers. *Energy* **2021**, *225*, 120261. [CrossRef]
17. Mamouri, A.R.; Khoshnevis, A.B.; Lakzian, E. Entropy generation analysis of S825, S822, and SD7062 offshore wind turbine airfoil geometries. *Ocean Eng.* **2019**, *173*, 700–715. [CrossRef]
18. Mamouri, A.R.; Khoshnevis, A.B.; Lakzian, E. Experimental study of the effective parameters on the offshore wind turbine's airfoil in pitching case. *Ocean Eng.* **2020**, *198*, 106955. [CrossRef]
19. Chen, J.; Wang, Q.; Shen, W.Z.; Pang, X.; Li, S.; Guo, X. Design, Structural optimization study of composite wind turbine blade. *Mater. Des.* **2013**, *46*, 247–255. [CrossRef]
20. Ghiasi, H.; Fayazbakhsh, K.; Pasini, D.; Lessard, L. Optimum stacking sequence design of composite materials Part II: Variable stiffness design. *Compos. Struct.* **2010**, *93*, 1–13. [CrossRef]
21. Zhang, Z.Y. Structural Design of Large Horizontal Axis Wind Turbine Blade Based on Fluid-Structural Interation. Ph.D. Thesis, Lanzhou University of Technology, Lanzhou, China, 2014.
22. Liao, C.C.; Zhao, X.L.; Xu, J.Z. Blade layers optimization of wind turbines using FAST and improved PSO Algorithm. *Renew. Energy* **2012**, *42*, 227–233. [CrossRef]
23. Song, J.; Zhang, Y.K.; Guo, X.; Hao, H.; Wen, W.D.; Cui, H.T. Topology and shape optimization of twin-web turbine disk. *Struct. Multidiscip. Optim.* **2022**, *65*, 1–20. [CrossRef]
24. Rossow, M.P.; Taylor, J.E. A finite element method for the optimal design of variable thickness sheets. *AIAA J.* **1973**, *11*, 1566–1569. [CrossRef]
25. Bendsøe, M.P.; Kikuchi, N. Generating optimal topologies in structural design using a homogenization method. *Comput. Methods Appl. Mech. Eng.* **1988**, *71*, 197–224. [CrossRef]

26. Mlejnek, H.P.; Schirmacher, R. An engineer's approach to optimal material distribution and shape finding. *Comput. Methods Appl. Mech. Eng.* **1993**, *106*, 1–26. [CrossRef]
27. Joncas, S. Thermoplastic Composite Wind Turbine Blades: An Integrated Design Approach. Ph.D. Thesis, Delft University of Technology, Delft, The Netherlands, 2010.
28. Buckney, N.; Pirrera, A.; Green, S.D.; Weaver, P.M. Structural efficiency of a wind turbine blade. *Thin-Walled Struct.* **2013**, *67*, 144–154. [CrossRef]
29. Yu, X. Optimal Design of Vertical Axis Wind Turbine Blade Structure with Honeycomb Core Layer Inside the Main Beam. Ph.D. Thesis, Tianjin University of Technology, Tianjin, China, 2021.
30. Zhang, Y.Y.; Zheng, Y.J.; Chen, Y.Y.; Sun, M.M.; Tang, J.M. Structural topology optimization design of wind turbine blade. *Shanxi Archit.* **2017**, *43*, 203–204.
31. Aage, N.; Andreassen, E.; Lazarov, B.S.; Sigmund, O. Giga-voxel computational morphogenesis for structural design. *Nature* **2017**, *550*, 84–86. [CrossRef]
32. Zuo, W.; Saitou, K. Multi-material topology optimization using ordered SIMP interpolation. *Struct. Multidiscip. Optim.* **2017**, *55*, 477–491. [CrossRef]
33. Jonkman, J.; Butterfield, S.; Musial, W.; Scott, G. *Definition of a 5-MW Reference Wind Turbine for Offshore System Development*; National Renewable Energy Lab: Golden, CO, USA, 2009.
34. Mamouri, A.R.; Lakzian, E.; Khoshnevis, A.B. Entropy analysis of pitching airfoil for offshore wind turbines in the dynamic stall condition. *Ocean Eng.* **2019**, *187*, 106229. [CrossRef]
35. Mahrooghi, A.; Lakzian, E. Optimization of Wells turbine performance using a hybrid artificial neural fuzzy inference system (ANFIS)—Genetic algorithm (GA). *Ocean Eng.* **2021**, *226*, 108861. [CrossRef]
36. Davidson, A.A.; Salim, S.M. CFD Modelling of Rotating Annular Flow Using Wall y+, International MultiConference of Engineers and Computer Scientists. *Trans. Eng. Technol.* **2018**, *1*, 318–330.
37. Manatbayev, R.; Baizhuma, Z.; Bolegenova, S. Numerical simulations on static Vertical Axis Wind Turbine blade icing. *Renew. Energy* **2021**, *170*, 997–1007. [CrossRef]
38. Son, C.; Kim, T. Development of an icing simulation code for rotating wind turbines. *J. Wind Eng. Ind. Aerodyn.* **2020**, *203*, 104239. [CrossRef]
39. Madsen, P.H.; Risø, D.J.R.N.L. *Introduction to the IEC 61400-1 Standar*; Technical Standard; Risø National Laboratory, Technical University of Denmark: Kongens Lyngby, Denmark, 2008.

processes

MDPI

*Article*

# Study on the Aerodynamic Performance of Floating Offshore Wind Turbine Considering the Tower Shadow Effect

**Danmei Hu *, Liwei Deng and Li Zeng**

College of Energy and Mechanical Engineering, Shanghai University of Electric Power, Shanghai 200090, China; dengliwei_suep@163.com (L.D.); zengli1832507667@sina.com (L.Z.)
* Correspondence: hudanmei@shiep.edu.cn

**Abstract:** The aerodynamic performance of the floating offshore wind turbine (FOWT) is obviously affected by the motion of the platform, and becomes much more complicated considering the effect of tower shadow. In view of this, this paper aims at investigating the aerodynamic performance of the floating offshore wind turbine with and without a tower under the three most influential motions (surge, pitch and yaw) by computational fluid dynamic (CFD). The results show that the power of the wind turbine is reduced by 1.58% to 2.47% due to the tower shadow effect under the three motions, and the pressure difference distribution is most obviously interfered by the tower shadow effect under yaw motion and concentrates at the root and tip of the blade. In addition, the degree of interference of the tower shadow effect on the wake flow field is different under the three motions, resulting in a more complex wake structure. These conclusions can provide a theoretical basis and technical reference for the optimal design of floating offshore wind turbines.

**Keywords:** floating offshore wind turbine; tower shadow effect; computational fluid dynamic; aerodynamic performance; surge; pitch; yaw

**Citation:** Hu, D.; Deng, L.; Zeng, L. Study on the Aerodynamic Performance of Floating Offshore Wind Turbine Considering the Tower Shadow Effect. *Processes* **2021**, *9*, 1047. https://doi.org/10.3390/pr9061047

Academic Editor: Eugen Rusu

Received: 3 May 2021
Accepted: 11 June 2021
Published: 15 June 2021

**Publisher's Note:** MDPI stays neutral with regard to jurisdictional claims in published maps and institutional affiliations.

**Copyright:** © 2021 by the authors. Licensee MDPI, Basel, Switzerland. This article is an open access article distributed under the terms and conditions of the Creative Commons Attribution (CC BY) license (https://creativecommons.org/licenses/by/4.0/).

## 1. Introduction

With the consumption of traditional fossil fuels and serious environmental pollution, more and more countries in the world begin to attach importance to the development of renewable energy. As a kind of green, pollution-free and abundant renewable energy, wind energy has great potential for development [1]. Originally, wind turbines were mainly built on land, but due to the large noise of onshore wind turbines and relatively few wind and land resources, the wind power industry gradually developed to the sea [2]. From a worldwide point of view, the sea wind is rich in resources, and the wind is stable, which has become the irresistible general trend [3]. With the large-scale capacity of the offshore wind turbine, the size of the wind turbine and the height of the tower are increasing, resulting in a more obvious tower shadow effect [4]. Therefore, it is particularly important to study the unsteady aerodynamics under the tower shadow effect of FOWT.

Offshore wind power generation has obvious advantages over onshore wind power generation; however, FOWTs produce six degrees-of-freedom (6-DOF) [5] motions under the combined action of wind, waves and currents, resulting in more complex aerodynamics compared with onshore and offshore fixed wind turbines. In recent years, many scholars have studied the aerodynamic performance and structural characteristics of FOWTs from the aspects of experiments, models, research methods, etc. The blade element momentum (BEM) theory with two widely used engineering dynamic inflow models was used by Vaal [6] to investigate the effect of a periodic surge on the wind turbine. Ma [7] investigated the effects of the control system of the wind turbine and the motion of the floating platform on the blade aerodynamic performance during the representative typhoon time history. However, the BEM methods used to research aerodynamics lack the characteristics of capturing the physical details of the flow field, which the reasonability and accuracy are suspectable. Farrugia [8] used the results from the free-wake vortex simulations to

analyze the wake characteristics of the wind turbine under floating conditions. Complex wake phenomena under the influence of extreme wave conditions were observed. Wen et al. [9,10] also used the FVM method for numerical simulation and found that the power coefficient overshoot is caused by the time lag between the output power and the wind farm power. The time lag and the resultant power coefficient overshoot increase as the platform surge frequency increases. In pitch motion, with the increase of the reduced frequency, the mean power output decreases at a low tip speed ratio and increases at a high tip speed ratio. Salehyar [11] investigated the dynamic response of a spar-buoy-based floating wind turbine to non-periodic disturbances through a coupled aero-hydro-elastic numerical model, observing the ability of the wind turbine to recover to the balanced position after being disturbed. Lin [12] investigated the aerodynamic characteristics in system pitch and surge motions and the asymmetric and complicated wake was observed. Tran et al. [13–16] performed the CFD simulation based on the dynamic mesh technique and an advanced overset moving grid method, respectively, to accurately consider the aerodynamic loads of a three-dimensional wind turbine. Results summarized the comparisons of different aerodynamic analyses under periodic surge, pitch and yaw motions to show the potential differences between the applied numerical methods. Chen [17] proposed a model of a spar-buoy and a semi-submersible floating wind turbine to compare with the experimental results of the two. Nguyen [18] studied the fully coupled motion of FOWT and applied the six degrees-of-freedom solid motion solver to multi-motion coupling to study the coupling of the surge, pitch and yaw motions. Huang [19] discussed the dynamic response of the local relative wind speed and local angle of attack of the blade section and the wind–wave force acting on the floating platform to reveal the interaction mechanism between the aerodynamic load and the motion of the platform with different degrees of freedom. Fang [20,21] applied a 1:50 model FOWT to explore the aerodynamics and characteristics of its wake under surge and pitch motions. Chen [22,23] investigated the aerodynamic characteristics of the wind turbine under surge–pitch coupling and pitch–yaw coupling by the combination of dynamic mesh and sliding mesh. The results show that the fluctuation of the overall aerodynamic performance of the wind turbine dramatically with the increase of amplitude and frequency. Sivalingam [24] examined the predictions of numerical codes by comparing them with experimental data of a scaled floating wind turbine.

In addition to the research on changes in wind turbine performance caused by platform motions, a series of studies have also focused on the tower shadow effect of the wind turbine. Kim [25] and Quallen [26] found that the diameter of the tower has a greater effect on the wind turbine than the gap between the tower and the blade, and the root of the blade is more affected by the tower. Ke [27] proposed an effective method for calculating the aerodynamic load and aeroelastic response of a large wind turbine tower blade coupling structure under the yaw condition, taking full account of wind shear, tower shadow, aerodynamic interaction and rotation effect. Noyes [28] used unsteady aerodynamic experiments to analyze the influence of tower shadow effect on aerodynamic loads and blade-bending moments of downwind two-blade wind turbines. Zhang [29] found that the maximum displacement and Mises stress increase with the increase of the average wind speed under the tower shadow effect. Li [30] investigated the aeroelastic coupling effect under periodic unsteady inflows, indicating that the tower shadow effect causes dramatic changes in the tilting moment, thrust force and output power when the blade rotates in front of the tower. Wu [31] investigated the unsteady flow characteristics in the tip region of the blade, observing the static pressure distribution of different blades near the leading edge of the tip is very different due to the influence of turbulence intensity and tower shadow effect.

According to the above literature review, the influence of the six degrees-of-freedom motions of the platform on the FOWTs has been studied to a certain extent, and the investigations on the tower shadow effect are mostly focused on the land-based fixed wind turbine. Nevertheless, the effect of platform motions combined with the tower shadow effect is rarely mentioned. This paper aims to investigate the unsteady aerodynamic

characteristics of FOWTs under surge, pitch and yaw motions based on the tower shadow effect. The unsteady dynamic numerical simulation of the aerodynamic characteristics of the full-size wind turbine model in the rotating process was carried out using a UDF (user-defined function) and embedded sliding mesh, and the unsteady Reynolds-Averaged Navier–Stokes equations (RANS) and SST k-ω turbulence model are adopted. Considering the effect of the tower shadow effect, the power, thrust and the pressure distribution of blade sections under surge, pitch and yaw motions are compared and analyzed, and the near wake and far wake flow fields of the wind turbine are analyzed.

## 2. Model and Numerical Methods

### *2.1. Governing Equations and Turbulent Model*

The three laws of mass conservation equation, momentum conservation equation and energy conservation equation need to be followed in fluid mechanics. For incompressible fluids, the continuity equation and the momentum equation (Navier–Stokes equation) can be used to describe the law of conservation of mass and momentum of the fluid. Regodeseves [32] and Burmester [33] validated the accuracy of the model in simulating the aerodynamic characteristics of FOWTs by comparing the simulation results of the model with the experimental data.

The definition of the continuity equation, Reynolds equation and scalar Φ time-averaged transport equation expressed in the tensor form are expressed as follows:

$$\frac{\partial \rho}{\partial t} + \frac{\partial}{\partial x_i}(\rho u_i) = 0, \tag{1}$$

$$\frac{\partial}{\partial t}(\rho u_i) + \frac{\partial}{x_j}\left(\rho u_i u_j\right) = -\frac{\partial p}{\partial x_i} + \frac{\partial}{x_j}(\mu \frac{\partial u_i}{\partial x_j} - \rho\overline{u'_l u'_j}) + S_i, \tag{2}$$

$$\frac{\partial(\rho\phi)}{\partial t} + \frac{\partial(\rho u_j \phi)}{\partial x_j} = \frac{\partial}{\partial x_j}\left(\Gamma\frac{\partial \phi}{\partial x_j} - \rho\overline{u'_j \phi'}\right) + S, \tag{3}$$

$$\tau_{ij} = -\rho\overline{u'_l u'_j}, \tag{4}$$

where $\rho$ is the air density, $t$ is the time, $u_i$ and $u_j$ represent the Reynolds mean velocity components of fluid, $p$ is the pressure, $\mu$ denotes the coefficient of dynamic viscosity, $S$ is the generalized source term ($i$, $j$ = 1, 2, 3) and Γ represents the diffusivity. $\tau_{ij}$ corresponds to six different Reynolds stress terms, which is defined as Reynolds stress.

The SST *k-w* model combines the advantages of the *k-w* model in the near-wall region and the far-field calculation of the *k-ε* model, further modifies the turbulent viscosity and adds an orthogonal diffusion term, which can well predict the separation of the fluid under the negative pressure gradient. For the aerodynamic analysis of the wind turbine in this paper, the SST *k-w* model has obvious advantages, which is used in the later simulation.

The transport equation expression of SST *k-w* is as follows:

$$\frac{\partial(\rho k)}{\partial t} + \frac{\partial(\rho u_i k)}{\partial x_i} = \frac{\partial}{\partial x_j}\left(\Gamma_k \frac{\partial k}{\partial x_j}\right) + \overline{G}_k - Y_k + S_k, \tag{5}$$

$$\frac{\partial(\rho w)}{\partial t} + \frac{\partial(\rho u_i w)}{\partial x_i} = \frac{\partial}{\partial x_j}\left(\Gamma_w \frac{\partial w}{\partial x_j}\right) + G_w - Y_w + D_w + S_w, \tag{6}$$

where $\overline{G}_k$ is the turbulent energy caused by the average velocity gradient, $G_w$ is the turbulent dissipation rate, $\Gamma_k$ and $\Gamma_w$ represent the effective diffusivity of $k$ and $w$ caused by turbulence, respectively, $Y_k$ and $Y_w$ are the dissipation of $k$ and $\omega$, $D_w$ is the orthogonal divergence, both $S_k$ and $S_w$ represent user-defined source items.

### 2.2. Floating Foundation

The floating foundation wind turbine is affected by wind, waves and currents in the marine environment, which produces 6-DOF motions. As shown in Figure 1, the motion of the platform includes three rotational components (pitch about X, roll about Y and yaw about Z) and three translational components (sway in X, surge in Y and heave in Z). This paper chooses a Spar floating wind turbine foundation for its larger draft, small vertical excitation force and heave motion [34].

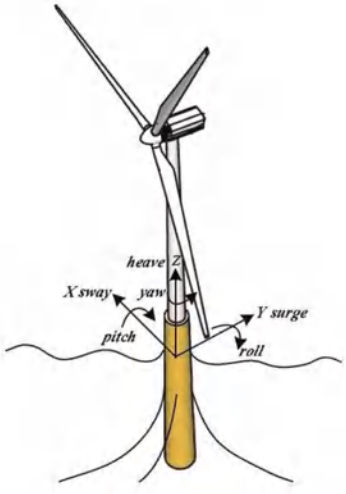


**Figure 1.** 6-DOF motions of a wind turbine floating foundation.

### 2.3. Wind Turbine Model

The NREL 5 MW wind turbine was selected as the research object, which is a three-bladed, upwind wind turbine and the power control adopts variable speed and variable pitch method. The diameter of the wind turbine is 126 m, and the hub height is 90 m. From root to tip, DU series airfoils of different thicknesses are used, and NACA series airfoils are used in the tip part. This study considers the existence of the tower, the bottom diameter of the tower is 6 m, and the top diameter is 3.87 m. The numerical simulation of the wind turbine is carried out under the rated operating conditions; the incoming wind speed is 11.4 m/s with the rotational speed of 12.1 r/min.

### 2.4. Flow Field and Boundary Conditions

As shown in Figure 2, the flow field calculation domain is divided into the external static domain and internal rotation domain. The rotational domain is used to define the rotation of the wind turbine relative to the external domain under the action of the inflow wind. The origin of the coordinate system is located in the center of the hub. The rotational domain is a cylinder with a diameter of 140 m and a height of 8 m. Considering the vastness of the sea area, the calculation domain should be divided large enough to reduce the influence of the boundary on the calculation accuracy [35]. The external flow field is a combination of a hemisphere with a diameter of 6.3 R (R is 63 m radius of the wind turbine rotor) and a cuboid with a width of 90 m. The inlet distance is 3.2 R from the rotation domain, and the outlet distance is 8 R from the rotation domain.

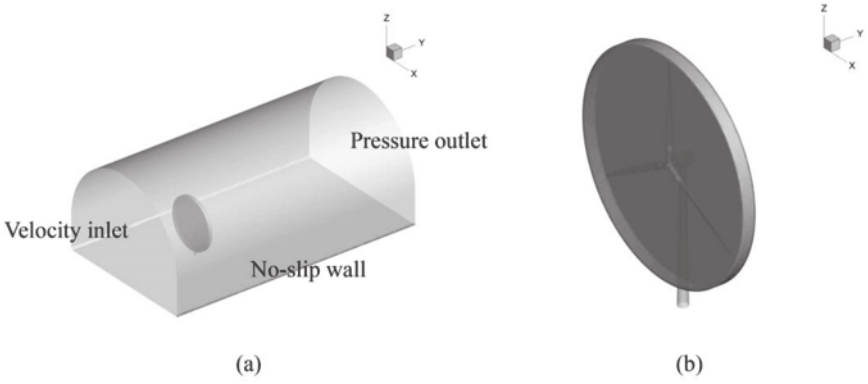


**Figure 2.** Computational domain of wind turbine flow field: (**a**) external domain; (**b**) rotational domain.

Due to the nested motion in the blade rotation domain, it is necessary to use the embedded sliding mesh to define its rotation. The area where the inner and outer domains are in contact with each other is set as the interface. There is a relative slip between the interfaces and the flow field information is transmitted. The inlet and outlet of the external flow field are set as velocity inlet and pressure outlet, respectively. Additionally, the surface of the blade and the surrounding boundary of the external flow field are set as non-slip walls.

### *2.5. Computational Mesh*

The internal and external flow field of the wind turbine is divided into unstructured grids by using MESH software. Figure 3 presents the grid generation in the overall computational domain. As the blade structure of the wind turbine model is complex and the tip position of the blade is too sharp, the grid size of the rotation region close to the blade needs to be set smaller, and the surface grid of the blade is further refined, which meets the requirements of the SST *k-w* turbulence model. As shown in Figure 3a, there are a total of 8.27 million grids in the whole flow field, of which the internal flow field grid is 6.21 million and the external field grid is 2.06 million.

### *2.6. Computational Methods*

The flow field of the wind turbine is simulated in ANSYS Fluent software, and the unsteady Reynolds-Averaged Navier–Stokes equations (RANS) is solved by using the SST *k-w* turbulence model considering the transition effects on the blade surface. The sliding grid method is used to simulate the rotation of the wind turbine, which is set as a transient calculation. The pressure-based solver is used, the SIMPLEC algorithm is selected for pressure-velocity coupling, in which the second-order upwind scheme is used for pressure term, convection term, turbulent kinetic energy equation and turbulent dissipation rate. Based on the steady calculation results, the unsteady calculation for 20 s is carried out, the additional calculation for 40 s is carried out in the case of platform motion, and the last platform motion period after convergence is taken as the analysis result. The residual of the continuity equation is reduced by at least four orders of magnitude in the process of calculation.

Figure 1 has defined the form of platform motions, including surge, pitch and yaw, which are the main factors affecting the aerodynamic performance of FOWTs. According to the situation of the literature [36], the suitable amplitude and frequency parameters of the floating foundation are selected, and the main motion parameters are shown in Table 1. In order to realize the above platform motions, the additional speed change is compiled by

the DEFINE_PFORILE macro of UDF. It is assumed that the motion of the FOWT floating foundation is harmonic; its expression can be written as:

$$\beta_i(t) = A_i \sin(\varepsilon_i t), \tag{7}$$

where $\beta_i(t)$, $A_i$ and $\varepsilon_i$ ($i$ = surge, pitch, yaw) denote the angle/displacement, amplitude and frequency of the platform motion.

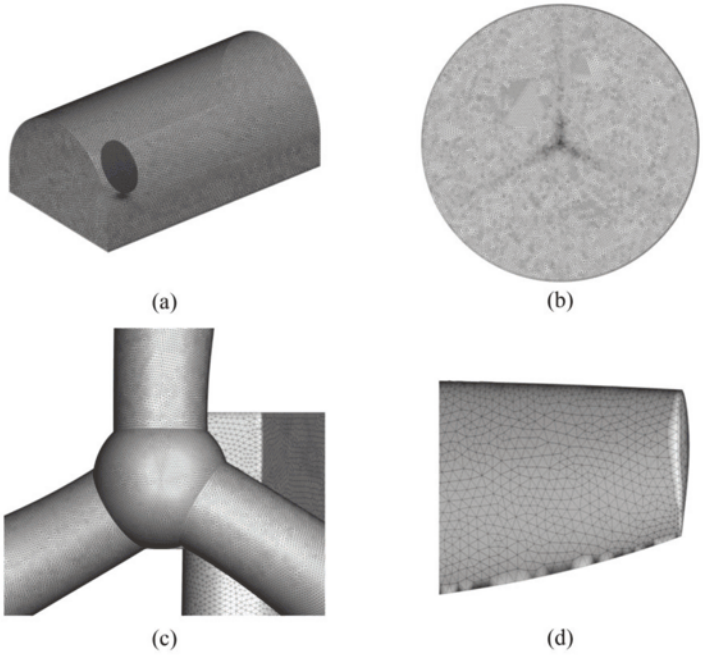


**Figure 3.** Computational mesh; (**a**) External domain; (**b**) Internal domain; (**c**) Hub surface mesh; (**d**) Blade surface mesh.

**Table 1.** Floating foundation motion conditions.

| Conditions | Motion | Displacement | Amplitude | Frequency |
|---|---|---|---|---|
| 1 | surge | −5–5 m | / | 0.05 Hz |
| 2 | pitch | / | −5–5° | 0.05 Hz |
| 3 | yaw | / | −15–15° | 0.05 Hz |

The motion of the floating foundation is described by the matrix between coordinate systems [37]. The incoming wind speed is set to $V = [V_x, V_y, V_z]^{\mathrm{T}}$, where $V_x$, $V_y$, $V_z$ represents the partial velocity in the direction of X, Y and Z, respectively. the relative inflow velocity of the platform during surge motion is converted into $V_S$, which can be written as

$$V_S = V(t) + \begin{bmatrix} 0 \\ \beta'_{surge}(t) \\ 0 \end{bmatrix} = \begin{bmatrix} 0 \\ V_y + \varepsilon_{surge} A_{surge} \cos(\varepsilon_{surge} t) \\ 0 \end{bmatrix}, \tag{8}$$

where $\beta'_{surge}(t)$ denotes the velocity of surge motion at each moment.

The pitch motion corresponds to the rotation $\beta_{pitch}$ of the floating platform around the $x$-axis, and the incoming flow velocity is converted to the relative velocity $V_P$, which can be presented as

$$V_P = \begin{bmatrix} 1 & 0 & 0 \\ 0 & \cos\beta_{pitch} & \sin\beta_{pitch} \\ 0 & -\sin\beta_{pitch} & \cos\beta_{pitch} \end{bmatrix} V = \begin{bmatrix} 0 \\ V_y\cos(A_{pitch}\sin(\varepsilon_{pitch}t)) \\ -V_y\sin(A_{pitch}\sin(\varepsilon_{pitch}t)) \end{bmatrix} \quad (9)$$

The yaw motion corresponds to the rotation $\beta_{yaw}$ of the floating platform around the $z$-axis, and the incoming flow velocity is converted to the relative velocity $V_Y$, which can be presented as

$$V_Y = \begin{bmatrix} \cos\beta_{yaw} & \sin\beta_{yaw} & 0 \\ -\sin\beta_{yaw} & \cos\beta_{yaw} & 0 \\ 0 & 0 & 1 \end{bmatrix} V = \begin{bmatrix} V_y\sin(A_{yaw}\sin(\varepsilon_{yaw}t)) \\ V_y\cos(A_{yaw}\sin(\varepsilon_{yaw}t)) \\ 0 \end{bmatrix} \quad (10)$$

## 3. Numerical Model Verification

### *3.1. Model Grid Independence Verification*

Table 2 exhibits the numerical value of the wind turbine torque under different meshing precision, which are refined along the circumference of wind turbine blades. The number of simulated grids is as follows: 2.86 million, 4.77 million, 6.71 million, 8.50 million and 10.08 million.

**Table 2.** Torque of different gird sizes.

| Cells Number (Million) | 2.86 | 4.77 | 6.71 | 8.50 | 10.08 | Reference Value |
|---|---|---|---|---|---|---|
| Torque (N m) | $3.54 \times 10^6$ | $3.82 \times 10^6$ | $3.90 \times 10^6$ | $3.98 \times 10^6$ | $4.03 \times 10^6$ | $4.01 \times 10^6$ |
| Relative error (%) | 11.72 | 4.74 | 2.74 | 0.75 | 0.50 | |

It can be found that with the refinement of the mesh, the error value of torque decreases constantly, and the decrease becomes smaller and smaller. The mesh of 8.50 million is selected for in-depth research due to the consideration of calculation accuracy and efficiency.

### *3.2. Model Power Verification*

Due to the lack of feasible experimental data, the experimental results of Jonkman [38] were selected for verifying the accuracy of the simulation. The cut-in wind speed of the NREL 5 MW wind turbine is 3 m/s. When the wind speed reaches more than 3 m/s, the wind turbine starts to operate. The rated wind speed is 11.4 m/s, and the rated speed is 12.1 rpm. When the wind speed exceeds the rated wind speed, the constant power control is realized by changing the pitch angle and reducing the lift-drag ratio.

Figure 4 illustrates the comparison of stable power between numerical simulation and experimental data under different incoming wind speeds. All of the results exhibited a high consistency before the incoming wind speed reached 11.4 m/s, indicating that the current simulation method has good accuracy and reasonable results.

### *3.3. Validation Considering the Tower under the Unsteady Condition*

It should be noted that the change of additional wind speed caused by the motion of the platform is synchronously added to the inlet velocity. The numerical model is verified with and without tower under unsteady calculation, respectively. A sufficient degree of steady condition calculation is carried out for the numerical model under rated conditions first, and the results of the steady calculation are taken as the initial flow field under unsteady wind speed conditions.

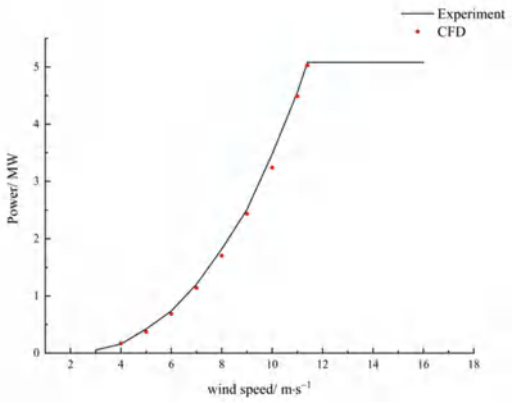


**Figure 4.** Power comparison of different wind speeds.

The uniform wind speed is 11.4 m/s, which is set at the inlet of the flow field. The speed of the wind turbine is 12.1 rpm. The time-step corresponding to 10° azimuth increment with 40 pseudo-time sub-iterations is 0.137741 s. The rotation time of the wind turbine for 4 cycles is calculated under unsteady conditions. Figure 5 shows the power fluctuation with and without the tower and it indicated that the power of the wind turbine tends to be stable after the wind turbine rotates for three cycles. Furthermore, a periodic rotation variation of the wind turbine in stable operation was observed locally. Compared with the non-tower, the existence of the tower makes the power decrease dramatically with an azimuth of 120° apart. This phenomenon is consistent with Wen [39]'s research, which verifies the influence of the tower shadow effect on the wind turbine.

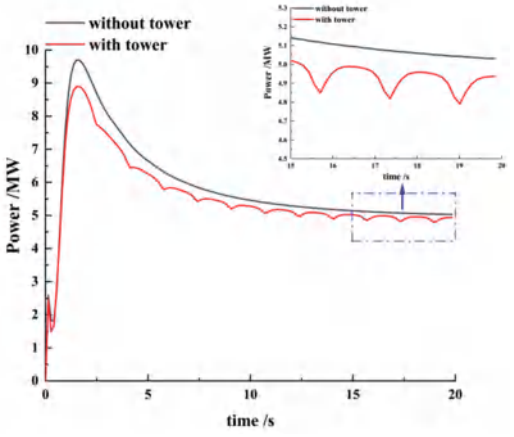


**Figure 5.** Power variation under unsteady rated condition.

## 4. Results and Discussion

Due to the obstruction of the tower to the airflow, the interference effect of the tower on the blades is different when the blades rotate to different azimuth angles. This paper takes the blades rotating to the azimuth directly above the tower as the starting point. The schematic diagram of the azimuth angle of the wind turbine blades is shown in Figure 6. $\theta$ is the angle between the two blades, $\gamma$ is the influence area of the tower shadow effect and the wind turbine rotates counterclockwise.

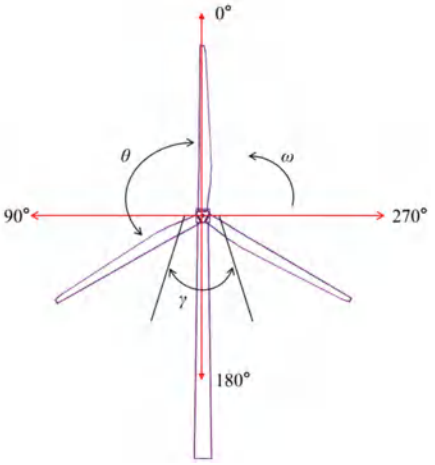


**Figure 6.** Schematic diagram of wind turbine blade-rotation phase angle.

### *4.1. Unsteady Aerodynamic Analysis under Surge Motion*

#### 4.1.1. Total Performance Analysis

Figure 7 illustrates the total power and thrust comparison with and without the tower under surge motion. It can be observed that the fluctuation period of power and thrust is consistent with the harmonic surge. The equilibrium position divides the power and thrust curve into rising and falling parts, mainly because the power and thrust are proportional to the relative wind speed. For f = 0.05 Hz, $A_s$ = 5 m, as shown in Figure 7b, the maximum power of the wind turbine without the tower is 6.98 MW, while the wind turbine with the tower is 6.85 MW. Both of these were larger than the rated power, while the existence of the tower reduced the maximum wind turbine power by 1.86%. The minimum power was 3.37 MW and 3.24 MW, respectively, and the power of the wind turbine with the tower was reduced by 3.86%. The average power generation was 5.12 MW and 5.01 MW, respectively; the latter was reduced by 2.15%. Further, the power fluctuated at a frequency thrice that of the rotation frequency under the combination of surge and tower shadow, while the surge motion played a leading role in the influence of power fluctuation. As shown in Figure 7c,d, the trend of the axial thrust fluctuation was similar to the power. The peak value of thrust without the tower was 888.3 KN; the wind turbine with the tower was 881.4 KN. Additionally, the valley value of thrust was 772.7 KN and 764.7 KN, respectively. It can be seen that the peak and valley values of thrust were basically the same with or without the tower. In addition, the average thrust was 772.7 KN and 764.7 KN, separately; the latter was reduced by 1.04%. It can be concluded that the influence of the tower shadow effect on thrust was less than that on power under the same condition of surge motion.

To further explore the variation mechanism of the aerodynamic load of the wind turbine under platform motion, the airfoil-induced velocity distribution under surge motion was analyzed, as shown in Figure 8. The surge motion of the platform produces an additional induced speed $V_{ind}$ to the wind turbine, which is obtained by superposing the surge speed with the free flow wind speed. When the platform moves forward, the $V_{ind}$ is opposite to the incoming wind speed, and the relative wind speed increases. When the platform moves backward, the $V_{ind}$ is in the same direction as the incoming wind speed, and the relative wind speed decreases. $V_{ind}$ can be decomposed into chord velocity $V_c$ and radial velocity $V_r$ on the rotating plane, the magnitude and direction of the relative velocity $V_{rel}$ acting on the rotating plane of the airfoil changes and the angle of attack changes accordingly. This theoretically expounds the essence of the fluctuation of the aerodynamic performance of the wind turbine under surge motion.

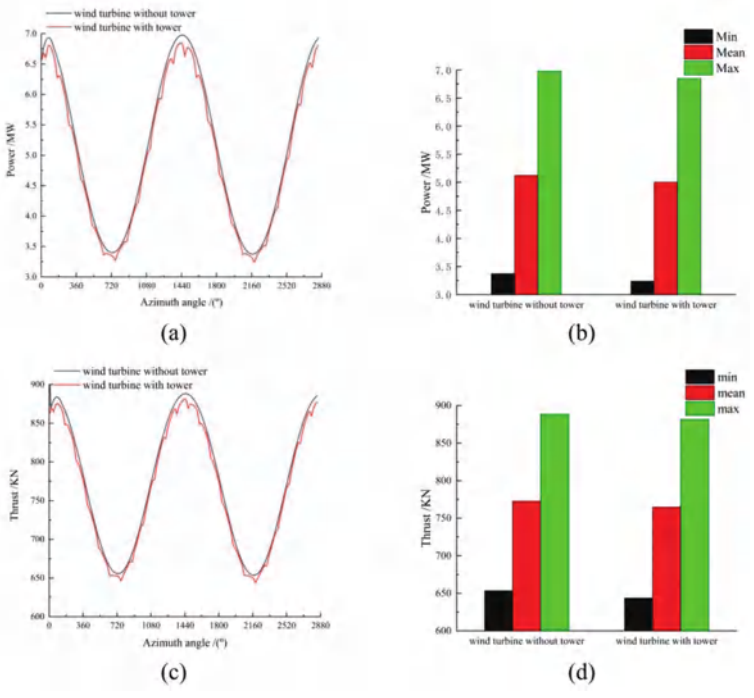


**Figure 7.** Total aerodynamic comparison of surge motion; (**a**) power versus azimuth angle; (**b**) extreme and average values of power; (**c**) thrust versus azimuth angle; (**d**) extreme and average values of thrust.

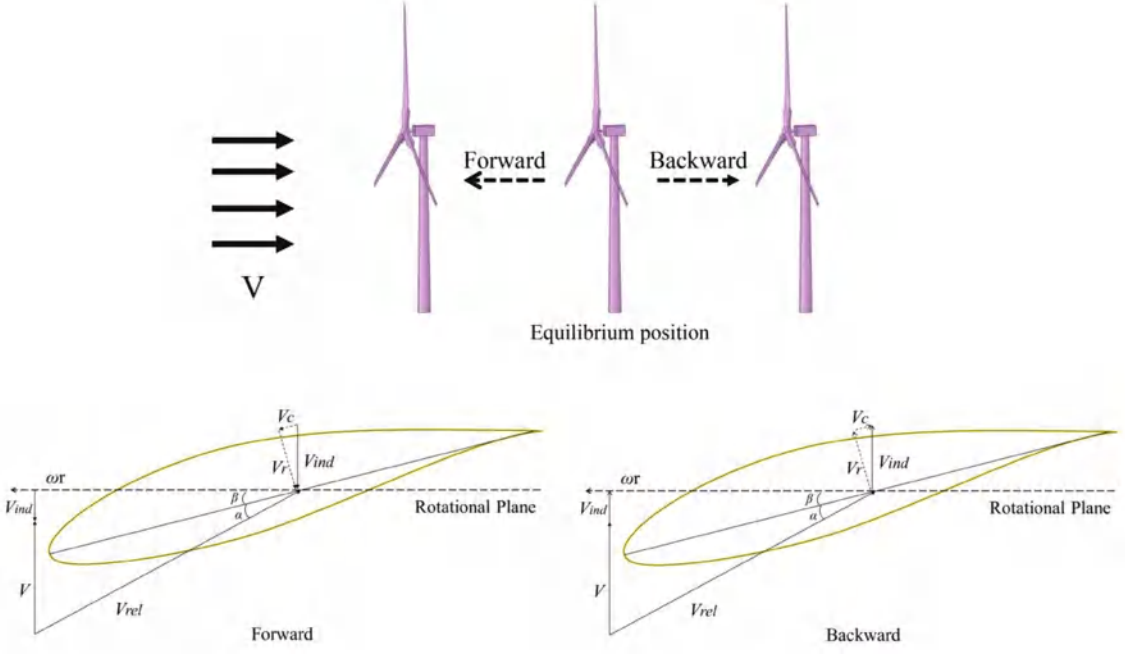


**Figure 8.** Schematic diagram of airfoil-induced velocity under surge motion.

4.1.2. Distribution of Pressure on the Blade Surface

Figure 9 shows the surge amplitude of the platform motion with reference to time. The second period of stable surge motion of the wind turbine is selected as the research object. Two typical positions were selected to analyze the pressure distribution on the blade surface.

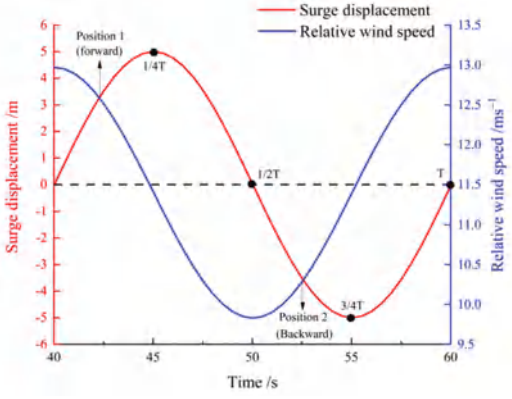


**Figure 9.** The two typical positions during surge motion.

The most fundamental influence of the tower shadow effect on the aerodynamic performance of the wind turbine is the interference of the tower on the blade; the blade surface pressure is the basic parameter to characterize the aerodynamic performance of the blade. This section selects two typical positions in which the blade rotates to the front of the tower under surge motion, and analyzes the pressure distribution under the root (r/R = 0.32), middle (r/R = 0.63) and tip (r/R = 0.94) sections of the blade. The abscissa is dimensionless as x/c (the abscissas of different points on the section/chord length of the section).

Figure 10 shows the distribution of pressure in each section of the blade with and without the tower at two typical positions in a surge cycle. It can be found that the pressure difference distribution at position 1 at the corresponding section is greater than that at position 2. It can be explained that the $V_{rel}$ at each blade section reaches larger values due to the forward surge velocity of the platform, while the $V_{rel}$ decreases when the platform surges backward. From the numerical point of view, the maximum pressure difference of the wind turbine without the tower at 0.32 R, 0.63 R, 0.94 R section is 1952 Pa, 4240 Pa and 7910 Pa, respectively. It can be seen that the closer to the tip of the blade, the greater the pressure difference on the blade surface. In addition, the tower shadow effect mainly affects the negative pressure value of the suction leading edge and the absolute value of the maximum negative pressure difference in each section is reduced by 10.56%, 7.61% and 5.36%, respectively. It can be inferred that the closer to the tip of the blade, the less obvious the interference of the tower shadow effect on the negative pressure of the suction surface.

4.1.3. Near Flow Field of Each Section of Blade

Figure 11 shows the interaction between the different blade sections and the tower when the blade rotates to the shadow area of the tower under surge motion. Position 1 was selected for further analysis. For the convenience of analysis, the variation of pressure fields near the blade surface and the distribution of absolute velocity streamline are discussed, respectively.

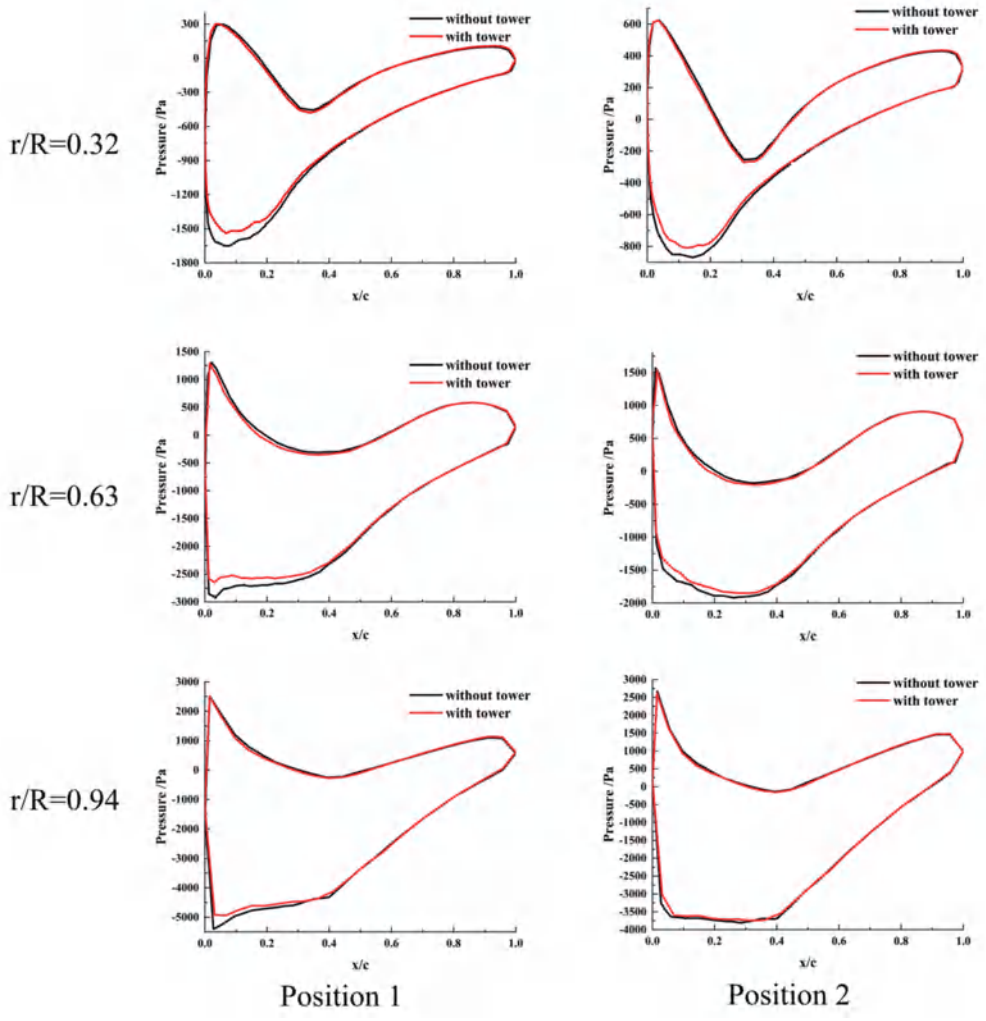


**Figure 10.** Distribution of pressure in each section of blade at position 1 and position 2.

By comparing the pressure field of the wind turbine with and without the tower at the same cross-section, it is seen that there is an obvious negative pressure field behind the suction surface of the blades. On the root and middle section of the blade, it can be observed that the suction leading edge negative pressure field of the wind turbine without the tower is larger and the negative pressure value is lower, while the pressure surface is basically the same, and the interference of the tower on the pressure field in the tip section is relatively small. These phenomena are in good agreement with the blade surface pressure distribution results described in the previous section. In addition, the whole negative pressure field at the root and middle section of the blade is obviously compressed due to the interference of the tower, which leads to a decrease in the pressure difference between the pressure surface and suction surface of the blade, thus reducing the overall work capacity of the blade. This further explains that the average power of the wind turbine decreases due to the influence of the tower shadow effect in the above results.

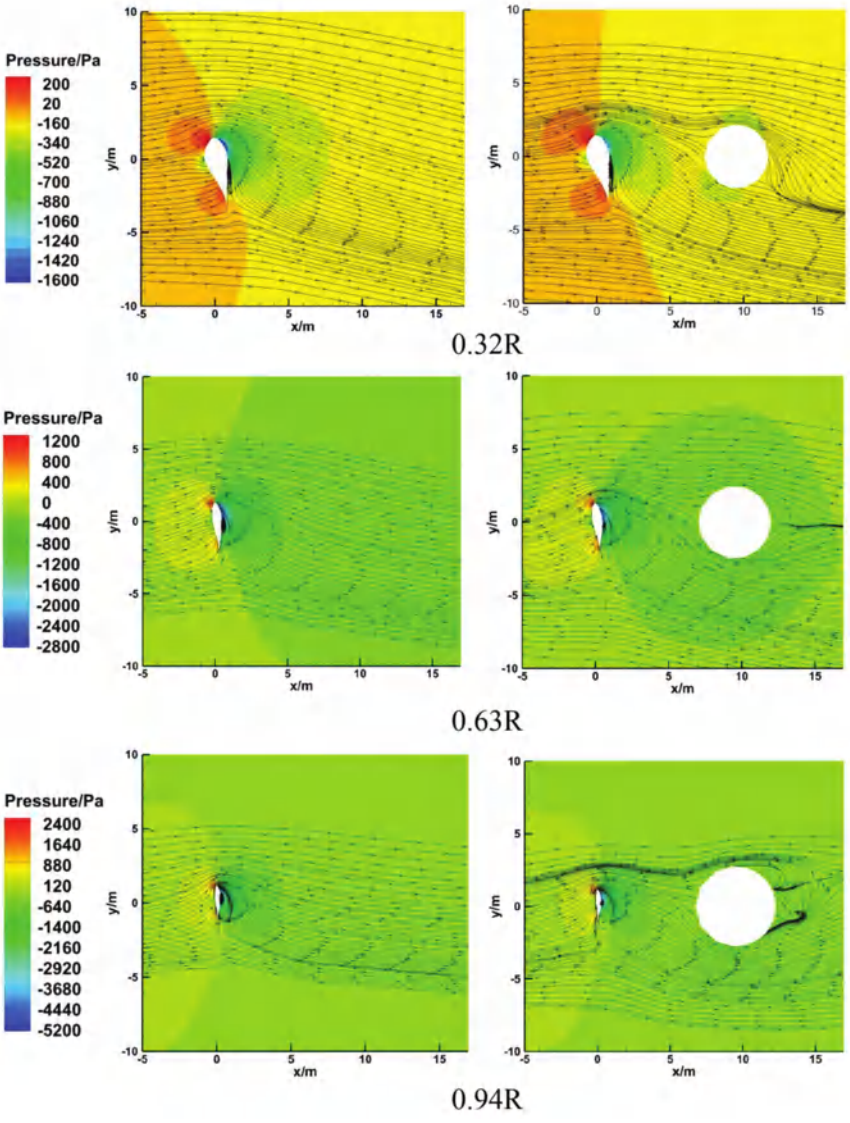


**Figure 11.** Streamline and pressure contours on different blade sections under surge motion.

Meanwhile, the streamline change of the wind turbine with the tower is not obvious compared with the wind turbine without the tower under surge motion, and the main change is concentrated in the wake of the tower. In the 0.32 R section, the streamline behind the tower shifts greatly, and the tower shadow effect is the most obvious in the interference of the flow field. In the 0.63 R section, the streamline on both sides of the tower shifts, and the flow field in this section is affected by both the tower shadow effect and the enhanced blade rotation effect. In the 0.94 R section, there is an obvious stall separation in the flow field behind the tower, and the separation point shifts to the direction of blade rotation. The area near the root of the blade is the main area affected by the tower shadow effect under surge motion, and the effect of the tower shadow effect weakens on the near wake flow field with the increase of blade height.

4.1.4. Wake Field behind the Wind Turbine

The main load source of the wind turbine is axial flow; the wake flow characteristics are particularly important for the analysis of wind turbine aerodynamics. By comparing the wake field with or without the tower, this section further illustrates the influence of platform motion on the aerodynamics of the wind turbine.

Figure 12 shows the velocity distribution of the wake field under platform surge motion. The symmetry of the wake field is disturbed and the flow field is slightly compressed. When the wind turbine moves forward, the average velocity of the wake field is greater than that of the backward motion. Considering the effect of the tower shadow, the influence range of the high-speed wake behind the hub expands, but it has little influence on the tip vortex, and the rear of the tower is accompanied by a large vortex shedding range and obvious vortex motion.

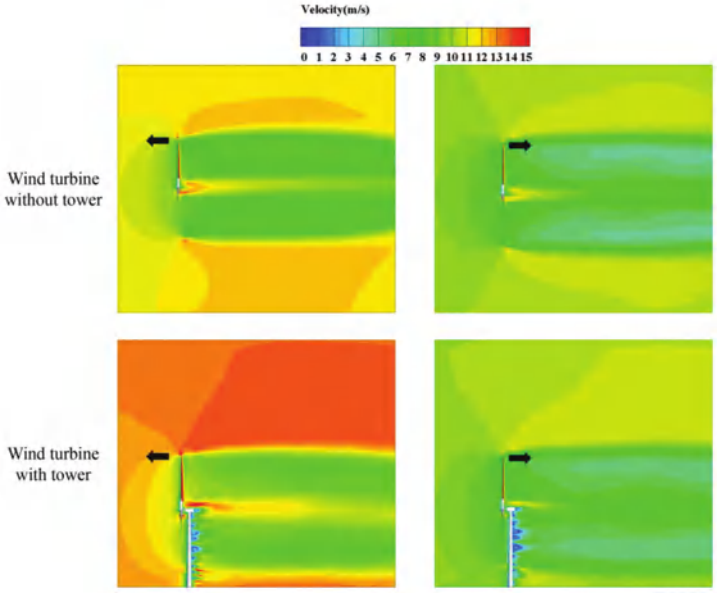


**Figure 12.** Velocity contours of wake field under surge motion.

*4.2. Unsteady Aerodynamic Analysis under Pitch Motion*

4.2.1. Total Performance Analysis

Figure 13 shows the overall power and thrust variation of the wind turbine with and without the tower. The pitch amplitude corresponds to the fluctuation of power and thrust values. For f = 0.05 Hz, $A_p = 5°$, as shown in Figure 13a, the power of the wind turbine fluctuates violently due to the existence of the tower, and it decreases sharply three times in one rotation cycle of the wind turbine. As shown in Figure 13b, the maximum power of the wind turbine without the tower was 5.16 MW, while the wind turbine with the tower was 5.11 MW. The minimum power of the former was 5.01 MW, while that of the latter s 4.70 MW. It can be seen that pitch motion slightly increases the peak and valley values of power, but the extreme value of the wind turbine decreases due to the existence of the tower. The average power generation was 5.06 MW and 4.98 MW, respectively; the latter was reduced by 1.58%. It can be found that the pitch motion of the platform increases the power of the wind turbine, but under the combination of pitch and tower shadow effect, the power fluctuation is larger and the increase is smaller. As shown in Figure 13c,d, the fluctuation trend of axial thrust is similar to that of power. The peak thrust and valley thrust of the wind turbine without the tower are 780.7 KN and 771.6 KN, and those with the tower are 777.9 KN and 751.1 KN, respectively. The average thrust was 774.5 KN and

769.0 KN, separately; the latter was reduced by 0.71%. That is, in terms of numerical values, the tower shadow effect slightly reduces the average power, while the average thrust is almost unchanged under pitch motion.

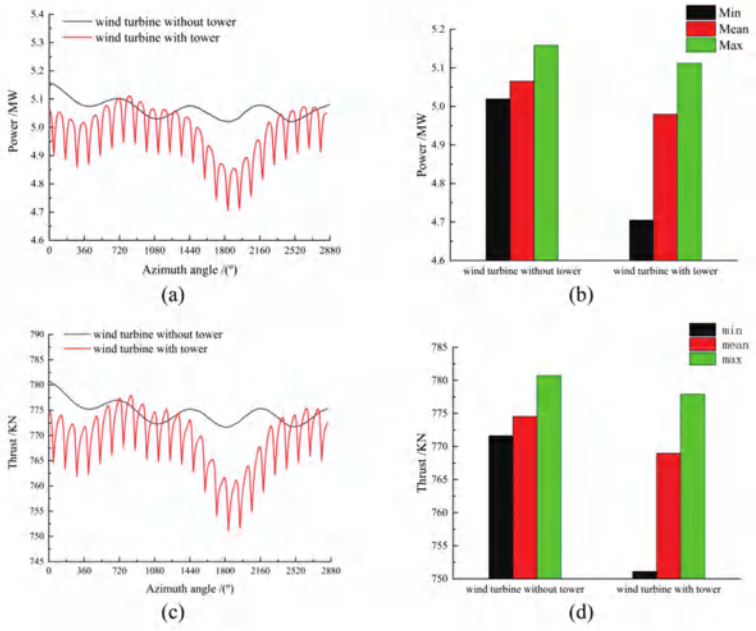


**Figure 13.** Total aerodynamic comparison of pitch motion; (**a**) Power versus azimuth angle; (**b**) Extreme and average values of power; (**c**) Thrust versus azimuth angle; (**d**) Extreme and average values of thrust.

Figure 14 shows the induced velocity distribution of airfoil under pitch motion. The pitch motion of the platform changes the angle between the incoming wind speed and the rotating plane of the wind turbine and produces an additional induced velocity $V_{ind}$. $V_{ind}$ can be decomposed into chord velocity $V_c$ and radial velocity $V_r$ on the rotating plane, in which the direction of chord velocity component $V_c$ depends on the positive or negative angle of pitch motion, which changes the relative velocity and direction of the rotating plane of the airfoil, and the angle of attack changes correspondingly. It leads to the fluctuation of the overall aerodynamic performance of the wind turbine under pitch motion.

4.2.2. Distribution of Pressure on the Blade Surface

Figure 15 shows the pitch amplitude and angular velocity of the platform motion with reference to simulation time. The second period of stable pitch motion of the wind turbine was selected as the research object, and the two typical positions of the wind turbine moving forward and backward to the front of the tower were selected for further analysis.

Figure 16 shows the pressure distribution in each section of the blade with and without the tower at two typical positions in a pitch cycle. In terms of numerical values, the maximum pressure difference of the wind turbine without the tower at 0.32 R, 0.63 R and 0.94 R sections is 1711 Pa, 3630 Pa and 7030 Pa, respectively. It can be found that the pressure difference of each section of the blade under pitch motion is smaller than that of surge motion. Comparing the pressure difference distributions of different sections at two typical positions, it can be seen that the pressure difference distributions on the pressure surface and the suction surface are basically the same. The change of the pressure difference is not obvious under pitch motion. Besides, affected by the tower shadow effect, the absolute value of the maximum negative pressure difference at the leading edge of

suction in each section of the blade decreases by 9.02%, 7.31% and 4.93%, respectively. Compared with surge motion, it can be seen that under pitch motion, the interference of the tower shadow effect on each section of the blade is also mainly concentrated in the root and tip of the blade, but the degree of interference is less than that of surge motion.

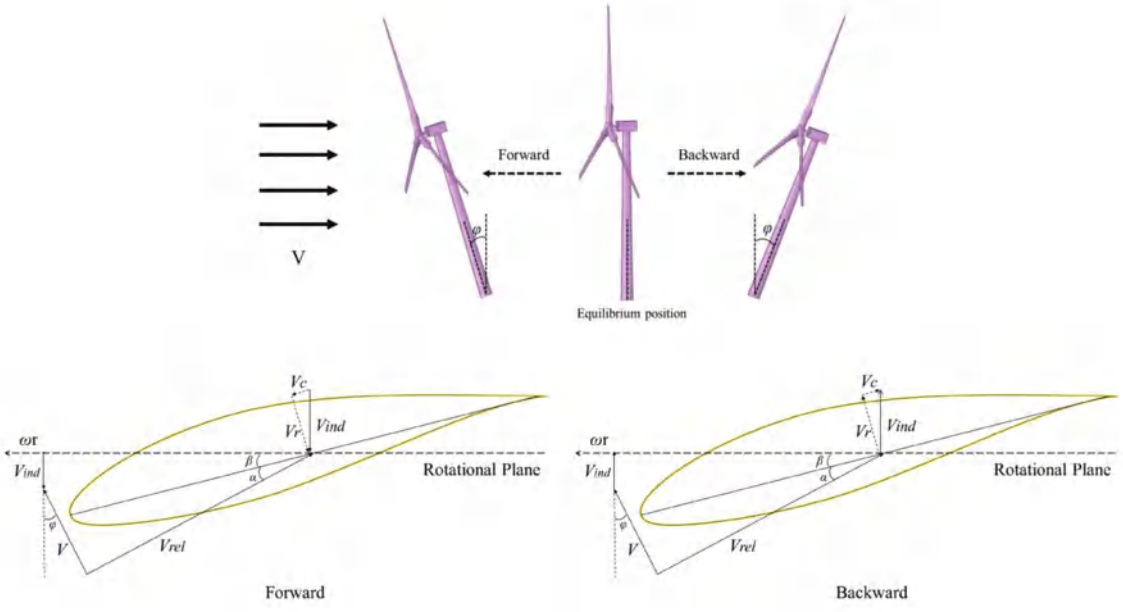


**Figure 14.** Schematic diagram of airfoil-induced velocity under pitch motion.

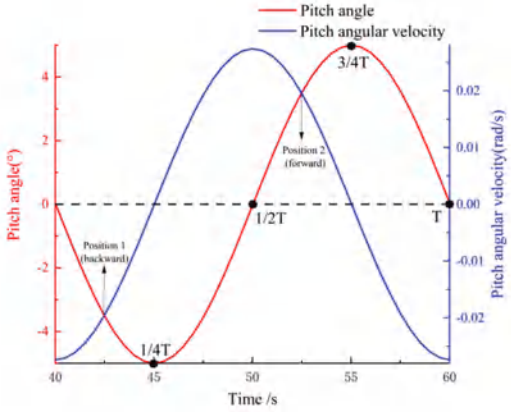


**Figure 15.** The two typical positions during pitch motion.

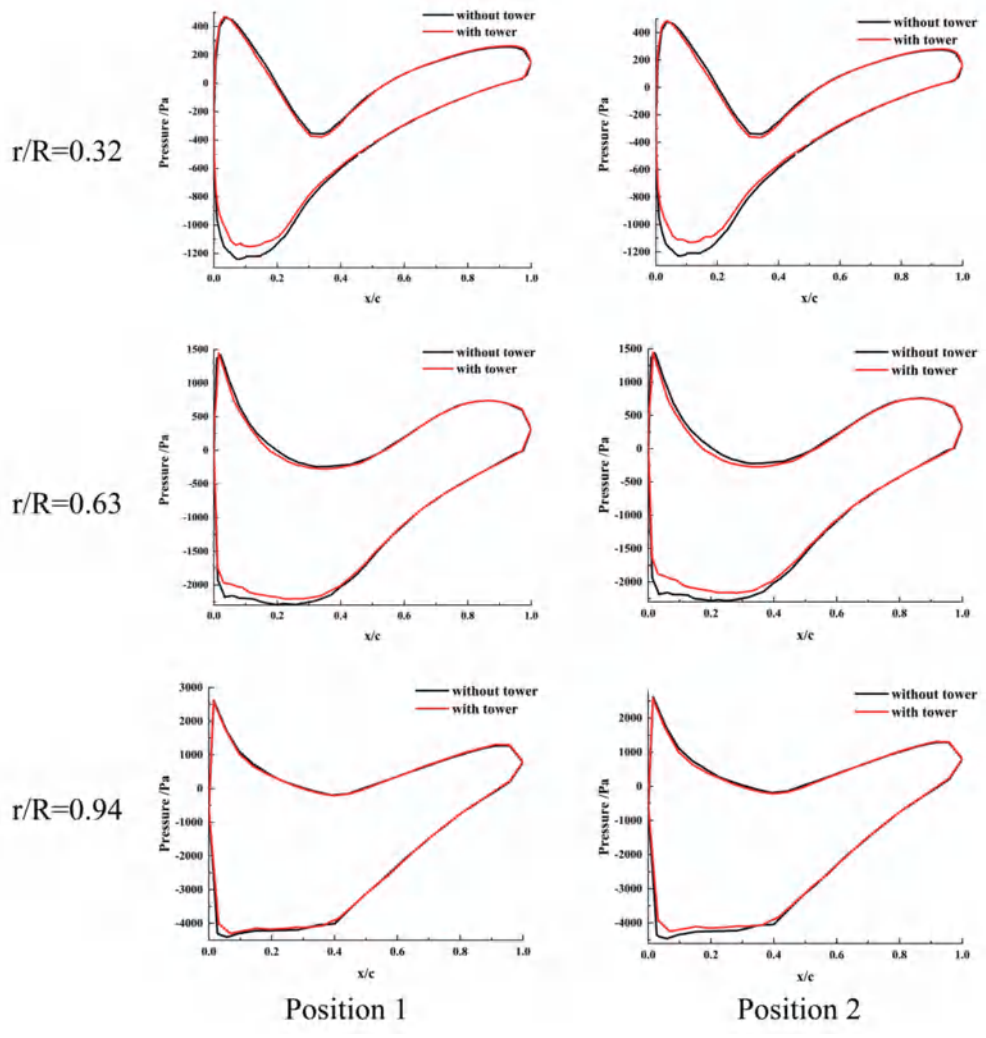


**Figure 16.** Distribution of pressure in each section of blade at position 1 and position 2.

4.2.3. Near Flow Field of Each Section of Blade

Figure 17 shows the interaction between the different blade sections and the tower when the blade rotates to the shadow area of the tower under pitch motion. The pitch motion of the platform to the rear and the rotation of the wind turbine to position 1 directly in front of the tower are selected for further analysis.

Comparing the pressure field on different blade sections with or without the tower under pitch motion, it can be seen that the pressure difference distribution of the blade surface is still concentrated on the leading edge of the blade. Under the influence of the tower shadow effect, the range of the negative pressure field near the suction surface of 0.32 R section and 0.63 R section is reduced, and the absolute value of negative pressure is smaller, but the negative pressure field of the suction surface of 0.94 R section has no obvious change. This further shows that the influence of the tower shadow effect on the pressure field is mainly concentrated in the root and the middle of the blade.

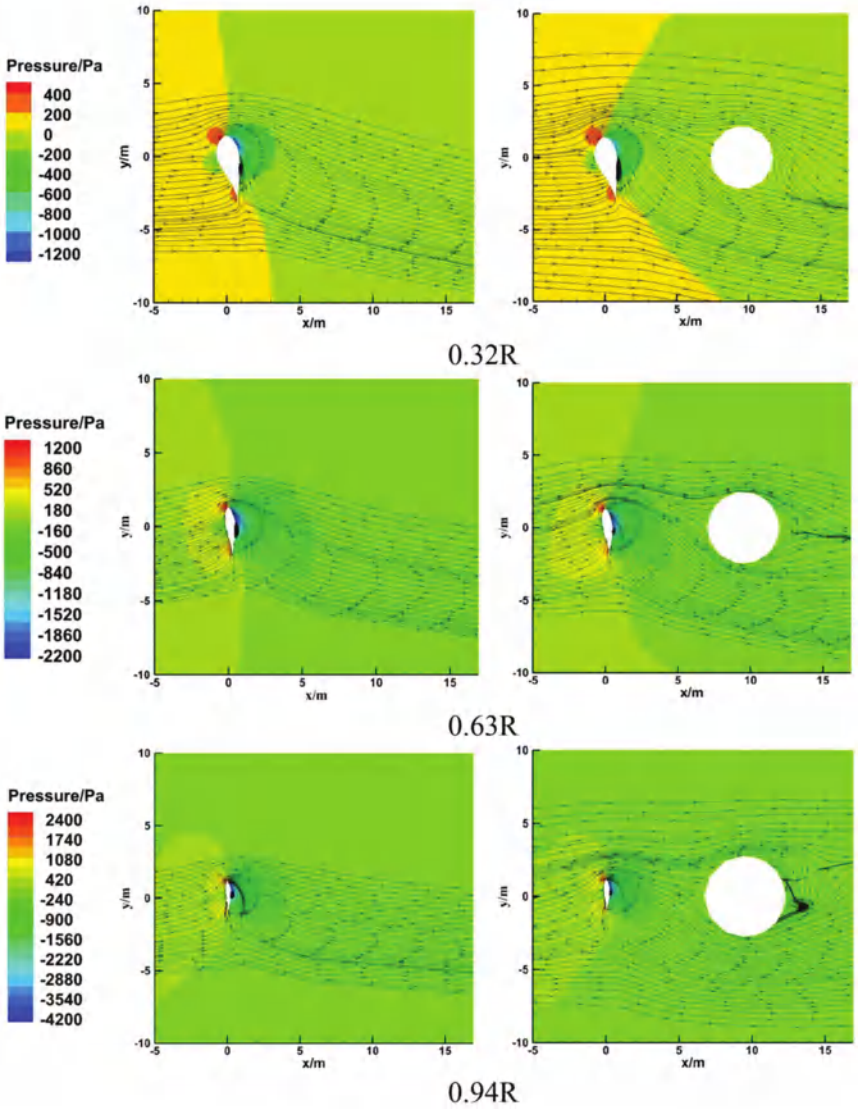


**Figure 17.** Streamline and pressure contours on different blade sections under pitch motion.

Observing the streamline distribution shown in Figure 17, the main difference is still concentrated in the near wake flow field of the tower. It can be seen that the distribution of the streamline at 0.32 R section and 0.63 R section is similar under surge motion, but there is an obvious stall separation vortex under the pitch motion at 0.94 R section, because compared with the surge motion moving only in the horizontal direction, the pitch motion applies a relative partial velocity in the vertical direction to the wind turbine when the azimuth of the wind turbine changes. The angle between the direction of the incoming flow velocity and the rotating plane of the wind turbine is constantly changing, which makes the flow field more complex.

4.2.4. Wake Field behind the Wind Turbine

Figure 18 shows the velocity distribution of the wake field under platform pitch motion. The two moments when the wind turbine is in the balanced position and pitches forward and backward, respectively, are selected for further analysis. It can be seen that when the wind turbine without the tower is in the equilibrium position, the mutual interference between the blade and the wake flow field is small, and the wake is more stable compared with surge motion. Nevertheless, the symmetry of the flow field behind the same wind turbine with the tower is affected, and there is an obvious low-speed disturbance zone behind the tower, which increases the complexity of the wake.

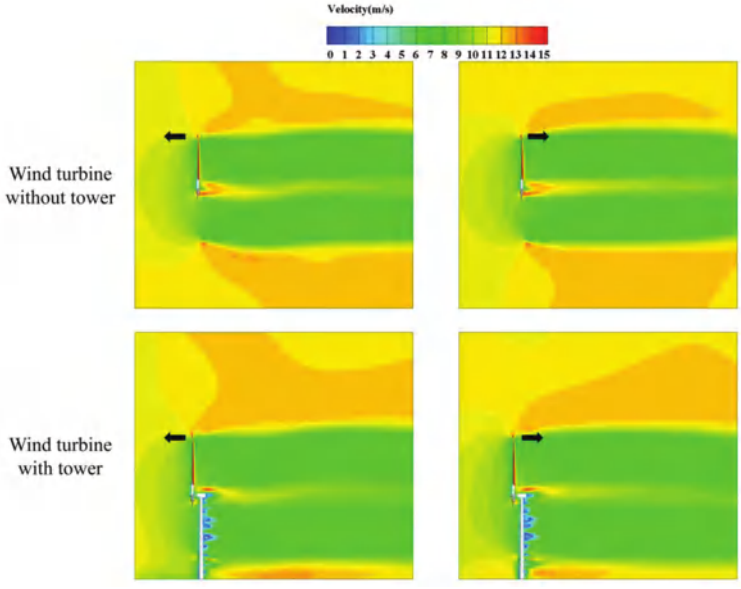


**Figure 18.** Velocity contours of wake field under pitch motion.

*4.3. Unsteady Aerodynamic Analysis under Yaw Motion*

4.3.1. Total Performance Analysis

Figure 19 shows the total power and thrust comparison with and without the tower under yaw motion. Similarly, the yaw amplitude corresponds to the fluctuation of power and thrust values. For f = 0.05 Hz, $A_y = 15°$, as shown in Figure 19a, it can be seen that the power of the wind turbine with the tower is always lower than that of the wind turbine without the tower under the same azimuth, and the power rises after three sharp drops in a wind turbine rotation cycle, which is the result of the combined action of the tower shadow effect and yaw motion. As shown in Figure 19b, under the effect of tower shadow, the maximum, average and minimum power of wind turbines are reduced by 1.94%, 2.47% and 4.16%, respectively. It can be concluded that the tower shadow effect aggravates the change of power extremum under yaw motion. As shown in Figure 19c,d, the fluctuation of the axial thrust value is consistent with that of the power value similarly; that is, they reach their respective extremes at the same azimuth. Under the effect of tower shadow, the maximum, average and minimum thrust of the wind turbine is reduced by 0.76%, 1.1% and 1.86%, respectively. It can be deduced that under yaw motion, the amplitude of the power drop is obviously affected by the tower shadow effect, while the thrust decreases slightly.

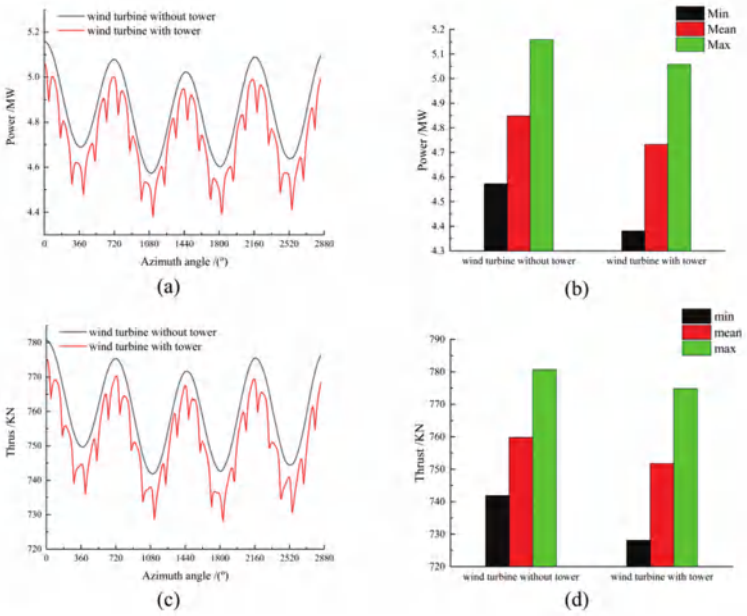


**Figure 19.** Total aerodynamic comparison of yaw motion; (**a**) Power versus azimuth angle; (**b**) Extreme and average values of power; (**c**) Thrust versus azimuth angle; (**d**) Extreme and average values of thrust.

Figure 20 shows the induced velocity distribution of airfoil under yaw motion. The yaw motion of the platform produces an additional induced velocity perpendicular to the rotation plane, and the direction of the $V_{ind}$ can be determined according to the right-hand rule. When the platform rotates to the left, the angle between the direction of the inflow velocity and the direction of $V_{ind}$ is an obtuse angle, and its relative inflow velocity increases; on the contrary, when the platform rotates to the right, the angle between the direction of the inflow velocity and the direction of $V_{ind}$ is an acute angle, and its relative inflow velocity decreases. $V_{ind}$ can also be decomposed into chord velocity $V_c$ and radial velocity $V_r$ on the rotating plane. *Vr* changes the rotation effect of the blade, and $V_c$ causes periodic fluctuations in the angle of attack and the sectional load of the blade.

4.3.2. Distribution of Pressure on the Blade Surface

Figure 21 shows the yaw amplitude and angular velocity of the platform motion with reference to simulation time. The second period of stable yaw motion of the wind turbine and two typical positions in front of the tower were selected for further analysis.

Figure 22 shows the pressure distribution in each section of the blade with and without the tower at two typical positions in a yaw cycle. The azimuth moment of 180° and 900° rotation of the wind turbine is selected to study when the wind turbine is at a certain yaw angle to both sides and the wind turbine is directly in front of the tower. In terms of numerical values, the maximum pressure difference of the wind turbine without the tower at 0.32 R, 0.63 R, 0.94 R sections is 1620 Pa, 3455 Pa and 6890 Pa, respectively. It can be found that the pressure difference of each section of the blade under yaw motion is smaller than that of pitch motion. Comparing the pressure distributions of the two kinds of wind turbines at two typical positions, it can be found that the distributions are consistent. The change of pressure difference at the different positions of yaw motion is also not obvious; however, affected by the tower shadow effect, the absolute value of the maximum negative pressure difference at the leading edge of suction in each section of the blade decreases by 11.01%, 8.23% and 5.80%, respectively. It can be inferred that under yaw motion, the

interference degree of the tower shadow effect on the negative pressure on the suction surface of the blade is greater than that of surge motion.

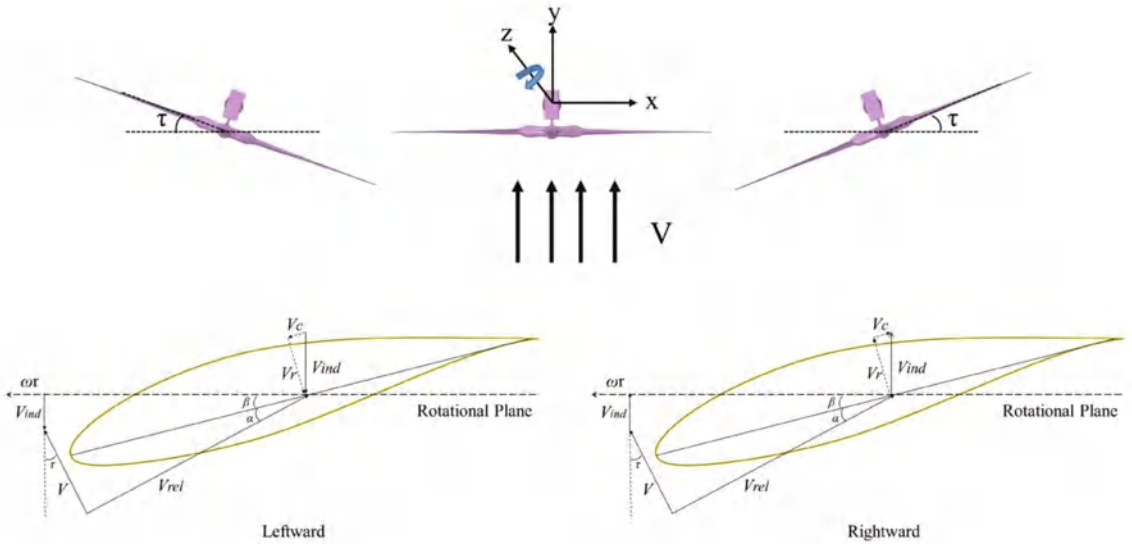


**Figure 20.** Schematic diagram of airfoil-induced velocity under yaw motion.

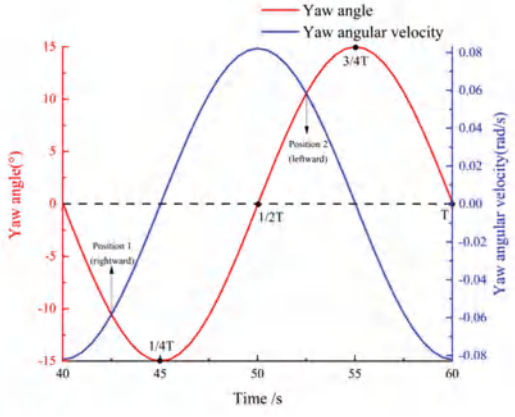


**Figure 21.** The two typical positions during yaw motion.

4.3.3. Near Flow Field of Each Section of Blade

Figure 23 shows the interaction between the different blade sections and the tower when the blade rotates to the shadow area of the tower under yaw motion. Position 1 was selected for further analysis.

Under yaw motion, the distribution trend of the pressure field in each section of the blade with or without the tower is similar to that of surge and pitch motions; the maximum negative pressure is still concentrated near the leading edge of the suction of the blade, and the tower compresses the negative pressure field and reduces the absolute value of the maximum negative pressure. The main influence range of the tower shadow effect is in the root and middle of the blade. From a numerical point of view, the blade surface pressure difference of the same section under yaw motion is lower than that of surge and pitch motions, which further shows that the work capacity of the wind turbine under yaw motion is the worst among the three motions.

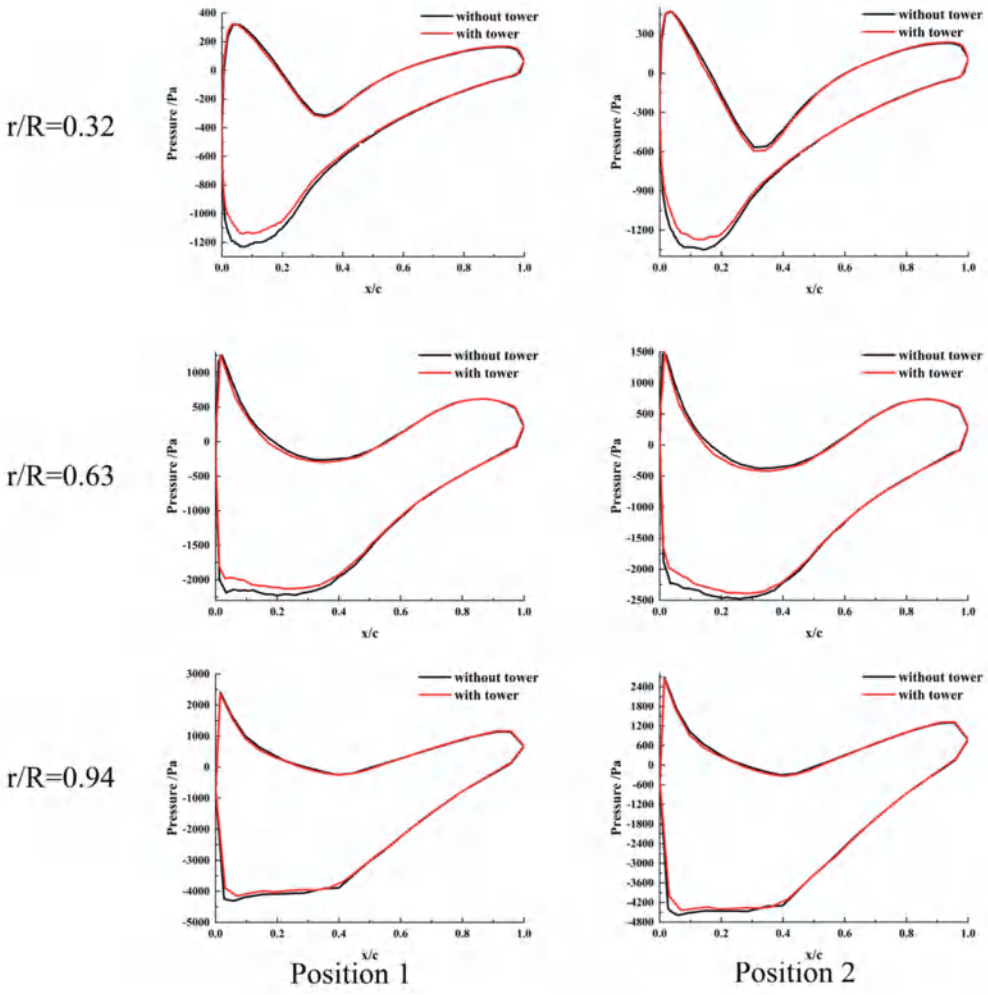


**Figure 22.** Distribution of pressure in each section of blade at position 1 and position 2.

By comparing the streamline of each section of the blade with or without the tower, the influence area of the tower shadow effect is still mainly concentrated in the wake flow field of the tower, and the streamline shifts behind the tower toward the trailing edge of the blade at 0.32 R section, which is mainly the interference of the tower. The streamline at 0.63 R section shifts in the opposite direction on both sides of the tower, which is the result of the joint action of the tower shadow effect and the enhanced rotation effect. At 0.94 R section, in addition to the weakening of the tower shadow effect and the enhancement of the rotation effect, the yaw motion changes the upwind area of the incoming flow and the rotating plane of the wind turbine, resulting in additional induced tangential velocity. The streamline behind the tower shifts to a greater extent along the rotation direction of the wind turbine.

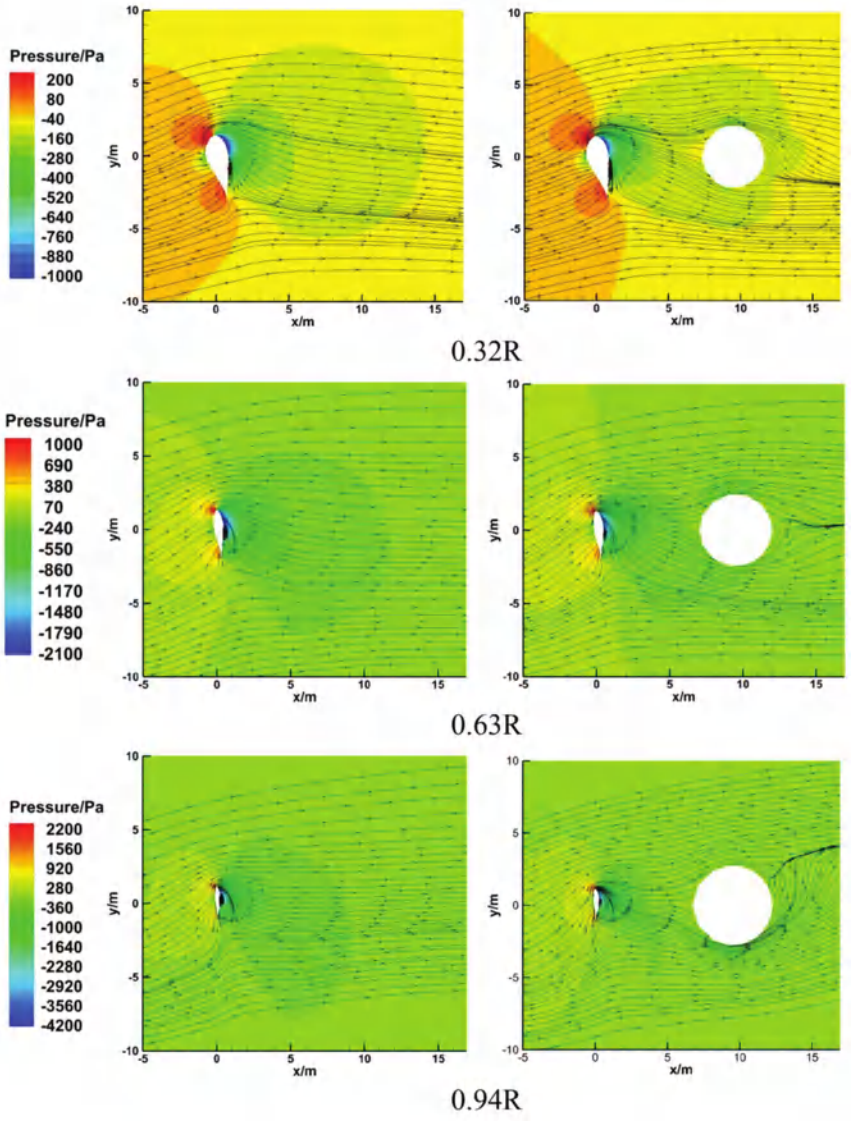


**Figure 23.** Streamline and pressure contours on different blade sections under yaw motion.

4.3.4. Wake Field behind the Wind Turbine

Figure 24 shows the velocity distribution of the wake field under platform yaw motion. The two moments when the wind turbine is in the equilibrium position and begins to yaw to the left and right side was selected for further analysis. The wake area of the wind turbine without the tower shows a nearly symmetrical distribution under the balanced position of yaw motion. Meanwhile, the high-speed wake area near the hub is smaller than that under pitch motion; it can be concluded that the yaw motion could reduce the induced velocity behind the hub. Furthermore, under yaw motion, the tower shadow effect similarly leads to the asymmetric distribution of the wake field.

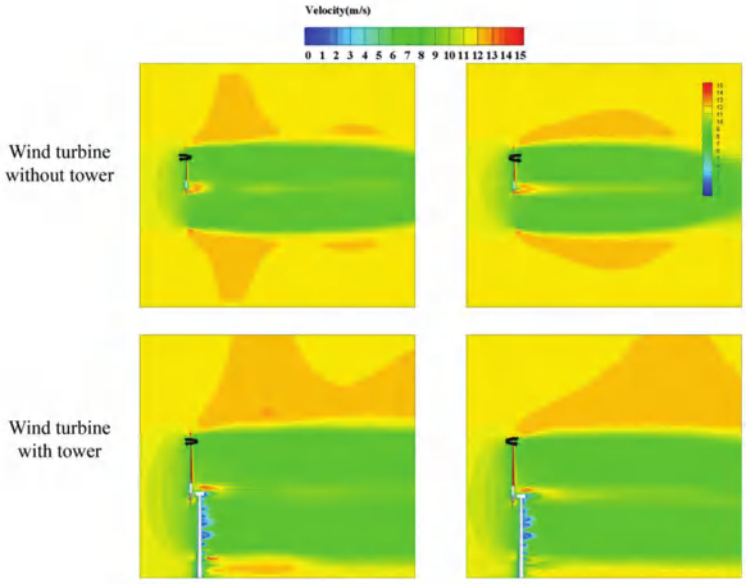


**Figure 24.** Velocity contours of wake field under yaw motion.

## 5. Conclusions

This paper investigated the aerodynamic performance of NREL 5 MW FOWT with a rigid blades turbine considering the tower shadow effect under surge, pitch and yaw motions, respectively. The motion form of the platform is equivalent to the change of relative velocity of the wind turbine. The dynamic inlet wind speed is compiled for unsteady numerical simulation using the UDF function. The accuracy of the numerical simulation was verified by proper computational grids. Three independent platform motions and two models with or without the tower were considered for calculation. The results illustrate the wind turbine's aerodynamics, including power, thrust, pressure distribution and flow field. The conclusions can be drawn as follows:

(1) The fluctuation frequency of power and thrust is always consistent with the motion frequency of the platform. The power is more obviously affected by the tower shadow effect than the thrust, in which the decrease of power is the largest under yaw motion, second-largest under surge motion, and smallest under pitch motion, with a decreased range of 1.58–2.47%.

(2) The influence of the tower shadow effect on the pressure difference of the wind turbine is mainly concentrated at the suction leading edge of the blade under different platform motions, and the interference ability of the tower from the root to the tip of the blade weakens along the blade-spreading direction. The pressure difference under yaw motion is most obviously interfered with by the tower, and the average maximum negative pressure is reduced by 8.35%, which is not conducive to the output power of FOWTs.

(3) For the pressure field, the tower shadow effect obviously compresses the range of the negative pressure field of the root and middle sections of the blade, while the negative pressure field of the tip section is less affected. For the near wake flow field, the wake of the tower at the root section is the most seriously interfered by the tower; the influence of the tower shadow effect decreases with the increase of the blade height and the additional induced velocity produced by yaw and pitch motions makes the near wake flow field of the tower more complicated.

(4) The wake field changes most violently under surge motion; the wake flow field is relatively stable under pitch and yaw motions. Besides, the tower shadow effect leads to

the increase of the velocity gradient near the hub, and the influence range of the high-speed wake of the tower wind turbine hub is the farthest under surge motion.

In view of these findings, the platform motion and the tower shadow effect have a great impact on the steady operation of FOWTs, and the combination of the two causes greater interference to the flow field. However, this paper only considers the aerodynamic characteristics of FOWTs under single-degree-of-freedom (surge, pitch and yaw) motion, and future research on factors such as heave, roll, sway and multi-degree-of-freedom coupling motions are worthy of more in-depth discussion.

**Author Contributions:** Conceptualization, L.D. and L.Z.; Formal analysis, L.D.; Investigation, L.D. and L.Z.; Methodology, L.D.; Project administration, D.H.; Software, L.D.; Supervision, D.H.; Validation, L.D.; Writing—original draft, L.D.; Writing—review and editing, L.D. All authors have read and agreed to the published version of the manuscript.

**Funding:** This research was funded by the Science and Technology Commission of Shanghai Municipality and the National Natural Science Foundation of China, grant number 18DZ1202302 and 50706025.

**Institutional Review Board Statement:** Not applicable.

**Informed Consent Statement:** Not applicable.

**Data Availability Statement:** The data are not publicly available.

**Acknowledgments:** This research work is sponsored by the Science and Technology Commission of Shanghai Municipality (18DZ1202302). Additionally, the support of the National Natural Science Foundation of China under project No. 50706025 is gratefully acknowledged.

**Conflicts of Interest:** The authors declare no conflict of interest.

## Abbreviations

| | |
|---|---|
| FOWT | Floating Offshore Wind Turbine |
| CFD | Computational Fluid Dynamic |
| 6-DOF | Six Degrees-of-Freedom |
| BEM | Blade Element Momentum |
| FVM | Free Vortex Method |
| UDF | User-Defined Function |
| RANS | Reynolds-Averaged Navier–Stokes equations |
| $V$ | Incoming Wind Speed |

## Nomenclature

| | |
|---|---|
| $V_S$ | the relative inflow velocity under surge motion |
| $V_P$ | the relative inflow velocity under pitch motion |
| $V_Y$ | the relative inflow velocity under yaw motion |
| $\theta$ | the angle between two blades |
| $\gamma$ | the influence area of the tower shadow effect |
| $\omega$ | the rotational speed of the wind turbine |
| $V_{ind}$ | the induced velocity of platform motion |
| $V_{rel}$ | the relative velocity |
| $A_s$ | surge amplitude |
| $A_p$ | pitch amplitude |
| $A_y$ | yaw amplitude |

## References

1. Cheng, P.; Huang, Y.; Wan, D.C. A numerical model for fully coupled aero-hydrodynamic analysis of floating offshore wind turbine. *Ocean Eng.* **2019**, *173*, 183–196. [CrossRef]
2. Shen, X.; Hu, P.; Chen, J.E.; Zhu, X.C.; Du, Z.H. The unsteady aerodynamics of floating wind turbine under platform pitch motion. *Proc. Inst. Mech. Eng. Part A J. Power Energy* **2018**, *232*, 1019–1036. [CrossRef]

3. Wu, X.N.; Hu, Y.; Li, Y.; Yang, J.; Duan, L.; Wang, T.G.; Adcock, T.; Jiang, Z.Y.; Gao, Z.; Lin, Z.L.; et al. Foundations of offshore wind turbines: A review. *Renew. Sustain. Energ. Rev.* **2019**, *104*, 379–393. [CrossRef]
4. Cai, X.; Gu, R.R.; Pan, P.; Zhu, J. Unsteady aerodynamics simulation of a full-scale horizontal axis wind turbine using CFD methodology. *Energy Convers. Manag.* **2016**, *112*, 146–156. [CrossRef]
5. Sebastian, T.; Lackner, M. Analysis of the Induction and Wake Evolution of an Offshore Floating Wind Turbine. *Energies* **2012**, *5*, 968–1000. [CrossRef]
6. De Vaal, J.B.; Hansen, M.O.L.; Moan, T. Effect of wind turbine surge motion on rotor thrust and induced velocity. *Wind Energy* **2014**, *17*, 105–121. [CrossRef]
7. Ma, Z.; Li, W.; Ren, N.A.X.; Ou, J.P. The typhoon effect on the aerodynamic performance of a floating offshore wind turbine. *J. Ocean Eng. Sci.* **2017**, *2*, 279–287. [CrossRef]
8. Farrugia, R.; Sant, T.; Micallef, D. A study on the aerodynamics of a floating wind turbine rotor. *Renew. Energy* **2016**, *86*, 770–784. [CrossRef]
9. Wen, B.R.; Dong, X.J.; Tian, X.L.; Peng, Z.K.; Zhang, W.M.; Wei, K.X. The power performance of an offshore floating wind turbine in platform pitching motion. *Energy* **2018**, *154*, 508–521. [CrossRef]
10. Wen, B.R.; Tian, X.L.; Dong, X.J.; Peng, Z.K.; Zhang, W.M. On the power coefficient overshoot of an offshore floating wind turbine in surge oscillations. *Wind Energy* **2018**, *21*, 1076–1091. [CrossRef]
11. Salehyar, S.; Li, Y.; Zhu, Q. Fully-coupled time-domain simulations of the response of a floating wind turbine to non-periodic disturbances. *Renew. Energy* **2017**, *111*, 214–226. [CrossRef]
12. Lin, L.; Wang, K.; Vassalos, D. Detecting wake performance of floating offshore wind turbine. *Ocean Eng.* **2018**, *156*, 263–276. [CrossRef]
13. Tran, T.; Kim, D.; Song, J. Computational Fluid Dynamic Analysis of a Floating Offshore Wind Turbine Experiencing Platform Pitching Motion. *Energies* **2014**, *7*, 5011–5026. [CrossRef]
14. Tran, T.T.; Kim, D.H. The aerodynamic interference effects of a floating offshore wind turbine experiencing platform pitching and yawing motions. *J. Mech. Sci. Technol.* **2015**, *29*, 549–561. [CrossRef]
15. Tran, T.T.; Kim, D.H. The platform pitching motion of floating offshore wind turbine: A preliminary unsteady aerodynamic analysis. *J. Wind Eng. Ind. Aerodyn.* **2015**, *142*, 65–81. [CrossRef]
16. Tran, T.T.; Kim, D.H. A CFD study into the influence of unsteady aerodynamic interference on wind turbine surge motion. *Renew. Energy* **2016**, *90*, 204–228. [CrossRef]
17. Chen, J.H.; Hu, Z.Q.; Wan, D.C.; Xiao, Q. Comparisons of the dynamical characteristics of a semi-submersible floating offshore wind turbine based on two different blade concepts. *Ocean Eng.* **2018**, *153*, 305–318. [CrossRef]
18. Wu, C.-H.K.; Vinh-Tan, N. Aerodynamic simulations of offshore floating wind turbine in platform-induced pitching motion. *Wind Energy* **2017**, *20*, 835–858. [CrossRef]
19. Huang, Y.; Wan, D.C. Investigation of Interference Effects Between Wind Turbine and Spar-Type Floating Platform Under Combined Wind-Wave Excitation. *Sustainability* **2020**, *12*, 246. [CrossRef]
20. Fang, Y.; Duan, L.; Han, Z.L.; Zhao, Y.S.; Yang, H. Numerical analysis of aerodynamic performance of a floating offshore wind turbine under pitch motion. *Energy* **2020**, *192*, 116621. [CrossRef]
21. Fang, Y.; Li, G.; Duan, L.; Han, Z.L.; Zhao, Y.S. Effect of surge motion on rotor aerodynamics and wake characteristics of a floating horizontal-axis wind turbine. *Energy* **2021**, *218*, 119519. [CrossRef]
22. Chen, Z.W.; Wang, X.D.; Guo, Y.Z.; Kang, S. Numerical analysis of unsteady aerodynamic performance of floating offshore wind turbine under platform surge and pitch motions. *Renew. Energy* **2021**, *163*, 1849–1870. [CrossRef]
23. Chen, Z.W.; Wang, X.D.; Kang, S. Effect of the Coupled Pitch-Yaw Motion on the Unsteady Aerodynamic Performance and Structural Response of a Floating Offshore Wind Turbine. *Processes* **2021**, *9*, 290. [CrossRef]
24. Sivalingam, K.; Martin, S.; Wala, A.A.S. Numerical Validation of Floating Offshore Wind Turbine Scaled Rotors for Surge Motion. *Energies* **2018**, *11*, 2578. [CrossRef]
25. Kim, H.; Lee, S.; Lee, S. Influence of blade-tower interaction in upwind-type horizontal axis wind turbines on aerodynamics. *J. Mech. Sci. Technol.* **2011**, *25*, 1351–1360. [CrossRef]
26. Quallen, S.; Tao, X. An Investigation of the Blade Tower Interaction of a Floating Offshore Wind Turbine. In Proceedings of the 25th International Offshore and Polar Engineering Conference, Big Island, HI, USA, 21 June 2015.
27. Ke, S.T.; Wang, T.G.; Ge, Y.J.; Tamura, Y. Aerodynamic loads and aeroelastic responses of large wind turbine tower-blade coupled structure in yaw condition. *Struct. Eng. Mech.* **2015**, *56*, 1021–1040. [CrossRef]
28. Noyes, C.; Qin, C.; Loth, E.; Schreck, S. Measurements and predictions of wind turbine tower shadow and fairing effects. *J. Wind Eng. Ind. Aerodyn.* **2018**, *179*, 297–307. [CrossRef]
29. Zhang, J.; Zhen, G.; Xing, Z.; Liang, G.; Hu, D. Dynamic analysis of offshore wind turbine blades under the action of wind shear and fluctuating wind. *J. Vibroeng.* **2018**, *20*. [CrossRef]
30. Li, Z.W.; Wen, B.R.; Dong, X.J.; Peng, Z.K.; Qu, Y.G.; Zhang, W.M. Aerodynamic and aeroelastic characteristics of flexible wind turbine blades under periodic unsteady inflows. *J. Wind Eng. Ind. Aerodyn.* **2020**, *197*, 104057. [CrossRef]
31. Wu, W.M.; Liu, X.F.; Dai, Y.J.; Li, Q.Y. An in-depth quantitative analysis of wind turbine blade tip wake flow based on the lattice Boltzmann method. *Environ. Sci. Pollut. Res.* **2020**, *13*. [CrossRef]

32. Regodeseves, P.G.; Morros, C.S. Unsteady numerical investigation of the full geometry of a horizontal axis wind turbine: Flow through the rotor and wake. *Energy* **2020**, *202*, 117674. [CrossRef]
33. Burmester, S.; Vaz, G.; el Moctar, O. Towards credible CFD simulations for floating offshore wind turbines. *Ocean Eng.* **2020**, *209*, 107237. [CrossRef]
34. Chen, D.; Gao, P.; Huang, S.S.; Fan, K.; Zhuang, N.; Liao, Y.D. Dynamic response and mooring optimization of spar-type substructure under combined action of wind, wave, and current. *J. Renew. Sustain. Energy* **2017**, *9*, 063307. [CrossRef]
35. Wang, X.D.; Ye, Z.L.; Kang, S.; Hu, H. Investigations on the Unsteady Aerodynamic Characteristics of a Horizontal-Axis Wind Turbine during Dynamic Yaw Processes. *Energies* **2019**, *12*, 3124. [CrossRef]
36. Jonkman, J.M. *Dynamics Modeling and Loads Analysis of an Offshore Floating Wind Turbine*; National Renewable Energy Lab. (NREL): Golden, CO, USA, 2007.
37. Hu, D.M.; Ji, S.Q.; Wu, Z.X. Study on Aerodynamic Performance of Offshore Floating Wind Turbine with Fusion Winglets. *J. Sol. Energy Eng. Trans. ASME* **2020**, *142*, 051007. [CrossRef]
38. Jonkman, J.M.; Butterfield, S.; Musial, W.; Scott, G. *Definition of a 5MW Reference Wind Turbine for Offshore System Development*; Office of Scientific & Technical Information Technical Reports; National Renewable Energy Lab. (NREL): Golden, CO, USA, 2009.
39. Wen, B.R.; Wei, S.; Wei, K.X.; Yang, W.X.; Peng, Z.K.; Chu, F.L. Power fluctuation and power loss of wind turbines due to wind shear and tower shadow. *Front. Mech. Eng.* **2017**, *12*, 321–332. [CrossRef]

energies

MDPI

*Article*

# Reliability Updating of Offshore Wind Substructures by Use of Digital Twin Information

**Dawid Augustyn [1,2,*], Martin D. Ulriksen [3] and John D. Sørensen [1]**

[1] Department of the Built Environment, Aalborg University, 9220 Aalborg, Denmark; jdas@build.aau.dk
[2] Ramboll Energy, 6700 Esbjerg, Denmark
[3] Department of Energy Technology, Aalborg University, 6700 Esbjerg, Denmark; mdu@et.aau.dk
* Correspondence: dja@build.aau.dk

**Abstract:** This paper presents a probabilistic framework for updating the structural reliability of offshore wind turbine substructures based on digital twin information. In particular, the information obtained from digital twins is used to quantify and update the uncertainties associated with the structural dynamics and load modeling parameters in fatigue damage accumulation. The updated uncertainties are included in a probabilistic model for fatigue damage accumulation used to update the structural reliability. The updated reliability can be used as input to optimize decision models for operation and maintenance of existing structures and design of new structures. The framework is exemplified based on two numerical case studies with a representative offshore wind turbine and information acquired from previously established digital twins. In this context, the effect of updating soil stiffness and wave loading, which constitute two highly uncertain and sensitive parameters, is investigated. It is found that updating the soil stiffness significantly affects the reliability of the joints close to the mudline, while updating the wave loading significantly affects the reliability of the joints localized in the splash zone. The increased uncertainty related to virtual sensing, which is employed to update wave loading, reduces structural reliability.

**Keywords:** offshore wind substructures; reliability updating; probabilistic fatigue assessment; digital twins; uncertainty quantification

**Citation:** Augustyn, D.; Ulriksen, M.D.; Sørensen, J.D. Reliability Updating of Offshore Wind Substructures by Use of Digital Twin Information. *Energies* **2021**, *14*, 5859. https://doi.org/10.3390/en14185859

Academic Editor: Eugen Rusu

Received: 5 August 2021
Accepted: 9 September 2021
Published: 16 September 2021

**Publisher's Note:** MDPI stays neutral with regard to jurisdictional claims in published maps and institutional affiliations.

**Copyright:** © 2021 by the authors. Licensee MDPI, Basel, Switzerland. This article is an open access article distributed under the terms and conditions of the Creative Commons Attribution (CC BY) license (https://creativecommons.org/licenses/by/4.0/).

## 1. Introduction

The offshore wind industry has experienced significant growth over the last decade [1]. As a result, the number of offshore wind turbines operating in Europe has reached 5402 in 2020 [2], with much more planned to be installed worldwide in the close future [3]. The typical lifetime of an offshore wind turbine ranges between 20 and 25 years, which means that over the coming years a large number of these structures reach their intended lifetime, and operators will have to take actions regarding their assets. Potential actions, denoted as decision models, can be to decommission, re-power, perform inspections, or extend lifetime. An optimal decision depends on what specific business model the operator pursues, but, regardless of the business aspect, an accurate and precise estimation of the structural reliability is key in making such a decision [4].

A digital twin-defined as a digital replica of a physical asset [5,6]-can help us to assess the structural integrity of existing structures more accurately and precisely compared to predictions from generic design practices because consistent and updated information of the structure is available. This has been successfully demonstrated in the oil and gas industry [7,8], in aerospace engineering [9], and in the offshore wind industry as well [10]. In fact, a number of wind standardization committees, including Det Norske Veritas (DNV) [11,12], International Electrotechnical Commission (IEC) [13], and Federal Maritime and Hydrographic Agency (BSH) [14], are working on design recommendations on how to use measurement data and inspection information to optimize decision models for existing

wind turbines. Currently, a key missing aspect is how to use the improved structural models contained in digital twins to subsequently improve the decision models.

Although fully physics-based digital twins have not yet been applied to improve decision models for wind turbines, some publications already indicate how measurement data can be used to achieve such an improvement. Nielsen and Sørensen [15] applied dynamic Bayesian networks to calibrate a Markov deterioration model based on past inspection data of wind turbine blades. Ziegler and Muskulus [16] investigated the feasibility of lifetime extension for offshore wind monopile substructures, with particular focus on identifying important parameters to monitor during the operational phase of the turbines. Leser et al. [17] presented a general framework for fatigue damage estimation based on in situ measurements. Mai et al. [18] focused on prediction of the remaining useful lifetime of wind turbine support structure joints using met-ocean in situ data. Augustyn et al. [19] extended a conceptual framework for updating decision models based on information from a digital twin, initially proposed by Tygesen et al. [7], to be applied to offshore wind substructures. In the framework, a digital twin is established with an updated structural and load model, and subsequently the digital twin is used to quantify uncertainty and update the structural reliability.

In the present paper, we outline the framework by Augustyn et al. [19] beyond its conceptual level and propose a probabilistic method for updating the structural reliability of offshore wind turbine substructures based on new information obtained from digital twins. Depending on the information type available, various methods for updating reliability can be used [20]. If information on the structural integrity becomes available, for example, by an inspection of joints to identify potential cracks, risk-based inspection methods can be applied [21–24]. Even though the inspection planning methodology is matured and well-proven in industrial applications [25], its feasibility for the majority of offshore wind applications is questionable due to the profound inspection costs [26]. A more economically feasible alternative, in the form of condition-based monitoring, is typically investigated for offshore wind applications [27,28]. In this context, condition monitoring data can be applied to identify structural damage, and then the resulting integrity information can be employed for updating reliability [29]. Application studies have been presented for mechanical components in turbine [30] and wind turbine blades [4]. However, in these studies, the condition monitoring data merely provide structural integrity information at a global level-that is, if damage is present or not. In the present study, we aim at enhancing the spatial resolution of the integrity assessment and hereby provide information at a local (joint) level. Consequently, this paper proposes a framework where condition monitoring data are used to update structural models; these updated models are subsequently used to update structural reliability, including uncertainty stemming from the updating procedure.

The contribution of this paper consists of: (1) proposing a method on how the uncertainties related to the structural dynamics and load modeling in fatigue damage accumulation can be quantified and updated based on updated distribution functions of model parameters, which can be acquired with the aid of a digital twin. Subsequently, (2) we present a framework where the updated uncertainty is used to update the structural reliability based on a well-established probabilistic model [31,32]. Generally, the framework can be used for optimization of operation and maintenance of existing turbines and design of new structures. The framework is exemplified based on two numerical case studies, in which digital twins established in previous studies by the authors [33,34] are included.

The remainder of this paper is organized as follows. In Section 2, we outline the concept of structural reliability estimation and convey the motivation for the proposed structural reliability updating framework, which is presented in Section 3. The two following sections address the numerical case studies used to exemplify the framework for existing and new substructures; Section 4 describes the setup of the case studies and Section 5 presents the appertaining results. Finally, this paper closes with concluding remarks in Section 6.

## 2. Background and Problem Statement

A wind turbine consists of structural components, for which reliability analysis is performed using structural reliability theory [35], and electrical/mechanical components, for which classical reliability models can be used, with the main descriptor being the failure rate or the mean time between failure (MTBF). Regardless of the component type being addressed in the reliability analysis, a probabilistic model describing the component's integrity is required. The reliability of electrical/mechanical components is typically modeled by a Weibull model for the time to failure and the components are assumed to be statistically independent. Using, for example, failure tree analysis (FTA) and failure mode and effect analysis (FMEA), system reliability models can be established and the reliability update can be performed when new information becomes available [36–38]. In the present paper, jacket-type steel wind turbine substructures are considered, so structural reliability techniques are required to model loads, resistances, and model uncertainties and to account for the correlation between the components. The fatigue damage is often design driving for the structural components of offshore wind substructures, such as joints. In this instance, fatigue damage accumulation can be expressed in terms of probability of failure or, equivalently, by the reliability index [39].

Let $g(t)$ be the fatigue limit state at year $t \in \mathbb{N}$ for an offshore wind substructure; then [32,40],

$$g(t) = \Delta - \sum_{i=1}^{l} \sum_{j=1}^{z} \frac{N_{i,j} p_i t}{K \Delta s_{i,j}^{-m}} (X_d X_l X_s)^m, \tag{1}$$

where $\Delta$ is the fatigue resistance and the double summation expresses the accumulated fatigue damage. In particular, $\Delta$ is a stochastic variable representing the limit value of the accumulated fatigue damage estimated using, for example, SN curves, including the uncertainty related to application of Miner's rule for linear fatigue damage accumulation. In the expression for the fatigue damage, $p_i$ is the yearly probability of occurrence for sea state $i$ (including wind and wave parameters), $N_{i,j}$ is the number of cycles for the $i$th sea state and $j$th stress range $\Delta s_{i,j}$, and $K$ and $m$ are the parameters related to the SN curve, with $m$ being the Wöhler exponent [41]. The uncertainties related to the SN curve approach are included by modeling $K$ as a stochastic variable. $X_d$, $X_l$, and $X_s$ are stochastic variables that model the uncertainties associated with the structural dynamics, load modeling and stress concentration.

If $g(t) \leq 0$, the limit state is exceeded and the structure fails, while $g(t) > 0$ implies that the structure is safe. The probability of fatigue failure in the time interval $t \in [0, T]$, $P_f(t) = P(g(t) \leq 0)$ can be estimated by first-order and second-order reliability methods [39] or, as is the case in this paper, by Monte Carlo methods [42]. The corresponding reliability index, $\beta$, can be computed as $\beta(t) = -\Phi^{-1}\left(P_f(t)\right)$, where $\Phi$ is the standard normal distribution function. The annual reliability index, $\Delta\beta$, can be calculated analogically assuming a reference period of one year.

We note that (1) $X_d$ and $X_l$ may be correlated, and, in this instance, they should be modeled by a joint probability density function with correlation coefficient $\rho$ and (2) a linear formulation of the limit state equation can be readily generalized for a bi-linear formulation of the SN curve. The parameters in model (1) are elaborated in Section 2.1.

### *2.1. Uncertain Parameters and Their Modeling*

The uncertainty modeling related to structural reliability due to fatigue damage is summarized in Figure 1. In the framework proposed in Section 3, we focus on updating stochastic variables related to structural dynamics and loading uncertainty, as schematically indicated by the dark blue boxes in Figure 1. The remaining part of the uncertainty (the light blue boxes in Figure 1) can be quantified based on experiments and data. This is not considered in the proposed framework, but a brief discussion is provided in the present subsection for the sake of completeness.

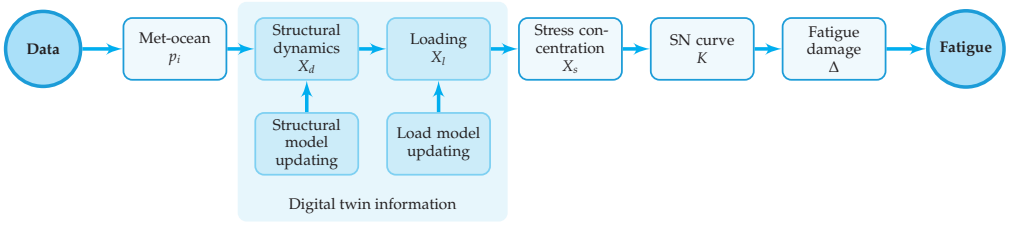


**Figure 1.** Stochastic variables modeling uncertainty in fatigue damage accumulation. The stochastic variables from the probabilistic model (1) are represented by separate boxes. The light blue boxes indicate stochastic variables estimated based on generic, design-based recommendations. The dark blue boxes indicate stochastic variables that can be quantified and updated based on new information from a digital twin.

#### 2.1.1. Met-Ocean Model

The joint probability distributions of the wind-wave climate is discretized by a finite number of short-term sea state simulations including random wind and wave seeds to model a stochastic process [40]. Met-ocean uncertainty is included in (1) by the yearly probability of each sea state, denoted $p_i$. The met-ocean uncertainty can be quantified if long-term climate parameters are monitored [18,43].

#### 2.1.2. Structural Dynamics

Estimating dynamic system properties is associated with uncertainties [44]. The uncertainties stem from environmental and operational variability, non-stationary sea states (fluctuating mean sea water level), time-variant structural conditions (corrosion, scour), output noise, and the formulation of the structural model, including modeling of highly uncertain parameters such as soil stiffness, joint stiffness and damping. We note that the output noise relates to the noise in the acceleration and/or strain signals, which is propagated through system identification procedures and results in uncertainty of the updated structural model parameters [44]. The structural dynamics uncertainty is included in (1) through the stochastic variable $X_d$.

#### 2.1.3. Loading

Depending on the location of the wind turbine, the loading may include the following exogenous sources and their inherent uncertainties:

- Hydrodynamic loading-uncertainty related to calculating wave loads that stems from different wave theories (linear vs. non-linear), Morison's equation, stretching and mass and drag coefficients.
- Aerodynamic loading-uncertainty related to calculating wind loads that stems from wind turbulence, wake model, and shear coefficient.
- Ice loading-uncertainty related to calculating ice loads, for example, ice thickness, ice crushing strength and ice failure regime.
- Earthquake loading-uncertainty related to calculating earthquake loads, for example, earthquake acceleration profile, structural response, soil-structure integration, and force transfer.

If loading uncertainty is quantified based on information from digital twins, the main part of the uncertainty is related to obtaining the structural response due to external loading. This response is typically estimated based on virtual sensing methods, which are associated with uncertainties [34,45]. The loading uncertainty is included in (1) through the stochastic variable $X_l$.

#### 2.1.4. Stress Concentration

Stress ranges in specific locations can be estimated based on simplified parametric equations, for example, Efthymiou [46] or detailed finite element (FE) models. The stress concentration uncertainty is included in (1) through the stochastic variable $X_s$. The stress

concentration uncertainty can be quantified if a detailed FE model is used to establish hot spot stresses [47] or if hot spot stresses are measured directly.

#### 2.1.5. SN Curve

The uncertainty in parameter estimation from the SN curve approach [48] is included in (1) through the stochastic variable $K$ and the deterministic parameter $m$. If a bi-linear SN curve is used, then stochastic variables are used to model the two branches of the SN curve. The SN curve uncertainty can be quantified if fatigue testing is performed [48].

#### 2.1.6. Fatigue Damage

Uncertainties related to the accumulated fatigue damage model (Miner's rule [49]) and the crack propagation method (Paris–Erdogan [50] or fracture mechanics) is included in (1) by modeling the resistance, $\Delta$, as a stochastic variable.

### *2.2. Current State-of-Practice for Reliability Updating*

Design standards define a specific level of reliability that offshore wind substructures must fulfill, for example, a target annual reliability index of $\Delta\beta = 3.3$ in IEC 61400-1 [31,40]. Reliability levels indicated in standards assume a generic level of uncertainty representative for all types of substructures and locations. Because the uncertainty is assumed to cover a wide range of structures and locations, the resulting design is, in many cases, conservative. The level of conservatism can be quantified when new information specific to a particular structure becomes available. One way of obtaining such information is by means of digital twins, which can be used to quantify the uncertainty and subsequently update the structural reliability.

## 3. Structural Reliability Updating Framework

In this paper, we propose a probabilistic framework in which digital twin information is used to update the uncertainties associated with the fatigue damage accumulation, which are then used to update the structural reliability. In particular, we use the updated parameters from the established digital twins to quantify the model uncertainties of the structural dynamics, $X_d$, and load modeling, $X_l$. The updated uncertainties are quantified based on a forward propagation method, which allows quantifying separate uncertainty sources stemming from specific model parameters. Having updated the relevant uncertainty contributions from the updated model parameters, the reliability is updated based on the linear probabilistic limit state Equation (1). Finally, the updated reliability serves as a decision basis for a decision model update. A schematic illustration of the framework is seen in Figure 2, and steps one to six are described in Sections 3.1–3.6.

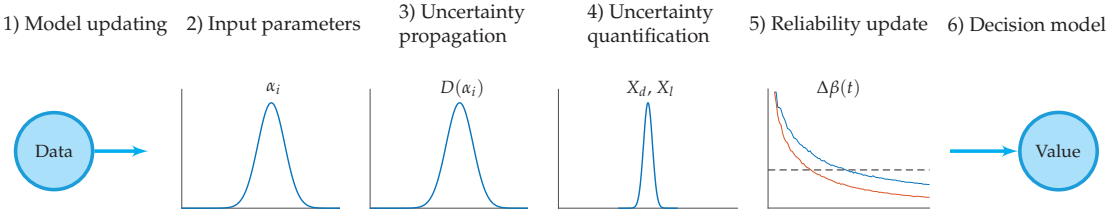


**Figure 2.** Structural reliability updating framework based on information from a digital twin. Updated parameters from the digital twin are used to quantify uncertainty in fatigue damage accumulation. Subsequently, the structural reliability is updated.

### *3.1. Model Updating*

It is assumed that an updated structural model (step one) is available, which can be obtained based on well-established model formulation and updating procedures [51].

### 3.2. Input Parameters

The distribution functions of the updated model parameters (available from step one) are used in step two as input for the uncertainty quantification procedure. The stochastic variables reflect both the aleatory and epistemic uncertainties, which constitute the updated $X_d$ and $X_l$ uncertainties.

### 3.3. Uncertainty Propagation

The effect of the updated model parameters on the fatigue damage accumulation is established by a Monte Carlo uncertainty propagation method [52], as indicated in step three in Figure 2. Based on the uncertainty in the input parameters (i.e., the distribution functions of the updated numerical model parameters), we obtain the distribution of fatigue damage, hence quantifying the uncertainties in fatigue damage due to the updated model parameters. The uncertainty quantification procedure is described next. The aim is to express the uncertainty as a stochastic variable multiplied to the fatigue stress ranges.

The uncertainty in fatigue damage accumulation due to an uncertain parameter, $\alpha_j \in \boldsymbol{\alpha}$, can be quantified by simulating $n$ realizations from this parameter's distribution function and calculating the corresponding fatigue damage. When calculating fatigue damage, the remaining parameters are assumed to be deterministic. Moreover, the fatigue damage is calculated assuming one sea state parameter. In this way, the introduced uncertainty is solely governed by the variability of $\alpha_j$, hence quantifying this parameter's contribution to the fatigue damage accumulation uncertainty. For example, a distribution function of updated soil stiffness implies structural dynamics uncertainty, while a distribution function of an updated inertia coefficient in Morison's equation implies loading uncertainty.

Among a number of uncertainty quantification methods [53], a Bayesian framework [54] is recommended by a number of standard committees, for example, IEC and Joint Committee on Structural Safety (JCSS), due to its sound theoretical basis and wide range of applicability. However, a main challenge in the Bayesian framework is the requirement of a prior distribution on the parameters to be quantified. In the context of offshore wind uncertainties, information on prior distributions is not available in the background documents for the above mentioned standards and committees. Consequently, in the proposed framework, we implemented a simplified method where we start with the uncertainty modeling consistent with the design standard of wind turbines [40], and subsequently we quantify the uncertain parameters already included in (1) using the maximum likelihood method.

Assuming the fatigue damage, modeled as a stochastic variable depending on the uncertain parameter $\alpha_j$, is normally distributed, $D(\alpha_j) \sim \mathcal{N}\left(\mu_{D_j}, \sigma^2_{D_j}\right)$, the fatigue damage distribution (mean value $\mu_{D_j}$ and standard deviation $\sigma_{D_j}$) can be found through the maximum likelihood method, where the likelihood is defined as

$$L\left(\mu_{D_j}, \sigma_{D_j}\right) = \prod_{i=1}^{n} \frac{1}{\sqrt{2\pi}\sigma_{D_j}} \exp\left(-\frac{1}{2}\left(\frac{D_i - \mu_{D_j}}{\sigma_{D_j}}\right)^2\right), \tag{2}$$

with $D_i$ being the fatigue damage associated with the $i$th realization of $\alpha_j$ computed based on the updated structural model contained in the digital twin.

The log-likelihood function becomes

$$\ln L\left(\mu_{D_j}, \sigma_{D_j}\right) = -n \ln\left(\sqrt{2\pi}\sigma_{D_j}\right) - \sum_{i=1}^{n} \frac{1}{2}\left(\frac{D_i - \mu_{D_j}}{\sigma_{D_j}}\right)^2, \tag{3}$$

and the optimal parameters are found to be

$$\underset{\mu_{D_j}, \sigma_{D_j}}{\operatorname{argmax}} \ln L\left(\mu_{D_j}, \sigma_{D_j}\right). \tag{4}$$

### *3.4. Uncertainty Quantification*

The procedure outlined in the previous subsection quantifies uncertainty in fatigue damage accumulation. However, the probabilistic model (1) requires uncertainty in stress ranges rather than in the fatigue damage. Therefore, it is now described how uncertainty in fatigue damage can be transformed into uncertainty in stress ranges, as indicated in step four in Figure 2.

The fatigue damage accumulation, $D$, is proportional to the stress ranges, $\Delta s$, according to $D \propto \Delta s^m$ (assuming a linear SN curve), from which it follows $\Delta s \propto D^{1/m}$. The stress range distribution parameters can be computed from Monte Carlo simulations. Alternatively, assuming the damage distribution function is normal, the stress range distribution's mean, $\mu_{\Delta s}$, and coefficient of variation (CoV), $c_{\Delta s}$, can be approximated as

$$\mu_{\Delta s} = \mu_i^{1/m} \tag{5}$$

and

$$c_{\Delta s} = \frac{c_i}{m}, \tag{6}$$

where $\mu_i$ and $c_i$ are the mean and CoV of the fatigue damage distribution due to the uncertainty associated with $\alpha_j$.

### *3.5. Reliability Update*

The quantified and updated uncertainties can be consistently included in the probabilistic framework to update the reliability level. The probabilistic model (1) is used to derive an annual reliability level, $\Delta\beta(t)$, given the updated uncertainties. This procedure is indicated in the fifth step in Figure 2, where two reliability curves (with and without using information from a digital twin) are schematically presented. The outcome of the reliability update (increase or decrease) depends on the outcome of uncertainty quantification (increased or decreased).

### *3.6. Decision Models*

Given new information from digital twins becomes available (either during operation or already in the design stage), the decision models can be updated as indicated by the last step in Figure 2. The digital twin information can be included based on Bayesian decision theory [24,55]. For existing structures, an operation and maintenance decision plan can be optimized based on an updated reliability level, for example, an updated inspection plan or lifetime reassessment. More specifically, a reliability-based inspection planning technique can be implemented [56] and some of the inspections can be removed (if any were planned during the lifetime of the structure in question) or new inspections can be included if the structural integrity is compromised. For new structures, the expected outcome of a future digital twin can be used to optimize structures already at the design stage (before the digital twin information becomes available) by the use of Bayesian pre-posterior theory [54].

## 4. Case Study Setup

To demonstrate an application of the proposed framework, we consider an example where information from a digital twin of an offshore wind jacket substructure is used to update the structural reliability of the substructure. The numerical models of the substructure and the turbine are described in Sections 4.1.1 and 4.1.2, followed by a description of the analyzed load case scenarios in Section 4.1.3. Based on the simulation results (in the form of stress range distributions), the structural reliability of selected joints is calculated in Section 4.2.1 by assuming a generic level of uncertainty. The results are nominal and are, in Section 5, compared with the results obtained by using digital twin information.

### *4.1. Modeling*

We simulate a numerical model of a 7 MW jacket-supported turbine using the procedure outlined by Nielsen et al. [57] and applied by, e.g., Augustyn et al. [34]. The simulation procedure consists of the following steps: (1) the substructure model and corresponding wave loading are reduced to a Craig–Bampton superelement [58] with 30 internal modes accounting for internal substructure dynamics. A convergence study has been performed to ascertain that the reduced model (including 30 modes) adequately captures the relevant modal parameters of the non-reduced system. Subsequently, (2) the wind loading is computed through aero-elastic analyses, in which the substructure superelement is included. Finally, (3) the force-controlled recovery run outlined by Nielsen et al. [59] is performed, where the response of the substructure is recovered and relevant measurements are extracted. The applied model is formulated using state-of-the-art modeling approaches included in a typical design procedure for jacket substructures, and the model has been validated to accurately and precisely represent the structural dynamics of a combined substructure and wind turbine system [60,61].

#### 4.1.1. Substructure

The jacket substructure and its appertaining wave loading were modeled using ROSAP (Ramboll Offshore Structural Analysis Programs), version 53 [62]. The jacket substructure considered in this study, which is depicted in Figure 3, has a total height of approximately 75 m. The substructure comprises three legs, each with a diameter ranging between 1.2 and 1.7 m, and four brace bays, each with a diameter ranging between 0.8 and 1.1 m. The substructure model includes, i.a., soil-pile interaction, local joint flexibility, scour, marine growth and appurtenance masses. The water depth is 55 m and the soil conditions are characterized as clay. The substructure includes 50 m grouted piles. The soil-structure interaction is modeled by the use of soil curves linearized according to the API method [63]. The structural damping was modeled according to a Rayleigh model [64] with 0.5% and 1% modal damping in the first and second bending modes, respectively.

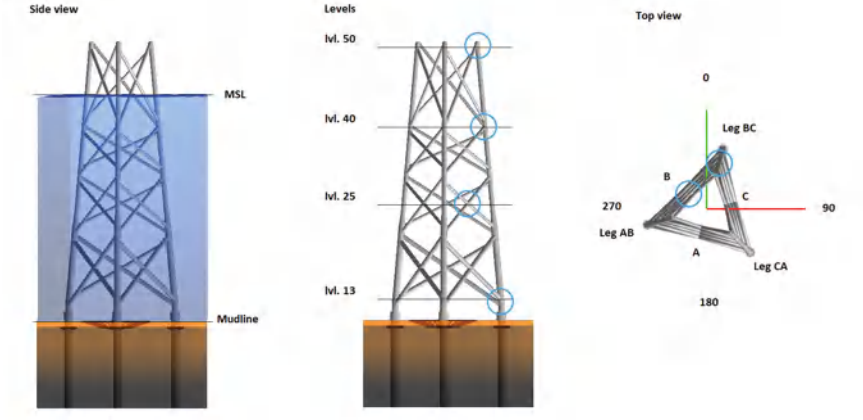


**Figure 3.** Substructure model used in the case studies. (**A**) Side view, (**B**) side view with indication of levels (blue circles indicate joints analyzed in the case studies) and (**C**) top view with indication of directions, side and leg names. NB: a wind turbine model is not shown in the figure.

The locations of the selected joints considered in the case studies are indicated in Figure 3B. The joint levels range between 13 (mudline) to 50 (top of the jacket). Results for sides B and C of the jacket, see Figure 3C, are provided. The joints are named in the following way: 50CL, where 50 indicates the level, C is the jacket side, and L indicates the lower element in the joint.

#### 4.1.2. Wind Turbine

The substructure carries a representative 7 MW turbine, which is modeled in LACflex aero-elastic code [65]. The turbine includes a 90 m tubular tower with a diameter ranging between 4 and 6 m. Along the tower, three concentrated masses are assumed to emulate the effect of secondary-structures. The aero-elastic code employs a modal-based representation of the turbine (including the tower, rotor and blades). An aerodynamic damping contribution is included through the fluid-structure interaction when calculating aero-elastic forces. The wind turbine model was originally developed for industrial purposes, where it was applied in commercial projects. A rather similar model (albeit a 5 MW turbine instead of 7 MW), which adheres to the same modeling principles, has been applied in other studies on structural dynamics of wind turbines [34,66].

#### 4.1.3. Load Cases

In this study, we consider the fatigue failure mode in the normal operating condition (design load case (DLC) 1.2 [40]). For a typical offshore wind jacket substructure, this DLC accounts for most of the fatigue damage [67].

The met-ocean parameters applied in this study are derived based on measurements from a representative North Sea site [68] and are summarized in Table 1. The wind speed ranges between 4 and 31 $\mathrm{ms}^{-1}$, resulting in $n_b = 15$ wind speed bins. For each wind speed bin, representative wave parameters, i.e., the significant wave height and peak period, are assigned. The significant wave height ranges from 0.1 to 7.9 m while the peak period ranges from 3.0 to 9.6 s. The met-ocean parameters along with their yearly probability of occurrence are derived from a site-specific joint probability distribution function, which is a common design practice [40]. A total of $n_d = 12$ wind directions are analyzed (wind and waves are assumed fully aligned). For each wind speed, a total of $n_{TI} = 5$ turbulence intensity quantiles, namely, $q \in [q_{10}, q_{30}, q_{50}, q_{70}, q_{90}]$, are considered. The quantiles for each wind speed are calculated based on the Weibull distribution according to the IEC standard [40] for turbulence class B. The turbulence intensities for the given site ranges from 0.09 to 0.31. The fatigue damage is scaled with the corresponding turbulence intensity quantile probability, hence representing the target Weibull distribution. Every load case (wind speed, wave height, peak period and turbulence intensity) is simulated with $n_s = 6$ seeds. The total number of load cases analyzed is $n_t = n_b n_d n_{TI} n_s = 5400$.

**Table 1.** Load case definitions according to IEC [40] and representative site-specific parameters.

| Turbine State | DLC | Wind Speed, $U$ ($\mathrm{ms}^{-1}$) | Turbulence, TI (-) | Wave Height, $H_s$ (m) | Wave Period, $T_p$ (s) | Direction (deg) |
|---|---|---|---|---|---|---|
| Operational | 1.2 | 4–31 | 0.31–0.09 | 0.1–7.9 | 3.0–9.6 | 0–330 |

### *4.2. Nominal Results*

The structural reliability of selected joints of the jacket substructure is evaluated based on model (1) and the variables are summarized in Table 2. The stress ranges, $\Delta\sigma$, and number of cycles, $N$, were obtained from simulations. The SN curves for tubular joints in air and in seawater with cathodic protection are used according to [48]. The SN curve for the air environment are applied to the joint at level 50. For the remaining joints, the SN curve for seawater with cathodic protection is applied. For tubular joints exposed to seawater with cathodic protection, negative inverse slopes of $m_1 = 3$ and $m_2 = 5$ and intercepts of $\log K_{c_1} = 12.18$ and $\log K_{c_2} = 16.13$ are assumed to calculate the characteristic SN curve. For tubular joints in air environment, the following values can be used: $\log K_{a1} = 12.48$ and $\log K_{a2} = 16.13$, while assuming the same $m$ values as for seawater environment. The mean SN curve for the probabilistic analysis was calculated from the characteristic SN curve's intercepts assuming a standard deviation of 0.20 [48].

**Table 2.** Variables used in the probabilistic model to estimate fatigue damage accumulation in the nominal case [32].

| Variable | Distribution | Mean | CoV | Std. Dev. | Ref. |
|---|---|---|---|---|---|
| $\Delta$ | N | 1.00 | 0.30 | N/A | [69] |
| $\log K_{c1}$ | N | 12.58 | N/A | 0.20 | [48] |
| $\log K_{c2}$ | N | 16.53 | N/A | 0.20 | [48] |
| $\log K_{a1}$ | N | 12.88 | N/A | 0.20 | [48] |
| $\log K_{a2}$ | N | 16.53 | N/A | 0.20 | [48] |
| $m_1$ | D | 3 | N/A | N/A | [48] |
| $m_2$ | D | 5 | N/A | N/A | [48] |
| $X_d$ | LN | 1.00 | 0.10 | N/A | [31] |
| $X_l$ | LN | 1.00 | 0.10 | N/A | [70,71] |
| $X_S$ | LN | 1.00 | 0.05 | N/A | [70] |

Distribution: N-normal, LN-logNormal, D-deterministic.

#### 4.2.1. Annual Reliability

The annual reliability index as a function of time, $\Delta\beta(t)$, is calculated based on the state-of-the-art probabilistic methods described in Section 2. The limit state Equation (1) was applied using the standard-based variables provided in Table 2. The reliability indices are presented in Figure 4 and Table 3 and are denoted as the nominal results. The results represent the situation where no additional knowledge from a digital twin is available. The results are provided for 10 selected joints, which are typically critical for a jacket design.

The structure is designed to have a fatigue lifetime of 25 years. The fatigue lifetime ends when the annual reliability index reaches the target value $\Delta\beta = 3.3$, which serves as the basis for reliability-based calibration of safety factors in recognized design codes [31,40]. For the considered case study, the design driving joints are 13BU and 40CU with a lifetime of 25 and 27 years. Joint 13BU is located close to the mudline, while joint 40CU is located slightly below the splash zone. Joints 40CL, 40BL, 25BU and 25BL have a lifetime between 50 and 100 years, while the remaining joints have a lifetime above 100 years.

**Table 3.** Fatigue lifetime derived based on probabilistic model (1) and stochastic variables presented in Table 2.

| Joint | Fatigue Lifetime (Years) |
|---|---|
| 50CL | >100 |
| 50BL | >100 |
| 40CL | 54 |
| 40BL | 77 |
| 40CU | >100 |
| 40BU | 25 |
| 13CU | 27 |
| 13BU | >100 |
| 25BL | 98 |
| 25BU | 86 |

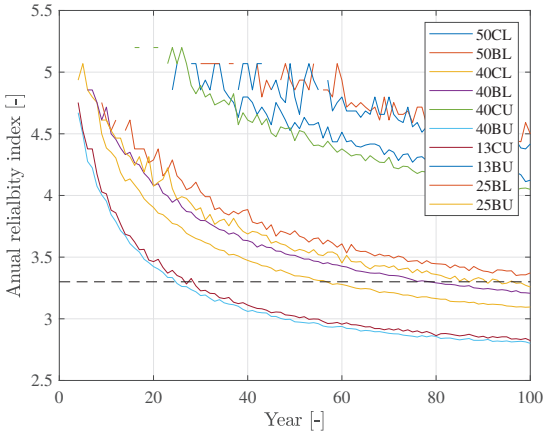


**Figure 4.** Structural reliability as function of time for the nominal model.

## 5. Case Study Results

In this section, we exemplify how new information from digital twins can be included in the proposed framework to quantify uncertainty and subsequently update structural reliability for the particular case study. We use information from previously established digital twins [33,34]. The effect of structural dynamics uncertainty, $X_d$, is investigated based on a model updating study presented in [33], where the soil stiffness, $k_s$, was calibrated based on in situ measurements. The effect of loading uncertainty, $X_l$, is investigated based on a virtual sensing study [34], where modal expansion was used to estimate unmeasured field quantities. The results are presented and discussed based on two design driving joints, namely, 13CU and 40BU.

### *5.1. Updating Structural Dynamics Uncertainty*

In this subsection, we present the updated structural reliability based on an updated structural dynamics uncertainty. First, we present a sensitivity study on updating soil stiffness, followed by a case study based on in situ soil stiffness calibration [33].

#### 5.1.1. Soil Stiffness Sensitivity

The effect of updating thesoil stiffness mean value, $\mu_{k_s}$, for joint 13CU is presented in Figure 5 and in Table 4. It is assumed that new information from a digital twin is obtained; in this particular case, the mean value of uncertainty related to structural dynamics, $\mu_{X_d}$, is updated. The results are derived by using the limit state Equation (1) with the standard-based variables provided in Table 2 and updated values for $\mu_{X_d}$.

As seen in Figure 5, the soil stiffness has a significant impact on the fatigue lifetime. Updating the soil stiffness by a factor of 0.5 (resulting in reducing the mudline pile stiffness by half) results in a reduction in lifetime by a factor of 0.3. In contrast, increasing the soil stiffness by a factor of 2.0 results in a lifetime increase by more than fourfold (>100 years). The effect of updating soil stiffness on joint 40BU is negligible, as indicated in Figure 6.

Note that in Figures 5 and 6 (and the other figures describing structural reliability as a function of time), the reliability generally decreases with time, albeit non-monotonically in some cases. For example, consider the green curve in Figure 5, where a local increase in reliability around year 20 is observed. This is due to a limited number of Monte Carlo simulations, but we note that this limitation does not qualitatively affect the conclusions drawn from the analyses.

**Table 4.** Fatigue lifetime derived for different distributions of $X_d$.

| $k_s$ | 13CU | | | 40BU | | |
|---|---|---|---|---|---|---|
| | $\mu_{X_d}$ | CoV $X_d$ | Lifetime | $\mu_{X_d}$ | CoV $X_d$ | Lifetime |
| 0.50 | 1.20 | 0.10 | 7 | 0.98 | 0.10 | 26 |
| 0.75 | 1.10 | 0.10 | 15 | 0.99 | 0.10 | 25 |
| 1.00 | 1.00 | 0.10 | 25 | 1.00 | 0.10 | 25 |
| 1.25 | 0.90 | 0.10 | 85 | 1.01 | 0.10 | 25 |
| 1.50 | 0.80 | 0.10 | >100 | 1.02 | 0.10 | 24 |
| 2.00 | 0.70 | 0.10 | >100 | 1.04 | 0.10 | 22 |

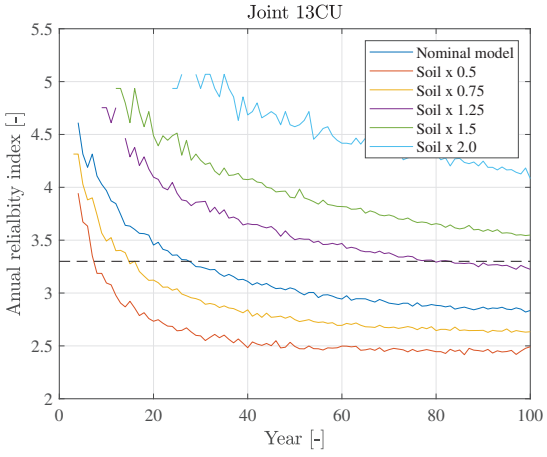


**Figure 5.** Impact of updating soil stiffness on structural reliability-joint 13CU.

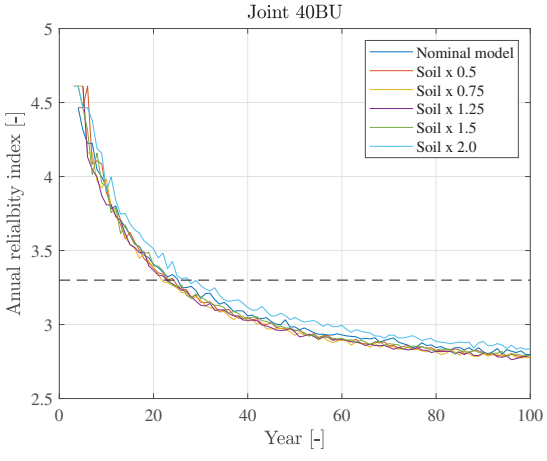


**Figure 6.** Impact of updating soil stiffness on structural reliability-joint 40BU.

#### 5.1.2. Reliability Update-Soil Stiffness

Based on the results presented in [33], we assume the soil stiffness distribution function after the update can be approximated by a normal distribution with mean value of 4.7 and CoV = 0.12, i.e., $k_s \sim \mathcal{N}\left(4.7, (4.7 \times 0.12)^2\right)$. The soil stiffness uncertainty is propagated through the numerical model, and the uncertainty on stress ranges was estimated according to the method presented in Section 3.3. It was assumed, for illustrative purposes, that

the soil stiffness is the only uncertain parameter affecting the $X_d$ uncertainty, i.e., $\boldsymbol{\alpha} = k_s$. The $X_d$ uncertainty is quantified and its updated value was applied together with the nominal uncertainty values for the remaining stochastic variables in (1). The updated $X_d$ distribution (mean value and CoV) as a result of the soil updating is presented in Table 5.

The soil stiffness update results in a reduction in the mean value of $X_d$ for all joints except three joints in the splash zone (joints 40CL, 40BL and 40CU). The CoV of $X_d$ is reduced for all joints because the CoV of $X_d$ is reduced from the initial value of 0.10 for all joints. The structural reliability after the soil update is presented in Figure 7 alongside the lifetime compared to the nominal model presented in Table 5. After the soil update, we can observe an increase in fatigue life in four joints close to the mudline (13CU and 13BU) and in the lowest X-joint (25BL and 25BU). Compared to the nominal model, we can conclude that for both critical joints (40BU and 13CU), the fatigue lifetime is increased after the update. Note that the fatigue lifetime in joint 40BL is reduced despite a reduced CoV. That is due to the fact that for this joint, two opposite effects of the soil update are merged; namely, the positive effect of the reduced CoV (0.006 vs. 0.10) and the negative effect of the increased mean value (1.07 vs. 1.00).

The general conclusion holds that if both the mean value and CoV are reduced, then the fatigue lifetime is increased, while if both of the values are increased, then the opposite result holds. If either mean or CoV is reduced while the other is increased, the fatigue lifetime can either increase or decrease depending on the extent of the increase/decrease in mean value and CoV.

**Table 5.** Effect of updating soil stiffness on fatigue lifetime.

| Joint | $\mu_{X_d}$ | CoV $X_d$ | Lifetime (Years) | Compared to Table 3 |
|---|---|---|---|---|
| 50CL | 0.98 | 0.004 | >100 | N/A |
| 50BL | 0.98 | 0.005 | >100 | N/A |
| 40CL | 1.04 | 0.004 | 62 | +8 |
| 40BL | 1.07 | 0.006 | 69 | −8 |
| 40CU | 1.05 | 0.003 | >100 | N/A |
| 40BU | 0.98 | 0.005 | 44 | +19 |
| 13CU | 0.65 | 0.058 | >100 | + |
| 13BU | 0.56 | 0.057 | >100 | N/A |
| 25BL | 0.90 | 0.013 | >100 | + |
| 25BU | 0.92 | 0.012 | >100 | + |

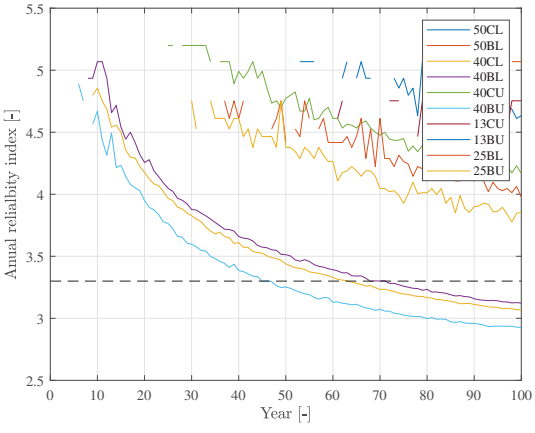


**Figure 7.** Structural reliability after the soil stiffness update. ($k_s$ update based on the study in [33]).

### *5.2. Loading Uncertainty Update*

In this subsection, we investigate the effect of updating loading uncertainty on the structural reliability. First, we present a sensitivity study on wave loading calibration, followed by updating the reliability based on load calibration using two virtual sensing configurations. The virtual sensing study is presented based on uncertainty quantified in [34]. In this subsection, the $X_l$ uncertainty is updated based on an updated $C_m$ parameter. It is assumed, similarly as in Section 5.1, that only one uncertain parameter affects the uncertainty modeling, i.e., $\boldsymbol{\alpha} = C_m$.

#### 5.2.1. Wave Loading Sensitivity

The effect of updating the wave loading coefficient, $C_m$, on the structural reliability of joint 13CU is presented in Figure 8 and in Table 6. The mean value of the wave loading coefficient is modified by a factor of 0.8–1.2, which results in modifications of the loading uncertainty. It is assumed that new information from the digital twin is obtained; in this particular case, the mean value of uncertainty related to loading uncertainty, $\mu_{X_l}$, is updated. The results are derived by using the limit state Equation (1) with the standard-based variables provided in Table 2 and updated values for $\mu_{X_l}$.

The wave loading modification has a medium impact on the fatigue lifetime. Updating the wave loading by a factor of 0.8 (reducing the inertia-induced wave loading by 20%) results in an increased lifetime by a factor of 1.6. Increasing the wave loading by a factor of 1.2 results in reducing the lifetime by a factor of 0.7. The effect of updating wave loading on joint 40BU is more pronounced, as indicated in Figure 9. For this joint, reducing the wave loading by 20% results in a lifetime increase by more than fourfold (>100 years), while a wave loading increase by 20% results in a lifetime reduction by a factor of 0.3.

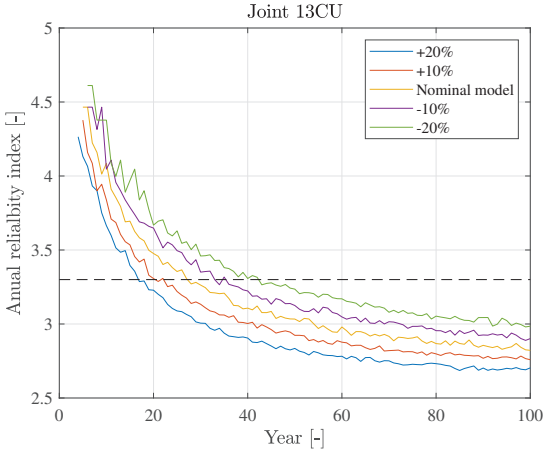


**Figure 8.** Impact of updating wave loading on structural reliability-joint 13CU.

**Table 6.** Fatigue lifetime derived for different distributions of $X_l$.

| $C_m$ | 13CU | | | 40BU | | |
|---|---|---|---|---|---|---|
| | $\mu_{X_l}$ | CoV $X_l$ | Lifetime | $\mu_{X_l}$ | CoV $X_l$ | Lifetime |
| 1.2 | 1.06 | 0.10 | 17 | 1.20 | 0.10 | 7 |
| 1.1 | 1.03 | 0.10 | 21 | 1.10 | 0.10 | 12 |
| 1.0 | 1.00 | 0.10 | 25 | 1.00 | 0.10 | 25 |
| 0.9 | 0.97 | 0.10 | 33 | 0.90 | 0.10 | 55 |
| 0.8 | 0.94 | 0.10 | 42 | 0.80 | 0.10 | >100 |

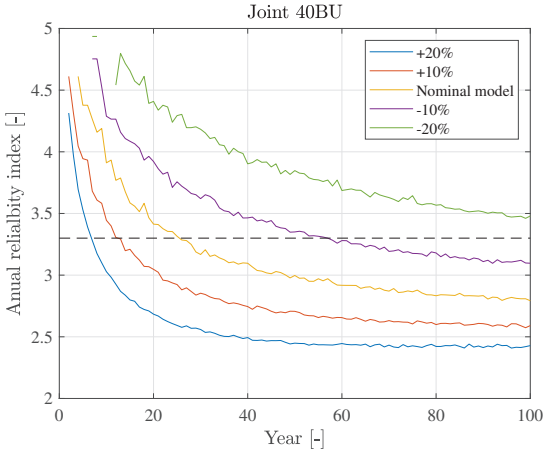


**Figure 9.** Fatigue lifetime derived for different distributions of $X_l$-joint 40BU.

#### 5.2.2. Reliability Update-Virtual Sensing Uncertainty

The virtual sensing uncertainty quantified for two virtual sensing configurations are considered based on results presented in [34]. The following virtual sensing uncertainty configurations are used: (1) basic setup: CoV = 0.10 and (2) extended setup: CoV = 0.05, while the mean value for both setups is assumed to be 1.00. The basic setup includes only acceleration sensors above the water level, while the extended one, in addition, includes sub-sea acceleration sensors and a wave radar sensor. It is assumed that the virtual sensing uncertainty are combined with the nominal $X_l$ uncertainty. Furthermore, it is assumed, for illustrative purposes, that the mean value of $X_l$ equals 0.9. The $X_l$ distribution parameters used in this study are summarized in Table 7 for joints 40CU and 13BU.

The results for joint 40BU are presented in Figure 10. As each model update configuration results in the same mean value update so the only difference in the stochastic model is the CoV, the higher the CoV, the shorter lifetime we should derive. This is confirmed in the results as the direct sensing method (measuring directly), with CoV = 0.00 resulting in a lifetime of 60 years, followed by the extended virtual sensing method (lifetime of 50 years and CoV = 0.05), while the most uncertain method (basic virtual sensing with CoV = 0.10) results in a fatigue lifetime of 40 years. In this case, each configuration derives a fatigue lifetime larger than the nominal one, i.e., 25 years. However, this is not the case for joint 13CU, where the fatigue lifetime using the basic virtual sensing configuration is 22 years, as depicted in Figure 11. Even though the mean value of the update results in reduced fatigue damage ($\mu_{X_l} = 0.97$ for this case), the negative effect of increased uncertainty (CoV $X_l = 0.14$) results in a fatigue lifetime reduction of 3 years.

**Table 7.** Fatigue lifetime updated based on various uncertain wave loading calibration methods. $X_l$ distribution is updated (mean and CoV).

| Configuration | 13CU | | | 40BU | | |
|---|---|---|---|---|---|---|
| | $\mu_{X_l}$ | CoV $X_l$ | Lifetime | $\mu_{X_l}$ | CoV $X_l$ | Lifetime |
| Nominal | 1.00 | 0.10 | 25 | 1.00 | 0.10 | 25 |
| Basic | 0.97 | 0.14 | 22 | 0.90 | 0.14 | 40 |
| Extended | 0.97 | 0.11 | 30 | 0.90 | 0.11 | 50 |
| Direct sensing | 0.97 | 0.10 | 35 | 0.90 | 0.10 | 60 |

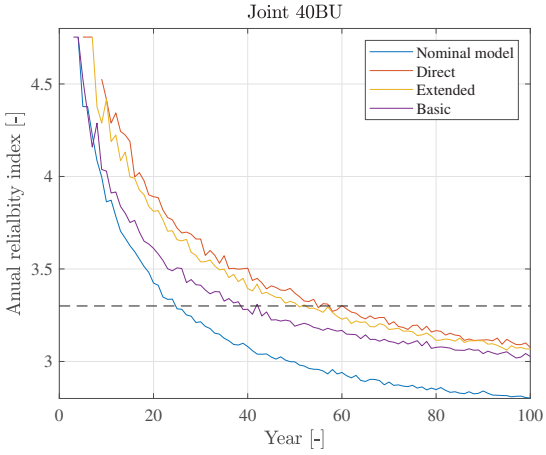


**Figure 10.** Impact of updating wave loading based on uncertain virtual sensing methods-40BU.

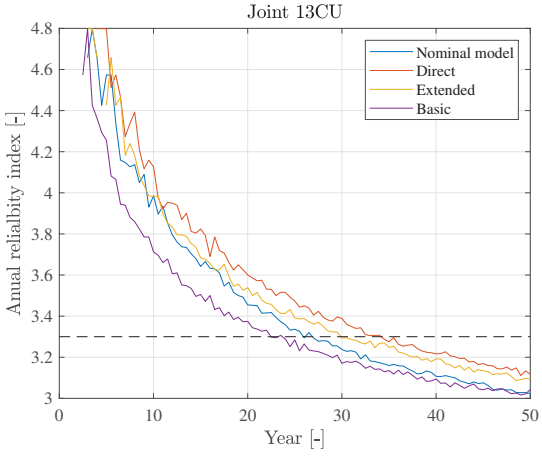


**Figure 11.** Impact of updating wave loading based on uncertain virtual. sensing methods-13CU.

### *5.3. Uncertainty Correlation*

In the previous subsections, the $X_d$ and $X_l$ uncertainties were investigated separately, hence neglecting a potential correlation. In this subsection, we consider updating both $X_d$ and $X_l$ with varying correlation coefficients. The correlation can stem from interaction between the structural dynamics and loading parameters. For example, the loading parameters can be calibrated based on responses from a previously updated structural model.

We assume the structural and loading uncertainties are quantified based on new information from a digital twin, resulting in updated mean values of structural and load uncertainties: $\mu_{X_d} = 0.80$ and $\mu_{X_l} = 0.97$ and using the reference uncertainty level CoV = 0.10. The updated uncertainty value corresponds to increasing the soil stiffness by 50%, $k_s = 1.5$, and reducing the wave loading coefficient by 10%, $C_m = 0.9$. The results are presented for joint 13CU.

Three scenarios of correlation between $X_d$ and $X_l$ are investigated: (1) $\rho = 0$ (no correlation), which can be the case if the load calibration was performed without using information from the updated structural model, (2) $\rho = 1$ (full correlation), when, for example, load calibration using mode shapes from an updated structural model and (3) an intermediate case with $\rho = 0.5$, where both analytical and measured mode shapes were used for load calibration.

The structural reliability calculated for various scenarios is presented in Figure 12. The nominal setup yields a fatigue lifetime of 25 years, while the updated uncertainty results in a fatigue lifetime ranging between 23 and 48 years, where the difference stems solely from varying correlations. The largest fatigue lifetime is obtained when assuming no correlation, while the lowest lifetime is derived for full correlation. Note that despite reducing the mean values of $X_d$ and $X_l$, the fatigue lifetime is reduced compared to the nominal result for the full correlation case. The results are in line with expectations, because positive correlation increases the combined $X_d X_l$ uncertainty.

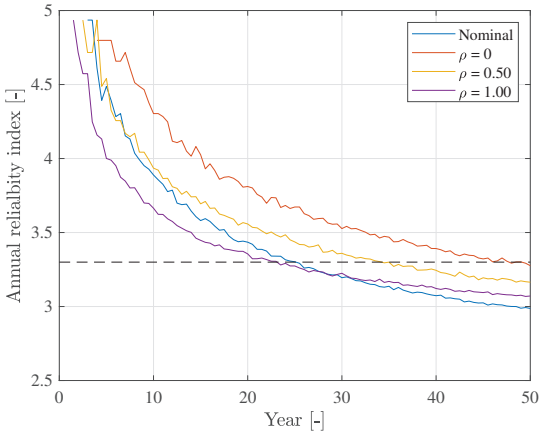


**Figure 12.** Impact of $X_d$ and $X_l$ correlation on structural reliability.

### *5.4. Application for New Structures*

Assuming a number of digital twins for similar structures have been established in the past, we can, by applying the proposed framework, obtain a distribution function of $X_d X_l$, which indicates what is the expected outcome of updating the structural and load model. This knowledge can be used at the design stage, resulting in an optimized design given the expected model update is realized. However, the updated information may be at a preliminary stage of validation and therefore subject to some degree of uncertainty, i.e., the expected model update outcome only represents our (best) knowledge. Hence, we must confirm our expectation by performing model updates during the structural lifetime and consider all potential outcomes of the experiment (model update) in the design stage. This is accounted for by preparing a decision rule, which for any outcome introduces an action that guarantees that the wind turbine has a sufficient reliability level until the intended lifetime is reached. The proposed application is based on Bayesian pre-posterior decision theory [54] and has, in the offshore wind industry, been applied in, for example, optimization of operation and maintenance of wind turbines [55].

In the following, an illustrative example is presented for this application to new structures. Assume that, based on previous digital twins, we obtain a prior distribution function of quantified uncertainties, $X_f = X_d X_l$. This prior distribution can be regarded as the future (yet to be realized) distribution of the updated uncertainties and can be used already at the design stage.

For the sake of illustration, we assume that the future outcome of model updates can be modeled as $X_f \sim \mathcal{N}\left(0.9, (0.9 \times 0.05)^2\right)$, as depicted in Figure 13. The prior distribution is used together with model (1) to design the optimized structure. This is obtained by assuming that the generic structural dynamics and loading uncertainty are substituted with the expected uncertainty quantified based on the future experiment, $X_d X_l = X_f$. The decision models are derived based on (1), where, depending on the outcome of the model update, different values of $X_f$ are assumed. The $X_f$ values are summarized in Table 8. As a result, we derive an optimized structure, which has sufficient reliability until the intended

lifetime is reached. This is indicated in Figure 14 by the blue curve. In the design, we have used the prior distribution of the updated uncertainty and assumed that updating the model is performed during the operation of the structure to confirm our expectation (obtain the posterior distribution). The point in time when updating the model must be performed can be derived by applying model (1) with the nominal uncertainty from Table 2, as shown in Figure 13 with the orange curve. Finally, we derive a point when the structure reaches the target reliability level and some action is needed to confirm its structural reliability. This is indicated by the orange curve in Figure 14.

When the model update time is reached, updating of the model is performed. As a result of model update, we can obtain one of the three outcomes for $X_f$, which will have an impact on the decision models, as depicted in Figure 15. In particular, we have the following potential outcomes:

- Most likely: the mean value of the derived model update is close to the mean value of the prior distribution assumed in the design stage, $\mu_{X_d X_l} = \mu_{X_f}$. In such a case, the structure is fit for operation for the intended lifetime and no further action is required. This scenario is indicated by the green line in Figure 15.
- Unlikely positive: the mean value is less than the value assumed in the design stage, $\mu_{X_d X_l} < \mu_{X_f}$. This results in a longer lifetime than expected and no further action is required. This scenario is indicated by the yellow line in Figure 15.
- Unlikely negative: the mean value is greater than the value assumed in the design stage, $\mu_{X_d X_l} > \mu_{X_f}$. This results in a shorter lifetime than expected and action is required to ensure a sufficient reliability during the intended lifetime of the structure. This scenario is indicated by the dashed red line in Figure 15.

Given the expected or positive outcome of updating the model is realized, no further action is required. However, if the outcome of updating the model is unexpectedly negative, the following mitigation actions can be considered to ensure the required level of reliability during the intended lifetime: (1) strengthening or (2) curtailing of the wind turbine (thereby reducing fatigue damage) and operating until the end of the intended lifetime. If it is economically infeasible to continue the operation of a particular turbine given the model updating outcome, one can consider premature decommissioning. The reliability level after the mitigation action is performed as indicated by the solid red line in Figure 15.

**Table 8.** Pre-posterior stochastic model.

| Case | $\mu_{X_f}$ | CoV $X_f$ | Comment | Information |
|---|---|---|---|---|
| Pre-posterior design | 0.9 | 0.05 | Prior knowledge on $X_f$ | Generic design |
| Determine model update time | 1.0 | 0.14 | Using no extra information from digital twin | Generic design |
| Model updating (expected outcome) | 0.9 | 0.05 | The same as prior knowledge, lifetime as expected, no action | Digital twin |
| Model updating (positive outcome) | 0.85 | 0.05 | Positive outcome, longer lifetime than expected, potential for lifetime extension | Digital twin |
| Model updating (negative outcome) | 0.95 | 0.05 | Negative outcome, shorter lifetime than expected | Digital twin |
| Model updating (negative outcome + mitigation) | 0.9 | 0.05 | Mitigation (extra cost) required, after mitigation expected (or longer) lifetime achieved | Digital twin + mitigation |

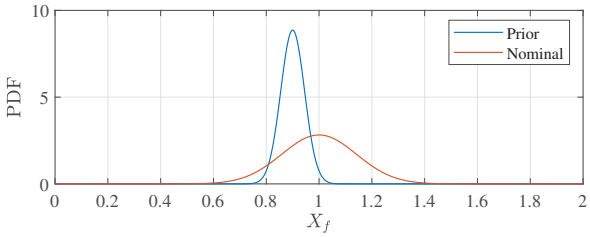


**Figure 13.** Stochastic model for pre-posterior design.

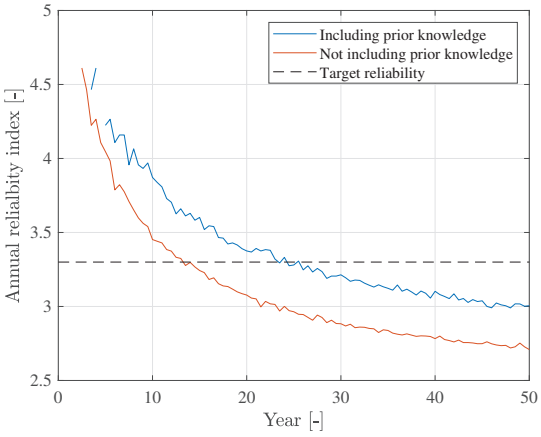


**Figure 14.** Benefit of including pre-posterior design (including prior knowledge on $X_f$).

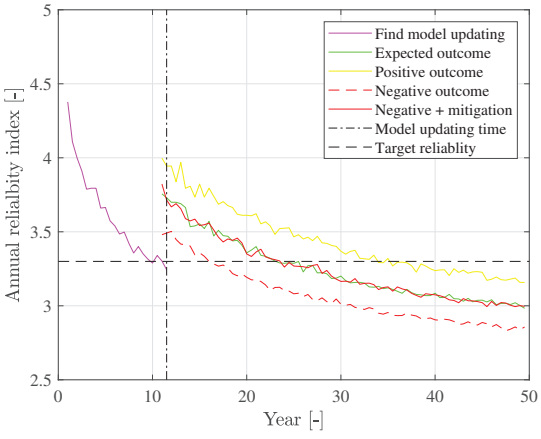


**Figure 15.** Pre-posterior design at inspection time.

## 6. Conclusions

In this paper, we propose a probabilistic framework for updating structural reliability of offshore wind substructures based on new information from digital twins. The digital twin information is consistently included in the framework by updating the uncertainty related to structural dynamics and load modeling and propagating this uncertainty to the fatigue damage accumulation. The resulting uncertainty is then converted into uncertainty of the stress ranges, which is included in a probabilistic model on structural reliability. The proposed framework is applicable to offshore wind substructures whose lifetimes are governed by fatigue damage accumulation.

The framework is applied to two case studies, where the potential for improved decision models for existing and new structures is demonstrated. In the former case, updating soil stiffness and wave loading is considered to investigate the potential for lifetime extension of fatigue critical joints. In the latter case, the framework is applied to optimize new structures by using Bayesian pre-posterior theory for future wave load calibration.

**Author Contributions:** Conceptualization, D.A., M.D.U. and J.D.S.; methodology, D.A., M.D.U. and J.D.S.; formal analysis, D.A., M.D.U. and J.D.S.; writing—original draft preparation, D.A., M.D.U. and J.D.S.; writing—review and editing, D.A., M.D.U. and J.D.S. All authors have read and agreed to the published version of the manuscript.

**Funding:** Innovationsfonden: 8053-00146B; Rambøll Fonden: A0.

**Institutional Review Board Statement:** Not applicable.

**Informed Consent Statement:** Not applicable.

**Data Availability Statement:** The study does not report any data.

**Acknowledgments:** The work presented herein is financially supported by Ramboll Foundation, Ramboll Energy and Innovation Fund Denmark. The financial support is highly appreciated. The first author would like to thank colleagues from Ramboll for their continuous support.

**Conflicts of Interest:** The authors declare no conflict of interest.

## References

1. U.S. Department of Energy. *2018 Offshore Wind Technologies Market Report*; Technical Report; U.S. Department of Energy: Washington, DC, USA, 2018.
2. Wind Europe. *Offshore Wind in Europe. Key Statistics 2020*; Technical Report; Wind Europe: Brussels, Belgium, 2020.
3. Global Wind Energy Council. *Global Offshore Wind Report 2020*; Technical Report; Global Wind Energy Council: Brussels, Belgium, 2020.
4. Nielsen, J.S.; Tcherniak, D.; Ulriksen, M.D. A case study on risk-based maintenance of wind turbine blades with structural health monitoring. *Struct. Infrastruct. Eng.* **2021**, *17*, 302–318. [CrossRef]
5. Grieves, M. *Digital Twin: Manufacturing Excellence through Virtual Factory Replication*; White Paper; Michael W. Grieves, LLC: Winooski, VT, USA, 2015.
6. Grieves, M.; Vickers, J. Digital Twin: Mitigating Unpredictable, Undesirable Emergent Behavior in Complex Systems. In *Transdisciplinary Perspectives on Complex Systems: New Findings and Approaches*; Springer International Publishing: Cham, Switzerland, 2017; pp. 85–113. [CrossRef]
7. Tygesen, U.; Jepsen, M.; Vestermark, J.; Dollerup, N.; Pedersen, A. The True Digital Twin Concept for Fatigue Re-Assessment of Marine Structures. In Proceedings of the ASME 2018 37th International Conference on Ocean, Offshore and Arctic Engineering OMAE2018, Madrid, Spain, 17–22 June 2018. [CrossRef]
8. Pedersen, E.B.; Jørgensen, D.; Riber, H.J.; Ballani, J.; Vallaghé, S.; Paccaud, B. True Fatigue Life Calculation Using Digital Twin Concept and Operational Modal Analysis. In Proceedings of the Twenty-Ninth (2019) International Offshore and Polar Engineering Conference, Honolulu, HI, USA, 16–21 June 2019; Volume 1.
9. Kritzinger, W.; Karner, M.; Traar, G.; Henjes, J.; Sihn, W. Digital Twin in manufacturing: A categorical literature review and classification. *IFAC-PapersOnLine* **2018**, *51*, 1016–1022.
10. Sivalingam, K.; Sepulveda, M.; Spring, M.; Davies, P. A Review and Methodology Development for Remaining Useful Life Prediction of Offshore Fixed and Floating Wind turbine Power Converter with Digital Twin Technology Perspective. In Proceedings of the 2018 2nd International Conference on Green Energy and Applications (ICGEA), Singapore, 24–26 March 2018; pp. 197–204. [CrossRef]
11. DNVGL-ST-0262. *Lifetime Extension of Wind Turbines*; Technical Report; Det Norske Veritas Germanischer Lloyd: Høvik, Greater Oslo, Norway, 2016.
12. DNVGL-ST-0263. *Certification of Lifetime Extension of Wind Turbines*; Technical Report; Det Norske Veritas Germanischer Lloyd: Høvik, Greater Oslo, Norway, 2016.
13. IEC 61400-28 ED1. *Wind Energy Generation Systems-Part 28: Through Life Management and Life Extension of Wind Power Assets (Committee Draft)*; Technical Report; International Electrotechnical Commission: Geneva, Switzerland, 2021.
14. BSH-7005. *Standard Design. Minimum Requirements Concerning the Constructive Design of Offshore Structures within the Exclusive Economic Zone (EEZ)*; Technical Report; Bundesamt für Seeschifffahrt und Hydrographie: Hamburg, Germany, 2015.
15. Nielsen, J.S.; Sørensen, J.D. Bayesian Estimation of Remaining Useful Life for Wind Turbine Blades. *Energies* **2017**, *10*, 664. [CrossRef]
16. Ziegler, L.; Muskulus, M. Fatigue reassessment for lifetime extension of offshore wind monopile substructures. *J. Phys. Conf. Ser.* **2016**, *753*, 092010. [CrossRef]
17. Leser, P.E.; Warner, J.E.; Leser, W.P.; Bomarito, G.F.; Newman, J.A.; Hochhalter, J.D. A digital twin feasibility study (Part II): Non-deterministic predictions of fatigue life using in-situ diagnostics and prognostics. *Eng. Fract. Mech.* **2020**, *229*, 106903. [CrossRef]
18. Mai, Q.A.; Weijtjens, W.; Devriendt, C.; Morato, P.G.; Rigo, P.; Sørensen, J.D. Prediction of remaining fatigue life of welded joints in wind turbine support structures considering strain measurement and a joint distribution of oceanographic data. *Mar. Struct.* **2019**, *66*, 307–322. [CrossRef]

19. Augustyn, D.; Tygesen, U.T.; Ulriksen, M.D.; Sørensen, J.D. Data-Driven Design and Operation of Offshore Wind Structures. In Proceedings of the Twenty-Ninth (2019) International Offshore and Polar Engineering Conference, Honolulu, HI, USA, 16–21 June 2019; Volume 1, pp. 491–498.
20. Straub, D. Reliability updating with equality information. *Probabilistic Eng. Mech.* **2011**, *26*, 254–258. [CrossRef]
21. Zhang, R.; Mahadevan, S. Model uncertainty and Bayesian updating in reliability-based inspection. *Struct. Saf.* **2000**, *22*, 145–160. [CrossRef]
22. Schneider, R.; Thöns, S.; Straub, D. Reliability analysis and updating of deteriorating systems with subset simulation. *Struct. Saf.* **2017**, *64*, 20–36. [CrossRef]
23. Straub, D.; Faber, M.H. Risk based inspection planning for structural systems. *Struct. Saf.* **2005**, *27*, 335–355. [CrossRef]
24. Sørensen, J.D. Framework for risk-based planning of operation and maintenance for offshore wind turbines. *Wind Energy* **2009**, *12*, 493–506. [CrossRef]
25. Singh, M.; Markeset, T. A methodology for risk-based inspection planning of oil and gas pipes based on fuzzy logic framework. *Eng. Fail. Anal.* **2009**, *16*, 2098–2113. [CrossRef]
26. Hevia-Koch, P.; Klinge Jacobsen, H. Comparing offshore and onshore wind development considering acceptance costs. *Energy Policy* **2019**, *125*, 9–19. [CrossRef]
27. Netland, Ø.; Sperstad, I.B.; Hofmann, M.; Skavhaug, A. Cost-benefit Evaluation of Remote Inspection of Offshore Wind Farms by Simulating the Operation and Maintenance Phase. *Energy Procedia* **2014**, *53*, 239–247. EERA DeepWind' 2014, 11th Deep Sea Offshore Wind R&D Conference. [CrossRef]
28. Ulriksen, M.D. Damage Localization for Structural Health Monitoring: An Exploration of Three New Vibration-Based Schemes. Ph.D. Dissertation, Aalborg University, Aalborg, Denmark, 2018.
29. Simoen, E.; De Roeck, G.; Lombaert, G. Dealing with uncertainty in model updating for damage assessment: A review. *Mech. Syst. Signal Process.* **2015**, *56–57*, 123–149. [CrossRef]
30. Nielsen, J.S.; Sørensen, J.D. Computational framework for risk-based planning of inspections, maintenance and condition monitoring using discrete Bayesian networks. *Struct. Infrastruct. Eng.* **2018**, *14*, 1082–1094. [CrossRef]
31. Sørensen, J.D.; Toft, H.S. *Safety Factors-IEC 61400-1 ed. 4-Background Document*; Technical Report, DTU Wind Energy-E-Report-0066(EN); Technical University of Denmark (DTU): Lyngby, Denmark, 2014.
32. Velarde, J.; Kramhøft, C.; Sørensen, J.D.; Zorzi, G. Fatigue reliability of large monopiles for offshore wind turbines. *Int. J. Fatigue* **2020**, *134*, 105487. [CrossRef]
33. Augustyn, D.; Smolka, U.; Tygesen, U.T.; Ulriksen, M.D.; Sørensen, J.D. Data-Driven Model Updating of an Offshore Wind Jacket Substructure. *Appl. Ocean. Res.* **2020**, *104*, 102366. [CrossRef]
34. Augustyn, D.; Pedersen, R.R.; Tygesen, U.T.; Ulriksen, M.D.; Sørensen, J.D. Feasibility of modal expansion for virtual sensing in offshore wind jacket substructures. *Mar. Struct.* **2021**, *79*, 103019. [CrossRef]
35. Madsen, H.; Krenk, S.; Lind, N. *Methods of Structural Safety*, 2nd ed.; Dover Publications: New York, NY, USA, 2006.
36. Tavner, P. *Offshore Wind Turbines: Reliability, Availability and Maintenance*; Institution of Engineering and Technology: Stevenage, UK, 2012.
37. Arabian-Hoseynabadi, H.; Oraee, H.; Tavner, P. Failure Modes and Effects Analysis (FMEA) for wind turbines. *Int. J. Electr. Power Energy Syst.* **2010**, *32*, 817–824. [CrossRef]
38. Nguyen, T.A.; Min, D.; Choi, E.; Lee, J.W. Dependability and Security Quantification of an Internet of Medical Things Infrastructure based on Cloud-Fog-Edge Continuum for Healthcare Monitoring using Hierarchical Models. *IEEE Internet Things J.* **2021**. [CrossRef]
39. Madsen, H.O.; Krenk, S.; Lind, N.C. *Methods of Structural Safety*; Courier Corporation: Washington, DC, USA, 2006.
40. IEC-61400-1:2019. *Wind Energy Generation Systems-Part 1: Design Requirements*; Technical Report; International Electrotechnical Commission: Geneva, Switzerland, 2019.
41. Szala, G.; Ligaj, B. Effect of the Exponent in the Description of Wöhler Fatigue Diagram on the Results of Calculations of Fatigue Life. *Key Eng. Mat.* **2014**, *598*, 231–236. [CrossRef]
42. Naess, A.; Leira, B.; Batsevych, O. System reliability analysis by enhanced Monte Carlo simulation. *Struct. Saf.* **2009**, *31*, 349–355. [CrossRef]
43. Hübler, C.; Gebhardt, C.G.; Rolfes, R. Methodologies for fatigue assessment of offshore wind turbines considering scattering environmental conditions and the uncertainty due to finite sampling. *Wind Energy* **2018**, *21*, 1092–1105. [CrossRef]
44. Reynders, E.; Pintelon, R.; Roeck, G. Uncertainty bounds on modal parameters obtained from stochastic subspace identification. *Mech. Syst. Signal Process.* **2008**, *22*, 948–969. [CrossRef]
45. Iliopoulos, A.; Weijtjens, W.; Van Hemelrijck, D.; Devriendt, C. Fatigue assessment of offshore wind turbines on monopile foundations using multi-band modal expansion. *Wind Energy* **2017**, *20*, 1463–1479. [CrossRef]
46. Efthymiou, M.; Durkin, S. Stress concentrations in T/Y and gap/overlap K-joints. In Proceedings of the 4th International Conference on Behaviour of Offshore Structures, Delft, The Netherlands, 1–5 July 1985; p. 12.
47. Lee, J.M.; Seo, J.K.; Kim, M.H.; Shin, S.B.; Han, M.S.; Park, J.S.; Mahendran, M. Comparison of hot spot stress evaluation methods for welded structures. *Int. J. Nav. Archit. Ocean Eng.* **2010**, *2*, 200–210. [CrossRef]
48. DNVGL-RP-C203. *Fatigue Design of Offshore Steel Structures*; Technical Report; Det Norske Veritas Germanischer Lloyd: Høvik, Greater Oslo, Norway, 2016.

49. Miner, M.A. Cumulative Damage in Fatigue. *J. Appl. Mech.* **2021**, *12*, A159–A164. [CrossRef]
50. Paris, P.; Erdogan, F. A Critical Analysis of Crack Propagation Laws. *J. Basic Eng.* **1963**, *85*, 528–533. [CrossRef]
51. Friswell, M.I.; Mottershead, J.E. *Finite Element Model Updating in Structural Dynamics*; Kluwer Ademic Publishers: Amsterdam, The Netherlands, 1995.
52. Anderson, G. Error propagation by the Monte Carlo method in geochemical calculations. *Geochim. Cosmochim. Acta* **1976**, *40*, 1533–1538. [CrossRef]
53. ISO 13587:2012. *Three Statistical Approaches for the Assessment and Interpretation of Measurement Uncertainty*; Technical Report; International Electrotechnical Commission: Geneva, Switzerland, 2012.
54. Raiffa, H.; Schlaifer, R. *Applied Statistical Decision Theory*; Wiley & Sons: Hoboken, NJ, USA, 2000. [CrossRef]
55. Nielsen, J.J.; Sørensen, J.D. On risk-based operation and maintenance of offshore wind turbine components. *Reliab. Eng. Syst. Saf.* **2011**, *96*, 218–229. [CrossRef]
56. Onoufriou, T. Reliability based inspection planning of offshore structures. *Mar. Struct.* **1999**, *12*, 521–539. [CrossRef]
57. Nielsen, M.B.; Jensen, J.F.; Harper, C.; Knudsen, L.S.; Pedersen, R.R. State-of-the-art framework for design of offshore wind jacket foundations. *Steel Constr.* **2019**, *12*, 209–214. [CrossRef]
58. Craig, R.R.; Bampton, M.C.C. Coupling of substructures for dynamic analyses. *AIAA J.* **1968**, *6*, 1313–1319. [CrossRef]
59. Nielsen, M.B.; Jensen, J.F.; Augustyn, D.; Pedersen, R.R. Efficient response recovery procedures for detailed design of jacket foundations. In *Insights and Innovations in Structural Engineering, Mechanics and Computation*, 1st ed.; Taylor & Francis: London, UK, 2016; Volume 1, pp. 2060–2065. [CrossRef]
60. van der Valk, P.; Voormeeren, S. An overview of modeling approaches for complex offshore wind turbine support structures. In Proceedings of the ISMA2012-USD2012, Leuven, Belgium, 17–19 September 2012; pp. 1–4.
61. Passon, P. Offshore Wind Turbine Foundation Design. Ph.D. Thesis, DTU Wind Energy: Roskilde, Denmark, 2015.
62. Ramboll. *ROSAP-Ramboll Offshore Structural Analysis Package, Version 53*; Technical Report; Ramboll: Esbjerg, Denmark, 2018.
63. API-RP-2A. *Recommended Practice for Planning, Designing and Constructing Fixed Offshore Platforms*; Technical Report; American Petroleum Institute: Washington, DC, USA, 2014.
64. Liu, M.; Gorman, D. Formulation of Rayleigh damping and its extensions. *Comput. Struct.* **1995**, *57*, 277–285. [CrossRef]
65. Ramboll. *LACflex-Aeroelastic Simulation Tool*; Technical Report; Ramboll: Aarhus, Denmark, 2018.
66. Augustyn, D.; Cosack, N.; Ulriksen, M. On the influence of environmental and operational variability on modal parameters of offshore wind support structures. *Mar. Struct.* **2021**. submitted.
67. Kelma, S.; Schaumann, P. Probabilistic Fatigue Analysis of Jacket Support Structures for Offshore Wind Turbines Exemplified on Tubular Joints. *Energy Procedia* **2015**, *80*, 151–158. [CrossRef]
68. Anonymous. *Met-Ocean Report*; Technical Report; Confidential Publisher: New York, NY, USA, 2016.
69. Rasmus Folsø, S.O.; Parmentier, G. Reliability-based calibration of fatigue design guidelines for ship structures. *Mar. Struct.* **2002**, *15*, 627–651. [CrossRef]
70. Sørensen, J. Reliability-based calibration of fatigue safety factors for offshore wind turbines. *Int. J. Offshore Pol. Eng.* **2012**, *22*, 234–241.
71. JCSS. *Probabilistic Model Code*; Technical Report; Joint Committee on Structural Safety: Copenhagen, Denmark, 2001.

energies

MDPI

*Article*

# A Study on Directly Interconnected Offshore Wind Systems during Wind Gust Conditions

**Cathal W. O'Donnell [1,*], Mahdi Ebrahimi Salari [2] and Daniel J. Toal [1]**

[1] Centre for Robotics & Intelligent Systems, University of Limerick, V94 T9PX Limerick, Ireland; Daniel.Toal@ul.ie
[2] MaREI Centre, University College Cork, P43 C573 Cork, Ireland; MEbrahimiSalari@ucc.ie
* Correspondence: Cathal.W.ODonnell@ul.ie

**Abstract:** An investigation of the effects of wind gusts on the directly interconnected wind generators is reported, and techniques toward the mitigation of the wind gust negative influences have been proposed. Using a directly interconnected system approach, wind turbine generators are connected to a single synchronous bus or collection grid without the use of power converters on each turbine. This bus can then be transformed for transmission onshore using High Voltage Alternating Current, Low-Frequency Alternating Current or High Voltage Direct Current techniques with shared power conversion resources onshore connecting the farm to the grid. Analysis of the potential for instability in transient conditions on the wind farm, for example, caused by wind gusts is the subject of this paper. Gust magnitude and rise time/fall time are investigated. Using pitch control and the natural damping of the high inertial offshore system, satisfactory overall system performance and stability can be achieved during these periods of transience.

**Keywords:** direct interconnection; wind gust; offshore wind; power generation

**Citation:** O'Donnell, C.W.; Ebrahimi Salari, M.; Toal, D.J. A Study on Directly Interconnected Offshore Wind Systems during Wind Gust Conditions. *Energies* **2022**, *15*, 168. https://doi.org/10.3390/en15010168

Academic Editors: Eugen Rusu, Kostas Belibassakis and George Lavidas

Received: 16 November 2021
Accepted: 24 December 2021
Published: 27 December 2021

**Publisher's Note:** MDPI stays neutral with regard to jurisdictional claims in published maps and institutional affiliations.

**Copyright:** © 2021 by the authors. Licensee MDPI, Basel, Switzerland. This article is an open access article distributed under the terms and conditions of the Creative Commons Attribution (CC BY) license (https://creativecommons.org/licenses/by/4.0/).

## 1. Introduction

Offshore wind will play a significant role in both Ireland's and Europe's decarbonisation plans. Ireland's large offshore territory, coupled with high wind availability across each season [1,2], make it an ideal candidate for offshore wind development. In line with the National Energy and Climate plan, 5 GW of offshore wind is planned for deployment in Ireland by 2030 [3]. According to the Sustainable Energy Authority of Ireland (SEAI)'s wind energy road map, Ireland has potential to far exceed this 5 GW of offshore wind with a predicted installed capacity of 30 GW by 2050 [4]. This growth prediction coincides with a general decrease in onshore wind farm planning applications. Harper et al. have evaluated the regulatory effects of wind turbine planning and financing in the United Kingdom [5]. This study identified onshore wind as having a 44% success rate compared with 89% in the offshore wind sector.

Wind gust analysis has been extensively performed for traditional wind turbine systems. Turbulence and wake effects and extreme load predictions for horizontal axis wind turbines have been studied by Brand et al. [6–8]. The effect of wind gusts on vertical axis wind turbines using Computational Fluid Dynamics (CFD) has been examined by Onol et al. [9]. The distribution of extreme gusts has been previously investigated for traditionally interconnected wind turbines by Cheng et al. [10]. Gust detection and prediction methods using Doppler LiDAR are an area of current development for wind farms [11]. The use of LiDAR for wake management has also been explored showing a wind farm power increase of 7.552% with a reduction in downwind turbulence [12].

This rapid expansion within the sector leaves an opportunity for the development of new interconnection technology such as the Direct Interconnection Technique (DIT) which is considered in this paper. This technique is a method of integrating renewable generation first proposed by Pican et al., 2011 [13]. This technique of integration minimises

the utilisation of Back to Back Power Converters (B2BC) in offshore turbines by connecting each turbine to a common offshore synchronous bus which can then be transmitted back to shore by High Voltage Alternating Current (HVAC), High Voltage Direct Current (HVDC) or Low-Frequency Alternating Current (LFAC) [14,15]. The power conversion equipment can be relocated to a single offshore site allowing for better access and optimisation or where transmission constraints permit, relocated entirely onshore.

Power electronic conversion systems exhibit a high failure rate among wind turbine subassemblies [16,17]. This resultant downtime, coupled with the difficulty and cost of servicing offshore turbines [18], demonstrates the potential that DIT has for improving reliability and reducing costs associated with offshore wind. While detection and protection methods can aid in reducing power electronic converter failures [19–21], offshore maintenance of these power converters has been noted as a critical element in the levelised cost of energy [22], given the requirement for transport of parts and technicians to these offshore locations. According to a case study conducted by Su et al. failure of electrical subsystems accounted for the third highest rate of failure, accounting for 14% and 26% of total failures for the two farms studied. This accounted for 301 hours of downtime in project 1 and 693 h in project two [23].

DIT begins by spinning a pilot generator connected to the offshore bus establishing the bus reference voltage and frequency. Each subsequent generator is then spun up and connected to the bus with the pilot generator governing system frequency and voltage, and load sharing controllers optimising behaviour on subsequent generators. This high inertia system electrical bus is then transmitted onshore through the use of HVAC, LFAC or HVDC as required and grid interconnection is performed by a large scale B2BC. This method has also been extended to Airborne Wind Energy (AWE) systems by Salari et al. 2018 [24]. The difference between traditional interconnection and direct interconnection can be observed in Figures 1 and 2.

In the case of the traditional interconnection, each generator is effectively separated from the local wind farm bus by the B2BC in the wind tower. This facilitates separation of the generator, and transients caused by wind gusts for example, from the local farm bus, and the individual B2BC provides a means of dealing with transient conditions on the generator side [25]. With DIT, as multiple generators are directly interconnected to the same bus, any gust generated transient condition experienced initially by a leading-turbine-to-wind will affect the interconnected system of generators.

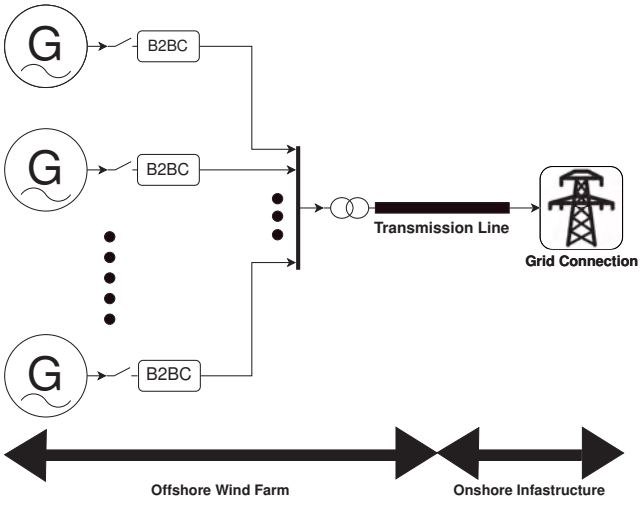


**Figure 1.** Traditional Interconnection.

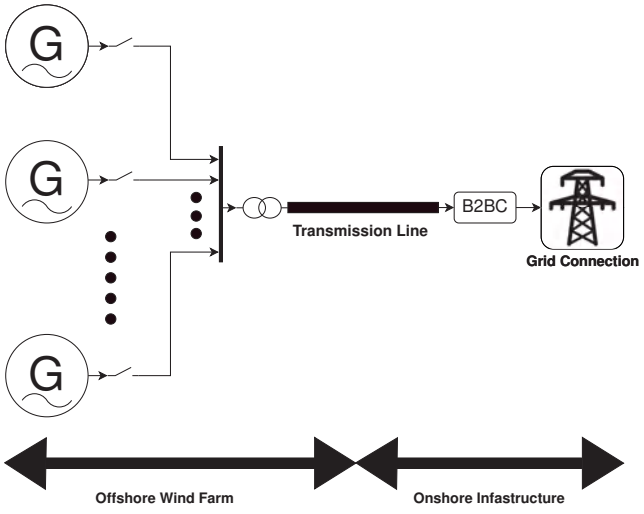


**Figure 2.** Direct Interconnection.

This paper studies the effects of wind gusts by simulating a directly interconnected wind farm and introducing a wind gust to a leading turbine. Gusts of varying types, magnitudes and transient times are applied to a leading turbine and overall system responses are investigated as described in detail in the simulation methodology section. Gust tolerance levels are measured and discussed with comparison to real-world coastal wind data.

## 2. Simulation Methodology

Gusts modelled in this study are created through the use of IEC standardised descriptions of gusts available in IEC 61400-3-1:2019 [26]. This offshore wind turbine standard in section 6.4.3.1 directly refers back to IEC 61400-1:2019 [27], an onshore wind turbine standard that describes the mean wind speed based wind gust profiles. In this standard, five extreme wind conditions are proposed: Extreme Operating Gusts (EOG), Extreme Direction Change (EDC), Extreme Coherent Gusts (ECG), Extreme Coherent Gusts with direction change (ECD) and Extreme Wind Shear (EWS). This study focuses on EOG and ECG. ECGs are considered as the increase in wind speed is sustained once the maximum gust speed is reached. This gust profile is useful for identifying any saturation limits of the system whereas the Mexican hat shape of EOGs present the greatest rate of change during the gust and therefore challenge the system due to the maximum rate of change of pitch angle. This worst-case analysis approach does not consider direction change of the wind, as the greatest amount of energy and therefore the most challenging input for the directly interconnected bus, occurs when the wind is directly incident on the turbine blades [28]. All gusts are applied with the hub facing directly into the wind with no yaw control considered. Future work may include an analysis of the other conditions. EOG and ECG profiles are generated using Equations (1) and (2).

$$u(z,t) = \begin{cases} \bar{U}(z) - 0.37U_{gust}sin(\frac{3\pi t}{T})(1 - cos(\frac{2\pi t}{T})) & 0 \leq t \leq T \\ \bar{U}(z) & otherwise \end{cases} \quad (1)$$

As defined in IEC 61400-1, $U_{gust}$ is the hub height magnitude defined by extreme wind speed recurrences for a particular site along with other physical factors such as rotor diameter. This $U_{gust}$ factor is varied along with the period $T$ to peak gust speed and settling time. $\bar{U}(z)$ is the average wind speed upon which the wind gust is superimposed.

$$u(z,t) = \begin{cases} \bar{U}(z) & t < 0 \\ \bar{U}(z) + 0.5U_{cg}(1 - cos(\frac{\pi t}{T})) & 0 \leq t \leq T \\ \bar{U}(z) + U_{cg} & t > T \end{cases} \quad (2)$$

In Equation (2), $\bar{U}(z)$ is the average wind speed, $U_{cg}$ is the magnitude of the coherent gust and T represents the rise time of the gust. Once the gust is complete the wind speed remains at this new value of $\bar{U}(z) + U_{cg}$. A sample of each gust type with the same rise time of five seconds is shown in Figure 3.

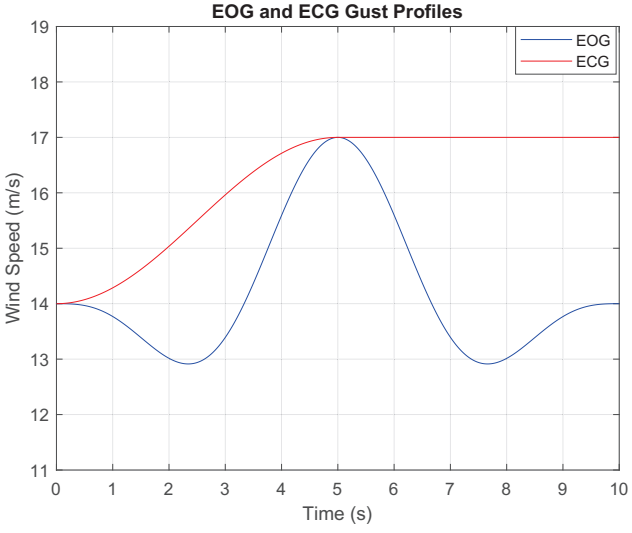


**Figure 3.** EOG and ECG profiles with rise times of 5 s.

The characteristic time for ECGs/EDCs stated in IEC 61400-1:2019 6.3.3.6 is 10 s [27]. This represents a rise time of 10 s between the base wind speed and the maximum wind speed value. However, in the case of EOGs in section 6.3.3.3, the characteristic time is 10.5 s. This time represents the length of the entire gust. Therefore the corresponding rise time would be 5.25 s. For this study, we round down this rise time to 5 s and consider rise times of 3 s, 5 s and 10 s to investigate these gusts on a like for like basis. These values are representative of the gust profiles as described in the standard, but also push beyond the values to investigate system limits.

Each turbine utilises a Permanent Magnet Synchronous Generator (PMSG) with a rated power of 800 kVA and is based on a real-world turbine characterisation [29]. The rated speed was selected at 14 m/s. The simulation begins with all wind turbines interconnected as per the direct interconnection algorithm described in [13]. Turbine 5 is selected as the pilot generator responsible for the maintenance of the frequency and voltage of the interconnected bus. This turbine in the real world would be selected as a turbine towards the centre of the wind park, thus minimising the risk of this turbine being the first to experience a wind disturbance. Each turbine has its own local dump load for spin up and disconnection from the main bus. A simulation diagram is shown in Figure 4. Disconnection could be required for dispatching down, in line with Transmission System Operator (TSO) instructions [30] or during times when the wind speed is outside of cut in and cut out speeds.

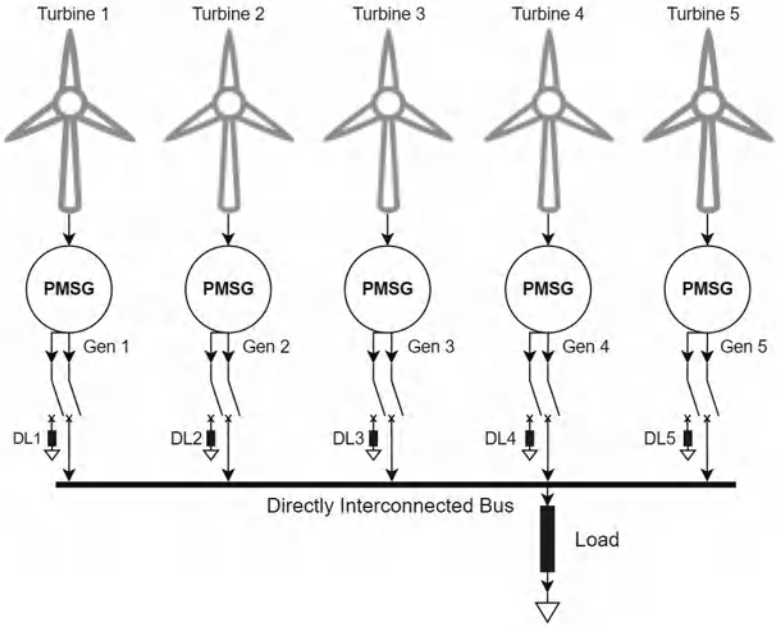


**Figure 4.** Simulation Diagram Showing the five turbines with their respective dump loads, the directly interconnected bus and the main load for the farm.

### *2.1. Simulation Model*

#### 2.1.1. Permanent Magnet Synchronous Generator model

As defined in [31] the PMSG model behaviour is described in Rotor Reference Frame (RRF) as follows:

$$\frac{d}{dt}i_d = \frac{1}{L_d}v_d - \frac{R}{L_d}i_d + \frac{L_q}{L_d}p\omega_m i_q \tag{3}$$

$$\frac{d}{dt}i_q = \frac{1}{L_q}v_q - \frac{R}{L_q}i_q - \frac{L_d}{L_q}p\omega_m i_d - \frac{\lambda p\omega_m}{L_q} \tag{4}$$

$$T_e = \frac{3}{2}p[\lambda i_q + (L_d - L_q)i_d i_q] \tag{5}$$

where $R$ is the resistance of the stator windings, $p$ is the number of pole pairs, $T_e$ is electrical torque, $L_d$ and $L_q$ are the $dq$ axis inductances, $\omega_m$ is angular velocity of the rotor, $\lambda$ is amplitude of induced flux, $v_d$ and $v_q$ are $dq$ voltages and $i_d$ and $i_q$ are $dq$ currents. Equations (3) and (4) represent the ouput currents and volatges in $dq$ frame and Equation (5) calculates electromagnetic torque.

$L_q$ and $L_d$ represent the relation between the phase inductance and the rotor position due to the saliency of the rotor. For a round rotor, there is no variation in the phase inductance therefore $L_d = L_q = \frac{L_{ab}}{2}$.

#### 2.1.2. Wind Turbine Model

The Wind turbine is modelled using the Matlab Simulink wind turbine model with a nominal mechanical output power of 800 kW and a base wind speed of 14 m/s. The output of this block is applied to the generator shaft in per unit of generator ratings. We assume a direct drive system where mechanical efficiency ($\eta\_m$) is 1. This wind turbine characteristic can be seen in Figure 5.

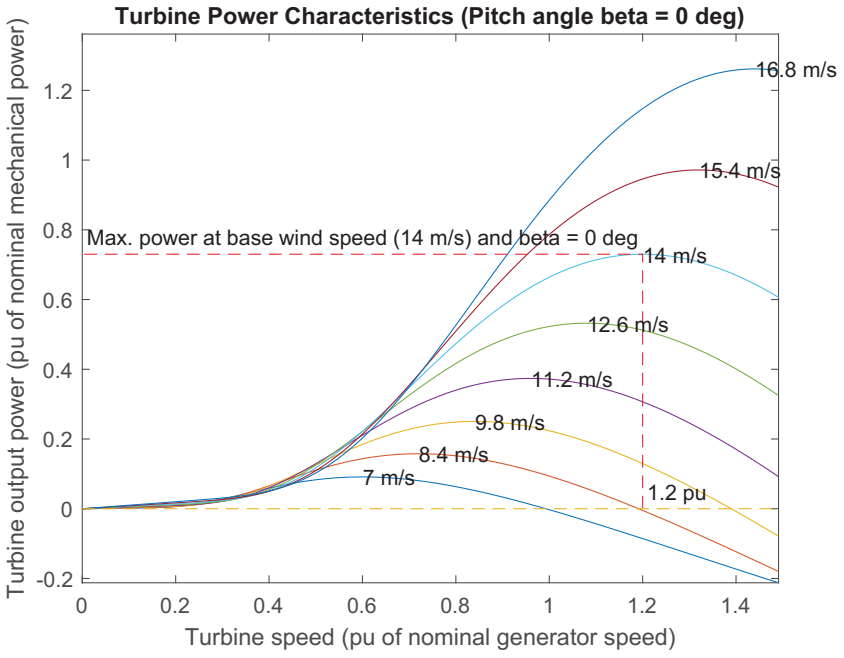


**Figure 5.** Wind Turbine Model Power Characteristic Curve.

A PID blade pitch angle controller is used with a rate of change limitation of eight degrees per second. This is to account for the fact that pitch angle cannot be varied instantaneously. This rate of change limitation value can be found in the NREL 5 MW reference wind turbine report [32]. A full control and simulation diagram can be found for both the pilot generator in Figure 6 and for non-pilot generators in Figure 7. For the pilot generator, the control system utilises a frequency setpoint and feedback loop to maintain the farm bus frequency. This pilot generator is set to a chosen power level and excluded from the farm power control loop. Non-pilot generators use a power reference and feedback loop to vary their active power contribution to the bus. The setpoint for these turbines is determined by a farm power level supervisor which takes the current farm power level and set point and distributes individual power levels to the turbines. For further information on the direct interconnection algorithm, see [13,24,29].

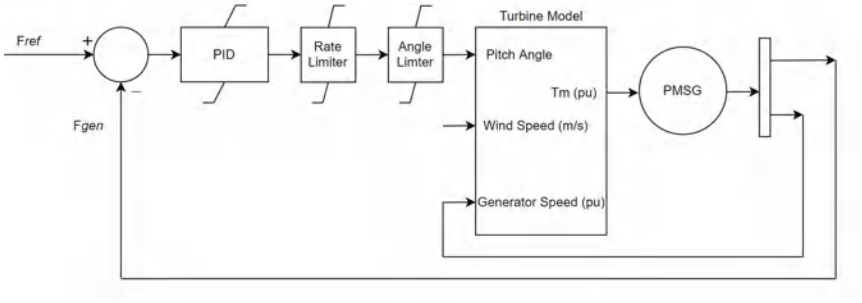


**Figure 6.** Control and Simulation Diagram for the Pilot Generator.

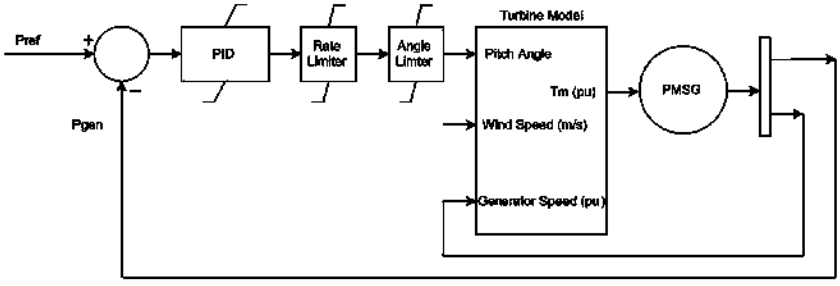


**Figure 7.** Control and Simulation Diagram for the Non-Pilot Generators.

### *2.2. Simulation Parameters*

The simulation parameters utilised in this study are provided by the company JSPM, a subsidiary of the Areva group, and represent a real-world PMSG turbine [33]. These values are applied to each PMSG model in the simulation. This characterisation is employed to provide a consistent simulation analysis approach for DIT. These parameters displayed in Table 1 as used by Pican and Ebrahimi Salari [24,29], provide a basis for comparison of DIT in varying configurations and conditions. The farm size selection of 5 turbines is presented as the base number of turbines which would realistically be deployed in the field. Larger farms could be made up of a single directly interconnected bus or multiple strings of directly interconnected buses, each consisting of varying numbers of turbines due to transmission, resource availability or geographical constraints [34–36]. A larger number of interconnected generators, similar to the traditional AC power gird, will facilitate better sharing of disturbances and simplify the frequency and power response of the system.

**Table 1.** Simulation Parameters [33].

| Parameter | Value |
|---|---|
| PMSG number of pole pairs | 45 |
| PMSG nominal frequency (Hz) | 18.6 |
| PMSG stator resistance (mΩ) | 47 |
| PMSG flux linkage (Wb) | 6.86 |
| Main load resistance (Ω) | 0.1 |
| Rotational Speed (RPM) | 24.8 |

### *2.3. Gust Factor and Variation Limits*

Gust Factor is a representation of the peak average $\tau$ second wind speed as a fraction of the $T$ seconds moving average wind speed [37]. This is shown in Equation (6), where $U_{max,\tau}$ is the maximum $\tau$ second moving average wind speed in a $T$-second averaging period and $\overline{U_T}$ is the $T$-second average wind speed. Typical values for $\tau$ are 1–10 s with common values for $T$ are 10 min to 1 h [37]. The gust factors of all test gusts applied are calculated and analysed.

$$G_{T,\tau} = \frac{U_{max,\tau}}{\overline{U_T}} \tag{6}$$

The tolerance threshold for both measured parameters of the simulation is selected as 5% (±2.5%). This threshold is selected to closely follow current grid connection codes on the farm side of the power converter [38]. This paper shows the differing gird requirements that the power conversion system of wind turbines are required to comply with. By limiting variation of frequency and active power to 5%, the power conversion system will be able to ensure grid interconnection compliance [30].

## 3. Results

### *3.1. Baseline System Response*

The baseline system response is generated applying the reference wind gust to the leading turbine while all pitch controllers on turbines 1–5 are disabled. This shows the reaction of the interconnected system of wind turbines in the absence of controllers assisting in dealing with gust disturbances. As shown in Figure 8 without any pitch control the system behaves similar to a single synchronous machine causing the collective bus frequency to increase while active power is inserted at the lead turbine. This relatively small disturbance causes both the bus active power and bus frequency responses to vary outside the 5% (±2.5%) tolerance threshold.

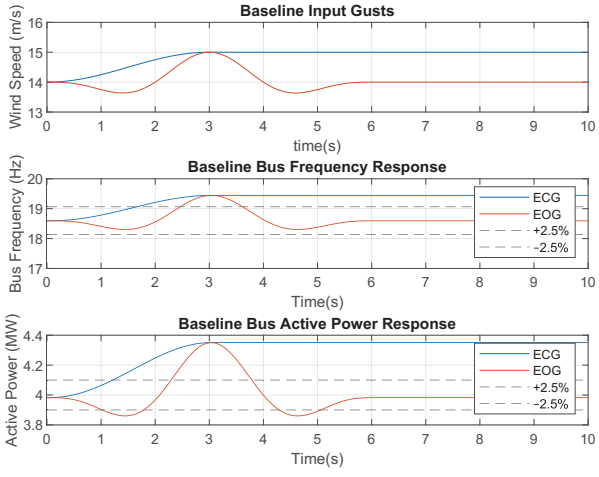


**Figure 8.** Baseline system test for both ECG and EOG. $\Delta T = 3$ s $V_{gust}$ max = 15 m/s.

### *3.2. Extreme Coherent Gust Responses*

The following section displays simulations results for Extreme Coherent Gusts (ECG) as described in the IEC Standard [27]. The test gust is applied to generator one with the system at a steady state at time zero. All generators are synchronised and interconnected to the main bus before time zero and have reached a steady state. Extreme coherent gust simulations are preformed at $\Delta T$ values of 3 s, 5 s and 10 s respectively. Example test gusts for $\Delta T = 3$ s are displayed in Figure 9.

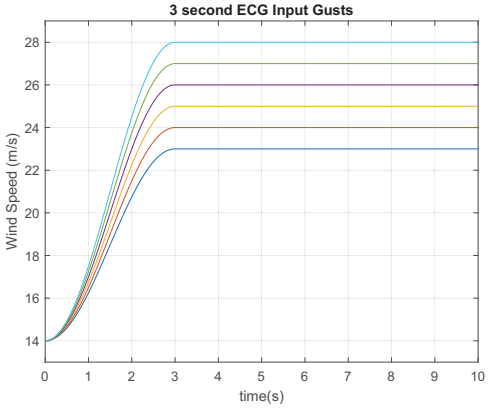


**Figure 9.** 3 s ECG test gusts applied.

For each rise time $V_{gust}$ max is varied from 15 m/s to 30 m/s in 1 m/s increments. The corresponding gust factors of these gusts can be calculated by Formula (6), where $U_{max,\tau}$ is the maximum $\tau$ second moving average wind speed in a $T$-second averaging period and $\overline{U_T}$ is the $T$-second average wind speed [37]. The gust factors for the input ECG test gusts applied are displayed in Table 2 assuming a ten minute moving average base wind speed $\overline{U_T}$ = 14 m/s and $\tau = 1$ s.

**Table 2.** ECG Input Gust Factors.

| $V_{gust}$ max | Gust Factor |
|---|---|
| 23 m/s | 1.64 |
| 24 m/s | 1.71 |
| 25 m/s | 1.79 |
| 26 m/s | 1.86 |
| 27 m/s | 1.93 |
| 28 m/s | 2.00 |
| 29 m/s | 2.07 |
| 30 m/s | 2.14 |

Figure 10 displays the frequency responses of each gust measured at the offshore bus. As can be clearly seen the 28 m/s gust response exceeds the limit of 5% (±2.5%) variation. This is due to the rate of change limitation of pitch angle variation of turbines. With an 8 degree per second maximum rate the pitch control is not capable of maintaining the 5% maximum variation. However, it can be seen that the system can damp the variation and return to steady state in all of the input gust cases. The 27 m/s gust also approaches the negative 2.5% limit but does not exceed it and therefore can be taken to be the maximum boundary limit with regard to our frequency response criteria.

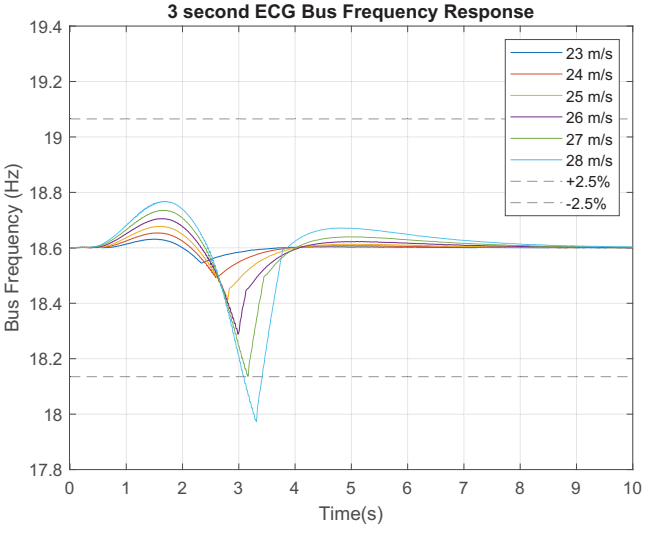


**Figure 10.** System frequency response to 3 s ECG gusts.

As can be seen in Figures 10 and 11, the active power and the frequency response are directly linked. As the 28 m/s ECG is rejected due to the frequency response criteria it can already be discounted. The 26 m/s, 27m/s and 28 m/s responses all fall outside the

negative boundary leaving the 25 m/s as the maximum boundary within the limit with regard to the active power criteria. It can therefore be said that for the system modelled any ECG with $\Delta T$ of 3 s and magnitude up to and including 25 m/s can be tolerated.

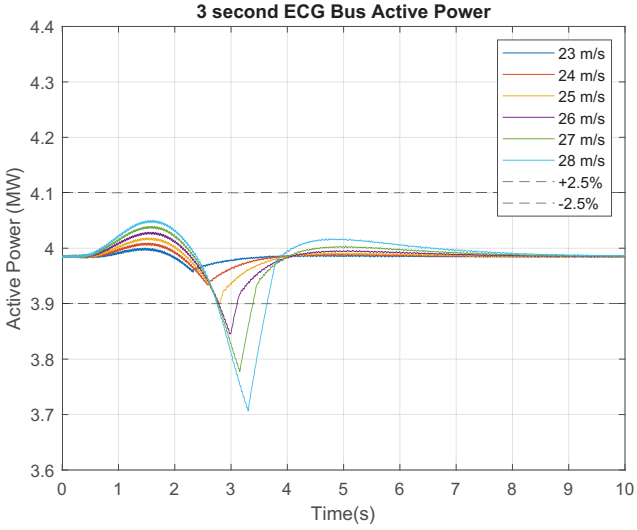


**Figure 11.** Bus active power response to 3 s ECG gusts.

The remaining simulations for ECGs with $\Delta = 5$ s and $\Delta = 10$ s all show performance within the 5% tolerance level. The 8 degrees/s of pitch angle control is capable of damping response without becoming saturated. The results of all the simulations are tabulated in Table 3. The light blue segments denote the respective criteria are satisfied while dark blue denotes that one or both of the $\pm 2.5\%$ threshold levels have been exceeded. Considering the 5 s and 10 s rise time simulations, it can be observed that ECGs up to 30 m/s can be tolerated by the system. The maximum gust factors for these events of 1.64 through 2.14 are well beyond the gust factors measures at the coastal wind site in Frøya [37]. The 3 s ECG is within limits up to and including a $V_{Gust}$ max of 25 m/s. With a gust factor of 1.79 from Table 2, this 25 m/s gust is well above the measured gust factors at this site with a mode value of 1.20.

**Table 3.** This table displays the results of all ECG simulations completed. Light Blue demonstrates the respective responses remain within the $\pm 2.5\%$ boundary limitations with dark blue showing the criteria has not been met. The minimum and maximum values of both frequency and active power reached during each gust are displayed.

| ΔT | 3s | | | | 5s | | | | 10s | | | |
|---|---|---|---|---|---|---|---|---|---|---|---|---|
| Peak Gust Velocity | Frequency (Hz) | | Active Power (MW) | | Frequency (Hz) | | Active Power (MW) | | Frequency (Hz) | | Active Power (MW) | |
| | Min | Max | Min | Max | Min | Max | Min | Max | Min | Max | Min | Max |
| <23m/s | 18.555 | 18.632 | 3.957 | 4.000 | 18.598 | 18.602 | 3.980 | 3.988 | 18.599 | 18.601 | 3.982 | 3.987 |
| 24 m/s | 18.493 | 18.654 | 3.934 | 4.009 | 18.598 | 18.602 | 3.980 | 3.988 | 18.599 | 18.601 | 3.982 | 3.987 |
| 25 m/s | 18.411 | 18.678 | 3.898 | 4.019 | 18.597 | 18.602 | 3.980 | 3.989 | 18.599 | 18.601 | 3.982 | 3.987 |
| 26 m/s | 18.288 | 18.705 | 3.845 | 4.029 | 18.598 | 18.602 | 3.980 | 3.989 | 18.599 | 18.601 | 3.982 | 3.987 |
| 27 m/s | 18.136 | 18.735 | 3.777 | 4.039 | 18.598 | 18.602 | 3.980 | 3.989 | 18.599 | 18.601 | 3.982 | 3.987 |
| 28 m/s | 17.973 | 18.768 | 3.707 | 4.050 | 18.598 | 18.603 | 3.980 | 3.989 | 18.599 | 18.601 | 3.982 | 3.987 |
| 29 m/s | 17.808 | 18.801 | 3.635 | 4.061 | 18.598 | 18.603 | 3.980 | 3.989 | 18.599 | 18.601 | 3.982 | 3.987 |
| 30 m/s | 17.593 | 18.879 | 3.543 | 4.100 | 18.596 | 18.603 | 3.979 | 3.989 | 18.599 | 18.601 | 3.982 | 3.987 |

### *3.3. Extreme Operating Gust Responses*

This section outlines the Extreme Operating Gust responses for $\Delta T$ values of 3 s, 5 s and 10 s. The same initial conditions of synchronisation and steady state are utilised with the gust being applied to turbine 1 at time t = 0. The $V_{Gust}$ max values are incremented by 1 m/s from 15 m/s to 30 m/s. Example 3 s EOG input gusts can be seen in Figure 12.

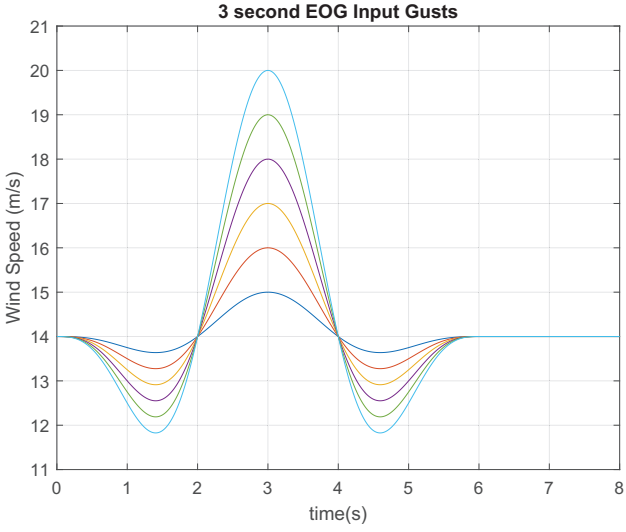


**Figure 12.** 3 s EOG test gusts applied.

The corresponding gust factors for the 3 s, 5 s and 10 s rise time EOGs are calculated by integrating (1) with limits of $\pm 0.5$ s of the peak gust time giving the sliding window of $\tau = 1$ s and are displayed in Table 4. The 10 min moving average wind speed $U_T = 14$ m/s.

**Table 4.** EOG Input Gust Factors.

| $V_{gust}$ max | Gust Factor 3 s | Gust Factor 5 s | Gust Factor 10 s |
|---|---|---|---|
| 15 m/s | 1.035 | 1.037 | 1.039 |
| 16 m/s | 1.126 | 1.137 | 1.141 |
| 17 m/s | 1.189 | 1.205 | 1.212 |
| 18 m/s | 1.252 | 1.273 | 1.283 |
| 19 m/s | 1.315 | 1.341 | 1.353 |
| 20 m/s | 1.378 | 1.410 | 1.424 |
| 21 m/s | 1.441 | 1.478 | 1.494 |
| 22 m/s | 1.504 | 1.546 | 1.565 |

Considering Figure 13, it can clearly be seen that the wind farm struggles to maintain electrical frequency through EOGs, when compared with ECGs of the same magnitude displayed in the previous section. This is to be expected as now the leading turbine first experiences a dip in wind speed prior to the sharp rise to $V_{gust}$ max. It can be observed that EOGs with magnitudes greater than 18 m/s lead to a violation of the 5% pk-pk limitation on bus frequency. The initial negative dip in wind speed preceding the rise causes a greater $dV_{Gust}/dt$ which saturates the 8 degree per second rate of change limitation on the pitch controller.

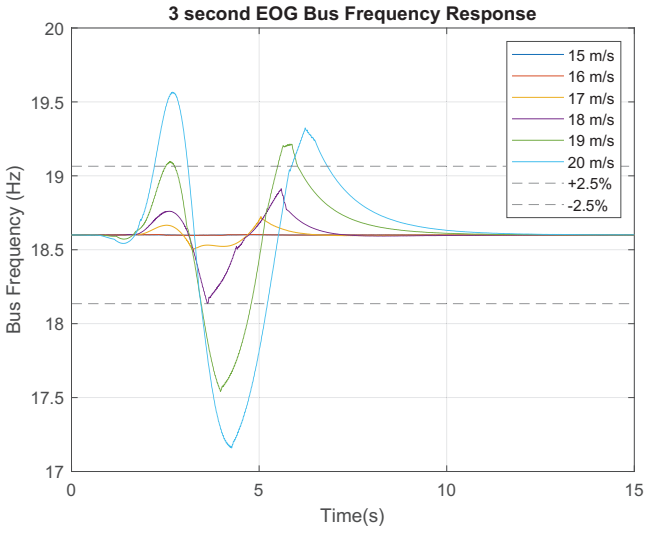


**Figure 13.** System frequency response to 3 s EOG gusts.

Figure 14 displays the active power variation on the main bus through the event. It can be seen that the 18 m/s gust displayed in purple, while within tolerance levels for frequency variation, fails to remain within 5% limitation on active power. However, as the active power only exceeds this limitation by 100 kW, it is possible that it could be considered tolerable in some electrical power conversion systems, particularly those which incorporate storage. This simulation assumes that all wind turbines remain connected to the bus throughout the transience however in the higher cases of $V_{gust}$ max, it is likely that the turbine would be forced to disconnect from the main bus. This case however is outside the scope of this study and may be explored in future work.

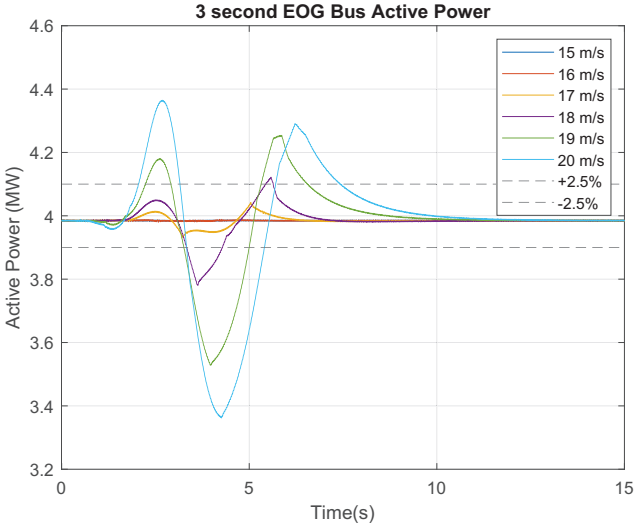


**Figure 14.** Bus active power response to 3 s EOG gusts.

The system frequency responses as shown in Figure 15 display a similar trend to that of the three second EOG tests. We can see however that the 19 m/s is within tolerable limits with the 20 m/s forming the boundary condition with regard to system frequency.

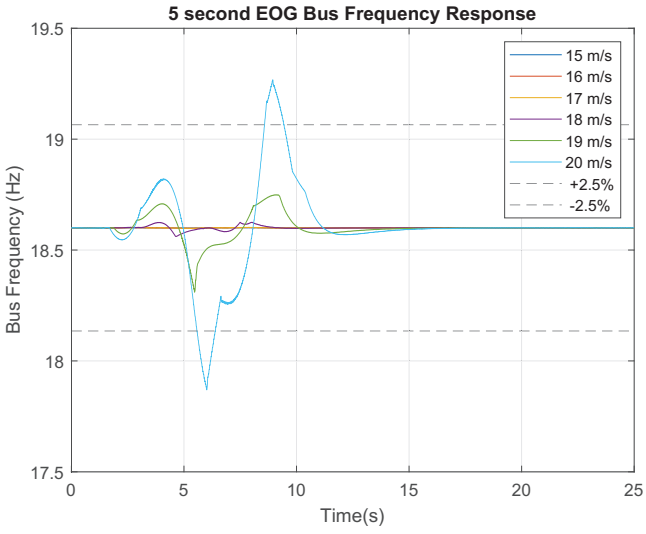


**Figure 15.** EOG Bus Frequency Responses $\Delta T = 5$ s.

Figure 16 displays the bus active power variation for the 5 s EOG tests. It can be observed that the 19 m/s EOG trace shown in green falls outside the negative 2.5% variation limit for a short period of time. For the purposes of this study, this will be declared outside the tolerance range.

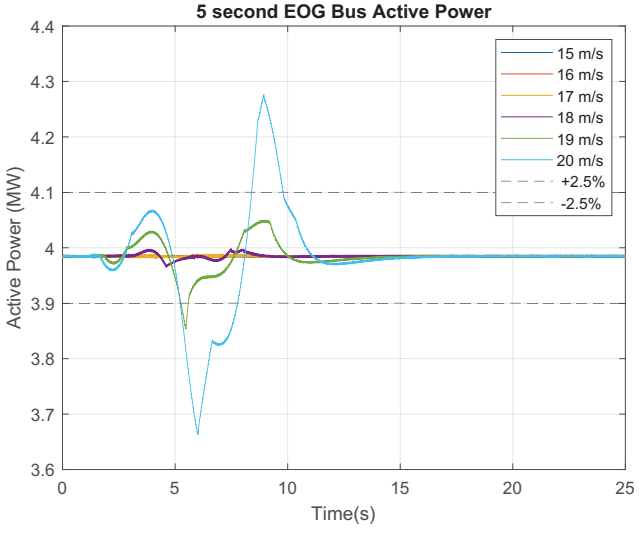


**Figure 16.** EOG Bus Active Power Responses $\Delta T = 5$ s.

All test runs are displayed in Table 5. The light blue denotes the output remains within the respective boundary condition with dark blue showing that one or both of the $\pm 2.5\%$ boundaries have been exceeded.

**Table 5.** This table displays the results of all EOG simulations completed. Light Blue demonstrates the respective responses remain within the ±2.5% boundary limitations with dark blue showing the criteria has not been met.

| ΔT | 3s | | | | 5s | | | | 10s | | | |
|---|---|---|---|---|---|---|---|---|---|---|---|---|
| Peak Gust Velocity | Frequency (Hz) | | Active Power (MW) | | Frequency (Hz) | | Active Power (MW) | | Frequency (Hz) | | Active Power (MW) | |
| | Min | Max | Min | Max | Min | Max | Min | Max | Min | Max | Min | Max |
| 15m/s | 18.597 | 18.602 | 3.981 | 3.987 | 18.598 | 18.602 | 3.821 | 3.987 | 18.599 | 18.601 | 3.982 | 3.987 |
| 16 m/s | 18.596 | 18.603 | 3.979 | 3.982 | 18.598 | 18.602 | 3.982 | 3.988 | 18.599 | 18.601 | 3.982 | 3.987 |
| 17 m/s | 18.485 | 18.725 | 3.930 | 4.042 | 18.597 | 18.603 | 3.980 | 3.989 | 18.599 | 18.601 | 3.982 | 3.987 |
| 18 m/s | 18.137 | 18.913 | 3.780 | 4.122 | 18.561 | 18.625 | 3.965 | 3.998 | 18.598 | 18.602 | 3.982 | 3.988 |
| 19 m/s | 17.542 | 19.215 | 3.528 | 4.254 | 18.310 | 18.749 | 3.854 | 4.050 | 18.575 | 18.649 | 3.972 | 4.009 |
| 20 m/s | 17.159 | 19.566 | 3.362 | 4.365 | 17.870 | 19.268 | 3.663 | 4.276 | 18.506 | 18.716 | 3.939 | 4.037 |
| 21 m/s | 17.135 | 20.086 | 3.347 | 4.569 | 17.300 | 19.672 | 3.420 | 4.443 | 18.355 | 18.791 | 3.869 | 4.066 |
| >22m/s | 16.493 | 20.640 | 3.117 | 4.784 | 16.879 | 19.683 | 3.241 | 4.447 | 18.086 | 18.916 | 3.749 | 4.113 |

Analysing Table 5, it can be observed that the EOG gusts present a much greater challenge to the DIT bus parameters than ECGs. The 10 s rise time EOGs are the most effectively controlled which is to be expected as they have the lowest rate of change of $V_{gust}$ max. The gust factors for these gusts are higher than the gust factors for shorter rise time gusts of the same magnitude. This is due to the wind speed cresting the maximum point for a greater time on either side of the maximum, therefore increasing the 1 s sliding average value. For a rise time of 10 s, the maximum gust factor which was successfully controlled by blade pitch angle control is 1.424. This gust factor is significantly below the 10 s for ECGs of 2.14 and above. Comparing this to the findings of Bardal et al., it can be observed that gust factors of 1.4 and above at the 100 m hub height are very rare [37]. As the average hub heights of modern offshore turbines are greater than 100 m, the 100 m data is the most relevant to this study.

If we consider the 3 and 5 s EOG data the corresponding boundary gust factors of 1.189 and 1.273 are within the range of values experienced offshore [37], however, the majority of gusts in the study fall below these values. This study also includes gust factors of gusts which may have occurred during times when the average wind speed may have been above the typical cut out speed of the turbine of 25 m/s and therefore the farm would not have been operating [39]. Gusts of this nature that do occur during the operation of a DIT wind farm would require further mitigation techniques outside of pitch angle control to maintain the 2.5% variation parameter studied.

## 4. Discussions & Conclusions

Extreme Operating and Coherent wind gust responses for directly interconnected systems have been investigated and discussed. It has been shown that through the use of pitch control on individual turbines the majority of wind gusts can be tolerated and the boundaries of this tolerance have been identified. The respective gust factors for these gust events have been calculated and compared to real coastal wind data [37]. These boundaries as presented in Tables 3 and 5 form the basis for further study on DITs interconnection to the grid. Power converter design and location can be investigated to further improve the gust tolerance of DIT systems. Additional analysis of large wind data sets will provide estimates of the frequency of gusts with gust factors greater than the tolerance levels described, facilitating comparison of DIT and traditionally interconnected wind systems in terms of capacity factor, capital expenditure (CapEx) and operational expenditure (OpEx).

Extreme operating gusts pose a greater challenge when compared to the extreme coherent gust conditions due to the higher rate of change in wind speed occurring throughout the gust. This study has not used B2BC which ordinarily provide a means on an individual turbine by turbine basis, of dealing with variations on the wind side while maintaining power on the grid side within specified limits of frequency and voltage. In the proposed DIT topology it is still intended to use B2BCs for a number of turbines as shown in Figure 2. Employing the farm level B2BC control and the pitch control as analysed in this paper

will facilitate a greater tolerance range of gusts for DIT systems and will be the subject of future work. It is possible that with wind prediction methods such as LiDAR and more sophisticated machine learning-based control systems, that the boundaries could be further improved thereby reducing the load on the pitch control system and the power conversion systems down steam of the interconnected bus.

In conclusion, the Direct Interconnection Technique has been shown to be capable of tolerating wind gust conditions. The boundary of tolerance has been established and methods for further improvement have been proposed.

**Author Contributions:** C.W.O. carried out the reported research work, writing the paper and revisions. M.E.S. and D.J.T. supervised the research work, revisions and editing. The content of this paper is discussed by the authors and they all contributed to the final article. All authors have read and agreed to the published version of the manuscript.

**Funding:** This publication has emanated from research supported by the Science Foundation Ireland under the MaREI Centre research programme (Grant No. 12/RC/2302, and 14/SP/2740) and LERO Science Foundation Ireland grant 13/RC/2094. It is also co-funded under the European Regional Development Fund through the Southern and Eastern Regional Operational Programme to MaREI (www.marei.ie (accessed on 20 December 2021)) and Lero (www.lero.ie (accessed on 20 December 2021)) centres.

**Institutional Review Board Statement:** Not applicable.

**Informed Consent Statement:** Not applicable.

**Data Availability Statement:** Data Available on request.

**Conflicts of Interest:** The authors declare that the publication of this article has no conflict of interest.

## References

1. Gallagher, S.; Tiron, R.; Whelan, E.; Gleeson, E.; Dias, F.; McGrath, R. The nearshore wind and wave energy potential of Ireland: A high resolution assessment of availability and accessibility. *Renew. Energy* **2016**, *88*, 494–516. [CrossRef]
2. Jung, C.; Schindler, D.; Buchholz, A.; Laible, J. Global Gust Climate Evaluation and Its Influence on Wind Turbines. *Energies* **2017**, *10*, 1474. [CrossRef]
3. Department of the Environment, Climate and Communications. *Ireland's National Energy and Climate Plan 2021–2030*; Government of Ireland: Dublin, Ireland, 2021. Avaliable online: https://www.gov.ie/en/publication/0015c-irelands-national-energy-climate-plan-2021-2030/ (accessed on 20 December 2021).
4. SEAI. Wind Energy Roadmap 2011–2050. 2011. Available online: https://www.seai.ie/publications/Wind_Energy_Roadmap_2011-2050.pdf (accessed on 20 December 2021).
5. Harper, M.; Anderson, B.; James, P.A.B.; Bahaj, A.S. Onshore wind and the likelihood of planning acceptance: Learning from a Great Britain context. *Energy Policy* **2019**, *128*, 954–966. [CrossRef]
6. Brand, A.J.; Peinke, J.; Mann, J. Turbulence and wind turbines. *J. Phys. Conf. Ser.* **2011**, *318*, 072005. [CrossRef]
7. Moriarty, P.J.; Holley, W.E.; Butterfield, S. Effect of Turbulence Variation on Extreme Loads Prediction for Wind Turbines. *J. Sol. Energy Eng.* **2002**, *124*, 387–395. [CrossRef]
8. Ebrahimi, A.; Sekandari, M. Transient response of the flexible blade of horizontal-axis wind turbines in wind gusts and rapid yaw changes. *Energy* **2018**, *145*, 261–275. [CrossRef]
9. Onol, A.O.; Yesilyurt, S. Effects of wind gusts on a vertical axis wind turbine with high solidity. *J. Wind. Eng. Ind. Aerodyn.* **2017**, *162*, 1–11. [CrossRef]
10. Cheng, P.W.; Bierbooms, W.A.A.M. Distribution of extreme gust loads of wind turbines. *J. Wind. Eng. Ind. Aerodyn.* **2001**, *89*, 309–324. [CrossRef]
11. Zhou, K.; Cherukuru, N.; Sun, X.; Calhoun, R. Wind Gust Detection and Impact Prediction for Wind Turbines. *Remote Sens.* **2018**, *10*, 514. [CrossRef]
12. Dhiman, H.S.; Deb, D.; Muresan, V.; Balas, V.E. Wake Management in Wind Farms: An Adaptive Control Approach. *Energies* **2019**, *12*, 1247. [CrossRef]
13. Pican, E.; Omerdic, E.; Toal, D.; Leahy, M. Direct interconnection of offshore electricity generators. *Fuel Energy Abstr.* **2011**, *36*, 1543–1553. [CrossRef]
14. Meng, Y.; Yan, S.; Wu, K.; Ning, L.; Li, X.; Wang, X.; Wang, X. Comparative economic analysis of low frequency AC transmission system for the integration of large offshore wind farms. *Renew. Energy* **2021**, *179*, 1955–1968. [CrossRef]
15. Rahman, S.; Khan, I.; Alkhammash, H.I.; Nadeem, M.F. A Comparison Review on Transmission Mode for Onshore Integration of Offshore Wind Farms: HVDC or HVAC. *Electronics* **2021**, *10*, 1489. [CrossRef]

16. Spinato, F.; Tavner, P.J.; Bussel, G.J.W.v.; Koutoulakos, E. Reliability of wind turbine subassemblies. *IET Renew. Power Gener.* **2009**, *3*, 387–401. [CrossRef]
17. Zhao, Y.; Li, D.; Dong, A.; Kang, D.; Lv, Q.; Shang, L. Fault Prediction and Diagnosis of Wind Turbine Generators Using SCADA Data. *Energies* **2017**, *10*, 1210. [CrossRef]
18. Ren, Z.; Verma, A.S.; Li, Y.; Teuwen, J.J.E.; Jiang, Z. Offshore wind turbine operations and maintenance: A state-of-the-art review. *Renew. Sustain. Energy Rev.* **2021**, *144*, 110886. [CrossRef]
19. Hossain, M.L.; Abu-Siada, A.; Muyeen, S.M. Methods for Advanced Wind Turbine Condition Monitoring and Early Diagnosis: A Literature Review. *Energies* **2018**, *11*, 1309. [CrossRef]
20. Lu, B.; Sharma, S.K. A Literature Review of IGBT Fault Diagnostic and Protection Methods for Power Inverters. *IEEE Trans. Ind. Appl.* **2009**, *45*, 1770–1777. [CrossRef]
21. Qiao, W.; Lu, D. A Survey on Wind Turbine Condition Monitoring and Fault Diagnosis—Part I: Components and Subsystems. *IEEE Trans. Ind. Electron.* **2015**, *62*, 6536–6545. [CrossRef]
22. Johnston, B.; Foley, A.; Doran, J.; Littler, T. Levelised cost of energy, A challenge for offshore wind. *Renew. Energy* **2020**, *160*, 876–885. [CrossRef]
23. Su, C.; Yang, Y.; Wang, X.; Hu, Z. Failures analysis of wind turbines: Case study of a Chinese wind farm. In Proceedings of the 2016 Prognostics and System Health Management Conference (PHM-Chengdu), Chengdu, China, 19–21 October 2016; pp. 1–6. [CrossRef]
24. Ebrahimi Salari, M.; Coleman, J.; Toal, D. Power Control of Direct Interconnection Technique for Airborne Wind Energy Systems. *Energies* **2018**, *11*, 3134. [CrossRef]
25. Li, S.; Haskew, T.A.; Swatloski, R.P.; Gathings, W. Optimal and Direct-Current Vector Control of Direct-Driven PMSG Wind Turbines. *IEEE Trans. Power Electron.* **2012**, *27*, 2325–2337. [CrossRef]
26. IEC. *EN IEC 61400-3-1:2019 Part 3-1: Design Requirements for Fixed Offshore Wind Turbines*; International Electrotechnical Commission: Geneva, Switzerland, 2019.
27. IEC. *EN IEC 61400-1:2019 Wind Energy Generation Systems—Part 1: Design Requirements*; International Electrotechnical Commission: Geneva, Switzerland, 2019.
28. Yang, J.; Fang, L.; Song, D.; Su, M.; Yang, X.; Huang, L.; Joo, Y.H. Review of control strategy of large horizontal-axis wind turbines yaw system. *Wind Energy* **2021**, *24*, 97–115. [CrossRef]
29. Pican, E.; Omerdic, E.; Toal, D.; Leahy, M. Analysis of parallel connected synchronous generators in a novel offshore wind farm model. *Energy* **2011**, *36*, 6387–6397. [CrossRef]
30. Eirgrid. *General Conditions of Connection and Transmission Use of System*; Eirgrid Group: Dublin, Ireland, 2013.
31. Grenier, D.; Dessaint, L.A.; Akhrif, O.; Bonnassieux, Y.; Le Pioufle, B. Experimental nonlinear torque control of a permanent-magnet synchronous motor using saliency. *IEEE Trans. Ind. Electron.* **1997**, *44*, 680–687. [CrossRef]
32. Jonkman, J.; Butterfield, S.; Musial, W.; Scott, G. *Definition of a 5-MW Reference Wind Turbine for Offshore System Development*; Technical Report NREL/TP-500-38060, 947422; National Renewable Energy Laboratory: Golden, CO, USA, 2009; [CrossRef]
33. Leroy, F. *JSPM Filial of AREVA NP*; Areva, S.A.: Courbevoie, France, 2011.
34. Bahirat, H.J.; Mork, B.A.; Høidalen, H.K. Comparison of wind farm topologies for offshore applications. In Proceedings of the 2012 IEEE Power and Energy Society General Meeting, San Diego, CA, USA, 22–26 July 2012; pp. 1–8. [CrossRef]
35. Sedighi, M.; Moradzadeh, M.; Kukrer, O.; Fahrioglu, M. Simultaneous optimization of electrical interconnection configuration and cable sizing in offshore wind farms. *J. Mod. Power Syst. Clean Energy* **2018**, *6*, 749–762. [CrossRef]
36. Wu, Y.; Zhang, S.; Wang, R.; Wang, Y.; Feng, X. A design methodology for wind farm layout considering cable routing and economic benefit based on genetic algorithm and GeoSteiner. *Renew. Energy* **2020**, *146*, 687–698. [CrossRef]
37. Bardal, L.M.; Sætran, L.R. Wind Gust Factors in a Coastal Wind Climate. *Energy Procedia* **2016**, *94*, 417–424. [CrossRef]
38. Singh, B.; Singh, S.N. Wind Power Interconnection into the Power System: A Review of Grid Code Requirements. *Electr. J.* **2009**, *22*, 54–63. [CrossRef]
39. Dupont, E.; Koppelaar, R.; Jeanmart, H. Global available wind energy with physical and energy return on investment constraints. *Appl. Energy* **2017**, *209*, 322–338. [CrossRef]

Journal of
*Marine Science and Engineering*

MDPI

*Article*

# Environmental Compatibility of the Parc Tramuntana Offshore Wind Project in Relation to Marine Ecosystems

**Koldo Diez-Caballero [1], Silvia Troiteiro [2,*], Javier García-Alba [3,†], Juan Ramón Vidal [1], Marta González [2], Sergi Ametller [2] and Raquel Juan [2]**

[1] Tecnoambiente S.L., 08290 Cerdanyola del Vallès, Spain; koldo.diezcaballero@tecnoambiente.com (K.D.-C.); joanramon.vidal@tecnoambiente.com (J.R.V.)
[2] SENER Ingeniería y Sistemas S.A., 08290 Cerdanyola del Vallès, Spain; marta.gonzalez@sener.es (M.G.); sergi.ametller@sener.es (S.A.); raquel.juan@sener.es (R.J.)
[3] IHCantabria—Instituto de Hidráulica Ambiental de la Universidad de Cantabria, 39011 Santander, Spain; javier.garciaalba@unican.es
* Correspondence: silvia.troiteiro@sener.es
† Contribution of the hydrodynamical studies on the Golf de Roses.

**Abstract:** Parc Tramuntana is the first offshore wind project being promoted in the Catalonian waters, and due to this newness, it has generated a strong social debate surrounding expected environmental and socioeconomic impacts traditionally associated to marine wind farms, as there are no relevant references in this area. The objective of this report is to provide a specific analysis of some of the main potential impacts, based on detailed information and quantitative data, in order to place these impacts in a realistic context and determine their actual magnitude. This analysis is fed by diverse and detailed studies carried out over the last two years to assess the environmental impact of the project, in accordance with current regulations. According to environmental impact assessment, which is based on a standardized methodology, the impact of the project is objectively qualified as MODERATE on vectors such as turbidity and sedimentation, underwater noise, hydrodynamic circulation or the alteration of electromagnetic fields, and NOT SIGNIFICANT on aspects such as the proliferation of invasive exotic species. As this is an ongoing assessment process, this report presents initial conclusions that do not yet address all possible impacts. Nevertheless, the authors stress the importance of framing the debate on offshore wind in Catalonia in the context of the urgency of the climate emergency and its inevitable impacts on the natural environment.

**Keywords:** offshore wind impacts; turbidity; sediment dispersion; electromagnetic fields; acoustic impact; marine hydrodynamics; invasive species

**Citation:** Diez-Caballero, K.; Troiteiro, S.; García-Alba, J.; Vidal, J.R.; González, M.; Ametller, S.; Juan, R. Environmental Compatibility of the Parc Tramuntana Offshore Wind Project in Relation to Marine Ecosystems. *J. Mar. Sci. Eng.* **2022**, *10*, 898. https://doi.org/10.3390/jmse10070898

Academic Editors: Barbara Zanuttigh and Eugen Rusu

Received: 18 May 2022
Accepted: 21 June 2022
Published: 29 June 2022
Corrected: 26 December 2022

**Publisher's Note:** MDPI stays neutral with regard to jurisdictional claims in published maps and institutional affiliations.

**Copyright:** © 2022 by the authors. Licensee MDPI, Basel, Switzerland. This article is an open access article distributed under the terms and conditions of the Creative Commons Attribution (CC BY) license (https://creativecommons.org/licenses/by/4.0/).

## 1. Introduction

Currently Catalonia, as well as the surrounding regions and countries, faces a situation of climate emergency, a situation that has been recognized both by the Generalitat de Catalunya [1], the Spanish Government [2], and the European Parliament [3].

It is hence a situation that involves the adoption of urgent measures to reduce the carbon emissions for which our energy and production model is responsible. It is therefore not only advisable, but essential, among other actions, to propose important changes in Catalonia's energy generation model, which involve the progressive replacement of non-renewable sources, which currently provide more than the 80% of the electricity generated, with renewable sources, including offshore wind. This strategy has been developed in Catalonia through the *Pacte Nacional per a la Transició Energètica de Catalunya* (National Agreement for the Energy Transition of Catalonia) and has been embodied in the Preliminary Draft of the Energy Transition Law, which contemplates large, medium, and small-scale renewable electricity generation, mainly by local sources (Strategy n° 12) [4].

According to the energy prospective studies for Catalonia with a 2050 horizon (PROENCAT 2050) [5], in order to meet the energy and environmental objectives Catalonia has been committed to comply, by 2030 it will be necessary to incorporate up to 12,000 MW of renewable production into the system (of which 1000 MW should correspond to offshore wind), a figure that should grow to more than 61,000 MW by 2050 (with a total contribution of 3500 MW from offshore wind). This new renewable capacity should make it possible to supply a demand characterized by a greater electrification of the economy, facing the expected closure of nuclear power plants and drastically reducing the current dependence on non-renewable sources, of foreign origin and with a high impact on greenhouse gas emissions.

Once the need to develop offshore wind energy in Catalonia has been assumed, its spatial development should be approached on the basis of criteria that incorporate and allow the complexity of the marine environment to be assessed, weighing the advantages and disadvantages of each area and the benefits and impacts of offshore wind farms on the whole of the territory and Catalan society.

Marine spatial planning plays an important role in this task. In recent years, the Spanish Ministry for Ecological Transition and the Demographic Challenge (*MITERD*) has been working, in coordination with many other Spanish state administrations and each of the autonomous communities of the Atlantic and Mediterranean arc, to develop Marine Spatial Management Plans (POEM) [6], which are currently under review following the presentation of their draft for public information and consultation, in order to incorporate the relevant modifications resulting from the allegations received, as a step prior to their approval by Royal Decree.

It should be noted that these plans are not arbitrary or based solely on economic or territorial interests, but that their approach responds to the assessment of a set of criteria that ensure that the combined pressure of activities in the marine environment is maintained at levels compatible with the achievement of good environmental status (GES), and that they do not compromise the capacity of marine ecosystems to respond to changes induced by human activity. An ecosystem approach has therefore been followed for its definition, considering both the interactions between land and sea, as well as the expected changes resulting from climate change.

Besides that, the challenges that the development of offshore wind in Catalonia and Spain face are not few, largely due to the newness of this type of project in Spain. One of these challenges is the adaptation of new projects to a constantly evolving regulatory framework to incorporate this new technology into the Spanish energy model, but also with a certain social rejection, characteristic of any change in strategy and implementation of new technologies for the first time in the country. The influence of this regulatory framework, especially regarding the environmental impact assessment process of this kind of project was already analyzed by Salvador et al. (2018) [7].

From the point of view of the possible social reticence to the development of offshore wind power in Catalonia by some economic stakeholders and some members of the scientific community, the social debate on this new technology is often justified on the basis of the lack of specific references of similar projects in operation in the Mediterranean that allow to accurately foresee the possible impacts that this type of projects can generate in the area of implementation, generating uncertainty.

While onshore and fixed founded offshore wind farms are quite widely installed around the world and provide relevant references on their impacts on the environment along their entire life-cycle (see e.g., Verma et al., 2022 [8] or Kouloumpis and Azapagic, 2022 [9]), and the adverse environmental impacts of different wind generation technologies have been already assessed (mainly in onshore context) [10], there are still many effects that cannot be directly extrapolated to floating offshore wind farms, producing a significant knowledge gap regarding the impacts of this technology in the environment.

This lack of applicable references means that some voices tend to assimilate as their own, without a rigorous analysis, other offshore wind experiences in the North Sea or

the Baltic, where both the technological characteristics of wind farms (mostly with fixed foundations) and the environment (depth, dynamics, ecosystems, etc.) are very different from those of the projects proposed in Catalonia.

It should be noted in this regard that, although there are currently no floating offshore wind projects in operation, the French Government has already taken the first step to be the pioneers in the Mediterranean, approving the installation of a pilot floating offshore wind farm, called "*Eoliennes Flottantes du Golfe du Lion*" (EFGL), and two other pilot farms ("*Eolmed*" and "*Provence Grand Large*") are in progress.

The EFGL wind farm consists of three 10 MW turbines, to be installed 16 km off the coast of Leucate, and within the perimeter of a protected area of the Natura 2000 Network, the marine natural park of the Gulf of Lion, the due Environmental Impact Study having been carried out and its impact considered compatible with the conservation objectives of this protected area. The other two wind farms are also planned with three turbines each, with power ratings between 8 and 10 MW, and at a distance from the coast of between 14 and 18 km.

In addition, on 14 March 2022, the French government confirmed its intention to build an additional 500 MW of floating offshore wind power in the Mediterranean by 2030.

## 2. Motivation

In this context, given the urgency of developing new renewable generation projects, due to the limited time available to meet emission reduction targets, and the periods required for the processing and technical development of projects, several developers specialized in offshore wind have begun to work, both in Catalonia and in other regions of Spain, to respond in the imminent future to the demand for these types of facilities.

One of these developments, pioneered in Catalonia in terms of technical maturity and coordination with the territory, Parc Tramuntana, proposes the installation of a floating offshore wind farm off the coast of the Empordà.

This project is being developed with the premise of integrating the participation of the territory from the earliest stages of conception, applying all the way and in all aspects of the design the best existing practices at the state-of-the-art level to ensure compliance with the so-called Precautionary Principle, which supports the adoption of protective measures against the possibility of a technological risk to the environment, without yet having a definitive scientific proof of such risk.

Likewise, the project, which has not yet been submitted for environmental processing, will follow all the way the environmental and administrative procedures required under current legislation, which includes the preparation and processing of the due Environmental Impact Study, including the process of public information and consultation with all the competent administrations.

The process leading to the selection of the most suitable site and the design proposal of the offshore wind facility has been and will continue to be a living and evolving process. It has started from an initial approach, based on the energy demand, the availability of connection to the electricity grid, the conditioning factors imposed by the legislation in force (environmental, sectorial, town planning, etc.), maritime and airspace planning and the characteristics of the site, and has evolved (in size and technical solutions) through the incorporation of additional requirements and conditioning factors derived from the conversations held with different stakeholders of the territory and society.

This report analyzes some of the aspects and potential impacts of the project that have generated some debate in the scientific community. This is the case of the recent publication of the article by Lloret et al. (2022) in the journal Science of the Total Environment [11], intending to serve as a reference for the evaluation of environmental impacts related to floating wind technology in the western Mediterranean. This purpose is also oriented towards introducing accuracy in the data analysis and promoting the debate with some sectors who systematically express opposition to this type of renewable generation project without a detailed analysis of its impacts on the environment.

## 3. General Description of the Parc Tramuntana Project

The Tramuntana Floating Offshore Wind Farm Project consists of the installation of an offshore renewable energy generation farm on the continental shelf of the province of Girona, at a distance of approximately 24 km from the coast of the Bay of Roses, in a range of depths between 120 and 180 m and on thick silty and detritic seabed, with a total absence of rocky outcrops. The turbine closest to the coast is located 14 km from Cap de Creus.

The wind farm is located within the area designated in the draft of the *POEM* for the Levantine-Balearic demarcation as a priority area for offshore wind (LEBA-2, Figure 1), being the only area identified in Catalonia as suitable for this type of activity. This site also partially coincides with a permanent closed area for trawling and is located outside protected natural areas.

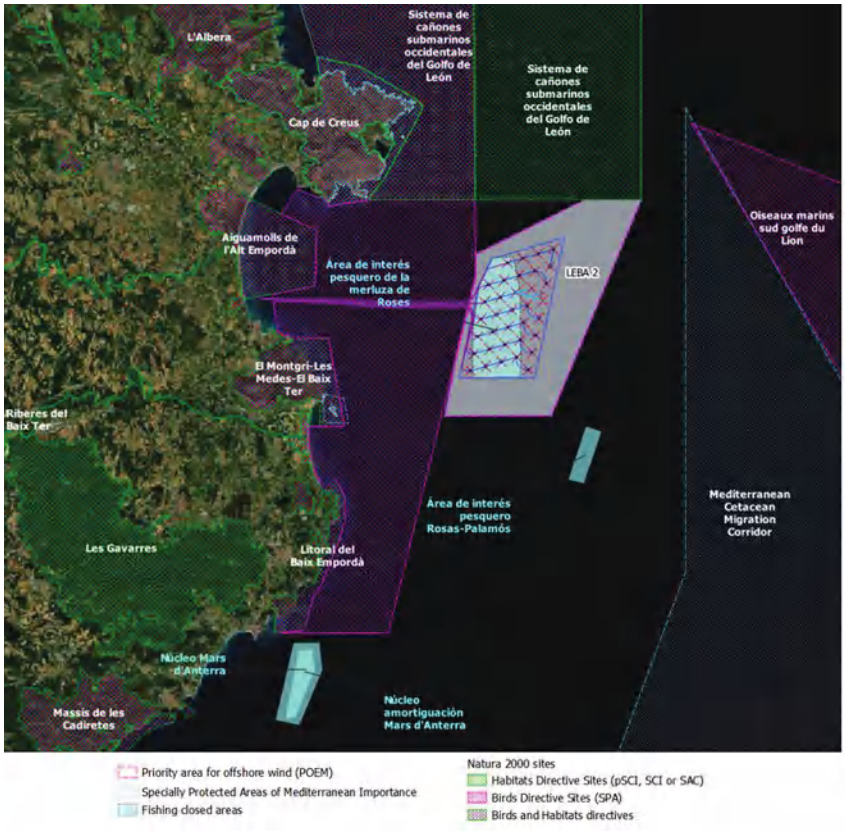


**Figure 1.** Location of the Tramuntana Floating Offshore Wind Farm Project in relation to environmental protected sites and other uses of maritime space.

The proposed solution consists of the following elements (Figure 2):

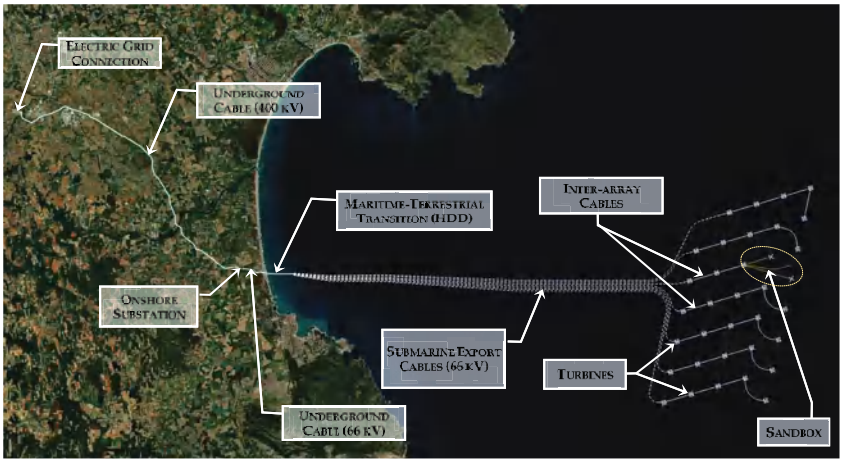


**Figure 2.** General layout of the Tramuntana Floating Offshore Wind Farm Project.

- Wind farm: it will have a total of 36 renewable energy generation positions, arranged in 7 rows perpendicular to the coast, in ENE direction (~N73° E). Initially, it will consist of 33 turbines of 15 MW and an R + D + i platform equipped with 3 positions for testing experimental devices (sandbox), with a total combined power of 500 MW. When fully developed, this sandbox will be replaced by 2 additional turbines of 15 MW each, with a maximum power of 525 MW;
- Submarine electrical cabling system for the interconnection of devices (inter-array cables) and subsequent export of the energy generated to shore (export cables). The export cables, which will be buried, run 24 km to the coast, in the municipality of Sant Pere Pescador;
- Maritime-terrestrial transition to the cable landing area on the coast, by means of HDD technique, and connection between the submarine cables and the terrestrial cables by transition boxes at the landing point;
- Terrestrial underground cabling (66 kV) for the connection between the transition boxes and the electrical substation, located approximately 1 km from the coast;
- Transformer substation, to raise the export voltage to 400 kV and provide the export electric circuit with the appropriate characteristics for connection to the onshore power grid.
- Terrestrial underground high-voltage conduction system (400 kV), to discharge the energy generated to the Spanish grid through the Santa Llogaia substation, near Figueres.

The estimated net energy production is approximately 1800 GWh/year, equivalent to 45% of the current consumption of the province of Girona, both household and industrial. The project includes a research platform, which will be developed in collaboration with the *Institut de Recerca d'Energia de Catalunya* (IREC) and will serve as a sandbox for different lines of R + D + i in the field of offshore renewable energy harnessing, as well as in other compatible uses of marine space such as aquaculture, fishing recovery, etc.

The wind farm takes up an area of approximately 95 $km^2$ where floating turbines and their anchoring systems are located. This area represents less than 0.12% of the surface of the Exclusive Economic Zone (EEZ) corresponding to Catalonia.

The 15 MW turbines have a total height of 261 m and a rotor diameter of 236 m, and are installed with a separation between turbines of between 1.2 and 2.5 km. They are attached to the seabed by 3 or 4 catenaries, each about 650 m long, attached to an anchor that remains buried about 14 m below the seabed.

The turbines are connected to each other by dynamic inter-array cables, which partially rest on the seabed, and from the end of each row of turbines comes an export cable, buried

between 1.5 and 2 m below the seabed, which carries the generated energy to land. In the land–sea transition zone, a solution using small diameter perforations (Horizontal Directional Drilling or HDD) has been adopted to facilitate the landing of the cable without altering the seabed or the biological communities settled on it.

From the grounding point to the connection with the electrical grid, all the high voltage conduits are projected buried, to minimize the environmental and landscape impact.

Keeping this development proposal as an objective, since it is considered necessary to provide the Catalan system with this minimum capacity of marine renewable generation, the possibility of a phased development of the project is also proposed, so that a single array can be initially executed together with the sandbox facility. This would allow to advance in the installation of the general energy export infrastructures, and to have for a certain period of time a testing and demonstration facility to validate these types of wind farms in the Mediterranean and to verify their environmental and socioeconomic compatibility.

## 4. Methods of Analysis

In the analysis of impacts carried out in the Environmental Impact Study of the project, still under development, an identification and quantification methodology was used, which is based on the methodology proposed by *Conesa* (1995) [12], in accordance with the requirements included in Annex VI of Law 21/2013, modified by Law 9/2018, regarding the identification, quantification, and assessment of the foreseeable significant effects of the projected activities on the environment.

It is important to differentiate, regarding impacts, those occurring during the construction phase, which has a more limited duration in time, from those occurring during the operational phase, which may be prolonged throughout the service life of the facility. In addition, due to the nature of this project, which extends over both the marine and terrestrial areas, it is necessary to differentiate between the two areas when assessing the environmental factors affected.

In this report, a preview of the assessment of some of the main impacts on the marine environment, related to the conservation of biodiversity and the good environmental status of the area, is made in order to dispel doubts regarding some of the potential impacts that represent a major concern for the authors of the article of Lloret et al. (2022) [11]. It is important to mention that, for each of the potential impacts preliminarily identified by means of a Leopold matrix, each of the following attributes were characterized (Table 1).

**Table 1.** Impact classification table.

| Attribute | | Degree | Description | Value |
|---|---|---|---|---|
| Nature (Sign) | Beneficial (+) or detrimental (-) nature of the impact. | Beneficial impact | Improvement in the current situation | + |
| | | Detrimental impact | Loss in current situation | - |
| Extension (EX) | Theoretical area of influence of the impact in relation to the project's surroundings (% of area with respect to the surroundings in which the effect is manifested). | Isolated | | 1 |
| | | Partial | | 2 |
| | | Extensive | | 4 |
| | | Total | | 8 |
| | | Critical | | 12 |
| Persistence (PE) | Time of permanence of the effect from its appearance, after which the initial conditions prior to the action are recovered. | Sporadic | <1 year | 1 |
| | | Temporary | 1–10 years | 2 |
| | | Permanent | >10 years | 4 |
| Synergy (YES) | Reinforcement of two or more single effects caused by simultaneous actions. | No synergies | - | 1 |
| | | Synergist | Moderate synergism | 2 |
| | | Very synergist | Highly synergistic | 4 |
| Effect (EF) | Cause–effect relationship, form of manifestation of the effect on a factor as a consequence of an action. | Indirect | It has an immediate impact on the relationship of one environmental factor to another | 1 |
| | | Direct | With immediate effect on an environmental component | 4 |
| Recoverability (MC) | Possibility of total or partial reconstruction and return to the initial conditions prior to the action, by means of human intervention (introduction of corrective measures). | Short-term/immediately recoverable | <1 year | 1 |
| | | Recoverable in the medium term | 1–10 years | 2 |
| | | Mitigable | Alteration that can be reduced by corrective measures | 4 |
| | | Irrecoverable | Alteration impossible to repair | 8 |
| Intensity (IN) | Degree of impact of the action on the factor, in the specific area in which it acts. | Short | | 1 |
| | | Medium | | 2 |
| | | High | | 4 |
| | | Very high | | 8 |
| | | Total | | 12 |
| Moment (MO) | Manifestation period or time elapsing between the occurrence of the action and the beginning of the effect. | Long term | >10 years | 1 |
| | | Medium term | 1–10 years | 2 |
| | | Short term | <1 year | 3 |
| | | Immediate | 0 | 4 |

**Table 1.** *Cont.*

| Attribute | | Degree | Description | Value |
|---|---|---|---|---|
| Reversibility (VR) | Possibility of returning to the initial conditions prior to the action, by natural means, once the action ceases to act on the environment. | Short term | <1 year | 1 |
| | | Medium term | 1–10 years | 2 |
| | | Long term | 10–15 years | 3 |
| | | Irreversible | >15 years | 4 |
| Accumulation (AC) | Progressive increase in the manifestation of the effect, when the action that generates it persists continuously or repeatedly. | Simple | No side effects or cumulative effects | 1 |
| | | Cumulative | It increases in severity over time | 4 |
| Periodicity (PR) | Regularity of manifestation of the effect. | Irregular | Appears in and irregular manner | 1 |
| | | Periodic | Appears periodically | 2 |
| | | Continuous | Appears in a constant manner over time | 4 |

The combination of the valuation of the attributes described above for each analyzed impact was carried out in accordance with the methodology proposed by Conesa (1995) [12], according to the following formula:

$$I = 3IN + 2EX + MO + PE + RV + SI + AC + EF + PR + MC \quad (1)$$

results in a standardized and objective characterization of its significance, which may be COMPATIBLE, MODERATE, SEVERE, or CRITICAL impact. In order to properly understand how these impact categories are defined, their definitions are included below:

- Compatible Environmental Impact (C): impact whose recovery is immediate after the cessation of the activity, not requiring protective or corrective actions. $I \leq 25$;
- Moderate Environmental Impact (M): impact whose recovery does not require intensive protective or corrective practices, and in which the achievement of the initial environmental conditions requires a certain amount of time. $25 < I \leq 50$;
- Severe Environmental Impact (S): impact in which the recovery of environmental conditions requires the application of protective or corrective measures, and in which, even with these measures, recovery requires a long period of time. $50 < I \leq 75$;
- Critical Environmental Impact (Cr): impact whose magnitude is greater than the acceptable threshold. This results in a permanent loss of the quality of environmental conditions, with no possible recovery, even with the adoption of protective and corrective measures. $I > 75$.

It is worth noting that the analysis focused on a set of negative impacts, leaving in the background the more positive aspects of the project, mainly related to the contribution to the reduction of GHG emissions, which will indirectly help mitigate the serious deterioration of marine ecosystems associated with climate change.

## 5. Results and Discussion of the Analysis of the Main Impacts of Offshore Wind, Applied to Parc Tramuntana

### *5.1. Analysis of the Impact of the Project on Water Turbidity and Sedimentation*

The increase in water turbidity is one of the main impacts detected, and it happens both during the execution phase, where it is of greater importance, and during the operation phase. The effects that sediment resuspension can cause indirectly in the transport and deposition of suspended sediment were also analyzed.

The installation of anchors, chains, and cables on sedimentary substrate, and the consequent sediment resuspension, are likely to cause direct effects on water quality (turbidity, alteration of the trophic and chemical states), and in turn indirect effects on the biota that may be affected by the turbidity plume, particularly hard-bottom filtering and suspension-feeding species. It should be noted that no such seabed has been detected in the project area, the seabed affected being composed entirely of fine sands and muds.

In general, regarding the alteration in water turbidity, the main effects on marine fauna are a decrease in visibility (affecting the behavior of certain species in their ability, among other aspects, to capture prey or detect predators) or, if prolonged over time, affecting the feeding and breathing capacity of suspension-feeding and filter-feeding animals, including fish, whose gills may suffer physical damage due to the presence of abrasive particles in the water.

Reduced light penetration also affects the depth of the photic zone (the layer where sufficient light reaches for photosynthesis) and thus the primary production capacity of algae and phanerogams.

The subsequent deposition of suspended sediment on the seabed would have its greatest impact on sessile species, particularly on those species most sensitive to sedimentation.

Considering these effects, the area with the greatest sensitivity and potential impact due to turbidity is considered to be the *Cymodocea nodosa* meadow in the shallower area, at depths below 20 m, close to the exit of the route through the HDD. In the remaining area

affected by the evacuation route and the area where the wind turbines will be installed, no significant presence of structuring sessile species was detected.

The increase in turbidity may also have an associated impact on water quality, when possible pollutants present in the sediment are mobilized. This potential impact is dismissed, given that the analysis of sediment samples taken in the area affected by the project shows no evidence of significant contamination.

In the Tramuntana project, during construction, the foreseeable increase in turbidity is mainly associated with the activities of drilling execution (HDD) in the maritime-terrestrial zone and export submarine cable burial by jetting for its protection. Both actions are temporary (with a permanence of the impact in the order of hours) and their effects on turbidity are reversible. In this phase, anchoring activities of anchor and mooring lines are short-time events, and have a lower capacity to generate turbidity, as well as the laying of inter-array cables, a part of whom can rest directly on the seabed, without the need for burial.

During operation of the wind farm, since most of the submarine cables are buried and immobile, the only contribution to increased turbidity on the seabed is that associated with the wind turbine anchoring systems, due to the resuspension of sediments from the seabed that may be produced by the movements of the mooring lines under the effect of waves and wind.

#### 5.1.1. Impact of HDD on Turbidity and Sedimentation (Construction Phase)

The HDD is a small diameter borehole that is drilled between the entrance pit, located on land behind the beach dunes, and the exit point in the sea 1770 m away from the previous one, at a depth of about 16 m. This is the technical solution proposed to allow the landing of the submarine cables without affecting the seabed surface and the biological communities present on it, some *Cymodocea nodosa* meadows of high ecological value.

These boreholes are drilled using drill heads operated from land and assisted by a jack-up structure (platform with legs) near the exit point (Figure 3).

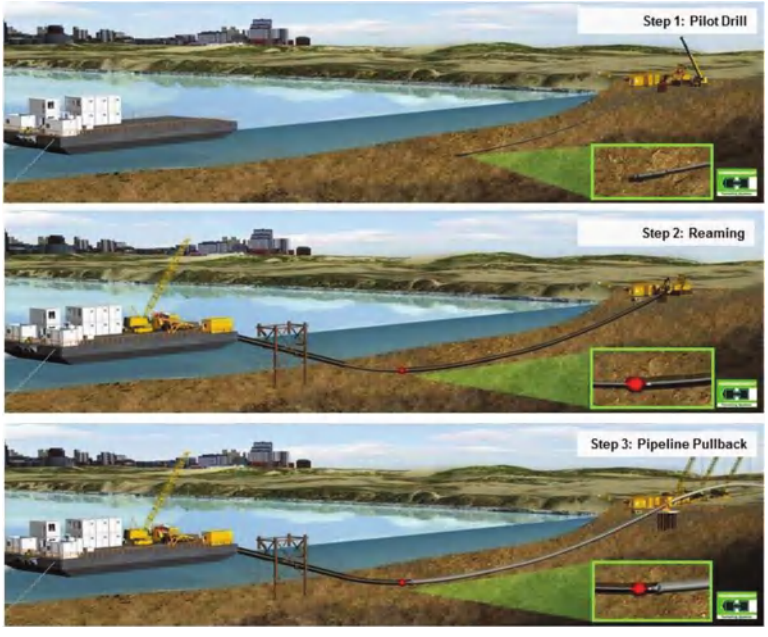


**Figure 3.** HDD drilling scheme for land–sea transition. Source: Herrenknecht.

The drilling system requires the use of bentonite fluid (composed of water, bentonite, which is a natural clay, and a small proportion of polymeric additives, wetting and dispersing agents), to facilitate drilling and to extract the excavated material, which is constantly recirculated and recycled to an onshore separation plant. Only at the exit of the drilling head at the end of drilling path is the loss of a limited volume of this fluid foreseeable. This fluid would temporarily increase turbidity around the exit point.

To reduce the dispersion and sedimentation of these bentonite clays around the exit point, containment measures are planned to be implemented by temporarily casing the exit point, to allow collection and recycling of the clays.

Based on the dispersion studies of the most unfavorable bentonite fluid emission scenarios, carried out by means of the MOHID numerical model, the predicted impact, characterized by the exceeding of the reference turbidity level (defined in accordance with Additional Provision IX of Law 22/1988 of 28 July 1988 on Coasts as 1.5 times the normal average of suspended solids measured in pre-operational state, i.e., 6.75 mg/L), is temporary (lasting less than 2 h), of low intensity (with maximum values not exceeding 40 mg/L), and limited to the immediate surroundings (distances of approximately 30 m).

5.1.2. Impact of Jetting Operations on Turbidity (Construction Phase)

The jetting technique consists of opening a trench in the seabed by applying pressurized water jets that causes the soil beneath and around the cable to fluidize, allowing the cable to sink through the suspended sediments to the bottom of the trench, to the required burial depth (Figure 4).

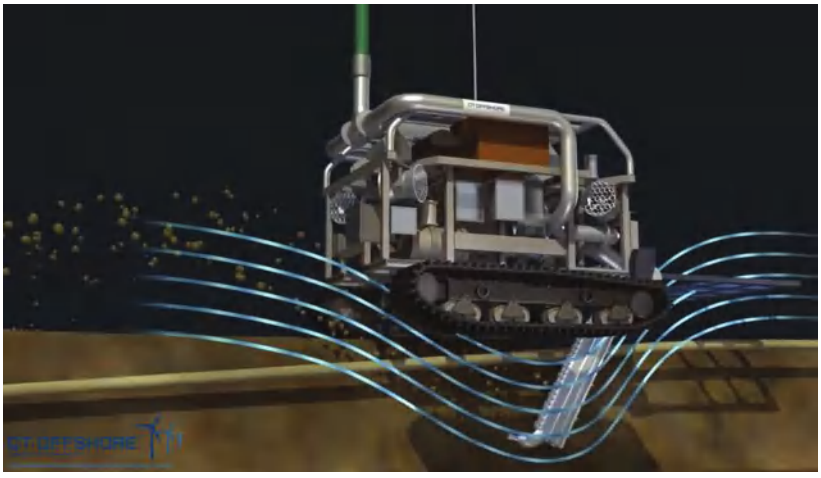


**Figure 4.** Example of subsea cable burial by jetting. Source: CT Offshore.

This technique minimizes the impact footprint and sediment resuspension, being the cable installation and burial method that generates less spatial impact (reduced trench width) and less temporal impact (reduced execution time) of those analyzed in the project.

This burial technique would be applied from the drilling exit point (HDD) to the wind farm site, about 24 km away.

To assess the effect of this operation, the sediment dispersion generated per m of advance was simulated again by the MOHID numerical model, considering a conservative hypothetical situation, in which it is assumed that all the sediment in a 2 m $\times$ 1 m trench is resuspended. The results of suspended solids concentration in the water column under this assumption show that the time duration of significant concentrations (above 6.75 mg/L) near the bottom is, in all cases, low: 3 h in the shallowest areas and those closest to the phanerogam meadows (<20 m) and up to 5 h in the deepest ones (120 m).

The impacts are therefore temporary (no more than 3–5 h above the reference threshold of 6.75 mg/L), of low intensity (maximum values below 40 mg/L), and limited again to the immediate surroundings (distances of less than 30 m), and mostly in areas of soft, non-vegetated substrate, so that the effects of the temporary increase in turbidity in the benthic zone on the physical environment and biota are considered compatible, temporary, and of low magnitude. By way of comparison, it should be noted that these levels of suspended solids and their persistence are equivalent to those usually produced during sea storms around the meadows.

Sedimentation in the shallow zone is limited to the area near the trench, and at a distance of more than 30 m does not exceed 2 cm. In the 30 m closest to the trench, 3 cm of thickness can occasionally be reached, between 30 and 60 m distance, 2 cm are not exceeded, and at more than 60 m, 1 cm is not exceeded.

It should be emphasized that the numerical modeling carried out is very conservative, since it considers the suspension of all the material present in the trench. In real observations made in other projects for laying and burying submarine power cables [13,14], the volume of resuspended material has been less than 30% of the trench volume, and the mobilized material accumulates mostly in a short radius around the trench (at a distance of less than 10 m).

5.1.3. Turbidity Impact of the Movement of Turbine Mooring Lines (Operation Phase)

The anchoring systems for floating turbines are composed of three to four mooring lines, consisting of chains connecting the floating platforms with anchors buried more than 10 m below the seabed (Figure 5). Part of these catenaries rest on the seabed to counteract the movement of the turbines under the effect of wind and waves with its weight.

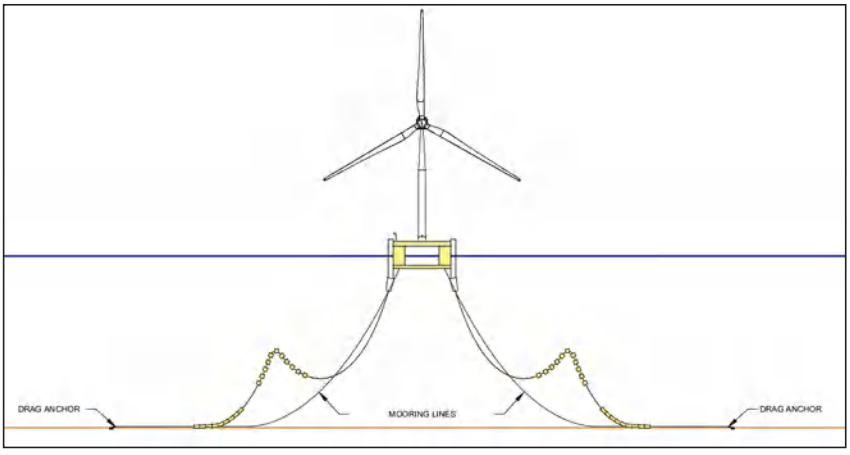


**Figure 5.** Schematic of the subsea mooring and cabling system of a floating turbine. Source: SENER.

A part of this resting section, approximately 330 m long, will be subject to certain movements that may cause the sediment to resuspend along its contact with the bottom, which may have indirect effects on the biota present in the area, in this case mostly benthic macrofauna that colonize the soft bottoms, as well as demersal species (e.g., hake).

It is estimated that the area affected by this effect is of the order of 1650 $m^2$ for each catenary (along the resting section and with a maximum arc of movement of 4°), or up to 6600 $m^2$ for each turbine (considering 4 mooring lines). Considering the area affected by the 35 planned turbines (0.23 $km^2$) compared to the total area where the wind farm would be installed (about 95 $km^2$), the area affected by this impact is about 0.24%. By contrast, the area currently subject to resuspension and turbidity on the seabed due to trawling activities in the Gulf of Roses (assuming a fleet of 21 vessels with an average operation of 180 days

per year, with 5 h of fishing periods) is estimated at 950 $km^2$ (95,000 Ha). In addition, this activity generates turbidity values much higher than those associated with the mobility of the mooring lines of a wind farm [11].

Based on the studies carried out, analyzing the possible movements in the catenaries, low speed movements are expected and the effects are not likely to reach a distance greater than 5 m at both sides of the chain, but will be limited to the furrow of maximum amplitude of the footprint considered for the catenary. The level of turbidity generated would therefore be close to that observed due to natural variability, and lower than that usually produced during episodes of strong currents or anthropogenic activity (e.g., if compared to the effect on turbidity produced by trawling, which turbidity plumes can exceed 100 m of thickness and reach suspended solids concentration of 200 mg $L^{-1}$ close to the sea bottom [15]).

The temporal effects of turbidity, although significant, will therefore be of low magnitude and low periodicity occurrence, considering the slowed movement of the chains. These effects on the physical environment are considered compatible, considering the adaptive capacity of the species that colonize the affected sedimentary bottoms.

#### 5.1.4. Overall Assessment of the Impact on Turbidity and Sedimentation

During the construction phase, the impact on the increase in turbidity and sedimentation is considered significant in the shallow area, considering that it happens in waters of protected natural areas (RN2000) and the presence of the marine phanerogam *Cymodocea nodosa* meadow in the landing area, despite the fact that the effect is temporary (hours) and the rate and spatial extent of sedimentation is limited.

By assessing the different descriptors of each impact (turbidity and sedimentation), according to the described methodology, a Moderate impact rating is obtained for both during the construction phase, as shown in Table 2:

**Table 2.** Overall assessment of the impact on turbidity and sedimentation during the construction phase.

| Attribute | Turbidity | | Sedimentation | |
|---|---|---|---|---|
| | **Characterization** | **Rating** | **Characterization** | **Rating** |
| Sign | Negative | (−) | Negative | (−) |
| Extension | Partial | 2 | Partial | 2 |
| Persistence | Temporary | 2 | Permanent | 4 |
| Synergy | Synergistic | 2 | Synergistic | 2 |
| Effect | Direct | 4 | Direct | 4 |
| Recoverability | Immediate | 1 | Immediate | 1 |
| Intensity | Medium | 2 | Low | 1 |
| Moment | Immediate | 4 | Immediate | 4 |
| Reversibility | Short period | 1 | Medium period | 2 |
| Accumulation | Simple | 1 | Cumulative | 4 |
| Periodicity | Continuous | 4 | Continuous | 4 |
| TOTAL RATING | MODERATE | −29 | MODERATE | −32 |

In terms of the impact on this vector during the operation phase, the expected impacts on turbidity are very limited, restricted to less than 1% of the project area, which in relation to the current impact of trawling in the area occupied by the park where this activity would cease (about 600 ha, equivalent to 6% of the park's surface), represents, both in terms of the extent and magnitude of the impact, a relative improvement in terms of turbidity conditions and recoverability of the seabed from sediment resuspension. From the modeling carried out, it is concluded that the levels of suspended solids in the water column derived from the movement of the chains are scarcely significant (less than 2 mg/L at distances of less than 25 m) at all times, being considered of low intensity and persistence (levels of less than 1 mg/L in less than 2 h).

The assessment of these impacts in the operation phase is summarized in Table 3:

**Table 3.** Overall assessment of the impact on turbidity and sedimentation during the operation phase.

| Attribute | Turbidity | | Sedimentation | |
|---|---|---|---|---|
| | Characterization | Rating | Characterization | Rating |
| Sign | Negative | (−) | Negative | (−) |
| Extension | Partial | 2 | Partial | 2 |
| Persistence | Permanent | 4 | Permanent | 4 |
| Synergy | Synergistic | 2 | Synergistic | 2 |
| Effect | Direct | 4 | Direct | 4 |
| Recoverability | Immediate | 1 | Immediate | 1 |
| Intensity | Low | 1 | Low | 1 |
| Moment | Immediate | 4 | Immediate | 4 |
| Reversibility | Short period | 1 | Medium period | 2 |
| Accumulation | Simple | 1 | Cumulative | 4 |
| Periodicity | Continuous | 4 | Continuous | 4 |
| TOTAL RATING | MODERATE | −28 | MODERATE | −32 |

### *5.2. Analysis of the Project's Impact on Underwater Noise*

The project has the potential to alter the acoustic environment of the area, both during the construction and operation phases.

In the study area, background underwater noise (reference situation), which is related to natural sources (e.g., wind) and artificial sources (e.g., maritime traffic, professional fishing), was measured by means of PAM (Passive Acoustic Monitoring) equipment. The recorded noise values reach peaks (SPL) of 156–159 dB re 1 μPa and cumulative averages (SEL) of 134–139 dB re 1 μPa at the wind farm proposed location. The greatest contribution is from maritime traffic, highlighting the important fishing activity linked to the port of Roses.

Underwater noise has the potential to alter the acoustic environment of the area and affect several species, especially marine mammals, with special attention to cetaceans present in the study area (mainly bottlenose dolphins), and chelonians such as loggerhead turtles (with less presence in the area).

The acoustic impact will depend on the distance to the source of the receptor. Considering the distribution of cetaceans in the study area, observed during the monitoring campaigns carried out during the last year, the main type of detected cetaceans are dolphins (bottlenose and striped dolphins), associated with a medium frequency hearing range (150–160 kHz), and to a lesser extent species with a low frequency hearing range (7–35 kHz), such as the fin whale.

In relation to the potential effect on turtles (loggerhead turtle), a reference level RMS of 166–175 dB re 1 μP [16] is considered to be the range for behavioral change effects, based on experimental measurements with species in captivity.

According to *MAGRAMA* [17], the reference levels for the definition of exclusion zones are 160 and 180 dB rms, corresponding to thresholds for which behavioral changes and physiological damage are detected in cetaceans, respectively.

#### 5.2.1. Noise Impact during the Construction Phase

During the construction phase, the main source of noise is associated with the vessels that will install the wind turbines and their anchoring systems and lay the cable. The underwater noise emission is proportional to the speed of the vessels, which, due to the nature of the work to be carried out, will generally be low (between 3 and 5 knots).

Other sources of noise identified in this phase are the use of acoustic devices for positioning during cable laying or anchor installation (echo sounders, sonars, acoustic positioning systems), the use of pumping equipment and the pressurized water jetting system (jetting), displacement along the bottom, sliding (dragging), and finally machinery on board for lifting and lowering equipment.

One of the main differences between the projected wind farm (with floating foundations) and most wind farms in the world (which have fixed foundations) is that in this case no pile driving activities are carried out for the execution of foundations. Pile hammering is the main source of underwater noise impact identified by the scientific community in association with offshore wind farms, having been analyzed in a large number of studies that show its impact on certain marine species, particularly cetaceans. Consequently, this important impact does not happen in a project such as Parc Tramuntana, as no impulsive, high-energy noise will be generated during construction.

Thus, the noise that may be generated during the construction phase does not differ much from noise associated with other types of maritime works, associated with low frequencies (e.g., navigation), and is of a temporary nature.

According to the consulted literature, the noise generated by cable-laying ships in shallow waters is of the order of 164–188 dB re 1 µPa, at 1 m from the source, acting at frequencies between 0.7 and 50 kHz: surface ship 180 dB (CEDA, 2011) [18], 164–170 dB (Nexans Skagerrak). In relation to underwater activities, a reference of burial works at 1 m from the source is available, with emissions up to 188.5 dB (at 11 kHz) [19] or 174 dB [20]. It should also be noted that modern newly built vessels reduce acoustic emissions and vibrations from engine operation very significantly.

The effects of the construction phase on this variable are considered significant, although the existing risk of direct effects is limited to the presence of wildlife in the vicinity of the noise source, noting that the negative effects would be temporary and that noise generation would be progressive, with a chasing effect that avoids further damage to the animals. The assessment of this impact in the installation phase is therefore moderate (Table 4):

**Table 4.** Assessment of the impact on submarine noise during the construction phase.

| Attribute | Characterization | Rating |
|---|---|---|
| Sign | Negative | (−) |
| Extension | Extensive | 4 |
| Persistence | Temporary | 2 |
| Synergy | Synergistic | 2 |
| Effect | Direct | 4 |
| Recoverability | Immediate | 1 |
| Intensity | Medium | 2 |
| Moment | Immediate | 4 |
| Reversibility | Short period | 1 |
| Accumulation | Simple | 1 |
| Periodicity | Continuous | 4 |
| TOTAL RATING | MODERATE | −28 |

As the main corrective measure, the use of modern workboats with low noise emission certifications (e.g., Silent-E) is proposed [21].

5.2.2. Noise Impact during the Operation Phase

During the operation phase of the wind farm, the main source of underwater noise generation will be the wind turbines themselves, which will produce continuous noise due to the movement of the blades, transmitted mainly through vibrations along the floating platform and the bottom-anchoring chains, and to a much lesser extent directly through the water surface, since the change in medium (air/water) produces a significant attenuation of atmospheric sound.

There will also be transient noise related to the movement of the anchor chains on the bottom due to the movement of the floating turbines.

In addition to the noise from the wind turbines, there will be noise from the vessels responsible for maintenance/repair tasks, similar in nature to that expected during the con-

struction phase. The impact of these vessels will have a limited frequency (20 days/year), similar to those currently caused by marine and fishing traffic.

In order to characterize the impact of underwater noise produced by the turbines, the existing literature on the subject was analyzed, coming from the scarce experiences in other floating offshore wind farms, specifically the studies and measurements of underwater noise in the Hywind Tampen wind farm [22], the first floating technology wind farm installed off the coast of Norway, in the North Sea.

In this wind farm, the noise recorded during operation was characterized as continuous and low frequency (25, 50, and 125 Hz). The results did not exceed in any case an SPL of 160 dB re 1μPa (reference level adopted as a threshold to determine the limit of the cetacean disturbance zone, according to *MAGRAMA* recommendations [17]), and the isophone range of 120 dB re 1 μPa, assimilable to the background noise recorded at the Hywind Tampen wind farm site), occurs, according to the developed acoustic modeling on the basis of measurements, at circa 2 km from the wind turbines, with a maximum noise footprint of approximately 40 $km^2$.

Similar experiences in the environmental monitoring phase of a fixed foundation (jackets) wind farm operating at a depth of 25 m off New York Bay, the Block Island Wind Farm [23], show maximum noise values generated during operation of up to 120 dB re 1 μPa at a distance of 50 m from the turbines, at a site with a background noise of 110 dB re 1 μPa.

These levels are considered an approximation to the underwater acoustic footprint that may be produced by Parc Tramuntana, whose increase in the acoustic scenario around the wind turbines will be cumulative depending on the number of wind turbines and the environmental conditions of the surroundings. It is estimated that this acoustic increase will be attenuated to the background noise levels existing at a distance of approximately 2 km or less (since in the case of Tramuntana the background noise is more intense than that existing in the other reference wind farms analyzed).

The expected RMS levels from this distance (around 120 dB re 1 uPa) are significantly lower than the background noise and the thresholds that would cause annoyance to the most sensitive species identified (dolphins and sea turtles), which are not highly abundant in the wind farm site area.

After this analysis, the effects of the operation phase on this variable are considered significant, of partial extension (affecting the area near the wind farm's footprint), and of medium magnitude due to the acoustic levels generated. The risk of direct effects is limited to the presence of fauna in the vicinity of the noise source, which is irregular and periodically distributed. The assessment of this impact during the operation phase is shown in Table 5:

**Table 5.** Assessment of the impact on submarine noise during the operation phase.

| Attribute | Characterization | Rating |
|---|---|---|
| Sign | Negative | (−) |
| Extension | Extensive | 4 |
| Persistence | Permanent | 4 |
| Synergy | Synergistic | 2 |
| Effect | Direct | 4 |
| Recoverability | Immediate | 1 |
| Intensity | Medium | 2 |
| Moment | Immediate | 4 |
| Reversibility | Short period | 1 |
| Accumulation | Cumulative | 4 |
| Periodicity | Continuous | 4 |
| TOTAL RATING | MODERATE | −38 |

The applicable measures are the monitoring of acoustic levels and the recording of cetacean activity in the area, through visual censuses and the installation of hydrophones, to verify the levels and activity of potentially affected fauna.

*5.3. Analysis of the Project's Impact on Electromagnetic Fields (EMF)*

This potential impact is only likely to occur during the operation phase, as it is associated with the transmission of electricity generated by the wind farm through the submarine cables.

The interconnection cables (inter-array) installed in the offshore wind farm and the export cables will operate in alternating current at 66 kV–50 Hz. An analysis of the EMF generated by these cables was carried out using numerical modeling based on the *Biot–Savart* analytical calculation for the different cable segments (both the dynamic inter-array cables, which connect the turbines to each other, and the buried export cables, which connect the wind farm to shore). This model adopted a conservative calculation, considering the most unfavorable possible scenario (cable operation at full load), and without considering the shielding effects due to the cable protection armor.

This simulation of EMF levels (see Figure 6) obtains magnetic field levels (B) for the maximum inter-array cables at the surface of the conductors of 90 μT and, for the evacuation cable, a maximum level of 5 μT on the seabed.

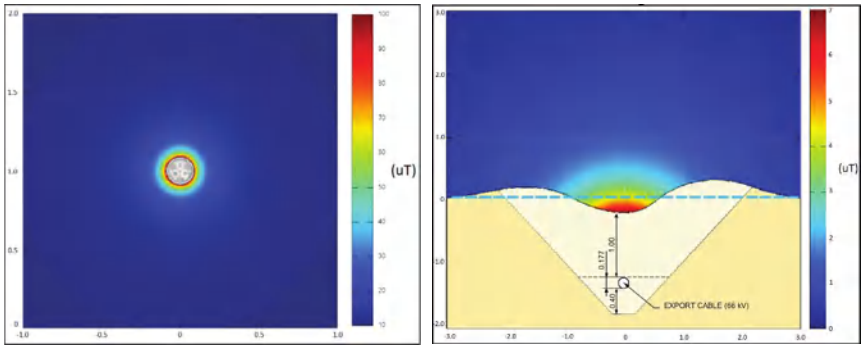


(**a**) (**b**)

**Figure 6.** EMC modeling for the inter-array (**a**) and export (**b**) cables.

The electric field (E) induced by the 66 kV conductors will be zero on the outside of the cables, since it is blocked by the metallic screen of the cable itself.

The potential effects of EMF on aquatic fauna include the possible disorientation of migratory species that use the terrestrial magnetic field for orientation during navigation, behavioral alteration with attraction or repulsion effects (barrier effect), as well as potential physiological damage at the cellular level.

As a reference, it should be noted that normal values of the earth's geomagnetic field can range from 20 to 75 μT, depending on the geographical location.

In order to assess which of these effects could be relevant to the project, a large amount of literature was consulted to analyze the effects of EMF on different species (Table 6):

**Table 6.** Documented effects of EMF on marine species.

| Species | Threshold Value | Effect | Source |
|---|---|---|---|
| Eel (*Anguilla anguilla*) | 5 μT (direct current) | Course deviation during migration | Westerberg and Begout-Anras (2000) [24] |
| Turtle (*Caretta caretta)* | 4.9 μT_ | Disorientation of juveniles during migrations periods | Fuxjager et al. (2011) [25] |
| Mussel (*Mytilus galloprovincialis)* | 300–1000 μT_ | Alteration of cellular processes for adults in the laboratory | Ottaviani et al. (2002) [26]<br>Malagoli et al. (2004) [27] |
| Shrimp (*Crangon crangon*) | 10–100 μT_<br>800 μT_ | Behavioral disturbance in adults<br>Attraction effect on adults | Hutchinson et al. (2018) [28] |
| Fish and macroinvertebrates | 1–3.2 mT_ | No significant long-term behavioral effects detected | Woodruff et al. (2012) [29]<br>Bochert and Zettler (2004) [30] |
| Elasmobranchs | 91 μV/m | Alteration of behavior by attraction or repulsion | CMACS (2003) [31]<br>Gill and Taylor (2001) [32] |
| | 60,000 μV/m | Narcosis | Smith (1974) [33] |
| Elasmobranchs and rajoids | 1/8 to 8 Hz | Electrosensitivity within the frequency range | Kalmijin (2000) [34]<br>Walker et al. (2003) [35] |

In relation to species sensitive to electric fields, elasmobranchs would be the most potentially affected group, whose ability to detect these fields is very sensitive, detecting levels of less than 0.5 V/m (5 nV/cm).

Among the species considered in the bibliography, the most important because of their potential presence and migratory habits are the loggerhead turtle (*Caretta caretta*), the bottlenose dolphin (*Tursiops truncatus*), devil fish (*Mobula mobular*), and the main protected species of elasmobranchs with a potential presence in the study area due to their conservation status: common thresher (*Alopias vulpinus*), basking shark (*Cetorhinus maximus*), tope shark (*Galeorhinus galeus*), bluntnose sixgill shark (*Hexanchus griseus*), shortfin mako shark (*Isurus oxyrinchus*), smooth-hound (*Mustelus* spp.), blue shark (*Prionace glauca*), and spiny dogfish (*Squalus acanthias*).

The maximum magnetic fields generated by the project are within the range of values detectable by marine fauna.

The field generated by the inter-array cables in the wind farm area (up to 90 μT) will be detectable by potentially present species of interest. Considering that the cables analyzed do not alter the electric field, significant effects on elasmobranchs are dismissed, although their behavior will be analyzed during the operation phase. This effect is localized in the closeness of the cables, as the magnetic field levels attenuate rapidly a few meters away.

The potential effects on fauna are considered locally limited; it should be noted that the cable's footprint in the sea bottom is approximately 10,000 $m^2$, less than 1% of the wind farm's area, and barely perceptible (<5 μT) at short distances (<1 m). Due to the extent of these fields and the magnitude of EMF and derived effects, they are not considered to have a significant barrier effect on migratory species.

In the case of the fields associated with the export cables (<5 μT), these are of limited magnitude, close to the levels of natural electromagnetic disturbances that regularly happen (*Nyqvist* et al., 2020) [36], and are therefore expected to be barely perceptible by potentially affected fauna, as the cable is buried deep enough for the field to attenuate to levels that are practically imperceptible at the seabed surface.

It should be noted that in EMF monitoring surveys of buried electrical interconnections, levels of the order of nT are usually detected. Considering its continuous route to the coast, the species of interest potentially affected would be the loggerhead turtle, in the event of passing through to nest on nearby beaches, and the bottlenose dolphin, due to its local presence. However, due to the magnitude of the impact, as described above, the effect on these species is considered insignificant. These values can also be extrapolated to the subway cable line through the HDD.

On the other hand, it should be noted that it is foreseeable that in the operating phase the EMF generated will be lower than that modeled, considering the maximum regular

operating loads contemplated and the additional shielding provided by the cable protection armor; according to the literature consulted, these levels would not be capable of causing physiological damage or significant changes in the behavior of the fauna present in the project area.

Anyway, the increase in EMF during the wind farm's operation phase was considered a significant effect, mainly in the wind farm's footprint area (where the inter-array cables are located). This impact is considered moderate, according to the following attribute classification (Table 7).

**Table 7.** Assessment of the impact of EMF on marine fauna.

| Attribute | Characterization | Rating |
|---|---|---|
| Sign | Negative | (−) |
| Extension | Partial | 2 |
| Persistence | Permanent | 4 |
| Synergy | Simple | 1 |
| Effect | Direct | 4 |
| Recoverability | Immediate | 1 |
| Intensity | Medium | 2 |
| Moment | Immediate | 4 |
| Reversibility | Short period | 1 |
| Accumulation | Simple | 1 |
| Periodicity | Continuous | 4 |
| TOTAL RATING | MODERATE | −30 |

Among the main mitigation measures, in addition to the design of the cables to reduce EMF through shielding and burial in the evacuation route, it is proposed to monitor EMF levels in the inter-array cables and in the evacuation route, as well as the monitoring of cetaceans, turtles, pelagic communities (including elasmobranchs), and benthic macrofauna.

### *5.4. Analysis of the Project's Impact on Marine Circulation and Nutrient Distribution*

Once the offshore wind farm is in operation, the operation of the wind turbines could generate changes in the atmospheric and oceanic dynamics due to the capture and modification of wind energy. On the other hand, the floating platforms, with a draft of −15 m, could generate a certain wave reduction effect or local alteration of the currents.

The main expected effect could be the reduction in wind energy in the area of the wind farm, associated to the wake effect, which consists of the reduction of wind speed and kinetic energy downwind of the wind farm.

It is considered that the capacity of the underwater structures to alter the hydrodynamic regime of the Gulf of Roses is very low, considering the depth at which the wind farm is located (>100 m) and that the installed structures (floating platform, chains, anchors, and inter-array cables) are not large enough to produce a significant reduction in current flows, stratification, or vertical transport phenomena in the water column.

Although these effects may happen, they will be very localized in the immediate surroundings of the structures and of little entity at the level of the Gulf of Roses (where they will probably be imperceptible), which does not confer the ability to become cumulative or synergistic downstream. The effect of this potential reduction in the wind and hydrodynamic regime on the development of species and habitats is assumed to be low, due to the expected low incidence of the reduction in physical effects on the column and seabed of the installed wind turbines, as well as the capacity of biological adaptation of the species potentially affected to small changes in the circulation.

This impact has first been assessed on the basis of a critical analysis of the existing literature, and a rigorous study by IHCantabria about the impact of the project on wind fields and marine currents has also been undertaken, by means of numerical modeling. This study, whose methodology has been presented to the Spanish National Research Council (CSIC) experts for their approval, and no objections have been received from them, will

provide quantitative information on the foreseeable variation in current speeds in the area of the Gulf of Roses.

As a result of the bibliographic analysis, some scientific publications that analyze and document wind field alteration effects were identified, mainly based on wind farms located in the North Sea [37]. In some cases, it is suggested that these alterations could lead to increases in precipitation, although the predicted changes are so small in magnitude that it is difficult to distinguish them from natural variability. According to Platis et al. (2018) [38], the wake effect is greater under stable atmospheric conditions than under turbulent conditions. When conditions are turbulent, such as those associated with the Tramuntana winds that will feed the wind farm, the wake effect is restricted to the local area inside the wind farm and the immediate surroundings.

It should also be noted that in general, regarding wind disturbance, the numerical models give overestimated values with respect to the field measurements. This divergence between modeled and measured values indicates deficiencies in the knowledge of the effects. Measurements made in the "Horn Rev" and "Nysted" fields in the Baltic Sea show reductions of 8–9% immediately after the field, and 2% at distances between 5 and 20 km [39]. As for the regional effect, it is estimated to be small, the energy loss in the first kilometer of the atmosphere being 0.007%. The conclusion is that floating wind farms may have a minor to moderate impact on atmospheric and oceanic dynamics (depending on the location and size of the wind farm), although there is insufficient specific knowledge of the cascading effects of large-scale atmospheric and oceanic processes to reduce the current uncertainty.

In relation to the possible effect of the alteration of currents on the distribution of nutrients, Van Berkel et al. (2020) [40] point to the potential upwelling effect associated with the wake, causing the upwelling of deep-water mass to the surface. However, this effect depends on the relative direction between the wind and the coast, being a frequent phenomenon on the Atlantic coast but not so in the western Mediterranean.

It should be noted that the bibliographic references in which appreciable variations in the current regime have been observed as an indirect consequence of the presence of a wind farm correspond to cases in shallow areas, with fixed foundation wind farms, and with a high concentration of turbines, being scenarios not very comparable with the project scenario.

The results of the hydrodynamical study by means of numerical modeling developed by IHCantabria show that the effect of the wind farm over the surface currents and those averaged over the water column in the coastal area is very small, with an averaged difference in the currents magnitude below 1 cm/s and maximum values of 1 cm/s during 98% of the time.

In the proximities of the wind farm in the open sea, the differences obtained, in both surface and averaged water column, remain below 1 cm/s at the north, east, and west from the farm, while at the south this difference is up to 2 cm/s, which represents an averaged variation inferior to 3.5% of the average speed registered in the study area by the buoy of *Puertos del Estado*.

In any case, to confirm the potential impact, the mitigation measures and Environmental Monitoring Plan propose monitoring the wind and current regime of the involved area, as well as monitoring the thermohaline structure of the main indicators of the water masses (temperature, salinity, turbidity), nutrients in the water column, and monitoring the evolution of the main pelagic and benthic communities in the affected area, whose evolution will be analyzed with a Before-After Control-Impact (BACI) study approach.

The impact is considered significant, permanent (during the life of the wind farm), and synergistic. Due to the uncertainty of the effect and the fact that mitigation measures cannot be developed, a medium magnitude is assigned to it. The resulting classification is shown at Table 8:

**Table 8.** Assessment of the impact on marine hydrodynamics.

| Attribute | Characterization | Rating |
|---|---|---|
| Sign | Negative | (−) |
| Extension | Extensive | 4 |
| Persistence | Permanent | 4 |
| Synergy | Synergic | 2 |
| Effect | Direct | 4 |
| Recoverability | Immediate | 1 |
| Intensity | Medium | 2 |
| Moment | Immediate | 4 |
| Reversibility | Short period | 1 |
| Accumulation | Cumulative | 4 |
| Periodicity | Continuous | 4 |
| TOTAL RATING | MODERATE | −38 |

*5.5. Analysis of the Impact of the Project on the Proliferation of Invasive Alien Species*

Another aspect that has been identified by scientists as a possible threat to marine biodiversity, in association with offshore wind farms, is their potential to promote the proliferation of invasive alien species.

According to the available knowledge by the scientific community on the proliferation of allochthonous species in the Mediterranean, either introduced intentionally or by chance by different ways, it is currently considered that this phenomenon could be one of the main causes of biodiversity loss in the Mediterranean. The number of invasive alien species inventoried in this sea in 2012 reached almost a thousand (more than 5% of the species present in this sea), with more than 300 identified in the western basin [41].

There is a wide variety of species with the potential to become invasive, although organisms with the ability to attach to hard surfaces (biofouling), including mollusks, are generally the most notorious. The known introduction ways are numerous, one of the most relevant being the opening of the Suez Canal in 1869, which involved communication between the Red Sea and the Mediterranean Sea, favoring the migration of numerous species from the Red Sea to the Eastern Mediterranean, some of which have come to spread throughout the Mediterranean basin [42].

Other known ways of anthropogenic introductions are the transport of sessile species attached to the hull of merchant ships or other structures moving from one place to another, the discharge of ballast water, which carries planktonic and nektonic organisms (some of which are larval stages of invasive species), the introduction of species of interest for mariculture and fish farming (which often carry parasitic organisms), the intentional or accidental release of specimens by aquariums, or even the recent proliferation of microplastics in the seas [43].

Regarding this threat, it is also worth noting the effect that climate change is likely to have on this phenomenon, since it is expected to affect, by modifying water temperature, the structure of marine communities, providing more opportunities for exotic species to disperse and compete with and displace native species [42].

Based on current knowledge, and in relation to the structures and actions foreseen in the project, the following possible routes of entry of allochthonous species into the project area are contemplated:

- Through adherence to the structures of the foundation floaters, during their towing from the manufacturing or assembly port:
  The structures are expected to be manufactured either in western Mediterranean ports, with a low probability of introduction of new species, or from the Atlantic ports of the Iberian Peninsula. The rest of the elements that will remain on the seabed (submarine cables, anchors, and chains) are not expected to be exposed to marine colonization outside the park, since they will be transported aboard ships.

In both cases, the main means of transport will be semi-submersible vessels between the manufacturing port and the wind turbine assembly port (e.g., in Tarragona), so possible adhesions will only occur during transport between the port of Tarragona and the wind farm site. The probability of introduction of allochthonous species is therefore very low, and comparatively lower than that which may be due to the transit of merchant ships coming from the Strait of Gibraltar or the Suez Canal to ports in the western Mediterranean.

- By attachment to working vessels during construction (cable-layers, tugboats, etc.):
  These vessels are highly specialized and generally work in all the world's oceans, so there is a possibility that they may carry allochthonous species attached to their hulls, with potential for invasion and displacement of native species.
  However, this is not a significant threat, in relation to the number of vessels with which it is associated, compared to the intense maritime traffic of merchant ships, pleasure craft, fishing boats, or cruise ships that sail the waters of the western Mediterranean from other seas.
- By releasing ballast water from the foundation platforms:
  The floating turbine foundation platforms have ballast systems that involve filling or emptying tanks integrated into their structure to contribute to the stability of the whole. The partial filling of these tanks will be carried out at the assembly port (Tarragona), ending at the location of the wind farm.
  It is therefore not foreseeable, as has been argued above in the case of the adhesion entry route, that these ballast waters will constitute a significant entry route for invasive non-native species.

Finally, the potential effect of the floating structures themselves, as well as the anchoring system and the inter-array cables, which will be the only elements exposed to marine colonization, should be evaluated as possible elements of attraction and settlement of invasive alien marine species. This effect, far from introducing new species, could only contribute to a greater growth of the species present in the area. Its effect would be equivalent to that provided by any structure capable of providing a substrate for the settlement of sessile organisms, especially if it is located within the photic zone, where photosynthesis occurs and with it the greatest growth of biomass. That is, it would be equivalent to that associated with boat hulls, buoys, fishing gear, artificial reefs, or shallow rocky bottoms.

It should also be noted, in the case of platforms, that these structures are protected against corrosion and biofouling by means of cathodic protection systems and/or impressed current, which significantly minimizes biological adhesion. Therefore, only the surface of the chains and inter-array cables would be exposed to colonization at a relevant level.

It is possible that the presence of the floating structures may generate slight changes in the behavior of pelagic species, which may be attracted or repelled in their immediate environment depending on their feeding, predatory, shelter, or reproduction habits. However, these effects are not considered to be relevant in terms of compromising the conservation of these species, especially when compared to other pressures on these species in the project area, such as trawling or maritime traffic.

For all of the above reasons, the effect of the project on the proliferation of invasive alien species was considered not significant for the purposes of impact assessment.

## 6. Conclusions

The social controversy related to the introduction of offshore wind power in Catalonia has scaled to a scientific debate about its environmental compatibility, and specifically in relation to the Parc Tramuntana project. Recent publications have contributed to sustaining this debate, without being adequately based on rigorous analysis of both the characteristics of the project and its specific location within the Gulf of Roses, so it has been considered appropriate to provide an exhaustive analysis of the main impacts identified by the scientific community in relation to offshore wind farms.

The aim of this report was therefore to dispel some of the uncertainty that motivates this opposition, based on detailed information and quantitative data, in order to place these impacts in a realistic context and determine their true magnitude.

This is possible because a series of diverse and detailed studies have been developed over the last two years to assess the environmental impact of the project, which are relatively advanced and ready to provide some well-founded conclusions. In the meantime, the study continues to be prepared and, once the relevant studies are completed, it will be submitted as part of the documentation required by current legislation for the environmental processing of the project. Although this procedure contemplates a 30-day public information phase, it is desired to maintain a less limited channel of dialogue and prior communication, for which reason the promoter commits to advance as far as possible the conclusions that emerge from the environmental studies and to make them available to any interested person through the project's web page.

It should be noted that both the project and the corresponding environmental impact study are being developed in accordance with current environmental processing regulations and based on the Scope Document submitted by the General Directorate for Environmental Quality and Assessment of the Ministry of the Environment. Likewise, the design of the wind farm's infrastructure is in accordance with the conditions established by urban and sectorial regulations.

Based on the studies carried out, which are based on a standardized methodology, the impact of the project is objectively classified as MODERATE on vectors such as turbidity and sedimentation, underwater noise, hydrodynamic circulation, or the alteration of electromagnetic fields, and NOT SIGNIFICANT on aspects such as the proliferation of invasive exotic species (Table 9).

**Table 9.** Summary of analyzed environmental impact ratings and characterization.

| Impact Assessment | Phase | Rating (-) | Characterization |
|---|---|---|---|
| Turbidity | Construction | 29 | MODERATE |
| | Operation | 28 | MODERATE |
| Sedimentation | Construction | 32 | MODERATE |
| | Operation | 32 | MODERATE |
| Submarine noise | Construction | 28 | MODERATE |
| | Operation | 38 | MODERATE |
| EMF on marine fauna | Construction | N/A | N/A |
| | Operation | 30 | MODERATE |
| Marine hydrodynamics | Construction | N/A | N/A |
| | Operation | 38 | MODERATE |
| Proliferation of invasive exotic species | Construction | N/A | N/A |
| | Operation | N/A | N/A |

Impacts on turbidity and sedimentation are expected along the evacuation cables track during construction stage and only in the close vicinity of turbine moorings during the operational stage.

Submarine noise is expected also during both stages, mainly associated to construction equipment and ships during construction and to both maintenance ships and turbine structure vibrations during operation, although emission levels are not expected to be higher than current background noise in the area or to cause severe damage to sensitive species present in the area.

EMF are only expected in operational stage, being significant mainly in the close vicinity of the floating inter-array cables. Generated fields are expected to be detectable by sensitive species, but not strong enough to cause severe alterations in their behavior.

The impact on marine hydrodynamics, based on numerical modeling, is expected to be low, limited to changes in currents magnitude of 1–2 cm/s in the vicinity of the wind farm during operational stage.

Finally, the effect of the project on the potential proliferation of invasive species was considered not significant, as there are small chances for the introduction of alien species associated to project structures, being irrelevant when compared with other identified introduction vectors in the area.

In general, the studies carried out allow to anticipate a low impact of the floating offshore wind farm project on marine biodiversity in the area of implementation, which makes it compatible with the conservation of such biodiversity.

In addition, most of the significant impacts identified allow the application of measures to mitigate their effects, as well as their follow-up during the environmental monitoring derived from the environmental processing, which will make it possible to know the evolution of the wind farm's effects on the environment, as well as the adoption of additional measures if necessary.

These initial conclusions address only certain environmental aspects of the project that have been identified as being of greatest concern to some members of the scientific community. As the environmental impact study progresses, it is expected that conclusions regarding other potential environmental or socioeconomic impacts will also be published.

It is clear that any project, of whatever nature, introduces certain changes in the environment and therefore has an associated impact. However, it is equally true that it is imperative to slow down climate change by all available means, among which the transformation of the energy generation model to a renewable model is a priority.

It should be remembered that the effects of climate change predicted by the IPCC for the coming decades (many of which are already occurring today, including in the Mediterranean) include an increase in the temperature of the planet and its oceans, the extinction and anomalous migration of species, colonization by invasive species, the modification of marine currents and acidification of the seas, droughts, and catastrophic climatic phenomena.

Therefore, the suitability or otherwise of offshore wind power in Catalonia should not be evaluated solely from the perspective of its effect on biodiversity, especially considering that climate change itself will certainly introduce much more drastic changes in Mediterranean ecosystems than those that can be attributed to any individual project, resulting in more severe, lasting, and irreversible impacts on marine biodiversity.

Thus, from an equanimous and global vision, the assessment of a project such as Parc Tramuntana should be carried out with scientific rigor and without falling into the tunnel vision that only focuses on the local negative impacts, without placing them in context. Because, according to environmentalists [44], even if it is accepted that, like any other renewable energy project or any other type of project, it may have a certain level of impact on local biodiversity, the relationship between this impact and the protection of biodiversity throughout the Mediterranean is largely in favor of the latter.

Finally, in response to the arguments calling for a halt to marine renewables under a precautionary principle that only greater scientific knowledge can overcome, it is necessary to indicate that unfortunately the time available for the study is limited, since the climate emergency is already a reality and requires an urgent response. It is therefore a priority to join efforts to ensure the optimal response to the climate challenge, as is being done in neighboring countries.

**Author Contributions:** Conceptualization, K.D.-C. and S.T.; methodology, K.D.-C.; software, J.G.-A.; formal analysis, J.G.-A.; investigation, K.D.-C. and S.T.; supervision, S.A.; writing—original draft preparation, S.T. and K.D.-C.; writing—review and editing, S.A., R.J., M.G. and J.R.V.; project administration, M.G. All authors have read and agreed to the published version of the manuscript.

**Funding:** This research received no external funding.

**Institutional Review Board Statement:** Not applicable.

**Informed Consent Statement:** Not applicable.

**Data Availability Statement:** Not applicable.

**Conflicts of Interest:** Mr. Koldo Diez-Caballero and Mr. Juan Ramón Vidal are employees of Tecnoambiente S.L., an environmental consultant that has developed the hydrographic, geophysical and environmental surveys of the project area, and is developing the Environmental Impact Assessment studies of the offshore wind farm project. Ms. Silvia Troiteiro, Ms. Marta González, Mr. Sergi Ametller and Ms. Raquel Juan are employees of SENER Ingeniería y Sistemas, S.A., a company of the SENER Group. The offshore wind farm mentioned in the article is being developed by BlueFloat Energy International, S.L.U. together with SENER Renewable Investments, S.L. (a company of the SENER Group) as minority partner. Ms. Silvia Troiteiro, Ms. Marta González, Mr. Sergi Ametller and Ms. Raquel Juan have participated in the elaboration of the study referred to in the article and have had access to all information produced by such study. Mr. Javier García-Alba is an employee of the IHCantabria, a non-profit research organization that has developed the specialized hydrodynamic studies to determine the impact of the wind farm on marine dynamics.

## References


1. Acord de Govern de la Generalitat de Catalunya, de 14 de Maig de 2019, de Aprovació de la Declaració de Emergència Climàtica a Catalunya. Available online: https://govern.cat/govern/docs/2019/05/14/15/12/9ff53be9-20cc-4ce1-9c7c-cdd5dc762187.pdf (accessed on 26 April 2022).
2. Acuerdo del Consejo de Ministros el 21 de Enero de 2020 Por el que se Aprueba la Declaración del Gobierno Ante la Emergencia Climática y Ambiental. Available online: https://www.miteco.gob.es/es/prensa/declaracionemergenciaclimatica_tcm30-506551.pdf (accessed on 26 April 2022).
3. European Parliament Resolution of 28 November 2019 on the Climate and Environment Emergency (2019/2930(RSP)). Available online: https://www.europarl.europa.eu/doceo/document/TA-9-2019-0078_EN.pdf (accessed on 26 April 2022).
4. Institut Català de l'Energia. Llei de Transició Energètica de Catalunya i Transformació de l'Institut Català d'Energia at l'Agència d'Energia de Catalunya. Available online: http://icaen.gencat.cat/ca/participacio/llei-de-transicio-energetica-de-catalunya-i-transformacio-de-linstitut-catala-denergia-en-lagencia-denergia-de-catalunya/ (accessed on 26 April 2022).
5. Institut Català de l'Energia. Prospectiva Energètica de Catalunya 2050 (PROENCAT 2050). Documento Resumen Presentado el 4 de Febrero de 2022. Available online: http://icaen.gencat.cat/es/l_icaen/prospectiva_planificacio/ (accessed on 26 April 2022).
6. Ministerio para la Transición Ecológica y el Reto Demográfico. Proyecto de Real Decreto/2021 por el que se Aprueban los Planes de Ordenación del Espacio Marítimo de las Cinco Demarcaciones Marinas Españolas. 2021. Available online: https://www.miteco.gob.es/es/costas/temas/proteccion-medio-marino/ordenacion-del-espacio-maritimo/default.aspx (accessed on 26 April 2022).
7. Salvador, S.; Gimeno, L.; Sanz Larruga, F.J. The influence of regulatory framework on environmental impact assessment in the development of offshore wind farms in Spain: Issues, challenges and solutions. *Ocean. Coast. Manag.* **2018**, *161*, 165–176. [CrossRef]
8. Verma, S.; Akshoy, R.P.; Nawshad, H. Selected Environmental Impact Indicators Assessment of Wind Energy in India Using a Life Cycle Assessment. *Energies* **2022**, *15*, 3944. [CrossRef]
9. Kouloumpis, V.; Azapagic, A. A model for estimating life cycle environmental impacts of offshore wind electricity considering specific characteristics of wind farms. *Sustain. Prod. Consum.* **2022**, *29*, 495–506. [CrossRef]
10. Chowdhury, N.E.; Shakib, M.A.; Xu, F.; Sayedus, S.; Islam, M.R.; Bhuiyan, A.A. Adverse environmental impacts of wind farm installations and alternative research pathways to their mitigation. *Clean. Eng. Technol.* **2022**, *7*, 100415. [CrossRef]
11. Lloret, J.; Turiel, A.; Solé, J.; Berdalet, E.; Sabatés, A.; Olivares, A.; Gili, J.M.; Vila-Subirós, J.; Sardá, R. Unravelling the ecological impacts of large-scale offshore wind farms in the Mediterranean Sea. *Sci. Total Environ.* **2022**, *824*, 153803. [CrossRef]
12. Conesa, V. *Guía Metodológica para la Evaluación del Impacto Ambiental*, 4th ed.; Mundi-Prensa: Madrid, Spain, 2010.
13. Seacon. *Sediment Spillage during Array Cable Installation at Nysted Offshore Wind Farm*; Report 0402-1-1-L001 rev.1; GS SEACON APS: Ringsted, Denmark, 2005.
14. Elliott, J.; Smith, K.; Gallien, D.R.; Khan, A.A. Observing Cable Laying and Particle Settlement During the Construction of the Block Island Wind Farm. In *Final Report to the U.S. Department of the Interior*; Bureau of Ocean Energy Management, Office of Renewable Energy Programs: Washington, DC, USA, 2017; p. 225.
15. Martín, J.; Puig, P.; Palanques, A.; Ribó, M. Trawling-induced daily sediment resuspension in the flank of a Mediterranean submarine canyon. *Deep. Sea Res. Part II Top. Stud. Oceanogr.* **2014**, *104*, 174–183. [CrossRef]
16. McCauley, R.D.; Duncan, A.J.; Penrose, J.D.; McCabe, K.A. Marine Seismic Surveys: A Study of Environmental Implications. *APPEA J.* **2000**, *40*, 692–708. Available online: http://citeseerx.ist.psu.edu/viewdoc/download?doi=10.1.1.624.3763&rep=rep1&type=pdf (accessed on 26 April 2022). [CrossRef]

17. Ministerio de Agricultura, Alimentación y Medio Ambiente. Documento Técnico Sobre Impactos y Mitigación de la Contaminación Acústica Marina. Madrid. 2012, p. 146. Available online: https://www.miteco.gob.es/es/costas/temas/proteccion-medio-marino/doc-tecnico-impactos-mitigacion-contaminacion-acustica-marina_tcm30-157028.pdf (accessed on 26 April 2022).
18. CEDA. Ceda Position Paper: Underwater Sound in Relation to Dredging. *Terra Aqua* **2011**, *125*, 23–28.
19. Taormina, B.; Bald, J.; Want, A.; Thouzeau, G.; Lejart, M.; Desroy, N.; Carlier, A. A review of potential impacts of submarine power cables on the marine environment: Knowledge gaps, recommendations and future directions. *Renew. Sustain. Energy Rev.* **2018**, *96*, 380–391. [CrossRef]
20. Nedwell, J.R.; Workman, R.; Parvin, S.J. *The Assessment of Likely Levels of Piling Noise at Greater Gabbard and Its Comparison with Background Noise, Including Piling Noise Measurements Made at Kentish Flats*; Report No. 633R0115; Subacoustech Environmental Limited: Southampton, UK, 2005.
21. DNVGL. Rules for Classification, Ships. Part 6 Additional Class Notations, Chapter 7 Environmental Protection and Pollution Control. Edition January 2017. Available online: https://rules.dnv.com/docs/pdf/DNV/ru-ship/2017-01/DNVGL-RU-SHIP-Pt6Ch7.pdf (accessed on 26 April 2022).
22. Martin, B.; MacDonnell, J.; Vallarta, J.; Lumsden, E.; Burns, R. HYWIND Acoustic Measurement Report: Ambient Levels and HYWIND Signature. Technical Report for Statoil by JASCO Applied Sciences. 2011. Available online: https://www.equinor.com/content/dam/statoil/documents/impact-assessment/hywind-tampen/Equinor-Hywind-Acoustic-Measurement-Report-JASCO-00229-December-2011.pdf (accessed on 26 April 2022).
23. HDR. Field Observations during Wind Turbine Operations at the Block Island Wind Farm, Rhode Island. Final Report to the U.S. Department of the Interior, Bureau of Ocean Energy Management, Office of Renewable Energy Programs. OCS Study BOEM 2019-028. 2019; p. 281. Available online: https://espis.boem.gov/final%20reports/BOEM_2019-028.pdf (accessed on 26 April 2022).
24. Westerberg, H.; Bégout, M.L. Orientation of silver eel (*Anguilla anguilla*) in a disturbed geomagnetic field. Advances in Fish Telemetry. In Proceedings of the 3rd Conference on Fish Telemetry, Norwich, UK, 1 January 2000; pp. 149–158.
25. Fuxjager, M.; Eastwood, B.; Lohmann, K. Orientation of Hatchling Loggerhead Sea Turtles to Regional Magnetic Fields along a Transoceanic Migratory Pathway. *J. Exp. Biol.* **2011**, *214*, 2504–2508. Available online: https://www.researchgate.net/publication/51489400_Orientation_of_hatchling_loggerhead_sea_turtles_to_regional_magnetic_fields_along_a_transoceanic_migratory_pathway (accessed on 26 April 2022). [CrossRef]
26. Ottaviani, E.; Malagoli, D.; Ferrari, A.; Tagliazucchi, D.; Conte, A.; Gobba, F. 50 Hz Magnetic fields of varying flux intensity affect cell shape changes in invertebrate immunocytes: The Role of potassium ion channels. *Bioelectromagnetics* **2002**, *23*, 292–297. [CrossRef] [PubMed]
27. Malagoli, D.; Gobba, F.; Ottaviani, E. 50 Hz magnetic fields activate mussel immunocyte p38 MAP kinase and induce HSP70 and 90. *Comp. Biochem. Physiol. C Toxicol. Pharmacol.* **2004**, *137*, 75–79. [CrossRef] [PubMed]
28. Hutchison, Z.; Sigray, P.; He, H.; Gill, A.; King, J.; Gibson, C. *Electromagnetic Field (EMF) Impacts on Elasmobranch (Shark, Rays, and Skates) and American Lobster Movement and Migration from Direct Current Cables (No. BOEM 2018-003)*; Bureau of Ocean Energy Management (BOEM): Narragansett, RI, USA, 2018. Available online: https://espis.boem.gov/final%20reports/5659.pdf (accessed on 26 April 2022).
29. Woodruff, D.L.; Ward, J.A.; Schultz, I.R.; Cullinan, V.I.; Marshall, K.E. Effects of Electromagnetic Fields on Fish and Invertebrates. In *Task 2.1.3: Effects on Aquatic Organisms Fiscal Year 2011 Progress Report-Environmental Effects of Marine and Hydrokinetic Energy (No. PNNL-20813 Final)*; Pacific Northwest National Laboratory (PNNL): Richland, WA, USA, 2012. Available online: https://www.pnnl.gov/main/publications/external/technical_reports/PNNL-20813Final.pdf (accessed on 26 April 2022).
30. Bochert, R.; Zettler, M.L. Long-Term Exposure of Several Marine Benthic Animals to Static Magnetic Fields. *Bioelectromagnetics* **2004**, *25*, 498–502. Available online: https://www.researchgate.net/publication/8338761_Long-term_exposure_of_several_marine_benthic_animals_to_static_magnetic_fields (accessed on 26 April 2022). [CrossRef] [PubMed]
31. CMACS. A Baseline Assessment of Electromagnetic Fields Generated by Offshore Windfarm Cables. COWRIE Report EMF-01-2002-66. 2003. Available online: https://tethys.pnnl.gov/sites/default/files/publications/COWRIE_EMF_Offshore_Cables.pdf (accessed on 26 April 2022).
32. Gill, A.B.; Taylor, H. The Potential Effects of Electromagnetic Fields Generated by Cabling between Offshore Wind Turbines upon Elasmobranch Fishes. Countryside Council for Wales 2001. CCW Contract Science Report No 488. Available online: https://tethys.pnnl.gov/sites/default/files/publications/Gill%20and%20Taylor%202001.PDF (accessed on 26 April 2022).
33. Smith, E. Electro-physiology of the electrical shark-repellant. *Trans. Korean Inst. Electr. Eng.* **1974**, *65*, 1–20.
34. Kalmijn, A.J. Detection and Processing of Electromagnetic and Near-field Acoustic Signals in Elasmobranch Fishes. *Philos. Trans. R. Soc. Lond. Board Biol. Sci.* **2000**, *355*, 1135–1141. [CrossRef]
35. Walker, M.M.; Diebel, C.E.; Kirschvink, J.L. Detection and use of the Earth's Magnetic Field by Aquatic Vertebrates. In *Sensory Processing in Aquatic Environments*; Collins, S.P., Marshall, N.J., Eds.; Springer: New York, NY, USA, 2003; pp. 53–74.
36. Nyqvist, D.; Durif, C.; Johnsen, M.G.; de Jong, K.; Forland, T.N.; Sivle, L.D. Electric and Magnetic Senses in Marine Animals, and Potential Behavioral Effects of Electromagnetic Surveys. *Mar. Environ. Res.* **2020**, *155*, 104888. [CrossRef]
37. Farr, H.; Ruttenberg, B.; Walter, R.; Wang, Y.-H.; White, C. Potential environmental effects of deepwater floating offshore wind energy facilities. *Ocean. Coast. Manag.* **2021**, *207*, 16. [CrossRef]
38. Platis, A.; Siedersleben, S.; Bange, J.; Lampert, A.; Bärfuss, K.; Hankers, R.; Canadillas, B.; Foreman, R.; Schulz-Stellenfleth, J.; Djath, B.; et al. First in situ evidence of wakes in the far field behind offshore wind farms. *Sci. Rep.* **2018**, *8*, 2163. [CrossRef]

39. Christiansen, M.B.; Hasager, C.B. Wake effects of large offshore wind farms identified from satellite SAR. *Remote Sens. Environ.* **2005**, *98*, 251–268. [CrossRef]
40. Van Berkel, J.; Burchard, H.; Christensen, A.; Mortensen, L.O.; Svenstrup Petersen, O.; Thomsen, F. The Effects of Offshore Wind Farms on Hydrodynamics and Implications for Fishes. *Oceanography* **2020**, *33*, 108–117. [CrossRef]
41. Zenetos, A.; Gofas, S.; Morri, C.; Rosso, A.; Violanti, D.; García Raso, E.; Cinar, M.E.; Almogi-Labin, A.; Ates, A.S.; Azzurro, E.; et al. Alien species in the Mediterranean Sea by 2012. A contribution to the application of European Union's Marine Strategy Framework Directive (MSFD). Part 2. Introduction trends and pathways. *Mediterr. Mar.* **2012**, *13*, 328–352. [CrossRef]
42. Otero, M.; Cebrian, E.; Francour, P.; Galil, B.; Savini, D. Monitoreo de Especies Marinas Invasoras at áreas Marinas Protegidas (AMP) del Mediterráneo: Estrategia y Guía Práctica Para Gestores. UICN 2013. p. 136. Available online: https://portals.iucn.org/library/efiles/documents/2013-008-Es.pdf (accessed on 26 April 2022).
43. Subías-Baratau, A.; Sànchez-Vidal, A.; Di Martino, E.; Figuerola, B. Marine biofouling organisms on beached, buoyant and benthic plastic debris in the Catalan Sea. *Mar. Pollut. Bull.* **2022**, *175*, 113405. [CrossRef] [PubMed]
44. Pastor, X. L'eòlica Marina, Una Aliada de la Biodiversitat. Published at el Diari de Girona, on 6 March 2022. Available online: https://www.diaridegirona.cat/opinio/2022/03/06/l-eolica-marina-aliada-biodiversitat-63484707.html (accessed on 26 April 2022).

Journal of
*Marine Science and Engineering*

MDPI

*Article*

# A Numerical Simulation of a Variable-Shape Buoy Wave Energy Converter

**Shangyan Zou [1,†] and Ossama Abdelkhalik [2,*,†,‡]**

[1] School of Civil and Constructional Engineering, Oregon State University, Corvallis, OH 97331, USA; shangyan.zou@oregonstate.edu
[2] Department of Aerospace Engineering, Iowa State University, Ames, IA 50011, USA
* Correspondence: ossama@iastate.edu
† These authors contributed equally to this work.
‡ 2241 Howe Hall, 537 Bissell Road, Ames, IA 50011, USA.

**Abstract:** Wave energy converters (WECs) usually require reactive power for increased levels of energy conversion, resulting in the need for more complex power take-off (PTO) units, compared to WECs that do not require reactive power. A WEC without reactive power produces much less energy, though. The concept of Variable Shape Buoy Wave Energy Converters (VSB WECs) is proposed to allow continuous shape-change aiming at eliminating the need for reactive power, while converting power at a high level. The proposed concept involves complex and nonlinear interactions between the device and the waves. This paper presents a Computational Fluid Dynamics (CFD) tool that is set up to simulate VSB WECs, using the ANSYS 2-way fluid–structure interaction (FSI) tool. The dynamic behavior of a VSB WEC is simulated in this CFD-based Numerical Wave Tank (CNWT), in open sea conditions. The simulation results show that the tested device undergoes a significant deformation in response to the incoming waves, before it reaches a steady-state behavior. This is in agreement with a low-fidelity dynamic model developed in earlier work. The resulting motion is significantly different from the motion of a rigid body WEC. The difference in the motion can be leveraged for better energy capture without the need for reactive power.

**Keywords:** ocean wave energy; flexible wave energy converters; Computational Fluid Dynamics; fluid–structure interaction; highly nonlinear dynamics

**Citation:** Zou, S.; Abdelkhalik, O. A Numerical Simulation of a Variable-Shape Buoy Wave Energy Converter. *J. Mar. Sci. Eng.* **2021**, *9*, 625. https://doi.org/10.3390/jmse9060625

Academic Editor: Eva Loukogeorgaki

Received: 10 May 2021
Accepted: 31 May 2021
Published: 4 June 2021

**Publisher's Note:** MDPI stays neutral with regard to jurisdictional claims in published maps and institutional affiliations.

**Copyright:** © 2021 by the authors. Licensee MDPI, Basel, Switzerland. This article is an open access article distributed under the terms and conditions of the Creative Commons Attribution (CC BY) license (https://creativecommons.org/licenses/by/4.0/).

## 1. Introduction

Wave energy conversion has been attracting more research attention due to the rising demand for renewable energy and its advantages including high power density [1], large energy potential, and consistency. Yet, wave energy conversion is still in the pre-commercial phase. In the last decade, the dynamics and control of WECs were significantly investigated. Starting from linear models, which are widely applied in developing optimal controls [2–5], to nonlinear hydrodynamics (especially nonlinear FK force) [6,7], to high-fidelity CNWT simulations of wave energy converters [8,9]. In recent years, significant research effort has been made to improve the economic index of wave energy conversion. Yet, some challenges still exist; one of which is the need for reactive power to optimize energy production. Some conventional optimal control methods [4] aim to achieve resonance between the device and ocean waves to maximize energy production; yet a complex PTO unit would be required to produce reverse power flow, which represents a high expenditure and the generated power quality is poor (large fluctuation) [10,11]. On the other hand, using damping control does not require reactive power, but the performance of the WEC is degraded in terms of power production.

The concept of VSB WECs was recently proposed to address this challenge. The VSB WEC has a'soft' buoy, allowing relatively rapid shape-changing in response to pressure variations. This is unlike the conventional rigid WECs and unlike the concept of variable

geometry WECs [12–15] in which a rigid WEC changes shape occasionally and slowly in response to changing wave conditions. The VSB WEC involves nonlinear interaction between the device and the waves (continuous deformation in response to the waves). This interaction can be leveraged to produce more power without the need for reactive power. The motion of the device can be excited due to the deformation as pointed out in reference [16], which employs a physics-based low-fidelity model.

Since the proposed device involves complex and nonlinear hydrodynamics, a tool for high-fidelity simulation is developed in this paper to investigate the behavior of VSB WEC. Due to the nature of this problem, a FSI tool that can handle variable-shape (morphing) structure is needed in the CNWT. This is unlike most existing high-fidelity WEC simulation tools [8], which can handle only rigid body FSI. The FSI capability employed in this paper implements 2-way FSI; the data is transferred between the solid domain (finite element analysis (FEA) model) and the fluid domain (CFD model). As far as the simulation software is concerned, ANSYS® and OpenFOAM are both widely applied in developing CNWTs and solving FSI [17]. The ANSYS 2-way FSI (system coupling simulation) is used in this paper. As detailed in this paper, this type of problem requires large mesh motions; this is accommodated in this paper using the diffusion-based mesh smoothing method.

The main contribution of this paper is to develop a high-fidelity simulation tool that enables the investigation of the recently proposed VSB WECs, which are characterized by their nonlinear hydrodynamics. The tool presented in this paper will enable the validation of other low fidelity models for VSB WECs that are usually used for WEC control design and analysis. The paper is organized as follows: numerical modeling is introduced in Section 2 and mesh generation is introduced in Section 3. Sections 4 and 5 present the simulation results and discussion, respectively. Finally, the conclusion is drawn in Section 6 with the plan for future work.

## 2. Numerical Modeling

The details of the numerical simulation approach applied in this study are introduced in this section. A schematic view of the proposed device and the computational domain is presented in Figure 1. As shown in the figure, the dimensions of the computational domain are 80 × 60 × 60 m. The height of the Free Surface Level (FSL) is 40 m measured from the global coordinate system, which is also shown in the figure. Since the proposed device is allowed to change the shape in response to the waves, a significant interaction between the device and waves is expected. By applying ANSYS 2-way FSI, the data transfers between solid and fluid are created on the interface between solid and surrounding fluids (denoted as FSI 1) and the interface between solid and internal gas (denoted as FSI 2). The device initially has a shape of a hollow sphere with a radius of 2 m and a thickness of 0.3 m.

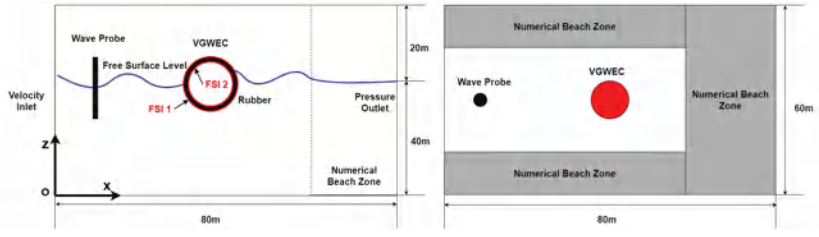


**Figure 1.** Computational domain layout.

### 2.1. Governing Equations

Three stratified phases including the environmental air, environmental water and chamber gas are applied in this simulation. Although the environmental air and water are assumed to be incompressible, the chamber gas is assumed to be compressible since the chamber has a large volumetric change due to the interaction between VSB WEC and

waves. The conservation equations for unsteady compressible fluid simulation can be written as:

$$\begin{aligned} &\frac{\partial \rho}{\partial t} + \nabla \cdot (\rho \vec{v}) = 0 \\ &\frac{\partial}{\partial t}(\rho \vec{v}) + \nabla \cdot (\rho \vec{v} \vec{v}) = -\nabla p + \nabla \cdot (\bar{\bar{\tau}}) + \rho \vec{g} + \vec{F} \\ &\frac{\partial}{\partial t}(\rho E) + \nabla \cdot (\vec{v}(\rho E + p)) = \nabla \cdot (k_e \nabla T) \end{aligned} \tag{1}$$

where $\rho$ is the fluid density, $\vec{v}$ is the flow velocity vector in the continuity equation. In the momentum equation, $\bar{\bar{\tau}}$ is the stress tensor, and $\rho \vec{g}$ represents the gravitational body force. Since in this study, the wave absorption zone is included near the pressure outlet, the source term $\vec{F}$ is added in the momentum conservation due to the applied numerical beach treatment. Further, in the energy equation, $E$ is the energy, and $k_e$ is the effective thermal conductivity. A transient Reynolds Averaged Navier Stokes (RANS) solver is applied with the governing equations discretized over the fluid domain by using finite volume method. The fluid simulation (CFD) is further coupled with transient structural analysis (FEA).

### 2.2. Physics Modeling

The turbulence model applied in this study is the realizable $k - \epsilon$ model, which is considered robust and computational efficient [17]. Compared to the widely applied standard $k - \epsilon$, the applied model provides more robustness, which is more suitable in this study since the interaction between the device and the waves is highly nonlinear. The transport equations for turbulent kinetic energy ($k$) and dissipation rate ($\epsilon$) will be solved. Details about the mathematical modeling of the k-epsilon turbulent model can be found in [18,19]. Furthermore, since the chamber gas has a negligible motion with respect to the device, the internal fluid domain is considered to be laminar.

The Volume of Fluid (VOF) method is applied to simulate the multi-phase flow. Environmental air is assumed to be the primary phase, and the environmental water and chamber gas are both assumed to be the secondary phase. To track the interface (e.g., free surface) between different phases, the volume fraction equation is applied:

$$\frac{\partial (\alpha_q \rho_q)}{\partial t} + \nabla \cdot (\alpha_q \rho_q \vec{v}_q) = 0 \tag{2}$$

where $\rho_q$ and $\alpha_q$ are the density and volume fraction of the $q$th fluid (phase $q$). The volume fraction $\alpha_q$ varies between 0 and 1 in a cell. For each cell, it is possible that:

$$\begin{aligned} &\alpha_q = 0 \text{ if the cell is empty of phase } q \\ &0 < \alpha_q < 1 \text{ if the cell contains interface} \\ &\text{between phase } q \text{ and other phases} \\ &\alpha_q = 1 \text{ if the cell is full of phase } q \end{aligned} \tag{3}$$

Furthermore, the summation of the volume fraction of all phases should be unity:

$$\sum_{q=1}^{n} \alpha_q = 1 \tag{4}$$

To further sharpen the free surface between environmental air and water, the interfacial anti-diffusion is enabled by adding a negative diffusion source term in the volume fraction equation [20]:

$$\frac{\partial \alpha_q}{\partial t} + \nabla \cdot (\vec{v}_q \alpha_q) = -\nabla \cdot (\vec{v}_c \alpha_q (1 - \alpha_q)) \tag{5}$$
$$\vec{v}_c = \gamma |\vec{v}_q| \frac{\nabla \alpha_q}{|\nabla \alpha_q|}$$

where $\vec{v}_c$ and $\vec{v}_q$ represent the compression velocity normal to the interface and cell velocity, respectively, and $\gamma$ is the compression factor.

Moreover, the large mesh motion due to the highly nonlinear interaction is accounted by diffusion-based smoothing dynamic mesh method. The pressure–velocity coupling problem is solved by the coupled algorithm to achieve aggressive convergence in transient simulation of the proposed challenging model. The density, momentum, turbulence, and energy are spatially discretized based on the second-order upwind scheme. The applied transient formulation is first-order implicit.

### *2.3. Domain and Boundary Conditions*

The boundary conditions applied in this study are summarized in Figure 2. The waves are generated from the velocity inlet, and the downstream boundary is specified as a pressure outlet. Symmetry boundary conditions are applied for the top, bottom, and sides boundary conditions. The purpose of setting the symmetry boundary conditions is to construct an open sea condition for the simulation where the deep water and infinite air assumptions are applied. As addressed in [21], velocity inlet and slip wall are also considered as appropriate selections for the top, bottom, and sides boundary conditions if the boundaries are located far away from the device (which is the case in this study). The interface between the surrounding fluids and the solid and between the chamber gas and the solid are both defined as adiabatic walls. A mesh will be morphed around the solid to account for the motion and deformation of the device.

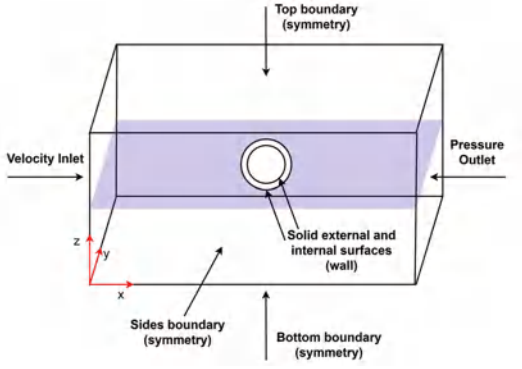


**Figure 2.** Boundary conditions applied in the simulation.

Since open sea conditions are applied in this study, the generated waves are assumed to be deep water waves with regard to a water depth 60 m. To prevent the drifting of the device, the flow current velocity is assumed to be zero. The Person–Monskowitz (PM) wave spectrum is applied as the irregular wave spectrum:

$$S_{PM}(\omega) = \frac{5}{16} \frac{H_s^2 \omega_p^4}{\omega^5} e^{-\frac{5\omega_p^4}{4\omega^4}} \tag{6}$$

where $H_s$ is the significant wave height and $\omega_p = \frac{2\pi}{T_p}$ is the peak frequency. The irregular wave that has a significant height of $H_s = 1$ m and a peak period of $T_p = 6$ s is applied in this paper given the fact that typical peak period of ocean waves varies from 6 s to 12 s. The frequency range of the wave is from 0.2 rad·s$^{-1}$ to 4 rad·s$^{-1}$ and the number of frequencies is 20. Moreover, deep water waves are normally multidirectional waves, thus the directional spreading function also needs to be specified. The widely applied cos-2$s$ directional spreading function [22–24] is applied in this study:

$$G(\theta) = G(s)\cos^{2s}\left(\frac{\pi}{2\theta_s}(\theta - \theta_p)\right) \tag{7}$$

where $s$ is the frequency independent cosine exponent, which is a positive integer. $\theta_p$ is the mean wave heading angle, and $\theta_s$ is angle spreading from $\theta_p$. In this paper, $s$ is selected as 30 for deep water waves as suggested in [25]. The mean wave heading angle is 0° and the spreading angle is 90°, which is found to be a good assumption for directional spreading when $s > 5$ [25]. Additionally, the number of angular components is chosen as 10. The resulting wave spectrum is the multiplication of the frequency spreading and directional spreading:

$$S(\omega, \theta) = S_{PM}(\omega)G(\theta) \tag{8}$$

The final wave field will be generated based on the wave spectrum by taking superposition of different wave components:

$$\eta(r,t) = \sum_{i=1}^{N_f}\sum_{j=1}^{N_a} a_{ij}cos(k_{x,ij}x + k_{y,ij}y - \omega_i t + \phi_{ij}) \tag{9}$$

where $a = \sqrt{2\int_{\theta-\frac{\delta\theta}{2}}^{\theta+\frac{\delta\theta}{2}}\int_{\omega-\frac{\delta\omega}{2}}^{\omega+\frac{\delta\omega}{2}} S(\omega,\theta)d\omega d\theta}$ is the amplitude of each wave component. Further, $k_{x,ij} = k_i\cos(\theta_j)$ and $k_{y,ij} = k_i\sin(\theta_j)$, where $k_i$ is the wave number of the $i$th wave component (which has a frequency of $\omega_i$) and $\theta_j$ is the $j$th wave heading. Random phase shift $\phi_{ij}$ is used in generating the wave field, which is uniformly distributed in $[0, 2\pi]$.

A multiple-directional numerical beach (as shown in Figure 1) is implemented in the vicinity of the downstream and the sides to suppress the wave reflection. A damping sink term is added in the momentum equation for this damping zone:

$$S = -[C_1\rho V + \frac{1}{2}C_2\rho \mid V \mid V]f(z)f(x) \tag{10}$$

where $C_1 = 116.24631$/s and $C_2 = 3192.6571$/m are the linear and quadratic damping resistance, respectively. $V$ is the vertical velocity, $z$ is the distance measured from FSL, and $x$ is the distance along the flow direction. The length of the multi-directional beach in the downstream (beach direction $[1, 0, 0]$) is specified as twice the wave length ($D = 2\lambda$) [26,27] and the length of the damping zone in the sides (beach direction $[0, 1, 0]$ and $[0, -1, 0]$) is defined as one wave length ($D = \lambda$).

## 3. Mesh Generation

Mesh quality is critical for free surface flows and the proposed challenging model, which involves highly nonlinear interaction between VSB WEC and the waves. Although a structured mesh provides better efficiency and accuracy in the simulation, it has the difficulty in tracking curved or complex geometries. On the other hand, the unstructured mesh is suitable to track complex geometries and change the mesh size locally, while a significant number of cells are required to ensure accuracy [28]. Therefore a hybrid mesh generation is performed in the fluid domain using ANSYS FLUENT meshing application. The structured mesh is applied in the background with a larger element size and the unstructured mesh is applied near the hull of the device and the internal gas domain with

smaller element size. Though hybrid mesh has the advantages of computationally efficient and tracking features accurately, the resulting mesh is non-conformal due to different mesh topologies applied in different zones. Thus, the meshes are matched in the faces that are meshed with different topologies in the calculation.

The mesh of the overall computational domain is presented in Figure 3. As shown in the figure, the unstructured mesh is applied in a refined region, which has a box shape and internal gas domain with a smaller mesh size. The mesh is also locally refined in the regions that require extra accuracy. It is clearly visible in Figure 3 that the mesh in the expected free surface is refined. In addition, as shown in Figure 4, the mesh is also refined in the interface between surrounding fluids and solid and the interface between the internal fluid and the solid to capture the geometry and motion of the device. Moreover, inflation layers are placed in the boundary layer along the surface (with respect to the surrounding fluids) of VSB WEC to capture the rapid velocity change. As shown in Figure 5, the unstructured mesh is also applied in the solid domain to capture the geometry. Since the applied geometry is a simple hollow sphere, no local mesh refinement is used in the solid domain.

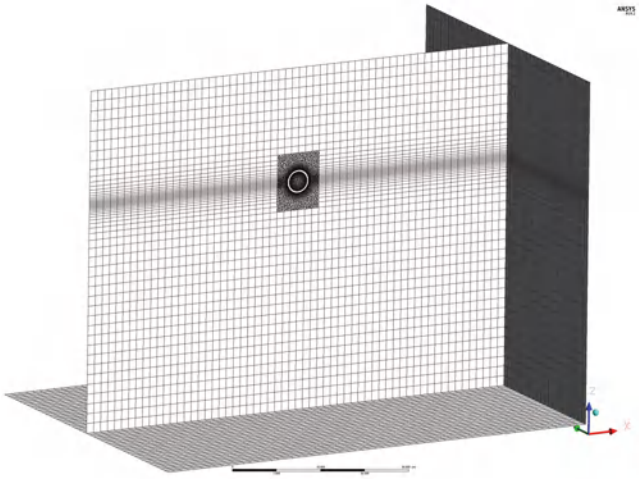

**Figure 3.** Mesh generation of the overall computational domain. Faces selected for presentation are bottom, outlet, and a cross-sectional face located at $y = 30$ m.

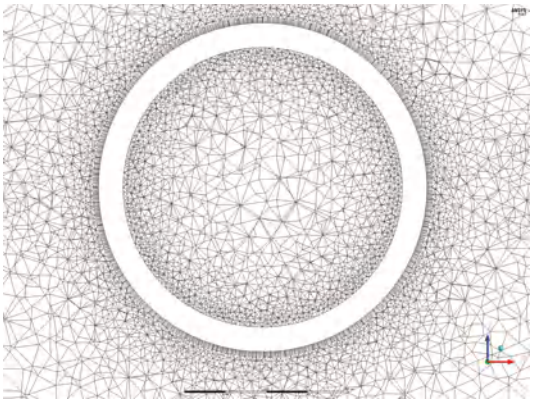

**Figure 4.** Mesh generation around the body surface with the mesh refinement at the interfaces and the boundary layer.

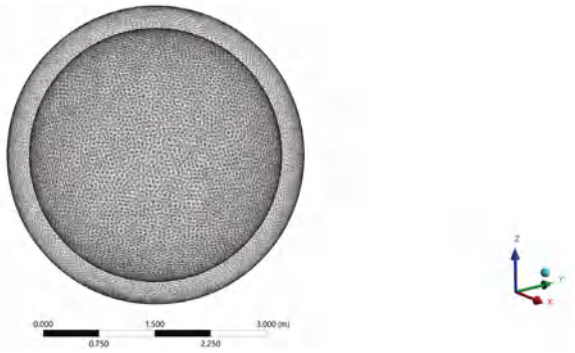


**Figure 5.** Mesh generation for the solid domain.

To select an appropriate grid resolution, a mesh sensitivity analysis is performed with three different levels of mesh resolutions (coarse, medium, and fine). The device is assumed to be rigid body (fixed-shape) in this analysis, and the details of each grid resolution are summarized in Table 1. The structured mesh is applied in the background, which occupies around 99.8% of the fluid domain, while only 18.4% of the cells of the fluid domain are formed in the background when the medium mesh is applied. On the other hand, nearly 81.6% of the cells (unstructured mesh) are concentrated in less than 0.2% of the fluid volume. The presented mesh arrangement allows a significantly reduced number of cells in the background to accelerate the calculation and keeps the accuracy of the simulation near the wave and structure interaction. The three-dimensional motions of the center of gravity (CoG) of the device (assumed rigid body) versus different mesh resolutions are plotted in Figures 6–8. As shown in the figures, the medium mesh is considered to be an appropriate mesh resolution since it provides close accuracy as the fine mesh while significantly saves the computational cost. Notably, the motion of the device in the y-direction is predicted inaccurately by applying the coarse mesh. The corresponding mesh size applied in different domains of the medium mesh is summarized in the following. The grid resolution applied on the body surfaces is 0.06 m (most refined) and applied in the background is 1.7 m. Moreover, the mesh is refined in the Refined Region (unstructured) with a mesh size of 0.42 m and the free surface is locally refined with a grid resolution of 0.17 m. The resulting minimum cell volume and maximum cell volume of the fluid domain are $2.12 \times 10^{-6}$ $m^3$ and 3.25 $m^3$, respectively. The similar mesh size (medium mesh) will be applied for the following simulations of VSB WEC (without assuming fixed-shape).

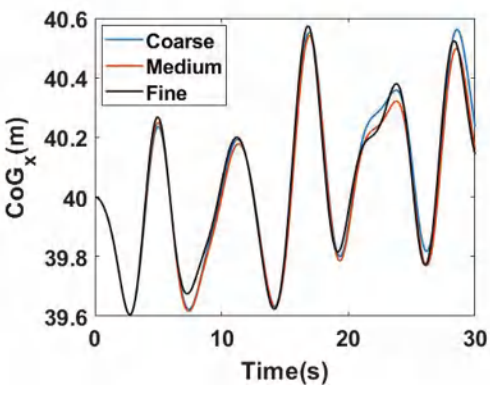


**Figure 6.** x-directional motion of the center of gravity of the device with different mesh resolutions.

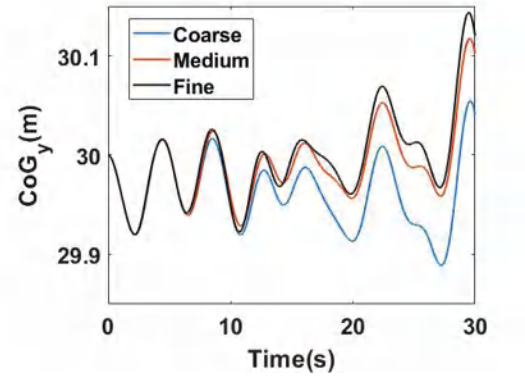


**Figure 7.** y-directional motion of the center of gravity of the device with different mesh resolutions.

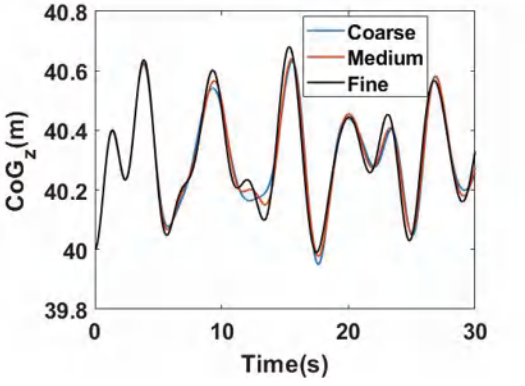


**Figure 8.** z-directional motion of the center of gravity of the device with different mesh resolutions.

**Table 1.** The breakdown of different types of mesh applied in mesh sensitivity analysis.

| Mesh Types | Number of Cells | | Total |
|---|---|---|---|
| | Background | Refined Region | |
| Coarse | 112,536 | 281,661 | 394,197 |
| Medium | 144,300 | 640,014 | 784,314 |
| Fine | 331,996 | 1,628,346 | 1,960,342 |

## 4. Numerical Results

The system coupling simulations are carried out on Iowa State University's High-Performance Computer (HPC). The number of processors used in the parallel simulation is 36 and the corresponding elapsed time for the simulation of VSB WEC with medium mesh is approximately 96.6 hrs including post-processing. To guarantee the flow current number is close to 1, the time step is selected as 0.01 s and a total of 3000 steps will be solved (simulation end time is 30 s). Although, a more robust analysis (may be conducted in the future) can be conducted by significantly extending the simulation timeseries (e.g., 20 min simulation for varied wave conditions). Giving that the computational cost of this simulation is extremely high, only a short time period (30 s) will be simulated and analyzed. Additionally, the applied simulation end time covers part of the steady-state responses, which provides meaningful results for both transient and steady-state analysis.

### 4.1. Free Decay Test

To validate the proposed simulator, a free heave decay test is first performed. The device (assumed rigid body in the decay test) is initially placed 1.3 m away from the equilibrium point with no initial velocity. As shown in Figure 9, the natural decay period of the device is found to be around 2.6 s. Moreover, the energy given to the device can be successfully dissipated by the implemented multi-directional numerical beach, and the device stays at the equilibrium without being excited by reflected waves (absorbed).

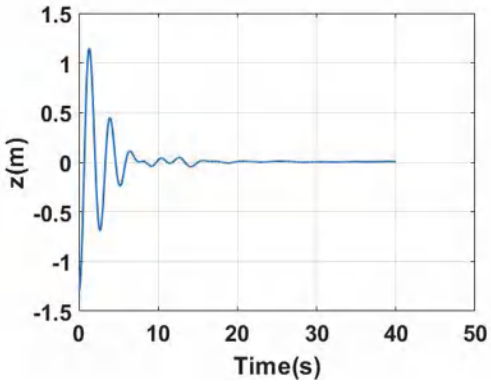


**Figure 9.** Heave decay test.

### 4.2. Irregular Wave Generation

As described in Section 2.3, multi-directional irregular waves will be applied in this study to simulate open sea conditions. A wave probe is placed between the inlet and the device (at $y = 30$ m) to monitor the free surface elevation (as shown in Figure 1). As suggested in [29], the distance between the inlet and the wave probe is $1L = 11$ m. The surface elevation measured at the free surface ($\alpha_{air} = 0.5$) by the wave probe is shown in Figure 10.

The wave pattern on the free surface is presented in Figures 11–14 at different time instants when the most significant interaction between waves and the device happens and at the end of the simulation. It is visible in the figure that the wave pattern (which is multidirectional) is significantly affected around the device due to the strong interaction. Although, a wavy water surface is assumed initially, the wave pattern near the outlet and the sides is flattened during the simulation (as shown in Figure 14). To better illustrate the influence of the wave forces on the motion and deformation of VSB WEC, Figures 15 and 16 show the dynamic pressure field around the device at two different time instants. A large dynamic pressure acts on the bottom of the device at $t = 0.5$ s with a peak pressure around $2.89 \times 10^3$ Pa, which not only causes a motion, but also a deformation of the hull (compress the device). At $t = 1.5$ s, there is also a significant deformation of the bottom half of the device (mainly at the sides) and peak dynamic pressure is around $0.696 \times 10^3$ Pa acts on the wet surface in upstream. By presenting these figures, we can claim the challenging interaction between the waves and the device is successfully captured by the proposed CFD model.

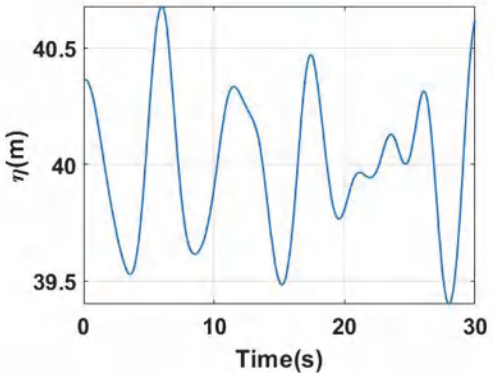


**Figure 10.** Free surface elevation measured at the wave probe.

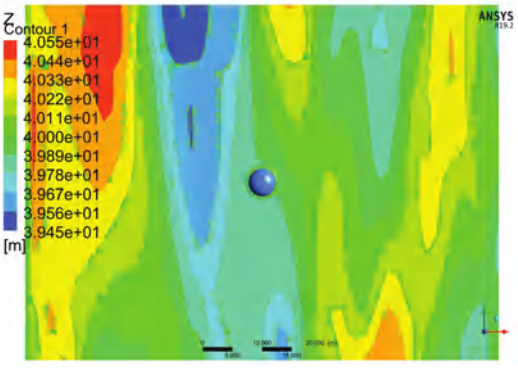


**Figure 11.** Wave pattern on the free surface at $t = 0.5$ s.

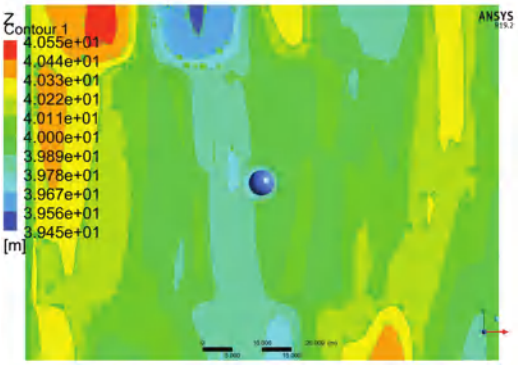


**Figure 12.** Wave pattern on the free surface at $t = 1$ s.

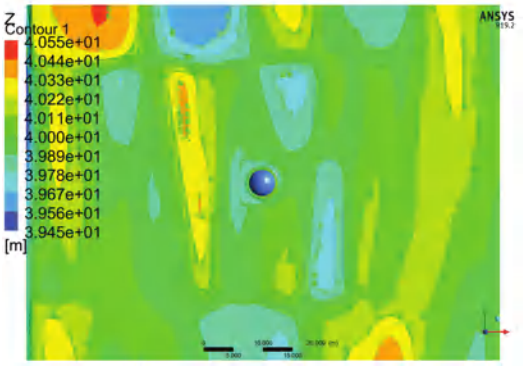


**Figure 13.** Wave pattern on the free surface at $t = 1.5$ s.

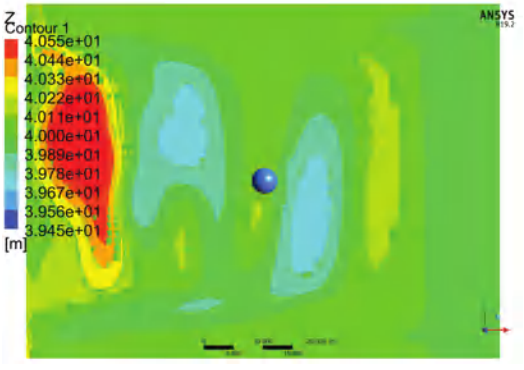


**Figure 14.** Wave pattern on the free surface at $t = 30$ s.

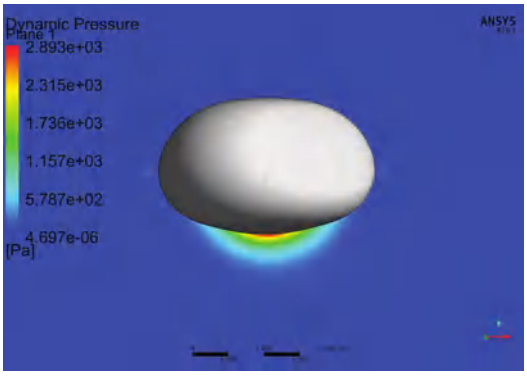


**Figure 15.** Dynamic pressure field measured around the device at $t = 0.5$ s.

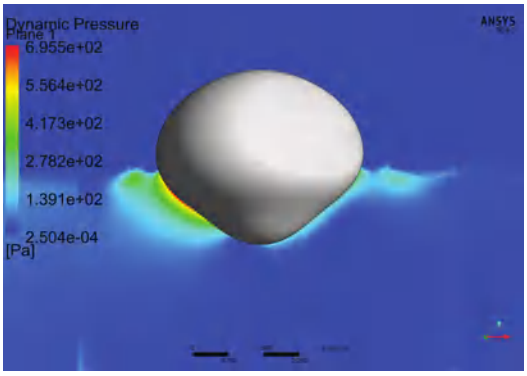


**Figure 16.** Dynamic pressure field measured around the device at $t = 1.5$ s.

### *4.3. VSB WEC Deformation*

Since the proposed device allows significant deformation in response to the waves, it is interesting to study the geometry variation in free motion. As shown in Figure 17, although the geometry of the device varies significantly from 0 s to 1.5 s, the shape of the device at 1.5 s indicates a trend of recovering to the original shape (at 0 s). Thus, a periodic change of the shape is expected, which is also reasonable since the gas chamber is a restoring mechanism. This periodic phenomenon can be better explained in the following figures. Figures 18 and 19 show the vertical motion of two nodes where the U=pper Node denotes the node defined originally at $(40, 30, 42)$ m and the Lower Node denotes the node defined at $(40, 30, 38)$. Figure 18 shows the individual motion of two nodes with respect to their original location. For a conventional fixed-shape buoy WEC (FSB WEC), the motions of these two nodes are expected to be identical since rigid body motion is assumed. Although, in this study, their motion patterns are different. The relative vertical distance between these two nodes is plotted in Figure 19. The original distance between these two nodes is 4 m, which will be kept as a constant for a FSB WEC. While the vertical distance of these two nodes for the VSB WEC changes periodically and finally reaches a steady-state deformation (approximately when $t > 15$ s). The natural period of steady-state deformation is around 1.96 s, which is almost one third of the wave peak period. The relation between the natural period of the shape deformation and the wave period can be more rigorously studied in the future by simulating the dynamic behavior of VSB WEC with varied wave conditions, which may benefit future optimization of the proposed device.

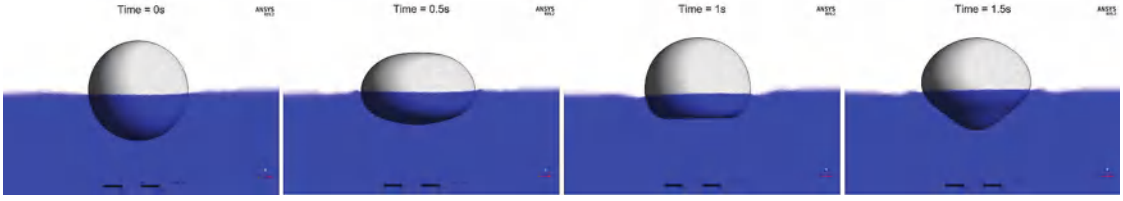


**Figure 17.** Snapshots of the deformation of VSB WEC at different time instants.

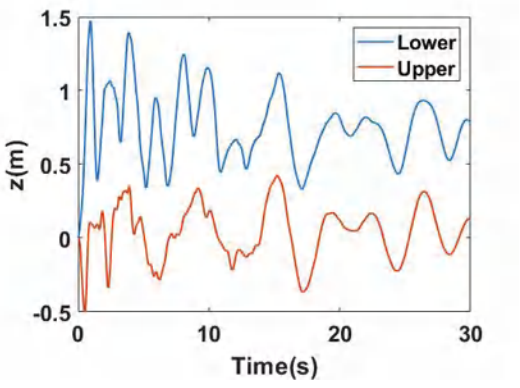


**Figure 18.** Motions of the upper node and the lower node with respect to their original location.

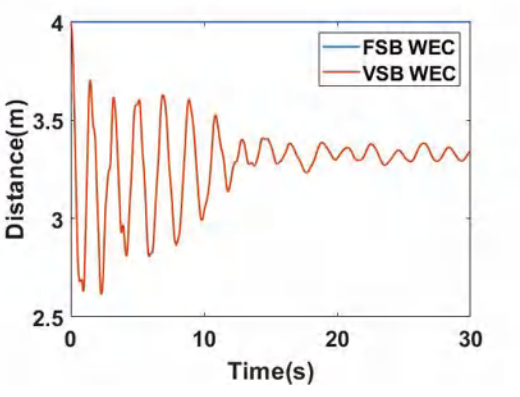


**Figure 19.** Relative vertical distance between the upper node and the lower node during operation.

*4.4. VSB WEC Motion*

The motion of VSB WEC is presented in detail in this section and it will be compared with FSB WEC motion under the same wave condition to highlight the difference in motions introduced by changing the shape. The motion difference can be later controlled and utilized to produce more wave power. Additionally, the mass and dimensions of FSB WEC are the same as VSB WEC (undeformed shape). The motions of the center of gravity of VSB WEC and FSB WEC in x, y, and z directions are shown from Figures 20–22, respectively. The motion of VSB WEC significantly differs from FSB WEC in three dimensions both in terms of phase and magnitude. The difference in vertical motion between the two devices is presented in Figure 23. The maximum difference is around 0.26 m, and the maximum z-directional motion of FSB WEC is around 0.64 m, which indicates a maximum 40.6% change in the heave motion caused by the introduction of geometry variation. This large difference represents a room for improving the performance of wave energy conversion by introducing appropriate control.

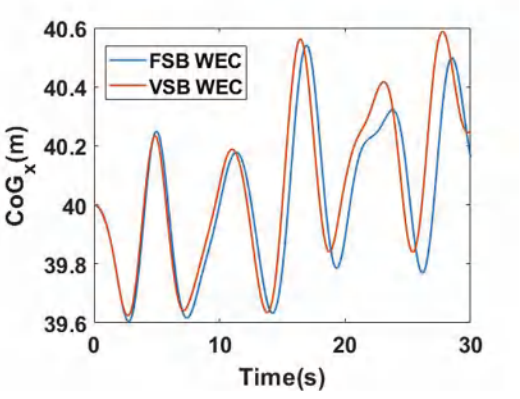


**Figure 20.** x-directional motion of center of gravity compared between FSB WEC and VSB WEC.

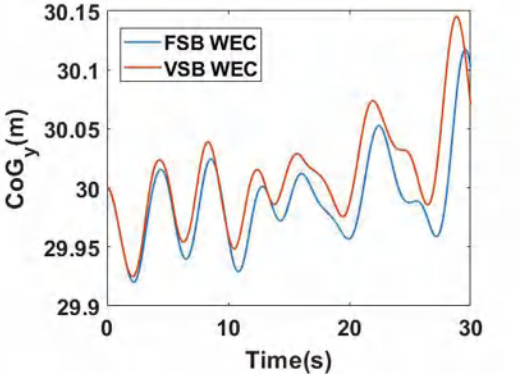


**Figure 21.** y-directional motion of center of gravity compared between FSB WEC and VSB WEC.

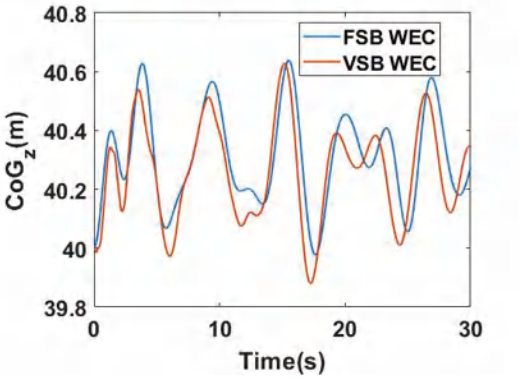


**Figure 22.** z-directional motion of center of gravity compared between FSB WEC and VSB WEC.

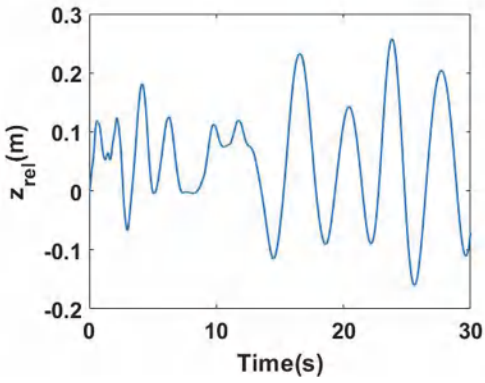


**Figure 23.** Difference in motions of FSB WEC and VSB WEC in heave direction.

## 5. Discussion

In this paper, a 3D numerical simulation architecture is introduced to simulate the fluid–structure interaction of the proposed VSB WEC. The simulation results show the proposed device has a significant shape-changing due to the highly nonlinear interaction between waves and the device. The resulting motion of VSB WEC also significantly differs from the motion of a conventional FSB WEC with the same mass and dimensions. It is noted that the design of VSB WEC can be further optimized in terms of energy extraction since this paper focuses on presenting a framework of the high-fidelity simulation of this device. The applied design is simple in terms of geometry and mechanism. For instance, a possible design presented in [16] is a VSB WEC that has a rigid body part (cylindrical shape) and a shape-changing part (truncated conical shape). A control valve is included to control the pressure oscillation in the gas chamber. As found in [16], a restoring mechanism (gas chamber in this study) is required to keep a steady-state deformation of the device in order to harvest more energy. The presented framework is applicable to simulate the performance of other designs of VSB WEC.

Hyperelastic material is applied in this study since the proposed device is required to be 'soft'. The material applied in the simulation obeys Neo-Hookean hyperelasticity with an initial shear modulus of 0.1 Mpa and an initial bulk modulus of 2000 Mpa, and the density of the material is 1000 $kg{\cdot}m^{-3}$. The corresponding strain–stress curve of the applied material is shown in Figure 24. Unlike vulcanized rubber [30] (initial shear modulus is 0.41 Mpa and initial bulk modulus is 414.5 Mpa), which only allows small deformation, the material used in this study is 'softer', which allows more deformation. In addition, unlike neoprene rubber (initial shear modulus is 0.027 Mpa and initial bulk modulus is 13.86 Mpa), which is too soft such that the deformation is too large to keep a stable simulation. More advanced dynamic mesh techniques need to be applied to address this challenging mesh motion. The study of the effect of different materials is interesting, though beyond the scope of this paper, therefore a material that has the hyperelastic properties between vulcanized rubber and neoprene rubber is applied such that the simulation is stable with a considerable deformation of the device.

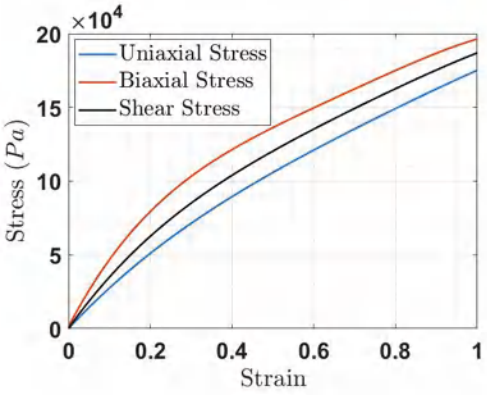


**Figure 24.** Material properties of the applied hyperelastic material.

## 6. Conclusions

A high-fidelity CFD-based numerical wave tank simulation for a VSB WEC is presented in this paper. This numerical tool is demonstrated to be able to simulate a VSB spherical WEC. This highly nonlinear interaction between the device and the waves is simulated using a 2-way FSI technique. Open sea conditions are applied in this study by assuming infinite air, deep water, and multi-directional waves. The numerical results in this paper capture the shape deformation in response to the varying surface pressure from the simulated ocean waves. It was shown that the VSB spherical WEC exhibits a transient response period before it reaches a steady-state motion and deformation. It was shown that this resulting motion of the VSB WEC significantly differs from that of a FSB WEC of the same shape as that of the non-deformed VSB WEC. This difference in response characteristics (difference in motion trajectories) is key for investigating the advantage of the VSB WEC power production over the FSB WEC.

**Author Contributions:** S.Z. implementation of numerical experiment, investigation, data analyses, visualization, original draft; O.A. conceptualization of the study, investigation, funding acquisition, refining of draft. All authors have read and agreed to the published version of the manuscript.

**Funding:** This research is funded by National Science Foundation (NSF), USA, under Grant Number 2023436.

**Institutional Review Board Statement:** Not applicable.

**Informed Consent Statement:** Not applicable.

**Data Availability Statement:** Not applicable.

**Acknowledgments:** This material is based upon work supported by the National Science Foundation (NSF), USA, under Grant Number 2023436.

**Conflicts of Interest:** The authors declare that they have no conflict of interest.

## References

1. Clément, A.; McCullen, P.; Falcão, A.; Fiorentino, A.; Gardner, F.; Hammarlund, K.; Lemonis, G.; Lewis, T.; Nielsen, K.; Petroncini, S.; et al. Wave energy in Europe: Current status and perspectives. *Renew. Sustain. Energy Rev.* **2002**, *6*, 405–431. [CrossRef]
2. Li, G.; Weiss, G.; Mueller, M.; Townley, S.; Belmont, M.R. Wave energy converter control by wave prediction and dynamic programming. *Renew. Energy* **2012**, *48*, 392–403. [CrossRef]
3. Bacelli, G.; Ringwood, J.V. Numerical optimal control of wave energy converters. *IEEE Trans. Sustain. Energy* **2014**, *6*, 294–302. [CrossRef]
4. Falnes, J. *Ocean Waves and Oscillating Systems: Linear Interactions Including Wave-Energy Extraction*; Cambridge University Press: Cambridge, UK, 2002.

5. Zou, S.; Abdelkhalik, O.; Robinett, R.; Bacelli, G.; Wilson, D. Optimal control of wave energy converters. *Renew. Energy* **2017**, *103*, 217–225. [CrossRef]
6. Giorgi, G.; Ringwood, J.V. Computationally efficient nonlinear Froude–Krylov force calculations for heaving axisymmetric wave energy point absorbers. *J. Ocean Eng. Mar. Energy* **2017**, *3*, 21–33. [CrossRef]
7. Penalba, M.; Mérigaud, A.; Gilloteaux, J.C.; Ringwood, J.V. Influence of nonlinear Froude–Krylov forces on the performance of two wave energy points absorbers. *J. Ocean Eng. Mar. Energy* **2017**, *3*, 209–220. [CrossRef]
8. Yu, Y.H.; Li, Y. Reynolds-Averaged Navier–Stokes simulation of the heave performance of a two-body floating-point absorber wave energy system. *Comput. Fluids* **2013**, *73*, 104–114. [CrossRef]
9. Anbarsooz, M.; Passandideh-Fard, M.; Moghiman, M. Numerical simulation of a submerged cylindrical wave energy converter. *Renew. Energy* **2014**, *64*, 132–143. [CrossRef]
10. Hong, Y.; Waters, R.; Boström, C.; Eriksson, M.; Engström, J.; Leijon, M. Review on electrical control strategies for wave energy converting systems. *Renew. Sustain. Energy Rev.* **2014**, *31*, 329–342. [CrossRef]
11. Penalba, M.; Ringwood, J.V. A review of wave-to-wire models for wave energy converters. *Energies* **2016**, *9*, 506. [CrossRef]
12. Tom, N.; Lawson, M.; Yu, Y.H.; Wright, A. Preliminary analysis of an oscillating surge wave energy converter with controlled geometry. In Proceedings of the 11th European Wave and Tidal Energy Conference, Nantes, France, 6–11 September 2015.
13. Tom, N.; Lawson, M.; Yu, Y.H.; Wright, A. Spectral modeling of an oscillating surge wave energy converter with control surfaces. *Appl. Ocean Res.* **2016**, *56*, 143–156. [CrossRef]
14. Tom, N.; Lawson, M.; Yu, Y.; Wright, A. Development of a nearshore oscillating surge wave energy converter with variable geometry. *Renew. Energy* **2016**, *96*, 410–424. [CrossRef]
15. Kelly, M.; Tom, N.; Yu, Y.H.; Thresher, R.; Abbas, N. Development of the Second-Generation Oscillating Surge Wave Energy Converter With Variable Geometry. In Proceedings of the 27th International Ocean and Polar Engineering Conference, San Francisco, CA, USA, 25–30 June 2017;
16. Zou, S.; Abdelkhalik, O. Modelling Of A Variable-Geometry Wave Energy Converter. *IEEE J. Ocean. Eng.* **2020**. [CrossRef]
17. Windt, C.; Davidson, J.; Ringwood, J.V. High-fidelity numerical modelling of ocean wave energy systems: A review of computational fluid dynamics-based numerical wave tanks. *Renew. Sustain. Energy Rev.* **2018**, *93*, 610–630. [CrossRef]
18. Fluent, A. *ANSYS Fluent Theory Guide, Release 2019 R2*; ANSYS Inc.: Canonsburg, PA, USA, 2019.
19. Alberello, A.; Pakodzi, C.; Nelli, F.; Bitner-Gregersen, E.M.; Toffoli, A. Three dimensional velocity field underneath a breaking rogue wave. In *Volume 3A: Structures, Safety and Reliability, Proceedings of the ASME 2017 36th International Conference on Ocean, Offshore, and Arctic Engineering, Trondheim, Norway, 25–27 June 2017*; V03AT02A009; American Society of Mechanical Engineers: New York, NY, USA, 2017.
20. Gupta, V.K.; Khan, M.; Punekar, H. Development and Application of Interfacial Anti-Diffusion and Poor Mesh Numerics Treatments for Free Surface Flows. In Proceedings of the 2015 IEEE 22nd International Conference on High Performance Computing Workshops, Bengaluru, India, 16–19 December 2015; pp. 12–18.
21. Tezdogan, T.; Demirel, Y.K.; Kellett, P.; Khorasanchi, M.; Incecik, A.; Turan, O. Full-scale unsteady RANS CFD simulations of ship behaviour and performance in head seas due to slow steaming. *Ocean Eng.* **2015**, *97*, 186–206. [CrossRef]
22. Lee, C.; Jung, J.S.; Haller, M.C. Asymmetry in directional spreading function of random waves due to refraction. *J. Waterw. Port Coastal Ocean Eng.* **2009**, *136*, 1–9. [CrossRef]
23. Guo, Q.; Xu, Z. Simulation of deep-water waves based on JONSWAP spectrum and realization by MATLAB. In Proceedings of the 2011 19th International Conference on Geoinformatics, Shanghai, China, 24–26 June 2011; pp. 1–4.
24. Simanesew, A.; Krogstad, H.E.; Trulsen, K.; Borge, J.C.N. Development of frequency-dependent ocean wave directional distributions. *Appl. Ocean Res.* **2016**, *59*, 304–312. [CrossRef]
25. Gilloteaux, J.; Babarit, A.; Clément, A. Influence of spectrum spreading on the SEAREV wave energy converter. In Proceedings of the International Ocean Energy Conference, Vancouver, BC, Canada, 29 September–4 October 2007.
26. Kamath, A.M. Calculation of Wave Forces on Structures Using Reef3d. Master's Thesis, Institutt for Bygg, Anlegg og Transport, Trondheim, Norway, 2012.
27. Lloyd, C.; O'Doherty, T.; Mason-Jones, A. Development of a wave-current numerical model using Stokes 2nd Order Theory. *Int. Mar. Energy J.* **2019**, *2*, 1–14. [CrossRef]
28. Beneš, P.; Kollárik, R. Preliminary computational fluid dynamics (CFD) simulation of EIIB push barge in shallow water. *Sci. Proc. Fac. Mech. Eng.* **2011**, *19*, 67–73. [CrossRef]
29. Luan, Z.; He, G.; Zhang, Z.; Jing, P.; Jin, R.; Geng, B.; Liu, C. Study on the Optimal Wave Energy Absorption Power of a Float in Waves. *J. Mar. Sci. Eng.* **2019**, *7*, 269. [CrossRef]
30. Treloar, L. Stress-strain data for vulcanised rubber under various types of deformation. *Trans. Faraday Soc.* **1944**, *40*, 59–70. [CrossRef]

Journal of
*Marine Science and Engineering*

MDPI

*Article*

# Investigations of Hydraulic Power Take-Off Unit Parameters Effects on the Performance of the WAB-WECs in the Different Irregular Sea States

**Mohd Afifi Jusoh, Zulkifli Mohd Yusop, Aliashim Albani, Muhamad Zalani Daud and Mohd Zamri Ibrahim ***

Renewable Energy & Power Research Interest Group (REPRIG), Eastern Corridor Renewable Energy Special Interest Group, Faculty of Ocean Engineering Technology and Informatics, Universiti Malaysia Terengganu, Kuala Nerus 21030, Terengganu, Malaysia; mohd.afifi.jusoh@gmail.com (M.A.J.); zul_12521@yahoo.com (Z.M.Y.); a.albani@umt.edu.my (A.A.); zalani@umt.edu.my (M.Z.D.)
* Correspondence: zam@umt.edu.my; Tel.: +60-96683328

**Abstract:** Hydraulic power take-off (HPTO) is considered to be one of the most effective power take-off schemes for wave energy conversion systems (WECs). The HPTO unit can be constructed using standard hydraulic components that are readily available from the hydraulic industry market. However, the construction and operation of the HPTO unit are more complex rather than other types of power take-off, as many components parameters need to be considered during the optimization. Generator damping, hydraulic motor displacement, hydraulic cylinder and accumulator size are among the important parameters that influence the HPTO performance in generating usable electricity. Therefore, the influence of these parameters on the amount of generated electrical power from the HPTO unit was investigated in the present study. A simulation study was conducted using MATLAB/Simulink software, in which a complete model of WECs was developed using the Simscape fluids toolbox. During the simulation, each parameters study of the HPTO unit were separately manipulated to investigate its effects on the WECs performance in five different sea states. Finally, the simulated result of the effect of HPTO parameters on the amount of generated electrical power from the HPTO unit in different sea states is given and discussed.

**Keywords:** ocean wave energy; wave-activated-body; hydraulic power take-off

**Citation:** Jusoh, M.A.; Yusop, Z.M.; Albani, A.; Daud, M.Z.; Ibrahim, M.Z. Investigations of Hydraulic Power Take-Off Unit Parameters Effects on the Performance of the WAB-WECs in the Different Irregular Sea States. *J. Mar. Sci. Eng.* **2021**, *9*, 897. https://doi.org/10.3390/jmse9080897

Academic Editor: Eugen Rusu, Kostas Belibassakis and George Lavidas

Received: 13 July 2021
Accepted: 13 August 2021
Published: 20 August 2021

**Publisher's Note:** MDPI stays neutral with regard to jurisdictional claims in published maps and institutional affiliations.

**Copyright:** © 2021 by the authors. Licensee MDPI, Basel, Switzerland. This article is an open access article distributed under the terms and conditions of the Creative Commons Attribution (CC BY) license (https://creativecommons.org/licenses/by/4.0/).

## 1. Introduction

Ocean waves are considered as one large untapped and predictable renewable energy resource on earth. Ocean waves contain tremendous of usable energy and have the potential to contribute to a significant share of global renewable energy sources. Ocean wave energy has many advantages such as high energy density, high source availability, source predictability and low environmental impact compared to other renewable energy (RE) sources [1]. The energy density of ocean waves is the highest among all renewable energy sources, which is around 50–100 kW/m [2]. Approximately, 8000–80,000 TWh/year ocean wave energy is available globally [2]. Due to its advantages, electrical energy production from the ocean waves has received a great deal of attention over the past several decades. Numerous wave energy converter systems (WECs) with different harnessing methods have been invented to convert the kinetic energy contained in the ocean waves into usable electricity, as reported in [3–6]. The existing WECs can be classified into wave-activated-body (WAB), oscillating water column (OWC) and overtopping device based on their working principles.

The WAB wave energy converters (WAB-WECs) are also known as oscillating bodies wave energy converters and point absorber wave energy converters. WAB-WECs can be defined as a single body or multiple bodies devices being oscillated by the wave excitation force [7]. WAB-WECs covers a kinds of WEC and recent development of WAB-WECs

around the world has been reported in [4,6,8,9]. In general, these WAB-WECs consist of three main subsystems, namely wave energy converter (WEC), power take-off (PTO) unit, and control system (CS) unit. WEC is a front-end device that absorbs the kinetic energy from the ocean waves. The absorbed energy is then converted to electricity through the PTO unit, whereas the control system unit is used to optimize the electrical energy produced from the WECs during its operation.

PTO is one of the most essential subsystems of WAB-WECs. In recent decades, a wide variety of PTOs have been designed, developed and experimentally tested for numerous types of WEC device, as reported in [10]. The various kinds of PTO concepts can be classified based on their main working principles, such as mechanical–hydraulic, direct mechanical, direct electrical drive, air and hydro turbine. The hydraulic power take-off (HPTO) unit is one of the most reliable and effective PTOs for the WECs [11,12]. The HPTO unit has excellent characteristics, such as high efficiency, wide controllability, well-suited to the low-frequency and large power density of ocean waves, etc. The HPTO unit can also be assembled using standard hydraulic components that are readily available from the hydraulic equipment suppliers. In [11], a review of the most popular HPTO concepts used in WAB-WECs is reported. From the study, the HPTO concepts can be classified into two main groups, i.e., a variable-pressure and a constant-pressure concept. The constant-pressure concept has received more attention. Based on the report in [13], the efficiency of the constant-pressure concept is much higher than that of the variable-pressure concept, which can reach up to 90%. According to [14], several crucial parameters may influence the efficiency of the HPTO unit, such as the mounting position and piston size of the hydraulic actuator, volume capacity and pre-charge pressure of the accumulator, displacement of hydraulic motor and damping coefficient of the electric generator.

Recently, several kinds of research into the HPTO in WAB-WECs have been published for various objectives, for example in [15–21]. From the literature, most of the studies have concentrated on the performance of the HPTO unit without investigating the influence of the important parameters of HPTO. Only a few studies have discussed this issue, e.g., [14,16]. In [14], the influence of the HPTO unit parameters on the power capture ability of two-raft-type of WEC was studied. However, the HPTO concept used in [14] is very different from the HPTO concept considered in the present study. The effects of the HPTO unit on the percentage of power reduction were not discussed in this study. Meanwhile, in [16], the sensitivity of the generator damping coefficient on the average generated electrical power was investigated. From the simulation results, the authors concluded that the generator damping coefficient is relatively sensitive to the changes in wave height and period. However, the sensitivity of the other HPTO parameters was not discussed in [16]. Since there is a lack of published articles on this issue, the present study proposes an investigation of the HPTO unit parameters on the performance of the WAB-WECs. The main objective of the study is to investigate the effect of these important parameters on the electrical power generated from the HPTO unit. The findings can be a useful reference to other researchers for improvement of WECs in future.

The remainder of this paper is organized as follows. Section 2 presents the design of the considered WECS and Section 3 describes the simulation study for investigation of the HPTO parameters. Section 4 presents the results and discussion. Finally, the conclusion and future work are discussed in Section 5.

## 2. Design of WEC with HPTO Unit

The WEC concept based on [20] is considered in the present study. The simplified concept is shown in Figure 1A. The WECs consist of a single floating body (floater) attached to the fixed body via a hinged arm, which is also known as the WEC device. This WEC device design is almost similar to the concepts used in [13,22–24]. The WEC device is unique due to its ability to convert both wave kinetic energy and wave potential by utilizing the pitch motion of the floater and hinged arm, as presented in Figure 1A. In this system, the WEC is connected to the fixed-body directed to the dominant wave direction to optimally

absorb the kinetic energy from the ocean waves. The WEC device is then connected to the HPTO and the CS unit is placed in the HPTO house to convert the mechanical energy from the WEC device into usable electricity.

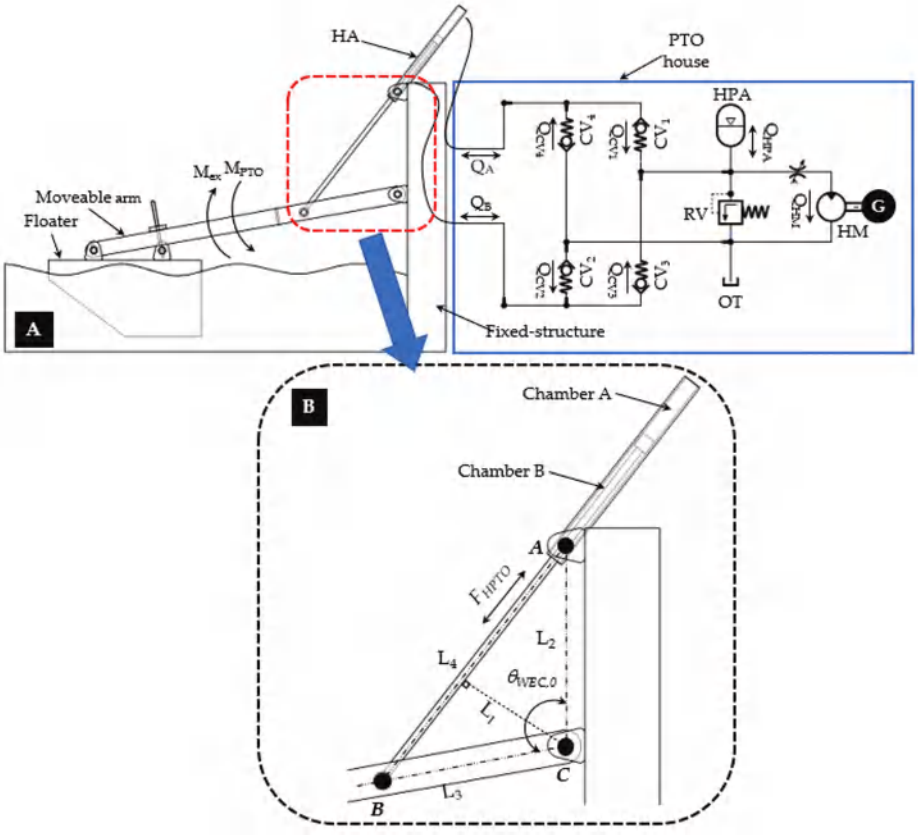


**Figure 1.** An illustration of WEC with the HPTO unit concept. (**A**) A complete layout design, and (**B**) Enlarge image of the interconnection between HA, floater's arm and fixed structure.

Figure 1A presents the simplified diagram of the HPTO unit which includes a hydraulic actuator (HA), hydraulic hose (HH), check valve rectifier module ($CV_1$, $CV_2$, $CV_3$ & $CV_4$), oil tank (OT), high-pressure and low-pressure accumulators (HPA & LPA), pressure relief valve ($RV_1$ & $RV_2$), hydraulic motor (HM) and electric generator (G). In this concept, double-acting with a single rod type of HA is considered. HA is used as a linear pump to absorb the mechanical energy from the reciprocating motion of the WEC. The piston rod of the HA is attached to the floater's arm using a rod end clevis while the barrel of the HA is attached to the fix-structure. Then, the HA is connected to the check valve rectifier module, an arrangement of four check valves in a bridge circuit configuration, as shown in Figure 1A. The check valve rectifier used in this HPTO unit is similar to the Graetz bridge concept, which is used for conversion of an alternating-current (AC) input into a direct-current (DC) output. For the HPTO, the check valve rectifier module is used to control the fluid flow direction ($Q_A$ & $Q_B$) from the HA to the HM. Thus, the large chamber (chamber A) of the HA barrel is connected to the inlet and outlet of $CV_1$ and $CV_4$, while the small chamber (chamber B) of the HA barrel is terminated to the inlet and outlet of $CV_2$ and $CV_3$, respectively. The check valve rectifier module is then connected to the HPA and LPA. The HPA is included in the HPTO unit to constrain the pressure of the HM in

the desired ranges. Finally, the generation module which consists of fixed-displacement of HM coupled to G is placed between the HPA and OT. In addition, the pressure relief valves $RV_1$ & $RV_2$ are placed to prevent the HPTO unit from over-pressurized fluid flows.

During the operation of WECs, the passing of ocean waves causes a WEC device to pitch upward and downward simultaneously. Then, the reciprocating motion of the WEC device causes back-and-forth motions of the piston and directly generates the high-pressure fluid flow from the HA chambers. During the upward movement of the WEC device, the high-pressure fluid flows from chamber A to chamber B through $CV_1$, HPA, HM, LPA, and $CV_2$. On the other hand, during the downward movement, the high-pressure fluid flows from chamber B to chamber A through the $CV_3$, HPA, HM, LPA, and $CV_4$ of the WEC device. The high-pressure fluid flowing through the HM causes the HM and G to rotate simultaneously in one direction and thus produces usable electricity. Overall, the speed and torque of the HM depend highly on the characteristics of ocean wave motions such as speed, frequency, wavelength, and amplitude [25]. They also depend on the important parameters of the HPTO unit itself.

### 2.1. Formulation of Hydrodynamic Pitch Motion of WEC

The hydrodynamic pitch motion of WEC in real waves can be formulated in the time domain to account for the non-linear effects such as the hydrodynamics of a floater, HPTO force, etc. So, the equation for the pitch motion of the WEC device can be expressed by:

$$M_D = M_{ex} - M_{rad} - M_{res} - M_{HPTO} \quad (1)$$

where $M_D$ is the D'Alembert moment of inertia, and $M_{ex}$, and $M_{rad}$ are the moments due to the diffracted and radiated ocean waves. $M_{res}$ and $M_{HPTO}$ are the moments due to hydrostatic restoring and HPTO unit interactions, respectively. The hydrodynamic pitch motion of the WEC equation above can be extended as follows:

$$(J_{WEC} + J_{add,\infty})\alpha_{WEC}(t) + \int_0^t k_{rad}(t-\tau)\ \omega_{WEC}(t) + k_{res}\,\theta_{WEC}(t) + M_{HPTO}(t) = \int_{-\infty}^{\infty} h_{ex}(t-\tau)\eta_W(\tau)d\tau \quad (2)$$

where $J_{WEC}$ is the moment of inertia of WEC (includes floater and hinged arm), $J_{add,\infty}$ is the added mass at the infinite frequency. $\tau$ is the time delay. $\theta_{WEC}$, $\omega_{WEC}$ and $\alpha_{WEC}$ are the angular position, angular velocity and angular acceleration of WEC during the pitch motion, respectively. $\theta_{WEC} = 0$ corresponds to the WEC device at rest. $k_{rad}$ and $k_{res}$ are the radiation impulse response function and the hydrostatic restoring coefficients. $h_{ex}$ is the excitation force coefficient and $\eta_W$ is the undisturbed wave elevation at the center point of the floater. The coefficients of $k_{rad}$, $k_{res}$ and $h_{ex}$ can be determined from the dynamic diffraction analysis using computational fluid dynamics (CFD) software, such as ANSYS/AQWA, as previously implemented in [20,26–30]. Alternatively, these coefficients also can be obtained using the boundary element method (BEM) toolbox in WAMIT software, as suggested in several studies [31–35].

Since the non-linear effect of the HPTO unit is considered in Equation (2), the moment due to the HPTO unit $M_{HPTO}$ can be described using Equation (3). According to Figure 1B, $F_{HPTO}$ is the feedback force of the PTO unit applied to the WEC device. $L_1$ is the perpendicular distance between HA and point *C*, which can be obtained using Equation (4), where $L_2$ and $L_3$ are the distance between points *A*-*C* and *B*-*C*, respectively. $L_{4,0}$ is the initial distance between points *A*-*B*. $\theta_{WEC,0}$ and $\theta_{WEC}$ are the initial and instantaneous angle of the WEC device. $x_p$ is the linear displacement of the piston. Based on Equation (4), $L_1$ is always relatively changes according to the change of the arm angle, as illustrated in Figure 1B.

$$M_{HPTO} = F_{HPTO}L_1 \quad (3)$$

$$L_1 = \frac{L_2 L_3 \sin(\theta_{WEC,0} - \theta_{WEC})}{L_{4,0} + x_{HA}} \quad (4)$$

$$x_p = L_{4,0} - \sqrt{{L_2}^2 + {L_3}^2 - 2L_2L_3\cos(\theta_{WEC,0} - \theta_{WEC})} \tag{5}$$

*2.2. Formulation of HPTO Unit*

Technically, the force generated by the HPTO unit, $F_{HPTO}$ is represented by the feedback force applied by the HA to the WEC device. The nonlinear $F_{HPTO}$ is generated due to the dynamic pressure in chambers A and B ($P_A$ & $P_B$) and the piston friction force ($F_{fric}$) of the HA. The $F_{HPTO}$ can be expressed using Equation (6), where $A_{p,A}$ and $A_{p,B}$ are the sectional areas of the piston in chambers A and B, respectively. $A_{p,A}$ and $A_{p,B}$ can be obtained using Equations (7) and (8), where $d_p$ and $d_r$ are the piston and rod diameter of the HA. Meanwhile, the dynamics of $P_A$ and $P_B$ can be calculated according to the fluid continuity function, as described in Equations (9) and (10), where $\beta_{eff}$ is the bulk modulus of the hydraulic fluid. $Q_{CV1}$ to $Q_{CV4}$ are the flow rates across the check valves $CV_1$ to $CV_4$. $L_s$, $x_p$ and $\dot{x}_p$ are the stroke length, linear displacement and linear velocity of the piston, respectively.

$$F_{HPTO} = P_A A_{p,A} - P_B A_{p,B} + F_{fric} \tag{6}$$

$$A_{p,A} = \pi {d_p}^2/4 \tag{7}$$

$$A_{p,B} = \pi\left({d_p}^2 - {d_r}^2\right)/4 \tag{8}$$

$$\frac{d}{dt}P_A = \frac{\beta_{eff}}{A_{p,A}(L_s - x_p)}\left(\dot{x}_p A_{p,A} + Q_{CV4} - Q_{CV1}\right) \tag{9}$$

$$\frac{d}{dt}P_B = \frac{\beta_{eff}}{A_{p,B}(L_s - x_p)}\left(\dot{x}_p A_{p,B} + Q_{CV2} - Q_{CV3}\right) \tag{10}$$

The flow rates $Q_{CV1}$ to $Q_{CV4}$ can be generally calculated using Equation (11), where $C_d$ and $A_{CV}$ are the discharge coefficient and the working area of each check valve. $P_{CVin}$ and $P_{CVout}$ are the inlet and outlet pressure of each check valve. $\rho_{oil}$ is the hydraulic oil density.

$$Q_{CV} = \begin{cases} C_d A_{CV}\sqrt{\frac{2}{\rho_{oil}}|P_{CVin} - P_{CVout}|} & ,if\ P_{CVin} > P_{CVout} \\ 0 & ,if\ P_{CVin} < P_{CVout} \end{cases} \tag{11}$$

On the other hand, the fluid volume ($V_{HPA}$) and flow rate ($Q_{HPA}$) which enters the accumulator can be calculated using Equations (12) and (13), where $V_{HPA,cap}$ is a capacity, $P_{HPA,0}$ is the initial pressure and $P_{HPA,in}$ is the inlet gauge pressure of HPA, and $n$ is the specific heat ratio, respectively. The initial pressure in the accumulators depends on the pre-charge pressure of the nitrogen gas in the HPA bladder.

$$V_{HPA} = \begin{cases} V_{HPA,cap}\left[1 - \left(\frac{P_{HPA,0}}{P_{HPA,in}}\right)^{\frac{1}{n}}\right] & ,\ if\ P_{HPA,in} > P_{HPA,0} \\ 0 & ,\ if\ P_{HPA,in} \le P_{HPA,0} \end{cases} \tag{12}$$

$$Q_{HPA} = \dot{V}_{HPA} = \begin{cases} \frac{1}{n}V_{HPA,cap}\left(1 - \frac{P_{HPA,0}}{P_{HPA,in}}\right)^{\frac{1-n}{n}}\frac{P_{HPA,0}\dot{P}_{HPA,in}}{{P_{HPA,in}}^2} & ,\ if\ P_{HPA,in} > P_{HPA,0} \\ 0 & ,\ if\ P_{HPA,in} \le P_{HPA,0} \end{cases} \tag{13}$$

Meanwhile, the flow rate across the HM ($Q_{HM}$) and the actual torque of HM ($\tau_{HM}$) can be obtained using Equations (14) and (15), where $D_{HM}$, $\omega_{HM}$ and $\Delta P_{HM}$ are the displacement, angular speed and the internal pressure difference of HM. $\eta_{HM,\,V}$ and $\eta_{HM,\,M}$ are the volumetric and mechanical efficiency of HM.

$$Q_{HM} = D_{HM}\omega_{HM}/\eta_{HM,V} \tag{14}$$

$$\tau_{HM} = \Delta P_{HM} D_{HM}\eta_{HM,M}/2\pi \tag{15}$$

Finally, the electric power generated by the electric generator ($P_G$) can be expressed using Equation (16), where $\omega_G$, $\tau_G$ and $\eta_G$ are angular speed, the torque and overall efficiency of the electrical generator. Since the electrical generator and HM are rotating simultaneously, the $\omega_G$ and $\tau_G$ are equal to $\omega_{HM}$ and $\tau_{HM}$, respectively.

$$P_G = 2\pi\omega_G\tau_G\eta_G = 2\pi\omega_{HM}\tau_{HM}\eta_G \quad (16)$$

### 2.3. Main Parameters of HPTO Unit

As previously mentioned in [14], there are several important parameters affecting the performance of the HPTO unit such as piston diameter, the volume capacity of HPA, displacement of HM, etc. Table 1 provides the important parameters of the HPTO unit that are summarized from Equations (3)–(16). For some parameters, the higher and lower values can reduce the performance of the HPTO unit. To investigate this problem, a detailed study regarding the influence of these parameters on the overall performance of WECs is performed in the present study.

**Table 1.** Important parameters of the HPTO unit.

| No. | Important Parameters of HPTO | Unit |
|---|---|---|
| 1 | Vertical mounting of HA, $L_2$ | m |
| 2 | Piston diameter, $d_p$ | m |
| 3 | Volume capacity of HPA, $V_{HPA,cap}$ | L |
| 4 | Pre − charge gas pressure of HPA, $P_{HPA,0}$ | bar |
| 5 | Displacement of HM, $D_{HM}$ | cc/rev |
| 6 | Damping coefficient of the generator, $d_G$ | Nm/(rad/s) |

In the present study, the complete simulation investigation of HPTO unit parameters was implemented in the MATLAB/Simulink software (Version: 2018b). The detailed methodology of the present study is described in the following subsections.

## 3. Simulation Investigation of HPTO Unit Parameters

### 3.1. Simulation Set-up of WEC with HPTO Unit

The MATLAB/Simulink software was used in this study to model a complete WEC system shown in Figure 1. The WECs consists of two main parts, the WEC model and the HPTO model. The WEC model was developed using a mathematical function block based on Equations (1)–(5). The wave elevation data, $\eta_W$ and $F_{HPTO}$ are the inputs, while the $x_p$ is the output of the WEC model. According to Equations (1) and (2), the hydrodynamics parameters of the WEC device such as $k_{rad}$, $k_{res}$, $h_{ex}$, added mass coefficient ($k_{add}$) and impulse response function ($k_{imp}$) are required to develop the considered WEC model. The hydrodynamic parameters of the WEC model from the previous study in [20] were used, since a similar WEC concept was considered in this study. In [20], these hydrodynamic parameters were obtained from the frequency domain analysis study that was carried out using ANSYS/AQWA software. The obtained hydrodynamic parameters are presented in Figure 2.

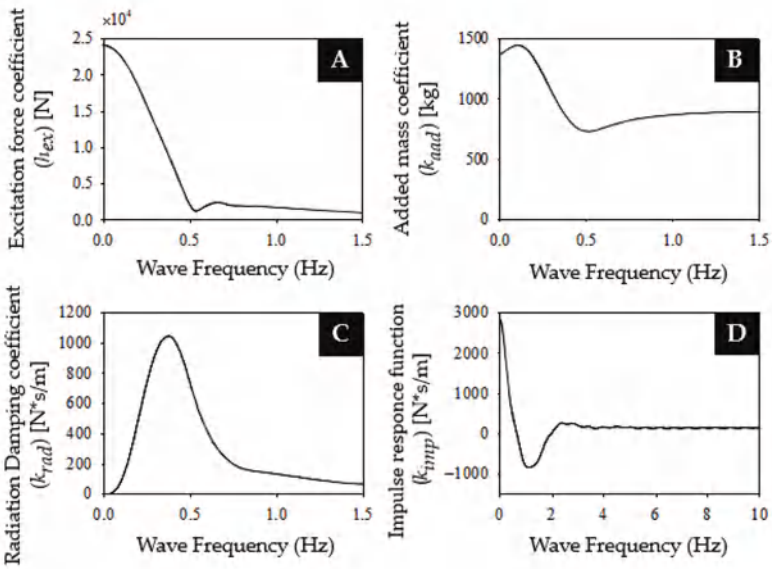


**Figure 2.** Hydrodynamic parameters of WEC device. (**A**) Excitation force coefficient, (**B**) Added mass coefficient, (**C**) Radiation damping coefficient, and (**D**) Impulse response function.

Meanwhile, the Simscape SimHydraulic toolbox in MATLAB/Simulink was used to develop the HPTO unit model. The snapshot of the developed model in MATLAB/Simulink is depicted in Figure 3. As illustrated in the figure, $x_p$ is the input of the HPTO unit. Using $x_p$ signal, the linear velocity of the piston, $\dot{x}_p$ is obtained using a first-order lag-based linear displacement to linear velocity converter. The double-acting hydraulic cylinder (DAC) component was used as HA. In the Simscape SimHydraulic toolbox, the DAC component is constructed based on the translational hydro-mechanical converter and translational hard stop blocks. The rod motion is limited with the mechanical translational hard stop block. The ideal force sensor block was connected to the HA rod to measure the $F_{HPTO}$. The pressure and flow rate sensor blocks were also connected to the HA to measure the dynamic pressure and flow rate of HA. To account for the friction loss along the pipe length and the fluid compressibility, the hydraulic pipeline blocks were used to connect some of the components, as illustrated in Figure 3. The thermodynamic transformation in the HPA was assumed to be isentropic, which is reasonable considering the cycle time in the device. Furthermore, for ease of control, a simple rotational damper with varying damping coefficients was used to represent the electric generator unit. In this way, the resistive torque imposed by the electric generator can be manipulated by varying the value of the damping coefficient ($d_G$). The generated electric power from the electric generator can be calculated using Equation (16). In this study, the initial parameters of the HPTO unit were manual tuned. However, these parameters are not optimal yet. The detailed specifications of each component in the developed HPTO model are provided in Table 2. Finally, the developed HPTO unit model in MATLAB/Simulink was then experimentally validated using an actual HPTO test rig in the dry lab environment.

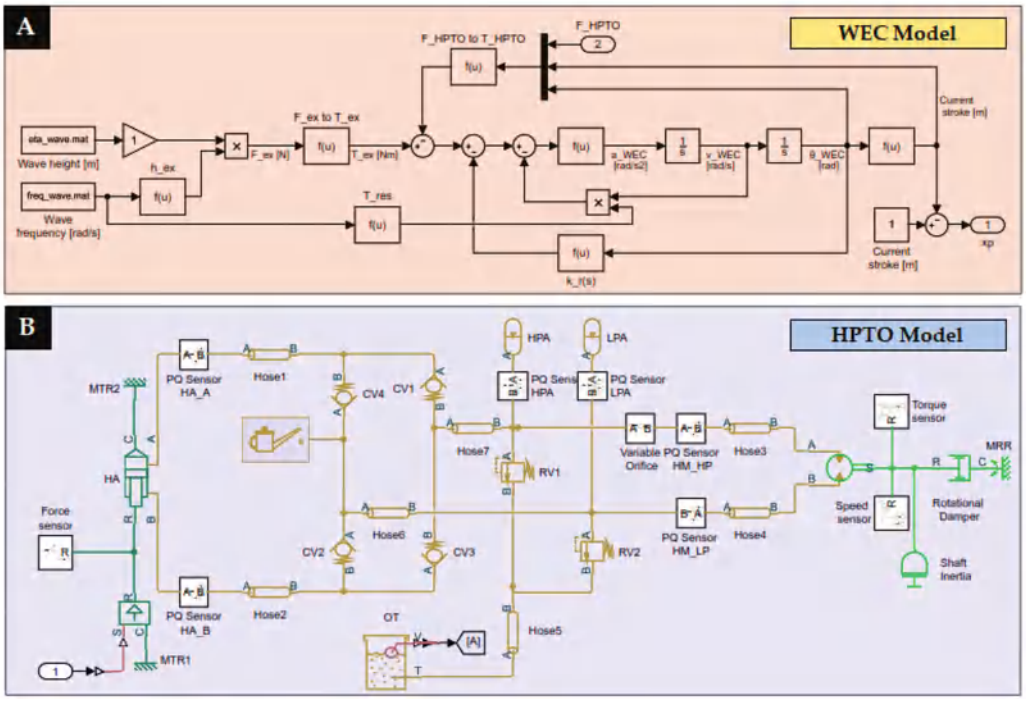


**Figure 3.** A complete model of WEC with HPTO unit in MATLAB/Simulink. (**A**) WEC device model, and (**B**) HPTO unit model.

**Table 2.** Detailed specifications of the developed HPTO unit.

| Component Descriptions | | Value | Unit |
|---|---|---|---|
| Hydraulic actuator | Piston diameter, $d_p$ | 0.035 | m |
| | Piston rod diameter, $d_r$ | 0.022 | m |
| | Stroke length, $L_s$ | 0.3 | m |
| | Initial stroke length, $L_{s,0}$ | 0.15 | m |
| | Vertical distance mounting, $L_2$ | 0.5 | m |
| | Horizontal distance mounting, $L_3$ | 0.5 | m |
| | Initial rod length (point A to B), $L_4$ | 0.766 | m |
| High-pressure accumulator | Pre-charge pressure, $P_{HPA,0}$ | 46.9 | bar |
| | Volume capacity, $V_{HPA,cap}$ | 2.8 | L |
| | Adiabatic index, $\gamma$ | 1.4 | - |
| Low-pressure accumulator | Pre-charge pressure, $P_{LPA,0}$ | 3.2 | bar |
| | Volume capacity, $V_{LPA,cap}$ | 4.0 | L |
| | Adiabatic index, $\gamma$ | 1.4 | - |
| Hydraulic motor | Displacement, $D_{HM}$ | 8.4 | cc/rev |
| | Nominal shaft angular velocity, $\omega_{HM,\,nom}$ | 200 | rpm |
| | Volumetric efficiency at nominal condition, $\eta_{HM,\,V}$ | 0.92 | - |
| | No-load torque, $\tau_{HM,\,no}$ | 0.05 | Nm |
| Electric generator | Rated power, $P_{G,\,rated}$ | 100 | W |
| | Rated speed, $\omega_{G,\,rated}$ | 200 | rpm |
| | Rated torque, $\tau_{G,\,rated}$ | 6.0 | Nm |
| | Damping coefficient, $d_G$ | 0.03 | Nm/(rad/s) |
| | Moment of inertia | 0.0036 | $kg/m^2$ |
| Fluid properties | Density, $D_{oil}$ | 50 | $kg/m^3$ |
| | Viscosity, $Vis_{oil}$ | 850 | cSt |

### 3.2. Simulation of WEC with HPTO Unit Using Five Irregular Sea States

The simulation analysis was started with the performance evaluation of the WEC with the HPTO model, using five different irregular wave input conditions. This simulation was intended to evaluate the effect of the significant wave height ($H_W$) and the peak wave period $T_W$ on the electrical output power produced by the HPTO unit. Five different sea states were considered as summarized in Table 3. Sea state A is the nominal wave condition for the developed WEC with the HPTO model, in which the significant wave height and the peak wave period were set to 0.8 m and 2.5 s, respectively. Sea state B and C were considered for wave height case studies, while sea state D and E are for wave period case studies. For sea states B and C, the significant wave heights were set to 0.6 m and 1.0 m, which is ±0.2 m of the wave height in sea state A. Meanwhile, the peak wave periods for both states were maintained at the nominal value. For sea states D and E, the significant wave height was maintained at the nominal value, while the peak wave periods were set to 2.0 s and 3.0 s, which is ±0.5 s of the nominal wave period.

**Table 3.** The parameters of five different sea states.

| Sea State | Significant | | Remarks |
|---|---|---|---|
| | Wave Height, $H_W$ (m) | Wave Period, $T_W$ (s) | |
| **A** | 0.8 | 2.5 | Nominal wave condition |
| **B** | 0.6 | 2.5 | Wave height case |
| **C** | 1.0 | | |
| **D** | 0.8 | 2.0 | Wave period case |
| **E** | | 3.0 | |

### 3.3. Investigation Studies of HPTO Unit Parameters

A further simulation proceeded with the investigation of the HPTO unit parameters study. As previously mentioned, the main purpose of the study is to investigate the influence of the important parameters on the performance of the HPTO unit. Thus, from this study, how the performance of the HPTO unit varies to its configuration parameters was discovered. To achieve the objective, several case studies were conducted on the developed simulation model of WECs. A summary of the case studies is provided in Table 4. The regulating condition of each case was selected based on the availability of the components from the hydraulic equipment market.

**Table 4.** Detailed of the case studies.

| Case | Important Parameters of HPTO | Default Value | Regulating Condition | | Unit |
|---|---|---|---|---|---|
| | | | Ranges | Step | |
| 1 | Vertical Mounting of HA, $L_2$ | 0.5 | 0.1–0.7 | 0.1 | m |
| 2 | Piston diameter, $d_p$ | 0.035 | 0.025–0.060 | 0.005 | m |
| 3 | Volume capacity of HPA, $V_{HPA,cap}$ | 2.8 | 0.5–10.5 | 2.0 | L |
| 4 | Pre-charge gas pressure of HPA, $P_{HPA,0}$ | 46.9 | 20–80 | 10.0 | bar |
| 5 | Displacement of HM, $D_{HM}$ | 8.4 | 6–18 | 2 | cc/rev |
| 6 | Damping coefficient of the generator, $d_G$ | 0.287 | 0.1–1.3 | 0.2 | Nm/(rad/s) |

## 4. Results and Discussion

The results from the investigation simulations are presented and discussed in three sections. The first Section 4.1 presents the experimental validation of the developed WEC with the HPTO unit model. The second Section 4.2 provides the performance analysis of the developed WEC with the HPTO unit model in different sea states and the third Section 4.3 presents the finding from the investigations of the influence parameters on the HPTO unit performance.

### 4.1. Experimental Validation of the HPTO Model

Figure 4A shows the hardware in the loop (HIL) test rig of the HPTO unit. In general, the HIL test rig was developed based on the design of WECs in Figure 1 and several sensors were installed to monitor the variations of HPTO force, oil pressure, the oil level in the oil tank and as the hydraulic motor shaft speed, as illustrated in Figure 4B. The servo-electric actuator was also installed in the HIL test rig to replicate wave-induced relative pitch motion to drive the HPTO unit to capture the wave energy. A servo motor controller based on Labview/Arduino integration and the data acquisition system for data collection from the sensors were placed in the control system unit. The relative pitch motion generated by the electric actuator is according to the input wave state. To simulate the condition that is close to real-world application, the hydrodynamic parameters from the CFD analysis and the feedback HPTO force were considered to calculate the produced excitation force applied to the floater's arm. The sinusoidal wave input with the amplitude and period of 0.4 m and 2.5 s were considered for the validation of HPTO model. The captured image of maximum upward and downward motions of the HIL test rig during the experimental validation of the HPTO unit is depicted in Figure 4C,D.

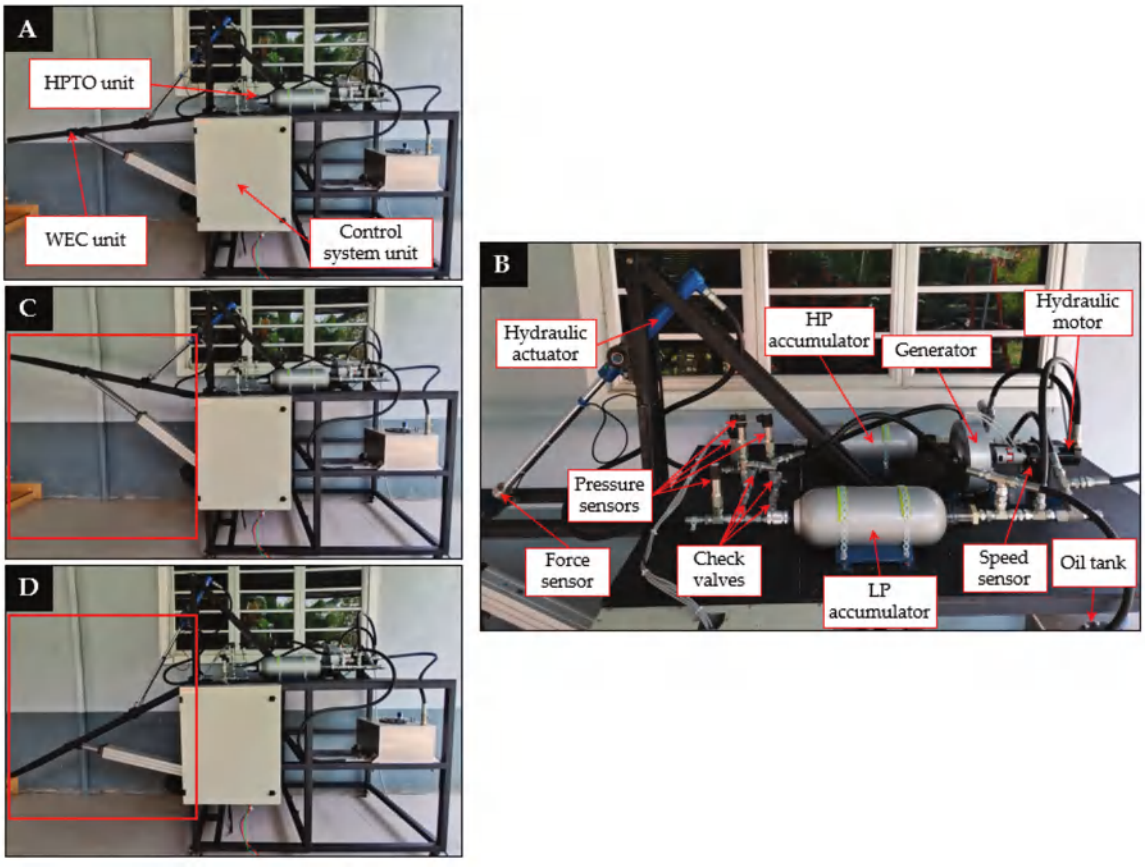


**Figure 4.** Experimental evaluation of WEC with hydraulic PTO unit. (**A**) A complete dry-lab test rig, (**B**) Enlarge image of HPTO unit setup, (**C**) Maximum upward, and (**D**) Maximum downward position of the WEC device.

Figure 5 shows the results of the behaviour of the HPTO unit in a regular wave condition with an amplitude and period of 0.4 m and 2.5 s. From the figure, it can be seen that the simulation results of the developed WEC with the HPTO unit model in

MATLAB/Simulink is in good agreement with the results obtained from the HIL test rig. However, slight differences and some fluctuations in hydraulic motor speed and HPTO force results were obtained during the experiment, as depicted in Figure 5A,B. These differences and fluctuations may be attributed to the errors in the manufacture and assembly of the test rig, the measuring errors of the transducers, the vibration of the hydraulic motor, and the leakage in the hydraulic motor, cylinders and joints. Such a good agreement presented in Figure 5A,B indicates that the developed WEC with HPTO unit model in MATLAB/Simulink presented in the present study would be effective and reliable as a tool for predicting the amount of power that can be generated from the ocean waves.

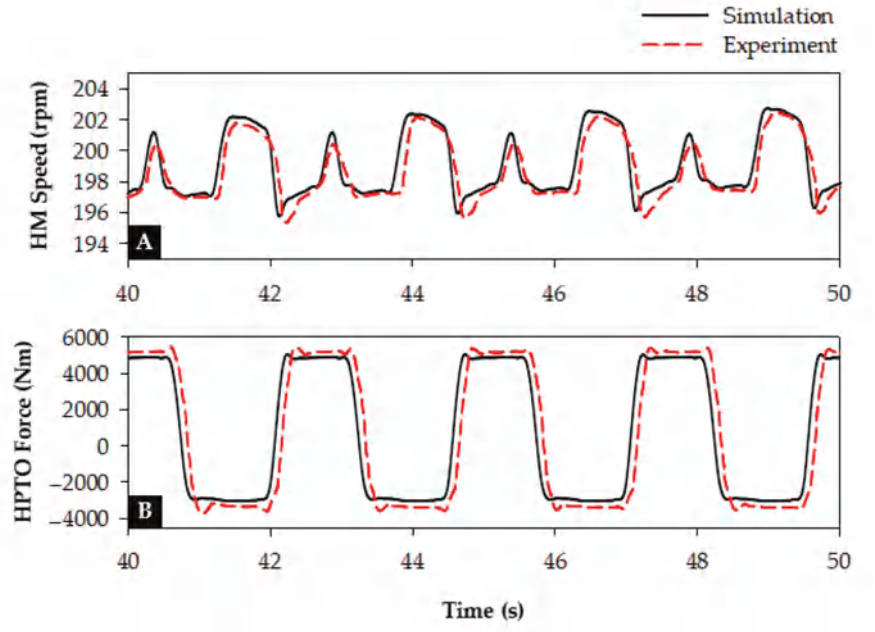


**Figure 5.** Behaviour of HPTO unit in a regular wave condition. (**A**) Speed of hydraulic motor and (**B**) HPTO force applied to the floater's arm.

*4.2. Performance of WEC with HPTO Model in Five Irregular Sea States*

The simulations of the developed WEC with the HPTO unit model using different sea states was first carried out in the present study. This simulation was intended to evaluate the performance of the developed model against the different wave heights and periods. The simulation was started with the nominal sea state (sea state A) and the results from the simulation are presented in Figures 6 and 7. Figure 6A shows the responses of WEC and the hydraulic cylinder piston against the irregular wave input in sea state A. The figure shows that the displacement of the WEC device was slightly lower than the wave elevation, particularly during the upward motion. This is due to influencing factors such as the hydrostatic restoring moment, the moment due to the HPTO unit and the initial moments of floater and arm [36]. Based on the results, the average displacement of the WEC device and hydraulic piston was 70% and 15% of the wave elevation. The figure also depicts that the displacements of the WEC device and piston were slightly delayed from the wave elevation. Figure 6B presents the profile of the HPTO force applied to the WEC device. On average, the HPTO forces applied to the WEC device during upward and downward motion equaled 3.64 kN and 1.99 kN, respectively. The unbalanced HPTO force applied to the WEC device is due to the unsymmetrical effective area of the piston. A larger effective area of piston produced a higher force rather than a smaller effective area piston.

Figure 6C shows the profile of HPA pressure. From the figure, the pressure of HPA reached up to 49 bar several times, which was a 4.5% increased from its pre-charge pressure setting.

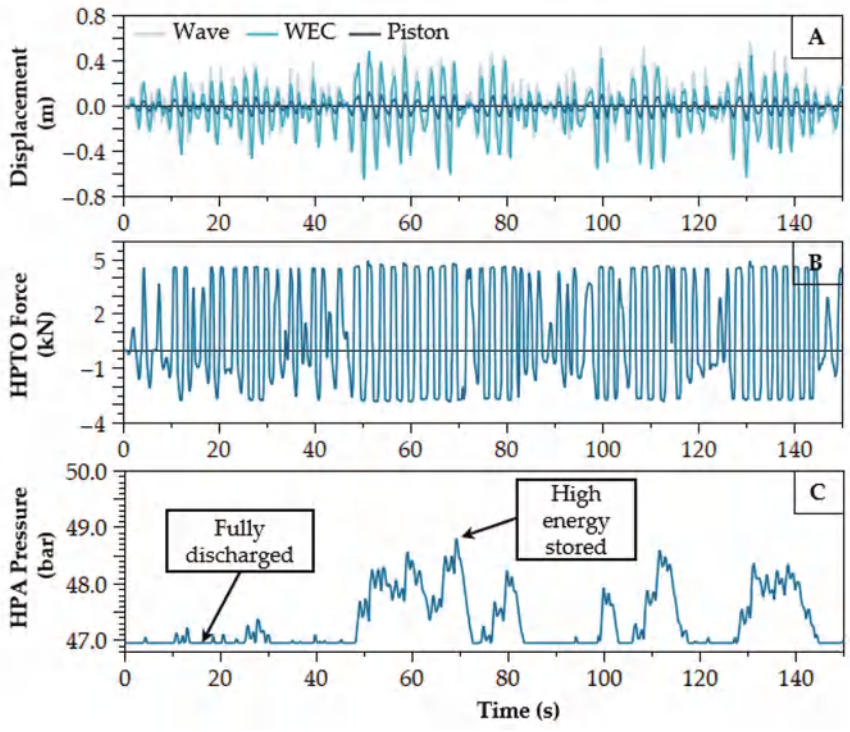


**Figure 6.** Performance of WEC with HPTO unit in sea state A, (**A**) Displacement of Wave, WEC and hydraulic cylinder piston, (**B**) HPTO force applied to WEC device, and (**C**) Pressure of high-pressure accumulator.

Meanwhile, Figure 7A,B show the pressure and speed profile of the HM. It can be seen from the figures that the pressure and the speed of the hydraulic motor reached up to 49 bar and 200 rpm. The smoothing effect of the HPA unit on the hydraulic motor pressure can be seen in Figure 7A. The HPA was able to reduce the fluctuation of the hydraulic motor pressure, particularly after 50 s of HPTO operation. Figure 7C illustrates the profile of the generated power from the HPTO unit. The average power generated from the generator was 70.9% of its rated capacity (100 W). The figure also demonstrates that some fluctuations exist in the generated power from the generator, particularly at the early stage of the operation. The comparison simulation results of the WEC with HPTO unit in each sea state are summarized in Table 5. From the table, the simulation result showed that the significant wave height and peak wave period were affected by the overall performance of the WEC with the HPO unit. First, the table reveals that the averaged angular displacement of the WEC device was increased and decreased, relatively, with increases and decreases of the significant wave height and peak wave period. From the table, the angular displacement of the WEC device in sea states B and D were reduced by 38% and 33% (upward) and 24% and 21% (downward) of its angular displacement in the nominal sea state. Meanwhile, the angular displacement in the sea states C and E were increased by 21% and 16% (upward) and 28% and 18% (downward), respectively. The increase and decrease of the angular displacements are due to the increase and decrease HPTO force applied to the WEC device, which can be obtained in Table 5. The increase and decrease of WEC displacement, relatively, also increase and decrease the generated

output power from the HPTO unit. As can be seen, the average power generated from the HPTO unit in sea states B and D were decreased by 41% and 34% of power from sea state A, while 15.5% and 10.4% were increased in sea states C and E. Overall, the generated power from the HPTO unit in each sea state is below its rated capacity. Thus, several parameter optimization methods, as suggested in [20], can be further implemented to increase the generated power from the HPTO unit.

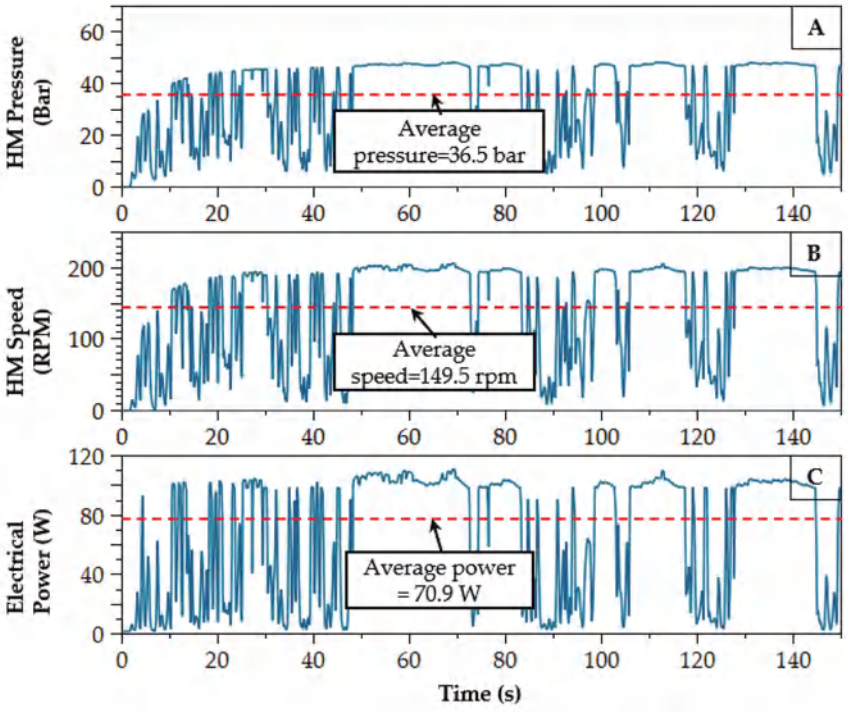


**Figure 7.** Performance of WEC with HPTO unit in sea state A (continue), (**A**) Pressure of hydraulic motor, (**B**) Speed of hydraulic motor, and (**C**) Electrical power generated from HPTO unit.

**Table 5.** Performance of WEC with HPTO unit in different sea states.

| Performance Description (Unit) | | Sea State | | | | |
|---|---|---|---|---|---|---|
| | | A | B | C | D | E |
| Averaged Angular Displacement of WEC (°) | upward | 5.73 | 3.53 | 6.94 | 3.84 | 6.67 |
| | downward | 6.95 | 5.26 | 8.87 | 5.49 | 8.17 |
| Averaged piston displacement (m) | upward | 0.033 | 0.019 | 0.041 | 0.022 | 0.038 |
| | downward | 0.035 | 0.026 | 0.043 | 0.028 | 0.040 |
| Averaged HPTO force (kN) | upward | 3.64 | 3.49 | 4.45 | 3.54 | 4.09 |
| | downward | 1.99 | 1.63 | 2.42 | 1.73 | 2.24 |
| Averaged operating pressure of HM (bar) | - | 36.5 | 27.4 | 41.9 | 29.2 | 39.7 |
| Averaged speed of generator (rpm) | - | 149.5 | 109.1 | 173.6 | 117.2 | 164.4 |
| Averaged generated electrical power (W) | - | 70.9 | 41.7 | 81.8 | 47.1 | 78.2 |

### *4.3. Investigation Studies of HPTO Unit Parameters*

In this subsection, the influence of each HPTO unit parameter on the generator power in five different sea states is discussed. From this subsection, how the power of the generator varies with the considered HPTO parameters and their corresponding to the sea states can be discovered in the following subsection.

4.3.1. Case 1: Position of Hydraulic Cylinder

The influence of HA position on the power of the generator was firstly investigated in this study. For this case, the position of HA was manipulated by adjusting the $L_2$ and $L_3$, as indicated in Figure 1. In this case, $L_2$ was incrementally varied by 0.1 m within the range of 0.1 to 0.7 m. To be fair, during adjustment of the HA position, the initial rod length of HA from point A to B ($L_4$) was maintained as default for every sequence. Figure 8 depicts that the averaged power generated from the generator varies with the vertical mounting distance of HA for different sea states. The figure clearly illustrates that the averaged power generated from the generator increases along with the increase of the horizontal mounting of HA for all sea states. Then, it decreases after reaching the optimal mounting position. From the figure, the optimal values for $L_2$ are different for each sea state. For the small wave height and period sea states (sea states B and D), the optimal value for $L_2$ is smaller than for the case of large wave height and period sea states. At the optimal mounting position, averaged generated power for the sea states A to E were around 72 W, 42 W, 84 W, 47 W and 79 W, respectively. At the lower $L_2$, averaged generated power for all sea states were significantly reduced compared to the bigger value of $L_2$, as depicted in Figure 8. For example, at $L_2$ equal to 0.1 m, the averaged generated power from the generator for the sea states A to E were reduced by 88%, 91%, 82%, 90% and 84% of their optimal values. While at $L_2$ equal to 0.7 m, the averaged power generated from the generator for sea states A to E were reduced by 43%, 53%, 32%, 51% and 38% of their optimal values, respectively. The percentage of averaged power reduction also indicates that the mounting position of HA relies on the wave height and wave period. The percentage of averaged power reduction shows that the mounting position of HA was more affected by low height and a small period for the sea states. Technically, the huge reduction of the averaged power generated at the lower $L_2$ is due to the larger HPTO force applied to the WEC device. So, from these investigation results, it can be suggested that the distance of $L_2$ should be equal or larger than $L_3$ to prevent huge losses due to the mounting position of HA.

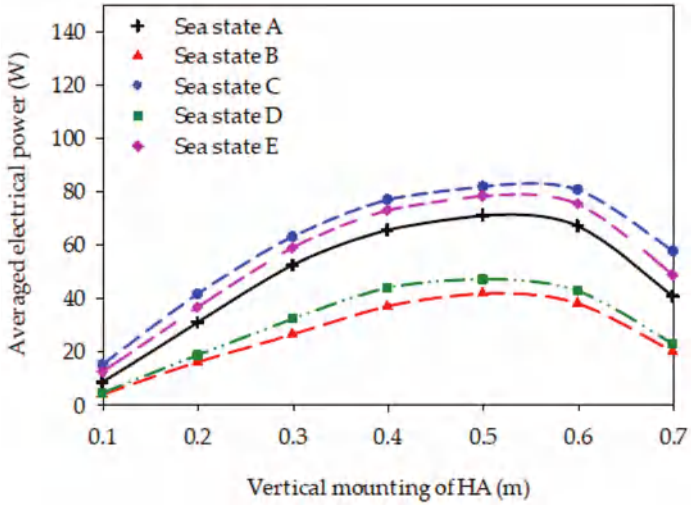


**Figure 8.** Averaged power of generator versus horizontal mounting distance corresponding to different sea states.

4.3.2. Case 2: Piston Size of the Hydraulic Actuator

The influence of the effective area of the piston in both hydraulic actuator chambers is also a concern in this study. As previously shown in Equation (6), the effective piston area relatively affects the amount of feedback HPTO force $F_{HPTO}$ applied to the WEC device. From Equations (7) and (8), the effective area of the piston in both hydraulic chambers can

be calculated via the diameter size of piston and rod ($d_p$ and $d_r$). Since a double-acting with single rod hydraulic actuator was considered in this study, the effective piston area in chamber B is affected by the rod size. This means that the effective piston area in chamber A is larger than that in chamber B. To investigate, the wide range of $d_p$ was used to examine the performance of the HPTO unit. In this case, the values of $d_p$ was incrementally varied by 0.005 m within the range of 0.025 to 0.060 m. In this case, the minimum range was selected based on the smallest piston size that is currently available in the hydraulic equipment market. While the value of $d_r$ remains as the initial parameter setting. Figure 9 presents the effect of the piston and rod diameter on the averaged power generated from the generator in different sea states. From the figure, it can be observed that the averaged generated power is influenced by the piston size of the hydraulic actuator. The figure depicts that the averaged generated power first increases with the increase of the piston diameter size and then starts to decrease after obtaining the optimal value of $d_p$. From the figure, it is clearly shown that the smaller significant wave height and peak period sea states were more affected by the piston size. The result shows that the average generated power for sea states B and D started to decrease after 0.045 m size of the piston, while for the bigger wave height and period sea states, such as sea state A, C and E, the average generated power started to decrease after 0.050 m and 0.055 m, respectively. This may be due to the lower wave forces during sea states B and D compared to wave forces for sea states A, C and E. Technically, more high-pressured fluid can be supplied to the hydraulic motor by a hydraulic actuator with a larger piston size. As a result, the average generated power at the optimal point for sea states A, C and E were found to be 94 W, 118 W and 110 W. Meanwhile, the average generated power at the optimal point for sea states B and D were found to be 64 W and 70 W, respectively.

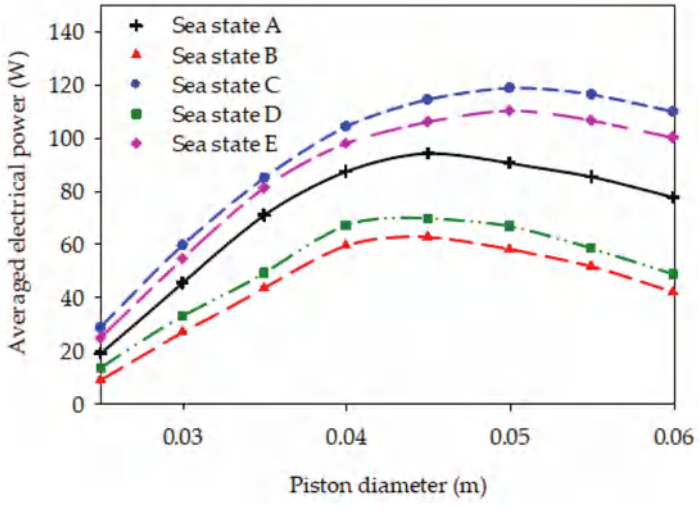


**Figure 9.** Averaged power of generator versus piston diameter corresponding to different sea states.

4.3.3. Case 3: Volume Capacity of HPA

The accumulator plays an important role in mitigating the power fluctuation during a dynamic process of wave power conversion. By using HPA and a robust control strategy, the HPTO unit enables conversion of the high fluctuating wave power into a smooth and continuous electrical power. Since the HPA is more important to the HPTO unit, a further investigation into the main parameters of HPA, such as volume capacity ($V_{HPA,cap}$) should be conducted. Hence, the effect of the volume capacity of HPA on the HPTO performance was explored in the present study. A wide range of $V_{HPA,cap}$ was used to evaluate its effect on the averaged generator power corresponding to the different sea states. In this

case, the value of $V_{HPA,cap}$ was incrementally varied by 2 L within the range of 0.5 to 10.5 L, as previously mentioned in Table 4. Figure 10 presents the effect of $V_{HPA,cap}$ on the averaged generated power from the generator for the different sea states. The figure showed that the averaged power generated from the generator is influenced by the increase of $V_{HPA,cap}$, particularly for large significant wave height and peak period sea states, while there was a less significant effect for small significant wave height and peak period sea states. From the result, the average generated power, particularly for sea states C and E significantly reduced by the increase of $V_{HPA,cap}$. By changing the value of $V_{HPA,cap}$ from 0.5 L to 10.5 L, the average generated power for sea states C and E were reduced by 28% and 20%, respectively. This power reduction can be attributed to more energy accumulated in the HPA, rather than directly flowing to the hydraulic motor when the large capacity of the HPA is implemented.

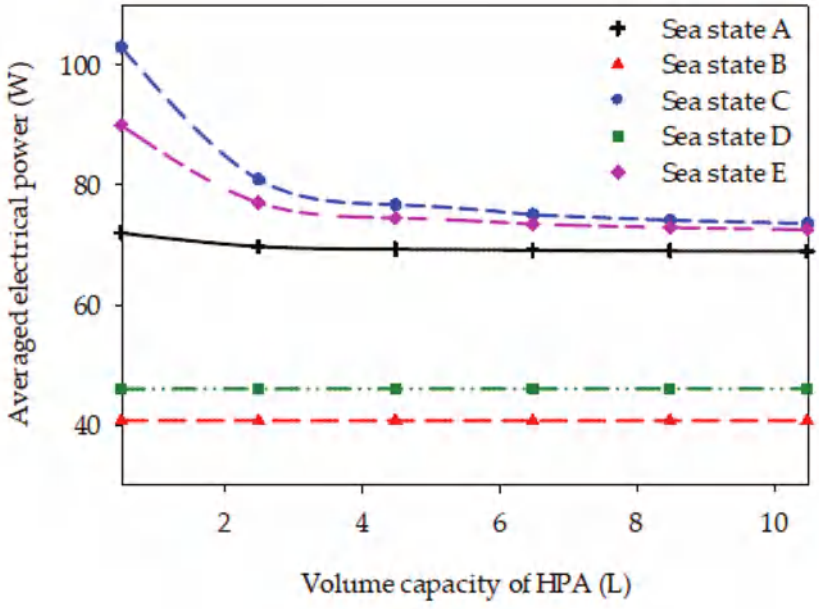


**Figure 10.** Averaged power of generator versus volume capacity of HPA corresponding to different sea states.

4.3.4. Case 4: Pre-Charge Pressure of HPA

The pre-charge pressure of HPA ($P_{HPA,0}$) is another important parameter of the HPTO. Technically, $P_{HPA,0}$ determines how much hydraulic fluid will remain accumulated in the HPA. The charging process of HPA begins when hydraulic fluid flows into the fluid chamber when the HPTO unit pressure is greater than the $P_{HPA,0}$. During charging, the gas is compressed to store energy. Once the HPTO unit pressure is below $P_{HPA,0}$ level, the high-pressure nitrogen gas in the ballast forces hydraulic fluid from the fluid chamber into the hydraulic motor. For such a dynamic process, the investigation of the effect of the $P_{HPA,0}$ on the power of the generator was considered. In this case, the value of $P_{HPA,0}$ was incrementally increase by 10 bar within the range of 20 to 80 bar. Figure 11 presents the variation of $P_{HPA,0}$ on the averaged generated power from the generator for different sea states. As can be seen in the figure, for all sea states the average power of the generator slightly increased, and then tended to be steady after the $P_{HPA,0}$ reached an optimal of $P_{HPA,0}$. The figure showed that a higher level of $P_{HPA,0}$ can be used for large significant wave height and peak period sea states. For example, the level of $P_{HPA,0}$ can be set up to 70 bar for sea states C and E, while, the highest $P_{HPA,0}$ for sea states, B and D was only

up to 40 bar. This difference is due to the different operating pressure of HPTO in each sea state, in which the operating pressure of HPTO is higher in sea states C and E rather than sea state B and D. The averaged generated power at the optimal point for sea state A, C and E were reached up to 80 W, 124 W and 108 W, while for sea states B and D the averaged generated power at the optimal point only reached 43 W and 49 W, respectively.

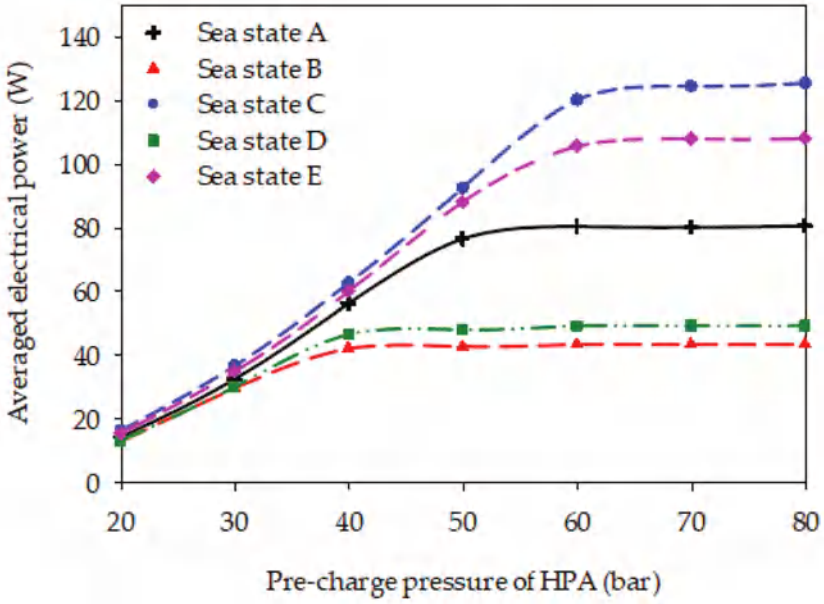


**Figure 11.** Averaged power of generator versus pre-charge pressure of HPA corresponding to different sea states.

4.3.5. Case 5: Displacement of Hydraulic Motor

The fluid displacement of the hydraulic motor ($D_{HM}$) is another important influencing parameter in the HPTO unit. Referring to Equation (14), $D_{HM}$ directly affects the power and torque of the hydraulic motor. Therefore, it is necessary to explore the effect of the $D_{HM}$ on the power of the hydraulic motor and generator. From the preliminary survey, the smallest size hydraulic motor currently available from the available hydraulic equipment for HPTO application 6 cc/rev. Thus, the variation range of $D_{HM}$ was set within 6 to 20 cc/rev and the value of $D_{HM}$ was incrementally varied by 2 cc/rev. Figure 12 illustrates the effect of $D_{HM}$ on the averaged generated power from the generator corresponding to different sea states. From the figure, it is clearly shown that the averaged generated power increases with the increase in $D_{HM}$ and then starts to decrease after reaching an optimal value of $D_{HM}$ for all sea states. The figure shows that a higher value of $D_{HM}$ can be implemented with a large significant wave height and peak period sea states. The result indicates that the value of $D_{HM}$ can be considered up to 10 cc/rev for sea states C and E, but only up to 8 cc/rev for sea states B and D. This may be due to the high operating pressure of HPTO during the large significant wave height and peak period sea states. At the optimal value of $D_{HM}$, the average generated power for sea states A to E can reach up to 72 W, 44 W, 102 W, 50 W and 90 W, respectively. Apart from that, the result also shows that the overestimated value of $D_{HM}$ was more affected in HPTO performance at the small significant wave height and peak period sea states. For example, the average generated power in sea states B and D was reduced by up to 59% and 60% once the value of $D_{HM}$ was increased from the optimal (8 cc/rev) to 18 cc/rev; while for sea states C and E, the average generated power in sea states C and E were reduced by up to 46% and 47% once the value of $D_{HM}$ was increased from the optimal (10 cc/rev) to 18 cc/rev. However, this was vice-versa

during the underestimated value of $D_{HM}$, in which the HPTO performance in the large wave height and period sea states was more affected by the $D_{HM}$. The figure clearly shows that the averaged generated power for sea states C and E were significantly reduced by 53% and 50%. Therefore, the result reveals that the underestimation and overestimation of the $D_{HM}$ can significantly reduce the power generated from the generator.

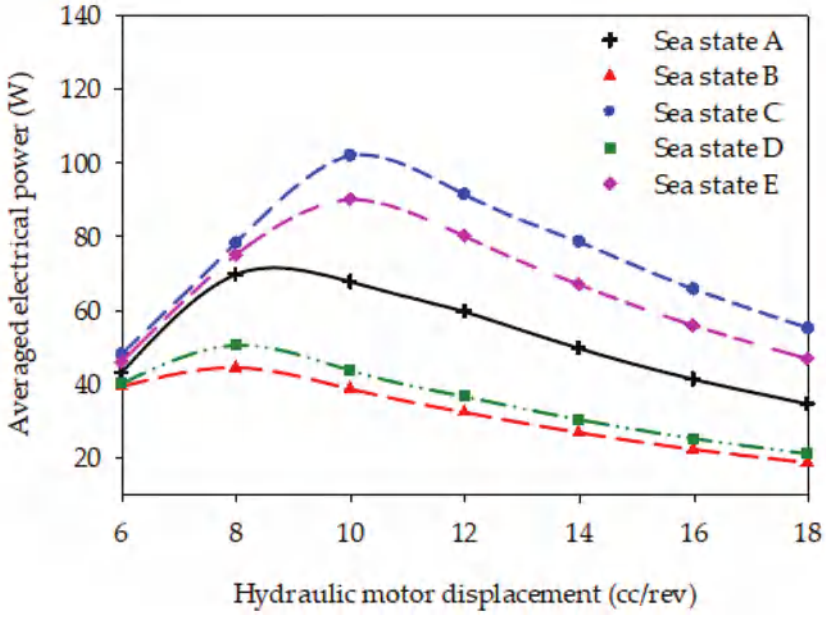


**Figure 12.** Averaged power of generator versus fluid displacement of HM corresponding to different sea states.

4.3.6. Case 6: Damping Coefficient of Electrical Generator

The damping coefficient ($d_G$) is different for each generator. As mentioned in [11], the $d_G$ of each generator is subjected to its type, capacity, etc. Technically, generated output power is affected by the $d_G$. Since the generator is one of the major components of the HPTO unit, the effect of the $d_G$ on the performance of the HPTO needs to be investigated. Thus, the effect of $d_G$ on the generated power from the HPTO unit was investigated in this study. In this case, the $d_G$ was varied from 0.1 to 1.2 Nm/(rad/s) with increments of 0.1 Nm/(rad/s) in each sequence. Figure 13 depicts the effect of $d_G$ on the averaged generated power corresponding to five different sea states. From the figure, it can be seen that the optimal $d_G$ that achieves the highest averaged power was sensitive to changes in significant wave height and peak wave period. During the nominal sea state, the optimal $d_G$ was found to around 0.3 Nm/(rad/s), while, for the short and long peak wave period sea states (sea states B and C), the optimal $d_G$ was found to be around 0.35 and 0.26 Nm/(rad/s). Meanwhile, for the small and large significant wave height sea states (sea states D and E), the optimal $d_G$ was found at around 0.34 and 0.24 Nm/(rad/s), respectively. The result also indicates that the overestimation of $d_G$ badly reduced the averaged generated power for all sea states, particularly sea states A, C and E. As can be seen in the figure, the average generated power for sea states A to E was reduced by 73%, 62%, 72%, 63% and 74% of its optimal value, respectively, due to overestimation of $d_G$ by up to 1.3 Nm/(rad/s). Hence, from the results, it can be said that the generator damping coefficient needs to be optimally controlled to maximize power absorption from the ocean. Thus, the use of several damping control strategies, as suggested in [17], can be considered in the HPTO unit.

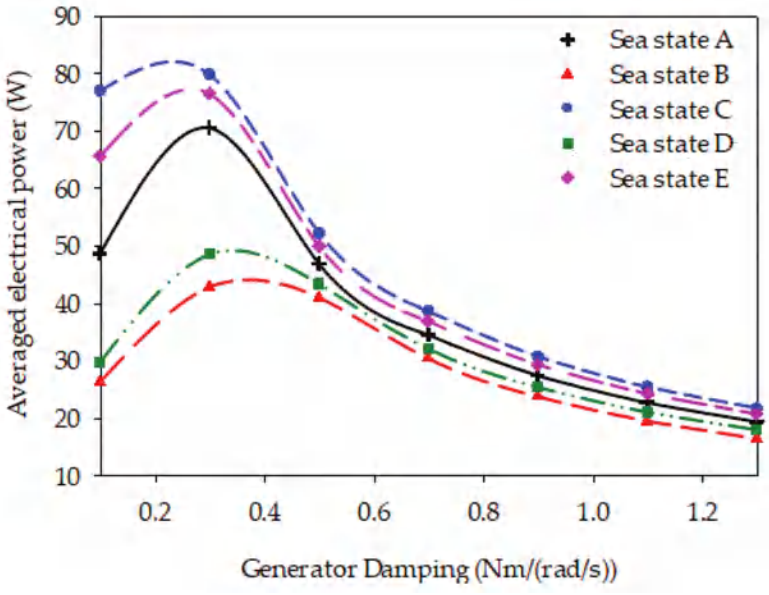


**Figure 13.** Averaged power of generator versus damping of generator corresponding to different sea states.

## 5. Conclusions

A comprehensive analysis of the effects of the important HPTO parameters on performance in generating usable electricity was conducted in the present study. Six critical parameters of the HPTO unit, including vertical mounting and the piston size of the HA, volume capacity and pre-charge pressure of HPA, displacement of HM and damping coefficient of the generator were considered. A simulation study was conducted using MATLAB/Simulink software, in which a complete model of WEC with the HPTO unit was developed using the Simscape fluids toolbox in MATLAB/Simulink. Five different irregular sea state inputs were used to evaluate the effect of each HPTO parameter against the different significant wave heights and peak periods. From the investigation, the following conclusion can be drawn:

(1) For case 1, the effect of the vertical mounting position ($L_2$) of the hydraulic actuator on the power generated by the generator was obtained. From the simulation result, it was found that the averaged power generated increased along with an increase of $L_2$ for all sea states and then decreased after reaching the optimal distance. At smaller $L_2$ (0.1 m), the averaged generated power for sea states A to E was reduced by 88%, 91%, 82%, 90% and 84% of their optimal values, respectively. The value of $L_2$ is sensitive to the significant wave height and peak wave period, in which the best of $L_2$ is larger during the large significant wave height and peak wave period sea state.

(2) For case 2, the averaged power generated was increased along with the increase of piston size ($d_p$) for all sea states. However, the average power was decreased for the over-sized of $d_p$ state. The simulation result shows a $d_p$ sensitive to the significant wave height and peak wave period. Thus, a large size of $d_p$ should be used in the large significant wave height and peak wave period sea state.

(3) For case 3, the simulation results demonstrate that the volume capacity of HPA ($V_{HPA,cap}$) is less sensitive to changes in small significant wave height and peak wave period sea state, and inversely for a large significant wave height and peak wave period sea state, where the increase of $V_{HPA,cap}$ reduced the averaged power generated. This is due to more power accumulated in the HPA rather than directly flowing to

the hydraulic motor. Thus, an appropriate $V_{HPA,cap}$ should be selected based on the HPTO capacity to avoid this power reduction.

(4) For case 4, the simulation result shows that the pre-charge pressure of HPA ($P_{HPA,0}$) should be higher for the large significant wave height and peak wave period sea state rather than the small significant wave height and peak wave period sea state.

(5) For case 5, the investigation results reveal that the underestimated and overestimated hydraulic motor displacement ($D_{HM}$) was significantly sensitive to wave height and peak wave period. Thus, a variable displacement hydraulic motor with a robust control strategy should be considered.

(6) For case 6, the simulation results found that overestimated damping coefficient of the generator ($d_G$) hardly reduced the averaged generated power. Thus, $d_G$ needs to be optimally controlled using appropriate damping control strategies to maximize power absorption from the ocean waves.

The present investigation studies may help researchers and engineers of WECs to improve the efficiency of their systems. The optimization of the critical parameters above is another attractive issue in terms of maximizing the generated power from the HPTO unit. Thus, it is suggested that further research regarding the HPTO parameter optimization using heuristic optimization algorithms should be conducted.

**Author Contributions:** M.A.J., conceptualization, methodology, software, data curation, analysis, writing—original draft; M.Z.I., writing—review and editing and supervision, project administration, funding acquisition; M.Z.D., conceptualization, methodology, writing—review and editing and supervision; Z.M.Y., software, data curation, analysis and writing—original draft; A.A. data curation, analysis and writing—review and editing. All authors have read and agreed to the published version of the manuscript.

**Funding:** This project was funded by the Ministry of Higher Education (MOHE) under the Fundamental Research Grant Scheme (FRGS/1/2019/TK07/UMT/01/1).

**Institutional Review Board Statement:** Not applicable.

**Informed Consent Statement:** Not applicable.

**Data Availability Statement:** Data available on request due to restrictions of privacy.

**Acknowledgments:** The authors would like to thank the Ministry of Higher Education (MOHE) and Universiti Malaysia Terengganu (UMT) for financial support for this research.

**Conflicts of Interest:** The authors declare no conflict of interest.

## References

1. Melikoglu, M. Current status and future of ocean energy sources: A global review. *Ocean Eng.* **2018**, *148*, 563–573. [CrossRef]
2. Farrok, O.; Ahmed, K.; Tahlil, A.D.; Farah, M.M.; Kiran, M.R.; Islam, M.R. Electrical power generation from the oceanic wave for sustainable advancement in renewable energy technologies. *Sustainability* **2020**, *12*, 2178. [CrossRef]
3. Ahamed, R.; McKee, K.; Howard, I. Advancements of wave energy converters based on power take off (PTO) systems: A review. *Ocean Eng.* **2020**, *204*, 107248. [CrossRef]
4. Al Shami, E.; Zhang, R.; Wang, X. Point absorber wave energy harvesters: A review of recent developments. *Energies* **2019**, *12*, 47. [CrossRef]
5. Falcão, A.F. Wave energy utilization: A review of the technologies. *Renew. Sustain. Energy Rev.* **2010**, *14*, 899–918. [CrossRef]
6. Yusop, Z.M.; Ibrahim, M.Z.; Jusoh, M.A.; Albani, A.; Rahman, S.J.A. Wave-Activated Body Energy Converter Technologies: A Review. *J. Adv. Res. Fluid Mech. Therm. Sci.* **2020**, *76*, 76–104. [CrossRef]
7. Sheng, W.; Lewis, A. Power takeoff optimization for maximizing energy conversion of wave-activated bodies. *IEEE J. Ocean. Eng.* **2016**, *41*, 529–540. [CrossRef]
8. Drew, B.; Plummer, A.R.; Sahinkaya, M.N. A review of wave energy converter technology. *Proc. Inst. Mech. Eng. Part A J. Power Energy* **2009**, *223*, 887–902. [CrossRef]
9. Titah-Benbouzid, H.; Benbouzid, M. An up-to-date technologies review and evaluation of wave energy converters. *Int. Rev. Electr. Eng.* **2015**, *10*, 52–61. [CrossRef]
10. Kukner, A.; Erselcan, İ.Ö. A review of power take-off systems employed in wave energy. *J. Nav. Sci. Eng.* **2014**, *10*, 32–44.
11. Jusoh, M.A.; Ibrahim, M.Z.; Daud, M.Z.; Albani, A.; Yusop, Z.M. Hydraulic power take-off concepts for wave energy conversion system: A review. *Energies* **2019**, *12*, 4510. [CrossRef]

12. He, X.; Xiao, G.; Hu, B.; Tan, L.; Tang, H.; He, S.; He, Z. The applications of energy regeneration and conversion technologies based on hydraulic transmission systems: A review. *Energy Convers. Manag.* **2020**, *205*, 112413. [CrossRef]
13. Hansen, R.H.; Kramer, M.M.; Vidal, E.; Hansen, R.H.; Kramer, M.M.; Vidal, E. Discrete displacement hydraulic power take-off system for the wavestar wave energy converter. *Energies* **2013**, *6*, 4001–4044. [CrossRef]
14. Liu, C.; Yang, Q.; Bao, G. Influence of hydraulic power take-off unit parameters on power capture ability of a two-raft-type wave energy converter. *Ocean Eng.* **2018**, *150*, 69–80. [CrossRef]
15. Zou, S.; Abdelkhalik, O. Control of Wave Energy Converters with Discrete Displacement Hydraulic Power Take-Off Units. *J. Mar. Sci. Eng.* **2018**, *6*, 31. [CrossRef]
16. Ding, B.; Cazzolato, B.S.; Arjomandi, M.; Hardy, P.; Mills, B. Sea-state based maximum power point tracking damping control of a fully submerged oscillating buoy. *Ocean Eng.* **2016**, *126*, 299–312. [CrossRef]
17. Jianan, X.; Tao, X. MPPT Control of Hydraulic Power Take-Off for Wave Energy Converter on Artificial Breakwater. *J. Mar. Sci. Eng.* **2019**, *8*, 304. [CrossRef]
18. Liu, C.; Yang, Q.; Bao, G. Performance investigation of a two-raft-type wave energy converter with hydraulic power take-off unit. *Appl. Ocean Res.* **2017**, *62*, 139–155. [CrossRef]
19. Xuhui, Y.; Qijuan, C.; Zenghui, W.; Dazhou, G.; Donglin, Y.; Wen, J.; Weiyu, W. A novel nonlinear state space model for the hydraulic power take-off of a wave energy converter. *Energy* **2019**, *180*, 465–479. [CrossRef]
20. Jusoh, M.A.; Ibrahim, M.Z.; Daud, M.Z.; Yusop, Z.M.; Albani, A. An Estimation of Hydraulic Power Take-off Unit Parameters for Wave Energy Converter Device Using Non-Evolutionary NLPQL and Evolutionary GA Approaches. *Energies* **2020**, *14*, 79. [CrossRef]
21. Jusoh, M.A.; Ibrahim, M.Z.; Daud, M.Z.; Yusop, Z.M.; Albani, A.; Rahman, S.J.; Mohad, S. Parameters estimation of hydraulic power take-off system for wave energy conversion system using genetic algorithm. In *Proceedings of the IOP Conference Series: Earth and Environmental Science*; Institute of Physics Publishing: Bristol, UK, 2020; Volume 463, p. 12129.
22. Hansen, A.H.; Asmussen, M.F.; Bech, M.M. Model predictive control of a wave energy converter with discrete fluid power power take-off system. *Energies* **2018**, *11*, 635. [CrossRef]
23. Gaspar, J.F.; Calvário, M.; Kamarlouei, M.; Soares, C.G. Design tradeoffs of an oil-hydraulic power take-off for wave energy converters. *Renew. Energy* **2018**, *129*, 245–259. [CrossRef]
24. Gaspar, J.F.; Calvário, M.; Kamarlouei, M.; Guedes Soares, C. Power take-off concept for wave energy converters based on oil-hydraulic transformer units. *Renew. Energy* **2016**, *86*, 1232–1246. [CrossRef]
25. Penalba, M.; Sell, N.P.; Hillis, A.J.; Ringwood, J.V.; Penalba, M.; Sell, N.P.; Hillis, A.J.; Ringwood, J.V. Validating a wave-to-wire model for a wave energy converter—Part I: The hydraulic transmission system. *Energies* **2017**, *10*, 977. [CrossRef]
26. Shadman, M.; Estefen, S.F.; Rodriguez, C.A.; Nogueira, I.C.M. A geometrical optimization method applied to a heaving point absorber wave energy converter. *Renew. Energy* **2018**, *115*, 533–546. [CrossRef]
27. Coiro, D.P.; Troise, G.; Calise, G.; Bizzarrini, N. Wave energy conversion through a point pivoted absorber: Numerical and experimental tests on a scaled model. *Renew. Energy* **2016**, *87*, 317–325. [CrossRef]
28. Chen, Z.; Zhou, B.; Zhang, L.; Sun, L.; Zhang, X. Performance evaluation of a dual resonance wave-energy convertor in irregular waves. *Appl. Ocean Res.* **2018**, *77*, 78–88. [CrossRef]
29. Sun, P.; Li, Q.; He, H.; Chen, H.; Zhang, J.; Li, H.; Liu, D. Design and optimization investigation on hydraulic transmission and energy storage system for a floating-array-buoys wave energy converter. *Energy Convers. Manag.* **2021**, *235*, 113998. [CrossRef]
30. Liu, Z.; Qu, N.; Han, Z.; Zhang, J.; Zhang, S.; Li, M.; Shi, H. Study on energy conversion and storage system for a prototype buoys-array wave energy converter. *Energy Sustain. Dev.* **2016**, *34*, 100–110. [CrossRef]
31. Liang, C.; Ai, J.; Zuo, L. Design, fabrication, simulation and testing of an ocean wave energy converter with mechanical motion rectifier. *Ocean Eng.* **2017**, *136*, 190–200. [CrossRef]
32. Zurkinden, A.S.; Ferri, F.; Beatty, S.; Kofoed, J.P.; Kramer, M.M. Non-linear numerical modeling and experimental testing of a point absorber wave energy converter. *Ocean Eng.* **2014**, *78*, 11–21. [CrossRef]
33. Rahmati, M.T.; Aggidis, G.A. Numerical and experimental analysis of the power output of a point absorber wave energy converter in irregular waves. *Ocean Eng.* **2016**, *111*, 483–492. [CrossRef]
34. Jama, M.A.; Noura, H.; Wahyudie, A.; Assi, A. Enhancing the performance of heaving wave energy converters using model-free control approach. *Renew. Energy* **2015**, *83*, 931–941. [CrossRef]
35. Forehand, D.I.M.; Kiprakis, A.E.; Nambiar, A.J.; Wallace, A.R. A Fully Coupled Wave-to-Wire Model of an Array of Wave Energy Converters. *IEEE Trans. Sustain. Energy* **2016**, *7*, 118–128. [CrossRef]
36. Windt, C.; Davidson, J.; Ringwood, J.V. High-fidelity numerical modelling of ocean wave energy systems: A review of computational fluid dynamics-based numerical wave tanks. *Renew. Sustain. Energy Rev.* **2018**, *93*, 610–630. [CrossRef]

energies

MDPI

*Article*

# Environmental Assessment of the Impacts and Benefits of a Salinity Gradient Energy Pilot Plant

**Etzaguery Marin-Coria [1,*], Rodolfo Silva [1,*], Cecilia Enriquez [2], M. Luisa Martínez [3] and Edgar Mendoza [1]**

[1] Instituto de Ingeniería, Universidad Nacional Autónoma de México, Ciudad Universitaria, Circuito Exterior S/N, Coyoacán, Mexico City 04510, Mexico; EMendozaB@iingen.unam.mx
[2] Campus Yucatan, Universidad Nacional Autónoma de México (UNAM), Mexico City 04510, Mexico; cenriqz@ciencias.unam.mx
[3] Instituto de Ecología, A.C. (INECOL), Xalapa, Veracruz 91073, Mexico; marisa.martinez@inecol.mx
* Correspondence: janeth.marin.coria@gmail.com (E.M.-C.); RSilvaC@iingen.unam.mx (R.S.)

**Abstract:** Although the technologies involved in converting saline gradient energy (SGE) are rapidly developing, few studies have focused on evaluating possible environmental impacts. In this work, the environmental impacts of a hypothetical 50 kW RED plant installed in La Carbonera Lagoon, Yucatan, Mexico, are addressed. The theoretical support was taken from a literature review and analysis of the components involved in the pressure retarded osmosis (PRO) and reverse electrodialysis (RED) technologies. The study was performed under a three-stage scheme (construction, operation, and dismantling) for which the stress-inducing factors that can drive changes in environmental elements (receptors) were determined. In turn, the possible modifications to the dynamics of the ecosystem (responses) were assessed. Since it is a small-scale energy plant, only local impacts are expected. This study shows that a well-designed SGE plant can have a low environmental impact and also be of benefit to local ecotourism and ecosystem conservation while contributing to a clean, renewable energy supply. Moreover, the same plant in another location in the same system could lead to huge modifications to the flows and resident times of the coastal lagoon water, causing great damage to the biotic and abiotic environment.

**Keywords:** salinity gradient energy; RED; PRO; coastal systems; stress factors; receptors; environmental impact

**Citation:** Marin-Coria, E.; Silva, R.; Enriquez, C.; Martínez, M.L.; Mendoza, E. Environmental Assessment of the Impacts and Benefits of a Salinity Gradient Energy Pilot Plant. *Energies* **2021**, *14*, 3252. https://doi.org/10.3390/en14113252

Academic Editor: Eugen Rusu

Received: 24 April 2021
Accepted: 28 May 2021
Published: 3 June 2021

**Publisher's Note:** MDPI stays neutral with regard to jurisdictional claims in published maps and institutional affiliations.

**Copyright:** © 2021 by the authors. Licensee MDPI, Basel, Switzerland. This article is an open access article distributed under the terms and conditions of the Creative Commons Attribution (CC BY) license (https://creativecommons.org/licenses/by/4.0/).

## 1. Introduction

As the supply of fossil fuels diminishes, the opportunity of switching to renewable sources of energy will put an end to some of the negative environmental impacts seen since the first industrial revolution [1,2]. The oceans are a major source of renewable energies, such as marine and tidal currents, wave energy, thermal, and salinity gradients, which can all be harnessed [3,4].

Chemical energy known as salinity gradients (SGE) or saline gradient potential (SGP) is available in coastal zones where two water flows of different saline content coincide, e.g., where a river meets the sea [5,6]. By controlling this mixture and capturing the energy before it is released, electricity can be produced without greenhouse gas emissions. It is possible to use only naturally occurring water flows, but it is also possible to employ hybrid systems, which use effluents of anthropic origin, such as residual waters from desalination plants [7–9]. Similarly, the effluent from wastewater treatment plants, of low salinity, could be used as input for an SGP system [10,11].

The methods for producing energy from a saline gradient are varied, but the most advanced methods are reverse electrodialysis (RED) and pressure retarded osmosis (PRO), both of which have already been tested outside the laboratory. Regarding RED, the companies WETSUS and REDstack have developed a 50 kW device in the Netherlands [12,13], while for PRO, the company Statkraft developed a 10 kW plant in Norway [14].

The International Energy Agency has reported that 15,102 TWh of electricity could be produced through salinity gradient in river mouths worldwide; that is 74% of global electricity consumption [15]. However, various physical and environmental limitations were not included in this estimation. Today, taking some of these restrictions into account, and counting only river mouths where this type of energy plant would be feasible, the estimation is 625 TWh, 3% of world consumption [5].

There have been many technological advances in PRO and RED around the world, but there is little information on the impacts the operation and maintenance of SGE plants could have on the functions of nearby ecosystems. The scientific literature surrounding the implementation of SGE at a given study site is scarce. Early works addressing environmental conditions to be monitored mention the amount of water to be extracted (defined as environmental flow, maximum extraction factor, extraction flow, design flow, the annual variation of flow, etc.), the physicochemical characteristics of the water, the physical and chemical characteristics of the input solutions (fresh, marine, treated) and other characteristics, such as salinity structure and temperature (temporal and annual variations) at the extraction and discharge sites [5,12,16–19]. Few works address the very important effects that the SGE implementation could cause on the sediment balance, care in the use of cleaning products (which when accidentally released pollute), and care and disposal of final effluents and membranes [16]. Other studies mention the importance of hydrodynamic studies and environmental forcings that may affect the thermohaline structure and therefore the amount of energy generated from the saline gradient [16]. Even so, there are very few case studies that mention potential environmental impacts. A study proposing a potential site for SGE at Lake Urmia, in Iran, (a Ramsar wetland with a Biosphere Reserve status with endemic species) only assessed in detail the economic implications of implementation [17]. One reason for this is that no operational devices exist.

Some papers mention that the impacts are similar to those of water treatment, desalination, or other renewable energy plants [1,18,20–22]. These works give an overview of potential impacts to habitat, local vegetation and associated fauna, water quality, sediment properties, and social issues related to fisheries and navigation rights and hydrodynamic modifications (changes in flows and their directions and mixing zones). All these impacts are caused by the location of the devices or their interactions with the environment. Specific work on the impact of saline gradient technology highlights potential impacts regarding water intake, final effluent disposal, and impacts associated with infrastructure [23]. However, the study in [22] summarises the overall potential impacts of SGE implementation using a three-phase scheme (construction, operation, and decommissioning).

This paper aims to present a scheme for an environmental impact assessment (EIA) that allows the identification of possible environmental impacts from the implementation of SGE in a coastal lagoon within an environmentally protected area. Through the description of stressors, receptors, and responses, an EIA is developed for the coastal system of La Carbonera, in the state of Yucatan, Mexico.

## 2. Materials and Methods

### *2.1. Study Area*

The area considered in this work is La Carbonera lagoon, in the northeast of the Yucatan Peninsula, Mexico (21°13′41.80″–21°14′4.79″ N, 89°53′21.66″–89°54′0.45″ W) (Figure 1) [24]. This coastal lagoon lies in a region of karst characteristics and is approximately 16.5 km$^2$ in area. More detailed information concerning the geology of the region can be found in Appendix A. The channel connecting it to the sea, the Gulf of Mexico, is quite recent, a result of the passage of Hurricane Gilbert, in 1988. The fresh water of the system comes from submarine groundwater discharges, or springs, carrying continental water, which is the result of regional precipitation. The main inlet of fresh water, locally called a 'peten', is located southwest of the system. 'Peten' is a colloquial Mayan name that refers to islands of vegetation which are associated with freshwater springs that allow the

development of perennial rainforests, frequently exposed to flooding [25]. It is a shallow lagoon, 0.30–2.0 m, and as such is very much influenced by the local atmospheric climate. The bathymetry of the lagoon and the coastal zone are presented in Appendix A. The mean annual rainfall is 1025 mm and there are three seasons: dry (March to June), rainy (July to October), and 'Nortes', characterised by a decrease in temperature, storm clouds, and heavy rains (November to February) [26–28]. The region is influenced by the transit of tropical storms during the summer months, which commonly intensify into hurricanes. Appendix A contains more detailed information on the climate of the study area.

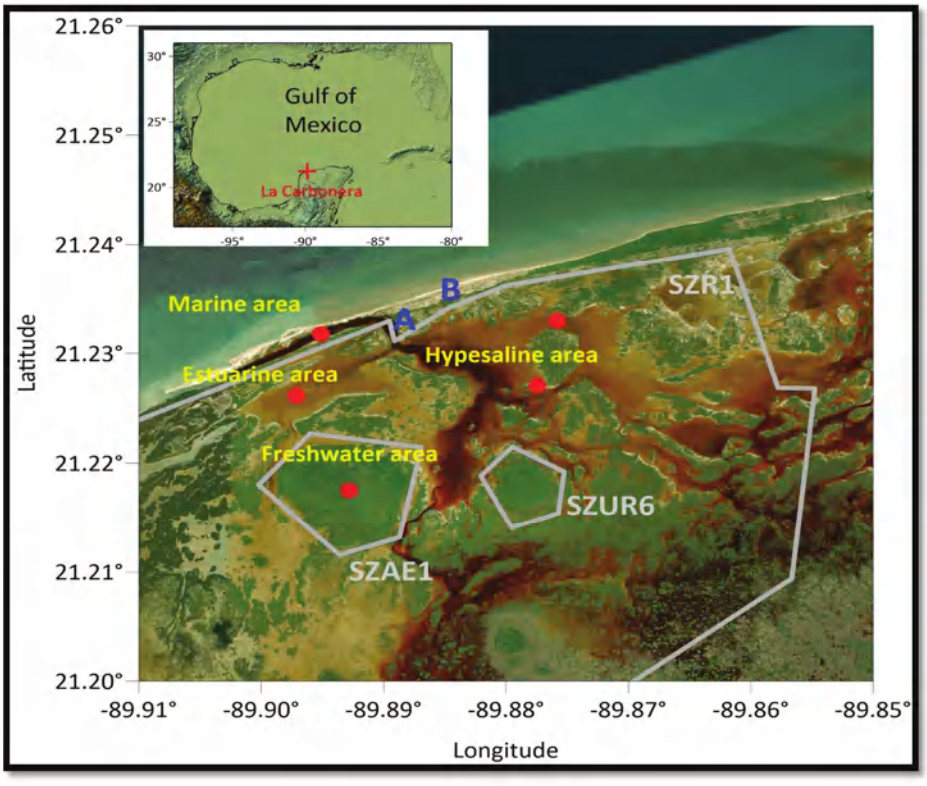


**Figure 1.** Location of La Carbonera lagoon, Yucatan, Mexico, showing areas with significant saline properties, the location of the CTD sensors (red dots), and sites proposed for the RED power plant (A and B). The polygons SZR1, SZAE1, and SZUR6 are areas with protection categories within the Cienegas and Manglares State Reserve of the North Coast of Yucatán (RECMY).

La Carbonera is part of a system of wetlands along the coast of Yucatan. It has a sand bar of 1.5 km in length, a sandy beach, and coastal dunes of medium height. Mangroves lie behind the dunes, around the lagoon, and sometimes further inland. There are springs and an area of swampland around the lagoon [29]. Geological data on the lagoon are given in Appendix A.4.

On the coast, the waves have low energy, except in the Nortes season or tropical storm or hurricane conditions, when the waves, currents, wind, and precipitation are extreme. The tidal regime is mixed, predominantly diurnal, with tides ranging from 0.40 m spring tides to 0.08 m neap tides. Appendix A has more information on the hydrodynamics, currents, and tides. The mean air temperature is between 24 °C and 26 °C, with variations

of up to 10 °C throughout the day, minimums in December and January and maximums in July and August [30].

### *2.2. Legal Framework*

This lagoon system is part of a Natural Protected Area (NPA) in the region known as the Cienegas and Manglares State Reserve of the North Coast of Yucatan (RECMY), which has a total surface area of 55,000 ha and covers several municipalities of the State of Yucatan. The aim of officially recognising the ecological importance of the region was to protect the coastal ecosystems there, which are mainly well-conserved mangroves. La Carbonera is in the west of the reserve, and within it, several polygons have been assigned categories according to their uses. The lagoon is within polygon SZR1, which has the category of Buffer Zone/Public Use. In this zone, current or future actions are given permits if they lead to sustainable development and, at the same time, create conditions to conserve the reserve's ecosystems in the long term. Recreation, leisure activities, group or individual tours are allowed in designated sites, approved for this purpose. Overnight stays and camping are permitted, as well as the development of low-impact infrastructure, in accordance with the Ecological Use Plan for the Coastal Territory of Yucatan. Such infrastructure must be subject to the corresponding authorisations and permits in terms of land and environmental use; including lodging infrastructure, walkways, trails, conditioning of water crossings, signage, and surveillance, which are aimed at sustainable use and the inspection and surveillance of such sites. The construction of new infrastructure, as well as actions that have an effect on hydrological flows, must comply with the relevant environmental impact requirements (Figure 1, polygon SZR1).

Within polygon SRZ1, there is a smaller polygon of category Core/Subzone Restricted Use Zone, SZUR6. This is a peten zone within the lagoon. It is better conserved, or little altered; an area that contains ecosystems, natural phenomena, and geohydrological processes of special interest, as well as species of flora and fauna that have special protection. In this polygon, only exceptional activities that do not modify the ecosystems and that are subject to strict control and supervision measures are allowed, subject to having a permit from the Reserve's authorities [31].

There is also another polygon with the category of Buffer Zone/Subzone of Special Use, SZAE1. This is where the main groundwater discharge to the lagoon is located. It is an area composed of vegetation mosaics with a certain degree of conservation. It contains natural resources which are essential for the social development of the inhabitants of the area. The exploitation of these resources must be carried out without damaging the ecosystem and without substantially modifying the landscape or causing irreversible environmental impacts, in appropriate ways, subject to limited, supervised load capacities. Ecotourism is therefore allowed if it is sustainable and compatible with the environment. For this, operators must have the corresponding permits and management plans, from the Reserve's authorities. The promotion of environmental management units for the intensive and extensive use of wild flora and fauna is also allowed, with the corresponding registers and authorised management plans. Similarly, artisanal and subsistence fishing activities are permitted, subject to surveillance and supervision, with fishing gear that has been authorised, for each case, in the specific sites of these subzones [31].

### *2.3. Geographical Boundaries and Current Uses*

Within its geographic margins, La Carbonera lagoon has no human settlements or infrastructure around it, although it is located between two towns, to the west, Sisal, and to the east, Chuburna. The current anthropic activities in the lagoon are local fishing, small-scale tourism promoted in the surrounding localities, and scientific research by various local and national institutions.

In the scientific literature, some characteristics are mentioned which imply that monitoring is necessary before and after the implementation of SGE exploitation: a very marked saline structure (a horizontal gradient, in this case), low tidal amplitude, and substantial

control of hydrodynamics with atmospheric forcings [16]. More specific biophysical details of La Carbonera are presented in the following sections.

### *2.4. Thermohaline Structure*

The thermohaline structure of this lagoon, similar to many coastal systems, has important variations at different temporal scales throughout the year, giving variations in the potential energy obtained from SGE. According to the salinity and temperature characteristics, La Carbonera has four defined zones [32–35] (Figure 1) as follows:

- A permanent fresh water effluent in the southwest of the lagoon (<5 psu (practical salinity units) with an almost constant temperature (27 °C));
- An estuarine zone in the central west of the system (where the salinity concentration varies with tides between 5 and 35 psu);
- A marine zone in the mouth of the sea inlet (around 35 psu);
- A hypersaline zone in the east of the system (60–100 psu).

The temperatures in zones 2, 3, and 4 show seasonal (15–37 °C) and daily variations of up to 10 °C and 20 psu or more in salinity. This lagoon has a strong horizontal salinity gradient, with hypersaline characteristics in the east, marine in the centre, estuarine in the west, and a freshwater zone in the southwest. In Appendix A, the salinity patterns of the lagoon are shown.

### *2.5. Theoretical Potential for Generating SGE*

Reyes-Mendoza et al. [35] have reported the theoretical potential of SGE available in La Carbonera lagoon, based on the thermohaline structure and environmental factors (evaporation, air temperature, etc.). There are three possible plant configurations to harness the saline gradient of the lagoon: freshwater/seawater (FW/SW), freshwater/hypersaline water (FW/HW), and seawater/hypersaline water (SW/HW). The energy available from these are the following:

- FW/SW: 0.244 $\pm$ 0.0889 kW, with a maximum of 0.527 kW in May, in the dry season;
- FW/HW: 1.111 $\pm$ 0.277 kW, which is the maximum average of the three plants' configurations;
- SW/HW: 0.413 $\pm$ 0.194 kW, with a maximum of 0.916 in December, in the Nortes season.

On the other hand, the great variations in the thermohaline structure determine the variability of the power potential throughout the year. For a capacity factor of 90%, the installed capacity for the FW/SW configuration should be 0.133 kWh, for the SW/HW configuration 0.25 kWh, and for the FW/HW configuration, 0.527 kWh [35]. These figures were obtained considering the mixing of 1 $m^3/s$ of saline and fresh water.

### *2.6. Biological Characteristics*

In this region, there are several species of economic importance (regional and local fisheries), ecosystemic and anthropogenic applications (medicinal, construction, tourism), or areas with some category of risk, according to the 059-Semarnat-2010 [36] or the International Union for Conservation of Nature (IUCN) (Table 1). Although many more species are reported, only those with anthropic importance and/or uses, or a protection category were assessed.

**Table 1.** Species reported in the north of Yucatan, detailing their ecological and commercial importance, anthropic uses, and protection category.

| Scheme 37 | Category of Protection | Importance and/or Uses |
|---|---|---|
| VEGETATION [37,38] | | |
| Mangrove | | |
| *Conocarpus erectus*<br>*Avicennia germinans*<br>*Rhizophora mangle*<br>*Laguncularia racemosa* | Threatened | Erosion control and soil conservation/construction. Key in the life cycle of various organisms (fish and crustaceans). Carbon reservoirs, natural filter for water quality. |
| Coastal dune | | |
| *Cordia sebestena*<br>*Jacquinia macrocarpa* | Uncategorised | Ornamental, medicinal, substrate fixation |
| *Bravaisia berlandieriana* | Uncategorised | Construction, medicinal, substrate fixation |
| *Metopium brownei* | Uncategorised | Toxic, substrate fixation |
| *Capparis incana*<br>*Gomphrena serrata*<br>*Rivina humilis*<br>*Capparis flexuosa* | Uncategorised | Medicinal, substrate fixation |
| *Acanthocereus tetragonus*<br>*Sideroxylon americanum* | Uncategorised | Edible, substrate fixation |
| *Pithecellobium keyense* | Uncategorised | Substrate fixation |
| Peten | | |
| *Ficus cotinifolia* | Uncategorised | Reclamation of degraded land |
| *Manilkara zapota*<br>*Sabal yapa* | Uncategorised | Medicinal, construction, and handicrafts |
| Lowland flooded forest | | |
| *Sporobolus pyramidatus* | Uncategorised | Primary cover resistant to saline soils |
| *Solanum nigrum* | Uncategorised | Edible |
| *Haematoxylum campechianum* | Uncategorised | Textile |
| *Ipomoea carnea* | Uncategorised | Medicinal, ornamental |
| Seagrasses | | |
| *Thalassia testudinum* | Minor concern | Key in the life cycle of various organisms (fish and crustaceans). Carbon reservoirs. |
| FISHES [39] | | |
| *Fundulus persimilis*<br>*Fundulus grandissimus* | Subject to special protection | Endemic |
| *Gambusia yucatana* | Uncategorised | Endemic |
| *Sphoeroides testudineus*<br>*Strongylura notata*<br>*Harengula clupeola* | Uncategorised | Traded for bait, resident, abundant species (vital in the food chain) |
| *Trachinotus falcatus*<br>*Lutjanus griseus*<br>*Lutjanus synagris*<br>*Floridichthys polyommus*<br>*Archosargus probatocephalus*<br>*Eucinostomus gula*<br>*Eucinostomu argenteusMugil curema*<br>*Mugil trichodon*<br>*Hyporhamphus unifasciatus*<br>*Chriodorus atherinoides* | Uncategorised | Marketed for local and regional consumption |
| *Poecilia velifera* | Subject to special protection | - |
| *Aetobatus narinari* | Almost threatened | Commercial importance in the region |
| CRUSTACEANS [40] | | |
| *Callinectes sapidus* | Uncategorised | Marketed for local and regional consumption |
| BIRDS [41] | | |
| *Phoenicopterus ruber*<br>*Phalacrocorax brasilianus*<br>*Cochlearius cochlearius*<br>*Platalea ajaja*<br>*Ardea alba* | Minor concern | For tourism (birdwatching) |
| *Campylorhiynchus yucatanicus* | Near threatened | Endemic |
| *Egretta rufescens* | Subject to special protection | For tourism (birdwatching) |
| REPTILES [42] | | |
| *Crocodylus moreletii* | Subject to special protection | For tourism (sighting) |
| *Eretmochelys imbricate* | Critically endangered | Tourism (controlled releases at turtle camps) |
| *Chelonia mydas* | Endangered | Tourism (controlled releases at turtle camps) |
| *Caretta caretta* | Endangered | Tourism (controlled releases at turtle camps) |
| ARTHROPODS [43] | | |
| *Limulus polyphemus* | Near threatened | Medicinal |

### 2.7. Environmental Impact Assessment

To ascertain the potential impacts of SGE implementation at La Carbonera, an Environmental Impact Assessment (IEA) was conducted [44–47]. The selection of the environmental impacts was based on the available scientific literature, such as [1,21–23].

The impact analysis used the [48] classification framework proposed for the impact assessment of other ocean renewable energies. The analysis was conducted for three phases: construction, operation, and decommissioning. This EIA considered stressors, receptors, and environmental responses and impacts. Stressors are those characteristics of the environment that may change due to the implementation of SGE in construction, operation, and decommissioning. Receptors are elements of the ecosystem with the potential for some form of response to the stressor, including the various biotic and abiotic components of the ecosystem with the potential to be affected. Effects, or responses, are how these receptors change, without indicating magnitude or significance. Finally, impacts address the severity, intensity, or duration of the effects and cover the direction of the effect, which can generate positive or negative outcomes.

The impacts of this technology are similar in the construction phase to those of seawater desalination plants, wastewater treatment plants, or other renewable energy plants. Since there is currently insufficient on-site experience on the impacts, the stressors considered were based on the analysis of the components of the PRO and RED technologies (Figure 2). This figure gives a general view of the main components of both technologies. In section A, the pipes and the filtering system are shown. In section B, depending on the technology used, and the expected production, the site will require several, repeated PRO or RED modules (membranes in both cases, in RED also electrolyte solutions), as well as hydraulic installations (turbines in PRO), sanitary installations and storage facilities for inputs and waste. Section C shows the electrical installations for power distribution/storage (should include cabling, towers, etc.). In both PRO and RED, a final by-product is a brackish water or seawater, depending on the scheme used (SW/FW, SW/HW, or FW/HW).

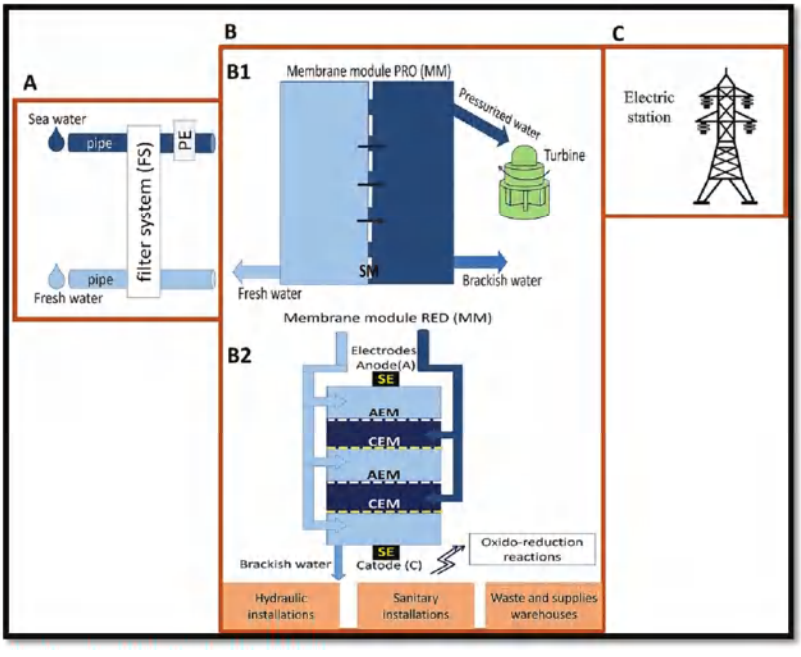


**Figure 2.** Components and processes involved in RED and PRO technologies that may produce environmental impacts in coastal systems. Abbreviations: PE (pressure exchanger), SE (electrolyte solution), AEM (anion exchange membrane), CEM (cation exchange membrane). The components by sections are shown (A, B and C).

For the determination of receptors, shown in Figure 2 (A–C), general impacts, similar to other engineering projects in coastal systems, are expected, including the following:

1. changes to land use (excavation, land newly used, etc.);
2. emission of pollutants (atmosphere, water, land, solid waste, etc.);
3. storage of waste (in situ, transport, waste sites, etc.);
4. overexploitation of resources (raw materials, energy consumption, water, flora, and fauna, etc.);
5. alterations in species composition and abundance (emigration, reduction in numbers, extinction, etc);
6. deterioration of the landscape (topography, vegetation, watercourses, surroundings, etc.);

Finally, from the revision of biotic and abiotic features of the system shown in the case study, an analysis of Stressors, Receptors, and general Responses to the implementation of SGE in potential systems was presented.

It is hoped that this work can serve as a guide for other cases elsewhere.

## 3. Results and Discussion

A general analysis of the environmental impacts of PRO and RED technologies in three phases (construction, operation, and decommissioning) is presented. These impacts can also be applied to other potential systems that use salinity gradients for energy production (river mouths, estuaries, coastal lagoons). The receptors highlight those characteristics of coastal environments that may be susceptible to change due to the SGE (Figure 3). The responses were analysed for each receptor, revealing the potential impacts of this technology (Figure 3).

In this overview of possible impacts on potential systems, it is important to mention that these may be minor or major impacts, depending on several factors, such as the size of the plant, the characteristics of each system (biotic and abiotic), and scheme used for energy harvesting (natural solutions or anthropic effluents). In the case of La Carbonera, the exploitation scheme proposed is in line with the regulations in force and adapted to the specific characteristics of the site.

The scheme for La Carbonera is the hypothetical implementation of net output of 50 kW RED power plant of the size and production of the RED prototype located in Afsluitdijk, in the Netherlands. This plant included three water storage tanks, two pretreatment systems (concentrated and dilute solution), and eight membrane stacks. The proposed infrastructure is therefore low impact.

For the size and energy production of this hypothetical plant, it is important to consider first that many of the environmental impacts in each phase will depend on the characteristics of the site where the plant is built. Therefore, some aspects taken into account to select a location, with consideration to possible responses, are reported in Figure 3 and include the following:

- Consider the proximity of the resource (freshwater, marine, hypersaline);
- Choose building sites on land with sparse vegetation;
- Consider smaller areas for excavation and the introduction of pipelines;
- Consider that permanent effects (such as changes to hydrodynamics) have greater effects on receptors than temporary effects (such as construction noise or increased turbidity) in resilient systems, such as coastal lagoons [41];
- Consider final effluent discharge area;
- Consider areas accessible to tourism;
- Consider species conservation.

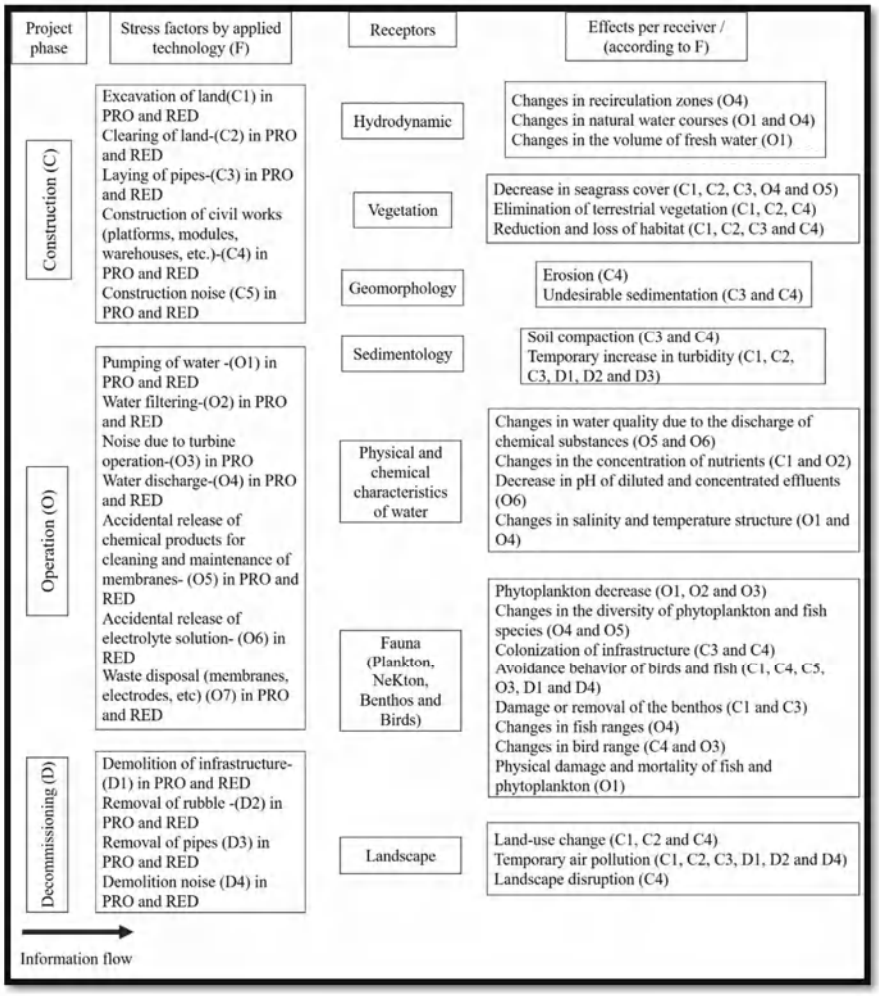


**Figure 3.** Stressors, receptors, and possible effects due to the implementation of SGE in La Carbonera lagoon in a three-stage scheme (construction, operation, and decommissioning) for the main components of the PRO and RED technologies. The letters indicate the number of stressors according to the phase of the project.

From these considerations, installing the RED plant behind a small jetty in the lagoon, A in Figure 1, would induce significantly greater environmental impacts than with option B of Figure 1. First, this result is because the excavation for the pipelines would be greater, as the hypersaline water must come further, and all the impacts associated with the various stressors (C1, C2, and C3, Figure 3) must be considered. Second, the pipeline would pass through several mangrove patches, and therefore, the vegetation here and its associated fauna would be severely affected. Thirdly, although the availability of seawater at this location (at the mouth of the lagoon) would be close to the RED plant, the interruption to the tidal flow entering the lagoon, due to the constant intake of this solution, would generate various negative impacts. One of the main impacts possible is that large areas of the hypersaline zone that depend on this sea–lake exchange could dry out. Exposed sediments would therefore be salinised, and large areas of mangroves would dry out. In addition, the interruption of this flow would change the hydrodynamic conditions that favour the distribution and abundance of the various fish species reported in Table 1.

Likewise, this would affect the sedimentation processes at the lagoon mouth. On the other hand, the discharge of effluent from this location into the sea would also imply greater excavation and the laying of pipes and damage to the mangrove and associated fauna (Figure 3).

Although the proposed infrastructure is small, the correct location of a plant and especially of the collecting and discharging zones may result in huge differences in terms of impacts: in this example, locating the plant at site A may generate several negative impacts that can be avoided with the location and design of plant at B (Figure 1). The design process, including location selection and analyses to be considered, are presented next.

### *3.1. Construction Phase*

The proposed location for the RED plant is on the coastline between La Carbonera lagoon and the coastal dune, outside the main SRZ1 polygon, and under the jurisdiction of the Federal Maritime Terrestrial Zone (ZOFEMAT) (A, Figures 1 and 4). At this location, several elements need to be constructed (roads and other infrastructure related to basic services). In the literature, as an example, the design of a PRO plant with a production capacity of 50 kW net output covers approximately 7000 $m^2$ (the approximate size of a football field) [49], while the area of the Afsluitdijk RED plant covers approximately 2750 $m^2$ (measured from Google maps). The total area proposed at La Carbonera is 5250 $m^2$, the RED plant elements will be distributed in 3000 $m^2$ (Figures 4 and 5), which includes three tanks for the concentrated (hypersaline), diluted water (marine or fresh), and the resulting effluent (brackish marine). There will also be space for the membrane modules and for a test laboratory. Finally, spaces for storage, waste storage, sanitary facilities, and an electrical station will be added (Figure 5).

**Figure 4.** Potential location of the RED pilot power plant; the dotted lines indicate the pipelines.

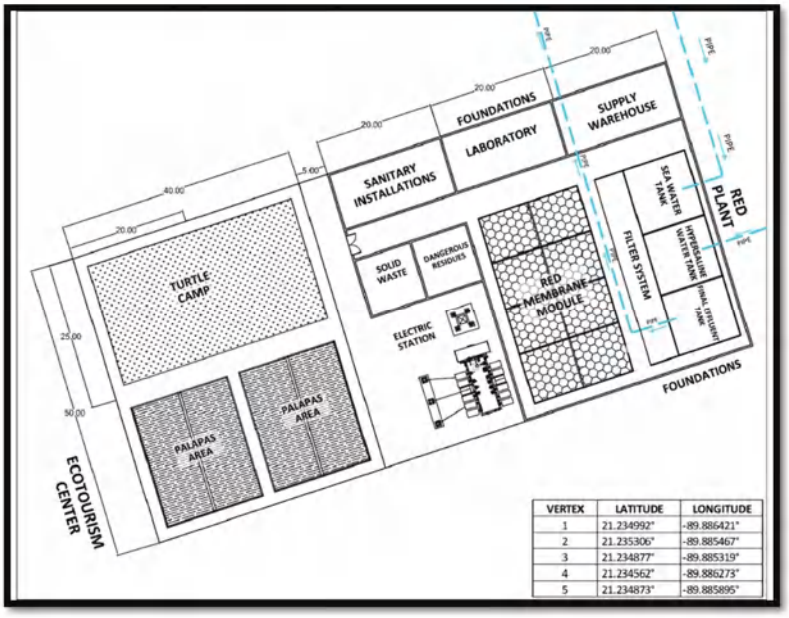


**Figure 5.** Distribution of space for the proposed RED plant and ecotourism centre at La Carbonera site, 5250 $m^2$.

La Carbonera, in spite of being a natural protected area, is becoming increasingly popular with tourists. This is encouraged since tourism is more profitable than fishing and agriculture. In line with regulations that allow minor infrastructure in the area, it is proposed that alongside the SGE plant a small ecotourism centre is built (with a total area of 2000 $m^2$), with cabins, viewpoints, rest areas, and a section for supplies, such as kayaks and boats. (Figures 4 and 5). This centre could include a turtle camp, as the area receives three protected species (*E. imbricata*, *C. mydas* and *C. caretta*, Table 1), arriving to lay their eggs. The incubation of the eggs, laid on the beach, would improve hatching success. The huts and nesting pens could be made using local palms (*Sabal yapa*, Table 1), widely used for this type of construction [50].

The ecotourism centre would benefit from the electricity generated at the RED plant. This energy could be used to charge mobile phones, cameras, or torches, in addition to the electricity needed for the turtle camp (mainly the nurseries), and in the future, could also supply energy for electric boats. The energy generated would be sufficient to make the plant self-sufficient in electricity. An ecotourism centre would provide well-paid jobs and also limit the pressures associated with the present mode of tourism; visitors coming into the area on day trips from other towns and villages which has brought various environmental problems to this area. The biological richness of the region is accessible in only a few places, and many features of the tourism model are misguided. Excessive growth in some of these areas has led to the infilling of swamp areas to build homes, damage to the coastal dunes due to road construction, and poor management of solid waste and residual water, in particular [42] (Figure 6). Using this site solely for ecotourism, scientific development, and species conservation could help to curb such chaotic, harmful growth around La Carbonera. In addition, the mangroves, swamps, and dune vegetation would be preserved because the ecotourism centre would not be built in these ecosystems. It would also promote environmental awareness among the local population.

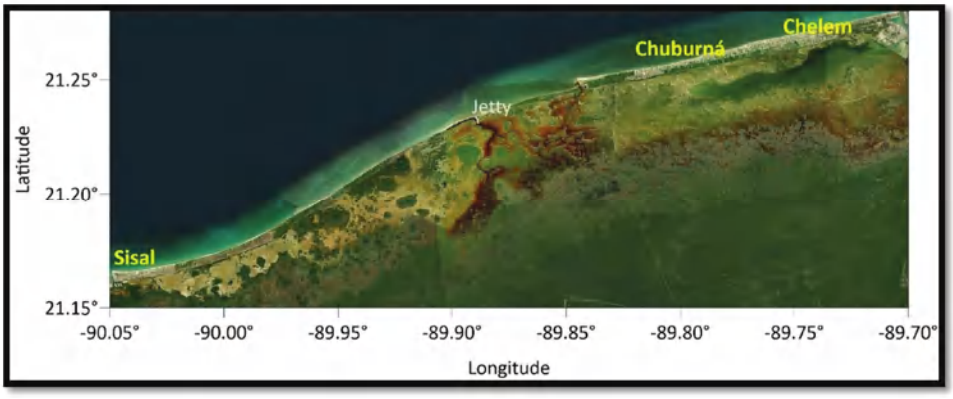


**Figure 6.** Aerial view of the villages around La Carbonera lagoon (the jetty is shown as a reference).

The stressors examined (Figure 3) include excavation, site preparation, placing pipelines, and the construction of platforms and modules. The impacts are similar to those of any other engineering project: removal of vegetation, habitat loss, erosion, unwanted sedimentation, soil compaction, temporary increase in turbidity, avoidance behaviour of birds and fish (due to construction noise), damage or removal of benthos, change of land use, temporary air pollution, and landscape disruption. Nevertheless, all of these will depend on the construction techniques and on the precautionary measures taken. The plant would be located on the seashore (Figure 2, section B), and as it would be affected by the tides, it is proposed that the RED plant be built on pillar-supported infrastructure (palafitte) that will allow water to flow beneath. These low-impact structures do not require extensive excavation [51] and would minimise some impacts on geomorphology and vegetation. They would also permit the free passage of wildlife, particularly useful in storm surge events. In terms of landscape disruption and land use change, as it is a small project, the impacts are expected to be minimal. Given that the site proposed for the plant will not modify the hydrodynamics of the lagoon, natural sediment transport changes are not expected. Additionally, any increase in turbidity, damage or elimination of benthos, erosion or soil compaction, and air pollution will only be temporary. In the case of vegetation and habitat loss, this location was chosen (Figure 4) precisely because there are no large patches of vegetation, except for some coastal dune species in the vicinity (Table 1).

During construction, in order to lay pipes, excavation work is required, which can lead to temporary increases in turbidity (due to sediment movement), loss of vegetation cover (terrestrial and aquatic) and associated habitat loss, removal of benthic organisms, and the release of nutrients and pollutants from the bottom of the lagoon (Figure 3).

The pumping system should be low cost and easy to maintain (to avoid algal blooms, oxygenation, and suspended particles). Three schemes are possible for the water intake in the lagoon: Marine Zone and Freshwater Zone (MW/FW); Marine Zone and Hypersaline Zone (MW/HW); or Freshwater Zone and Hypersaline Zone (FW/HW) (Figure 1). Water intakes should be close to the plant, both to minimise the impact of pumping losses on net power production and to avoid environmental impacts associated with some stressors (excavation) [52]. One option to avoid impacts from the excavation is to lay pipes on the surface and thus avoid the impacts associated with this stress factor. In the MW/FW and FW/HW schemes, the first problem is that the area where the fresh water emerges is within polygon SZAE1, and although ecotourism activities and the exploitation of flora and fauna can occur in this area with a permit, laying pipelines may not be compatible with the conservation laws of this polygon [31]. On the coasts of Yucatan, groundwater is used to supply fresh water to nearby settlements. Thus, the MW/FW and FW/HW schemes could be a possibility using wells or pumping to extract fresh or brackish water [53] in order to avoid negative effects on other processes and activities.

In the MW/HW scheme, which the plant is designed to use (Figure 4), hypersaline water would be taken from the hypersaline zone to the plant, and the pipeline would pass through parts of the SRZ1 polygon; however, low impact sustainable infrastructure would be used (Figure 4). Seawater would be brought to the plant directly from the sea, under the jurisdiction of the ZOFEMAT (Figure 4). Although another possibility for this region, where there is high radiation and evaporation, generating hypersaline conditions, would be to use seawater evaporation ponds. The volume of hypersaline water needed would therefore not be an impediment.

For the energy production expected, an inflow of 200 $m^3$/h of both solutions is required [52]. These inflows will pass through a hydraulic network, which includes the set of pipes, pumps, and other accessories (elbows, valves, etc.) that will allow the entry and exit of the solutions. For a flow of this volume, 10-inch diameter pipes are required; hence, the impacts associated with excavation will be less. The hypersaline water must be piped to the plant; options to avoid the mangrove patches in its path exist, and special attention must be paid to the protected mangrove species (*C. erectus*, *A. germinans*, *R. mangle* and *L. racemosa*) [36]. For the discharge pipe, the same factors apply. These species are important because they provide shelter and protection areas for birds and various species of fish, and they deliver ecosystem services such as filtering water discharges from the mainland to the sea [54] and protection from wind and waves that prevents coastal erosion in an area that is also affected by hurricanes [55].

In the construction phase of the proposed design, no large-scale pipes would be installed within the lagoon; therefore, the loss of seagrasses, the release of pollutants and nutrients from the bottom of the lagoon, and the removal of organisms from the benthos would be practically nil, and the increase in turbidity due to the movement of sediments would be only temporary (weeks). Regarding the seagrass ecosystem, in areas with high salinity, seagrasses are not found; therefore, in the water intake in the hypersaline zone, there will be no damage to seagrasses [56,57]. In the hypersaline zone, the depths are 50 cm or less (Figure 2), and therefore, the hydraulic network here should be able to pump hypersaline water from different points to prevent it from drying out.

On the other hand, regarding the avoidance behaviour of birds due to construction noise (Table 1), emblematic species such as the flamingo (*Phoenicopterus ruber*, Table 1) would probably modify their distribution in the area only temporarily (weeks). In addition, with RED technology, no turbines will be used in the operation phase; hence, noise pollution would only occur during construction.

### *3.2. Operation Phase*

In this phase, the impacts associated with water pumping and water pretreatment (Figure 3) are the first that should be considered. Pretreatment of the water intake is crucial for the operation of a RED system [58]. Such a system must ensure low-cost performance and effective sediment filtration [52]. In the RED plant of Afsluitdijk, the filtration system is of the drum and gravity type, and even with small intakes of very good quality water cartridges, filters can be used [52]. The impacts associated with water pumping and pretreatment are related to the amount of fresh water and hypersaline water that will be taken from the system and pass through it. These impacts include changes to natural watercourses, as well as changes in the nutrients and salinity of the water. Possibly, and depending on the intensity, these alterations may affect native species and natural ecosystems. For instance, it is known that changes in salinity alter the reproductive and feeding behaviour of flamingos and horseshoe crabs (*Limulus polyphemus*) [59].

Another impact is the possible decrease in phytoplankton biomass retained in the filtration system. The latter is a concern at the Afsluitdijk pilot plant because large quantities of plankton, fish, and larvae must be filtered, which has ecological implications and may also have economic implications [60]. Since the biomass of microorganisms at the base of food chains is affected by this, it can lead to imbalances in the food chain and local fisheries [23,48].

Detailed hydrological studies are therefore needed to determine the amount of water that can be extracted from the lagoon and how much it can be altered without generating the above-mentioned impacts. In the case of the Afsluitdijk pilot plant, the intakes in the sea and in the lagoon area of 200 $m^3/h$, assuming a technical potential of 1 $MJ/m^3$ of seawater and freshwater, can produce up to 50 kW net power output [52]. In La Carbonera, taking the concentrated solution from the lagoon (hypersaline water) counteracts the effects on the biomass of microorganisms to a certain extent, since the biomass is reduced due to the hypersalinity of the area [59]. The diluted solution could be taken from wells on the coast, in which case there would be no phytoplankton, due to the lack of light. On the other hand, it could be taken directly from the sea, and this would have fewer microorganisms than that of the estuarine and marine zones of the lagoon [61].

Another stress factor is the disposal of the final by-product of the RED process—the brackish water. Even if the intended scheme is MW/HW, the water mix would have a similar or higher salinity than seawater. The change in salinity of the effluent must be calculated in the laboratory. The effluent must be discharged in an appropriate area, at the appropriate time, and the dispersion of this effluent by the hydrodynamic actions of the system should not alter the natural salinity patterns in that ecosystem [32,33].

Depending on the volume of the water, pump diffusers may be needed (alternating or slanted) in the hydraulic network, to distribute the flows in different directions within the lagoon, or into the sea [62]. The discharge of water used may not induce negative impacts at sites where the hydrodynamic performance and salinity concentrations are known prior to the design for the effluent flow. This is so at sites where there has been salinity deterioration as a result of previous anthropogenic activities.

The change in salinity is only one of the environmental conditions responsible for the variety and abundance of fish reported for this lagoon (Table 1) [39]. In addition, salinity indirectly affects the distribution of species through its role in water density and the resulting hydrodynamics [63].

The spatial/temporal variation of water masses and their salinity is important for the distribution of organisms, especially of fish, which only live under certain salinity ranges, according to their tolerance to this parameter [64–66]. This is important for the distribution of various marine species of commercial interest (Table 1). Discharging a saline effluent into the lagoon, of marine salinity or slightly higher, in the hypersaline zone, will lower the salinity in this zone and thus limit the amount of hypersaline water available for power generation. In consequence, the impact on different species may be significant.

It is important to mention that there are many characteristics that make this an environment that harbours great diversity in fishes, but high salinities have been associated with a lower richness and diversity of fish [67]. Thus, for species distributed in marine/estuarine environments, such as *S. testudineus*, *S. notata*, *H. clupeola*, *T. falcatus*, *L. griseus*, *L. synagris*, *F. polyommus*, *A. probatocephalus*, *E. gula*, *E. argenteus*, *M. curema*, *M. trichodon*, *H. unifasciatus*, *C. atherinoides* and *A. narinari*, (Table 1) [39], a potential decrease in salinity in the hypersaline zone would alter the extent of their distribution areas.

However, to avoid changes in salinity and resulting limitations in resources, it is better to discharge this effluent into the sea since, being saline and of a small volume, it will not have the same effects as if it were brine [68]. On the other hand, stressors such as the accidental release of cleaning and maintenance chemicals and electrolyte solutions must be regulated against any facility handling hazardous chemicals.

Both in the pretreatment of solutions and in the cleaning of membranes and facilities, products such as chlorine are used, which can be toxic to the environment [23,48]. Usually, chlorine is used to avoid degradation of the membranes caused by biological growth in them. There is evidence that even small amounts of chlorine (e.g., 0.1 ppm) can have ecological impacts which induce a significant reduction in the productivity of dragged phytoplankton and species diversity [23]. Similarly, electrolyte solutions should be handled with caution [69]. The electrolyte solutions are stored in the electrode compartment which also contains the electrodes and is sealed with membranes that generally have

special properties to ensure the confinement of the electrolyte, recirculating it in a closed circuit [70]. There are reports of the toxicity of this type of element [23], but there is not much information on the toxic gases or compounds that are generated in the redox process within such a compartment (depending on the redox couple and the electrolyte used). Furthermore, in these compartments, some instability in pH control sometimes occurs since anion exchange membranes have a non-negligible proton transport number. This may allow an increase in the pH of the electrode solution, accompanied by a decrease in the pH of the effluent, and this may not be environmentally acceptable if it is too high [70]. Although the pH of the effluent would only change in the event of an accidental release, it is important to note that this parameter is an indicator of water quality. It affects the toxicity of certain compounds, such as ammonia, by controlling their ionisation, as well as the bioavailability of certain pollutants, such as heavy metals. For example, water with a pH range of 6.5 to 8.5 is suitable for many biological systems. Values of over 9.0 and lower than 5.8 limit the development and physiology of aquatic organisms [71].

Finally, it is worth noting the positive impacts that an SGE plant could have on La Carbonera. In the operational phase, the pipes will provide new spaces for colonization (bioincrustation) by sessile species [1]. These structures offer heterogeneity to the habitat and appropriate surfaces for algae and sessile organisms to colonise, especially on the muddy bottom. Fish and other invertebrates will be attracted by the hard surface, the shade, the changes in turbulence, the small spaces, and eventually, by the availability of food sources [48,72]. However, this type of infrastructure can also encourage the establishment of non-native species, invasive species, and blooms of harmful algae; therefore, the extent and composition of the colonisation are difficult to predict [73,74]. In the case of La Carbonera, pipes in the hypersaline zones would be easily colonised in the short term by barnacles, which live in the carbonated structures which stick to the surfaces and may cause deterioration. For this reason, their colonisation should be treated cautiously since they also damage RED membranes, encouraging the proliferation of microorganisms which impede the free passage of water or ions and thereby reduce the functionality of the system [75]. Although the production of 50 kW of electric energy from renewable sources is by no means a technological challenge, this work aims to provide electric power using the best technologies available, producing the smallest possible footprint, in harmony with the land use of this area (i.e., [76]).

With the present technological maturity of SGE techniques, these objectives do not yet yield low costs. Firstly, because the cost of the energy depends on the establishment of the market and industry; if the technological development is successful, the manufacturing of the parts will become cheaper. In the meantime, support from public funding is to be expected [77]. On the other hand, when environmental and social aspects are prioritised, a cost–benefit analysis based only on economic variables is not sufficient [78,79]. If the community face expensive-energy versus no-energy, their decision will be controversial.

For this specific case, the goal is not to urbanise the area or provide services that will promote urbanisation. The goal is to offer services that may assist environmental protection and conservation activities held in La Carbonera Lagoon and its surroundings where only low-density ecotourism is allowed. In this sense, a pilot plant using emergent technology is both suitable and affordable. Other technologies may not be feasible at this site. For example, although an established solar energy industry exists, the installation of solar panels may increase the air temperature around them, which is undesirable in environmentally sensitive areas. Additionally, a strategy for energy storage would be needed, thus increasing the final cost. There are similar disadvantages for wind energy, with additional construction difficulties [21]. Thus, an SGE plant, with the proposed additional facilities, seems to be a good strategy for promoting education, environmental conservation, and technology development.

### *3.3. Decommissioning Phase*

In this phase, few impacts are expected. A RED plant built on palafittes should not require large-scale activity using heavy machinery. In the case of the pipes that have been colonised by algae and sessile organisms, their removal will eliminate this artificial habitat and also the organisms that installed themselves there. The soil is not expected to be severely impacted by the type of foundations used. On the other hand, the noise associated with demolition may temporarily affect the behaviour of birds and fish. Finally, the infrastructure of the proposed ecotourism centre should not be demolished since these facilities offer attractive spaces for tourism and assist in the conservation of species in the area.

## 4. Conclusions

A preliminary environmental assessment of the potential impacts of a 50 kW net output RED power plant using SGE on the coastal lagoon of La Carbonera was carried out. Many impacts depend on the size and location of the SGE plant and the water intake or on the technology to be implemented. In this case, a small-scale SGE power plant, using the RED technology, combined with an ecotourism centre, would provide renewable energy and protection of resources for the lagoon system and the nearby area around it, as well as providing well-paid jobs for local people that may eventually encourage an improvement in the care of coastal ecosystems.

Although several water schemes can be used in this ecosystem (FW/MW, FW/HW, and MW/HW), everything will depend on the availability of saline water. In both cases, there are alternatives; for instance, to use the dilute solution (FW) through wells on the coast, and the concentrated solution (HW) directly from the lagoon (according to hydrological studies) or through marine water evaporation ponds.

In terms of the potential impacts, the most concerning are the change in the volume of water in the lagoon and the disposal of the final effluent. While many negative potential responses could be expected, if the EIA covers information on the biotic and abiotic characteristics of the ecosystem at a given point in time, in addition to the site characteristics, many of these impacts could be minimised or avoided.

While the study in [22] suggested that most of the impacts due to the implementation of SGE occur in the construction phase, this study shows that although the impacts then may be very evident, even with mitigation measures, the ecosystems in La Carbonera could recover from these temporary effects. More damaging to the ecosystems would be the permanent and constant changes in characteristics which an SGE plant would induce, such as in the hydrodynamics (changes in water flows or volume) and salinity gradients. Therefore, it must be taken into account that since they are highly variable ecosystems that have close hydrological connectivity with the surrounding systems, any modification can have implications for neighbouring systems.

From the results of the Receptors and Responses analysis, the importance of monitoring these features during and after the construction phase must be underlined [79]. Many of the Receptors analysed are also present in other systems with potential for SGE. Even though methodologies for their characterisation already exist for most of them, it is still difficult to find quantitative criteria which demonstrate how positive or negative these Receptors are when SGE technology is applied.

Even so, this work offers the first attempt to evaluate the potential changes induced by SGE plants. This analysis for La Carbonera is important at the present time even though the technology discussed is as yet untested at a large scale, and there are no plants using it in Mexico. Small pilot plants, such as that suggested here, could offer insights for successful larger developments in the future.

Finally, although this system is healthy at present, an EIA would serve to minimise negative impacts. In this way, the benefits of SGE, zero greenhouse gas emissions, and the use of renewable sources could be successfully harnessed at La Carbonera.

**Author Contributions:** Conceptualisation, E.M.-C. and R.S.; methodology, E.M.-C. and M.L.M.; software, E.M.-C.; validation, R.S., C.E., M.L.M., and E.M.; formal analysis, E.M.-C. and R.S.; investigation, E.M.-C.; writing—original draft preparation, E.M.-C. and R.S.; writing—review and editing, E.M.-C., R.S., C.E., M.L.M., and E.M.; visualisation, E.M.-C. and R.S.; supervision, C.E., M.L.M., and E.M.; project administration, R.S.; All authors have read and agreed to the published version of the manuscript.

**Funding:** This research was funded by the CONACYT-SENER-Sustentabilidad Energética project: FSE-2014-06-249795 Centro Mexicano de Innovación en Energía del Océano (CEMIE-Océano).

**Informed Consent Statement:** Not applicable.

**Data Availability Statement:** Data sharing not applicable. No new data were created or analysed in this study. Data sharing is not applicable to this article.

**Acknowledgments:** We are grateful to Jill Taylor for the English revision, and to Roberto Rivera for support in managing Autocad. The authors thank the Centro Mexicano de Innovación en Energía del Océano (CEMIEOcéano) for providing support in the research in the CONACYT-SENER-Sustentabilidad Energética project: FSE-2014-06-249795 Centro Mexicano de Innovación en Energía del Océano (CEMIE-Océano). Finally, thanks to the Civil Engineering Postgraduate of the UNAM and CONACYT for the grant awarded for the development of this project.

**Conflicts of Interest:** The authors declare no conflict of interest.

## Appendix A

*Appendix A.1. Precipitation, Evaporation, and Atmospheric Temperature*

The heaviest rains, associated with tropical systems in the peninsula, occur between June and October. In the winter, from November to February, it is also common for rain associated with the passing of cold fronts, or 'Nortes'. The annual precipitation varies between 444 mm and 1290 mm and is greater north to south, and east to west, in the state of Yucatan. The dry season, March to June, has very little rain, with high levels of solar radiation which generate extremely high temperatures [80].

As is typical in tropical areas, the evaporation exceeds the precipitation (approximately 1800 and 1290 mm/year, respectively). The atmospheric temperature has a defined annual oscillation, with maximums in summer. The annual average temperature is 26 °C, the maximum monthly average is around 36 °C, in May, and the minimum monthly average is 16 °C, in January [35,81].

*Appendix A.2. Tides, Winds, and Waves*

According to [82], the tides are diurnal, with higher high water = 0.590 m; mean high water = 0.461 m; mean water level = 0.326 m; mean low water = 0.238 m, and mean lower low water = 0.000 m.

As explained by [83], winds in the Yucatan Peninsula are mostly Trade winds, from the east and northeast, locally modified by a marked system of coastal breezes, with sustained averages of 5.5 m/s. The waves are of low energy, with a mean annual significant wave height of Hs = 0.78 m, mean peak period Tp = 4.6 s, and a predominant northeast direction (see Figure A1).

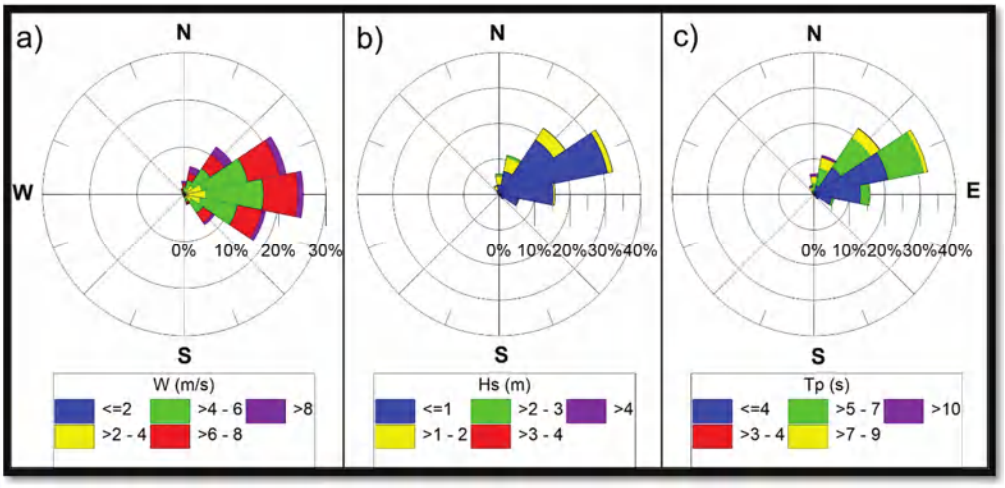


**Figure A1.** Roses showing the direction and magnitude of (**a**) wind velocity, (**b**) wave height, and (**c**) peak period. Reanalysis data from [83].

In addition, the region has atmospheric systems of short duration which modify these patterns: in summer there are tropical cyclones, which can become hurricanes, with sustained winds of up to 44 m/s, Hs > 10 m, and Tp > 12 s, and in winter, strong 'Nortes' can have winds of up to 15 m/s, Hs = 4.5 m, and Tp = 8.7 s [83].

*Appendix A.3. Bathymetry*

The inlet linking the lagoon with the sea has depths of 1.5–2 m, the shallow interior is only 0.5 m deep, with the exception of the channel that links the freshwater inflow area with the lagoon (southwest), where depths are 2 m close to the inflow, and 0.5 m towards the lagoon interior (Figure A2). The depths in the marine area show the shallow, extensive nature of the continental shelf off Yucatan.

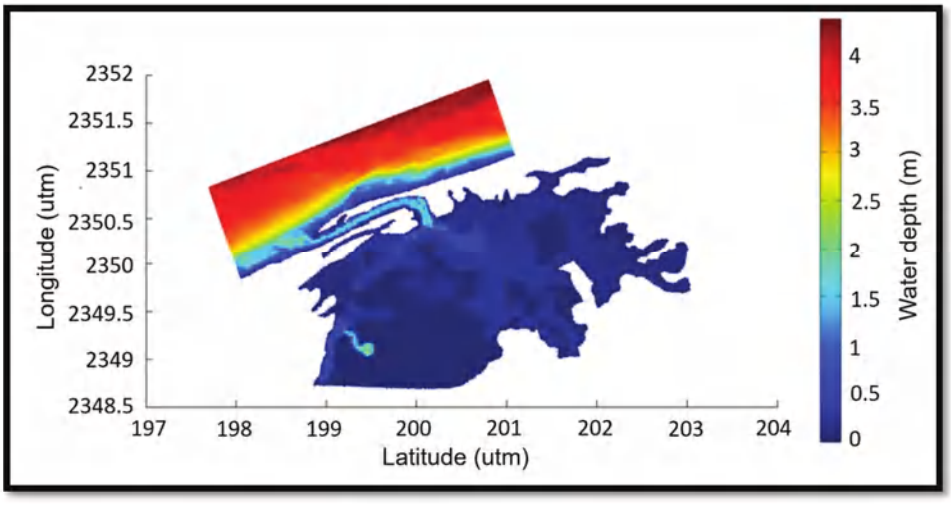


**Figure A2.** Bathymetry of the lagoon of La Carbonera and nearby marine area [33].

*Appendix A.4. Hydrogeological Characteristics*

La Carbonera is part of the karst system of the Peninsula of Yucatan (Batllori-Sampedro et al., 2006). In the lagoon, three types of sediment lie on top of the karst strata: sand, rocky sediment, and mud [24]. The orientation of the sandy beaches on the coast is predominantly north–northwest. The mean grain diameter is 0.2–0.5 mm [84,85].

The main hydrological feature of the coastal systems of the peninsula es that freshwater emerges from underground springs or seeps into lagoons and wetlands [86]. Once in the lagoon systems, it begins to mix and patterns of salinity and temperature develop between the fresh water and the water of the lagoon, producing a complex thermohaline circulation system [27]. Such is the case with the inflow in the southwest of the lagoon, where an estuarine gradient is produced.

*Appendix A.5. Hydrodynamics*

The main hydrodynamic drivers are the tides, the predominant winds of the region (Trade Winds, sea breezes, and Nortes). The study in [33] reported that inside the system, the residual currents are around 0.05 m/s, both when influenced by the local breezes as well as the winds (Figures A3 and A4). As can be seen, the tides entering through the inlet spread east, west, and southwards in the lagoon system (Figure A3). In the centre, south, and east of the lagoon, there are mixing zones, with higher values (close to 0.2 m/s) which are greater during 'Nortes' (Figure A4).

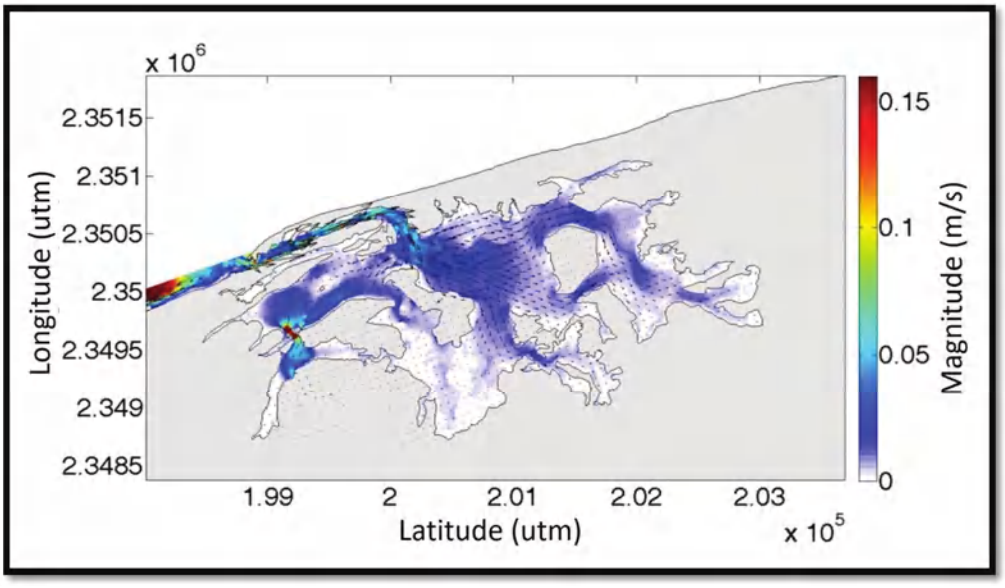


**Figure A3.** Example of the residual circulation pattern (m/s) during a spring tide with sea breeze forcing [33].

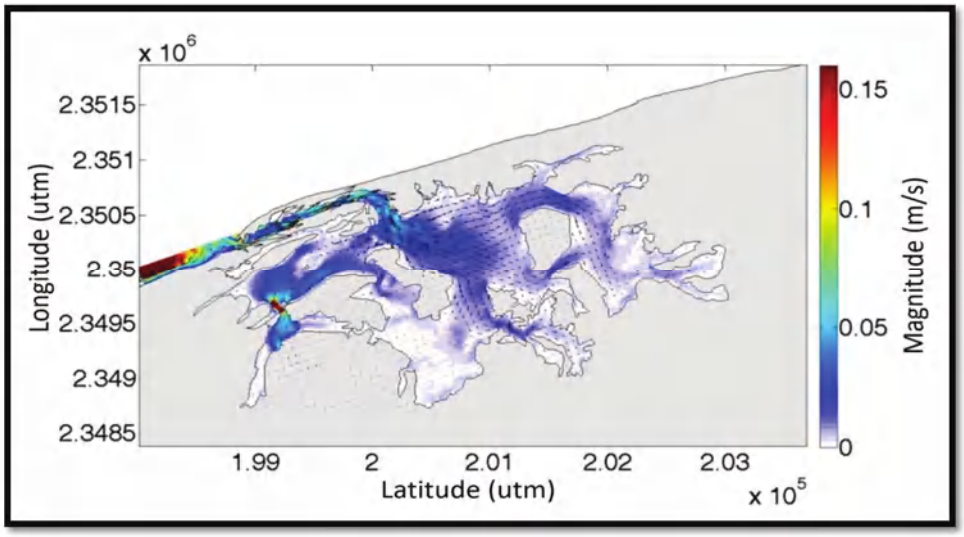


**Figure A4.** Example of the residual circulation pattern (m/s) during a spring tide with forcing from NE winds [33].

*Appendix A.6. Salinity Patterns*

The general patterns of salinity in the lagoon of La Carbonera are seen in Figure A5. During a tidal cycle, these patterns are very dynamic [33]. At high and low tides the estuarine, marine, and hiperhaline zones move, due to the influence of the tides and dominant winds, as well as the inflow from the underground spring, which can increase or decrease the salinity in the lagoon. At the highest tide level, and under the effects of strong winds, the seawater can move further into the hiperhaline zone. At low tide, brackish water can reach the mouth of the lagoon [33].

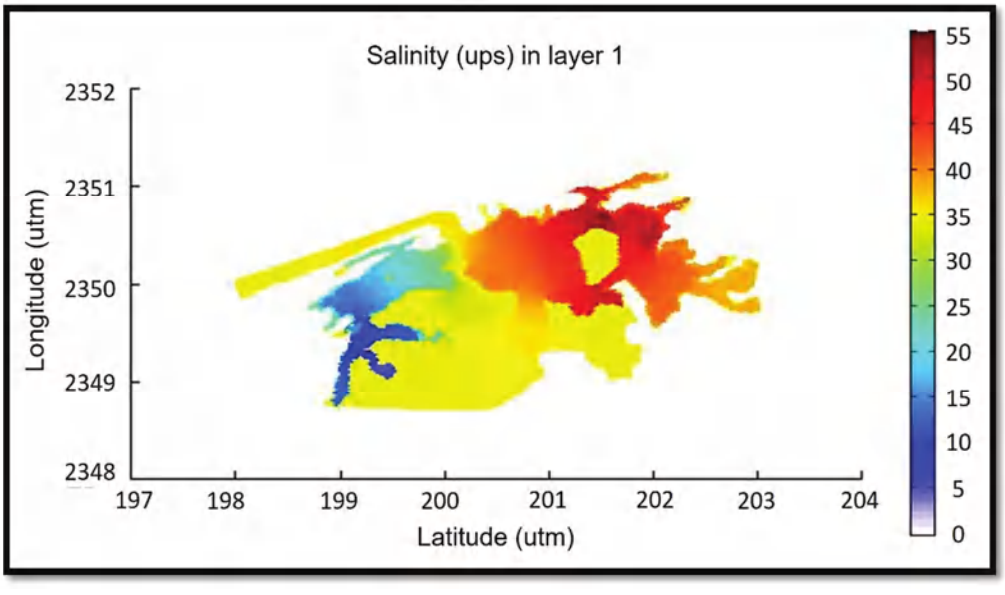


**Figure A5.** Example of salinity patterns in the La Carbonera lagoon. The hiperhaline zone can reach levels of over 80 ups [33].

## References


1. Mendoza, E.; Lithgow, D.; Flores, P.; Felix, A.; Simas, T.; Silva, R. A framework to evaluate the environmental impact of OCEAN energy devices. *Renew. Sustain. Energy Rev.* **2019**, *112*, 440–449. [CrossRef]
2. Zhao, S.; Zou, L.; Tang, C.Y.; Mulcahy, D. Recent developments in forward osmosis: Opportunities and challenges. *J. Membr. Sci.* **2012**, *396*, 1–21. [CrossRef]
3. Copping, A.; Sather, N.; Hanna, L.; Whiting, J.; Zydlewski, G.; Staines, G.; Gill, A.; Hutchison, I.; O'Hagan, A.; Simas, T.; et al. *Annex IV State of the Science Report: Environmental Effects of Marine Renewable Energy Development Around the World*; TETHYS: Richland, WA, USA, 2016. Available online: https://tethys.pnnl.gov/publications/state-of-the-science-2016 (accessed on 25 March 2017).
4. Edenhofer, O.; Seyboth, K.; Creutzig, F.; Schlömer, S. On the Sustainability of Renewable Energy Sources. *Ann. Rev. Environ. Resour.* **2013**, *38*, 169–200. [CrossRef]
5. Alvarez-Silva, O.A.; Osorio, A.F.; Winter, C. Practical global salinity gradient energy potential. *Renew. Sustain. Energy Rev.* **2016**, *60*, 1387–1395. [CrossRef]
6. Jia, Z.; Wang, B.; Song, S.; Fan, Y. Blue energy: Current technologies for sustainable power generation from water salinity gradient. *Renew. Sustain. Energy Rev.* **2014**, *31*, 91–100. [CrossRef]
7. Ahmad, M.; Williams, P. Application of salinity gradient power for brines disposal and energy utilisation. *Desalin. Water Treat.* **2009**, *10*, 220–228. [CrossRef]
8. Tedesco, M.; Cipollina, A.; Tamburini, A.; van Baak, W.; Micale, G. Modelling the Reverse ElectroDialysis process with seawater and concentrated brines. *Desalin. Water Treat.* **2012**, *49*, 404–424. [CrossRef]
9. Zhu, Y.; Wang, W.; Cai, B.; Hao, J.; Xia, R. The salinity gradient power generating system integrated into the seawater desalination system. *IOP Conf. Ser. Earth Environ. Sci.* **2017**, *52*, 012067. [CrossRef]
10. Ye, M.; Pasta, M.; Xie, X.; Cui, Y.; Criddle, C.S. Performance of a mixing entropy battery alternately flushed with wastewater effluent and seawater for recovery of salinity-gradient energy. *Energy Environ. Sci.* **2014**, *7*, 2295–2300. [CrossRef]
11. Yip, N.Y.; Brogioli, D.; Hamelers, H.V.M.; Nijmeijer, K. Salinity Gradients for Sustainable Energy: Primer, Progress, and Prospects. *Environ. Sci. Technol.* **2016**, *50*, 12072–12094. [CrossRef] [PubMed]
12. Berrouche, Y.; Pillay, P. Determination of salinity gradient power potential in Québec, Canada. *J. Renew. Sustain. Energy* **2012**, *4*, 053113. [CrossRef]
13. Micale, G.; Cipollina, A.; Tamburini, A. 1—Salinity gradient energy. In *Sustainability Energy from Salinity Gradients*; Cipollina, A., Micale, G., Eds.; Woodhead Publishing: Sawston, UK, 2016; pp. 1–17. [CrossRef]
14. Sanvik, S.O.; Skihagen, S.E. Status of Technologies for Harnessing Salinity Power and the Current Osmotic Power Activities. Article to the 2008 Annual Report of the International Energy Agency Implementing Agreement on Ocean Energy Systems Annex I: Review, Exchange and Dissemination of Information on Ocean Energy Systems. 2008. Available online: http://www.iea-oceans.org/publications.asp?id=1 (accessed on 28 May 2017).
15. IEA. *Key World Energy Statitics*; International Energy Agency: Paris, France, 2013; p. 82.
16. Alvarez-Silva, O.; Osorio, A.F. Salinity gradient energy potential in Colombia considering site specific constraints. *Renew. Energy* **2015**, *74*, 737–748. [CrossRef]
17. Emdadi, A.; Gikas, P.; Farazaki, M.; Emami, Y. Salinity gradient energy potential at the hyper saline Urmia Lake—ZarrinehRud River system in Iran. *Renew. Energy* **2016**, *86*, 154–162. [CrossRef]
18. Karunarathne, H.D.S.S.; Walpalage, S. Applicability of Pressure Retarded Osmosis Power Generation Technology in Sri Lanka. *Energy Procedia* **2013**, *34*, 211–217. [CrossRef]
19. Ortega, S.; Stenzel, P.; Alvarez-Silva, O.; Osorio, A.F. Site-specific potential analysis for pressure retarded osmosis (PRO) power plants—The León River example. *Renew. Energy* **2014**, *68*, 466–474. [CrossRef]
20. HydroQuebec. *A Renewable Energy Option: Osmotic Power*; HydroQuebec: Montreal, QC, Canada, 2015; ISBN 978-2-550-72233-5.
21. Martínez, M.L.; Vázquez, G.; Pérez-Maqueo, O.; Silva, R.; Moreno-Casasasola, P.; Lopez-Portillo, J.; Mcgregor, I.; Hecke, L.G.; Hernández-Santana, J.; García-Franco, J.; et al. A systemic view of potential environmental impacts of ocean energy production. *Renew. Sustain. Energy Rev.* **2021**, Subbmitted.
22. Seyfried, C.; Palko, H.; Dubbs, L. Potential local environmental impacts of salinity gradient energy: A review. *Renew. Sustain. Energy Rev.* **2019**, *102*, 111–120. [CrossRef]
23. Papapetrou, M.; Kumpavat, K. 10—Environmental aspects and economics of salinity gradient power (SGP) processes. In *Sustainability Energy from Salinity Gradients*; Cipollina, A., Micale, G., Eds.; Woodhead Publishing: Sawston, UK, 2016; pp. 315–335. [CrossRef]
24. Bonilla-Gómez, J.L.; Badillo-Alemán, M.; Gallardo-Torres, A.; Chiappa-Carrara, X. Temporal variation, growth and natural mortality of two species of mojarras (Perciformes Gerreidae) from a tropical coastal lagoon: La Carbonera, Yucatan, Mexico. *Rev. Cienc. Mar. Costeras* **2013**, *5*, 57–67. [CrossRef]
25. Carmona-Escalante, A.; Guadarrama, P.; Ramos-Zapata, J.; Castillo-Argüero, S.; Montaño, N.M. Arbuscular mycorrhizal fungi associated with coastal vegetation in Chuburna, Yucatan, Mexico. *Trop. Subtrop. Agroecosyst.* **2013**, *16*, 431–443.

26. Carbajal, N. *Hidrodinámica y Transporte de Contaminantes y Sedimentos en el Sistema Lagunar Nichupté-Bojórquez, Quintana Roo*; Informe final SNIB-CONABIO Proyecto No. CQ063; Instituto Potosino de Investigación Científica y Tecnológica: Mexico City, Mexico, 2009.
27. Sánchez-Santillán, N.; Lanza-Espino, G.; Sánchez-Trejo, R. Analysis of the dynamic climatology of the Yucatan Peninsula, Mexico. In *Recursos Acuáticos Costeros del Sureste Vol. II. Fondo Mixto—CONACYT—Gobierno del Estado de Yucatán*; Consejo de Ciencia, Innovación y Tecnología del Estado de Yucatán: Mérida, Yucatán, Mexico, 2012; pp. 353–374. ISBN 978-607-9060-08-4.
28. Vidal, R. *Climatic Regions of Mexico*; Institute of Geography, National Autonomous University of Mexico: Mexico City, Mexico, 2005; 216p.
29. Palacios-Sánchez, S.E.; Vega-Cendejas, M.E. Cambios alimenticios en tres especies de Sphoeroides (Tetraodontiformes: Tetraodontidae) posterior al huracán Isidoro en Bocana de la Carbonera, Sureste del Golfo de México. *Rev. Biol. Trop.* **2010**, *58*, 1223–1235. [CrossRef]
30. Mariño, I.; Enriquez, C. *Estudios batimétricos, Hidrodinámicos y de Calidad de Agua en Lagunas Costeras de Yucatán*; Reporte Técnico, Fondo mixto—CONACYT—Gobierno del Estado de Yucatán, Clave: 66254; Centro de Investigación y Estudios Avanzados del Instituto Politécnico Nacional Unidad Mérida: Mérida, Yucatán, México, 2011; 121p.
31. DOEY. *Diario Oficial del Estado de Yucatán*; Decreto Número 285, 19 de Marzo de 2010; Gobierno del Estado: Mérida, Mexico, 2010.
32. Jerónimo, G.; Gómez-Valdés, J.; Badillo, M.; López-Aguilar, K.; Galindo, C.; Gallardo, A.; Loera, J.; Arrollo-Pedraza, L.; Chiappa-Carrara, X. Variación Estacional de Temperatura y Salinidad en la Laguna la Carbonera, Yucatán, 2009–2010. In *En Recursos Acuáticos Costeros del Sureste*; Vol. II. Fondo Mixto—CONACYT—Gobierno del Estado de Yucatán; Consejo Nacional de Ciencia y Tecnología: Mexico City, Mexico, 2012; pp. 71–88. ISBN 978-607-9060-08-4.
33. Marin, E. *Modelación de la Hidrodinámica de un Sistema Lagunar en Humedal Costero con Descargas de Agua Subterránea (DAS)*; Universidad Nacional Autónoma de México: Mexico City, Mexico, 2016.
34. Marin-Coria, E.; Enriquez, C. Variaciones de temperatura y salinidad en el sistema lagunar La Carbonera, Yucatán, México. *Rev. Digit. E-BIOS* **2016**, *4*, 35–45.
35. Reyes-Mendoza, O.; Alvarez-Silva, O.; Chiappa-Carrara, X.; Enriquez, C. Variability of the thermohaline structure of a coastal hypersaline lagoon and the implications for salinity gradient energy harvesting. *Sustain. Energy Technol. Assess.* **2020**, *38*, 100645. [CrossRef]
36. SEMARNAT. *Norma Oficial Mexicana NOM-059-Semarnat-2001. Protección Ambiental-Especies Nativas de México de Flora y Fauna Silvestres-Categorías de Riesgo y Especificaciones para su Inclusión, Exclusión o Cambio-Lista de Especies en Riesgo*; Diario Oficial de la Federación, 6 de Marzo del 2002, Segunda Sección; Secretaría de Medio Ambiente y Recursos Naturales: Ciudad de México, México, 2002.
37. Guadarrama, P.; Salinas-Peba, L.; Chiappa-Carrara, X.; Ramos-Zapata, J.A. Florística, composición y estructura de las comunidades vegetales de la porción occidental de la Reserva Estatal Ciénegas y Manglares de la Costa Norte de Yucatán. *Rev. Mex. Biodivers.* **2018**, *89*, 784–805. [CrossRef]
38. Torres, W.; Méndez, M.; Dorantes, A.; Durán, R. Estructura, composición y diversidad del matorral de duna costera en el litoral yucateco. *Bol. Soc. Bot. Méx.* **2010**, *86*, 37–51. [CrossRef]
39. Gallardo-Torres, A.; Badillo-Alemán, M.; Galindo-de Santiago, C.; Loera-Pérez, J.; Rioja-Nieto, R.; Chiappa-Carrara, X. Listado Taxonómico de los Peces de la Laguna Boca de la Carbonera, Yucatán: Un Primer paso para el Manejo y Evaluación de los Recursos Costeros del Norte de Yucatán. In *En Recursos Acuáticos Costeros del Sureste*; Vol. II. Fondo Mixto—CONACYT—Gobierno del estado de Yucatán; Consejo Nacional de Ciencia y Tecnología: Mexico City, Mexico, 2012; pp. 270–288. ISBN 978-607-9060-08-4.
40. Poot-López, G.R.; López-Rocha, J.A.; González-Salas, C.; Guillen-Hernández, S.; Villegas-Hernández, H. Sex related differences in density, selectivity and vulnerability of the Atlantic blue crab, Callinectes sapidus (Rathbun, 1896), in the southern Gulf of Mexico. *Reg. Stud. Mar. Sci.* **2019**, *32*, 100846. [CrossRef]
41. Chiappa-Carrara, X.; Enríquez, C.; Mariño, I.; Badillo, M.; Gallardo, A.; Yáñez, C.; Marin-Coria, E.; Arena, L.; Guadarrama, P.; López, K.; et al. Monitoreo ambiental de largo Plazo, herramienta para evaluar la Resiliencia de sistemas costeros. In *Caracterización Multidisciplinaria de la Zona Costera de Sisal*; Garza-Pérez, J.R., Ize Lema, I., Eds.; El Laboratorio Nacional de Resiliencia Costera: Yucatán, México, 2017.
42. Santoyo, A. *Esbozo Monográfico de Sisal, Yucatán*; Reporte Técnico; Laboratorio Nacional de Resiliencia Costera: Yucatán, México, 2017; 119p.
43. Sandoval-Gio, J.J.; Zamora-Bustillos, R.; Avilés-Ramírez, G.A.; Ortiz-León, H.J.; Rosas-Correa, C.O. First report of a spawning site of Limulus polyhemus at Ría Lagartos Biosphere Reserve, Yucatan, Mexico. *Rev. Bio Cienc.* **2016**, *5*, e354.
44. Coria, I.D. El estudio de impacto ambiental: Características y metodologías. *Invenio* **2008**, *11*, 125–135.
45. Dellavedova, M. Guía Metodológica para la Elaboración de una Evaluación de Impacto Ambiental. Universidad de la Plata. 2011. Available online: http://blogs.unlp.edu.ar/planeamientofau/files/2013/05/Ficha-N%C2%BA-17-Gu%C3%ADa-metodol%C3%B3gica-para-la-elaboraci%C3%B3n-de-una-EIA.pdf (accessed on 13 January 2021).
46. Fernández-Vitora, V. *Guía Metodológica para la Evaluación del Impacto Ambiental*; Editorial Mundi-Prensa: Madrid, Spain, 2010.
47. Hyman, E.L. Combining Facts and Values. In *Environmental Impact Assessment: Theories and Techniques*, 1st ed.; Routledge: New York, NY, USA, 1988; p. 322. [CrossRef]
48. Boehlertm, G.; Gill, A. Environmental and Ecological Effects of Ocean Renewable Energy Development: A Current Synthesis. *Oceanography* **2010**, *23*, 68–81. [CrossRef]

49. Andrade Soriano, E.N. *Desarrollo de una Metodología para Diseñar una Planta de Energía Osmótica*; Universidad Distrital Francisco José de Caldas: Bogotá, Colombia, 2015.
50. Caballero, J.; Pulido, M.; Martínez-Ballesté, A. *The Use of the Guano Palm (Sabal Yapa) in the Tourism Industry in Quintana Roo, Mexico*; Forest Products, Livelihoods and Conservation. Case Studies on Non-Timber Forest Products Management Systems; Alexiades, M., Shanley, P., Eds.; CIFOR-CGIAR: Bogor, Indonesia, 2004; Volume 3.
51. Bahamón, A.; Álvarez, A.M. *Palafito: De Arquitectura Vernácula a Contemporánea*; Parramón: Lleida, Spain, 2009; p. 144.
52. Cipollina, A.; Micale, G.; Tamburini, A.; Tedesco, M.; Gurreri, L.; Veerman, J.; Grasman, S. 5—Reverse electrodialysis: Applications. In *Sustainability Energy from Salinity Gradients*; Cipollina, A., Micale, G., Eds.; Woodhead Publishing: Sawston, UK, 2016; pp. 135–180. [CrossRef]
53. Graniel, E.; Vera, I.; González, L. Dinámica de la interfase salina y calidad del agua en la costa nororiental de Yucatán. *Ingeniería* **2004**, *8*, 15–25.
54. Osland, M.J.; Feher, L.C.; López-Portillo, J.; Day, R.H.; Suman, D.O.; Guzmán Menéndez, J.M.; Rivera-Monroy, V.H. Mangrove forests in a rapidly changing world: Global change impacts and conservation opportunities along the Gulf of Mexico coast. *Estuar. Coast. Shelf Sci.* **2018**, *214*, 120–140. [CrossRef]
55. Capurro, L. A large coastal ecosystem: The Yucatán Península. *Adv. Perspect.* **2002**, *22*, 69–75.
56. Palko, H. *Exploring Potential Sites for Salinity Gradient Renewable Energy on the North Carolina Coast and Evaluating the Potential Effects of Local Salinity Regime Variation on SAV Communities due to Reverse Electrodialysis Effluent*; University of North Carolina: Chapel Hill, NC, USA, 2017.
57. Salas, M.; Gómez-López, D.; Duque, G. Estructura de las praderas de Thalassia testudinum en un gradiente de profundidad en la Guajira, Caribe colombiano. *Bol. Investig. Mar. Costeras* **2010**, *39*, 381–395.
58. Vermaas, D.A.; Kunteng, D.; Saakes, M.; Nijmeijer, K. Fouling in reverse electrodialysis under natural conditions. *Water Res.* **2013**, *47*, 1289–1298. [CrossRef] [PubMed]
59. Wojtarowski, A.; Martínez, M.L.; Silva, R.; Vázquez, G.; Enriquez, C.; López-Portillo, J.; García-Franco, J.G.; MacGregor-Fors, I.; Lara-Domínguez, A.L.; Lithgow, D. Renewable energy production in a Mexican biosphere reserve: Assessing the potential using a multidisciplinary approach. *Sci. Total Environ.* **2021**, *776*, 145823. [CrossRef]
60. Didde, R. Pilot Plant Brings "Blue Energy" Closer. 2014. Available online: https://resource.wur.nl/en/show/Pilot-plant-brings-blue-energy-closer.htm (accessed on 23 February 2021).
61. Gómez, L. Aspectos ecológicos y biotecnológicos. *Rev. Cub. Quím.* **2013**, *19*, 3–20.
62. CONAGUA. *Manual de Agua Potable, Alcantarillado y Saneamiento. Guía para el Diseño de Emisores Submarinos*; CONAGUA: México City, México, 2007.
63. Enriquez, C.; Mariño-Tapia, I.; Jeronimo, G.; Capurro-Filograsso, L. Thermohaline processes in a tropical coastal zone. *Cont. Shelf Res.* **2013**, *69*, 101–109. [CrossRef]
64. Blaber, S. *Fish and Fisheries of Tropical Estuaries*; Chapman & Hall: London, UK, 1997.
65. Telesh, I.V.; Khlebovich, V.V. Principal processes within the estuarine salinity gradient: A review. *Mar. Pollut. Bull.* **2010**, *61*, 149–155. [CrossRef]
66. Vega-Cendejas, M.E.; Hernández de Santillana, M. Fish community structure and dynamics in a coastal hypersaline lagoon: Rio Lagartos, Yucatan, Mexico. *Estuar. Coast. Shelf Sci.* **2004**, *60*, 285–299. [CrossRef]
67. Arceo-Carranza, D.; Chávez-López, R. Cambio Climático, Estuarios e Hipersalinidad. In *Tópicos de Agenda para la Sostenibilidad de Costas y Mares Mexicanos*; Rivera-Arriaga, E., Sánchez-Gil, P., Gutiérrez, J., Eds.; Universidad Autónoma de Campeche: Campeche, Mexico, 2019; pp. 275–290.
68. Dawoud, M.A. Environmental Impacts of Seawater Desalination: Arabian Gulf Case Study. *Int. J. Environ. Sustain.* **2012**, *1*, 22–37. [CrossRef]
69. Aaberg, R.J. Osmotic power: A new and powerful renewable energy source? *Refocus* **2003**, *4*, 48–50. [CrossRef]
70. Scialdone, O.; Guarisco, C.; Grispo, S.; Angelo, A.D.; Galia, A. Investigation of electrode material—Redox couple systems for reverse electrodialysis processes. Part I: Iron redox couples. *J. Electroanal. Chem.* **2012**, *681*, 66–75. [CrossRef]
71. Pérez-Castillo, A.G.; Rodríguez, A. Indice fisicoquímico de la calidad de agua para el manejo de lagunas tropicales de inundación. *Rev. Biol. Trop.* **2008**, *56*, 1905–1918. [PubMed]
72. Garner, S.B.; Boswell, K.M.; Lewis, J.P.; Tarnecki, J.H.; Patterson, W.F. Effect of reef morphology and depth on fish community and trophic structure in the northcentral Gulf of Mexico. *Estuar. Coast. Shelf Sci.* **2019**, *230*, 106423. [CrossRef]
73. Chen, Q.; Yuan, H.; Chen, P. Short-term effects of artificial reef construction on the taxonomic diversity and eco-exergy of the macrobenthic faunal community in the Pearl River Estuary, China. *Ecol. Indic.* **2019**, *98*, 772–782. [CrossRef]
74. Yang, X.; Lin, C.; Song, X.; Xu, M.; Yang, H. Effects of artificial reefs on the meiofaunal community and benthic environment—A case study in Bohai Sea, China. *Mar. Pollut. Bull.* **2019**, *140*, 179–187. [CrossRef]
75. Vaselbehagh, M.; Karkhanechi, H.; Takagi, R.; Matsuyama, H. Biofouling phenomena on anion exchange membranes under the reverse electrodialysis process. *J. Membr. Sci.* **2017**, *530*, 232–239. [CrossRef]
76. Hernández-Fontes, J.V.; Martínez, M.L.; Wojtarowski, A.; González-Mendoza, J.L.; Landgrave, R.; Silva, R. Is ocean energy an alternative in developing regions? A case study in Michoacan, Mexico. *J. Clean. Prod.* **2020**, *266*, 121984. [CrossRef]
77. Ciarreta, A.; Espinosa, M.P.; Pizarro-Irizar, C. Is green energy expensive? Empirical evidence from the Spanish electricity market. *Energy Policy* **2014**, *69*, 205–215. [CrossRef]

78. Silva, R.; Chávez, V.; Bouma, T.J.; van Tussenbroek, B.I.; Arkema, K.K.; Martínez, M.L.; Oumeraci, H.; Heymans, J.J.; Osorio, A.F.; Mendoza, E.; et al. The Incorporation of Biophysical and Social Components in Coastal Management. *Estuaries Coasts* **2019**, *42*, 1695–1708. [CrossRef]
79. Silva, R.; Oumeraci, H.; Martínez, M.L.; Chávez, V.; Lithgow, D.; van Tussenbroek, B.I.; van Rijswick, H.F.M.W.; Bouma, T.J. Ten Commandments for Sustainable, Safe, and W/Healthy Sandy Coasts Facing Global Change. *Front. Mar. Sci.* **2021**, *8*. [CrossRef]
80. Herrera-Silveira, J.A. Lagunas Costeras de Yucatan (SE, México) Investigación, Diagnóstico y Manejo. *Ecotropicos* **2006**, *19*, 94–108.
81. INEGI. *Estudio Hidrológico de la Península de Yucatán*, 1st ed.; Instituto Nacional de Estadística, Geografía e Informática y Gobierno del Estado de Yucatán: Yucatán, México, 2012.
82. SEMAR. Available online: https://oceanografia.semar.gob.mx/Templates/grafnum_progreso.html (accessed on 20 May 2021).
83. Silva, R.; Ruiz, G.; Posada, G.; Pérez, D.; Rivillas, G.; Espinal, J.; Mendoza, E. *Atlas de Clima Marítimo de la Vertiente Atlántica Mexicana*; Instituto de Ingeniería, Universidad Nacional Autónoma de México: Mexico City, Mexico, 2008.
84. Alcerreca, J.C.; Silva, R.; Mendoza, E. Simple settling velocity formula for calcareous sand. *J. Hydraul. Res.* **2013**, *51*, 215–219. [CrossRef]
85. Cuevas Jiménez, A.; Euán Ávila, J.I.; Villatoro Lacouture, M.M.; Silva Casarín, R. Classification of Beach Erosion Vulnerability on the Yucatan Coast. *Coast. Manag.* **2016**, *44*, 333–349. [CrossRef]
86. Kachadourian-Marras, A.; Alconada-Magliano, M.M.; Carrillo-Rivera, J.J.; Mendoza, E.; Herrerías-Azcue, F.; Silva, R. Characterization of Surface Evidence of Groundwater Flow Systems in Continental Mexico. *Water* **2020**, *12*, 2495. [CrossRef]

Journal of
*Marine Science and Engineering*

MDPI

*Article*

# Wind–Wave Coupling Effect on the Dynamic Response of a Combined Wind–Wave Energy Converter

**Jinghui Li [1], Wei Shi [1,*], Lixian Zhang [1], Constantine Michailides [2] and Xin Li [3]**

[1] State Key Laboratory of Coastal and Offshore Engineering, Deepwater Engineering Research Center, Dalian University of Technology, Dalian 116024, China; jinghuili@mail.dlut.edu.cn (J.L.); 2248742388@mail.dlut.edu.cn (L.Z.)
[2] Department of Civil Engineering and Geomatics, Cyprus University of Technology, Limassol 3036, Cyprus; c.michailides@cut.ac.cy
[3] Institute of Earthquake Engineering, Faculty of Infrastructure Engineering, Dalian University of Technology, Dalian 116024, China; lixin@dlut.edu.cn
* Correspondence: weishi@dlut.edu.cn; Tel.: +86-411-8470-8709

**Abstract:** There is a huge energy demand from offshore renewable energy resources. To maximize the use of various renewable energy sources, a combined floating energy system consisting of different types of energy devices is an ideal option to reduce the levelized cost of energy (LCOE) by sharing the infrastructure of the platform and enhancing the power production capacity. This study proposed a combined concept of energy systems by combing a heave-type wave energy converter (WEC) with a semisubmersible floating wind turbine. In order to investigate the power performance and dynamic response of the combined concept, coupled aero-hydro-servo-elastic analysis was carried out using the open-source code F2A, which is based on the coupling of the FAST and AQWA tools by integrating all the possible environmental loadings (e.g., aerodynamic, hydrodynamic). Numerical results obtained by AQWA are used to verify the accuracy of the coupled model in F2A in predicting dynamic responses of the combined system. The main hydrodynamic characteristics of the combined system under typical operational conditions were examined, and the calculated responses (motions, mooring line tension and produced wave power) are discussed. Additionally, the effect of aerodynamic damping on the dynamic response of the combined system was examined and presented. Moreover, a second fully coupled analysis model was developed, and its response predictions were compared with the predictions of the model developed with F2A in order for the differences of the calculated responses resulted by the different modeling techniques to be discussed and explained. Finally, the survivability of the combined concept has been examined for different possible proposed survival modes.

**Keywords:** wind–wave energy structures; wind turbine; fully coupled analysis; hydrodynamic response; aerodynamic damping; wave energy converters

**Citation:** Li, J.; Shi, W.; Zhang, L.; Michailides, C.; Li, X. Wind–Wave Coupling Effect on the Dynamic Response of a Combined Wind–Wave Energy Converter. *J. Mar. Sci. Eng.* **2021**, *9*, 1101. https://doi.org/10.3390/jmse9101101

Academic Editor: Eugen Rusu

Received: 10 September 2021
Accepted: 1 October 2021
Published: 9 October 2021

**Publisher's Note:** MDPI stays neutral with regard to jurisdictional claims in published maps and institutional affiliations.

**Copyright:** © 2021 by the authors. Licensee MDPI, Basel, Switzerland. This article is an open access article distributed under the terms and conditions of the Creative Commons Attribution (CC BY) license (https://creativecommons.org/licenses/by/4.0/).

## 1. Introduction

In recent years, the field of offshore wind power generation has developed rapidly and has become the fastest-growing energy source for marine renewable energy. As of the end of 2020, the global wind power capacity reached 744 GW, with 50% increase over 2019 [1]. With the rapid development of offshore wind technology, offshore wind turbines are increasing in scale and size, and the scale of wind farms is also increasing. The national renewable energy laboratory (NREL) 5-MW reference wind turbine [2] and DTU 10-MW reference wind turbine [3] have been widely used in comparative studies. The largest offshore wind turbine MySE 16.0-242 16 MW with rotor diameter of 242 m was launched by Ming Yang Smart Energy in August of 2021. To further exploit the offshore wind from deep water, various floating offshore wind concepts were proposed including mainly spar, semisubmersible, tension leg platform (TLP), and barge. Compared to TLP and spar, the

semisubmersible platform is more feasible in various water depths and has low installation costs of the mooring system. At present, the concepts of semisubmersible wind turbines mainly include WindFloat [4], Dutch Tri-floater [5], Windsea [6], Windflo [7], braceless [8], V-shaped [9], OC4-DeepCwind [10], and so on. Wave energy is also a large energy source, with a much higher power density than wind power, but this energy technology is not fully commercialized at present due to its high cost and reliability issue. WECs can generally be categorized as oscillating bodies, oscillating water columns, and overtopping devices [11].

By sharing space, supporting structures, cables, and other infrastructure, combining floating wind turbine system and WEC can not only reduce the cost of the device but also capture wind and wave energy and greatly improve the utilization of renewable energy of the ocean. At present, many studies on numerical simulations and model tests based on different floating offshore wind concepts (barge, TLP, spar, and semisubmersible) combined with WEC have been carried out. Aboutalebi et al. [12,13] proposed to install an oscillating water column WEC on the barge platform to reduce the fatigue movement of the platform. In Michailides et al. [14], the required wind–wave analysis for harsh environmental conditions has been examined. Ren et al. [15] carried out an experimental and numerical study of dynamic response of a new combined TLP wind turbine and wave energy converter. Bachynski et al. [16] proposed a TLP combined three-point absorber WECs system and studied the performance under operational and extreme sea cases. Russo et al. [17], Tomasicchio et al. [18], and Xu et al. [19] carried out experimental studies of the dynamic characteristics of Spar Buoy Wind Turbine and studied its dynamic behavior. Hu et al. [20] carried out the optimal design of WEC and dynamic characteristics analysis of a hybrid system combing a semisubmersible floating wind platform (WindFloat) and WECs. Sarmiento et al. [21] carried out a new floating semisubmersible structure combined with WECs (three oscillating water columns, OWC) in order to characterize the performance of the platform and OWCs. The MARINA Platform project funded by the European Union [22] proposed a combined system of semisubmersible platforms with point absorption and oscillating water column WEC. Peiffer et al. [23] and Aubault et al. [24] carried out coupled dynamic analysis through numerical models and experimental models. Muliawan et al. [25,26] proposed a comprehensive concept that combines a spar-type floating wind turbine with a torus WEC (named STC). Wan et al. [27–29] studied the dynamic response of an STC under typical operational conditions and extreme conditions based on numerical and experimental methods. Another concept that combines a floating semisubmersible wind turbine and a flap-type WEC (named SFC) was proposed. Michailides et al. [30–32] systematically studied the integrated operation of SFCs through numerical and experimental models. Ren et al. [33] carried out experimental and numerical studies on the hydrodynamic response of a new combined monopile wind turbine and a heaving-type WEC under typical operational conditions. In addition, Wang et al. [34] studied the hydrodynamic response of the combined system of the semisubmersible platform and heaving-type WEC.

With the development of the field of offshore wind turbines, the aero-hydro-servo-elastic coupling tool has become the key to solve the equation of motion and calculate the dynamic response of floating wind turbines. Different simulation tools have been developed so far. DeepLines [35,36], DARwind [37], Bladed, HAWC2, and FAST are the most well-known tools for fully coupled analysis of wind turbines. Jonkman et al. [38,39] developed a hydrodynamic module to consider the diffraction and radiation effects of floating platforms. Due to its open-source nature, it has also been used to participate in the development of a fully coupled framework. Kvittem et al. [40] combined AeroDyn with the non-linear finite element software SIMO/REFLEX. Shim [41] developed an interface that combines FAST with the fluid dynamic analysis tool CHARM3D. Recently, Yang et al. [42] developed a new aero-hydro-servo-elastic coupling framework based on FAST and AQWA (F2A) for dynamic analysis of FOWTs, combining the advantages of aero-elastic-servo of FAST and hydrodynamic analysis of AQWA [43].

In this study, with use of the recently proposed coupled analysis tool F2A, a fully coupled analysis is performed for a combined system consisting of a semisubmersible

platform and a heaving-type WEC. A numerical model of the combined structure that was capable of simulating its motion and dynamic responses under different typical operational conditions was developed and used with F2A. A second model with use of a different analysis tool is developed for performing fully coupled analysis. Different types of analysis and comparison were performed to examine the fully coupled responses of the combined structure but also for emphasizing the effect of different modeling methods/techniques on the response quantities of the combined system. The time-domain dynamic response characteristics, mooring characteristics, and PTO-produced power of the combined system are examined and presented in this study. Under the excitation of only waves, there was small difference between the two numerical models, while under irregular wave and turbulent wind conditions, the difference between two models was larger. The impact of aerodynamic loads as well as aerodynamic damping is significant. When the wind velocity is small, aerodynamic damping has a significant effect on reducing the resonance of surge and pitch, and there is an obvious positive relationship. When the wind velocity increases, wind thrust has a greater impact than aerodynamic damping. The rationality behind the efficient use of the two examined numerical tools for studying combined concepts has been presented. Finally, an extreme condition is studied to ensure the survivability of the combined system. The results show that the two models had significant differences in dynamic motion and mooring force prediction under irregular wave and turbulent wind condition due to the wind–wave coupling effect at low frequency range.

## 2. Theoretical Background

Different from offshore oil and gas platform, a floating wind turbine experiences the aerodynamic load and hydrodynamic load simultaneously. These loads are both important in the system design at the same order. The basic theories used in the combined system analysis are described in this section.

### *2.1. Aerodynamic Loads and Aerodynamic Damping*

Blade element momentum (BEM) theory is one of the efficient and most commonly used methods for calculating induced loads on wind turbine blades [44]. In this theory, the wind turbine blade is divided into many sections along the span direction, and these sections are called blade elements. The wind turbine blade is simplified as a finite element that is superimposed in the radial direction, so the three-dimensional aerodynamic characteristics of the wind turbine blade can be obtained by integrating the aerodynamic characteristics of the element in the radial direction [42].

The axial velocity $V_2$ and the circumferential velocity $V_3$ at the rotor plane are calculated as follows:

$$V_2 = (1 - a)V_1 \tag{1}$$

$$V_3 = \Omega r\left(1 + a'\right) \tag{2}$$

where $V_1$ is the incoming wind velocity, $a$ is the axial induction factor, and $a'$ is the angular induction factor. The axial velocity and the circumferential velocity vector are combined to obtain the resultant velocity $V_0$. The lift force ($L$) is formed perpendicular to the resultant velocity, and the drag force ($D$) is formed in the same direction as the incoming velocity. They can be calculated by the following equations:

$$L = \frac{1}{2}\rho V_0^2 A C_L \tag{3}$$

$$D = \frac{1}{2}\rho V_0^2 A C_D \tag{4}$$

where $A$ is the rotor sweeping area, $\rho$ is the air density, $C_L$ is the lift coefficient, and $C_D$ is the drag coefficient.

The lift coefficient $C_L$ and drag coefficient $C_D$ of the aerofoil are projected in the normal and tangential directions, respectively, to obtain the normal force coefficient $C_N$ and the tangential force coefficient $C_T$, as shown in the following equations:

$$C_N = C_L \cos\varphi + C_D \sin\varphi \tag{5}$$

$$C_T = C_L \sin\varphi - C_D \cos\varphi \tag{6}$$

Finally, the thrust force and torque on the blade section are calculated by the following equations:

$$dT = \frac{1}{2}\rho V_0^2 c C_N dr \tag{7}$$

$$dM = \frac{1}{2}\rho V_0^2 c C_T r dr \tag{8}$$

where $c$ is the aerofoil chord length.

When studying aerodynamic loads, the influence of aerodynamic damping cannot be ignored. Analyzed at the micro level, the aerodynamic damping of the wind turbine essentially comes from the relationship between the aerodynamic load of the wind turbine blades and the inflow wind velocity. Without considering the platform motion and elastic structure deformation [45], the following equation can be used:

$$V_0 = V_1\sqrt{(1-a)^2 + \left[\frac{\Omega r}{V_0}(1+a')\right]^2} = V_1 f_1 \tag{9}$$

The factor $f_1$ indicates that the relative inflow wind velocity at the blade is simultaneously affected by the axial induction factor, angular induction factor, structural deformation of the wind turbine, and rotational velocity [46].

Considering the relative movement of the platform, the relative velocity is written as follows:

$$V_0 = V_1 f_1 - L\dot{x}_5 \cos(x_5) - \dot{x}_1 \tag{10}$$

where $x_5$ is the pitch motion of the platform, $\dot{x}_5$ is the pitch velocity of the platform, and $\dot{x}_1$ is the surge velocity of the platform.

From Equation (7), the total thrust $T$ on the blade can be obtained as follows:

$$T \infty V_0^2 \infty \left(V_1 f_1 - L\dot{x}_5 \cos\left(\dot{x}_5\right) - \dot{x}_1\right)^2 \tag{11}$$

Ignoring the velocity components above the second order, the following equation is obtained:

$$\begin{array}{c} T \infty (V_1 f_1)^2 - 2V_1 f_1 L\dot{x}_5 \cos\left(\dot{x}_5\right) - 2V_1 f_1 \dot{x}_1 \\ \infty (V_1 f_1)^2 - 2V_1 f_1 L\dot{x}_5 - 2V_1 f_1 \dot{x}_1 \end{array} \tag{12}$$

The last two terms in the above equation represent aerodynamic damping and can be added to the left side of the equation of motion. The aerodynamic thrust is proportional to the square of the wind velocity, and the aerodynamic damping is proportional to the first power of the wind velocity. This shows that when the wind velocity is not particularly high, the effect of aerodynamic damping on the offshore floating wind turbine may be more obvious, and the relationship between them is positive. However, as the wind velocity increases, the influence of aerodynamic thrust may be much greater than that of aerodynamic damping. Of course, the aerodynamic damping force of offshore floating wind turbines is affected not only by wind velocity but also by other complex factors, such as aerodynamic induction factor. Thrust coefficient may even be affected by pitch angle and stall effect. Since F2A and AQWA were used for simulation in this study, the largest difference between them is whether considering aerodynamic damping.

### 2.2. Potential Flow Theory

The potential flow theory may be to calculate the hydrodynamic loads on marine structures. It is usually assumed that the fluid is non-rotating, non-viscous, and incompressible, and the fluid is assumed to be an ideal fluid [47,48]. Derived from the conservation of mass and the conservation of momentum, the governing equations of fluid motion, the Laplace equation are expressed as follows:

$$\nabla^2\phi = 0 \tag{13}$$

$$\frac{\partial u}{\partial t} + (u \cdot \nabla)u = -\nabla\left(gz + \frac{p}{\rho}\right) \tag{14}$$

where $\phi$ represents the three-dimensional velocity potential function and $\phi = \phi(x, y, z, t)$. The velocity potential can be decomposed into the following equation:

$$\phi = \phi^i + \phi^d + \phi^r \tag{15}$$

where $\phi^i$ is the velocity potential function of the incident wave, $\phi^d$ is the diffraction potential function, and $\phi^r$ is the radiation potential function.

For the fluctuation problem of linear periodic motion, the time factor can be separated by the variable separation method, and the velocity potential can be expressed as follows:

$$\phi = \mathrm{Re}\left[\varphi e^{-i\omega t}\right] \tag{16}$$

where $\omega$ is the angular frequency and Re represents the real part.

### 2.3. Viscous Loads

In potential flow theory, since the assumption is inviscidity, viscosity needs to be considered in practice. In this study, the Morrison model was added to consider the viscosity [48,49]. In AQWA, the viscosity was simulated by adding Morrison elements as follows:

$$f_d = 0.5 C_d \rho D \mu |\mu| \tag{17}$$

where $C_d$ represents the drag coefficient, and in this study, $C_d = 1.2$ was selected due to $d/L \geq 0.2$ and $H/d \leq 0.2$; $H$, $d$, and $L$ represent the wave height, water depth, and wavelength, respectively; $\mu$, D, and are the incoming flow velocity, structure diameter, and fluid density, respectively; and $f_d$ represents the drag force on a unit height of the structure.

### 2.4. Equation of Motion

In this study, the wind and wave energy combined system consists of two bodies having in total 12 degrees of freedom (six degrees for each body), which requires comprehensive consideration of multiple degree-of-freedom systems [29]. The multi-body equation of motion is given as follows:

$$\begin{gathered}\begin{pmatrix} (M+m)_{11} & m_{12} \\ m_{21} & (M+m)_{22} \end{pmatrix}\begin{pmatrix} \ddot{x}_1(t) \\ \ddot{x}_2(t) \end{pmatrix} + \int_0^t \begin{pmatrix} \kappa(t-\tau)_{11} & \kappa(t-\tau)_{12} \\ \kappa(t-\tau)_{21} & \kappa(t-\tau)_{22} \end{pmatrix}\begin{bmatrix} \dot{x}_1(\tau) \\ \dot{x}_2(\tau) \end{bmatrix} d\tau \\ + \begin{pmatrix} (R)_{11} & 0 \\ 0 & (R)_{22} \end{pmatrix}\begin{bmatrix} x_1(t) \\ x_2(t) \end{bmatrix} = \begin{bmatrix} f^{wind}(t) \\ 0 \end{bmatrix} + \begin{bmatrix} {f_1}^{wave}(t) \\ {f_2}^{wave}(t) \end{bmatrix} + \begin{bmatrix} {f_1}^{drag}(t) \\ {f_2}^{drag}(t) \end{bmatrix} \\ + \begin{bmatrix} {f_1}^{interface}(t) \\ {f_2}^{interface}(t) \end{bmatrix} + \begin{bmatrix} {F_1}^{PTO}(t) \\ {F_2}^{PTO}(t) \end{bmatrix}\end{gathered} \tag{18}$$

where $m$ is the added mass matrix, $x$, $\dot{x}$, and $\ddot{x}$ are the displacement, velocity, and acceleration matrix in the time domain, respectively, $\kappa(\tau)$ is the retardation function, which is based on the added mass and potential damping matrix, and $f$ is the summation of the external forces in time domain. The subscripts 1 and 11 refer to the variables of body 1 (braceless); subscripts 2 and 22 refer to the variables of body 2 (WEC); and subscripts 12 and 21 present the coupling terms between the braceless and WEC. The vertical (heave) quadratic damping of the braceless and WEC terms is modeled by the quadratic damping matrix on the left side of Equation (18). The term $f^{wind}$ denotes wind load on the turbine rotor, while $f^{wave}$ is the wave forces applied on the braceless platform and WEC. The

interface forces $f_1^{interface}$ between the two bodies include horizontal contact forces and vertical friction forces. $F^{PTO}$ is the PTO forces. Each term of the interface and PTO forces is applied on the two bodies with the same value but in different directions.

### 2.5. Brief Description of F2A

The baseline version of AQWA was incapable of predicting the aero-servo-elastic of floating offshore wind turbines, but it accepted time domain analysis of external forces implemented by dynamic link library (.dll). In order to enable AQWA to form a fully coupled analysis of floating offshore wind turbines, FAST was integrated in AQWA with some simulation function implemented [36]. Therefore, the coupling framework was "FAST2AQWA", denoted as F2A. The coupling of AQWA and FAST was accomplished by user_force.dll and source code subroutine of FAST. Related simulation capabilities of FAST were completely implemented in time domain analysis in the DLL that can be called by AQWA during the simulation.

## 3. Numerical Model of Combined System

The combined system was composed of a semisubmersible platform and a heaving-type WEC connected by a guide-roller system in the middle and an upper connecting system [50]. The wind turbine model used for this study is the NREL 5-MW baseline wind turbine. The main parameters of the 5-MW wind turbine are shown in Table 1 [2]. An illustration of the combined system is shown in Figure 1, and the main parameters of the combined system are shown in Table 2. In this study, the time-domain hydrodynamic simulation of the combined system was based on AQWA. Hydrodynamic panel models are shown in Figure 2.

**Table 1.** The main parameters of the 5-MW wind turbine.

| Rotor-Nacelle-Assembly t | 350 |
|---|---|
| Center of Gravity (CoG) m | (−0.2,0.0,70) |
| Tower mass t | 347.46 |
| Total WT mass moment of inertia about X axis ($I_{xx}$) kg*m$^2$ | 3,770,000,000 |
| Total WT mass moment of inertia about Y axis ($I_{yy}$) kg*m$^2$ | 3,660,000,000 |
| Total WT mass moment of inertia about Z axis ($I_{zz}$) kg*m$^2$ | 112,000,000 |

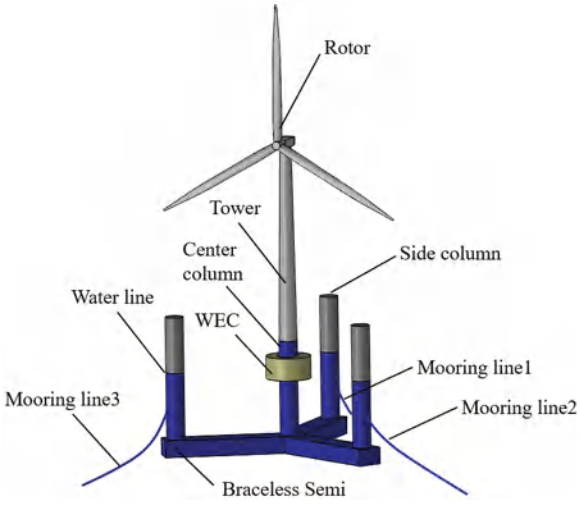


**Figure 1.** Sketch map of the combined system.

**Table 2.** The main parameters of the combined system.

| | Parameters | Values |
|---|---|---|
| Semisubmersible platform | Semisubmersible mass t | 9738 |
| | Diameter of the central column m | 6.5 |
| | Diameter of the three side columns m | 6.5 |
| | Water displacement $m^3$ | 10,298 |
| | Water depth m | 200 |
| | Operating draft m | 30 |
| | Center of semisubmersible m | (0,0,24.36) |
| WEC | Outer/Inner diameter m | 16/8 |
| | FigureHeight/Draft m | 8/3.5 |
| | Mass t | 463.5 |
| | Water displacement $m^3$ | 452.2 |
| | Center of mass m | (0,0,1) |

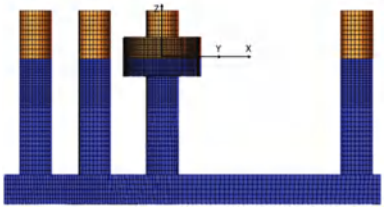

**Figure 2.** Panel models for the hydrodynamic analysis.

The PTO system (shown in Figure 3), which captures the wave energy through the relative heave motion of the semisubmersible platform and the WEC, was simplified as a linear spring and a linear damper. This model was accomplished by establishing a fender element in ANSYS/AQWA. Based on the discussion of damping coefficient of Fender and stiffness coefficient of linear spring [27–29,33,34,50], it was found that a large value of $B_{pto}$ value may lead to air compressibility that cannot be ignored, while a small $K_{pto}$ coefficient may ignore the influence of stiffness coefficient on the produced power [19]. Therefore, $1.5 \times 10^6$ $Ns^2/m$ was selected for $B_{pto}$ and 1 N/m for $K_{pto}$ in this study. The force of PTO was calculated by the following equation:

$$F_{pto} = B_{pto} \cdot (v_2 - v_1) + K_{pto} \cdot (x_2 - x_1) \quad (19)$$

where $B_{pto}$ and $K_{pto}$ are the linear damping coefficient and linear spring stiffness coefficient, respectively; $v_1$ and $x_1$ are the velocity and displacement of the semisubmersible platform; and $v_2$ and $x_2$ are the velocity and displacement of the WEC, respectively.

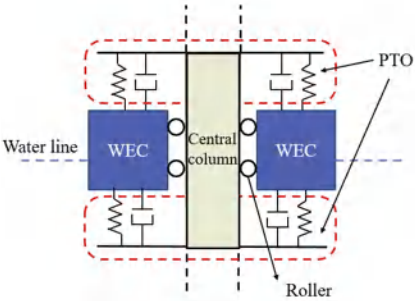


**Figure 3.** Simplified dynamic coupling model between the WEC and braceless.

Knowing the damping force of the PTO system and the relative velocity between the platform and WEC, the produced power of the WEC can be calculated through the following equation:

$$P_{PTO} = F_{PTO} \cdot (v_2 - v_1) \quad (20)$$

## 4. Results and Discussion

The simulations conducted in this study were primarily carried out under typical operational conditions and extreme conditions from a typical site at 61°21′ N latitude and 0°0′ E longitude near the Shetland Islands, northeast of Scotland, UK. The water depth at the site was 200 m [51]. The examined load cases are listed in Table 3. For regular wave case (LC1), the 1800 s–1900 s was used in the comparison to get rid of transient effect. For irregular wave cases (LC2–LC4), the total simulation time is 4600 s, and the first 1000 s has been excluded to avoid the transient effect. It should be noted that the time series results of the motion and force responses between 3500 to 3700 s are displayed to better present the difference between different codes.

**Table 3.** Load cases table.

| Load Case | Wind Velocity $U_{wind}$ (m/s) | Wave Height $H/H_s$ (m) | Wave Period $T/T_p$ (s) |
|---|---|---|---|
| LC1 | / | 2.0 | 9.0 |
| LC2 | 8.4 | 2.0 | 14.8 |
| LC3 | 11.4 | 2.4 | 10.9 |
| LC4 | 23.8 | 5.5 | 13.5 |
| LC5 | 50.0 | 13.8 | 19.2 |

### 4.1. Free Decay Test

A free decay test was performed in the numerical simulation to determine the natural frequencies of the surge, heave, and pitch of the platform. The natural frequencies are listed in Table 4. Figure 4 was the time domain curve of free decay test of platform. The results showed that the natural frequencies of the surge (Figure 4a) and heave (Figure 4b) of the platform were the same from two codes, and there is a difference of about 11.7% of the natural frequency of the platform pitch from two codes.

**Table 4.** Natural frequencies (rad/s) of platform.

| | Surge | Heave | Pitch |
|---|---|---|---|
| F2A | 0.078 | 0.256 | 0.239 |
| AQWA | 0.078 | 0.256 | 0.210 |

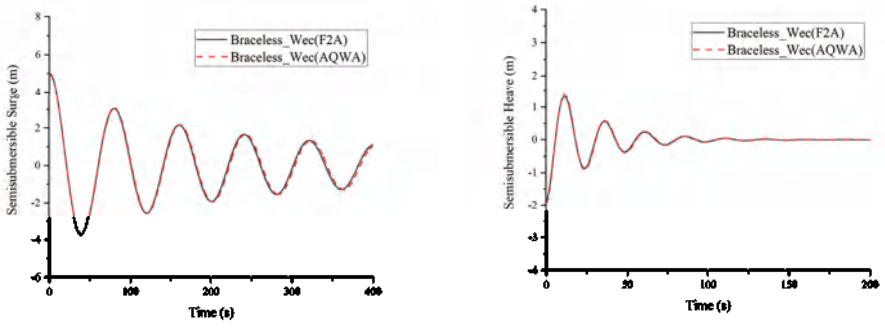


(**a**) (**b**)

**Figure 4.** *Cont.*

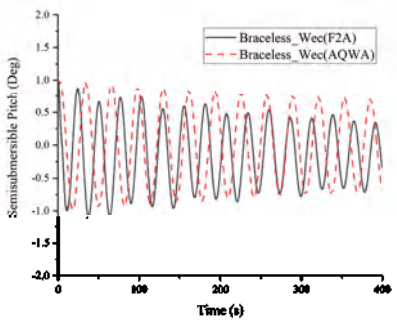


(**c**)

**Figure 4.** Time domain curve of free decay test of the semisubmersible platform: (**a**) Surge; (**b**) Heave; (**c**) Pitch.

### *4.2. Regular Wave Condition*

In this study, the simulation of typical regular wave conditions (LC1) was performed, and the characteristics of the motion response, mooring response, and produced power of multiple bodies (F2A and AQWA simulation) were compared.

#### 4.2.1. Motion Response

In this section, the motion response under a regular wave ($H$ = 2.0 m, $T$ = 9.0 s) was selected, and a motion response of three degrees of freedom (DOF) of the platform (surge, relative heave, pitch) is presented (Figure 5). The results were compared between the fully coupled framework F2A and the hydrodynamic software AQWA.

The surge motion of the platform is shown in Figure 5a. Compared with the multibody simulation results of F2A and AQWA, the amplitude was basically the same, but the simulation results of F2A at the wave peak were slightly larger. The relative heave motion responses simulated by F2A and AQWA were basically the same (Figure 5b). Slightly larger pitch response from F2A could be identified compared with AQWA results. Under only wave conditions, F2A and AQWA had good consistency in simulating multibody motion characteristics, especially in relative heave.

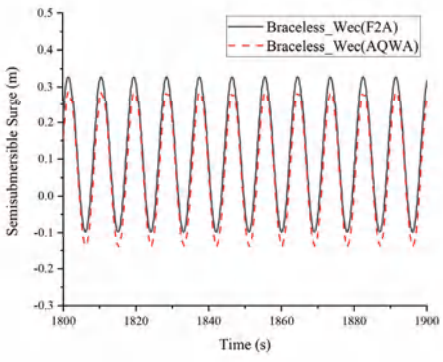


(**a**)

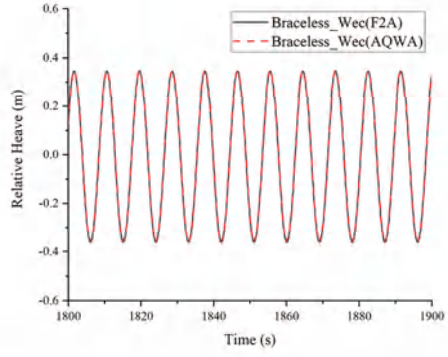


(**b**)

**Figure 5.** *Cont.*

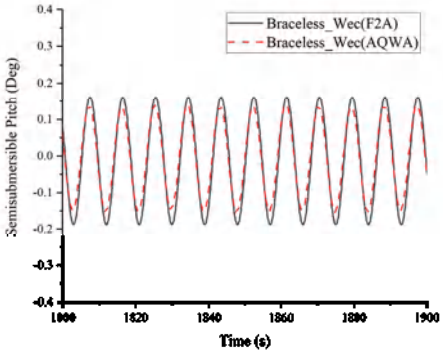


(**c**)

**Figure 5.** Time domain motion response of the semisubmersible platform: (**a**) Surge; (**b**) Relative Heave; (**c**) Pitch.

4.2.2. Mooring Line Force

Figure 6 shows the time-domain response of the mooring force of Mooring Line 1 (ML1) and Mooring Line 2 (ML2). The mooring line force of ML1 (downwind direction) was smaller than that of ML2 (upwind direction) when subjected to waves in the heading direction. Results from F2A have slightly larger mooring line force than those from AQWA simulation.

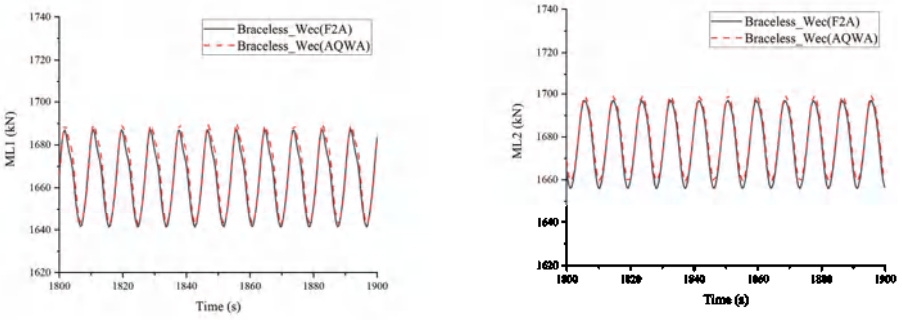


(**a**) (**b**)

**Figure 6.** Mooring force of: (**a**) ML1; (**b**) ML2.

4.2.3. Produced Wave Power

The wave energy was captured by PTO system. The relative heave velocity from both codes are similar to each other (Figure 7a). From Equation (19), the damping force can be observed in Figure 7b. Based on the relative heave velocity and damping force, the produced wave power could be identified, which is similar from F2A results and AQWA results (Figure 7c).

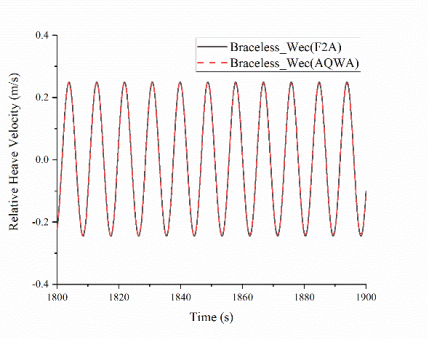


(**a**)

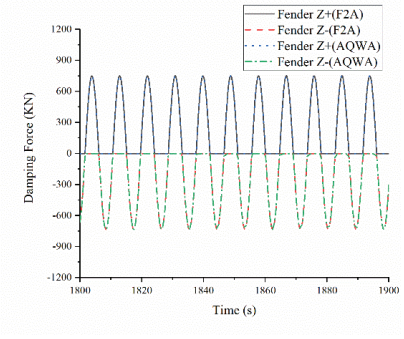


(**b**)

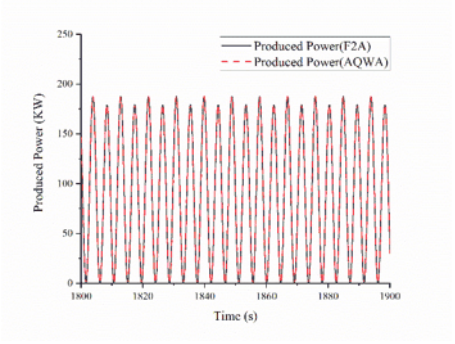


(**c**)

**Figure 7.** Time series of different responses of the combined structure under regular waves: (**a**) Relative Heave Velocity; (**b**) Damping Force; (**c**) Produced Power.

Under only wave conditions, F2A and AQWA had good consistency in simulations of the multibody dynamic response. This was because F2A integrates the AQWA hydrodynamic module.

### *4.3. Irregular Wave and Turbulent Wind Conditions*

This section presents the motion response, mooring force, and produced power under irregular wave and turbulent wind conditions.

#### 4.3.1. Motion Response

Figure 8 shows the motion response in surge, pitch, and heave directions under normal operation conditions in LC2 and LC3. The responses of surge and pitch in both load cases from F2A (Figure 8a,b) simulation are smaller than those predicted by AQWA (Figure 8e,f). This is due to the fact that the wind load in F2A and AQWA is differently implemented. In F2A, the wind field is pre-generated and both wind aerodynamic load and damping are considered due to the rotating turbine rotor. However, in AQWA, the wind load is implemented as an external load using dll function and no interaction and aerodynamic damping is included. The difference for the relative heave motions simulated by two tools was limited for both LC2 and LC3 (Figure 8c,d).

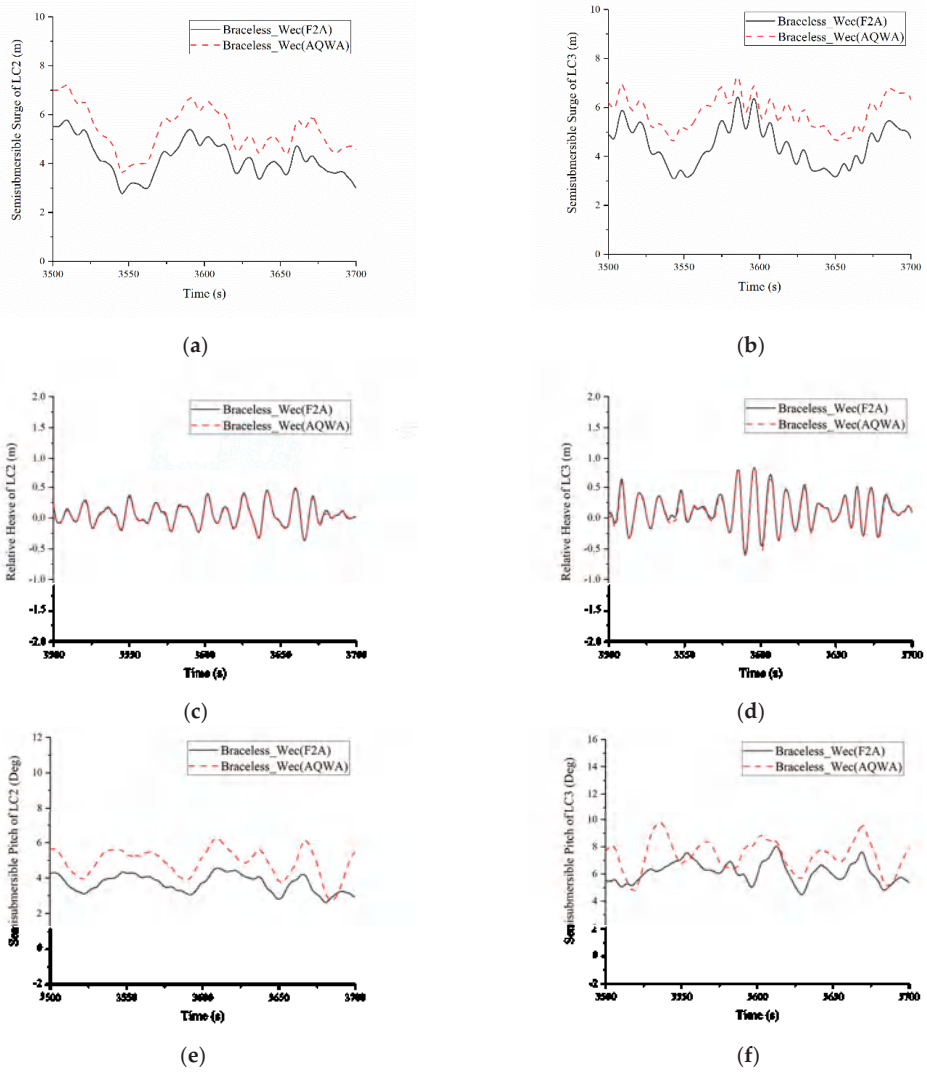


**Figure 8.** Time domain motion response of the semisubmersible platform: (**a**) Surge in LC2; (**b**) Surge in LC3; (**c**) Relative Heave in LC2; (**d**) Relative Heave in LC3; (**e**) Pitch in LC2; (**f**) Pitch in LC3.

Figure 9 shows motion response in LC4, in which the wind speed is larger than rated wind speed. Similar as the load case LC2 and LC3, the motion responses in surge and pitch direction from F2A are lower than those motions from AQWA due to the aerodynamic damping. The relative heave motions predicted from two codes are similar to each other.

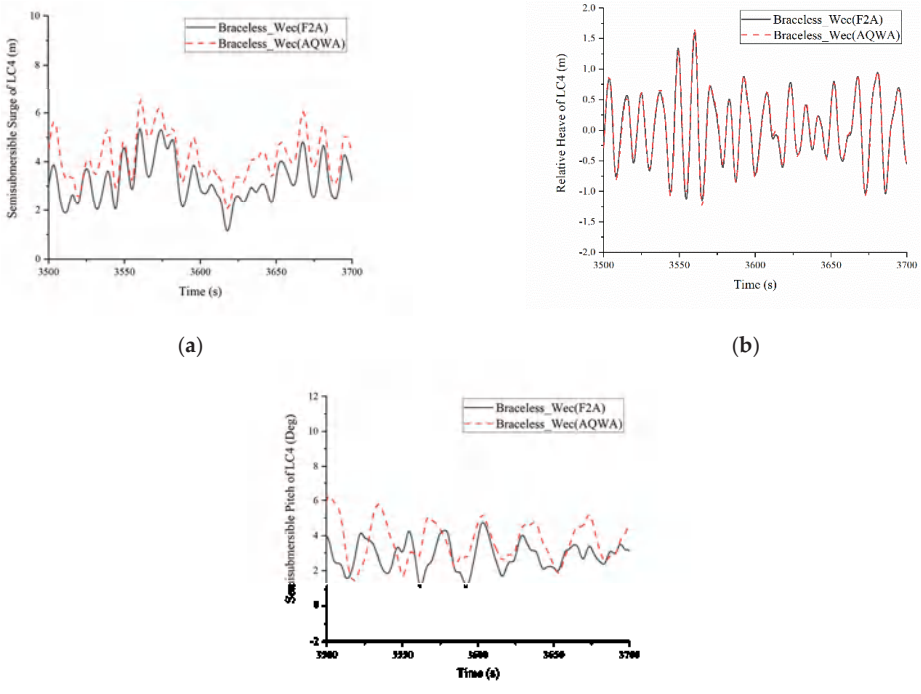


**Figure 9.** Motion responses of the semisubmersible platform in LC4: (**a**) Surge; (**b**) Relative Heave; (**c**) Pitch.

#### 4.3.2. Mooring Line Force

The mooring line forces of ML1 and ML2 from LC2, LC3, and LC4 were compared for F2A results and AQWA in Figure 10. Basically, the mooring line force of ML2 in the upwind direction is larger than the mooring line force of ML1 in the downwind direction because wind and wave will drive the combined system to move in a downwind direction from its equilibrium position. Therefore, ML1 will get relaxed and ML2 will get tensioned. For the mooring line force of ML1, the reduction of the mooring force from its force at equilibrium position from F2A simulation is less than the reduction of the force from AQWA simulation due to the difference of the surge motions from two codes in all three load cases. Thus, the mooring line forces of ML1 from F2A are larger than those from AQWA (Figure 10a,c,e). However, for mooring line force of ML2, the increasing of the mooring force from its force at equilibrium position from F2A simulation is less than the increasing of force from AQWA simulation. Therefore, the mooring line forces of ML2 from F2A are less than those from AQWA (Figure 10b,d,f). Due to the pitch control above the rated wind speed (LC4), the wind thrust force is much smaller than that in LC2 (below rated wind speed) and LC3 (at rated wind speed). Therefore, the aerodynamic damping effect is much smaller. In this case (LC4), the contribution from wave load is much larger than wind load, and the discrepancy from two codes is minimal. Therefore, there is a slight difference in the mooring line force of ML2 for LC4.

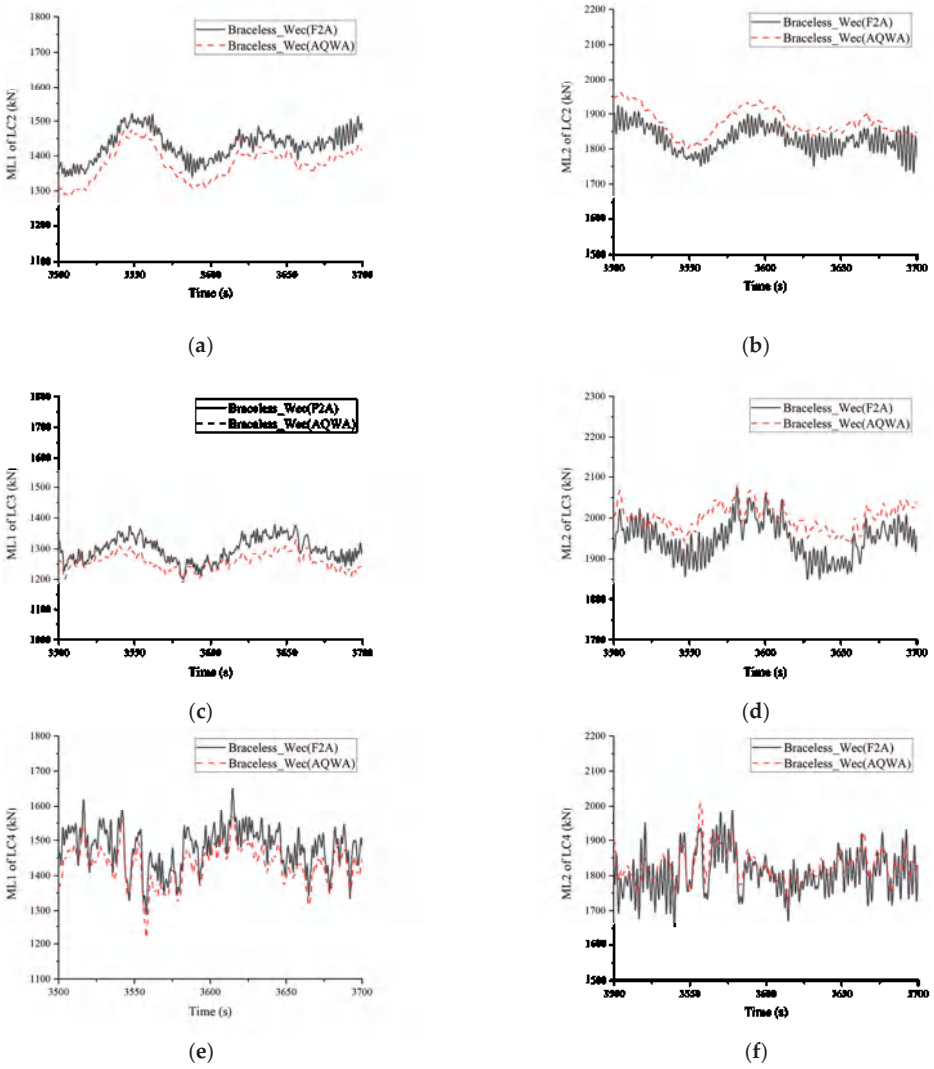


**Figure 10.** Mooring force of: (**a**) ML1 in LC2, (**b**) ML2 in LC2, (**c**) ML1 in LC3, (**d**) ML2 in LC3, (**e**) ML1 in LC4, (**f**) ML2 in LC4.

#### 4.3.3. Produced Wave Power

The relative heave velocities between the semisubmersible platform and the WEC, the damping force and produced power from WEC in LC2, LC3, and LC4, are presented in Figure 11. Due to less effect of aerodynamic damping on heave motion, no significant difference is identified for the relative heave velocities, damping force, and produced power. When the wave height increases from LC2 to LC4, the relative heave velocity (Figure 11a,c,e) also increases due to the large relative heave motion in a severe sea state, which is beneficial to capture wave energy. Figure 11b,d,f present the vertical damping force. The F2A and AQWA simulation results were similar. As the wave height increases, the vertical damping force increases significantly. Figure 11g,h,i show the produced energy power from WEC. With the sea state moving from mild to severe (LC2 to LC4), more power can be produced from the wave. Figure 11i is the produced power under severe sea conditions (LC4). It can be seen the maximum power in LC4 is even as large as 3.5 MW (not shown in Figure 11f), which is comparable to the power produced from the wind turbine.

However, the mean produced power is less than 600 kW, and it shows obvious instability, while the produced power of WEC is much smaller. Therefore, the wind power production for NREL 5 MW WT will make the main contribution to the total power production of the combined system under the severe sea conditions.

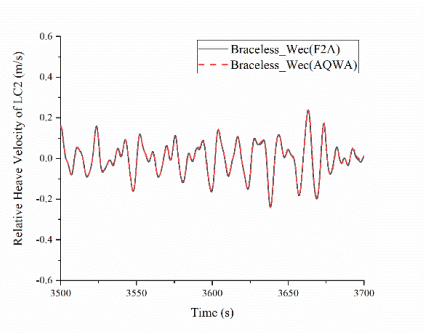


(**a**)

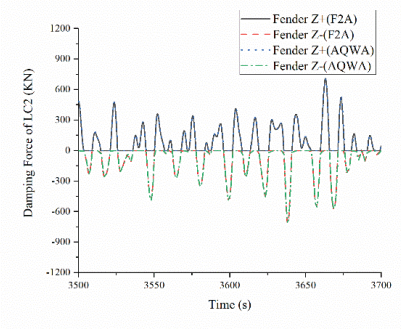


(**b**)

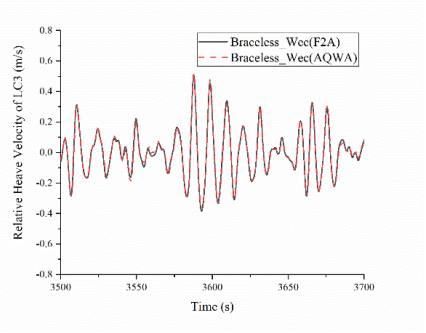


(**c**)

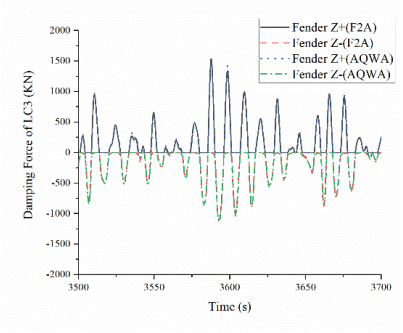


(**d**)

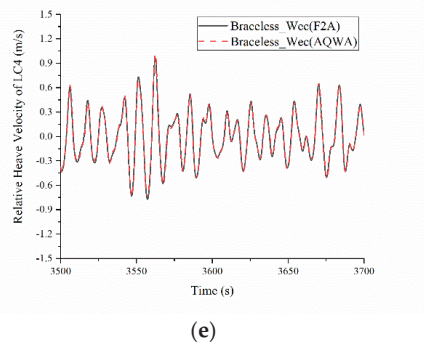


(**e**)

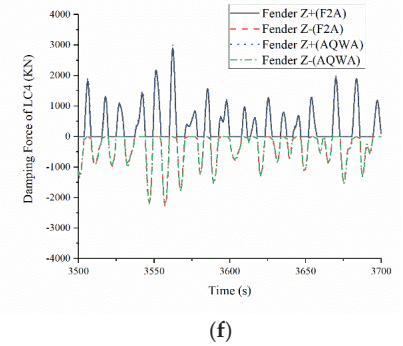


(**f**)

**Figure 11.** *Cont.*

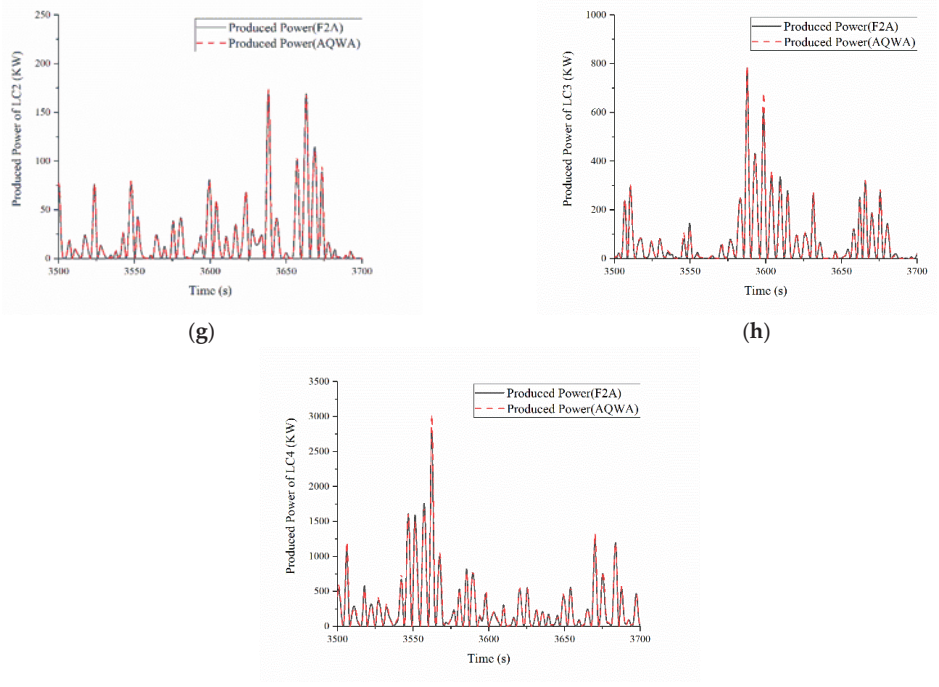


**Figure 11.** Time series of different responses of the combined structure: (**a**) Relative Heave Velocity of LC2, (**b**) Damping Force of LC2, (**c**) Relative Heave Velocity of LC3, (**d**) Damping Force of LC3, (**e**) Relative Heave Velocity of LC4, (**f**) Damping Force of LC4, (**g**) Produced Power of LC2, (**h**) Produced Power of LC3, (**i**) Produced Power of LC4.

#### 4.3.4. Statistical Analysis

Figure 12 displays the statistics of responses in operational conditions from both F2A simulation and AQWA simulation. The maximum and minimum values are determined as the highest crest and lowest trough of the corresponding time series. Figure 12a–c show that the simulation results of F2A and AQWA were different in the surge and pitch motion, and the heave motion results were slightly different, which was consistent with the previous results. When the wind velocity was the rated wind velocity of the wind turbine (12.4 m/s), the surge and pitch motion amplitudes of the platform were the largest, and the heave motion was greatly affected by the hydrodynamic load. When the wave height increases (LC2–LC4), the heave amplitude increases accordingly. Figure 12d shows that under the three operational conditions, the statistical values of the mooring force of ML2 simulated by F2A and AQWA were slightly different. Similarly, when the wind velocity was the rated wind velocity of 12.4 m/s (LC3), the mooring force of ML2 was the largest. Figure 12e shows that as the sea state becomes worse (LC2–LC4), the damping force and the produced power increase sharply. By comparing, aerodynamic loads were confirmed to have significant effects on surge and pitch motion and mooring forces, while hydrodynamic loads had significant effects on the vertical responses (heave, damping force, and produced power).

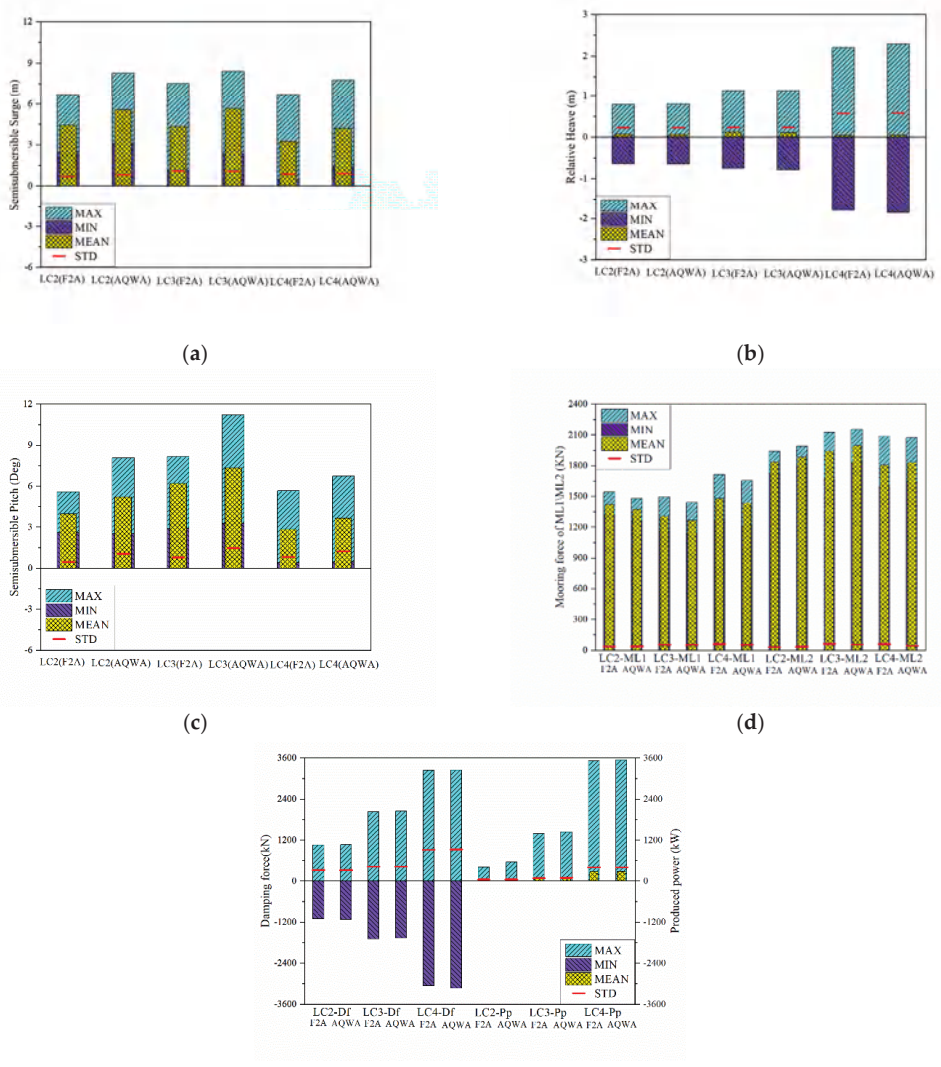


**Figure 12.** Comparison of the statistical results of in LC2, LC3, LC4: (**a**) Surge Motion; (**b**) Relative Heave Motion; (**c**) Pitch Motion; (**d**) Mooring Force of ML1 and ML2; (**e**) Damping Force (Df) and Produced Power (Pp).

### *4.4. Spectrum Analysis*

In this section, the power spectral density (PSD) of platform motion response, mooring line force, damping force, and produced wave power were presented and compared for F2A simulation and AQWA simulation.

#### 4.4.1. Motion Spectrum

Figure 13a,d,g display the PSD of the platform surge under the three load cases. The energy was mainly concentrated in the natural frequency of the surge and the wave frequency. For the mild sea state (LC2) in Figure 13a, there is a reduction for surge motion at the surge resonance peak in F2A simulation compared with AQWA simulation due to the aerodynamic damping effect. However, this reduction is not significant for worse sea state (LC3 and LC4) for surge motion in Figure 13d,g. For the relative heave motion, the

responses are dominated by the frequency from 0.3 to 0.9 rad/s which is related to the wave peak frequency. Therefore, both F2A simulation and AQWA simulation are very similar to each other (Figure 13b,e,h). Figure 13c,f,i are the PSD of the platform pitch motion. Observing the PSD curves of surge and pitch, the reason for the difference in the low frequency area around pitch resonance peak was the influence of aerodynamic damping considered in F2A simulation. It was obvious that when the wind velocity was small, aerodynamic damping obviously reduced the resonance response in the low-frequency region but had little effect on the wave frequency range. This phenomenon conforms well to the known characteristics of the general damping effect. However, when the wind velocity gradually increased (LC2–LC4), the influence of air damping gradually decreased. This was because the aerodynamic thrust acting on the rotor increases rapidly with increasing wind velocity, offsetting the increase in the aerodynamic damping effect caused by surge. Among these effects, aerodynamic damping and wind velocity had a first-order relationship, and aerodynamic thrust and wind velocity had a quadratic relationship. Therefore, at low wind velocities, aerodynamic damping had a greater influence, and at high wind velocities, aerodynamic thrust had a more obvious influence. It can be found that aerodynamic damping had a greater impact on pitch than surge and a stronger reduction in pitch motion.

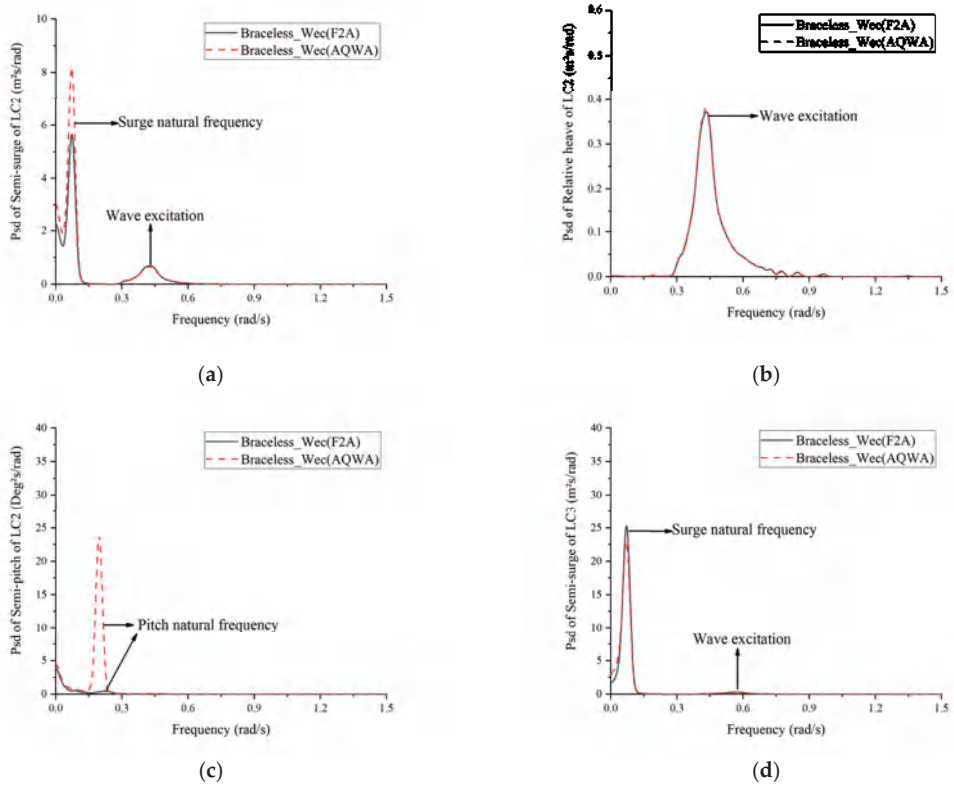


**Figure 13.** *Cont.*

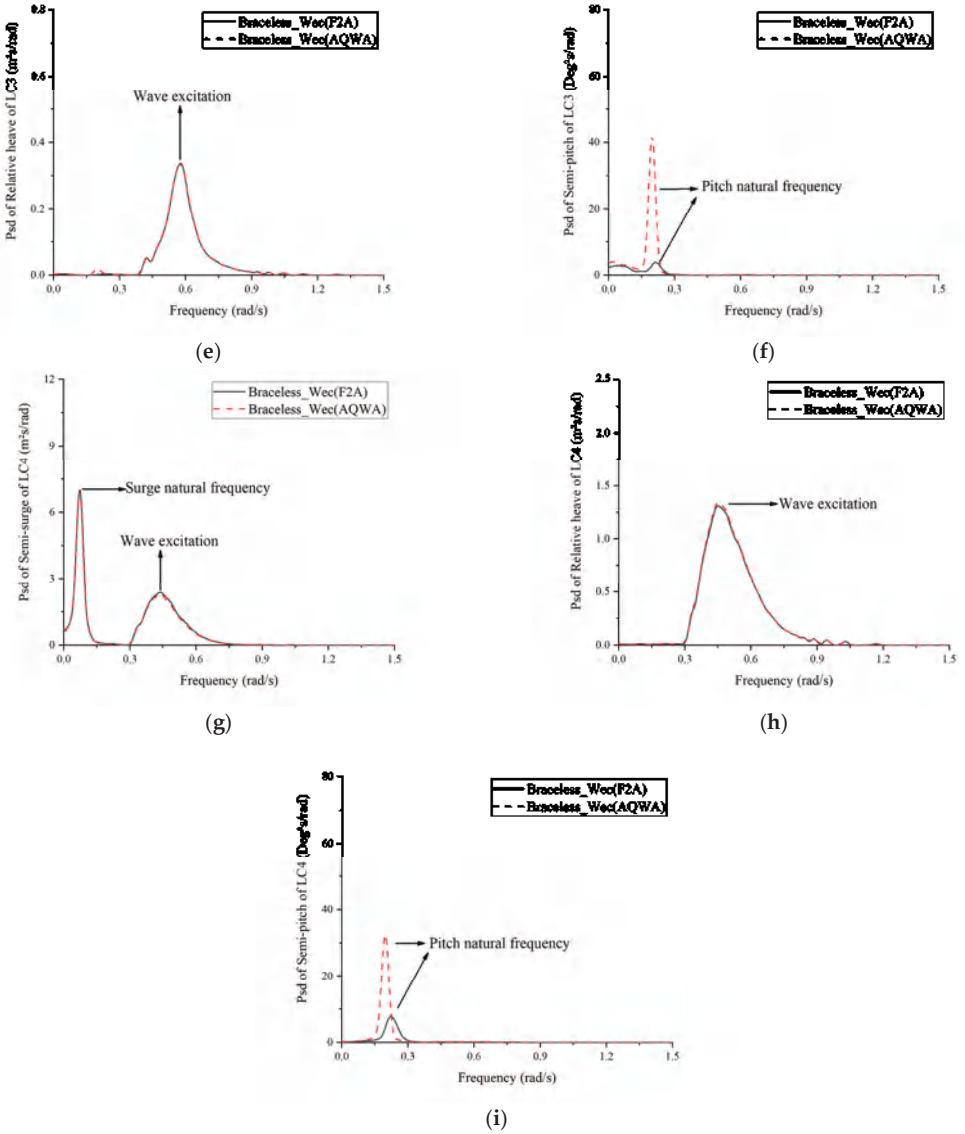


**Figure 13.** Comparisons of the PSD of the motion for LC2, LC3, and LC4: (**a**) Surge Motion of LC2; (**b**) Relative Heave Motion of LC2; (**c**) Pitch Motion of LC2; (**d**) Surge Motion of LC3; (**e**) Relative Heave Motion of LC3; (**f**) Pitch of LC3; (**g**) Surge Motion of LC4; (**h**) Relative Heave Motion of LC4; (**i**) Pitch Motion of LC4.

#### 4.4.2. Mooring Tension Spectrum

The mooring line responses in the frequency domain in the head sea under different load cases from F2A simulation and AQWA simulation are shown in Figure 14. For all the load cases, the most significant contribution to the ML 1 and ML2 tension comes from the low-frequency region (surge mode response). The contributions from pitch mode response are also identified. For worse sea state (LC4), the contributions to the ML1 and ML2 tension from the wave frequency range from 0.3 rad/s to 0.9 rad/s are comparable to the contribution from surge mode response. Similar to the PSD of the motion response, in the F2A simulation, aerodynamic damping had a weakening effect on the response

at surge and pitch natural frequencies. With the wind velocity increases (LC2–LC4), the aerodynamic damping effect gradually decreased.

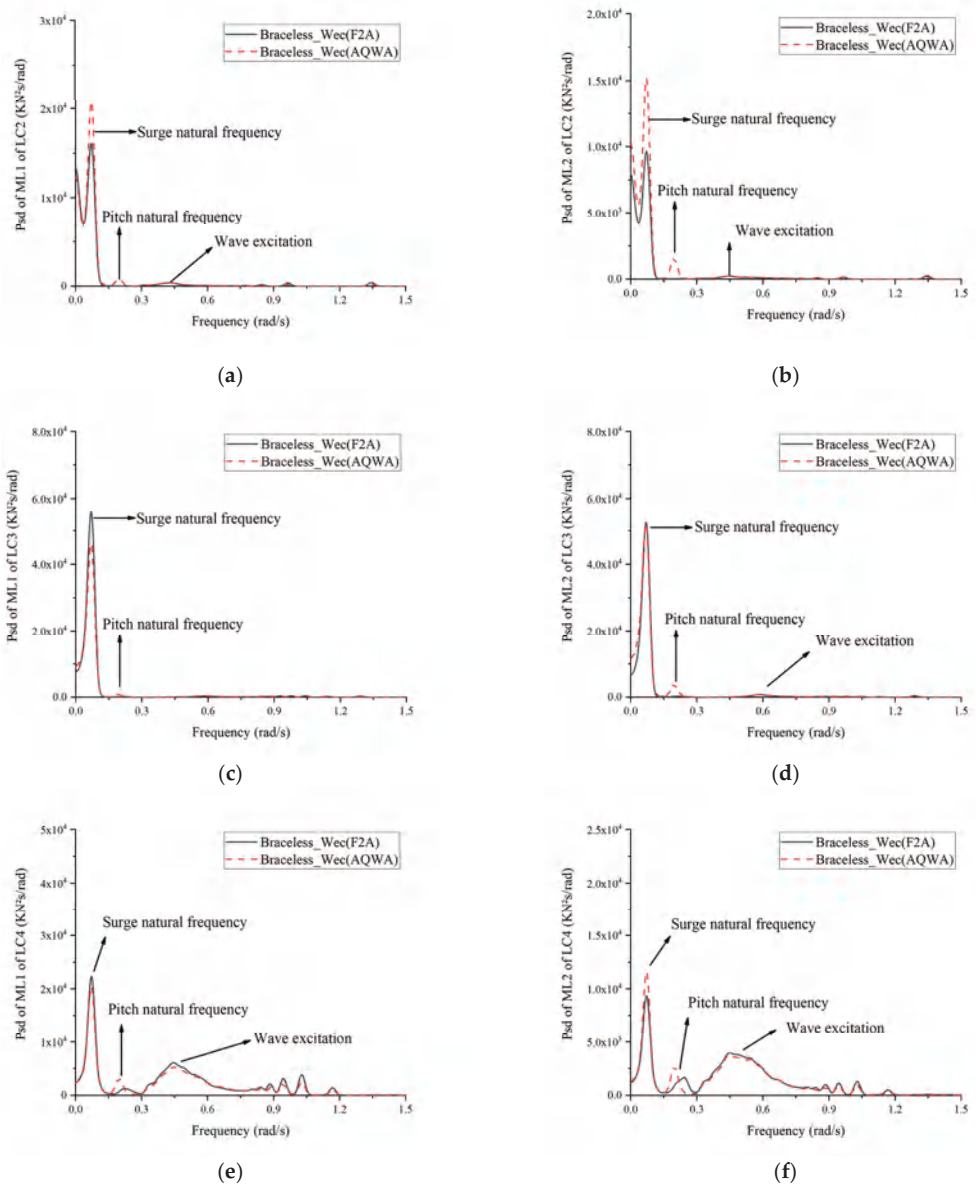


**Figure 14.** Comparisons of the PSD of the mooring line force of: (**a**) ML1 of LC2; (**b**) ML2 of LC2; (**c**) ML1 of LC3; (**d**) ML2 of LC3; (**e**) ML1 of LC4; (**f**) ML2 of LC4.

#### 4.4.3. Damping Force and Produced Wave Power Spectrum

Figure 15 shows the damping force in the vertical direction and the produced wave energy power. The simulation results of the two simulation tools are slightly different. The energy was mainly concentrated in the wave frequency. Figure 15b,d,f are the PSDs of the produced power. The produced wave power frequencies are located in the dou-

ble wave frequency and low frequency regions. There was no significant effect from aerodynamic damping.

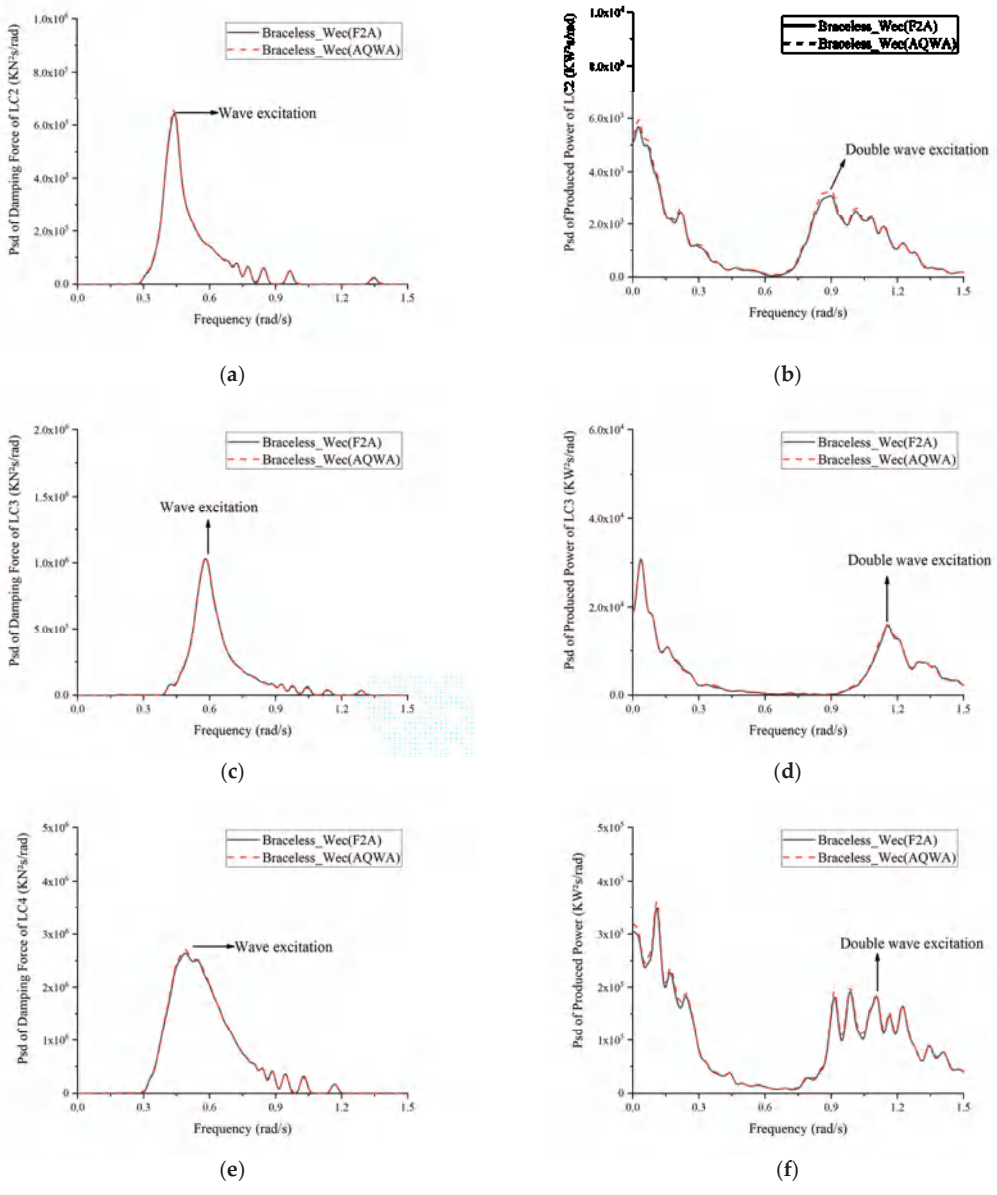


**Figure 15.** Comparisons of the PSD of: (**a**) Damping Force of LC2; (**b**) Produced Power of LC2; (**c**) Damping Force of LC3; (**d**) Produced Power of LC3; (**e**) Damping Force of LC4; (**f**) Produced Power of LC4.

### *4.5. Dynamic Responses in Extreme Conditions*

Under extreme condition (LC5), the WEC and the semisubmersible platform were locked to each other, and there was no relative motion. The PTO system and the wind turbine were parked. As shown in Figure 16a, the WEC and the semisubmersible platform had the same heave motion and were in a locked state. Figure 16b,c show the PSDs of the

platform surge and heave. The PSD of the platform surge was mainly dominated by the wave frequency and the natural frequency of the surge. The PSD of the platform heave was mainly dominated by the wave frequency. From the PSD of the pitch (Figure 16e), it can be seen that the energy was mainly concentrated on the wave frequency and the natural frequency of the pitch, but the resonance effect on the pitch simulated by AQWA was much smaller than the result of the F2A simulation. When using F2A simulation, the upper wind turbine was parked, and the pitch angle was set to 90°. Figure 16e,f show the mooring forces of ML1 and ML2. The energy was mainly dominated in the wave frequency range.

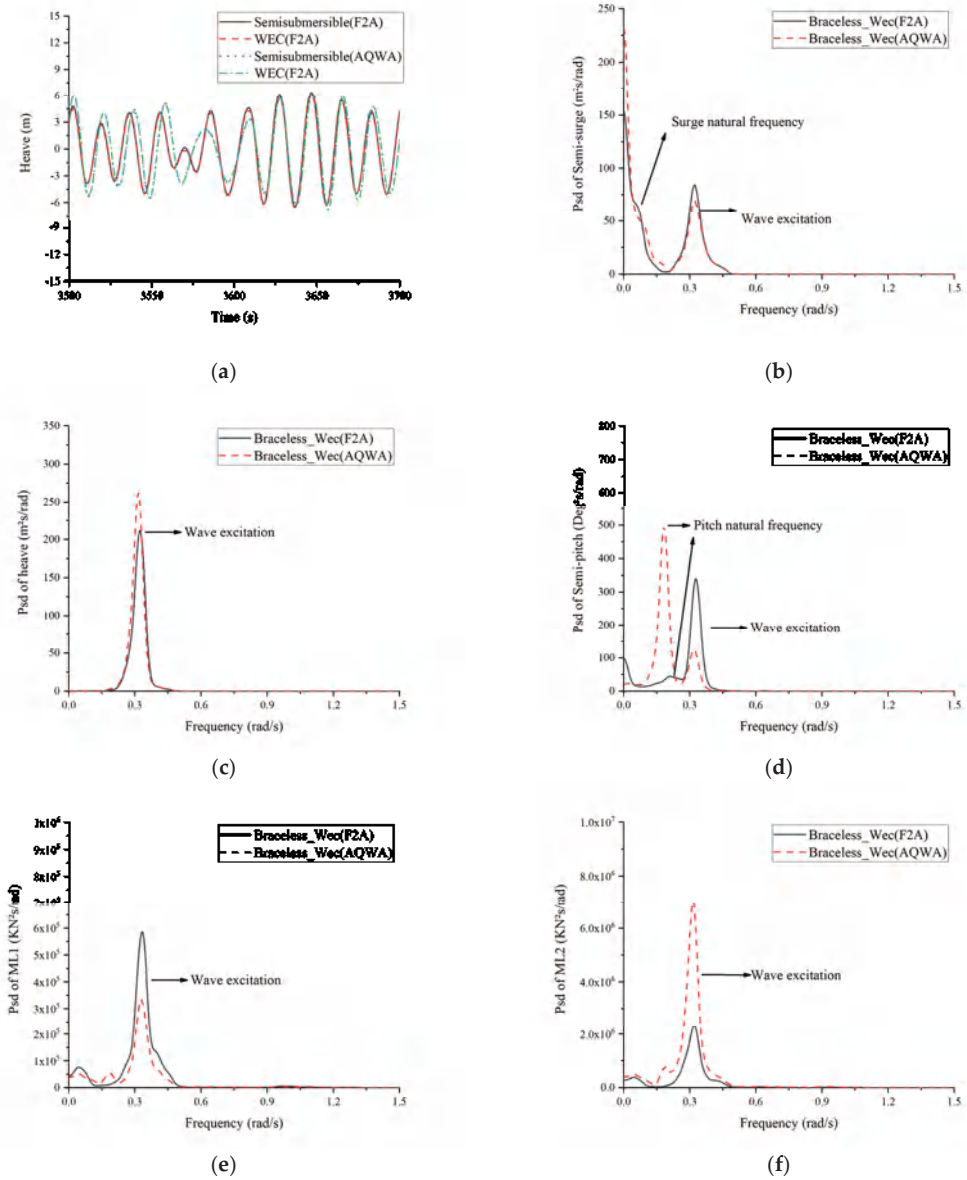


**Figure 16.** Motion and mooring force response of the platform under LC5: (**a**) Heave motion time series; (**b**) PSD of platform surge; (**c**) PSD of platform heave; (**d**) PSD of platform pitch; (**e**) PSD of ML1; (**f**) PSD of ML2.

## 5. Conclusions

In this study, through a recently proposed fully coupled analysis framework (F2A), a fully coupled analysis of a combined system consisting of a semisubmersible platform (braceless) and a heaving-type WEC was carried out. A numerical model of the combined structure that was capable of simulating its motion and dynamic responses under different typical operational and extreme conditions was developed and used. Different types of analysis and comparison were performed to examine the fully coupled responses of the combined structure. The primary results are summarized as follows:

(1) Under regular wave conditions, regardless of wind conditions, the simulation results of F2A and AQWA were basically similar in time domain motion, mooring force, and generated wave power. Since F2A integrated the AQWA hydrodynamic module, it shows that F2A has good consistency with AQWA.

(2) Under irregular wave and turbulent wind conditions, F2A and AQWA had significant differences in time domain motion and mooring force. It shows that F2A effectively reduces the dynamic response amplitude because of the aerodynamic damping effect in F2A; as the wave and wind velocity increased, the amplitude of time-domain motion and mooring force (ML2) are significantly affected by aerodynamic loads, and the dynamic response amplitudes are the largest at rated wind velocity. The trends of relative heave motion, damping force, and produced wave power were similar.

(3) Through the PSD analysis of the dynamic response, it was more obvious that aerodynamic damping used F2A effectively inhibited the resonance at the low frequency range, which was the largest difference compared to the prediction calculated with the simulation tool of AQWA. The relationship between aerodynamic damping and wind velocity was linear, and the relationship between aerodynamic thrust and wind velocity was quadratic. Therefore, when the wind velocity was small, the influence of aerodynamic damping was significant, and especially the resonance of surge and pitch was significantly reduced. When the wind velocity increased, the aerodynamic thrust had a significant effect. The inhibition effect of aerodynamic damping was mainly concentrated in the low-frequency region and had no obvious effect on the resonance caused by the wave frequency. The resonance was mainly excited near the wave frequency; there was a slight difference between F2A and AQWA simulation results close to resonance.

(4) Under extreme conditions, the WEC was locked on a semisubmersible platform as a way of survival to withstand the impact of large wave force. From the PSD analysis of time domain motion and mooring force, the energy was mainly concentrated near the wave frequency, and the wave influence was obvious.

**Author Contributions:** Conceptualization, W.S., L.Z., C.M. and X.L.; methodology, W.S., C.M. and X.L.; investigation, J.L., L.Z., W.S. and C.M.; writing—first draft preparation, J.L., L.Z., W.S. and C.M.; review and editing, W.S., C.M. and X.L.; supervision, W.S. and C.M.; project administration, W.S.; funding acquisition, W.S and X.L. All authors have read and agreed to the published version of the manuscript.

**Funding:** This research was funded by the National Natural Science Foundation of China (Grant No. 52071058, 51939002). This work is also partially supported by LiaoNing Revitalization Talents Program (XLYC1807208) and special funds for promoting high quality development from department of natural resources of Guangdong province (GDNRC [2020]016).

**Institutional Review Board Statement:** Not applicable.

**Informed Consent Statement:** Not applicable.

**Data Availability Statement:** Not applicable.

**Acknowledgments:** The authors would like to thank the Yang Yang from Ningbo University for his valuable discussion of simulation in F2A software.

**Conflicts of Interest:** The authors declare no conflict of interest.

## References


1. World Wind Energy Association. Available online: https://wwindea.org/worldwide-wind-capacity-reaches-744-gigawatts (accessed on 24 March 2021).
2. Jonkman, J.; Butterfield, S.; Musial, W.; Scott, G. *Definition of a 5-MW Reference Wind Turbine for Offshore System Development*; National Renewable Energy Laboratory (NREL): Golden, CO, USA, 2009.
3. Bak, C.; Zahle, F.; Bitsche, R.; Kim, T.; Yde, A.; Henriksen, L.C.; Hansen, M.H.; Blasques, J.P.A.A.; Gaunaa, M.; Natarajan, A. *The DTU 10-MW Reference Wind Turbine*; Danish Wind Power Research: Lyngby, Denmark, 2013.
4. Roddier, D.; Cermelli, C.; Aubault, A.; Weinstein, A. WindFloat: A floating foundation for offshore wind turbines. *J. Renew. Sustain. Energy* **2010**, *2*, 033104. [CrossRef]
5. Huijs, F.; de Bruijn, R.; Savenije, F. Concept design verification of a semi-submersible floating wind turbine using coupled simulations. *Energy Procedia* **2014**, *53*, 2–12. [CrossRef]
6. Lefranc, M.; Torud, A. Three wind turbines on one floating unit, feasibility, design and cost. In Proceedings of the Offshore Technology Conference, Houston, TX, USA, 2–5 May 2011.
7. Le Boulluec, M.; Ohana, J.; Martin, A.; Houmard, A. Tank testing of a new concept of floating offshore wind turbine. In Proceedings of the ASME 2013 32nd International Conference on Ocean, Offshore and Arctic Engineering, Nantes, France, 9–14 June 2013.
8. Luan, C.; Gao, Z.; Moan, T. Design and analysis of a braceless steel 5-MW semi-submersible wind turbine. In Proceedings of the ASME 2016 35st International Conference on Ocean, Offshore and Arctic Engineering, Busan, Korea, 19–24 June 2016.
9. Karimirad, M.; Michailides, C. V-shaped semisubmersible offshore wind turbine: An alternative concept for offshore wind technology. *Renew. Energy* **2015**, *83*, 126–143. [CrossRef]
10. Robertson, A.; Jonkman, J.; Masciola, M.; Song, H.; Goupee, A.; Coulling, A.; Luan, C. *Definition of the Semisubmersible Floating System for Phase II of OC4*; National Renewable Energy Laboratory (NREL): Golden, CO, USA, 2014.
11. Falcão, A.F.D.O. Wave energy utilization: A review of the technologies. *Renew. Sustain. Energy Rev.* **2010**, *14*, 899–918. [CrossRef]
12. Aboutalebi, P.M.; Zoughi, F.; Garrido, I.; Garrido, A.J. Performance analysis on the use of oscillating water column in barge-based floating offshore wind turbines. *Mathematics* **2021**, *9*, 475. [CrossRef]
13. Aboutalebi, P.M.; Zoughi, F.; Martija, I.; Garrido, I.; Garrido, A.J. Switching control strategy for oscillating water columns based on response amplitude operators for floating offshore wind turbines stabilization. *Appl. Sci.* **2021**, *11*, 5249. [CrossRef]
14. Michailides, C.; Gao, Z.; Moan, T. Response analysis of the combined wind/wave energy concept sfc in harsh environmental conditions. In Proceedings of the RENEW2014 1st International Conference on Renewable Energies Offshore, Lisbon, Portugal, 24–26 November 2014.
15. Ren, N.; Ma, Z.; Shan, B.; Ning, D.; Ou, J. Experimental and numerical study of dynamic responses of a new combined TLP type floating wind turbine and a wave energy converter under operational conditions. *Renew. Energy* **2020**, *151*, 966–974. [CrossRef]
16. Bachynski, E.E.; Moan, T. Point absorber design for a combined wind and wave energy converter on a tension-leg support structure. In Proceedings of the ASME 32nd International Conference on Ocean, Offshore and Arctic Engineering, Nantes, France, 9–14 June 2013.
17. Russo, S.; Contestabile, P.; Bardazzi, A.; Leone, E.; Iglesias, G.; Tomasicchio, G.R.; Vicinanza, D. Dynamic loads and response of a spar buoy wind turbine with pitch-controlled rotating blades: An experimental study. *Energies* **2021**, *14*, 3598. [CrossRef]
18. Tomasicchio, G.R.; Vicinanza, D.; Belloli, M.; Lugli, C.; Latham, J.P.; Iglesias Rodriguez, J.G.; Jensen, B.; Vire, A.; Monbaliu, J.; Taruffi, F.; et al. Physical model tests on spar buoy for offshore floating wind energy conversion. *Ital. J. Eng. Geol. Environ.* **2020**, *1*, 129–143.
19. Xu, X.; Day, S. Experimental investigation on dynamic responses of a spar-type offshore floating wind turbine and its mooring system behaviour. *Ocean Eng.* **2021**, *236*, 109488. [CrossRef]
20. Hu, J.; Zhou, B.; Vogel, C.; Liu, P.; Willden, R.; Sun, K.; Zang, J.; Geng, J.; Jin, P.; Cui, L.; et al. Optimal design and performance analysis of a hybrid system combing a floating wind platform and wave energy converters. *Appl. Energy* **2020**, *269*, 114998. [CrossRef]
21. Sarmiento, J.; Iturrioz, A.; Ayllón, V.; Guanche, R.; Losada, I.J. Experimental modelling of a multi-use floating platform for wave and wind energy harvesting. *Ocean Eng.* **2019**, *173*, 761–773. [CrossRef]
22. Marina Platform. Available online: https://www.msp-platform.eu/projects/marina-platform (accessed on 3 April 2020).
23. Peiffer, A.; Roddier, D.; Aubault, A. Design of a point absorber inside the WindFloat structure. In Proceedings of the ASME 2011 30th International Conference on Ocean, Offshore and Arctic Engineering, Rotterdam, The Netherlands, 19–24 June 2011.
24. Aubault, A.; Alves, M.; Sarmento, A.N.; Roddier, D.; Peiffer, A. Modeling of an oscillating water column on the floating foundation WindFloat. In Proceedings of the ASME 2011 30th International Conference on Ocean, Offshore and Arctic Engineering, Rotterdam, The Netherlands, 19–24 June 2011.
25. Muliawan, M.J.; Karimirad, M.; Moan, T. Dynamic response and power performance of a combined Spar-type floating wind turbine and coaxial floating wave energy converter. *Renew. Energy* **2013**, *50*, 47–57. [CrossRef]
26. Muliawan, M.J.; Karimirad, M.; Gao, Z.; Moan, T. Extreme responses of a combined spar-type floating wind turbine and floating wave energy converter (STC) system with survival modes. *Ocean Eng.* **2013**, *65*, 71–82. [CrossRef]
27. Wan, L.; Gao, Z.; Moan, T. Experimental and numerical study of hydrodynamic responses of a combined wind and wave energy converter concept in survival modes. *Coast. Eng.* **2015**, *104*, 151–169. [CrossRef]

28. Wan, L.; Gao, Z.; Moan, T.; Lugni, C. Experimental and numerical comparisons of a combined wind and wave energy converter concept under operational conditions. *Renew. Energy* **2016**, *93*, 87–100. [CrossRef]
29. Wan, L.; Gao, Z.; Moan, T.; Lugni, C. Comparative experimental study of the survivability of a combined wind and wave energy converter in two testing facilities. *Ocean Eng.* **2016**, *111*, 82–94. [CrossRef]
30. Michailides, C.; Gao, Z.; Moan, T. Experimental study of the functionality of a semisubmersible wind turbine combined with flap-type Wave Energy Converters. *Renew. Energy* **2016**, *93*, 675–690. [CrossRef]
31. Michailides, C.; Gao, Z.; Moan, T. Experimental and numerical study of the response of the offshore combined wind/wave energy concept SFC in extreme environmental conditions. *Mar. Struct.* **2016**, *50*, 35–54. [CrossRef]
32. Michailides, C.; Luan, C.; Gao, Z.; Moan, T. Effect of flap type wave energy converters on the response of a semi-submersible wind turbine in operational conditions. In Proceedings of the ASME 2014 33rd International Conference on Ocean, Offshore and Arctic Engineering, San Francisco, CA, USA, 8–13 June 2014.
33. Ren, N.; Ma, Z.; Fan, T.; Zhai, G.; Ou, J. Experimental and numerical study of hydrodynamic responses of a new combined monopile wind turbine and a heave-type wave energy converter under typical operational conditions. *Ocean Eng.* **2018**, *159*, 1–8. [CrossRef]
34. Wang, Y.; Zhang, L.; Michailides, C.; Wan, L.; Shi, W. Hydrodynamic response of a combined wind-wave marine energy structure. *J. Mar. Sci. Eng.* **2020**, *8*, 253. [CrossRef]
35. Le Cunff, C.; Heurtier, J.; Piriou, L.; Berhault, C.; Perdrizet, T.; Teixeira, D.; Ferrer, G.; Gilloteaux, J.C. Fully coupled floating wind turbine simulator based on nonlinear finite element method: Part I—Methodology. In Proceedings of the ASME 2013 32nd International Conference on Ocean, Offshore and Arctic Engineering, Nantes, France, 9–14 June 2013.
36. Perdrizet, T.; Gilloteaux, J.; Teixeira, D.; Ferrer, G.; Piriou, L.; Cadiou, D.; Heurtier, J.M.; Le Cunff, C. Fully coupled floating wind turbine simulator based on nonlinear finite element method: Part II—Validation Results. In Proceedings of the ASME 2013 32nd International Conference on Ocean, Offshore and Arctic Engineering, Nantes, France, 9–14 June 2013.
37. Chen, J.; Hu, Z.; Liu, G.; Wan, D. Coupled aero-hydro-servo-elastic methods for floating wind turbines. *Renew. Energy* **2019**, *130*, 139–153. [CrossRef]
38. Jonkman, J.M. Dynamics of offshore floating wind turbines-model development and verification. *Wind Energy* **2009**, *12*, 459–492. [CrossRef]
39. Jonkman, J.M. *Dynamics Modeling and Loads Analysis of an Offshore Floating Wind Turbine*; National Renewable Energy Laboratory (NREL): Golden, CO, USA, 2007.
40. Kvittem, M.I.; Bachynski, E.E.; Moan, T. Effects of hydrodynamic modelling in fully coupled simulations of a semi-submersible wind turbine. *Energy Procedia* **2012**, *24*, 351–362. [CrossRef]
41. Shim, S. Coupled Dynamic Analysis of Floating Offshore Wind Farms. Ph.D. Thesis, Texas A & M University, College Station, TX, USA, 2010.
42. Yang, Y.; Bashir, M.; Michailides, C.; Li, C.; Wang, J. Development and application of an aero-hydro-servo-elastic coupling framework for analysis of floating offshore wind turbines. *Renew. Energy* **2020**, *161*, 606–625. [CrossRef]
43. *AQWA Manual Release 19.0*; ANSYS Inc.: Canonsburg, PA, USA, 2018.
44. Moriarty, P.J.; Hansen, A.C. *AeroDyn Theory Manual*; National Renewable Energy Laboratory (NREL): Golden, CO, USA, 2005.
45. Chen, J.; Hu, Z. Experimental investigation of aerodynamic effect-induced dynamic characteristics of an OC4 semi-submersible floating wind turbine. *Proc. Inst. Mech. Eng. Part M J. Eng. Marit. Environ.* **2018**, *231*, 19–36. [CrossRef]
46. Karimirad, M.; Moan, T. Effect of aerodynamic and hydrodynamic damping on dynamic response of a spar type floating wind turbine. *Development* **2010**, *2*, 3.
47. Faltinsen, O. *Sea Loads on Ships and Offshore Structures*; Cambridge University Press: Cambridge, UK, 1993.
48. Li, Y.C.; Teng, B. *The Effect of Waves on Marine Buildings*, 3rd ed.; Ocean Publication: Beijing, China, 2015; pp. 270–273.
49. Morison, J.R.; Johnson, J.W.; Schaaf, S.A. The force exerted by surface waves on piles. *Pet. Trans. Aime* **1950**, *2*, 149–154. [CrossRef]
50. Wang, Y.; Shi, W.; Zhang, L.; Michailides, C.; Zhou, L. Hydrodynamic analysis of a floating hybrid renewable energy system. In Proceedings of the 30th International Society of Offshore and Polar Engineers, Shanghai, China, 14–19 June 2020.
51. Zhao, Y.; Yang, J.; He, Y.; Gu, M. Coupled dynamic response analysis of a multi-column tension-leg-type floating wind turbine. *China Ocean. Eng.* **2016**, *30*, 505–520. [CrossRef]

Journal of
*Marine Science and Engineering*

MDPI

*Article*

# 3D Numerical Study of the Impact of Macro-Roughnesses on a Tidal Turbine, on Its Performance and Hydrodynamic Wake

**Ilan Robin *, Anne-Claire Bennis and Jean-Claude Dauvin**

Morphodynamique Continentale et Côtière (UMR CNRS 6143), Université de Caen Normandie, Rouen Normandie, 14000 Caen, France; anne-claire.bennis@unicaen.fr (A.-C.B.); jean-claude.dauvin@unicaen.fr (J.-C.D.)
* Correspondence: ilan.robin@unicaen.fr

**Abstract:** Biofouling is an important factor to consider when calculating the energetic efficiency of tidal farms. Despite the fact that biofouling effects have been widely investigated in the past for naval applications, very few studies concern tidal turbines. This paper proposes a numerical approach to assess the impact of biofouling on tidal turbines, which is efficient for testing many configurations. Two turbulence models are tested (RANS k-$\omega$ SST and LES Smagorinsky) for the motionless blade case to validate them. Then we chose to use the Smagorinsky model for the case of a complete tidal turbine rotor with realistically fouled blades. The pressure coefficient is strongly affected by the barnacle in the motionless blade case and the power coefficient is slightly degraded in the complete rotor case. Motionless blade cases do not represent the real biofouling behaviour for two reasons. First, sessile species settle in the down flow part of the chord where their impact is less important. Then, the surrounding turbulence provoked by the blades rotation in the rotor case reduces the impact of biofouling. In the wake, biofouling generates small vortexes that propagate into the larger ones, causing them to spread their energy.

**Keywords:** marine renewable energy; tidal energy; fluid–structure interaction; biofouling; turbulence; numerical modelling

**Citation:** Robin, I.; Bennis, A.-C.; Dauvin, J.-C. 3D Numerical Study of the Impact of Macro-Roughnesses on a Tidal Turbine, on Its Performance and Hydrodynamic Wake. *J. Mar. Sci. Eng.* **2021**, *9*, 1288. https://doi.org/10.3390/jmse9111288

Academic Editor: Eugen Rusu

Received: 14 October 2021
Accepted: 9 November 2021
Published: 18 November 2021

**Publisher's Note:** MDPI stays neutral with regard to jurisdictional claims in published maps and institutional affiliations.

**Copyright:** © 2021 by the authors. Licensee MDPI, Basel, Switzerland. This article is an open access article distributed under the terms and conditions of the Creative Commons Attribution (CC BY) license (https://creativecommons.org/licenses/by/4.0/).

## 1. Introduction

When a surface is submerged in natural water, it is submitted to colonisation by numerous species. The accumulations of biological organisms on this surface is called biofouling. The first step of this phenomenon is the colonisation by micro-organisms like bacteria or micro-algae into a thin layer a few millimetres thick (biofilm) [1]. This thin film serves as a base for larger sessile species such as barnacles and mussels [2], which often organise in habitats allowing the arrival of mobile organisms (shrimps, crabs, ...). The speed, the kind and the arrangement of the colonisation depend on many factors [3]: depth, salinity, kind of surface, region, temperature, etc. Larvae are also able to select the substrate suitable for their development depending on the water streaming and chemical properties. Moreover, specific conditions can lead to particularities among the species. For example, in the Alderney Race located between France and United Kingdom, where the tidal stream is extremely energetic, the species evolving in such conditions are mainly smaller, with more developed fixing organs and a smoother surface [4]. Some studies show that biofouling also occurs on moving solids like ship propellers or tidal turbines. The biofouling is the origin of the artificial reef effect created by off-shore artificial constructions such as the wind turbine farms described in [5]. However, despite this positive effect, biofouling is a real challenge for the marine renewable implantation in sea water. Ref. [6] shows its negative impact on boat hulls. The experimental study shows a higher resistance on heterogeneous rough parts of the hull, which is very dependent on the position of the roughnesses [7]. More generally, studies of the effects of small roughnesses on the flow along a flat plate are well-understood in both air [8] and water [9]. Small structures promote

the boundary layer transition by making the boundary layer transition move upstream and also increase the rate of turbulence. With the development of renewable marine energies and some special cases in aviation, studies are aiming towards understanding the effects of various roughnesses on wing profiles [10]. Ref. [11] looks into the effect of ice accretion located on the leading edge and finds that the aerodynamic performance of the profile is significantly deteriorated by ice. Ref. [12] experimentally studied the effects of numerous cones distributed homogeneously over the surface of a blade in a wind tunnel. The study is carried out in stationary flow with solid cones ranging from 0.0035 c (chord) to 0.0285 c in height. Results show a strong increase in the drag. Ref. [13] investigates the aerodynamic impact of an isolated barnacle-shaped excrescence on a blade in a wind tunnel. The barnacle is 0.02 c high and is located at 60% of the chord. Three angles for the flow incidence are studied: 5°, 10° and 15° under two different operating modes: a stationary or oscillating blade. On the motionless blade, the barnacle has no impact on lift but considerably increases drag. The pressure coefficient field is very different between the 5° and 15° cases in the motionless case but seems very similar once the blade is set in motion.

Nevertheless, the marine environment at tidal sites is not easy to study in realistic conditions. So, the main parts of these studies are conducted in ideal conditions, easily replicable experimentally. In fact, marine currents are really strong and numerical approach is more suitable to predict biofouling in more realistic conditions. Most papers aim at developing models for small roughnesses. However with the development of CFD, more and more 2D studies are emerging: Ref. [14] investigates the effects of biofouling on a NACA0018 profile using numerous turbulence models (Reynolds Averaged Navier–Stokes (RANS): k-$\epsilon$, k-$\omega$ SST (Shear Stress Transport) and Large Eddy Simulation (LES): Smagorinsky). RANS k-$\omega$-SST and LES-Smagorinsky gave close results for the blade performances but RANS models are less efficient than LES models to compute the vortexes in the wake. The results show that if the biofouling species are placed on the first half of the blade chord, their effects are maximised. Conversely, when biofouling is in the second half, the effects are reduced.This phenomenon is explained by the isolated roughnesses that create an early detachment of the boundary layer. Nevertheless, biofouling generates three-dimensional effects in the flow [15,16]. A 2D study is therefore not sufficient to fully understand such effects.

To our knowledge, the only work relating to the impact of biofouling on the performance of tidal turbines applied to a complete turbine is [17], where biofouling is a surface finish applied with a wall function on the whole turbine. In this paper, we propose to investigate the impact of a realistic fouling on an entire turbine. After a short introduction, Section 2 explains the methodology and methods used to carry out the numerical tests. Section 3 is the validation of the model and its comparison with the experimental data of [13]. Section 4 shows our results that are discussed. Section 4 draws the conclusion.

## 2. Materials and Methods

The numerical simulations are divided into two parts. The first part is a 3D model of a single blade with only one barnacle. This aims to validate the numerical model using the experimental results. The second part relates to the modelling of a complete biofouled rotor. That allows us to study the impact of a realistic implantation of sessile species on the performance and the wake of the tidal turbine. Unlike the work of [17], biofouling is explicitly represented in the mesh by integrating the barnacles into the 3D structure and not by using a roughness model applied to the turbine.

### 2.1. Experimental Setups

Experiments were carried out by [13,18] and their data were used for comparison with the numerical results.

The results of the **motionless blade experiment** chosen for the validation of the numerical model comes from [13]. Their experimental method is described hereafter. The tests were carried out in the Handley–Page wind tunnel with dimensions of 1.61 m high ×

2.13 m wide × 2.74 m long. The air flow velocity was 45 m·s$^{-1}$ with 2.5% turbulence. The blade is made from a NACA 63-619 foil of 0.55 m chord. It passes completely through the height of the wind tunnel. The barnacle is represented by a solid cone with a radius of 20 mm at its base and 10 mm at its top and a height of 11 mm, dimensions nearby to the *Balanus crenatus* found in the Alderney Race [4]. A total of 25 pressure orifices are positioned on and around the barnacle in order to follow the evolution of the pressure field. Three angles of attack are studied: 5°, 10° and 15°. Sensor HDI series gauge sensors measured the dynamic stall while pressure transducers were used to sample the pressure evolution along the blade. The experimental setup also allowed blade oscillation, but unsteady tests were not used here.

The **full rotor simulation** is built according to [18] and uses the IFREMER-LOMC[1] horizontal axis turbine. The water velocity was fixed to 0.8 m·s$^{-1}$ with 3% of turbulence intensity. The rotor rotation was forced by a motor to fix the Tip Speed Ratio (TSR) to 4. TSR is defined as follows :

$$\lambda = \frac{|\Omega_x| R}{U_\infty}, \tag{1}$$

where $\Omega_x$ is the angular velocity, $R$ is the radius of the tidal turbine and $U_\infty$ is the inlet flow velocity. The rotor characteristics are presented in Table 1.

**Table 1.** General characteristics of the IFREMER-LOMC turbine

| Turbine Profile | IFREMER-LOMC NACA 63418 | Unit |
|---|---|---|
| Rotor Radius (R) | 350 | mm |
| Hub Radius | 46 | mm |
| Pitch | 0 | degrees |
| TSR | 4 | - |

Torque sensors were used to measure the power and drag coefficients of the entire structure, including the hub. Laser Doppler Velocimeters (LDV) were used to monitor the wake and vortexes.

### 2.2. Governing Equations

The numerical model is used for validation (in air) and investigation (in water) cases. For the numerical simulations, the following hypothesis are considered:

(i) Air and water are considered as viscous fluids.
(ii) Both fluids are considered incompressible. This hypothesis can be questioned in the case of air, but the validation cases in air have a Mach number of 0.14. It is generally accepted that for a flow with a Mach number below 0.3, the fluid can be considered incompressible.
(iii) Gravity is neglected.
(iv) The study is carried out in the middle of the water column, so wave and bottom effects are neglected.

The 3D Navier–Stokes equations are suitable to solve the fluid motion under the incompressible assumption (with $i$ = 1, 2, 3 representing the 3 directions in a Cartesian framework):

$$\frac{\partial u_i}{\partial x_i} = 0, \tag{2}$$

$$\frac{\partial u_i}{\partial t} + \frac{\partial u_i u_j}{\partial x_j} = -\frac{1}{\rho}\frac{\partial p}{\partial x_i} + \frac{1}{\rho} f_i + \nu \frac{\partial^2 u_i}{\partial x_j \partial x_j}, \tag{3}$$

where $u_i$ is the fluid velocity in the $i$-direction, $t$ is the time, $\rho$ is the fluid density (kg·m$^{-3}$), $p$ is the pressure, $f_i$ represents the volumetric forces in the $i$-direction, and $\nu$ is the kinematic viscosity.

The RANS k-$\omega$ SST and LES Smagorinsky turbulence models give close results for the calculation of blade forces. However, the RANS approaches, including the k-$\omega$ SST model, known to be cheaper, do not give accurate results for the calculation of the wake. On the other hand, LES models like Smagorinsky offer better results for the generation and development of vortices in the wake but the computational cost is high. Thus, the both turbulence models are compared in this work.

2.2.1. Reynolds-Averaged Navier-Stokes Turbulence Model

In RANS models, the velocity $u_i$ is decomposed into an averaged part ($\overline{u_i}$) and a fluctuating part ($u_i'$) such as:

$$u_i = \overline{u_i} + u_i. \tag{4}$$

The low-frequency component is obtained by applying the Reynolds average ($\overline{\cdot}$) to the instantaneous velocity. This average is also applied to the pressure leading to the same decomposition.

In this framework, the Navier–Stokes equations are :

$$\frac{\partial \overline{u_i}}{\partial x_i} = 0, \tag{5}$$

$$\frac{\partial \overline{u_i}}{\partial t} + \frac{\partial \overline{u_i}\,\overline{u_j}}{\partial x_j} = -\frac{1}{\rho}\frac{\partial \overline{p}}{\partial x_i} + \frac{1}{\rho}\overline{f_i} + \nu\frac{\partial^2 \overline{u_i}}{\partial x_j \partial x_j} - \frac{\partial \overline{u_i' u_j'}}{\partial x_j}, \tag{6}$$

where $\overline{p}$ is the mean pressure.

The mean value $\overline{u_i}$ is considered as varying slightly in time compared to the variation of fluctuation whereas the mean value of $u_i'$ is zero. In order to solve Equations (5) and (6), the knowledge of the Reynolds stress tensor $\overline{u_i' u_j'}$ is necessary. After approximating this term using a turbulence viscosity depending on both turbulence kinetic energy ($k$) and specific dissipation rate ($\omega$), the evolution equations for $k$ and $\omega$ need to be solved to determine these quantities [19]. They are initialised as :

$$k = \frac{3}{2}(I|U_\infty|)^2, \tag{7}$$

where $I$ is the turbulence intensity and $U_\infty$ is the reference velocity (undisturbed velocity),

$$\omega = \frac{k^{0.5}}{0.009^{0.25} L}, \tag{8}$$

where $L$ is a reference length scale equal to the chord of the profile (c) for the motionless blade simulation and to the rotor radius (R) for the full rotor simulation.

2.2.2. Large Eddy Simulation Turbulence Model

For LES, flow characteristics are separated into two parts according to the turbulent scales by applying a mathematical filter ($\tilde{\cdot}$). $\tilde{u_i}$ is composed of the large eddies whose size is greater than the size of the filter. $u^*$ carries the smaller eddies with a size inferior to the filter size. In the Smagorinsky turbulence model, the filter size is correlated with the mesh size and $\tilde{u_i}$ is solved explicitly by solving :

$$\frac{\partial \tilde{u_i}}{\partial t} + \frac{\partial \tilde{u_i}\tilde{u_j}}{\partial x_j} = \frac{1}{\rho}\left(-\frac{\partial \tilde{p}}{\partial x_i} + \tilde{f_i}\right) + (\nu + \nu_{sgs})\frac{\partial^2 \tilde{u_i}}{\partial x_j x_j} - \frac{\partial \tau_{ij}}{\partial x_i}, \tag{9}$$

where $\tilde{p}$ and $\tilde{f_i}$ are the filtered pressure and volumetric forces, respectively. $\nu_{sgs}$ is the turbulent eddy viscosity.In the original Smagorinsky model, $\nu_{sgs}$ is computed as :

$$\nu_{sgs} = (C_k \Delta)^2 \sqrt{2 S_{ij} S_{ij}}, \tag{10}$$

where $\Delta$ is the width of the filter and $S_{ij}$ is the resolved-scale strain rate tensor. However, the Sub Grid Scale Kinetic Energy (SGS TKE) variation of the Smagorinsky model is used here. This choice is made because of the ability of the SGS TKE to evaluate the forces and model the flows in the near walls. The classical Smagorisky model does not allow modelling of the viscous sub-layer of the boundary layer without drastically increasing the number of cells [20]. Thus, $\nu_{sgs}$ is written:

$$\nu_{sgs} = C_e \Delta k_1^{0.5}, \tag{11}$$

where $C_e$ is a constant of the SGS Kinetic Energy model constant and $k_1$ is the turbulent kinetic energy computed according to:

$$\frac{\partial k_1}{\partial t} + \tilde{u}_i \frac{k_1}{\partial x_i} = c_e \Delta_x \sqrt{k_1} \tilde{S_{ij}} \tilde{S_{ij}} - C_e \frac{k_1^{\frac{3}{2}}}{\Delta_x} - \frac{1}{\partial x_j} \left[ \left( \nu + \frac{c_e}{\sqrt{k_1}} \Delta \sqrt{k_1} \right) \frac{\partial k_1}{\partial x_i} \right], \tag{12}$$

### 2.3. Boundary Conditions

The boundary conditions are given by the following equations:

$$u_i|_{\delta\Omega_1} = U_\infty x_1, \tag{13}$$

$$p|_{\delta\Omega_2} = p_\infty, \tag{14}$$

$$\frac{\partial u_i}{x_i} n_i|_{\delta\Omega_{3,4,5,6}} = 0, \tag{15}$$

$$u_i|_{walls} = 0, \tag{16}$$

where $\delta\Omega_1$ is the inlet, $\delta\Omega_2$ is the outlet and $\delta\Omega_{3,4,5,6}$ are the four other surfaces (bottom, up, front and back). *walls* represents solid structures, the blade surfaces here. $n_i$ is the normal vector of the surface on which it is applied. $p_\infty$ is the undisturbed pressure.

Equation (13) is a velocity inlet condition set to a constant value ($U_\infty$) in the flow direction. Equation (14) describes the pressure outlet value (usually chosen to avoid to over-constrain the system). A slip velocity condition is considered on the surrounding surfaces to limit the side effects Equations (15) and (16) is a no-slip condition applied on the blades. This condition is only valid in the solid surface datum.

Meanwhile, the initial conditions were set to:

$$u_i|_\Omega = 0, \tag{17}$$

$$p|_\Omega = p_\infty, \tag{18}$$

where $\Omega$ is the computational domain.

### 2.4. Geometries, Meshes and Numerical Setups

For both cases, the 3D blade geometry is made using the open source software QBlade [21] that allows building of a blade using its various sections and twist. Two kinds of barnacles are studied to investigate the differences between them: a conical barnacle according to [13] experiment and a realistic barnacle generated using 3D digital imaging (Figure 1). The open CAD software Blender [22] is used to fix the barnacles to the structures.

SnappyHexMesh is a module of OpenFoam that generates unstructured meshes [19]. This module allows one to control the parameters of the mesh such as the number of refined layers near the walls, the size of the smallest computational cells, the skewness, the orthogonality, etc. Thus, all the meshes respect the following characteristics: skewness smaller than 4 and a non-orthogonality parameter lower than 60°. Near the walls, cells are always structured. The smallest cell length scale is $2.1875 \times 10^{-4}$ c and $5.6 \times 10^{-2}$ c for the biggest one. The meshes contain around 2 million cells for the motionless blade case and around 9 million for the full rotor simulation. The time step ($\Delta T$) is computed by